Biogenic silica diagenesis under early burial in hemipelagic marine sediments



Shahab Varkouhi

Thesis submitted to the University of Oxford

for the degree of Doctor of Philosophy

Department of Earth Sciences

St. Edmund Hall College

Trinity 2018

Supervised by Dr. Nick J. Tosca and Prof. Joe A. Cartwright

To my wonderful daughter:

Asal

Biogenic silica diagenesis under early burial in hemipelagic marine sediments

Thesis submitted for the degree of Doctor of Philosophy

Shahab Varkouhi

St. Edmund Hall College

Trinity 2018

Abstract

Four aspects of biogenic silica diagenesis are researched under this project: signatures of ongoing silica diagenesis in pore water, drivers leading to anomalous compaction (abrupt petrophysical changes), bottom-water temperature controls on silica dissolution and recycling, and temperature-time relationships in silica later diagenesis. Results of this project are discussed in Chapters 4–7.

Chapter 4 demonstrates, based on pore chemistry, mineralogy, and thermodynamic analyses, that solubility equilibrium is reached for diagenetic silica in pore water at opal-A to opal-CT transition zone captured by Ocean Drilling Program Sites 794 and 795 in Japan Sea; thus opal-CT is precipitating across the transition. It is also argued that ion transport mechanisms have failed to erase signatures of ongoing diagenesis.

Chapter 5 utilises texture and mineralogical analyses of hemipelagic sediments from Sites 794 and 795 to place anomalous compaction across the transition zone in a diagenetic context. A sharp decrease in opal-A content in the transition under dissolution causes a significant decrease in sediment stability which results in a porosity drop and other petrophysical variations. Subsequent precipitation of opal-CT has, however, had far less effects on porosity.

Chapter 6 models variations in silica dissolution and recycling with bottom-water temperatures using data from 22 representative Ocean Drilling Program sites. Though model expression of early diagenesis confirms a relationship between temperature and opal-CT formation in young sediments (< 4 Ma) near the seabed in the Antarctic, the established inverse temperature-time correlation in silica diagenesis contradicts main controls from low bottom temperature over a short geological time.

Chapter 7 investigates temperature-time relationships in silica diagenesis by examining 67 scientific drill sites where the opal-A to opal-CT transition zone lies in Cenozoic sediments. Based on these constraints, the reference opal-CT stability field is modified. The chapter also applies a model that formulates time-temperature dependence of silica diagenesis in representative Sites 794 and 795.

Biogenic silica diagenesis under early burial in hemipelagic marine sediments

Thesis submitted for the degree of Doctor of Philosophy

Shahab Varkouhi

St. Edmund Hall College

Trinity 2018

Extended abstract

This study integrates data derived from interrogation of the Ocean Drilling Program and Deep Sea Drilling Project database for borehole sites hosting silica diagenesis transition zones with the result of textural and mineralogical analysis of core samples from two representative Ocean Drilling Program wells, 794 and 795 in the sea of Japan, to investigate four principal aspects of biogenic silica diagenesis: potential proxy utilisation of interstitial-water chemistry tool for tracking the signatures of ongoing silica diagenesis, elucidation of diagenetic drivers leading to sediment anomalous compaction, bottom-water temperature role in biogenic silica early diagenesis, and temperature-time relationships for silica later diagenesis. The results of this work are discussed in Chapters 4–7.

Chapter 4 presents the first systematic study of the chemical signals of active silica diagenesis in the sediment pore-water scale. Pore-water chemistry, mineralogy, and thermodynamic analyses of Sites 794 and 795 demonstrate that solubility equilibrium is reached with respect to diagenetic silica at the opal-A to opal-CT transition zones captured by the biosiliceous hemipelagic deposits in the Japan Sea; implying that the precipitation of opal-CT is currently an ongoing process. The thermochemical equilibrium reached for opal-CT heavily suggests that the dissolved silica sink across the transition zones is essentially affected by active transformation of opal-A to opal-CT. Owing to the association of petrophysical changes with formation of opal-CT in the transition zones, ongoing silica diagenesis has markedly influenced other interstitial-water profiles, including those for major ions and primary chemical indicators. Under the slow to moderate sedimentation rates at these sites, ion transport mechanisms are potentially able to smooth the non-steady-state silica sink as well as the concentration gradient of major ions and primary indicators unless silica diagenesis is still ongoing and the dissolved species are continuously released into the interstitial water at rates higher than those of pore-water transport

mechanisms. This chapter discusses that though dissolved species have not been diffused in the sediment at rates comparable to those by pore-water advection, both advective and diffusive processes have ceased to operate recently or they are operating very slowly as they have failed to erase the signals of ongoing silica diagenesis. It is also argued that the porosity drop due to silica diagenesis in the transition zone at Sites 794 and 795 relates to a chemically-induced anomalous compaction event that causes sediment framework to lose its strength, allowing a collapse of the sediment matrix.

Chapter 5 describes the texture and composition of the sediments hosting silica diagenesis in Sites 794 and 795 to place anomalous compaction phenomenon (abrupt petrophysical variations) across the depth of opal-A to opal-CT transition zone in a diagenetic context. These analyses indicate that opal-A and opal-CT are the two major components in occurrence of anomalous compaction. Other authigenic phases as well as the authigenisation of clay minerals have no measurable effects on this process. Abrupt reduction of opal-A in the transition zone due to progressive dissolution causes a significant decrease in sediment stability which results in sudden compactional collapse, porosity drop, and other associated petrophysical changes. Mineralogical data show that the subsequent precipitation of opal-CT has far less influence on porosity than that of opal-A dissolution; therefore the anomalous compaction results basically from dissolution of biogenic silica. The abundant clayey material in the hemipelagic deposits of Sites 794 and 795 is an obstacle to massive precipitation of opal-CT, causing less availability of this mineral phase to fill the pore spaces and to decrease the porosity. The internal ordering of opal-CT with depth in the opal-CT precipitation interval is because the external cations, which retard the transformation of disordered to ordered cristobalite, are possibly consumed by other authigenic reactions. Correlation of lower opal-CT d-spacings with denser rocks and vice versa within this interval suggests that burial temperature and time are also essential controls on ordering of opal-CT.

Chapter 6 assesses the dissolution rates of biogenic opal deposited on the seabed and the benthic flux of dissolved silica for 22 Ocean Drilling Program borehole sites where the diagenetic transition zones are located in Neogene deposits for which there are existing data regarding the composition, and physical, chemical, and thermal properties. Empirical diagenetic models specified for two sediment types hosting

biosilica—detrital and carbonate—are developed to predict the variability of silica dissolution and recycling with present-day bottom-water temperatures. The temperature-dependent kinetic coefficient of silicic acid (dissolved silica) buildup and the saturation concentration increases with increasing bottom-water temperature. When these effects are incorporated into the models, prediction of dissolution rates and diffusive fluxes with temperature is more pronounced. The primary role of temperature in the process is to decrease the relative degree of pore-water saturation with opal while increasing the concentration of dissolved silica. The correlation between the dissolution rate and recycling with temperature is robust at carbonate-dominated sites. This is because the dissolution of carbonate provides the alkalinity necessary for both silica dissolution and clay formation, therefore the competition between these reactions for the available alkalinity strongly decreases. The linear expression of the early transformation reaction for silica in the sediments from this work confirms that there may be relationships between surface temperatures and the uncommon formation of low temperature (0–4 °C) opal-CT in a short geological time (< 4 Ma) at a few sub-seabottom locations near the seafloor in the Antarctic. This is acknowledged by an agreement between increases in model-predicted transformation ratios and temperatures with depth within the uppermost sediments from the seafloor down-core to the depth of opal-CT formation in the Antarctic Site 751. The role of temperature, however, is not as critical as previously thought because the established inverse correlation between temperature and time in silica diagenesis is in contrast with the possibility of a major control from low surface temperature on formation of diagenetic opal over a short period of geological age. Here, the relationship between solubility and surface area of biogenic opal can be sufficient to explain the formation of opal-CT in the Antarctic Site 751, where time seems to play a key role, more important than temperature. Since the solubility and surface area decrease with age, a ~4 Ma time would bring opal-A to the point that specific surface area is so low that its influence on solubility is nil. This process may lead to precipitation of opal-CT in low temperature settings near the seabed in the Antarctic.

Chapter 7 studies 67 Ocean Drilling Program and Deep Sea Drilling Project sites worldwide where opal-A to opal-CT transition zone lies in Cenozoic deposits to determine temperature-time relationships in silica diagenesis. This transition zone is a narrow depth interval ranging in thickness from 10 to 40 m. The sudden

petrophysical changes occurred over the transition zone are used to identify the depth of this interval. Controls on transition zone thickness are investigated and temperature is found to be the fundamental driver. This study extends the reference time-temperature stability field for the initiation of opal-CT precipitation. Ongoing silica diagenesis occurs over a long geological time (> 35 Ma) at low temperatures (< 30 °C), within 3 Ma at moderate temperatures (35–55 °C), and quickly at high temperatures (> 55 °C) regardless of burial depth, based on the modified stability field. The temperature-time data points for the transition zones involved in this study do not fit within the modified stability field. It is argued that some of these transitions with low temperatures and young ages (Middle Miocene and younger) are likely to be diagenetically-fossilised features. This chapter also discusses thermal gradient and sedimentation rate as the dominant controls on rate of biogenic silica diagenesis, and employs these drivers to reconstruct geothermal and burial history of sediments at Sites 794 and 795 which capture presently-active transitions. The rapid increase in temperatures from the Late Miocene onwards at these two sites corresponds to high accumulation rates in the opal-A unit. The higher burial temperatures achieved for the opal-A sediment under higher sedimentation rates and a steeper thermal gradient lead to an earlier transition zone at Site 795 (~5 Ma) as compared to Site 794 (~8 Ma). Kinetic models are formulated to represent the dependence of opal-A to opal-CT transformation on temperature and time. Due to higher burial heating and higher transformation rates, the ratio of reacted opal-A significantly increases in the opal-CT interval, as compared with low ratios of opal-CT in the opal-A unit. Opal-CT begins to precipitate in the opal-A unit and reaches its peak content at the transition zone. However, the transformation process is not completed until 6 Ma at Sites 794 and ca. 4.5 Ma at Site 795 elapse following the development of the transition zone.

Due to the significance of silica diagenetic studies for different aspects of basin analysis, reservoir evaluation, and silicon marine environmental and biogeochemical cycles, the outcome of present research should demonstrate useful for any future study conducted on biogenic silica diagenesis.

Acknowledgements

I would like to thank my supervisors, Dr. Nick Tosca and Prof. Joe Cartwright, for their valuable guidance during this research work.

Prof. Kevin Taylor from the University of Manchester and Dr. Stuart Robinson from the University of Oxford are gratefully acknowledged for serving, respectively, as the external and internal examiners on this D.Phil. project.

This study has greatly benefited from the Deep Sea Drilling Project/Ocean Drilling Program/International Ocean Discovery Program database. The International Ocean Discovery Program is warmly acknowledged for providing the sediment core samples.

I would also like to extend my appreciation to Dr. Jonathan Wade who helped me use the scanning electron microscope, to Mr. Jonathan Wells for the preparation of polished resin blocks, and to Mr. Owen Green for guiding me how to prepare smear slides.

Finally, I am thankful to my wife for always encouraging me and for supporting me especially over the lifetime of this project.

Table of contents

Abstract **i**

Extended abstract **iii**

Acknowledgements **vii**

Table of contents **ix**

List of figures **xvii**

List of tables **xxv**

Chapter 1: General introduction **1**

1.1 Rationale 1

1.2 Biogenic silica 5

1.2.1 Overview 5

1.2.2 Biogenic silica — Structure and physical properties 6

1.2.3 Marine productivity 8

1.2.4 Biogenic silica — Preservation versus dissolution 11

1.2.5 Recycling at the water-sediment interface 12

1.2.6 Burial and preservation in the sediments 13

1.2.7 Biogenic silica diagenesis 15

1.2.7.1 Controls on biogenic silica diagenesis 18

1.2.7.1.1 Temperature and time 18

1.2.7.1.2 Surface area 20

1.2.7.1.3 Pore-water chemistry 22

1.2.7.1.4 Host sediment lithology 25

1.2.7.1.5 Sediment permeability 27

1.2.7.2 Physical properties and silica diagenesis 27

1.3 Research goals 31

1.4 Thesis structure 35

Chapter 2: Geological setting **39**

2.1 Introduction 39

2.2 Regional tectonics 39

2.3 Sea of Japan — Physiography 42

2.4 Yamato Basin 44

2.4.1 Geological and tectonic setting 44

2.4.2 Crustal structure 45

2.4.3 Site 794 46

2.5 Japan Basin 51

2.5.1 Geological and tectonic setting 51

2.5.2 Crustal structure 52

2.5.3 Site 795 53

Chapter 3: Data and methods **57**

3.1 ODP- and DSDP-derived data 58

3.1.1 Interstitial-water geochemical data 58

3.1.1.1 Interstitial-water sampling 58

3.1.1.2 Interstitial-water chemical analysis 59

3.1.2 Physical properties data 60

3.1.2.1 Physical properties measurements 61

3.1.3 Other parameters 62

3.2 Core samples shipped by IODP 63

3.2.1 X-ray diffraction 66

3.2.1.1 Sample preparation 66

3.2.1.2 Sample analysis 67

3.2.2 Scanning electron microscopy 70

3.2.2.1 Sample preparation 70

3.2.2.2 Sample analysis 71

3.2.3 Smear slides 73

3.2.3.1 Sample preparation 73

3.2.3.2 Optical microscopy 76

Chapter 4: Pore-water chemistry — A proxy for tracking the signature of ongoing silica diagenesis 79

4.1 Abstract 79

4.2 Introduction 80

4.3 Study sites 85

4.3.1 Silica diagenetic fronts at Sites 794 and 795 89

4.4 Data acquisition and methodology 94

4.5 Results 99

4.5.1 X-ray diffraction mineralogy 99

4.5.2 Quantitative XRD 102

4.6 Discussion 108

4.6.1 Source of dissolved silica 108

4.6.2 Silica concentration profile: diagenetic signals and implications 112

4.6.3 Pore-water saturation conditions 116

4.6.4 Role of authigenisation on silica concentration in sediment pore water 119

4.6.5 Interstitial-water signatures of other major ions 121

4.6.6 Signals of ongoing reactions in pore-water primary indicators 127

4.6.7 Ongoing diagenesis signals from isotopic temperatures 132

4.6.8 Transport of dissolved species: advection versus diffusion 136

4.6.9 Controls on sediment porosity 138

4.7 Conclusions 143

Chapter 5: Anomalous compaction due to silica diagenesis — Textural and mineralogical evidence from hemipelagic fine-grained deep-sea sediments 147

5.1 Abstract 147

5.2 Introduction 148

5.3 Tectono-stratigraphy and lithology of study sites 152

5.4 Data and methodology 160

5.5 Data presentation and results 164

5.5.1 Physical properties — General trends and features 164

5.5.1.1 Correlation with stratigraphic units 165

5.5.2 $TZ_{A/CT}$ thickness 171

5.5.3 Smear-slides observations 174

5.5.4 Sediment microfabric 177

5.6 Interpretation and discussion 190

5.6.1 Silica diagenetic controls on sediment petrophysics —– Textural evidence 190

5.6.2 Sediment composition and physical properties 195

5.6.2.1 Diagenetic silica d-spacing and implications for petrophysical changes 201

5.6.3 Authigenisation reactions associated with silica diagenesis 206

5.7 Conclusions 209

Chapter 6: Bottom-water temperature controls on biogenic silica dissolution and recycling in surficial deep-sea sediments 213

6.1 Abstract 213

6.2 Introduction 215

6.3 Environmental setting 221

6.4 Data acquisition and methods 225

6.4.1 Early diagenetic equations for silica 228

6.5 Results 231

6.5.1 ODP-derived dataset 231

6.6 Discussion 235

6.6.1 Model parameters: Calibration 235

6.6.2 Dissolution rate and benthic efflux: Empirical models 238

6.6.3 Effects of pore-water undersaturation 245

6.6.4 Biogenic silica burial efficiency 249

6.6.5 Controls on the precipitation of low temperature near-surface opal-CT 252

6.7 Conclusions 259

Chapter 7: Temperature-time relationships in biogenic silica diagenesis 263

7.1 Abstract 263

7.2 Introduction 264

7.3 Data and methods 268

7.3.1 Temperature estimates 270

7.3.2 Age determination 275

7.4 Results 275

7.4.1 Overview of the silica diagenesis transition zone 275

7.4.2 Temperature-age relationship 283

7.5 Discussion and implications 287

7.5.1 Controls on $TZ_{A/CT}$ thickness 287

7.5.2 Revisiting the silica diagenesis stability field 289

7.5.3 Geothermal history of silica diagenesis 301

7.5.3.1 Thermal history: Case study 304

7.5.4 Modelling of silica diagenesis 305

7.6 Conclusions 314

Chapter 8: Conclusions and future research 317

8.1 Thesis conclusions 318

8.1.1 Conclusions of Chapter 4 318

8.1.2 Conclusions of Chapter 5 321

8.1.3 Conclusions of Chapter 6 322

8.1.4 Conclusions of Chapter 7 323

8.2 Research limitations 325

8.3 Future outlook 327

References 329

Appendices 373

Appendix I (Chapter 4) 373

Appendix II (Chapter 4) 379

Appendix III (Chapter 5) 385

Appendix IV (Chapter 5) 391

Appendix V (Chapter 5) 395

Appendix VI (Chapter 7) 397

List of figures

Figure 1.1. Scanning electron microscope images of the network structures of diatom cell walls constructed of almost closely-packed silica nano-spheres from: A) *Coscinodiscus asteromphalus*; B) *Thalassiosira pseudonana*; and C) *Stephanopyxis Turris*. D) Smooth appearance of the diatom cell wall from a *Coscinodiscus asteromphalus* 7

Figure 1.2. X-ray powder diffraction pattern of a diatomaceous ooze (biogenic opal-A) from the Section 201-1225C-27H-5 at ODP Site 1225 in the eastern equatorial Pacific 9

Figure 1.3. Regions of the global ocean characterised by intense upwelling (highlighted in yellow) 10

Figure 1.4. Nutrient cycling in a strong upwelling area 11

Figure 1.5. Pore-water silicic acid concentrations within the first few centimetres below the seafloor for several regions of the modern ocean 13

Figure 1.6. Distribution of biogenic silica in deep-sea sediments 15

Figure 1.7. Textural evidence for the dissolution-reprecipitation pathway followed during silica diagenesis 17

Figure 1.8. Diagram showing the temperature scale of silica phase changes 19

Figure 1.9. Occurrence of abrupt porosity and density contrasts across the opal-A to opal-CT transition zone at ODP Site 799/Leg 128. Note these petrophysical variations are tied to a high amplitude reflection on the seismic profile at 3.09 s 29

Figure 2.1. Geographical distribution of the ODP and DSDP sites penetrating the $TZ_{A/CT}$ in Quaternary deep-sea deposits 40

Figure 2.2. Sea of Japan 43

Figure 2.3. Crustal structure of Yamato and Japan Basins in the Sea of Japan 46

Figure 2.4. Map of the eastern Japan Sea tectonic zone in the vicinity of Well 794 area showing recognised faults, fold axes, and recent earthquake epicentres 48

Figure 2.5. Stratigraphic column for Sites 794 and 795 50

Figure 2.6. Schematic model of opening of the Japan Sea 52

Figure 2.7. Tectonic map of area surrounding Well 795 showing recognised faults, fold axes, and the 1940 earthquake epicentre (M = 7.0) 54

Figure 3.1. Schematic presentation of a core split into two half-cores named archive-half core and working-half core. Also shown are the relative orientation conventions 62

Figure 3.2. An example of the ODP core sample slabs shipped by the IODP 66

Figure 3.3. A) Agate mortar and pestle used for grinding the sediments from Sites 794 and 795 to a fine powder; B) Powder sample preparation kit used for packing the powdered sediment into a sample holder; C) The fine powder packed into a ring-shaped sample container; D) Sample changer with 15 sample holder positions; E) The PANalytical Empyrean Series 2 powder diffractometer, Department of Earth Sciences, University of Oxford 68

Figure 3.4. Preparation and analysis of resin-impregnated polished blocks from the sediment samples obtained for this study 72

Figure 3.5. Preparation and analysis of smear slides from the sediment samples for this study 75

Figure 3.6. Comparator charts for visual percentage estimation of different components of sediment 77

Figure 4.1. A) Location of ODP Leg 127, Sites 794 and 795 on crustal map of the Japan Sea; B) Map of the eastern Japan Sea tectonic zone in the vicinity of Site 794 area showing recognised faults and fold axes; C) Tectonic map of area surrounding Site 795 showing recognised faults and fold axes 86

Figure 4.2. Integration of physical property measurements, pore-water silica content, and lithology for identifying the opaline reaction boundary ($TZ_{A/CT}$) 88

Figure 4.3. A) Opal-A to opal-CT transition demonstrated by the existence of a bottom-simulating reflector on a multi-channel seismic profile of Site 794; B) Single-channel seismic line over Site 795 showing the $TZ_{A/CT}$ cutting across the stratal reflectors, but simulating the modern seabed 91

Figure 4.4. Depth profiles of lithium, potassium, calcium, magnesium, and strontium at Sites 794 and 795 95

Figure 4.5. Depth profiles of pH, sulphate, alkalinity, ammonia,

phosphate, salinity, sodium, and chloride at Sites 794 and 795 97

Figure 4.6. XRD integrated intensity versus 2θ for representative samples from opal-A zone (at Site 794) and opal-A to opal-CT transition zone (at Sites 794 and 795) 101

Figure 4.7. Relative abundance of tridymite and cristobalite in sediments at Sites 794 and 795 as determined by XRD analyses 103

Figure 4.8. Depth profile for dissolved silica as well as the distribution of opal-A deposits (using smear-slides analyses; green shaded area) as estimated by Shipboard Scientific Party (1990a, b). Also shown are the distribution of volcanic glass (grey shaded area) and normalised abundance of cristobalite (this study) 110

Figure 4.9. SEM photographs of diatom dissolution 111

Figure 4.10. SEM photographs of opal-CT formation 115

Figure 4.11. Pore-water saturation index versus burial depth for Sites 794 and 795 118

Figure 4.12. The relationship between the H_4SiO_4 concentration in pore waters of the sub-seabottom sediments is Sites 794 and 795 and the relative detrital content of the sediments 120

Figure 4.13. A) Lithium versus silica, Site 794; B) Lithium versus silica, Site 795 123

Figure 4.14. A) Calcium versus magnesium, Site 794; B) Calcium versus magnesium, Site 795 125

Figure 4.15. Sulphate reduction as a function of the organic carbon content of sediment samples, Site 794 128

Figure 4.16. Pore-water salinity versus sediment porosity, Sites 794 and 795 131

Figure 4.17. Oxygen isotope and temperature versus burial depth, Sites 794 (A) and 795 (B) 134

Figure 4.18. Correlation of pore-water saturation index with respect to silica polymorphs and the porosity values versus burial depth for Site 794 141

Figure 4.19. A) A porous opal-A facies from the biosiliceous ooze deposits in Site 794 (Sample 127-794A-11H-6, 37–38 cm, at 100.17 mbsf); B) Porous biosiliceous sediment from the opal-A zone in Site 795 (Sample 127-795A-16H-4, 101–102 cm, at 147.81 mbsf) 143

Figure 5.1. Location of ODP Sites 794 and 795 on crustal

map of the Japan Sea 153

Figure 5.2. Correlation of petrophysical measurements with lithology in Sites 794 and 795 155

Figure 5.3. Core photo images from sediment intervals accommodating and overlying the $TZ_{A/CT}$ in Sites 794 and 795 158

Figure 5.4. $TZ_{A/CT}$ thickness quantified using petrophysical properties of the sediments in Wells 794 and 795 173

Figure 5.5. Photomicrographs of biosiliceous sediments 175

Figure 5.6. Photomicrographs of siliceous sediments 176

Figure 5.7. Variation of porosity versus sub-seafloor depth 178

Figure 5.8. Porous biosiliceous sediments from the opal-A succession in Site 794 180

Figure 5.9. Siliceous sediments from the opal-CT-rich interval in Site 794 183

Figure 5.10. Biosiliceous sediments from the opal-A zone in Site 795 187

Figure 5.11. Siliceous sediments from the opal-CT-rich interval in Site 795 189

Figure 5.12. Relationships between porosity and biogenic silica content of the sediments from Sites 794 and 795 192

Figure 5.13. Sediment framework collapse due to silica diagenesis 193

Figure 5.14. Porosity variations with opal/clay ratios of the sediments, Sites 794 and 795 194

Figure 5.15. Diagenetic silica (tridymite and cristobalite from Tables 4.2 and 4.3 in Chapter 4) versus percent porosity for sediment samples from Sites 794 and 795 196

Figure 5.16. Variation in clay- to silt-sized grains ratios of sediment detrital fraction versus burial depth, Sites 794 and 795 198

Figure 5.17. A) SEM photomicrograph of a claystone (Sample 127-794A-33X-1, 0–1 cm, at 303.3 mbsf), showing pore spaces (some of which only partly filled with opal-CT lepispheres); B) A chert (Sample 127-795A-36X-CC, 36–37 cm, at 327.78 mbsf), showing a cavity part of which filled with opal-CT lepispheres 199

Figure 5.18. Opal-CT versus percent porosity for the sediments examined in this study. Opal-CT sediment data from the Santa

Barbara coastal area and the Point Pedernales are plotted for comparison 201

Figure 5.19. d(101) spacing and integrated intensity of opal-CT versus burial depth of siliceous sediments; d(101) spacing versus porosity, Sites 794 and 795 203

Figure 5.20. Integrated intensities of smectite and zeolite versus burial depth, Sites 794 and 795 208

Figure 6.1. Location of the investigated ODP borehole sites 222

Figure 6.2. The first-order variability of dissolution rate coefficient with bottom-water temperature at the detrital- and carbonate-hosted 22 selected ODP sites 237

Figure 6.3. Asymptotic silicic acid concentration as a function of present-day temperature of the clay- and carbonate-based surface sediments 237

Figure 6.4. Calculated dissolution rate of sedimentary biogenic opal versus bottom-water temperature for the investigated sites 240

Figure 6.5. Calculated benthic flux of silicic acid versus bottom-water temperatures at the investigated ODP sites 241

Figure 6.6. Dissolution rates of biogenic silica as a function of bottom-water temperature at the investigated sites 243

Figure 6.7. Benthic fluxes of dissolved silica as a function of bottom-water temperature at the studied sites 245

Figure 6.8. Dissolution rate of opal predicted using average parameter values versus bottom-water temperature at the studied ODP sites 247

Figure 6.9. Benthic fluxes of silicic acid versus bottom-water temperature for the various studied ocean regions 248

Figure 6.10. Degree of undersaturation with respect to opal versus bottom-water temperature at the studied ODP sites 249

Figure 6.11. The fraction of solid silica buried as a function of the opal rain rate emphasising the role of sedimentation rate in the preservation of biogenic silica 251

Figure 6.12. Linear transformation rate in the analysed surface sediments 254

Figure 6.13. Comparison of model-predicted and measured transformation ratios of opal-A to opal-CT, ODP Site 751 256

Figure 7.1. Location of the investigated borehole sites 269

Figure 7.2. A) APC tool components; B) WSTP probe assembly for temperature measurement and fluid sampling 274

Figure 7.3. Depth distribution of the opal-A to opal-CT transition zones in clay- and carbonate-rich sediments drilled at the studied borehole sites 277

Figure 7.4. $TZ_{A/CT}$ thickness as estimated by changes in the physical properties of the sediments for four representative borehole sites 278

Figure 7.5. Histogram showing the distribution of $TZ_{A/CT}$ thickness categories in clay-hosted (black bars) and carbonate-hosted (white bars) lithologies 279

Figure 7.6. Age distribution of silica diagenetic transition zones within the studied ODP and DSDP boreholes 281

Figure 7.7. A) Cross-plot illustrating the relationship between the $TZ_{A/CT}$ age and thickness in clay-dominated (solid squares) and carbonate-dominated (× marks) sediments; B) Age of the $TZ_{A/CT}$ relative to the opal content of the sediment hosting the $TZ_{A/CT}$ 282

Figure 7.8. Bar graph showing the distribution of temperature at $TZ_{A/CT}$ depth for clay-hosted (black bars) and carbonate-hosted (white bars) sites 284

Figure 7.9. Scatterplot showing the $TZ_{A/CT}$ temperature-zone thickness relationship in clay- and carbonate-dominated ODP and DSDP study sites 285

Figure 7.10. A) Inverse relationship between age and *in situ* temperature across the $TZ_{A/CT}$ at the studied ODP and DSDP sites; B) The age-temperature data points of Figure 7.10A as classified by their dominant host sediment types. The reference data of Hein et al. (1978) are also plotted for comparison 286

Figure 7.11. Temperature contrast through the $TZ_{A/CT}$ versus zone thickness for the studied ODP and DSDP sites 288

Figure 7.12. Stability field of diagenetic silica (opal-CT) formation based on age and temperature values at the $TZ_{A/CT}$ depths analysed in this study. The reference data of Hein et al. (1978) are shown for comparison 294

Figure 7.13. Distribution of the $TZ_{A/CT}$ temperature and time data from the studied ODP and DSDP sites within and around the modified stability field of opal-CT formation 298

Figure 7.14. Geothermal evolution versus age at the $TZ_{A/CT}$ for the study sites 302

Figure 7.15. Reconstructed burial and thermal histories for the sediments hosting the $TZ_{A/CT}$ at Sites 794 and 795 306

Figure 7.16. Calculated opal-A to opal-CT transformation rates versus *in situ* temperature measurements at ODP Sites 794 and 795 309

Figure 7.17. A) Modelled opal-A to opal-CT transformation at ODP Sites 794 and 795; B) Reference phase diagram for silica diagenesis; C) Comparison between modelled and observed transformation ratios in Site 794; D) Comparison of modelled and observed transformation ratios at Site 795 311

Figure 7.18. Modelled transformation of opal-A to opal-CT as a function of temperature and time 313

Figure 8.1. Connections between the research topics presented in this work, also their links to basinal and environmental research 319

I.1. XRD integrated intensity versus 2θ for sediment core samples from opal-A-rich interval at Site 794 373

I.2. XRD integrated intensity versus 2θ for sediment core samples from the upper part of the $TZ_{A/CT}$ at Site 794 374

I.3. XRD integrated intensity versus 2θ for sediment core samples from the lower part of the $TZ_{A/CT}$ at Site 794 375

I.4. XRD integrated intensity versus 2θ for sediment core samples from opal-A-rich interval at Site 795 376

I.5. XRD integrated intensity versus 2θ for sediment core samples from the lower part of opal-A zone (the uppermost (first) XRD graph in the photo) and the upper part of the $TZ_{A/CT}$ at Site 795 377

I.6. XRD integrated intensity versus 2θ for sediment core samples from the $TZ_{A/CT}$ (upper and lower parts) at Site 795 378

II.1. Additional SEM photomicrographs of biosiliceous sediments (opal-A interval) from Site 794 380

II.2. Additional SEM photomicrographs of biosiliceous sediments (opal-A interval) from Site 795 383

III.1. Additional photomicrographs of smear slides from Site 794 386

III.2. Additional photomicrographs of smear slides from

Site 795 389

V.1. Additional SEM photomicrographs of sediments from the opal-CT interval in Site 794 395

V.2. Additional SEM photomicrographs of sediments from the opal-CT interval in Site 795 396

List of tables

Table 3.1. Stratigraphic position, identification number, age, depth, and lithology of the samples acquired from Site 794 64

Table 3.2. Stratigraphic position, identification number, age, depth, and lithology of the samples acquired from Site 795 65

Table 4.1. Seismic structural and geometrical criteria for recognition of fossilised silica fronts 82

Table 4.2. Normalised mineral content based on X-ray diffraction analysis of random bulk sediment samples, Site 794 105

Table 4.3. Mineral content based on X-ray diffraction analysis of bulk sediment samples, Site 795 107

Table 4.4. Mean porosity, mean water content, and accumulation rate of the lithologic units, Sites 794 and 795. Also shown are the dependent parameters, including sediment diffusion coefficient and diffusion rate estimated for each unit 139

Table 5.1. Statistics for physical properties of the lithologic units capturing silica diagenesis at Site 794 167

Table 5.2. Statistics for petrophysical properties of the lithostratigraphic units overlying and capturing silica diagenetic transition zone at Site 795 169

Table 6.1. Description of ODP sites investigated in this study, including latitude and longitude, water depth, geographic location, and description of the first lithologic unit 223

Table 6.2. Dataset assembled from the ODP data sources for the uppermost sediment of the 22 study sites 232

Table 6.3. Site-specific benthic flux, burial flux, and rain rate of biogenic opal calculated using the early diagenetic equations 1.3, 1.4, and 1.5, respectively. Also shown are the relative diffused and buried fluxes (in percentage) at each site 250

Table 7.1. Parameters of the ODP and DSDP sites comprising the opal-A to opal-CT transition zone 271

Table 7.2. Likely-active opal-A to opal-CT transition

zones involved in this study and their characteristics 292

IV.1. The abundance of various components of sediments from Site 794 estimated based on the study of smear slides 391

IV.2. The abundance of various components of sediments from Site 795 estimated based on the study of smear slides 393

VI.1. Statistics related to the $TZ_{A/CT}$ thickness values presented in Table 7.1 in Chapter 7 397

VI.2. Statistics related to the $TZ_{A/CT}$ temperature values presented in Table 7.1 in Chapter 7 398

Chapter 1

General introduction

1.1 Rationale

Biogenic silica (also called opal-A or amorphous opal), known as a major constituent of Neogene hemipelagic sediments around the globe, is subject to early burial diagenetic transformations. Biogenic silica diagenesis represents a consecutive process involving two first-order transitional steps, from opal-A to opal-CT (cristobalite and tridymite) and from opal-CT to microcrystalline quartz.

Silica diagenesis has been broadly researched over the past four decades, largely incited by the Deep Sea Drilling Project (DSDP) (e.g., Hein et al., 1978) and Ocean Drilling Program (ODP) (e.g., Shipboard Scientific Party, 1987). The motivation for these projects was the presence of hard porcellanite and chert layers (containing opal-CT and microcrystalline quartz, respectively), developed through alteration of siliceous biogenic oozes (containing opal-A), that were a major drilling hazard. One of the principal findings of these scientific drilling programmes was that the transition from opal-A to opal-CT corresponds to marked changes in physical properties of Neogene marine sediments (i.e., anomalous compaction) and that the transition is distinctly manifested in the downhole logs acquired at most of the drilled sites (e.g., Shipboard Scientific Party, 1990a, b). Substantial petrophysical variations associated with the biosiliceous sediments undergoing transformation from opal-A to

opal-CT commonly result in a prominent regional seismic reflection that is sometimes evident on seismic profiles by a discordant attitude relative to the host sediment (e.g., Ireland et al., 2010).

One of the principal, and yet less understood, issues in silica diagenesis research is the determination whether diagenesis across the opal-A to opal-CT transition is currently stopped (arrested transition) or it is an ongoing process (active transition). So far, seismic reflection methods have been widely utilised for expressing the present-day diagenetic status of this boundary (e.g., Neagu et al., 2010). However, due to its limited vertical extent (being below the vertical resolution limit of the seismic data), the transition cannot be studied using seismic tools (at a regional scale) with precision. One aim of the thesis research presented herein is to utilise pore-water chemistry as a more reliable diagnostic tool to trace the associated chemical signatures of silica diagenesis. This research contributes to a better understanding of the geochemical controls on biogenic silica diagenesis and helps constrain the diagenetic drivers that account for sudden variations in the physical state of sediments. From a basin analysis perspective, the presence or absence of pore-water geochemical signals of silica diagenesis is key for understanding the thermal evolution of the sediments hosting significant accumulations of silica.

Another significant aspect of silica diagenesis studies that deserves further investigation is how diagenesis leads to the anomalous compaction of sediments. This part of the research characterises the sediment capturing silica diagenesis

texturally and mineralogically to unravel the diagenetic drivers responsible for changes in sediment petrophysics. Understanding anomalous compaction and its controlling factors is important economically, as in some locations hydrocarbons have been largely produced from siliceous mudstones, porcellanites, and cherts. For example, the Monterey Formation in California is well known for hosting significant hydrocarbon reservoirs in diagenetically-developed chert and diatomite. In basinal studies, analysing the controls from silica diagenesis on the evolution of sediment physical properties is essential to understanding the implications on fluid flow, rock deformation, and thermal history of depositional basins (Wrona et al., 2017).

Of importance in the context of this thesis is also the analysis of the role of bottom-water temperature in controlling the rate of opal-A dissolution and recycling of dissolved silica across the surficial deep-sea sediments during silica early diagenesis. The solubility of biogenic opal markedly increases with increasing temperature (e.g., Iler, 1979; Williams and Crerar, 1985; Atkins and de Paola, 2006; Boggs, 2009). The occurrence of most progressive dissolution of biogenic silica at the seawater-sediment interface may further emphasise the temperature dependence of silica solubility. Since a considerable part of the silicic acid, distributed below the water-sediment interface due to kinetic dissolution of opal-A during very early diagenesis, is released back to the seawater column through diffusion, understanding of the effects of variations in bottom-water temperature on the production of dissolved silica and on the benthic flux of silicic acid is essential to the development of predictive environmental and biogeochemical models of silica cycling in marine

settings. In addition, the remaining part of the silicic acid not diffused back to the water column and trapped in the pore water during burial is consumed during ongoing diagenetic reactions in the sediment. Therefore, quantifying bottom-water temperature controls on silica solubility is important for a better understanding of the silica early diagenesis process and the mechanisms behind later accumulation of diagenetic silica below the seafloor.

While it is accepted that the rate of silica diagenetic reactions depends exponentially on temperature, both temperature and time are first-order controls. Keeping this issue in mind, the roles of temperature and time during opal-A to opal-CT reaction are included as variables in this research. This is important because of the implications that the temperature-time relationship has for defining the stability field of opal-CT formation and for reconstructing the geothermal history of depositional basins accommodating silica diagenesis.

This research project is concentrated on the biosilica to opal-CT transformation. The project builds on interrogating accessible DSDP and ODP scientific databases for the borehole sites capturing silica diagenesis and on utilising new data collected from core samples of two ODP Sites 794 and 795 (Leg 127, the Sea of Japan) to tackle four significant aspects of opal-A to opal-CT diagenesis: pore-water chemical signals of silica diagenesis, controls on anomalous compaction, (bottom-water)temperature controls on production and recycling of silica during early diagenesis, and the role of temperature in relation to time on later diagenetic transformation of opal-A to opal-

CT.

This chapter summarises the current state of knowledge concerning the genesis of biogenic silica, its preservation versus dissolution in seawater and at the water-sediment interface, its burial in marine sediments, its diagenesis, and the impacts of silica diagenesis on the physical properties of biosiliceous host sediments, including anomalous compaction at what is commonly referred to as the silica diagenetic transition zone (e.g., Littke et al., 1991).

1.2 Biogenic silica

1.2.1 Overview

Over 70% of marine dissolved silicon is derived from riverine influxes generated by the chemical continental weathering of siliceous rocks (e.g., Hawkings et al., 2017), with the majority of this delivered to the ocean as silicate solution or silicic acid ($Si(OH)_4$ or H_4SiO_4). Silica (SiO_2; the most common naturally-occurring form of silicon) enters the ocean also through submarine weathering, groundwater, hydrothermal emissions, atmospheric deposition of particles, and glacial weathering (e.g., Tréguer and De La Rocha, 2013). Unlike the other major nutrients such as phosphate, nitrate, and ammonium, which are needed by almost all marine plankton, silica acts as an essential chemical requirement for very specific biota that use it to build their siliceous structures. Most of the dissolved silicon is removed from the seawater by the formation of siliceous tests primarily by surface-dwelling plankton, including diatoms and silicoflagellates, which are phytoplankton, and radiolaria,

which are protozoans. This biogenic precipitation of dissolved silica produces solid hydrated amorphous opal ($SiO_2 \cdot nH_2O$) (mostly called biogenic silica) through the complex polymerisation of silicic acid molecules (Robert, 2009). Amorphous opal is also produced by sponges, some groups of which secrete silica spicules, but this constitutes only a small fraction of the biogenic silica (Kershaw and Cundy, 2000).

1.2.2 Biogenic silica — Structure and physical properties

The nano-structure of biogenic silica is mostly characterised as nano-spheres composed of colloidal SiO_2 ranging between 10 and 100 nm in diameter. These silica nano-spheres are produced by growth of the highly-branched polysilicic acid (with the general formula $[SiO_X(OH)_{4-2X}]_n$) (Sumper and Kröger, 2004) that is taken up by the cells (microorganisms, such as diatoms, radiolarians, silicoflagellates, and siliceous sponges) through a process of active transport (Lewin and Chen, 1968), and acts as a silica nucleus. The silica nano-spheres commonly form a three-dimensional network constructing branched particle chains that are cross-linked by siloxane bonds (Si–O–Si) (Sumper and Kröger, 2004). In many cases, the void between the nano-spheres is filled with silica through flocculation, a process that nearly connects and close-packs silica spheres and gives the surface a smooth appearance as it is often found in the diatom cell wall (Figs. 1.1A–D). When the biogenic silica undergoes dissolution, the silica deposited between the nano-spheres commonly dissolves first, yielding a porous structure. The mean diameter of the pore spaces in modern and ancient biogenic silica is 5–10 nm with an overall porosity ranging from 35 to 50% (Hurd, 1983; DeMaster, 2003).

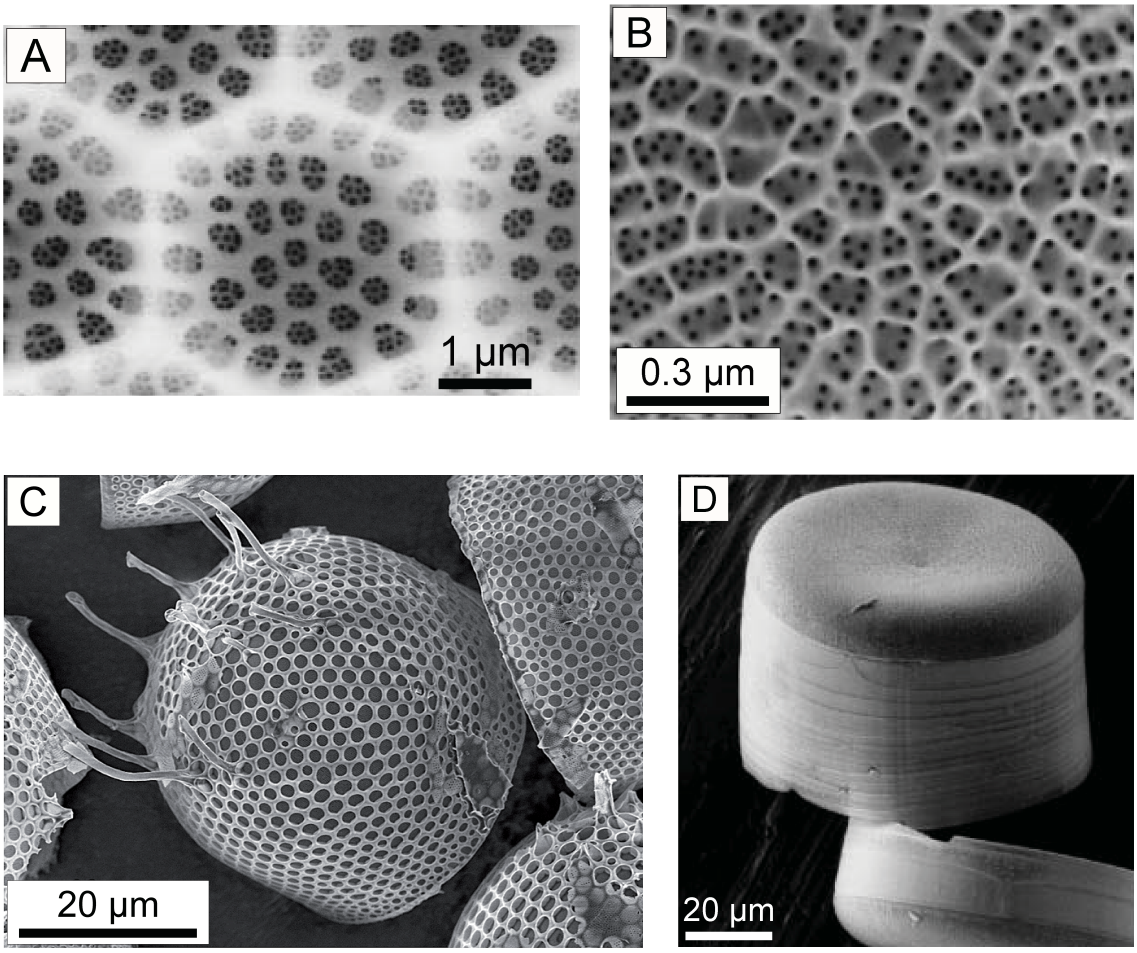


Figure 1.1. Scanning electron microscope images of the network structures of diatom cell walls constructed of almost closely-packed silica nano-spheres from: A) *Coscinodiscus asteromphalus*; B) *Thalassiosira pseudonana*; and C) *Stephanopyxis Turris*. D) Smooth appearance of the diatom cell wall from a *Coscinodiscus asteromphalus*.
Figures A, B, and D are modified from Sumper and Kröger (2004), Figure C from Jantschke et al. (2014).

The density of biogenic silica ranges from 2.6 to 1.15 g/cm^3 for diatoms, depending on their lipid content produced by photosynthesis (Railkin, 2003). The silica body density varies from 1.7 to 2.05 g/cm^3 for radiolarians and from 1.99 to 2.04 g/cm^3 for

siliceous sponge spicules (Hurd and Theyer, 1977). According to Mortlock and Froelich (1989) and Hendry and Andersen (2013), the average H_2O content of biogenic silica equals 12% of the molecular mass of SiO_2, the estimation that introduces $SiO_2 \cdot 0.4H_2O$ as the chemical formula for biogenic opal. Although dependent upon many factors, especially age and species, the water content of biogenic opal ranges between 2 and 15 wt% (Olivarez Lyle and Lyle, 2002). The specific surface area of the biogenic silica, in particular radiolarian and diatom tests, estimated by Hurd (1973) based on nitrogen adsorption measurements, ranges from 19 to 350 m^2/g with the median and average values being 92 and 117 m^2/g, respectively. Kastner et al. (1977) report surface areas for two age categories of radiolarians, being 7 m^2/g for Eocene radiolarian assemblages and 439 m^2/g for Quaternary radiolaria. Biogenic silica (mineralogically, called opal-A) is nearly X-ray amorphous, and shows a broad diffuse scattering feature occurring from 20 to 26° 2θ (from ~4.44 to ~3.43 Å) in its diffraction pattern with the greatest intensities near 23.10 and 22.10° 2θ (3.85 and 4·02 Å, respectively) (Fig. 1.2).

1.2.3 Marine productivity

Downward fluxes of biogenic silica in the global ocean derive dominantly from the productivity of diatoms (Longhurst and Harrison, 1989; Bidle and Azam, 1999) as abundant, and often predominant, members of the phytoplankton. Productivity fluxes and population dynamics are both limited by the availability of dissolved silicon since these phytoplankton have an obligate silicon requirement (in the form of silicic acid) for growth (Lewin, 1962), and that they have a stronger relative absorption of

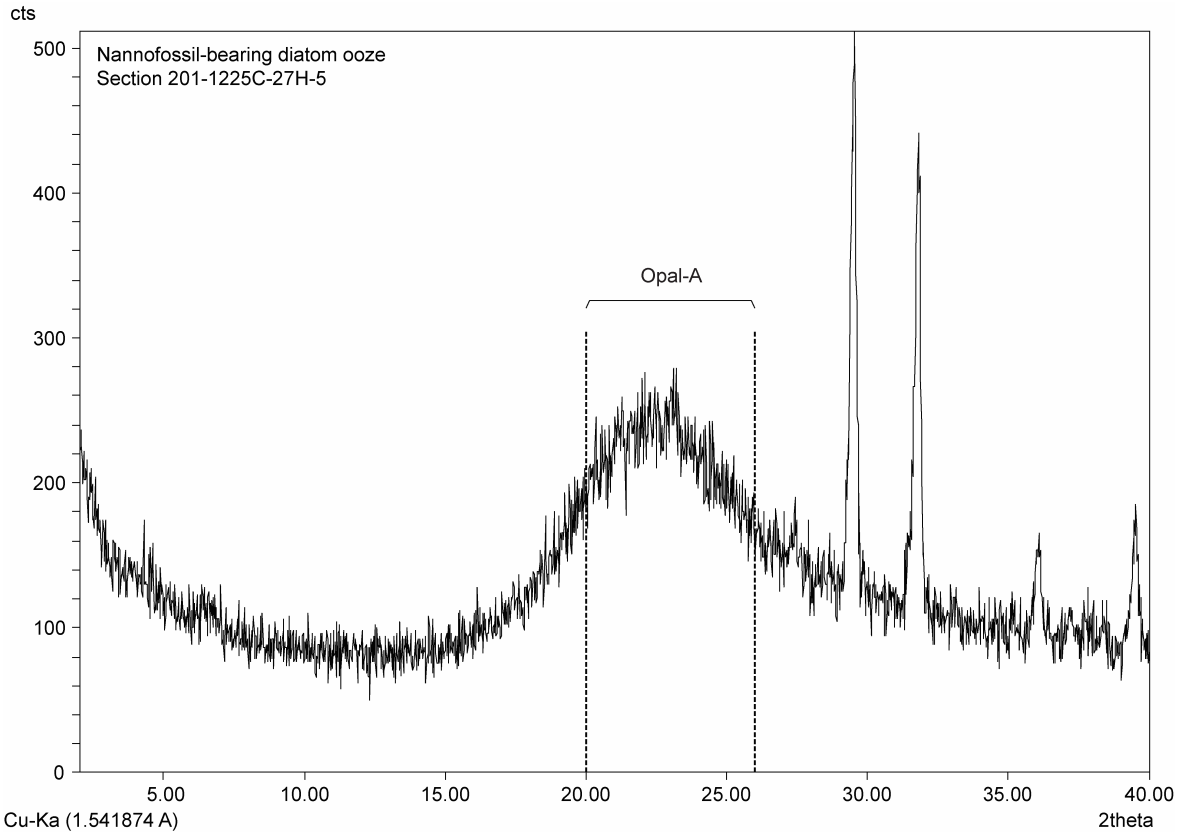


Figure 1.2. X-ray powder diffraction pattern of a diatomaceous ooze (biogenic opal-A) from the Section 201-1225C-27H-5 at ODP Site 1225 in the eastern equatorial Pacific (redrawn from Shipboard Scientific Party, 2003). The amorphous nature of the biogenic silica is apparent from the broad scattering feature that commonly occurs between 20 and 26° 2θ.

nutrients than the other pelagic micro-algae. Therefore, the silicic acid supply into the photic zone—largely by upwelling and silica dissolution—controls biogenic silica production, and consequently the biological uptake of atmospheric CO_2 by the ocean, over vast oceanic areas (Dugdale and Wilkerson, 1998).

Silicic acid concentrations are highest in areas exposed to upwelling because

nutrient-rich deep water is transported to the euphotic zone near the ocean surface. Upwelling involves divergence of wind-driven currents that bring deeper, cooler, and usually nutrient-rich waters to the ocean surface. As illustrated in Figure 1.3, upwelling regions are located at equatorial and sub-polar latitudes, as well as along the western continental margins (e.g., Rashid, 1985; Libes, 1992).

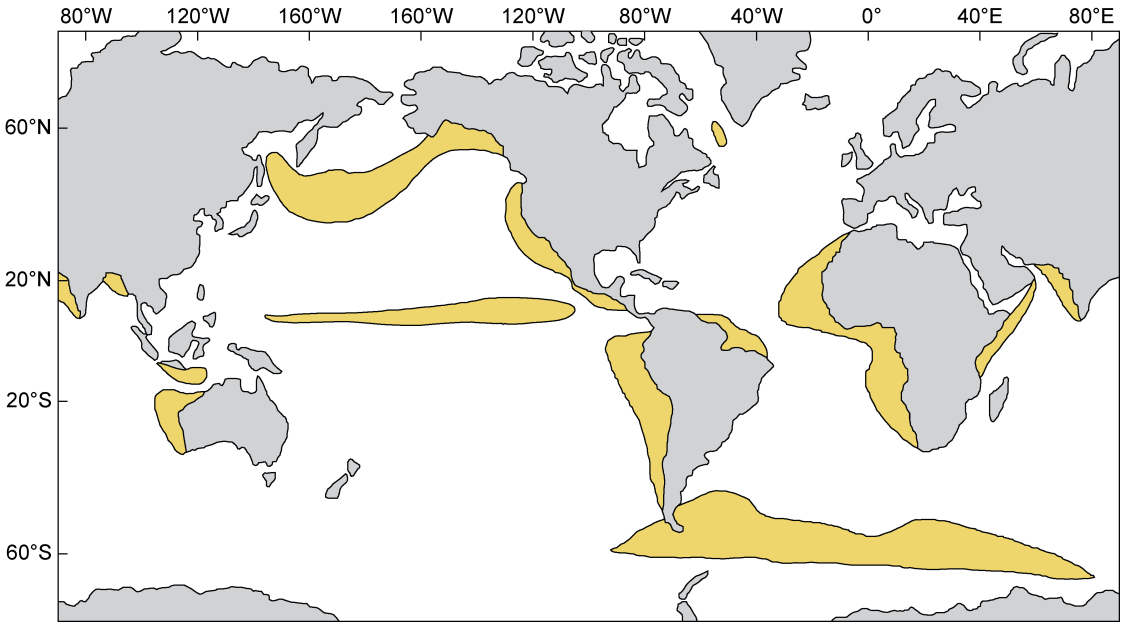


Figure 1.3. Regions of the global ocean characterised by intense upwelling (highlighted in yellow) (redrawn from Rashid, 1985; Libes, 1992).

The lack of density stratification in upwelling areas causes silicon and other nutrients (namely nitrate) to be recycled after the death of the organism and the sinking of siliceous tests, as shown in Figure 1.4. Upwelling transports the regenerated silicon and nutrients back to the euphotic zone, where they are reconverted into biogenic particles, primarily by diatoms. The silicon and nutrients are thus kept within the

upwelling zone, unless they sink fast enough to become buried in the sediments (Libes, 1992).

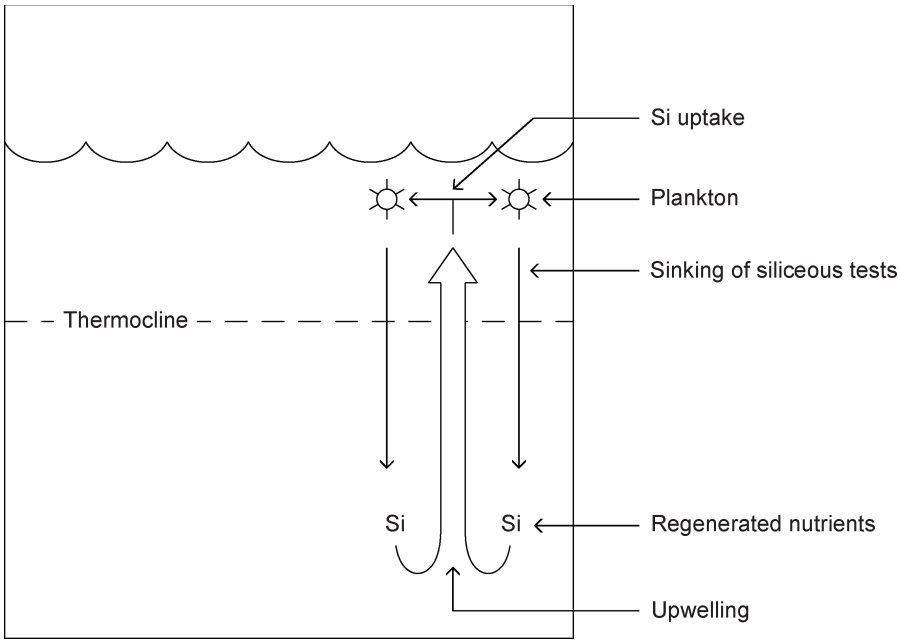


Figure 1.4. Nutrient cycling in a strong upwelling area (redrawn after Libes, 1992).

1.2.4 Biogenic silica — Preservation versus dissolution

Since seawater is highly undersaturated with respect to opal (seawater contains only 2─14 ppm SiO_2, according to Williams and Crerar, 1985), the siliceous tests are exposed to dissolution as they settle to the seafloor. However, the extent of dissolution depends not just on the degree of undersaturation, but also is controlled by the kinetics of dissolution relative to the residence time of biogenic opal in seawater (Sarmiento and Gruber, 2006) which may limit the extent of dissolution. Thus, a small percentage of biogenic silica produced by planktonic organisms in the

surface ocean can escape dissolution in the water column and reach the seafloor. The factors limiting the dissolution rate of biogenic opal also prevent seawater from achieving solubility equilibrium with respect to biogenic opal, which is why undersaturated conditions with respect to opal persist across the entire ocean.

1.2.5 Recycling at the water-sediment interface

According to Hesse and Schacht (2011), the proportion of opaline silica that survives dissolution in the seawater column and reaches the seafloor still undergoes progressive dissolution during very initial burial within the uppermost layers of sediment (an average of 80% dissolves prior to final burial; Ragueneau et al., 2002). Most progressive dissolution of opal occurs at the water-sediment interface, where the settled biogenic components are exposed to the deep ocean water, highly undersaturated with respect to opal, over a long period of time. This process makes the pore water rapidly enriched in silicic acid within the first few centimetres below the seafloor, the zone where the dissolved silica concentrations documented for various modern oceanic basins show an increase to an asymptotic value ranging from 200 to 800 μM (e.g., Rabouille et al., 1997; Ragueneau et al., 2000; Gallinari et al., 2002; Dixit and Van Cappellen, 2003; Hüneke and Henrich, 2011) (Fig. 1.5). The fact that these pore-water concentrations are all higher than the concentrations in the seawater column implies a continuous flux of silicic acid from the sediments into the highly-undersaturated seawater column (Hüneke and Henrich, 2011). The high dissolution efficiency at the water-sediment interface indicates that the dissolution of biogenic silica and the related benthic flux of silicic acid out of the sediment is

determined primarily by the pattern of opal rain to the sediment (Rabouille et al., 1997; Ragueneau et al., 2002). The higher the opal rain rate, the more intense the recycling, and therefore the sharper the rise in asymptotic dissolved silica concentration.

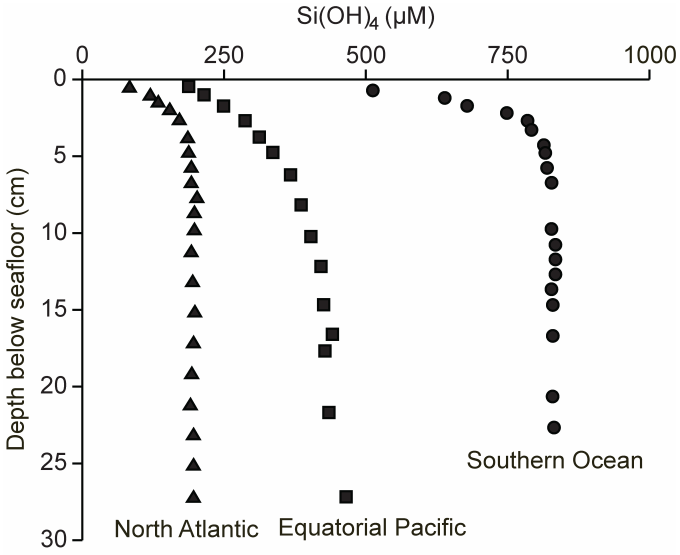


Figure 1.5. Pore-water silicic acid concentrations within the first few centimetres below the seafloor for several regions of the modern ocean. Symbols are triangle for the North Atlantic, square for the equatorial Pacific, and circle for the Southern Ocean (redrawn and modified from Ragueneau et al., 2000; Hüneke and Henrich, 2011).

1.2.6 Burial and preservation in the sediments

The efficiency of opal burial and preservation in the sediments is also a direct function of the rain rate of biogenic silica arriving at the seafloor (Ragueneau et al., 2000). If the opal rain reaching the seafloor exceeds the threshold silicic acid flux out

of the sediment (the theoretical upper boundary of silicic acid out-flux that is the bottom-water dissolved silica concentration, according to Dixit and Van Cappellen, 2003; Hüneke and Henrich, 2011), any excess rain above this flux leads obviously to burial. Areas with an opal rain rate above this threshold are considered to have a high opal burial efficiency (up to 30%), which promotes preservation as rapid burial isolates opal from the seawater, and therefore leads to high amounts of biogenic opal accumulated in the sediments. Of course, additional factors may influence opal burial and preservation; especially the relative accumulation rate of other particles and the degree of undersaturation of deep waters. For example, Libes (1992) suggested that sediments with high biogenic opal contents result from rapid burial which is caused by a high rain rate of opal and the accumulation rate of other particles is slow. These conditions are commonly met for the sediments beneath the equatorial and sub-polar upwelling regions, where the deposits with high concentrations of solid opaline silica are produced (after Leinen et al., 1986; Fig. 1.6). The sediments of the Pacific Ocean, located beneath the largest and most intense zone of equatorial upwelling, are known to have the highest opal content (in excess of 80 percent by mass). In the Pacific Ocean, horizontal segregation results in bottom waters with high silica concentrations; thus leading to significant variations in their degree of undersaturation. Additionally, the high rate of opal rain toward the ocean floor and a slow rain rate of other particles (including detrital) lead to strong preservation of biogenic opal in the sediments. Conversely, in coastal upwelling areas and on the continental margins where opal is commonly buried by other particle types, the relative contribution of opal to the sediment is diluted, despite large rates of opal rain

(Libes, 1992).

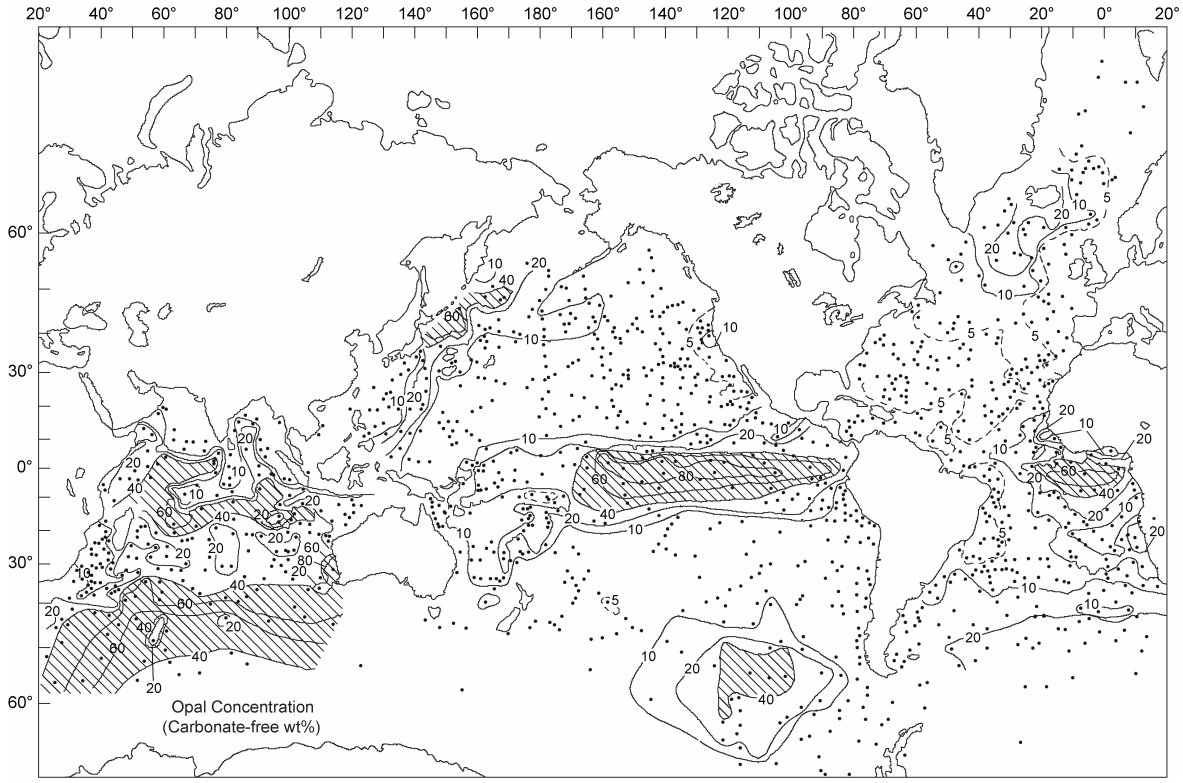


Figure 1.6. Distribution of biogenic silica in deep-sea sediments (redrawn from Leinen et al., 1986). All data are corrected for dilution by calcium carbonate. Contours are in weight percent. Shaded area has concentrations greater than 40 wt%.

1.2.7 Biogenic silica diagenesis

After burial, biogenic silica progresses from metastable opal-A (a highly-disordered near amorphous natural hydrous silica, according to Jones and Segnit, 1971) to the metastable phase of opal-CT (disordered interlayering of α-cristobalite and α-tridymite, according to Wilson, 2014) that is subsequently transformed into thermodynamically-stable microcrystalline quartz (also cryptocrystalline quartz or

chalcedony).

The progressive diagenesis of biosiliceous deposits to opal-CT porcellanite and chert involves a set of chemical, physical, and biological processes that occur under early burial (at depths commonly < 1000 mbsf), in sedimentary settings (this issue has been well documented in the geological literature; e.g., Schink et al., 1975; DeMaster, 2003; Hesse and Schacht, 2011). These diagenetic and catagenetic processes control the dissolution and re-precipitation mechanisms that lead to alteration of the amorphous structure of biogenic silica. Empirical evidence suggests that such a solution-redeposition pathway is inevitably followed by the silica diagenesis reactions (e.g., Kastner et al., 1977). The most explicit evidence is textural─in near-surface sediments partly-dissolved tests are rarely found; rather, most diatom frustules and radiolarians appear untouched by dissolution, although in places mechanically broken (Hein et al., 1978; Williams et al., 1985; Fig. 1.7A). As burial progresses, diatom and radiolarian tests undergo more intense fragmentation and begin to dissolve (Fig. 1.7B), with some re-precipitation of silica overgrowths in the form of opal-A′—a still amorphous transitional phase in the transformation of opal-A to opal-CT with almost unknown newly-formed crystallites of 20–27 Å in size larger than those of opal-A (12–16 Å)—virtually simultaneous to the opal-A dissolution (Hein et al., 1978; Fig. 1.7C). Following this, the opal-A′ is rapidly transformed to opal-CT (with the crystallite sizes ranging from 40 to 81 Å) by crystal growth within the siliceous tests and pore spaces as cements, lepispheres (opal-CT spherical aggregates formed under conditions of unobstructed diagenetic growth,

according to Flörke et al., 1976) (Fig. 1.7D), and blades (Hein et al., 1978; Williams et al., 1985).

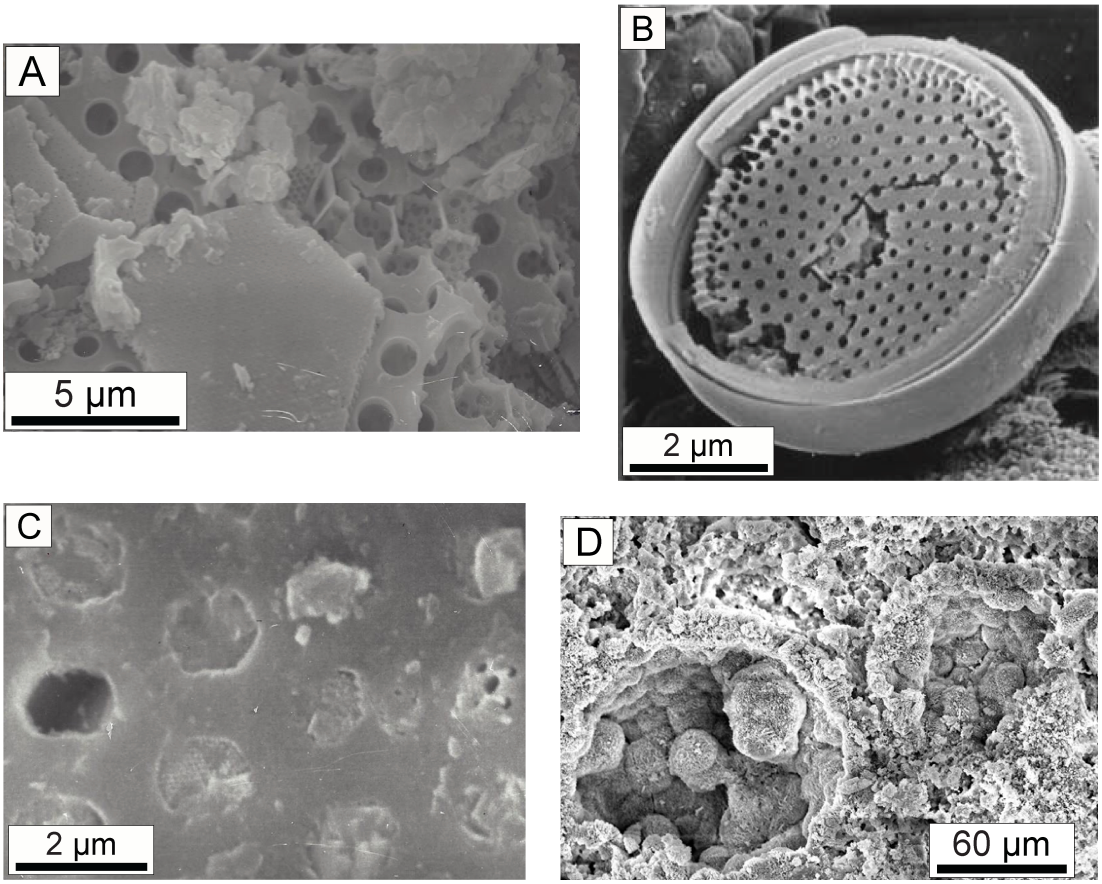


Figure 1.7. Textural evidence for the dissolution-reprecipitation pathway followed during silica diagenesis. A) A diatomaceous ooze containing fairly-pristine skeletons that show only mechanical breakage (from Williams et al., 1985); B) Mechanical breakage and dissolution of a diatom skeleton (from Fütterer, 2006); C) Silica overgrowths (deposition of opal-A′) as a pore-filling material in a diatom frustule (from Hein et al., 1978); and D) Opal-CT lepispheres occupying the cavities of radiolarian tests (from Tanaka and Ogawa, 2006).

1.2.7.1 Controls on biogenic silica diagenesis

The dissolution-reprecipitation pathway involved in the transformation from opal-A to opal-CT and then to quartz is controlled by temperature, time, specific surface area of siliceous tests, pore-water chemistry (i.e., pH, degree of saturation with respect to silica, ions in solution, additional minerals in the sediment, silica diffusion), host sediment composition (whether primarily calcareous, argillaceous, or siliceous), and sediment permeability (e.g., Lancelot, 1973; Kastner et al., 1977; Hein et al., 1978; Williams and Crerar, 1985; Nobes et al., 1992; Neagu, 2011).

Below, these controlling factors are discussed in more detail.

1.2.7.1.1 Temperature and time

Among the aforementioned factors controlling the rate of silica diagenetic reactions, temperature is commonly thought to be the dominant rate-determining control, as illustrated by the experiments of Kastner et al. (1977). The principal effect of temperature is to decrease the relative degree of supersaturation of pore solutions, while increasing silica concentration and therefore increasing the rate of diagenetic silica precipitation (after Ernst and Calvert, 1969; Stein and Kirkpatrick, 1976; Williams and Crerar, 1985).

Based on the temperature estimates (Keller and Isaacs (1985) and the comparable values by Pisciotto (1981a) using thermal gradients and reconstructed maximum burial depths from well data for the Miocene Monterey Formation), Behl (1999)

reported the initiation of opal-CT and quartz formation to occur at ~40–50 °C and ~65–80 °C, respectively (Fig. 1.8). Estimates made by Behl (1992) and Behl and Garrison (1994) for the purest siliceous sediments undergoing diagenesis, however, give temperatures as low as 2–33 °C and 36–76 °C for opal-A to opal-CT and opal-CT to quartz chert transitions, respectively. These values as well as other reported temperature estimates (e.g., see Hein et al., 1978; Pisciotto et al., 1992) imply that the temperatures required for opal-A to opal-CT and opal-CT to quartz transformations vary from 2 to 50 °C and from 36 to 80 °C, respectively.

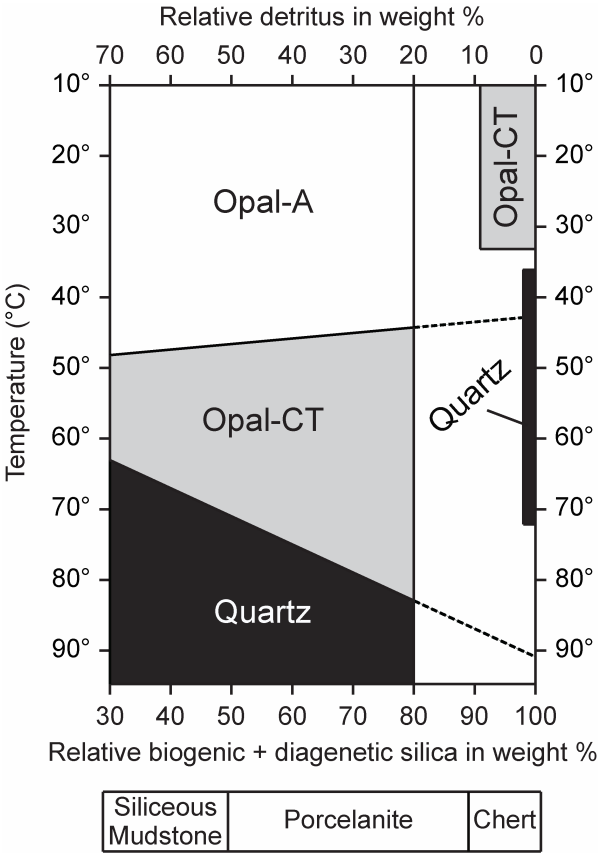


Figure 1.8. Diagram showing the temperature scale of silica phase changes (redrawn from Behl, 1999).

Given these wide temperature ranges for the silica conversion transitions, the reaction temperature must depend on other factors, such as time, surface area, pore-fluid chemistry, and host lithology. The Arrhenius Law used for thermodynamic expression of the rate constant illustrates the importance of time in playing a major role at various temperatures of diagenesis (especially at low temperatures), and relates both temperature and time as dominant controls on the reaction rate. The dependence of the rate of silica diagenesis mainly on temperature and time, instead of temperature alone, has been supported by many researchers; for example Mizutani (1970, 1977), Hein et al. (1978), Keller and Isaacs (1985); Hesse (1988), Kuramoto et al. (1992), Giles (1997), and Hesse and Schacht (2011). Following these studies, the current view is that the opal-A to opal-CT transformation occurs at lower temperatures in older sediments, while higher temperatures are required in younger successions. The formation of opal-CT takes place at relatively-deeper burial depth (> 500 mbsf) and moderate temperatures (35–55 °C) within 10 million years, while more than 30 million years is required for the silicification at shallow burial conditions (< 300 mbsf) and low temperatures (< 30 °C), according to Hein et al. (1978).

1.2.7.1.2 Surface area

Though the role of temperature and time as primary controls on silica diagenetic reactions is clear, the relationship between aqueous solubility of silica polymorphs and surface area suggests that the role of temperature and time may not be as critical as previously thought (Kastner et al., 1977; Williams et al., 1985). For example,

Hesse and Schacht (2011) argue that opal-A solubility is the principal rate-limiting factor for overall silica diagenetic processes, which is, in turn, a direct function of the specific surface area of biogenic silica fragments (Williams et al., 1985). Thus, the higher the surface area exposed to dissolution, the higher the solubility. At standard ambient temperature (25 °C), the aqueous solubility of amorphous silica is ~120–140 ppm (Siever, 1957). With burial (temperature) and age in the sediments, the reactive surface of the siliceous skeleton fragments decreases which results in a solubility decrease. Kastner et al.'s (1977) experiments at room temperature over a period of three weeks show that the high specific surface area of the Quaternary radiolarians, being 439 m^2/g, is responsible for increasing the silica content of the solution up to 1600 μM (96 ppm), whereas the significantly-reduced surface areas of Eocene radiolarians to 7 m^2/g sharply decreases the concentration of dissolved silica to 40 μM (2.4 ppm). Since there is no longer a net release of dissolved silica from the water-sediment interface to the pore waters in deep sediments, the changes in the specific surface area with depth and time reflect progressive elimination of reactive sites on the surfaces of biosiliceous particles (Van Cappellen, 1996), which is an important solubility-decreasing mechanism. The less soluble diagenetic silica polymorphs opal-CT and quartz (with aqueous solubilities of 27 ppm (Fournier and Rowe, 1962) and 6 ppm (e.g., Morey et al., 1962) at 25 °C, respectively) contain specific surface areas lower than that of biogenic opal (for comparison, the surface area of fine quartz is near 0.1 m^2/g, according to Van Lier et al., 1960).

Although it is primarily a function of surface area and crystal structure of solid silica

particles, the solubility of silica is also influenced by kinetic and thermodynamic factors, including temperature, pH and electrolyte composition of the porewater solution, and additional minerals in the sediment (Williams and Crerar, 1985; Van Cappellen, 1996).

1.2.7.1.3 Pore-water chemistry

The chemistry of pore fluid exerts controls on silica diagenesis through parameters that deal with the solubility of silica phases, such as pH, degree of saturation, presence of electrolytes, additional minerals in the sediment, and molecular diffusion.

— pH

At a pH value > 9, under standard ambient temperatures, silica solubility increases in the sense that it facilitates the ionisation, dissociation, and polymerisation of monomeric silicic acid as the predominant aqueous species in undersaturated solutions (Williams and Crerar, 1985).

— Saturation degree

In sediments where the pore water is highly undersaturated with respect to biogenic silica (commonly at the sub-seabottom depths near the water-sediment interface), the solubility of biogenic silica rapidly increases with increasing undersaturation (after DeMaster, 2003). In areas of steady pore-water undersaturation, the silica solubility gradually increases with burial depth. Progressive undersaturation with respect to

biogenic silica deeper in the sediments is mainly attributed to reduction in the reactive surface area which causes the silica solubility to decrease.

— Electrolytes in solution

It has been documented that the solubility of silica polymorphs is significantly enhanced by the presence of some electrolytes (especially alkali and earth alkali salts), such as NaCl, KCl, $MgCl_2$, and $CaCl_2$ (modified after Van Lier et al., 1960; Kamiya and Shimokata, 1976; Dove and Crerar, 1990; Dove and Elston, 1992; Dove and Nix, 1997; Dove, 1999). The mechanism behind this control is explained by Dove (1999) who proposed that the presence of alkali and earth alkali cations in the pore water enhances the nucleophilic properties of water; thus increasing the frequency of hydrolysis attacks at the silica surface. This matter confirms the catalytic effects of alkali and earth alkali ions on amplification of silica dissolution (Loucaides, 2009).

— Additional minerals and auxiliary processes in the sediment

The concentration of dissolved silica can decrease due to adsorption onto existing detrital particles and through neoformation of clays and zeolites, which is an observed part of diagenesis in many siliceous oozes (depending on overall sediment chemistry) (modified after Williams and Crerar, 1985; Williams et al., 1985).

Siever and Woodford (1973), Maynard (1975), and Williams and Crerar (1985) have demonstrated experimentally that a drop in silica concentration in pore waters can be

correlated with the silica uptake by detrital minerals such as clays. Although trace amounts of detrital minerals adsorb silica, they have a trivial or short duration effect on silica diagenesis because adsorption capacity is small relative to the total amount of silica in the system. However, large amounts of detrital minerals (in particular high area strongly-adsorbing clays) can reduce the total dissolved silica concentration, and hence the silica solubility considerably.

Silicic acid can also be removed from the pore water by auxiliary process of authigenic precipitation (neoformation) of clays, zeolites, and other silicates if the rates of nucleation and growth of silica polymorphs are lower than those of authigenic clay or other silicates (Williams et al., 1985). In extreme events (dissolved silica concentration is reduced below the quartz solubility limit), this should enhance dissolution of all silica polymorphs, and opal-A should transform directly to other silicate phases. In less extreme cases, however, this process only retards the formation of diagenetic silica due to its effect on degree of supersaturation (modified after Williams et al., 1985).

The degree of supersaturation can be reduced by a reduction in the activity of silicic acid, without changing the total dissolved silica concentration, via processes such as complexation, polymerisation, or dissociation that shift silica to some species other than H_4SiO_4 more rapidly than dissolution can re-establish equilibrium (Williams et al., 1985). Such a reduction in activity of silica occurs through changing the ratio of the activity of silicic acid to the activities of other dissolved species.

— Silica diffusion

The strongly-undersaturated status of ocean waters with respect to biogenic silica drives the diffusion of silica from sediments up into bottom waters (e.g., Hurd, 1973; Edmond et al., 1979; Williams and Crerar, 1985; James, 2005; Hesse and Schacht, 2011). Hurd (1973) calculated silica diffusion rates in the pore waters of near-surface sediments in the Central Equatorial Pacific, where the concentrations increased from the bottom-water value of < 100 to up to 500 μM within the first 10 cm of sediment depth. His calculated diffusion rates are quite low even at the water-sediment interface (the mean value being 4.1×10^{-6} moles/cm^2 yr), and decrease rapidly down in the sediment. Nevertheless, these low diffusion rates are still important to the solubility of biogenic opal, as high diffusion rates prevent dissolving silica from concentrating *in situ*, and the critical concentrations needed for precipitation of diagenetic opal cannot be achieved (Williams and Crerar, 1985).

1.2.7.1.4 Host sediment lithology

According to many researchers (e.g., Lancelot, 1973; Murata and Nakata, 1974; Kastner et al., 1977; Isaacs, 1982; Hinman, 1987; Hesse and Schacht, 2011), the rates of the mineralogical transformations in the opal-A → opal-CT → quartz diagenetic sequence are distinctly influenced by the composition of host sediment. The results of Kastner et al.'s (1977) experiments conducted on DSDP sediments under low and high temperatures (over a one-day to six-months period) show that the rate of transformation from opal-A to opal-CT is enhanced in carbonate-rich sediments relative to pure silica, and relative to clay-rich sediments, and that the

formation of opal-CT lepispheres is aided by the precipitation of nuclei composed mainly of magnesium hydroxide. In carbonate-rich sediments, the dissolution of carbonate provides the necessary alkalinity, and seawater provides Mg^{2+} for the magnesium hydroxide in the nuclei. In clay-rich sediments, conversely, the clay minerals compete with opal-CT formation for the available alkalinity from seawater. As a result, the clays are enriched in Mg, and the rate of opal-CT formation is dramatically reduced. The nature of the host sediment exerts controls not only on the rate of silica transformations, but also on mineralogical structure of the diagenetic phases. Observations of Keene (1976) for the biosiliceous deep-sea sediments of the Pacific indicate that the degree of disorder of the opal-CT crystallised in clay-rich sediments, and thus silica values in solution, is higher than in carbonate sediments of the same geologic age and thermal maturation level. Therefore, the mineralogical evolution of biogenic silica is a direct function of the lithologic composition of the sediment accommodating it.

The presence of organic matter in biosiliceous sediments is also another factor that influences the silica transformation rates. In organic-matter-rich sediments, the rate of silica diagenesis is reduced (Hinman, 1987). Organic acids released by organic matter maturation dissociate and lower the pH, thereby reducing the carbonate alkalinity. This, in turn, retards the silica conversion reactions by decreasing the silica polymerisation rate (Hesse and Schacht, 2011).

1.2.7.1.5 Sediment permeability

According to Lancelot (1973), disordered opal-CT is mostly confined to biosiliceous sediments in which clay minerals obstruct the circulation of pore waters and create a microenvironment in which pore spaces are small enough to keep the ratio of silica to other dissolved species (including cations) at relatively-low values. Such sediment systems, as well as many of the pores of the siliceous tests, are filled due to partial re-distribution of clays under burial, which further decreases the permeability. Wherever the permeability increases, such as in a large void, chalcedony and microcrystalline quartz can precipitate because of a sharp increase in the aforementioned ratio. In carbonate sediments, both the lack of aluminium and most cations, and the high permeability favour direct precipitation of microcrystalline quartz from opal-A without an intermediate opal-CT phase (Lancelot, 1973). In contrast to Lancelot (1973), Wise and Kelts (1971) noted only opal-CT lepispheres in a permeable Oligocene nannofossil chalk with only negligible amounts of clay minerals, and Wise and Weaver (1974) described the occurrence of opal-CT only, underlying a highly-permeable clay-free diatom ooze. Considering these explanations, it seems that permeability leads to variations in the silica/cation ratios rather than acting as a direct control over the diagenetic maturation sequence of silica.

1.2.7.2 Physical properties and silica diagenesis

Classical views of compaction in fine-grained sediments generally describe the evolution of physical properties, such as porosity, density, and permeability as

gradual (e.g., McSween et al., 2003; Fabricius, 2012). However, continuously-cored basinal sediments rich in biogenic silica in many scientific boreholes (drilled by the DSDP/ODP) show that abrupt physical property changes (anomalous compaction) often take place, and are linked to the silica diagenesis (e.g., Littke et al., 1991; Nobes et al., 1992; Kim et al., 2007). One of the most interesting results reported by the DSDP and ODP sources is that rapid decreases in porosity, water content, and permeability of sediments while increases in density and acoustic velocity, observed through the downhole logs for the drilled sites, are the result of opal-A to opal-CT transformation (e.g., Shipboard Scientific Party, 1990a). These petrophysical variations occur over a depth interval named the 'transition zone' (Littke et al., 1991) or 'diagenetic front' (Thein and von Rad, 1987). This is a relatively-narrow sub-seabottom boundary with tens of metres thick across which opal-A and opal-CT co-exist, however, it is mostly constructed of opal-CT. According to work based on the ODP and DSDP borehole data (e.g., von Rad et al., 1978; O'Brien et al., 1989; Shipboard Scientific Party, 1990c, d, e; Nobes et al., 1992; Guerin and Goldberg, 1996; Neagu, 2011 and the literature therein), prominent physical property variations due to diagenesis of biosiliceous ooze to opal-CT porcellanite and chert (porosity drop and bulk density increase) are associated with the formation and development of the opal-A to opal-CT transition zone ($TZ_{A/CT}$) (Fig. 1.9).

Less significant changes in petrophysical properties are observed deeper in the sediment where opal-CT is later transformed to microcrystalline quartz chert. These variations occur across a very narrow interval (at most < 3 m thick, after Nobes et al.,

1992), namely opal-CT to quartz transition zone ($TZ_{CT/Q}$). The study of opal-CT to quartz diagenesis and the characteristics of the $TZ_{CT/Q}$ are, however, beyond the scope of the present research.

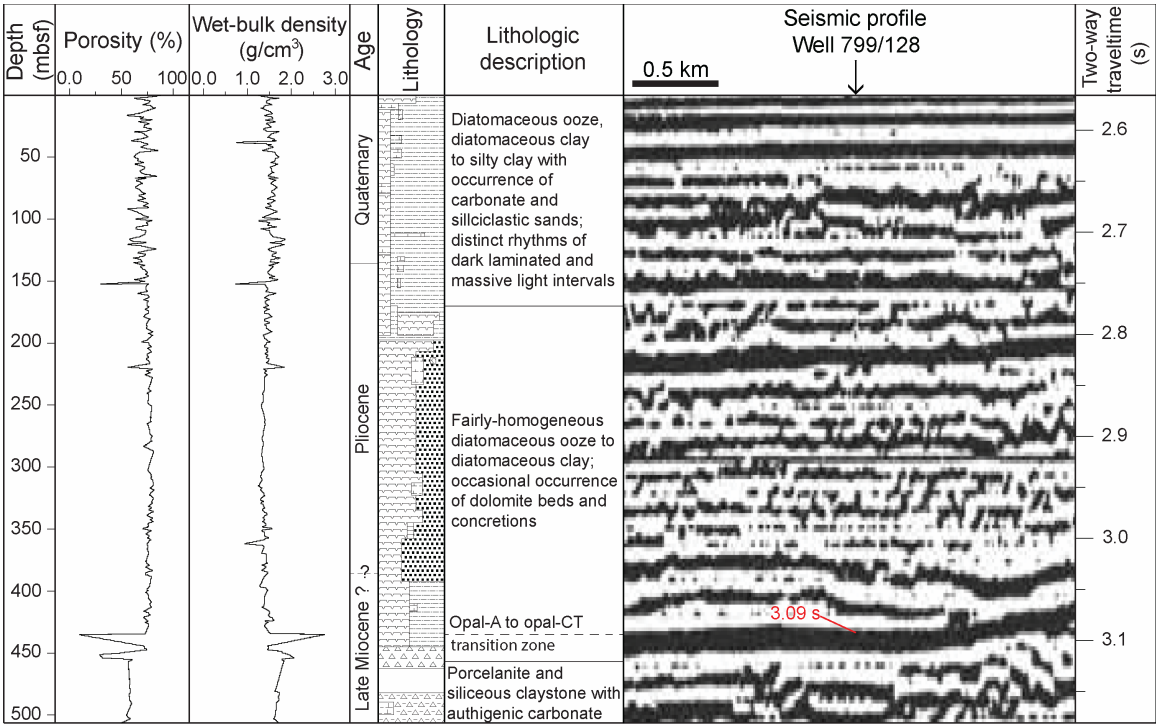


Figure 1.9. Occurrence of abrupt porosity and density contrasts across the opal-A to opal-CT transition zone at ODP Site 799/Leg 128. Note these petrophysical variations are tied to a high amplitude reflection on the seismic profile at 3.09 s. 0.1 s two-way traveltime roughly equates to 82 m sediment thickness in this profile (data in the Figure 1.9 are derived and modified from Shipboard Scientific Party, 1990e).

Opal-A is commonly recognised on borehole logs by its high porosity (the mean value for the ODP sites being 70%, according to Neagu, 2011) and the $TZ_{A/CT}$ recognised by an abrupt change in porosity, bulk density, or velocity (O'Brien et al.,

1989; Guerin and Goldberg, 1996). Neagu (2011) reports a range of 10 to 40% reduction in porosity and a bulk density increase between 0.15 and 0.55 g/cm^3 with the change from opal-A to opal-CT for typical ODP boreholes calibrating the $TZ_{A/CT}$. The lower values in the porosity contrast range are relating to lesser proportions of opal-A in the bulk sediment.

The anomalous compaction interval (the $TZ_{A/CT}$) has been also identified through studying biosiliceous sediments on land; the most extensive and well known outcrops being from the Monterey Formation fracture-dominated reservoir group 2 in California, where the alteration of soft diatomaceous sediments to tight porcellanite and fractured chert has resulted in a porosity decrease of at least 8% (Chaika and Dvorkin, 1997; Chaika, 1998; Chaika and Williams, 2001).

It has been demonstrated, based on both wellbore and on land data, that the major mechanism of porosity drop over the $TZ_{A/CT}$ is compaction associated with solution-precipitation of silica during diagenetic phase transformations and not a result of gradual mechanical compaction due to increasing sediment load (e.g., Isaacs, 1981). Supporting this conclusion, Hamilton (1976) notes that biosiliceous sediments are resistant to mechanical compaction; thus showing a considerable retention of high porosity during burial.

The prominent increase in bulk density and compressional velocity due to opal-A to opal-CT transformation results in dramatic changes in acoustic impedance, allowing

the $TZ_{A/CT}$ to be imaged on seismic profiles as a reflection event (Fig. 1.9) sometimes cross-cutting the host stratigraphy (e.g., Hein et al., 1978; Brekke, 2000; Davies, 2005; Ireland et al., 2010; Neagu et al., 2010). However, because of its limited vertical extent, the $TZ_{A/CT}$ is below or at the vertical resolution limit of the seismic data; thus it cannot be precisely studied at a regional scale. In particular, the limited availability and quality of the DSDP and ODP seismic data makes the study of silica diagenesis and anomalous compaction phenomena using seismic stratigraphy approach even more difficult.

1.3 Research goals

This research project has four main objectives:

Objective 1: The Assessment of chemical signals and thermodynamic status of silica diagenesis in interstitial waters

One of the outstanding issues in silica diagenesis research is the study of opal-A to opal-CT transitions over which silicification is an ongoing process. Studying the characteristics of active silica transformation is key for constraining physical and chemical diagenetic controls, particularly those causing petrophysical variations. It is essential for this part of the project to utilise the pore-water chemical profiles of dissolved species to look for the present-day signatures of silica diagenesis across the transition zone (Chapter 4). Although widely preferred as an analytical tool for monitoring the early diagenesis, pore-water chemistry has been rarely quantitatively examined for the associated signals of silica transformation.

This section is aimed to answer the following questions:

a. What is the major source of silica dissolved in the pore water ?

b. What patterns of concentration-depth profiles (in particular silica profile) suggest presently-active silica diagenesis ?

c. How does thermodynamic analysis determine whether precipitation of diagenetic opal across a silica transition zone is currently ongoing ?

d. What is the main mechanism for transport of dissolved ions and species in interstitial water during silica diagenesis ?

e. How does the pore-water chemistry influence silica diagenesis and therefore porosity reduction ?

Objective 2: The Elucidation of diagenetic processes leading to anomalous compaction

An essential aspect of silica diagenesis relates to early burial processes that force abrupt changes in the physical state of sediments across the opal-A to opal-CT transition zone. These physical and chemical driving factors are not well understood simply due to a paucity of inclusive research on characterising internal features and mineralogical evolution of the sediment capturing silica diagenetic transformation. Here, a greater understanding of sediment texture and mineralogical composition of silica transition zone and the interval overlying it is essential for accurate assessment of the dominant diagenetic driver (Chapter 5). The approach taken to achieve this goal is to document and quantify physical property variations and place them in a diagenetic context through relating these changes to variations in microfabric and

mineralogy of host sediment. The broader perspective for this part of the project is a process-based understanding of controls on anomalous compaction behaviour during silica diagenesis in sedimentary basins.

Under this umbrella, this research aims to answer the following:

a. What processes lead to framework collapse and sudden anomalous compaction across the opal-A to opal-CT transition ?

b. How does the fine-grained detrital fraction exert controls on precipitation of diagenetic silica and sediment porosity ?

c. Do petrophysical variations relate to changes in the d(101) spacing of cristobalite ?

d. How influential is smectite and zeolite authigenesis on the rate of silica diagenesis and porosity reduction at the opal-CT precipitation zone ?

Objective 3: Bottom-water temperature controls on silica dissolution and benthic flux from surficial sediments under early diagenesis

It is known that, due to the highly-undersaturated nature of seawater, biogenic silica dissolves at the water-sediment interface progressively, and that the dissolution of opal-A is heavily temperature dependent. Little is known on the role of bottom-water temperature in early diagenetic dissolution of biogenic opal and the benthic flux of silicic acid back to water column across the water-sediment interface (driven by dissolution of biogenic silica deposited at the seafloor). It is therefore essential for this part of the research to understand the impacts on the rate of these processes, and to model them versus present-day bottom-water temperature. This will clarify how

temperature influences the uppermost layer of deep-sea sediments during silica early diagenesis (Chapter 6).

This section answers the following questions:

a. What variables are critical for determining the model-derived silica dissolution rate and recycling ?

b. How does host sediment composition influence the rates of silica dissolution and benthic flux ?

c. What are the primary effects of bottom-water temperature on silica early diagenesis ?

d. To what extent do low temperatures (including bottom-water temperature and temperatures of a-few-metre-thick interval below seafloor) exert controls on the accumulation of opal-CT chert and porcellanite close to the seafloor ?

Objective 4: Temperature-time relationships for silica later diagenesis

Although silica dissolution rate as representative of the overall rate of opal-A to opal-CT transformation is exponentially temperature dependent (e.g., Atkins and de Paola, 2006), the thermodynamic expression of the rate constant based on Arrhenius Law suggests temperature and time as a principal control on the reaction rate. Following this conception for temperature and time relation in silica later diagenesis, a reference definition is presented by Hein et al. (1978) for the temperature-time stability field of diagenetic silica. Of importance for the present research is the modification of this reference field as it is defined based on a very limited number of

data points (only 6 data points) which are insufficient for an exact constraint of the temperature-time stability zone (Chapter 7). In a novel approach, recognising that silica diagenesis is mainly controlled by the geothermal history of the sediment (e.g., Mizutani, 1970), the temperature-time relationship is incorporated in modelling of opal-A to opal-CT transformation rate and ratio (Chapter 7).

This section aims to answer the following:

a. What factors control the thickness of opal-A to opal-CT transition zone ?

b. Does the temperature-time relationship in silica diagenetic transformation differentiate active versus fossilised transition zones ? If so, what transitions fit the temperature-time stability field of diagenetic silica ?

c. How does geothermal history influence silica diagenesis, and in turn what controls thermal history ?

d. What are the functional parameters in accurately modelling the opal-A to opal-CT transformation ?

e. What controls cause a significant difference between the amount of reacted biosilica in the opal-A-rich sediment above the transition zone and the opal-CT-rich interval below it ?

1.4 Thesis structure

In this chapter, an overview of the characteristics of biogenic silica, its productivity, preservation versus dissolution in seawater, at the water-sediment interface, and in sediments, biogenic silica diagenesis and its drivers, petrophysical variations due to

silica diagenesis, and the formation of opal-A to opal-CT transition zone were presented, followed by a statement of the aims of this research.

Chapter 2 outlines the global distribution and setting of the DSDP and ODP sites that penetrate the diagenetic transition from opal-A to opal-CT and gives an account of tectonic setting and descriptions of the two representative ODP sites (794 and 795) that are investigated in detail under the remit of this research project.

Chapter 3 introduces the data acquired from the DSDP, ODP, and IODP (International Ocean Discovery Program) sources, and provides detailed accounts of the laboratory techniques and analytical methods employed to produce the data and results presented in this work.

The research findings of this thesis are presented in Chapters 4–7.

Chapter 4 investigates variation in, and the potential proxy application of, interstitial-water inorganic chemistry for tracing the signatures of active silica diagenesis across the opal-A to opal-CT transition at Sites 794 and 795 of ODP Leg 127, Japan Sea. In a novel approach, the variability in concentrations of major ions (in particular silica) with burial depth is combined with data from microscopic, mineralogical, and thermodynamic analysis of sediments undergoing silica diagenesis to demonstrate the present-day release of opal-A dissolution products to the pore water and their subsequent precipitation as opal-CT. The pre-existing isotopic temperatures of

crystalline silica formation are used as an added constraint to provide further support on persistence of silica dissolution and precipitation across the transition zone.

Chapter 5 analyses microstructure and composition of the deep-sea sediments undergoing transformation of opal-A to opal-CT at the ODP Sites 794 and 795 to elucidate the processes that result in the sudden anomalous compaction event during silica diagenesis. The study documents and quantifies variations in different petrophysical properties, especially abrupt porosity reduction across the opal-A to opal-CT transition zone, and places them in a diagenetic context through providing textural and mineralogical evidence from the sediment. The chapter also investigates the implications that crystallographic habit of diagenetic silica as well as the authigenic processes accompanying silica diagenesis (including the formation of authigenic clay minerals) may possibly have for variations in the physical state of the sediment.

Chapter 6 compiles, analyses, and describes lithological data, temperature, pore-water silica concentrations, and physical properties measurements for surficial deep-sea sediments at 22 ODP sites from a range of ocean basins through the ODP databank to model silica early diagenesis processes, including dissolution rate of biogenic opal and its related recycling versus bottom-water temperatures. The chapter discusses the effects of temperature on these parameters, in particular through controls that temperature exerts on pore-water saturation status with respect to biogenic silica during early diagenesis. The study uses these results to account for

unusual accumulations of low temperature opal-CT porcellanites and cherts in a few deep-sea positions near the seafloor during selected geological intervals.

Chapter 7 interrogates the ODP and DSDP database to compile and analyse the downhole measurements for an assemblage of the borehole sites worldwide that drill the Cenozoic deposits accommodating the $TZ_{A/CT}$. This datapack is used to extract the information required for researching the relationships between temperature and time during silica later diagenesis. The physical property data are used to characterise the $TZ_{A/CT}$ in the sub-seafloor position at these sites. The age and thermal data from a group of the transition zones that represent likely-active silica diagenesis are utilised to modify the reference time-temperature stability zones for the onset of diagenetic opal. In this chapter, the influence of temperature history on silica diagenesis is reconstructed and discussed for the representative Wells 794 and 795. Finally, the transformation of biogenic to diagenetic silica is modelled, and the model is validated using a diagenetic phase diagram and the ODP-measured opal-A and opal-CT content of the sediment.

Chapter 8 presents a summary of the conclusions of this project and discusses the factors limiting the research reported in this thesis, followed by a statement of future outlook.

Appendices I─VI include additional data that support the conclusions of Chapters 4─7.

Chapter 2

Geological setting

2.1 Introduction

This work focuses on the ODP and DSDP scientific borehole sites drilling the $TZ_{A/CT}$ in biosiliceous deep-sea sediments. So far, more than 100 ODP and DSDP wells worldwide have sampled the $TZ_{A/CT}$ (Neagu, 2011) and in most of them the transformation zone is hosted in Palaeogene and Neogene deposits. The ODP and DSDP borehole sites that penetrate biosiliceous sediments have been broadly investigated over the last few decades for different purposes, including fluid flow and migration (e.g., Deyhle et al., 2004), evaluation of thermal history (e.g., Pisciotto, 1981b; Pisciotto et al., 1992), environmental and nutritional oceanic silicon cycles (e.g., Swann et al., 2017), and the significance of these scientific drilling projects on deep-water hydrocarbon prospectivity (e.g., Kvenvolden et al., 1989; Emeis et al., 1991). However, less attention has been given to the rates and mechanisms of biogenic silica diagenetic processes that occurs in the deep-sea sediments from these sites.

2.2 Regional tectonics

The global distribution of ODP and DSDP borehole sites that drill the Palaeogene and Neogene deposits accommodating the $TZ_{A/CT}$ is presented in Figure 2.1. In total, ~80% of the sites were drilled along the continental margins of North and South

America, West-Northwest Africa, and East (and Southeast) Asia.

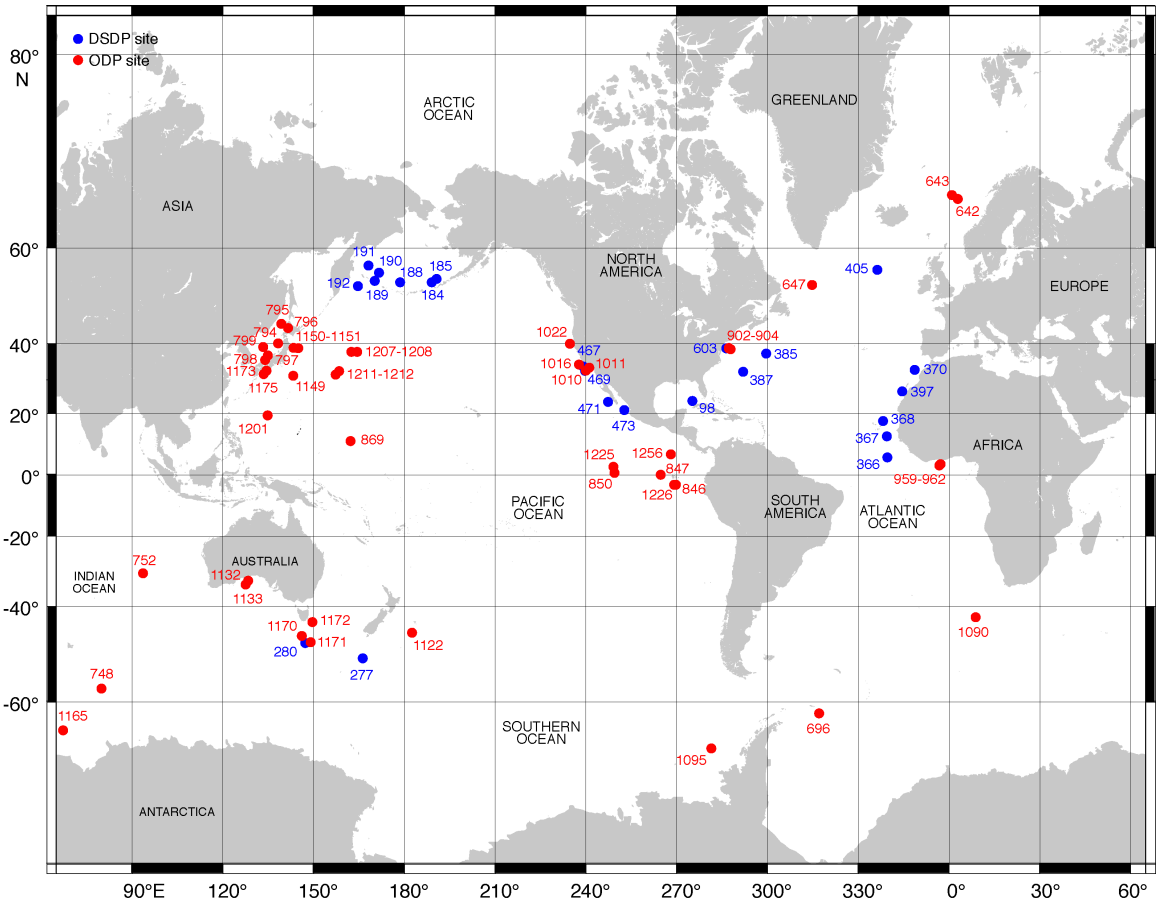


Figure 2.1. Geographical distribution of the ODP and DSDP sites penetrating the $TZ_{A/CT}$ in Quaternary deep-sea deposits (redrawn and modified from Ocean Drilling Program Site Maps, 2009).

Among these regional settings, the tectonic setting of West African coast varies considerably because the continent has been involved both in transform motion relative to South America and in crustal divergence away from North America (Schlee, 1980). The present-day structural configuration of South America and West

Africa coasts, defined as passive continental margins, results from a series of rifting events whose timing remains poorly constrained. The opening of the Equatorial Atlantic Gateway (EAG) driven by the oblique crustal separation of Africa and eastern South America is thought to have been initiated during the Early Cretaceous (after Pletsch et al., 2001; Kankeu et al., 2012). The onset of the separation of eastern North America from Africa, however, occurred in the Early Jurassic, according to Weishampel and Jianu (2011). The Central Atlantic seafloor spreading began in the Jurassic, following the separation of these two continental tracts. Both Atlantic-type margins along North America and West Africa show the complex interplay of differential subsidence, buildup of biogenic deposits, deposition of clastic sediments, and local tectonism (after Schlee, 1980); reflecting that these continental margins are only passive in that they are not active plate boundaries.

The continental margins of western North America on the eastern rim of the Pacific Ocean are chiefly active, affected first by multi-episodic rifting and then by plate-margin subduction and transcurrent faulting over a 700 million year period of time (Nelson, 2004; Nelson and Colpron, 2007). On the western rim of the Pacific Ocean, the compressional deformation of Pacific-type East Asian active margins has been interpreted to result from extrusion tectonics related to the India-Asia collision which started in the Early Eocene (after Tapponnier et al., 1982; Molnar et al., 1987; Chung et al., 1997, Flower et al., 1998; Yin, 2010). These regional compressional deformation events are associated with the basin fill and burial of sediments, especially those rich in carbon and silicon in the continental margins of East Asia.

Based on the amount of marine organic matter buried in continental margin deposits ((3–4) × 10^{13} gC/y; Hedges and Keil, 1995) and typical silica/carbon weight ratios in productive continental margins (~3), nearly half of the world's biogenic silica may be accumulating in continental margin sediments (DeMaster, 2001, 2003). Based on the accumulation rate of continental margin sediments rich in biogenic opal (with an average of 60 m/Ma; e.g., after Shipboard Scientific Party, 1990b), the continental margin of East Asia in the Pacific Ocean has been one of the major world depocentres for biogenic silica during the Middle Miocene to Early Pliocene. This is of particular significance in the context of present research as two of the ODP sites selected for this work (Sites 794 and 795) are located in the Sea of Japan along the continental margin of East Asia.

2.3 Sea of Japan — Physiography

The Sea of Japan (also named East Sea) is a semi-enclosed back-arc marginal basin between the Japanese archipelago (Japan Island Arc), the Korean Peninsula, and Russia (Fig. 2.2). At c. 25 Ma (million years ago) (in the Late Oligocene Epoch), the Japan Sea began to open causing the separation of Japan from the East Asia margin to form the present island arc (Taira et al., 2016), and during the Miocene, there was expansion of the Sea of Japan (Son et al., 2015). The sea mainly comprises the Japan Basin from the north to northwest regions, the Yamato Basin in the southeast region, the Ulleung Basin (Tsushima Basin) in the southwest region, and the Yamato Rise as the topographic high in the central region (Sato et al., 2014). The Japan Basin is ~700 km long trending NE-SW, is of oceanic origin, and its basin floor ranges in

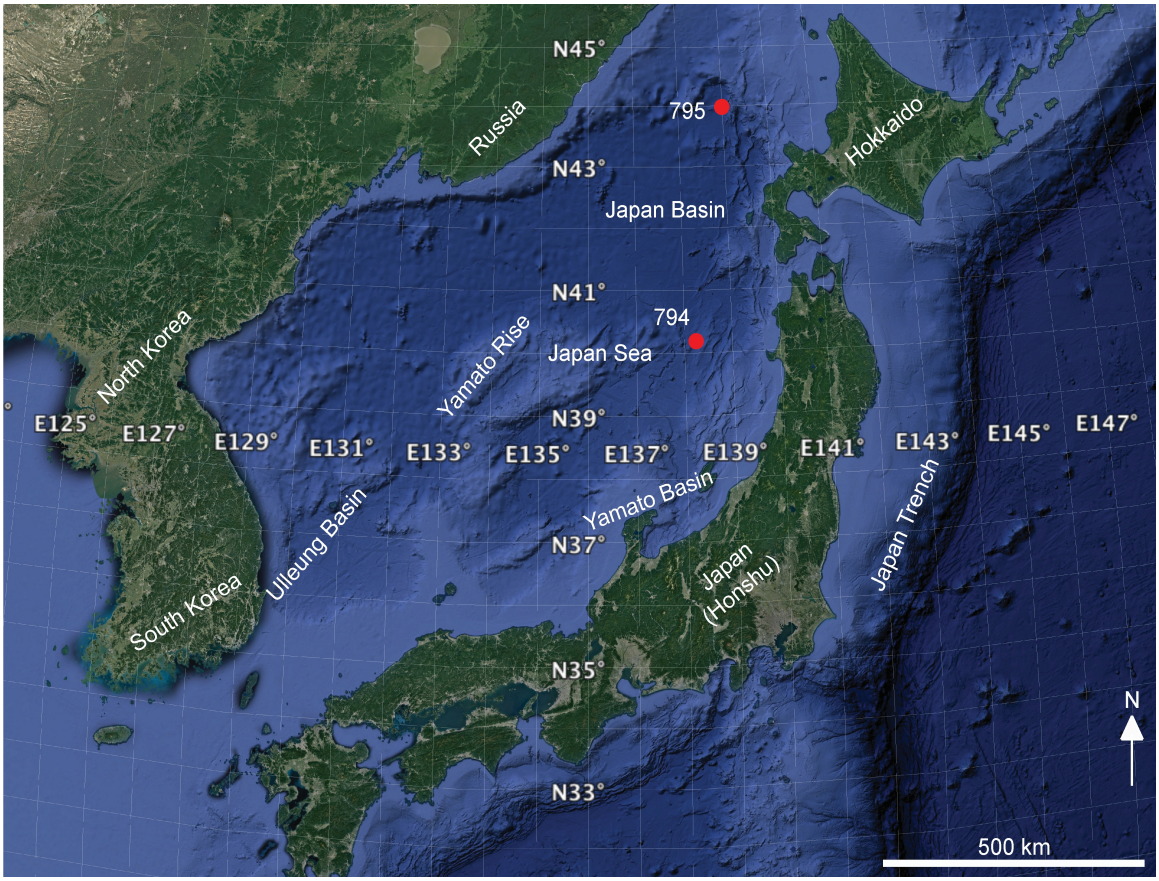


Figure 2.2. Sea of Japan (from Google Earth Pro 7.3, 2017). The sea comprises Japan, Yamato, and Ulleung Basins and Yamato Rise. Note the location of the ODP Sites 794 and 795 in the Yamato and Japan Basins, respectively.

water depth from 3300 to 3700 m (Chough et al., 2000). ODP Site 795 is located at 43.99°N and 138.97°E in the northernmost part of the Japan Basin (Fig. 2.2), where the water depth above the seafloor is the shallowest within the basin (3310 m, according to Shipboard Scientific Party, 1990b). The southeastern part of the sea, the Yamato Basin, is also trending NE-SW, but it is shallower than the Japan Basin with an average water depth of 2500 to 2700 m (maximum of 2970 m). ODP Site 794 is located at 40° 11.41´N and 138° 13.86´E along the northeastern end of the Yamato

Basin (Fig. 2.2), where the depth of water column above the seafloor is 2822 m (Shipboard Scientific Party, 1990a). The floors of the Japan and Yamato Basins are rather smooth and flat except for a few seamounts and hills that rise up to 2000 m above the surrounding basin floor (Chough et al., 2000).

Below, although the geologic and tectonic setting of the Yamato Basin and Japan Basin is discussed, the focus is clearly on tectonic and geology of these basins at and in the vicinity of the location of ODP Wells 794 and 795.

2.4 Yamato Basin

2.4.1 Geological and tectonic setting

To date, the age and formation of the Yamato Basin is still controversial (Kong et al., 1991). Based on palaeo-magnetic data, the clockwise rotation of southwest Japan 15 Ma has been used to argue for the rapid opening of the Sea of Japan and Yamato Basin by back-arc spreading (Otofuji and Matsuda, 1983, 1984; Hayashida and Ito, 1984; Otofuji et al., 1985). In contrast, Lallemand and Jolivet (1986) propose, based on structural data, the formation of a pull-apart basin along two right-lateral shear zones off Korea and northeast Honshu, followed by back-arc spreading in the Middle Miocene (after 21 Ma) due to the extensional stress field present behind the subducting Pacific plate (Kong et al., 1991). Based on the recognition of fold and thrust structures in seismic profiles of the continental slope off northeastern Japan (Kimura et al., 1987; Tamaki, 1988; Shipboard Scientific Party, 1990a), it is thought that the present regional stress field is, however, compressional. Tamaki (1988)

estimated the age of the Yamato Basin to be 10–30 Ma from sediment stratigraphic, basement depth, and heat flow data, and suggested that the back-arc spreading was related to the collision of the Indian and Eurasian continental plates. A rapid shift in benthic fauna type (Chinzei, 1986), and the uplift of sedimentary units in central Japan (Hayakawa and Takemura, 1987), is consistent with the opening of the Yamato Basin about 15 Ma (Kong et al., 1991).

2.4.2 Crustal structure

The crustal structure of the Yamato Basin (Fig. 2.3) has been inferred from seismic reflection and refraction data (Ludwig et al., 1975; Hirata et al., 1989; Shipboard Scientific Party, 1990a; Shinohara et al., 1992; Park et al., 1996). This analysis indicates that the upper crust (Layer 2 in Fig. 2.3), mainly composed of (basaltic)dolerite sills, is possibly interlayered with sediments at a depth of 3.5 to 4 km below sea level. Presently, the composition of the uppermost part of the (upper)crust is well constrained from ODP Site 794, suggesting that the upper crust is sub-parallel to the acoustic basement and constituted of a dolerite sill complex (Refer to Shipboard Scientific Party (1990a) for a review of the upper crustal lithology inference of the Yamato Basin based on the composition of acoustic basement). This rock complex comprises highly-altered dolerite (also basalt) that has been injected into soft sediments during the formation of the Yamato Basin at ~15 Ma (Shipboard Scientific Party, 1990a). The upper crust ranges in thickness from 1.5 to 3 km, and is characterised by an average P-wave velocity of ~4.2 km/s. The lower crust (Layer 3 in Fig. 2.3) is characterised by P-wave velocity in the range between

6.2 to 7.2 km/s, and lies at about 5 to 7 km below sea level. The depth to the upper mantle in this basin is 14 to ~17 km below sea level which is nearly twice as deep as that below normal oceanic crust.

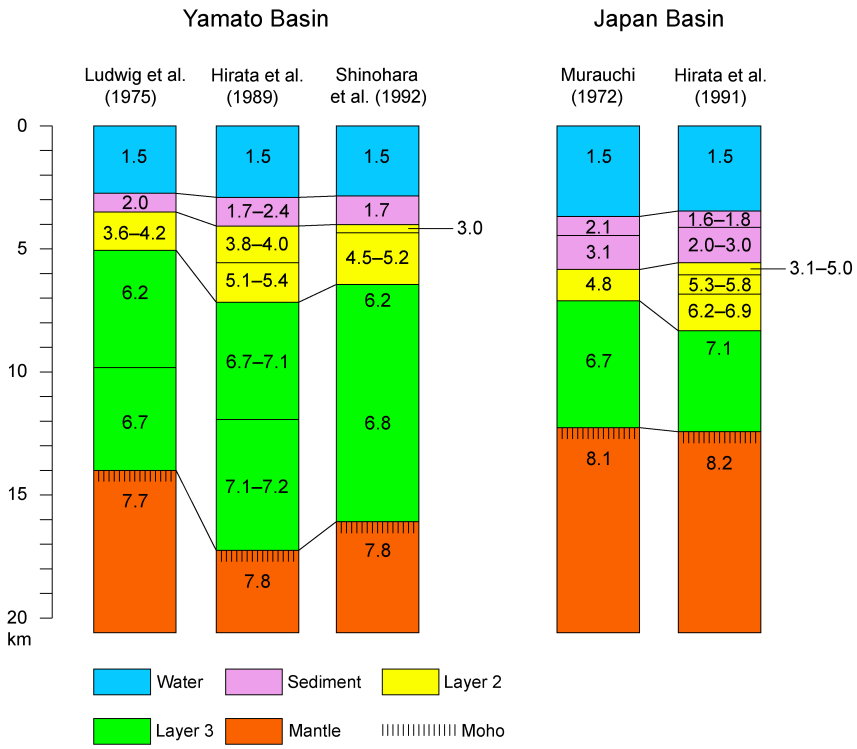


Figure 2.3. Crustal structure of Yamato and Japan Basins in the Sea of Japan. Numbers in the coloured rectangles denote P-wave velocity in km/s (redrawn and modified after Park et al., 1996; Chough et al., 2000).

2.4.3 Site 794

Tectonics

The tectonic setting in the vicinity of Site 794 is discussed here following Shipboard Scientific Party (1990a). Site 794 is at the northeastern margin of the Yamato Basin

near the transition from the continental crust of the Yamato Basin to the oceanic crust of Japan Basin and at the axial zone of the Yamato Basin. The site lies approximately 50 km west of the most active tectonic belt in the Sea of Japan (Fig. 2.4). This belt extends along the eastern shelf and slope of Hokkaido and northern Honshu and is characterised by a series of north-trending faults and folds, by linear ridge-basin morphology, and by shallow seismicity (Fukao and Furamoto, 1975; Seno and Eguchi, 1983; Tamaki and Honza, 1985; Tamaki, 1988; Shipboard Scientific Party, 1990a). Based on single-channel and multi-channel seismic data, many of the faults within this zone are thrust or reverse faults with moderate to steep, east or west dips. A number of these faults are coincident with seafloor escarpments and ridge flanks (Shipboard Scientific Party, 1990a). An eastward-dipping thrust fault is situated 50 km east of Site 794 (Fig. 2.4). The central Japan Sea earthquake of magnitude 7.7 in 1983 occurred in association with this fault (Tamaki and Honza, 1985). The focal mechanism solution suggests that this earthquake was compressional with an axis of N70°W (Ishikawa et al., 1984). Another earthquake of magnitude 6.9 occurred in 1964 just near this thrust fault. This earthquake was also compressional with an axis of N59°W (Fukao and Furamoto, 1975). The focal mechanism solutions for these earthquakes demonstrated that the failures occurred on the same east-dipping fault plane at depths of 14–19 km (Ichikawa, 1971). Occurrence of these earthquakes indicates that the present-day compressional stress field trends east-west to northwest-southeast in this part of the Japan Sea. Faults are also present on the eastern Yamato Rise about 75 km west of Site 794. The faults in this area are mostly steep normal faults involving acoustic basement. The principal

activity on these faults occurred prior to the Late Miocene during rifting of this part of the Japan Sea. North and south of Site 794, and also in the immediate vicinity of the site, structural disruption of acoustic basement and the overlying sedimentary pile is minimal.

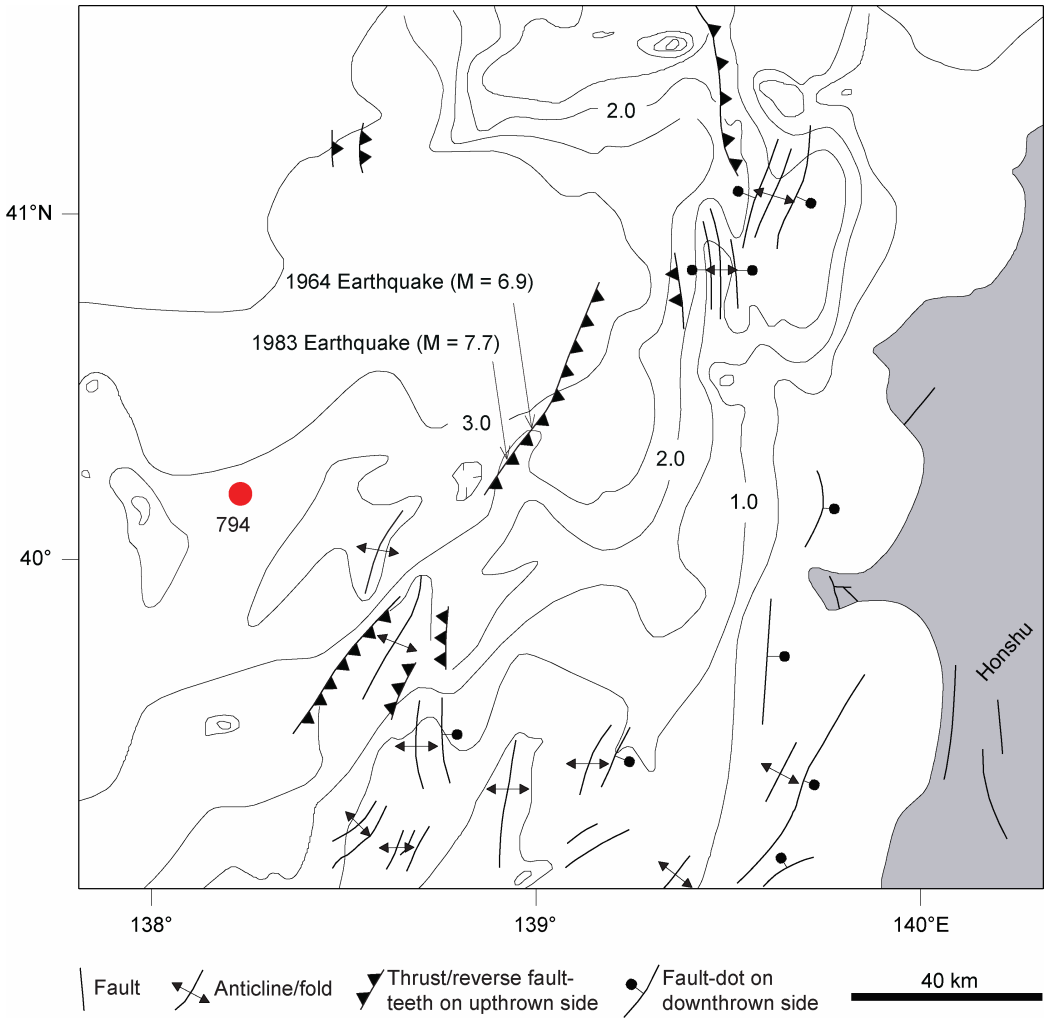


Figure 2.4. Map of the eastern Japan Sea tectonic zone in the vicinity of Well 794 area showing recognised faults, fold axes, and recent earthquake epicentres (redrawn after Shipboard Scientific Party, 1990a). Bathymetric contours are in kilometres.

Lithologic units

The sedimentary section that overlies the Yamato Basin dolerite sill basement at Site 794 is ~544 m thick. The section together with the first 110 m of the basement sum up to the 654 m thick sub-seafloor pile that was penetrated at this site (Fig. 2.5). The sedimentary section was cored in Holes 794A and 794B drilling to the depths of 351.3 and 549 mbsf, respectively. The section consists mainly of fine-grained hemipelagic sediments of Pleistocene to Middle Miocene age. The lithological composition of the five stratigraphic units penetrated by Site 794 (from top to base of the section) consists of: 92.3 m of clay and silty clay with a significant admixture of vitric ash (Unit I), 201.2 m of diatom ooze and clay (Unit II), 198.2 m of clay or claystone; diatoms are rare or absent, and silica in the unit consists mainly of opal-CT (Unit III), 28.9 m of tuff, lapilli tuff, and claystone (Unit IV), 23.7 m of claystone, silty claystone, and calcareous claystone, with minor glauconitic claystone and altered vitric tuff (Unit V). The stratigraphic Units II and III are each further divided into two subunits (Fig. 2.5) (Refer to Shipboard Scientific Party (1990a) for a complete review of the lithology of the sediments encountered at Site 794). The age of these units has been derived from the ODP 794 initial report (Shipboard Scientific Party, 1990a). Sediment ages for the depositional Units I and II were determined by ODP based on the age model of diatom zones. In addition, an excellent palaeo-magnetic reversal record is present up to depth of 150 mbsf (~5 Ma), which leads to accurate time marks from the Pleistocene to Pliocene. In Unit III, sporadically-occurred foraminifers, nannofossils, and radiolarians confirm diatom dates, but because of poor preservation they do not add precision. Below Unit

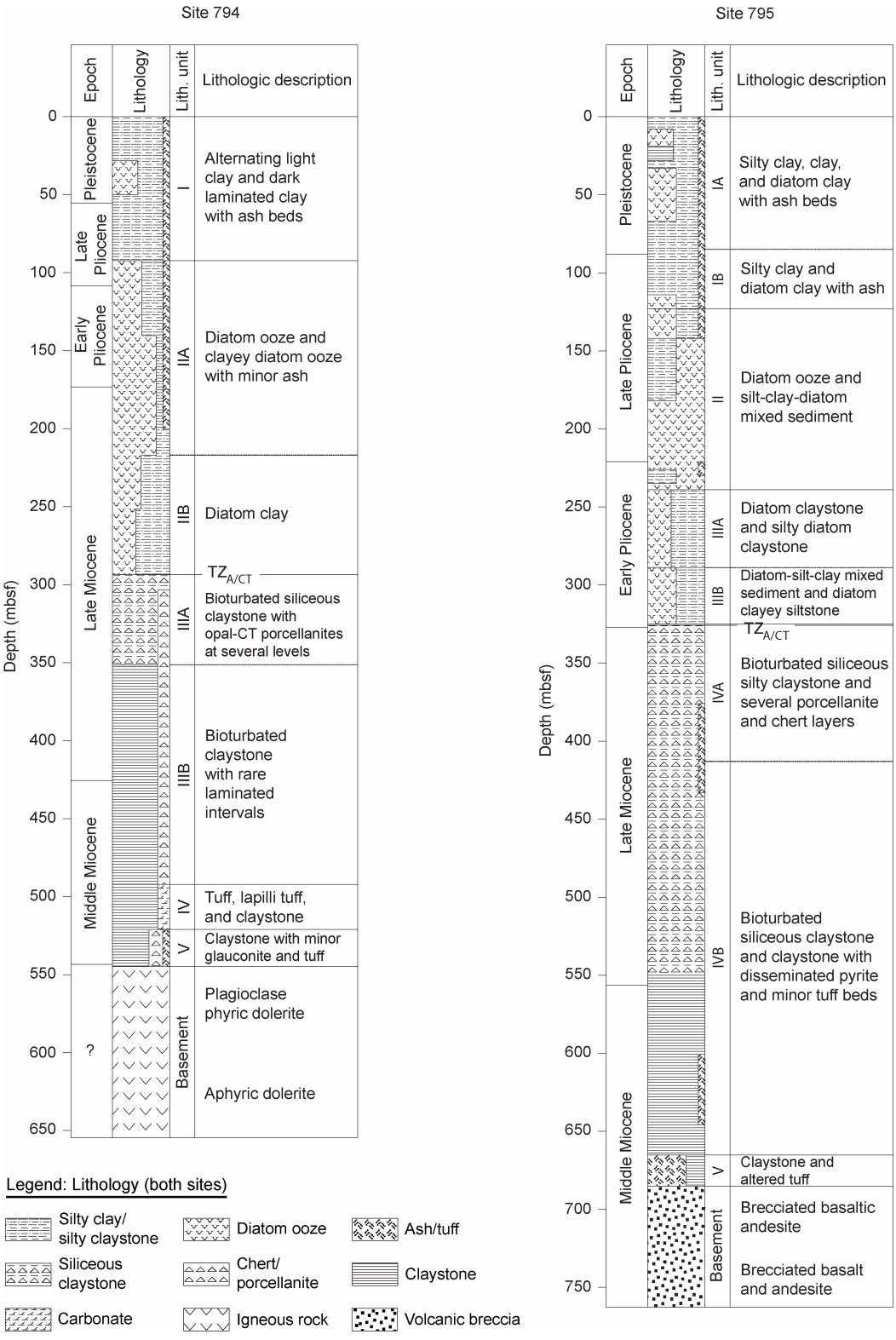


Figure 2.5. Stratigraphic column for Sites 794 and 795 (redrawn from Shipboard Scientific Party, 1990a, b).

III, only calcareous nannofossils and planktonic foraminifers provide age control. The depositional section at Site 794 is clearly intact with no overburden removal, implying the Middle Miocene subsidence of the back-arc rifted continental arcs to lower-middle bathyal depths, and the prevailing deposition of hemipelagic silicious overburden through the Early Pliocene.

2.5 Japan Basin

2.5.1 Geological and tectonic setting

According to Celaya and McCabe (1987), the Japan Basin was initially formed under a rifting process that was followed by the back-arc spreading and rotation of the Yamato Basin in the Early Miocene, in response to an oceanic arc collision in western Hokkaido. This is in accordance with the idea of a two-stage opening with the creation of the Japan Basin during the first stage and the Yamato Basin during the last stages as suggested by Hilde and Wageman (1975), Kobayashi and Isezaki (1976), Kobayashi (1983), and Lallemand and Jolivet (1986). Accordingly, the main opening at least of the Japan Basin during the Upper Oligocene/Lower Miocene was followed by the back-arc spreading and opening of the Yamato Basin (second opening) which may be associated with a small amount of rotation of southwest Japan during Middle Miocene (Fig. 2.6). The rhombohedral shape of the Japan Basin and the structure of its margins support the idea of rifting of a pull-apart basin accommodated along two large right-lateral shear zones (fault zones), east of Korea and west of northeast Japan (Oga-Tartary Fault), during the Early Eo-Oligocene (Lallemand and Jolivet, 1986). The rifting was followed, during the Upper

Oligocene/Lower Miocene, by active tectonism along the eastern and western margins and the main opening of the Japan Basin as a mega pull-apart event. The right-lateral movement is very important on both sides of the Japan Basin. The motion of the whole of Japan has been mainly southward along the East Korean Fault and the northeastern fault line, creating the Japan Basin with its rhombohedral shape (Fig. 2.6).

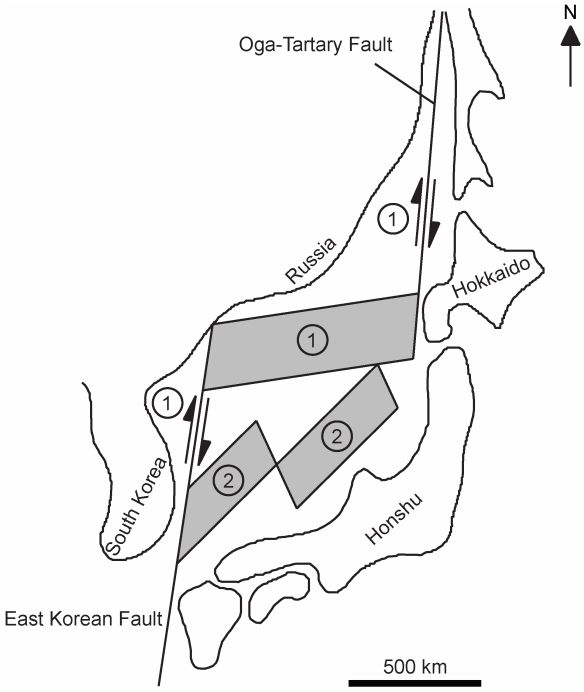


Figure 2.6. Schematic model of opening of the Japan Sea. 1 = first opening, pull-apart mechanism; 2 = second opening, back-arc spreading (redrawn and modified after Lallemand and Jolivet, 1986).

2.5.2 Crustal structure

Like that of the Yamato Basin, the crustal structure of the deep Japan Basin (Fig.

2.3) has been principally constrained with seismic refraction data (e.g., Murauchi, 1972; Gnibidenko, 1979; Hirata et al., 1991; Park et al., 1996). The upper crust (Layer 2), mainly composed of highly altered and vesicular basaltic andesite and basalt occurs at about 6 km below sea level (refer to Shipboard Scientific Party (1990b) for inferring the lithology of upper crust in the Japan Basin based on the composition of basement rocks). Layer 2 is 1 to ~2.5 km thick with velocities in the range 3.1–6.9 km/s. Capping this sequence is Layer 1, the sedimentary section which was continuously cored at Site 795. This layer varies from 0 to 3 km thick (Shipboard Scientific Party, 1990b) with velocities in the range between 1.6 and 3.1 km/s. Layer 3 (assumed lower crust) is 4 to ~5 km thick and has an average velocity of 6.9 km/s. The crustal thickness (upper + lower crusts) in the Japan Basin (~6–7 km, according to Hirata et al., 1991) lies within the range of oceanic crust (5–10 km), and is obviously lower than that in the Yamato Basin (10.5 to ~13 km, according to Ludwig et al., 1975; Hirata et al., 1989).

2.5.3 Site 795

Tectonics

Here, the tectonic setting in the vicinity of Site 795 is discussed following Shipboard Scientific Party (1990b). The linear complex of north-trending ridges, basins, and escarpments lying east of the site are part of an active tectonic zone which extends along the western-northwestern part of Japan (Tamaki and Honza, 1985). Thrust/reverse faults coincide with many of these escarpments, including the one just east of the site where fold axes are generally parallel to the ridges (Fig. 2.7). The

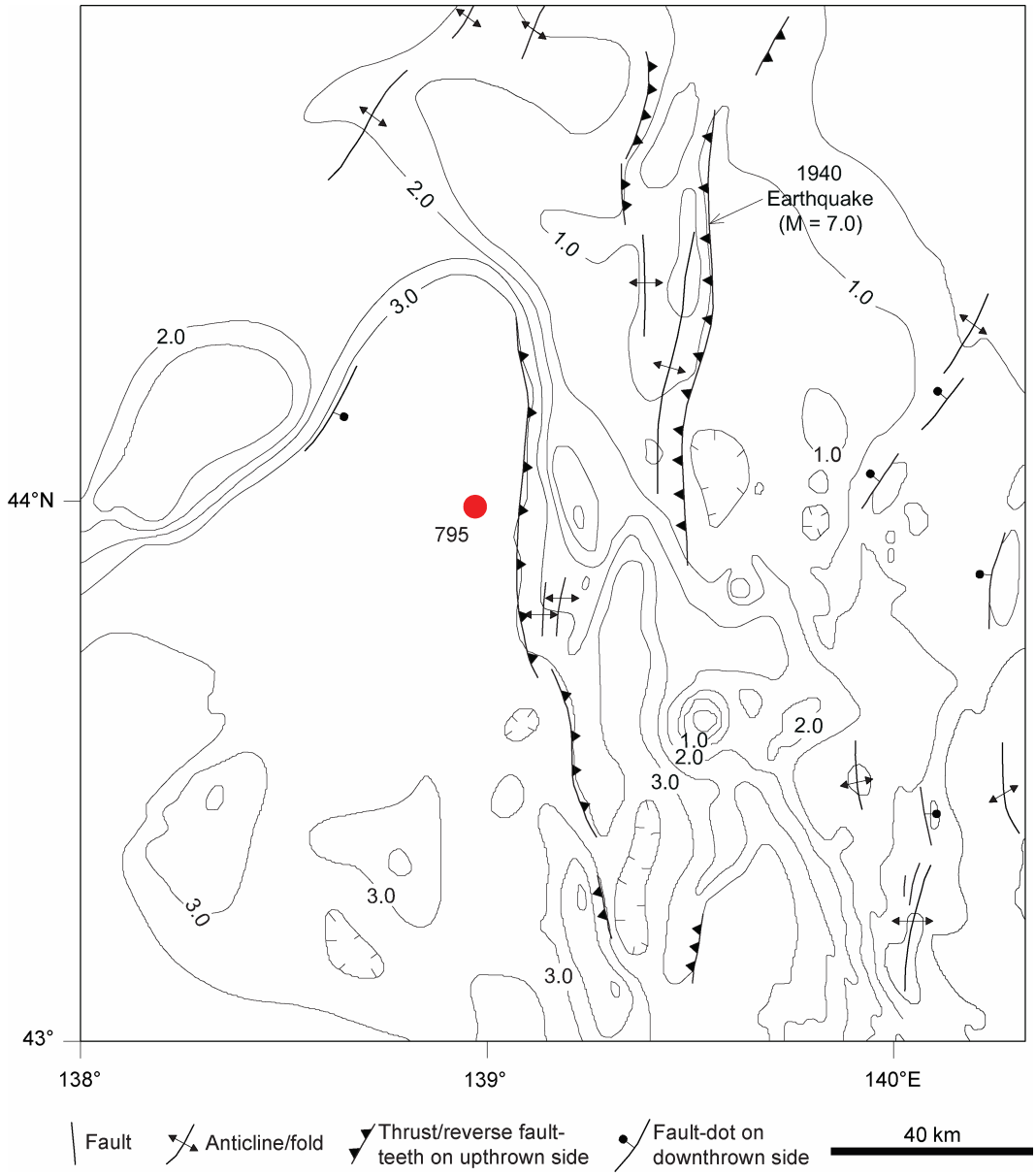


Figure 2.7. Tectonic map of area surrounding Well 795 showing recognised faults, fold axes, and the 1940 earthquake epicentre (M = 7.0) (redrawn after Shipboard Scientific Party, 1990b). Bathymetric contours are in kilometres.

most striking structural element in the area is an escarpment that begins at southwestern Hokkaido and extends to the northwest, finally merging with the steep north north-south escarpment which lies east and northeast of Site 795. In general,

the topographic and structural patterns east of Site 795 suggest an area of compression containing steep reverse faults, some of which cut the entire lithosphere (Shipboard Scientific Party, 1990b). Large compressional earthquakes occurred in the tectonic zone east of Site 795 which, as counterparts to the earthquakes in east of Site 794, support the presence of such active tectonism. Figure 2.7 shows the location of the epicentre of a magnitude 7.0 event (occurred in 1940) that lies about 70 km northeast of Site 795. The focal depth was at 33 km, slightly greater than the estimated thickness of the lithosphere in the Sea of Japan (Abe and Kanamori, 1970). The focal mechanism solution shows that this earthquake occurred on a north-south thrust or reverse fault (Fukao and Furumoto, 1975) cutting through the entire lithosphere. North, west, and south of Site 795, however, the structural style is less dramatic. The rise and highs south of the site have very little sedimentary cover suggesting that they have stood as high blocks since the Miocene. Their steep flanks appear to be normal faults which formed during rifting of this part of the Sea of Japan (Shipboard Scientific Party, 1990b).

Lithologic units

The sedimentary succession that overlies the acoustic basement of the Japan Basin at Site 795 is 685 m thick (Fig. 2.5). The succession was cored in Hole 795A, drilled to the depth of 365.9 mbsf. Hole 795B also drills the depositional section to the depth of 685 mbsf, and continues to penetrate below the sedimentary section in the basement to 762.2 mbsf. The sedimentary section consists of mostly fine-grained hemipelagic diatomaceous and terrigenous sediments of Middle Miocene to

Quaternary age. The lithological composition of the 5 lithostratigraphic units penetrated at Site 795 (from top to base of the section) consists of: 123 m of silty clay, clay, diatomaceous clay, and minor ash (Unit I), 116 m of diatom ooze, diatom silty clay, and diatom mixed sediment (Unit II), 86 m of silty diatom claystone and diatom-clay-silt mixed sediment (Unit III), 340 m of siliceous claystone and silty siliceous claystone, biogenic silica is rare or absent, opal-CT is permanently the dominant silica phase (Unit IV), 20 m of claystone and tuff (Unit V). Units I, III, and IV are each further subdivided into two subunits (Fig. 2.5) (Refer to Shipboard Scientific Party (1990b) for a complete review of the lithology of the sediments encountered at Site 795). The ODP 795 initial report (Shipboard Scientific Party, 1990b) was the source from which the age of these stratigraphic units has been derived. According to Shipboard Scientific Party (1990b), sediment ages were determined by diatom zones and palaeo-magnetic reversals in Unit I, and by diatoms in Units II and III. Units IV and V were dated by ODP using sporadic diatoms and sparse controls from foraminifers, radiolarians, and calcareous nannofossils. The depositional section of Site 795 more or less resembles that in Site 794. Its Neogene section, based on the study of benthonic foraminifers, was deposited in mid-bathyal and deeper waters, suggesting that water depths probably increased up-section (Shipboard Scientific Party, 1990b). Nevertheless, the Quaternary succession in Site 795 is slightly coarser-grained than the same section in Site 794. These relationships are consistent with the more proximal position to terrestrial sediment sources and the more isolated basinal setting of Site 795.

Chapter 3

Data and methods

The data used for this research work come from the two following sources:

- Interrogation of freely-accessible ODP and DSDP scientific databanks for the borehole sites hosting the $TZ_{A/CT}$
- The results of analysis of discrete core samples from the ODP Sites 794 and 795 in the Sea of Japan

These datasets are utilised to: 1) evaluate the thermodynamic status of silica diagenesis, 2) evaluate controls on abrupt petrophysical changes during silica diagenesis, 3) evaluate the role of bottom-water temperature in controlling the rate of biogenic silica early diagenesis, and 4) evaluate the temperature-time relationships in later silica diagenesis.

While the data and specific methodologies employed for every result chapter are described in the relevant sections (i.e., Chapters 4–7), here in this chapter the specifications of the dataset used in this thesis and the methods based on which these data have been produced and/or analysed are described in detail.

3.1 ODP- and DSDP-derived data

3.1.1 Interstitial-water geochemical data

The pore-water chemical data used in the present work include the concentrations of major ions and primary indicators that were measured by ODP in the sediment pore waters from Sites 794 and 795. The shipboard inorganic geochemistry programme for Sites 794 and 795 was focused exclusively on interstitial-water analysis. The pore-water concentrations of major ions, such as silica, lithium, potassium, calcium, magnesium, and strontium, and primary chemical variables, including pH, salinity, sodium, chloride, alkalinity, sulphate, ammonia, and phosphate at different depths were measured (Shipboard Scientific Party, 1990a, b). These data are available through open access to both the ODP initial reports and the IODP databank. The interstitial-water chemistry profiles for these ions and other aforementioned constituents are good in quality because of the high resolution of their sampling intervals (between 10–20 m).

Below, the pore-water sampling technique and chemical measurement methods used by the ODP are briefly described mainly following the ODP technical note of Rabinowitz and Garrison (1985).

3.1.1.1 Interstitial-water sampling

A new version of the Barnes *in situ* pore-water sampler (BW) has been used by the ODP for sampling. The instrument is adapted for open-hole fluid sampling as well as *in situ* filtration from sediments at the bottom of the hole. The tool is lowered down

the drill pipe on the sandline, and the filter probe extends more than one metre beyond the end of the drill bit. Interstitial-water core samples are placed in a Manheim squeezer (Manheim and Sayles, 1974). The squeezer is then placed in one of two Carver hydraulic presses that are capable of 25 tons constant pressure, and squeezed until a sufficient quantity of water is extracted, usually ~30 ml from a 500 cm^3 sample. The resultant pore water is filtered through a 0.45 μm filter.

3.1.1.2 Interstitial-water chemical analysis

The extracted water sample was first titrated for pH and alkalinity determination. This analysis was automated by interfacing a Metrohm 665 Dosimat autotitrator, Metrohm 605 pH meter, and an IBM PCAT-clone. Titrations of calcium, magnesium, and chlorinity can also be performed using a Metrohm 655 Dosimat, which is capable of dispensing titrant in microlitre amounts (Rabinowitz et al., 1990).

Colorimetric measurements of ionic concentrations in pore-water samples was conducted on the Bausch & Lomb Model 1001 Spectrophotometer. In a wavelength range from 190 to 950 nm, analyses are made of concentrations of silica, ammonia, phosphate, and other common pore-water constituents. For a complete review of the analytical steps for determining the ionic concentrations, see Gieskes et al. (1991).

Measurements of salinity were made with a temperature-compensated refractometer. Several drops of pore water were used for the analysis, with a resultant precision of

±1%.

A Dionex Ion Chromatograph (IC) was used by the ODP primarily for sulfate analyses of pore water. The IC was microprocessor-controlled and attached to the LAS (Lab Automation System). The shipboard IC had three columns: one for anions, a second for monovalent cations, and a third for divalent cations. The amounts of lithium, sulfate, calcium, magnesium, sodium, potassium, and strontium were measured, with the potential for chlorinity, nitrate, and phosphate measurements in interstitial water squeezed from whole-round core samples.

3.1.2 Physical properties data

The ODP- and DSDP-measured physical properties used in this study consist of P-wave velocity measurements, index properties (including wet-bulk density, dry-bulk density, grain density, porosity, water content, and void ratio), GRAPE (Gamma Ray Attenuation Porosity Evaluator) density, and resistivity. These data are available for most of the ODP and DSDP wells investigated in this research through both ODP/DSDP initial reports and IODP database. Due to their small sampling spacings, the quality of physical properties profiles are high. To allow cross-correlation of the results, index properties and electrical resistivity were obtained once per core section (each section is 1.5 m long) usually at 100 cm from the top of the core (Shipboard Scientific Party, 1990b). P-wave velocity was measured using a sampling spacing of 5 cm (4-s period), and the GRAPE density every 5 cm (5-s period) (modified after Blum, 1997).

Below, the methodology of ODP for measuring the physical properties is briefly explained by following the ODP technical note of Blum (1997).

3.1.2.1 Physical properties measurements

After cores arrive on deck they are cut into 1.5-m-long sections and stored in racks for temperature equilibration. The first measurement station is the multi-sensor track (MST), where the whole-core sections are loaded on a motorised core conveyor "boat" for the automatic measurement of GRAPE density, compressional (P-)wave velocity, magnetic susceptibility, and natural gamma radiation. Next, the cores are split into two half-cores designated as archive-half cores and working-half cores (Fig. 3.1). As shown in Figure 3.1, the relative core orientation conventions are established to place physical properties measurements in a geographic reference frame using absolute core orientation measurements when the core is cut. The archive-half cores are preserved in a pristine condition, whereas the working-half cores are available for measurements that physically disturb parts of the cores and for the removal of specimens for shipboard as well as shore-based studies. The working-half core is used for the measurement of P-wave velocity by using probes that are inserted into the soft sediment, shear strength by inserting a miniaturised vane into the sediment, similar strength measurements with the hand-held Torvane and penetrometers, and resistivity measurements using a component analyser.

For the final physical properties measurement, specimens are extracted from the working-half core to determine water content and average mineral density (moisture

and density (MAD) station). At the MAD station, the following are measured:

- wet-bulk mass and dry mass of the specimen (for moisture content and density)
- volume of dry (and optionally wet-bulk) specimen using gas pycnometry.

From these measurements, basic phase relationships such as porosity, bulk density, grain density, dry density, and void ratio are then calculated.

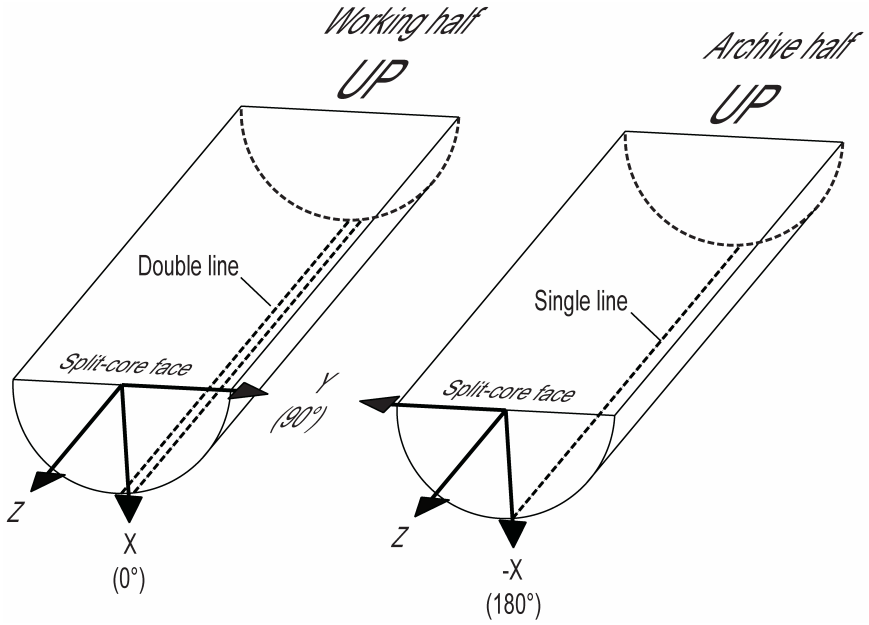


Figure 3.1. Schematic presentation of a core split into two half-cores named archive-half core and working-half core. Also shown are the relative orientation conventions (redrawn from Blum, 1997).

3.1.3 Other parameters

Thermal parameters of the ODP and DSDP sites investigated under remit of this

project as well as lithology, age, and accumulation rate of the sediment hosting the $TZ_{A/CT}$ at these sites, and the $TZ_{A/CT}$ characteristics were extracted from or computed based on the information from the ODP and DSDP initial reports and IODP sources. The methodologies employed by the ODP and DSDP to evaluate these parameters have been described in details in the ODP technical notes (e.g., see Mazzullo and Graham, 1988; Fisher and Becker, 1993; Blum, 1997). In Chapter 7, a comprehensive review will be made on the ODP and DSDP methods for measuring the age and temperature of the sediments regarding the functional role of these two parameters in the context of the present study.

3.2 Core samples shipped by IODP

A significant part of the present project relies on the results of different analyses conducted on the sediment core samples obtained from Sites 794 and 795 for the purpose of this study. In total, 67 deep-sea core samples (37 and 30 samples from Sites 794 and 795, respectively) were requested from the IODP for performing three sets of analyses, including X-ray diffraction (XRD), scanning electron microscopy (SEM), and smear slides. The initial selection of these samples obtained for the present study was on the basis of lithological characteristics and XRD data already acquired by the ODP for these two sites. The samples were obtained from both opal-A- and opal-CT-dominated sediment intervals. Tables 3.1 and 3.2 present the stratigraphic position, the ODP-assigned identification number, and the lithologic composition of acquired samples.

Table 3.1. Stratigraphic position, identification number, age, depth, and lithology of the samples acquired from Site 794.

Lithologic unit (based on Fig. 2.5 in Chapter 2)	Core, section, interval, cm	Age	Depth, mbsf	Lithological composition
IIA	127-794A-11H-6, 37–38 *	Late Pliocene	100.17	Clayey diatom ooze
	127-794A-17X-1, 48–49 *	Early Pliocene	149.98	Diatom ooze
	127-794A-22X-2, 113–114 *	Late Miocene	200.13	Clayey diatom ooze
IIB	127-794A-27X-3, 80–81 *	Late Miocene	249.8	Diatom clay
	127-794A-31X-5, 50–51	Late Miocene	291.1	Diatom-bearing clay
	127-794A-31X-6, 90–91 *	Late Miocene	293	Diatomaceous clay
IIIA	127-794A-32X-1, 22–23	Late Miocene	293.72	Clay
	127-794A-32X-2, 5–6 *	Late Miocene	295.05	Clay
	127-794A-32X-3, 46–47	Late Miocene	296.96	Clay
	127-794A-32X-CC, 34–35	Late Miocene	298.45	Clay
	127-794A-33X-1, 0–1 *	Late Miocene	303.3	Claystone
	127-794A-33X-1, 5–6	Late Miocene	303.35	Claystone
	127-794A-33X-1, 10–11	Late Miocene	303.4	Claystone
	127-794A-33X-1, 35–36	Late Miocene	303.65	Pyrite-bearing clay
	127-794A-33X-1, 70–71	Late Miocene	304	Pyrite-bearing clay
	127-794A-33X-1, 104–105	Late Miocene	304.34	Pyrite-bearing clay
	127-794A-33X-2, 9–10	Late Miocene	304.89	Claystone
	127-794A-33X-3, 68–69	Late Miocene	306.98	Claystone
	127-794A-33X-4, 119–120 *	Late Miocene	308.99	Clay with pyrite
	127-794A-33X-6, 20–21	Late Miocene	311	Semi-lithified Clay
	127-794A-34X-1, 40–41 *	Late Miocene	313	Clay
	127-794A-34X-2, 90–91	Late Miocene	315	Pyrite-bearing claystone
	127-794A-35X-1, 5–6 *	Late Miocene	322.25	Clay
	127-794A-35X-2, 30–31	Late Miocene	324	Clay
	127-794A-35X-3, 80–81	Late Miocene	326	Sapropel-bearing clay
	127-794A-35X-4, 130–131 *	Late Miocene	328	Sapropel-bearing clay
	127-794A-35X-6, 38–39 *	Late Miocene	330.08	Sapropelic clay
	127-794A-36X-1, 21–22	Late Miocene	332.11	Sapropel-bearing clay
	127-794A-36X-2, 55–56 *	Late Miocene	333.95	Clay
	127-794A-36X-3, 110–111 *	Late Miocene	336	Clay
	127-794A-36X-5, 54–55	Late Miocene	338.44	Clay
	127-794A-37X-1, 0–1	Late Miocene	341.6	Pyrite-bearing ashy claystone
	127-794A-37X-2, 19–20	Late Miocene	343.29	Claystone

Table 3.1. Continued.

IIIA	127-794A-37X-3, 40–41	Late Miocene	345	Claystone
	127-794A-37X-3, 140–141	Late Miocene	346	Claystone
	127-794A-37X-CC, 30–31	Late Miocene	346.63	Claystone
	127-794B-6R-CC, 5–6	Late Miocene	347.85	Claystone

* Samples selected for SEM analysis.

Table 3.2. Stratigraphic position, identification number, age, depth, and lithology of the samples acquired from Site 795.

Lithologic unit (based on Fig. 2.5 in Chapter 2)	**Core, section, interval, cm**	**Age**	**Depth, mbsf**	**Lithological composition**
IA	127-795A-1H-1, 124–125	Pleistocene	1.24	Ashy diatom silty clay
	127-795A-6H-1, 91–92 *	Pleistocene	48.21	Locally diatom-rich silty clay
IB	127-795A-13H-4, 43–44 *	Late Pliocene	118.73	Diatom silty clay
II	127-795A-16H-4, 101–102 *	Late Pliocene	147.81	Diatom ooze
	127-795A-22X-5, 128–129 *	Early Pliocene	198.48	Diatom ooze
IIIA	127-795A-27X-1, 34–35 *	Early Pliocene	240.24	Diatom claystone
	127-795A-30X-5, 10–11 *	Early Pliocene	275.4	Silty diatom clay
IIIB	127-795A-34X-1, 100–101	Early Pliocene	308.9	Diatom silt clay mixed sediment
	127-795A-34X-3, 100–101	Early Pliocene	311.9	Diatom clayey siltstone
	127-795A-34X-4, 105–106	Early Pliocene	313.45	Diatom clayey siltstone
	127-795A-34X-6, 101–102	Early Pliocene	316.41	Diatom clayey siltstone
	127-795A-35X-1, 101–102	Early Pliocene	318.61	Diatom clayey siltstone
	127-795A-35X-3, 100–101 *	Early Pliocene	321.6	Clayey silt diatom mixed sediment
	127-795A-35X-5, 84–85	Early Pliocene	324.44	Diatom clayey siltstone
	127-795A-35X-5, 128–129	Early Pliocene	324.88	Diatom clayey siltstone
IVA	127-795A-35X-6, 84–85	Early Pliocene	325.94	Siliceous silty claystone
	127-795A-35X-6, 136–137 *	Late Miocene	326.46	Siliceous silty claystone
	127-795A-35X-CC, 14–15	Late Miocene	326.74	Siliceous silty claystone
	127-795A-36X-1, 12–13	Late Miocene	327.32	Opal-CT chert
	127-795A-36X-CC, 36–37 *	Late Miocene	327.78	Opal-CT chert
	127-795A-37X-1, 0–1	Late Miocene	336.9	Siliceous silty claystone
	127-795A-37X-1, 47–48 *	Late Miocene	337.37	Siliceous silty claystone
	127-795A-37X-1, 101–102	Late Miocene	337.91	Siliceous silty claystone

Table 3.2. Continued.

IVA	127-795A-37X-1, 133–134 *	Late Miocene	338.23	Siliceous silty claystone
	127-795A-37X-CC, 35–36	Late Miocene	338.68	Siliceous silty claystone
	127-795A-38X-CC, 1–2 *	Late Miocene	346.61	Siliceous claystone
	127-795A-39X-CC, 0–1 *	Late Miocene	356.2	Siliceous claystone
	127-795B-1R-1, 18–19 *	Late Miocene	365.38	Silty siliceous claystone
IVB	127-795B-6R-1, 80–81 *	Late Miocene	414.6	Siliceous claystone
	127-795B-11R-3, 112–113	Late Miocene	465.82	Siliceous claystone

* Samples selected for SEM analysis.

The core samples shipped by the IODP are each a ~20 cm^3 slab (5 cm long by 2 cm wide by 2 cm deep (thickness); Fig. 3.2). These discrete samples are semi-consolidated in nature and, except for a few of them from the shallower part of Sites 794 and 795, display excellent fabric preservation.

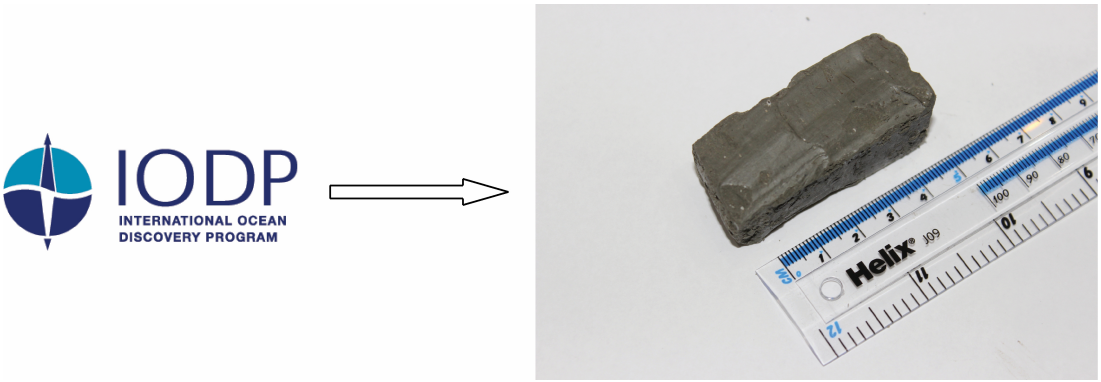


Figure 3.2. An example of the ODP core sample slabs shipped by the IODP.

3.2.1 X-ray diffraction

3.2.1.1 Sample preparation

A small fraction (1 gram) was carefully split from each core slab and oven-dried at

40 °C for 4 days to make certain that the sediment lacks any moisture and drying did not influence mineralogical transformations. The dried sample was ground to a fine powder (typically to produce particle sizes of less than 10 μm) using an agate mortar and pestle (Fig. 3.3A). With the aid of a powder sample preparation kit (Fig. 3.3B), the fine powder was then packed into a ring-shaped sample container (Fig. 3.3C) with the internal diameter and the thickness of the ring being 16 and 2.4 mm, respectively. Care was taken to create a flat upper surface for the sample to minimise sample height displacement error and to achieve a random distribution of lattice orientations.

3.2.1.2 Sample analysis

The powdered sediments contained in the sample holders were put in a sample changer with 15 positions for 15 sample holders (Fig. 3.3D) and analysed using a PANalytical Empyrean Series 2 powder diffractometer housed by the Department of Earth Sciences, University of Oxford (Fig. 3.3E). The Empyrean is configured for a range of diffraction experiments in the theta-theta geometry, and operates with a cobalt X-ray source (Co-Kα) having a step rate of 0.017°/s over a 2θ ranging from 5 to 85°. The priority of analysing the powdered sample with the Empyrean instrument is that the sample is recoverable after analysis. So, it can be returned to the sample bottle (glass vial) for future use.

Phase identification from the powder diffraction data acquired from the samples was performed using the analytical software Match!, Mac version. The software

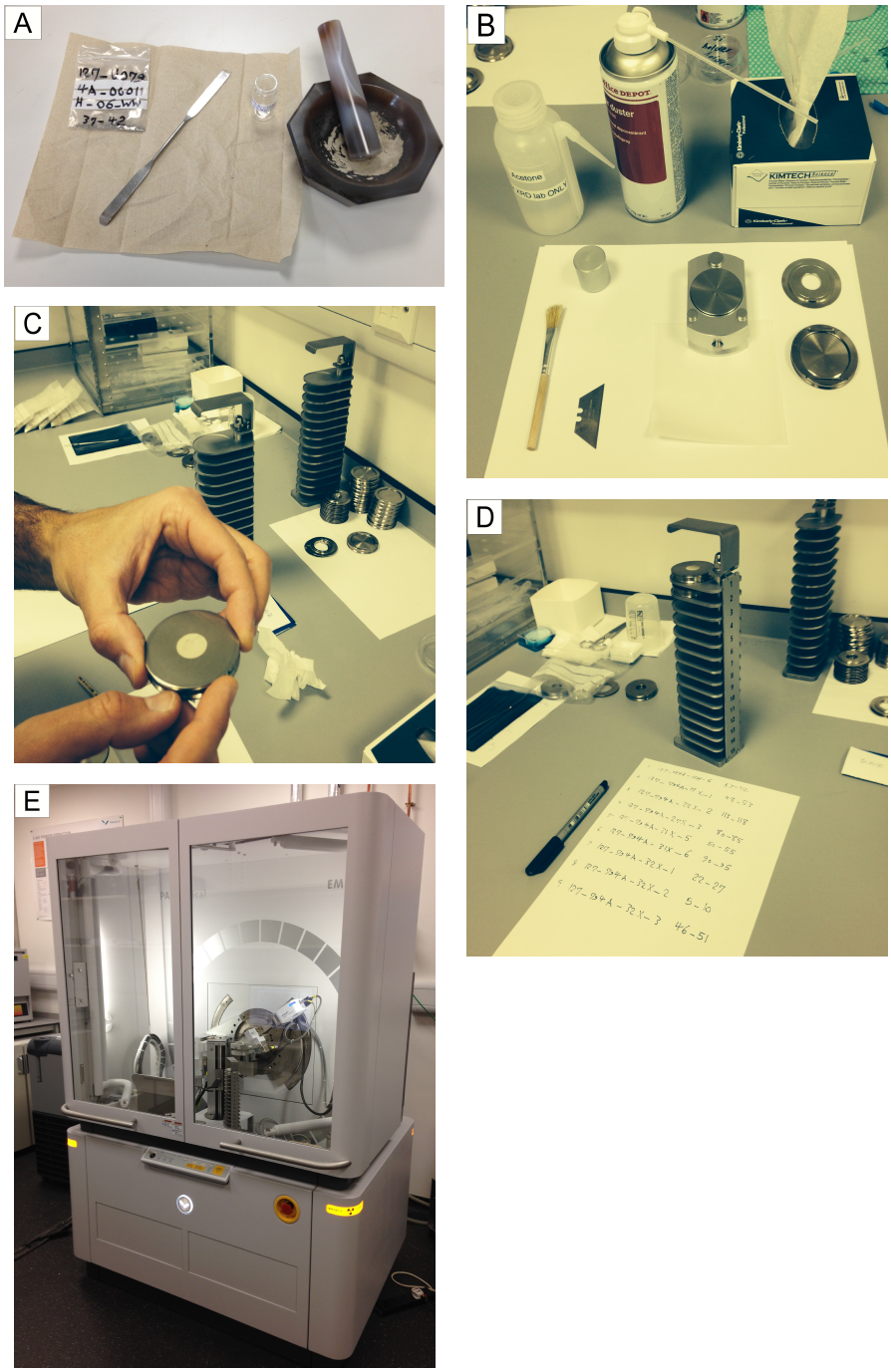


Figure 3.3. A) Agate mortar and pestle used for grinding the sediments from Sites 794 and 795 to a fine powder. The powdered sample is kept in a glass vial; B) Powder sample preparation kit used for packing the powdered sediment into a sample holder. The kit is comprised of a sample preparation table (onto which the

sample holder ring is clamped), a powder press block or piston, a dusting brush, and a stanley knife blade. Compressed air duster, acetone, and delicate task wipers are used for cleaning the kit before and after use. Also shown are sample holder bottom and sample holder top; C) The fine powder packed into a ring-shaped sample container; D) Sample changer with 15 sample holder positions; E) The PANalytical Empyrean Series 2 powder diffractometer, Department of Earth Sciences, University of Oxford.

compares the diffraction patterns of selected samples (experimental pattern) to a database containing reference patterns in order to identify the phases which are present. Based on agreement seen between the position and intensity of reference peaks and the experimental curves in the background, the matching phases were determined. This study has used the Reference Intensity Ratio (RIR) method to quantify crystalline components in the sediment samples. The RIR was first suggested by de Wolff and Visser (1964) as a method to place diffraction patterns on a relative-absolute intensity scale (Chung and Smith, 2000). The method scales all diffraction data from sediments containing multiple phases to the diffraction pattern of standard reference materials using a parameter named "scale factor". By convention, corundum (α–Al_2O_3) is used as an optimal international reference material (e.g., de Wolff and Visser, 1964) and the scale factor is calculated as the ratio of the intensity of analyte to the intensity of corundum (i.e., I/I_c). The RIR analysis can only be carried out if all the crystalline phases which have been selected as matching contain I/I_c factors. The method assumes that the weighted amounts of phases present in the sample add up to 100 wt% of the crystalline fraction of the

sediment.

3.2.2 Scanning electron microscopy

29 out of 67 core samples obtained from the IODP (14 samples from Site 794 and 15 from Site 795) were selected for preparation of resin-impregnated polished blocks for SEM analysis (samples marked by asterisk in Tables 3.1 and 3.2).

3.2.2.1 Sample preparation

A 1-cm-thick slab was sub-sampled from each of the semi-lithified core samples selected for preparation of resin-impregnated polished blocks. Since a few samples from the shallower part of Wells 794 and 795 were somewhat friable, a few small pieces of each sample from these depths were used for preparation of a resin block. The sub-sampled slabs were put in cylindrical moulds whose interior had been already lubricated using silicon grease, so that the cured resin block did not stick to the mould (Fig. 3.4A). The sample identification number has been written on the outer wall of the mould using a non-erasable marker pen. The moulds containing samples were put in a Logitech IU 30 vacuum impregnation machine for half a day, helping to dry them out (Fig. 3.4B). Under a fume hood, the samples in the moulds were then submerged in a standard low viscosity Epoxy Resin (e.g., following Kemp et al., 2001) (Fig. 3.4C), in this case Struers EpoFix was used). The samples were returned again into the vacuum impregnation machine for 30 minutes. This helps the epoxy resin solution completely embed the core sample and helps avoid air inclusions in the sediment. The samples were put again under the fume hood and left

there for 24 hr to cure. The hard cylindrical resin blocks were then taken out of the moulds, and the number marked on to them using a diamond scribe and further highlighted using a non-erasable pen. The rough surface of the samples was ground using a diamond grinding wheel and ethanediol until the sample surface was exposed (Fig. 3.4D), the blocks were then cleaned and dried off using task wiper. The resin blocks were then lapped by hand on a glass plate with 14 micron aluminium oxide powder and ethanediol until all scratches were removed from the surface of the sample (Fig. 3.4E). Drying the sample carefully and holding it up to the light will show if scratches are present or not. Once the samples were flat, they were cleaned in the ultrasonic bath with isopropanol (Fig. 3.4F), before the lower base of the cylindrical sample was stuck to a sample holder using hot wax. The sample (the upper base of the cylindrical resin block) was then polished using a polishing cloth (Texmet brand) and 0.25 μm diamond polishing compound lubricated using the Hyprez lubricant fluid (Fig. 3.4G). The polishing can take from 20 to 60 minutes depending on the sample, and the sample surface should become polished and shiny by the end of this process. The block was then taken out of the sample holder and its surface was cleaned using delicate task wipers ready for SEM analysis. It is very important to note that water must not be used instead of ethanediol during any part of this process as due to the fine-grained nature of the sediments it will produce mud during lapping the surface of the polished block.

3.2.2.2 Sample analysis

Before the start of SEM analysis, the resin-impregnated polished blocks were carbon

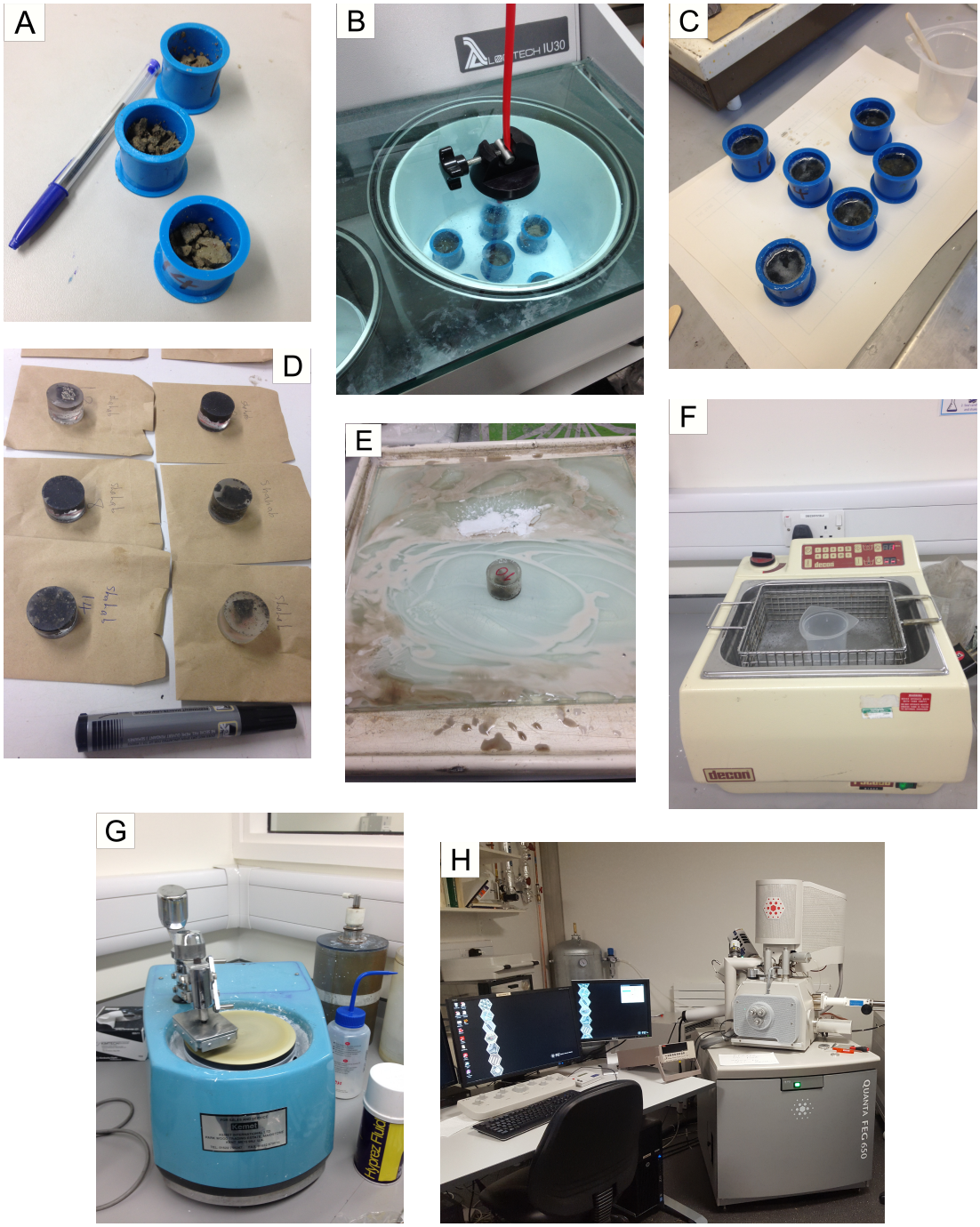


Figure 3.4. Preparation and analysis of resin-impregnated polished blocks from the sediment samples obtained for this study. A) Sediment pieces, sub-sampled from the core samples, put in cylindrical moulds; B) Vacuum impregnation machine used for drying out the samples; C) Samples submerged in Epoxy resin solution; D) The

surface of samples exposed after grinding; E) Lapping of the surface of a resin block for removing the scratches; F) Ultrasonic bath used for cleaning the resin blocks; G) Polishing machine. The resin blocks are polished using a polishing cloth (Texmet brand) covering the surface of rotating disk, and the diamond polishing compound lubricated using a lubricant fluid; H) The FEI Quanta 650 FEG (field emission gun) SEM, resided at the Department of Earth Sciences, University of Oxford, used for analysing the samples.

coated using a HHV Auto 306 vacuum coater. An FEI Quanta 650 FEG scanning electron microscope equipped with a field emission beam and a secondary electron detector (ETD), present in the Department of Earth Sciences, University of Oxford, was used for examining the samples (Fig. 3.4H). This instrument runs in a high vacuum (HV) mode (pressure range 10^{-2}–10^{-4} Pa), allowing for high-resolution imaging of conductive samples in a secondary electron mode. The system can accommodate multiple samples and one of its important accessories is the drift-correction mode for imaging highly-charging samples (the semi-consolidated deep-sea sediments from this study are commonly among the highly-charging samples).

3.2.3 Smear slides

3.2.3.1 Sample preparation

Smear slides were prepared for all the 67 sediment core samples obtained from the ODP Wells 794 and 795 for this study. A 3 gram piece of each core sample was sub-sampled and submerged in the 15 volume % solution of sodium hydrogen carbonate or sodium bicarbonate ($NaHCO_3$) for disaggregation (Fig. 3.5A). The samples were

left on a hotplate at roughly 90–95 °C in the fume-cupboard for 3 days. The samples were then washed with deionised water few times to make sure no sodium bicarbonate is left in the sediment. The suspensions (sediment + a few ml of deionised water) were transferred to glass vials (Fig. 3.5B).

Using liquid dropper pasteur pipettes, 2–3 drops of the suspension kept in the glass vial were deposited on a glass coverslip and 1 drop of non-ionic wetting agent (brand Ilford Ilfotol) was deposited over the sample. The wetting agent helps disaggregate the sediment on the coverslip when drying. The samples were then left on the hotplate, adjusted at the low temperature band (slightly higher than 90–95 °C), for 5 minutes to completely dry out (Fig. 3.5C). 2–3 drops of the optical adhesive (mounting medium) brand DPX were deposited on the dried sample, and the coverslip was then quickly affixed to a glass slide to make a smear slide (Fig. 3.5D). The slides were left on the edge of the hotplate adjusted at the low temperature mark of 2 (~50 °C) for 30 minutes in order for the coverslip to fix over the glass slide and to avoid air bubbles as much as possible. The prepared smear slides were then put on a horizontal surface (a laboratory table) at the standard lab temperature for 24 hr, giving sufficient time for the optical adhesive to completely harden.

The suspension made for preparation of smear slides could also approximate the proportions of major grain-size fractions in the terrigenous texture (being sand, silt, and clay) following the simple method of Marsaglia et al. (2013). It was observed that sand and silt grains rapidly settled from the suspension while it took a long

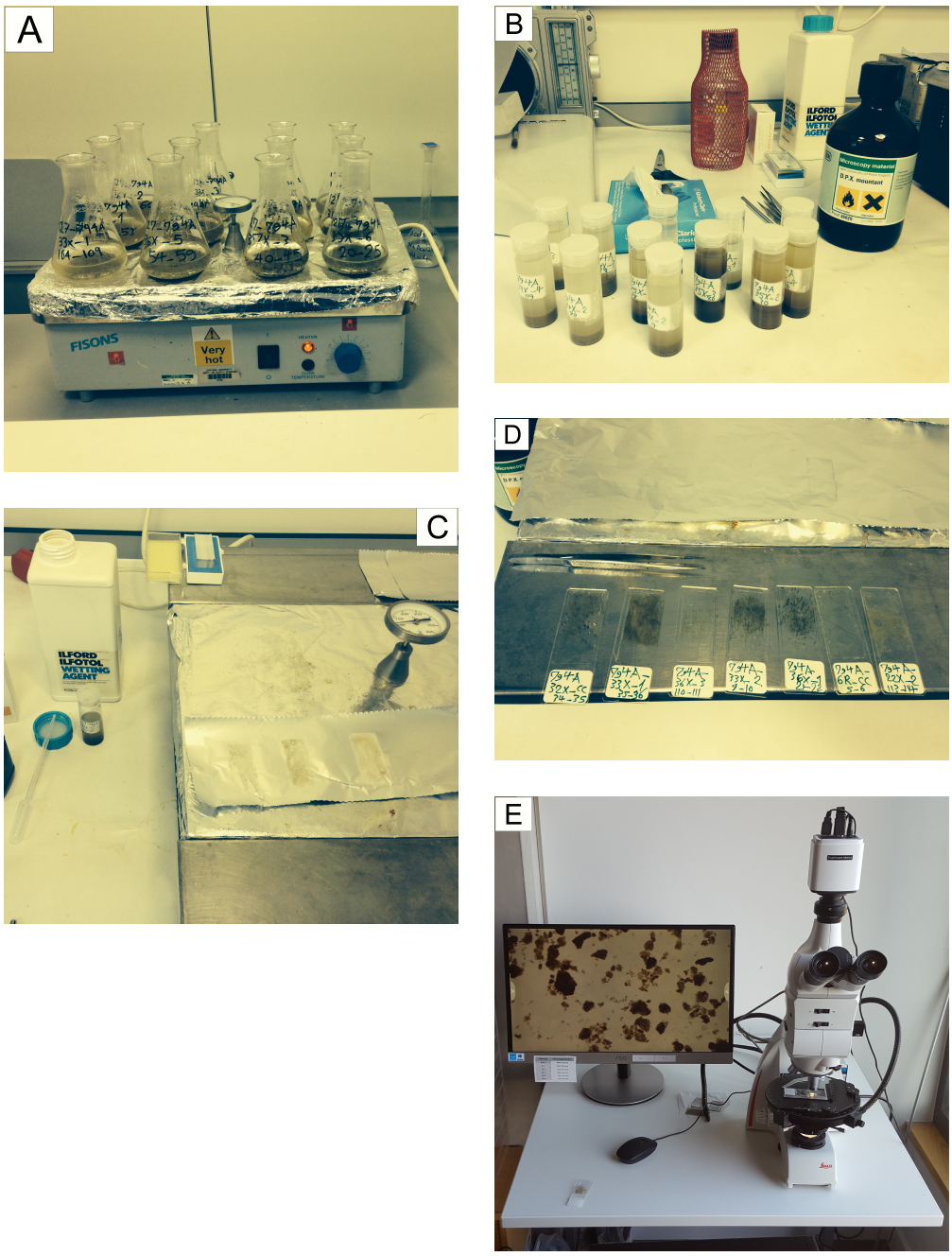


Figure 3.5. Preparation and analysis of smear slides from the sediment samples for this study (here, photos A–D capture the consecutive steps of smear-slides preparation conducted by the present work, and the samples shown in the photos are not necessarily the same in each of these photos). A) Sediment disaggregation using 15% solution of sodium hydrogen carbonate; B) Suspensions transferred to glass

vials after being washed with deionised water. Also shown are other necessary material for preparation of smear slides, such as mounting media, wetting agent, coverslips, and glass slides; C) Sediment suspensions deposited on coverslips left on a hotplate to dry. Also shown is a liquid dropper pipette using which the suspension and wetting agent are deposited on the coverslip; D) Prepared smear slides. The samples dried on the coverslips are affixed to glass slides using optical adhesive; E) Leica DM750 P polarising microscope used for studying the smear slides.

period of time for clay to settle (clays remain suspended in the water for a long period).

3.2.3.2 Optical microscopy

A Leica DM750 P polarising microscope, housed in the Department of Earth Sciences, University of Oxford (Fig. 3.5E), was used for studying the smear slides. The microscope is equipped with a reflected light illuminator with capability for brightfield, oblique, and polarised light. The standard comparator charts of Terry and Chilingarian (1955) (Fig. 3.6) were used to estimate the relative abundance of different components of the sediment identified under the microscope. These charts are useful for a quick visual percentage estimation when dealing with a large suite of samples (Mazzullo and Graham, 1988). Photomicrographs of the smear slides were made using a high speed measurement colour HDMI camera, model TrueChrome Metrics (Fig. 3.5E), attached to the Leica DM750 P microscope. The camera is precise at the micron scale, and the data can be accurate to 1/100 microns (TrueChrome Metrics, 2015).

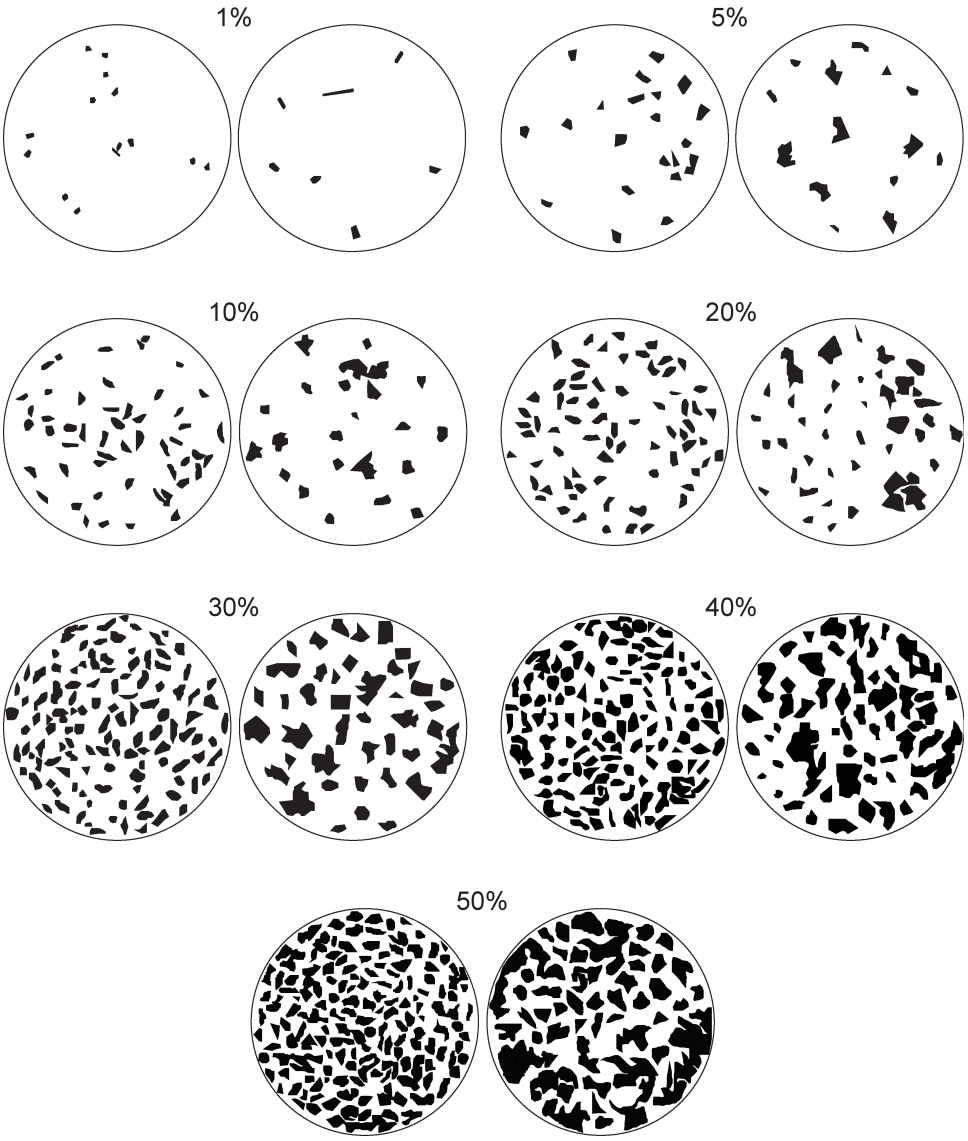


Figure 3.6. Comparator charts for visual percentage estimation of different components of sediment (redrawn from Terry and Chilingarian, 1955).

Chapter 4

Pore-water chemistry — A proxy for tracking the signature of ongoing silica diagenesis

4.1 Abstract

Silica diagenesis leads to dramatic petrophysical variations in the host sediment across the depth of an opal-A to opal-CT transition zone. Predicting the present-day diagenetic status of opal-A to opal-CT transition zones, i.e., active versus fossilised fronts, is essential to constraining the drivers that control abrupt changes in the physical state of sediment. This study assesses whether there are modern signatures of ongoing silica diagenesis in the sediment pore water, and demonstrates the potential for pore-water chemistry profiles for distinguishing between active opal-CT precipitation and fossil transition zones. Pore-water chemistry, mineralogy, and thermodynamic analyses of the Ocean Drilling Program Wells 794 and 795 indicate that solubility equilibrium has been reached with respect to opal-CT in the transition zones captured by the Neogene biosilica in the Sea of Japan. Even though silica dissolution might be triggering a reverse weathering process, the equilibrium reached with respect to diagenetic opal strongly suggests that the silica drop across the transition zones is mainly influenced by active opal-A to opal-CT transformation. Owing to abrupt petrophysical variations associated with opal-CT formation, other interstitial profiles─major ions and primary indicators─have been influenced by

silica diagenesis. The extremely-low silica diffusion fluxes in the sediment, the low permeable characteristics of host sediment, and the occurrence of considerable pore-water loss at the depth of the transition zone all support this conclusion that the dissolved species have not been diffused in the sediment at rates comparable to those by pore-water advection. Advection and diffusion, however, appear to have ceased to operate recently as they have failed to smooth the signature of ongoing silica diagenesis. The porosity drop during opal-A to opal-CT diagenesis at Sites 794 and 795 is attributed to chemically-induced anomalous compaction causing sediment framework to lose its strength, under fragmentation and extensive opal-A dissolution. Subsequent precipitation of pore-filling opal-CT further decreases the porosity.

Keywords: Pore water, Silica diagenesis, Opal-A, Opal-CT, Ocean Drilling Program, Japan Basin, Yamato Basin

4.2 Introduction

Diatomaceous sediments are widely distributed constituents of present day and ancient ocean floors. These extensive biosilica masses are subjected to diagenetic transformation from opal-A (a highly-disordered near amorphous natural hydrous silica; *sensu* Jones and Segnit, 1971) to opal-CT (disordered α-cristobalite and α-tridymite, according to Wilson, 2014) and subsequently to a stable phase of microcrystalline quartz during early burial. The transformation of opal-A to opal-CT occurs through a dissolution-reprecipitation mechanism (Leeder, 1982). This leads to

the anomalous compaction of biosiliceous successions, i.e., significant changes in the petrophysical properties (in particular a dramatic reduction in porosity; e.g., Isaacs et al., 1983; Tada, 1991; Nobes et al., 1992; Chaika and Dvorkin, 1997; Meadows and Davies, 2007). Such changes in the physical properties take place over a relatively-narrow depth interval (tens of metres thick) named the 'transition zone' (Littke et al., 1991) or 'diagenetic front' (Thein and von Rad, 1987). The porosity drop across the opal-A to opal-CT transition zone ($TZ_{A/CT}$) can produce a high amplitude reflector that is sometimes evident on seismic profiles by a discordant geometry with host stratigraphy (Hein et al., 1978; Brekke, 2000; Davies, 2005; Ireland et al., 2010; Neagu et al., 2010).

An essential aspect of constraining the diagenetic factors that drive abrupt changes in the physical state of sediments is the recognition and study of active silica fronts as opposed to currently-fossil transitions. Active transition zones are of particular importance for reconstructing the thermal history of the sediments hosting silica diagenetic reactions, too. By active, I here mean the transitions across which silica diagenesis is still occurring. Conversely, opal-A to opal-CT conversion has been stopped in fossilised transitions; this fossilised state is determined from the stratigraphic and structural relationships between the reaction front and the accommodating lithology (Davies and Cartwright, 2002).

The long established view of an active silica transition, being geometrically close to seabottom simulating─a reflection that roughly parallels the seafloor reflection (e.g.,

Dillon et al., 1993)─has been developed based on the discordant basin-wide seismic stratigraphic relationships between the $TZ_{A/CT}$ and the nearby strata (e.g., Hein et al., 1978; Meadows and Davies, 2007). Silica diagenetic reactions occur over thermodynamically-active fronts that migrate upwards, relative to the host lithology, at a recognisable rate (Neagu et al., 2010). Contrary to the notion of currently-active transitions, the seismic structural and stratigraphic criteria proposed by a few studies in the past two decades conducted on the diagenetic situation of $TZ_{A/CT}$ (Table 4.1) suggest that the silica fronts are unlikely to be active in their current sub-seafloor position.

Table 4.1. Seismic structural and geometrical criteria for recognition of fossilised silica fronts.

Criteria
- Exposure at present-day seafloor
- Deformation by polygonal faults ***(Brekke, 2000; Berndt et al., 2004; Neagu et al., 2010)***
- Thermal disequilibrium with present-day isotherms ***(Roaldset and He, 1995; Neagu et al., 2010)***
- Deformation as differential compaction folds ***(Neagu et al., 2010)***
- Taking anticlinal-synclinal form at a regional scale ***(Brekke, 2000; Davies and Cartwright, 2002; Neagu et al., 2010)***
- Not a bottom-simulating reflector ***(Brekke, 2000; Davies and Cartwright, 2002; Neagu et al., 2010)***

Seismic stratigraphic approaches help determine the position and geometry of the

opal-A to opal-CT diagenetic front. However, due to its limited vertical extent, the $TZ_{A/CT}$ is below or at the vertical resolution limit of the seismic data. The seismic geometrical method is thus fallible in determining the present-day diagenetic status of the transition zones, and silica diagenesis cannot be studied at a regional scale with precision. The accuracy of seismic criteria has been further challenged by Meadows and Davies (2007) who discussed the silica front cross-sectional morphologies in the Sea of Okhotsk. According to Meadows and Davies (2007), though a generally-discordant feature in relation to the modern seabed (this should represent a fossil transition following Neagu et al. (2010) and literature therein), the reaction over the front would not stop, and there has instead been a decrease in the rate of opal-A to opal-CT conversion in the latest phase of basin evolution.

Given the importance of identifying active versus fossil fronts and the limitations of seismic stratigraphy approach, the nomination of a more reliable diagnostic tool that allows such a distinction to be made on a case by case basis is of particular significance.

Although widely accepted as a preferred analytical procedure for monitoring the early diagenetic reactions, pore-water chemistry has been very rarely investigated for the present-day signals of silica transformation reactions. In this work, I assess whether there are associated chemical signatures of ongoing silica diagenesis found in the sediment pore water, and demonstrate the potential of pore-water chemistry for distinguishing between active opal-CT precipitation at the $TZ_{A/CT}$ and fossil transition

zones. Even minor changes affecting the solid phases, too small to be detected using common analytical techniques, can leave a large enough signal in the chemical composition of pore water to be picked up by routine hydrochemical analysis (Hesse and Schacht, 2011). Variations in pore-water composition may identify where diagenetic transformations remain active, as diffusion is generally too slow to eliminate chemical signals produced by ongoing reactions.

This work is derived from the accessible scientific database from Sites 794 and 795 of ODP Leg 127 in the Sea of Japan (Fig. 4.1A). I construct a high resolution record of chemical variations in the pore waters associated with the diagenesis of Neogene biosiliceous sediments. In particular, my analysis combines data from vertical concentration profiles with those based on SEM examination of siliceous frustules and their dissolution, and precipitation of diagenetic crystalline phases to elucidate the consumption of opal-A, the release of dissolution products to the pore water and their subsequent precipitation. Mineralogical analysis is conducted on sediments from these sites to determine the presence and abundance of diagenetic opal. Palaeo-temperatures of the sediments in which crystalline silica formation occurred, as estimated by Pisciotto et al. (1992) based on the oxygen isotope analyses of authigenic opal-CT and the adjoining pore waters, provide an added constraint to thermodynamically trace diagenesis through the opaline transformation boundary. The premise is that past sediment temperatures being lower than or comparable to present-day temperatures can further support the idea that silica dissolution and precipitation over the $TZ_{A/CT}$ are still persisting. I attempt to determine the

mechanisms that contributes most to the transport of dissolved phases pending active silicification reactions. Finally, I discuss the implications that interstitial water has on anomalous compaction phenomenon in the sediments penetrated by the ODP 794 and 795.

4.3 Study sites

The study Sites 794 (40° 11.41´N and 138° 13.86´E) and 795 (43.99°N and 138.97°E) are located in the Sea of Japan along the northeastern end of the Yamato Basin and the northernmost margin of Japan Basin, respectively (Fig. 4.1A).

Site 794 lies within a sudden crustal transition between continental crust of the Yamato Basin and oceanic crust of the Japan Basin. Thus, although basic volcanic rocks were expected, the spectrum of possible rock types comprising acoustic basement in the vicinity of this site is rather broad. The most active tectonic belt in the Japan Sea is situated in ~50 km east of Site 794 (Fig. 4.1B). The tectonic belt is characterised by a series of north-trending thrust/reverse faults, by linear ridge-basin morphology, and by shallow seismicity (Fukao and Furamoto, 1975; Seno and Eguchi, 1983; Tamaki and Honza, 1985; Tamaki, 1988; Shipboard Scientific Party, 1990a). Of particular importance in the vicinity of Site 794 are the steep normal faults that implicate acoustic basement. The major activity on these faults has occurred prior to the Late Miocene during rifting events along the northern Yamato Basin.

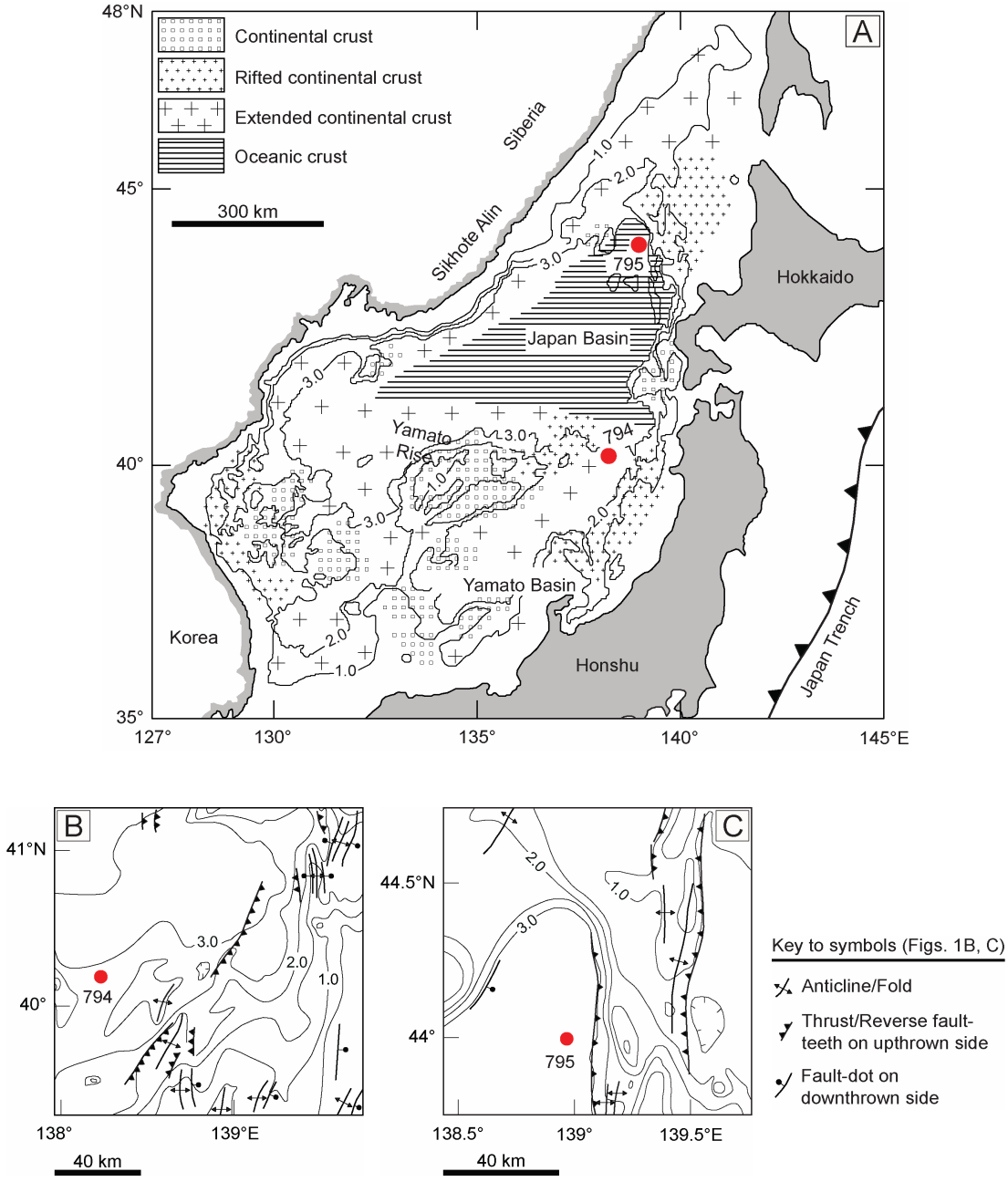


Figure 4.1. A) Location of ODP Leg 127, Sites 794 and 795 on crustal map of the Japan Sea (redrawn from Tamaki, 1988; Tamaki et al., 1992). Bathymetric contours on the map are in kilometres; B) Map of the eastern Japan Sea tectonic zone in the vicinity of Site 794 area showing recognised faults and fold axes (redrawn from Shipboard Scientific Party, 1990a). Bathymetric contours in kilometres; C) Tectonic map of area surrounding Site 795 showing recognised faults and fold axes (redrawn from Shipboard Scientific Party, 1990b). Bathymetric contours are in kilometres.

Site 795 lies within an active tectonic zone that extends along much of western Hokkaido and Honshu near the linear complex of north-trending ridges, basins, and escarpments (Tamaki and Honza, 1985). The structural patterns in the vicinity of Site 795 indicate an area of active compression containing reverse faults (Fig. 4.1C), some of which cut the entire lithosphere. Steep faults are coincident with many of the escarpments at this site. It is also possible that the area has been affected by oblique transcurrent faulting, where linear ridges represent transpressional bulges and the small associated basins result from transtension (Shipboard Scientific Party, 1990b).

The sedimentary section cored at Site 794 (Holes 794A and 794B) consists mostly of fine-grained hemipelagic sediments of Quaternary to Middle Miocene age with significant fractions of diatoms (Fig. 4.2A). Tuffs and tuffaceous sediments were recovered from Hole 794C between dolerite sills (Shipboard Scientific Party, 1990a). The section is obviously intact with little or no overburden removed. This implies, in view of the relatively-young age (15 Ma) of the Yamato Basin formation (Shipboard Scientific Party, 1990a), the Late Middle Miocene active subsidence of the back-arc setting to lower-middle bathyal depths, and having the prevailing deposition of hemipelagic silica overburden through the Early Pliocene.

The depositional section cored at Site 795 (Holes 795A and 795B) (685 m thick) overlies a brecciated basalt of Middle Miocene age. The section largely consists of Middle Miocene to Quaternary fine-grained detrital and pelagic diatom sediments (Fig. 4.2B). Based on benthonic biostratigraphy, the Neogene part of the sedimentary

section has been deposited in a mid-bathyal or a deeper setting, with the water depth probably increasing up-section. Noteworthy, the uppermost Pliocene-Quaternary succession in Site 795 is to some extent coarser-grained than the comparable section in Site 794 (Shipboard Scientific Party, 1990b). This suggests a more proximal position to terrestrial sources and the more isolated basinal setting of Site 795.

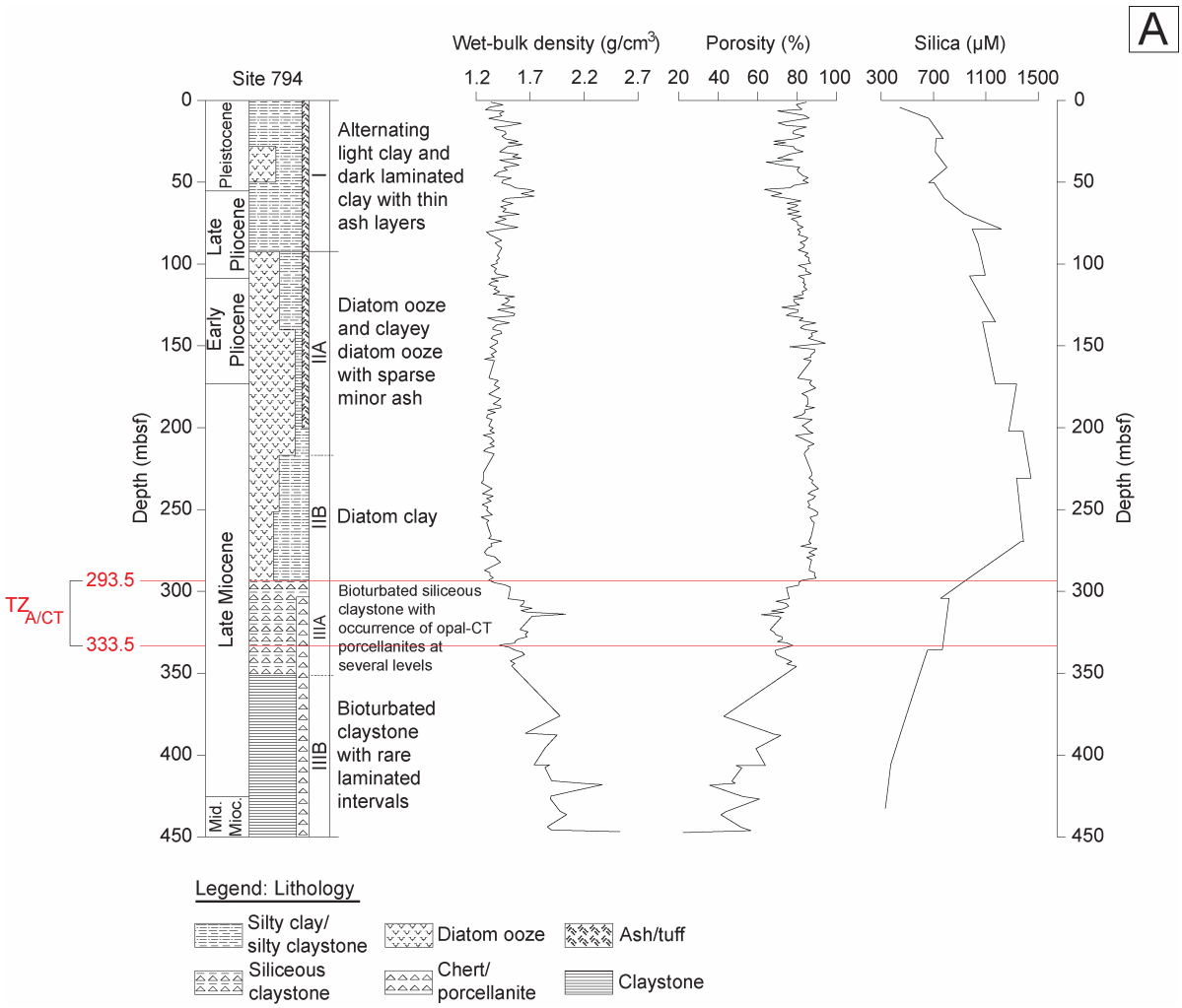


Figure 4.2. Integration of physical property measurements, pore-water silica content, and lithology for identifying the opaline reaction boundary ($TZ_{A/CT}$). A) Site 794 (redrawn and modified after Shipboard Scientific Party, 1990a); B) Site 795 (redrawn and modified after Shipboard Scientific Party, 1990b).

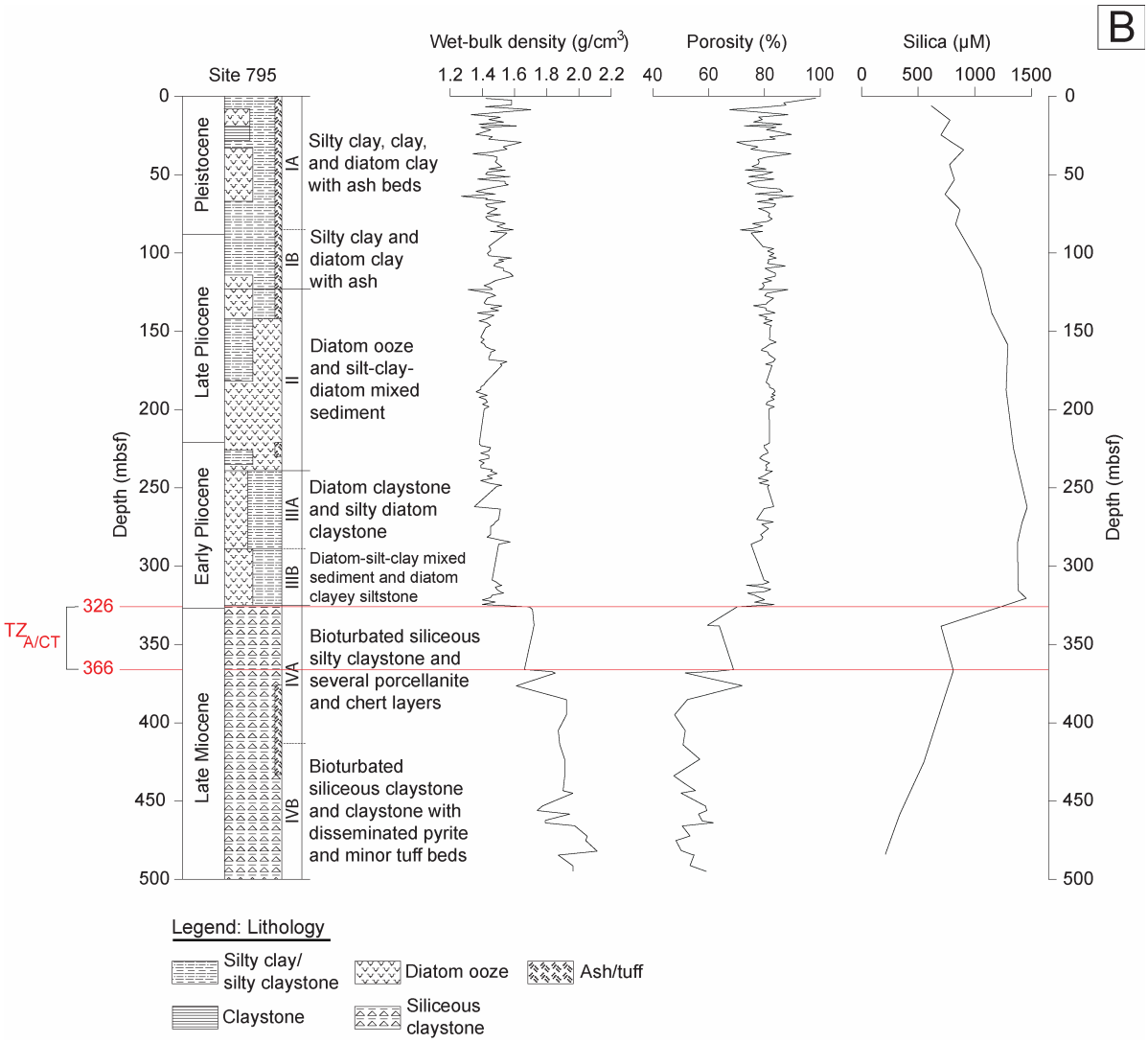


Figure 4.2. Continued.

4.3.1 Silica diagenetic fronts at Sites 794 and 795

The pronounced change of physical properties at relatively-shallow burial depths of ~293.5 mbsf and 326 mbsf respectively for Sites 794 and 795, marking the presence of the opal-A to opal-CT transition zone, is close to the depth below which occurs the greatest silica removal from the pore water (Figs. 4.2A, B). These physical and chemical variations are correlated with exhibition of stratified distinct bottom-

simulating reflectors (BSR) in the Yamato Basin and northern Japan Basin (Figs. 4.3A, B) which locally cross-cut nearby stratal reflections.

The opal-A to opal-CT transition at Site 794 is coincident with the boundary between lithologic Subunit IIB (216.9–293.5 mbsf), a largely-diatomaceous greenish grey clay, and the upper section of Unit III (293.5–351.3 mbsf), an olive-grey to grey-green siliceous claystone with abundant occurrence of porcellanite layers containing opal-CT (Fig. 4.2A). In Site 795, the transition zone is at the lithological boundary between the Subunit IIIB (288.8–325 mbsf), comprising diatom-silt-clay sediment mixture, and diatom clayey siltstone and Subunit IVA (325–413 mbsf), a siliceous silty claystone with several porcellanite and chert layers highly disturbed by drilling (Fig. 4.2B). The correlation between the shift in physical parameters at ~293.5 mbsf and the boundary between lithostratigraphic Units II and III for Site 794, also a similar correlation between physical property variations and boundary between Units III and IV in Site 795 may suggest that the petrophysical shift is controlled by the lithological change. However, there is evidence that support the changes in physical properties across the $TZ_{A/CT}$ are controlled by diagenetic processes:

The strongly-stratified character of the BSR interval, whose top is coincident with the $TZ_{A/CT}$, reflects the abundant occurrence of diagenetic opal-CT porcellanite layers within the top of the Unit III at Site 794. This is expressed by the sonic velocity log that displays a corresponding high variability (Shipboard Scientific Party, 1990a), suggesting intercalation of these layers with the physical properties. The lithological

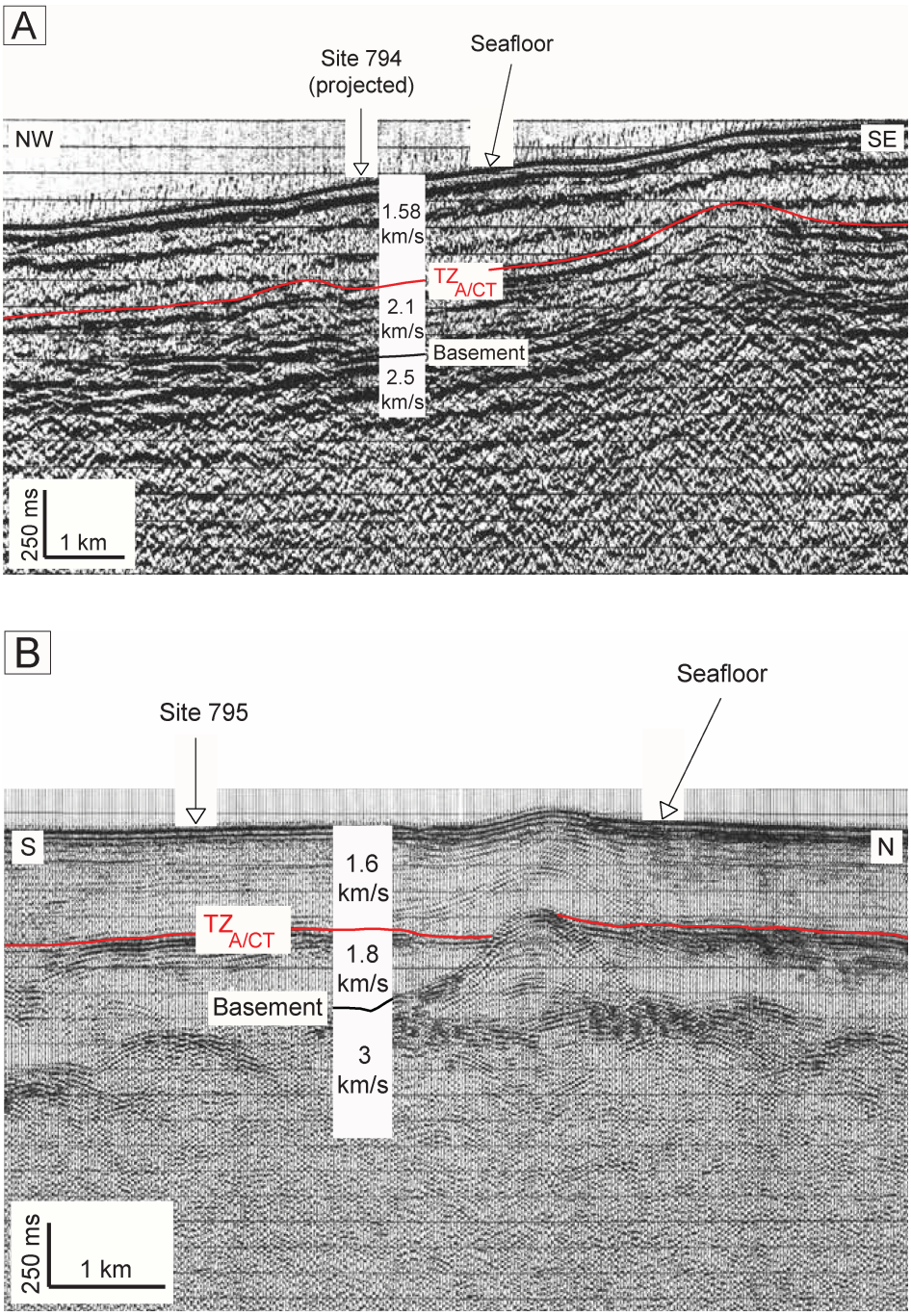


Figure 4.3. A) Opal-A to opal-CT transition demonstrated by the existence of a bottom-simulating reflector on a multi-channel seismic profile of Site 794 (after Shipboard Scientific Party, 1990a); B) Single-channel seismic line over Site 795 (after Shipboard Scientific Party, 1990b) showing the $TZ_{A/CT}$ cutting across the stratal reflectors, but simulating the modern seabed.

analogy between Sites 794 and 795, while with different physical properties profiles, suggests the lithological variations are only a subordinate control on petrophysical changes. The lithologic differences between Site 794 and the neighbouring cores of Site 797, likely drilling through the same transition zone, have apparently-little effect on the petrophysical and logging profiles across the $TZ_{A/CT}$ too, given the similarity of the physical property profiles of both sites (Nobes et al., 1992; also refer to Shipboard Scientific Party (1990c) for a review of the lithology and petrophysical properties of the sediments penetrated at ODP Site 797). These striking petrophysical similarities favour the idea this shift in properties is associated with the diagenetic transformation of opal-A to opal-CT.

Based on the parallel and consistent variations in the natural gamma and resistivity logs more than 10 m above the opal-A to opal-CT boundary and the lack of parallel response within 2 m below the boundary, the transition zone at Site 794 may be as much as 12 m thick (Nobes et al., 1992). Neagu (2011) picked up the top and base of the transition zone qualitatively by the depth of a great deflection in the curve indicating the variation of a certain physical property. This approach in the case of the porosity profile, for example, defines the top of the $TZ_{A/CT}$ interval by an abrupt negative deflection, while a subsequent positive deflection for the base of the $TZ_{A/CT}$. Due to the consistency observed between the qualitative definition of the $TZ_{A/CT}$ using physical property variations and the quantitatively-measured highest gradient between two adjacent values within this specific depth interval, Neagu's (2011) method is mostly accepted for determining the thickness of the $TZ_{A/CT}$. Following

this approach, the transition zones at Sites 794 and 795 are each a ~40-m-thick interval. It should be noted that other methods, such as X-ray diffraction (XRD), smear slides, core descriptive lithology, and seismic reflection can also determine the thickness of the $TZ_{A/CT}$, however, because of their limited stratigraphic resolution (Neagu, 2011) as compared with higher sampling intervals of the petrophysical properties measurement the latter method was preferred for defining the $TZ_{A/CT}$ thickness at the ODP sites included in this study.

The $TZ_{A/CT}$ at Sites 794 and 795 provide a highly-plausible active feature as:

- They are found in a continuous stratigraphic section, where there are no major breaks or unconformities in deposition;
- The fronts are clearly identifiable on seismic data;
- The transition lies parallel to the present-day seabed, while being non-parallel to overlying stratigraphy (i.e., discordant to host sediments but concordant with the seabed);
- The fronts are hosted in silica-rich relatively-young sediment sections (Late Miocene and younger). The age of depositional horizons in which the $TZ_{A/CT}$ is accommodated was constrained by diatom zones (see age versus depth relationship and Tables 5 in Shipboard Scientific Party, 1990a, b);
- The geothermal gradient at each site is very high (125 and 132 °C/km for Sites 794 and 795, respectively; Shipboard Scientific Party, 1990a, b).

These observations suggest that Sites 794 and 795 represent potential candidates for

the study of ongoing silica diagenesis at the pore-water sample scale.

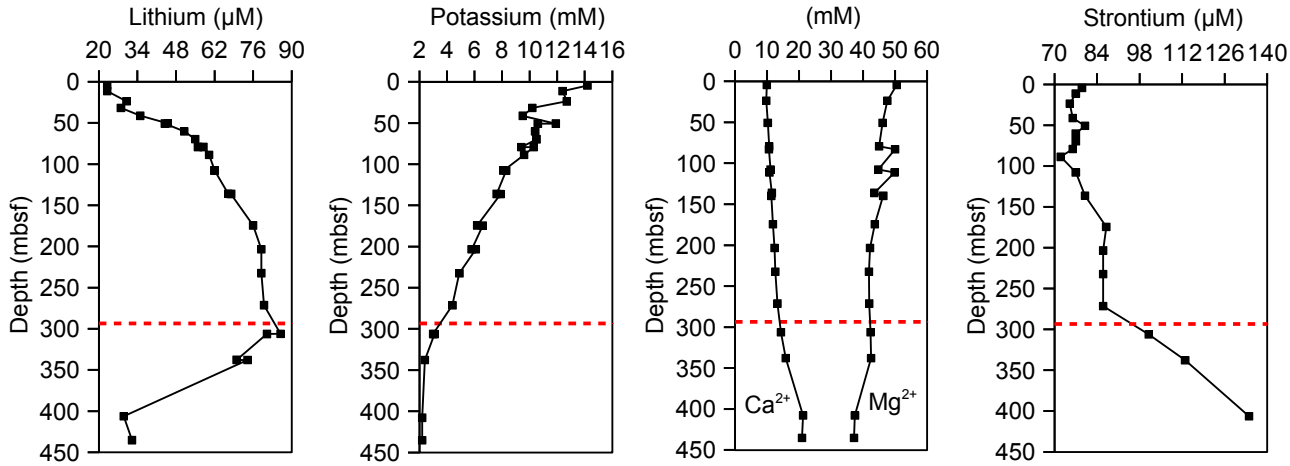
4.4 Data acquisition and methodology

Most information for this study comes from the results of pre-existing interstitial-water samples analyses for Sites 794 and 795 that are available through the ODP databank. The inorganic geochemistry programme, conducted by the ODP for Site 794, focused exclusively on analysis of 40 pore-water samples from a nearly-continuous cored section from the sediment-water interface to ~524 mbsf that were acquired using Barnes *in situ* water sampler (BW) and the standard steel ODP squeezer (Manheim and Sayles, 1974). Likewise, the shipboard inorganic geochemistry programme at Site 795 continued its focus on analysing 42 interstitial-water samples extracted from whole-round core samples squeezed by the ODP squeezers. The samples were gathered from a depth interval between ~6.0 and ~662 mbsf. In order to decrease the possible contamination of pore water by drill water, the Barnes *in situ* sampler was not used during ODP 795 (the standard stainless-steel ODP squeezer and a new plastic-lined Brumsack squeezer were used instead; Shipboard Scientific Party, 1990b).

The concentrations of major ions (Si, Li, K, Ca, Mg, and Sr) and several of the primary chemical indicators of interstitial water, including pH, salinity, sodium, chloride, alkalinity, sulphate, ammonia, and phosphate were measured during the ODP 794 and 795 programmes (Shipboard Scientific Party, 1990a, b). Due to their high resolution on acquisition and processing sampling intervals (being 10–20 m),

the interstitial-water chemistry profiles well represent variations in the sediment pore-water composition with depth (Figs. 4.4 and 4.5).

Site 794



Site 795

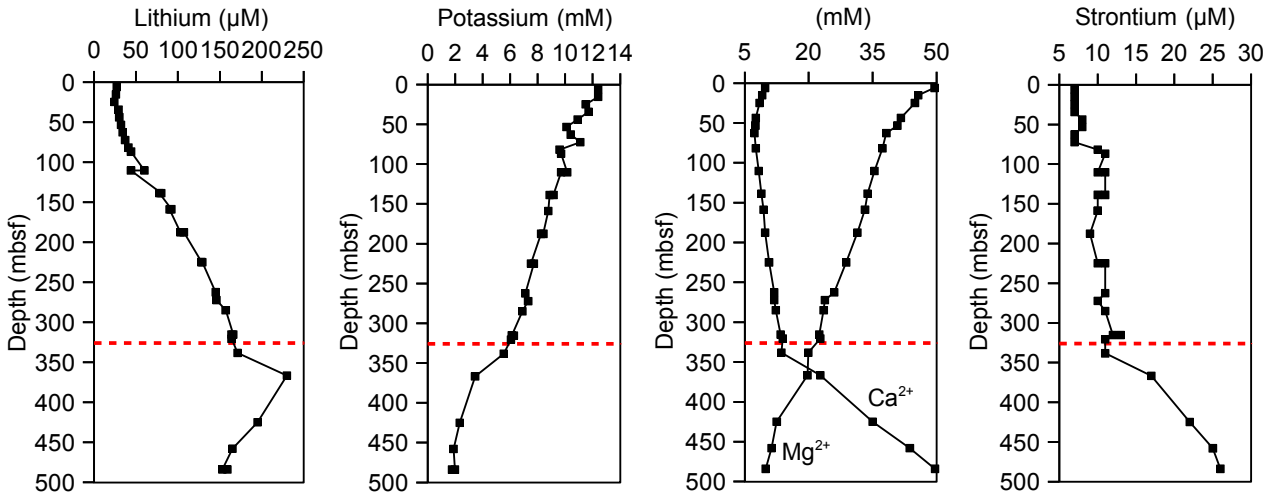


Figure 4.4. Depth profiles of lithium, potassium, calcium, magnesium, and strontium at Sites 794 and 795. The profiles are drawn based on the data from Interstitial Water (2014) accessible at IODP core database. Red dashed lines mark the top of opal-A to opal-CT transition zone ($TZ_{A/CT}$) as specified by sharp petrophysical properties variations (at ~293.5 and 326 mbsf for Sites 794 and 795, respectively).

Subsurface sediments in interaction with the interstitial waters were requested from the IODP to furnish supplemental mineralogical and textural information. I based my initial selection of 67 core samples for this study on the lithologic descriptions and bulk XRD data already acquired by ODP for Sites 794 and 795. The sample selection strategy focused on obtaining sediments from both opal-A and opal-CT depositional piles along the boreholes. There are no core samples from the first 100 mbsf at Site 794 as the main working-half sections no longer have any material. Samples were acquired from the sampling intervals ranging between ~40 and ~50 m within the diatomaceous Unit II in Site 794, while a wide range of sampling intervals (~1 to ~70 m) within the opal-A zone in Site 795. Due to accommodating the interval of interest ($TZ_{A/CT}$), closely-spaced samples (0.05 to ~7 m) were collected across the Subunit IIIA in Site 794. Depending on core recovery, samples within the Subunit IVA capturing the transition at Site 795 were collected at small intervals too (0.28 to ~10 m) (see the first four columns in Tables 4.2 and 4.3 for the stratigraphic position and identification of acquired samples).

The discrete core samples are semi-consolidated, and mostly display a well preserved fabric. A 1 gram fraction of each sample was oven-dried, finely powdered, and passed through an X-ray to determine the abundance and relative amounts of diagenetic opal-CT, and to designate the onset of silica diagenetic reactions. XRD scans were obtained using a PANalytical Empyrean Series 2 powder diffractometer and a cobalt X-ray source (Co-Kα) having a step rate of 0.017°/s over a 2θ range from 5 to 85°, at the Department of Earth Sciences, University of Oxford. Phase

identification from the powder diffraction data was performed using the analytical software Match! Version 3.2.1 Build 70, that compares the diffraction patterns of selected samples to a reference database in order to identify the phases present.

Site 794

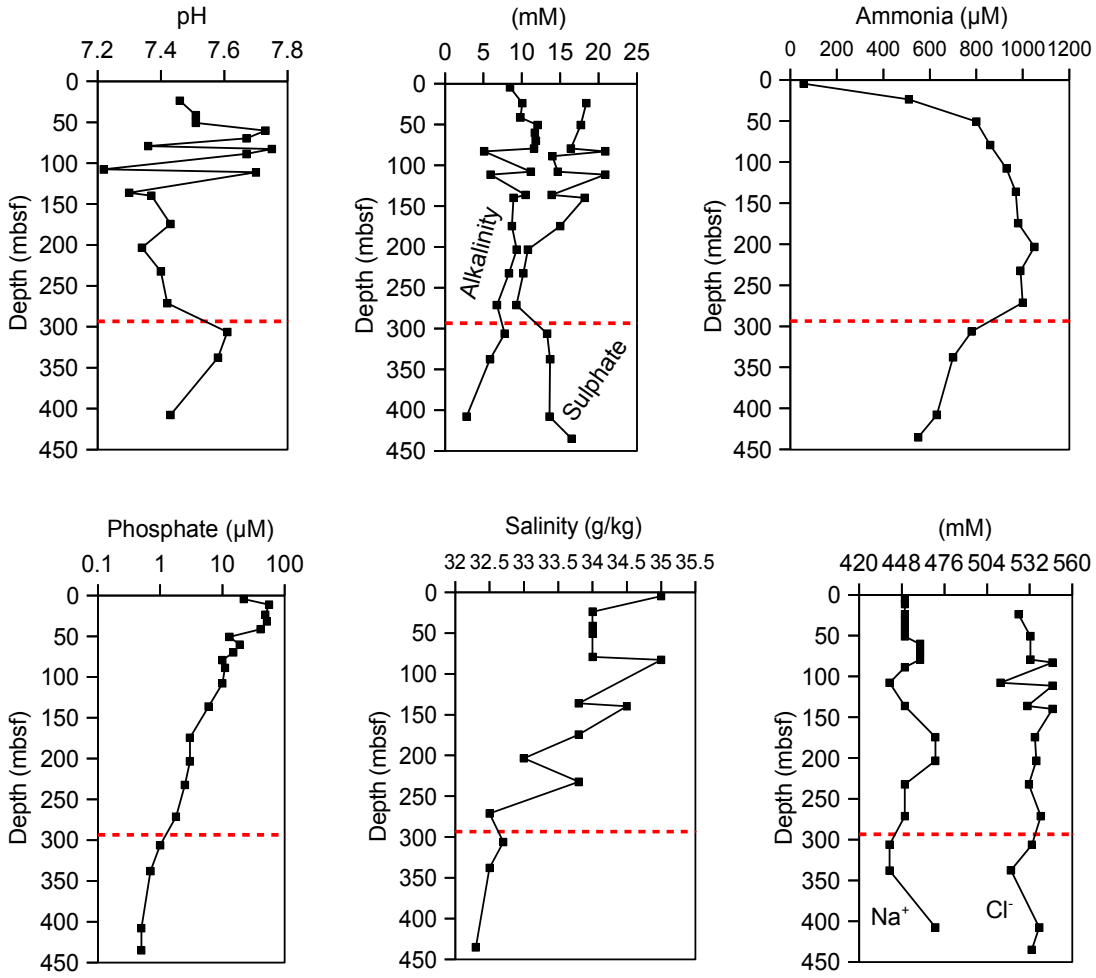


Figure 4.5. Depth profiles of pH, sulphate, alkalinity, ammonia, phosphate, salinity, sodium, and chloride at Sites 794 and 795. The profiles are drawn based on the data from Interstitial Water (2014) available at IODP core database. Red dashed lines indicate the top of the $TZ_{A/CT}$ as defined by abrupt petrophysical changes.

Site 795

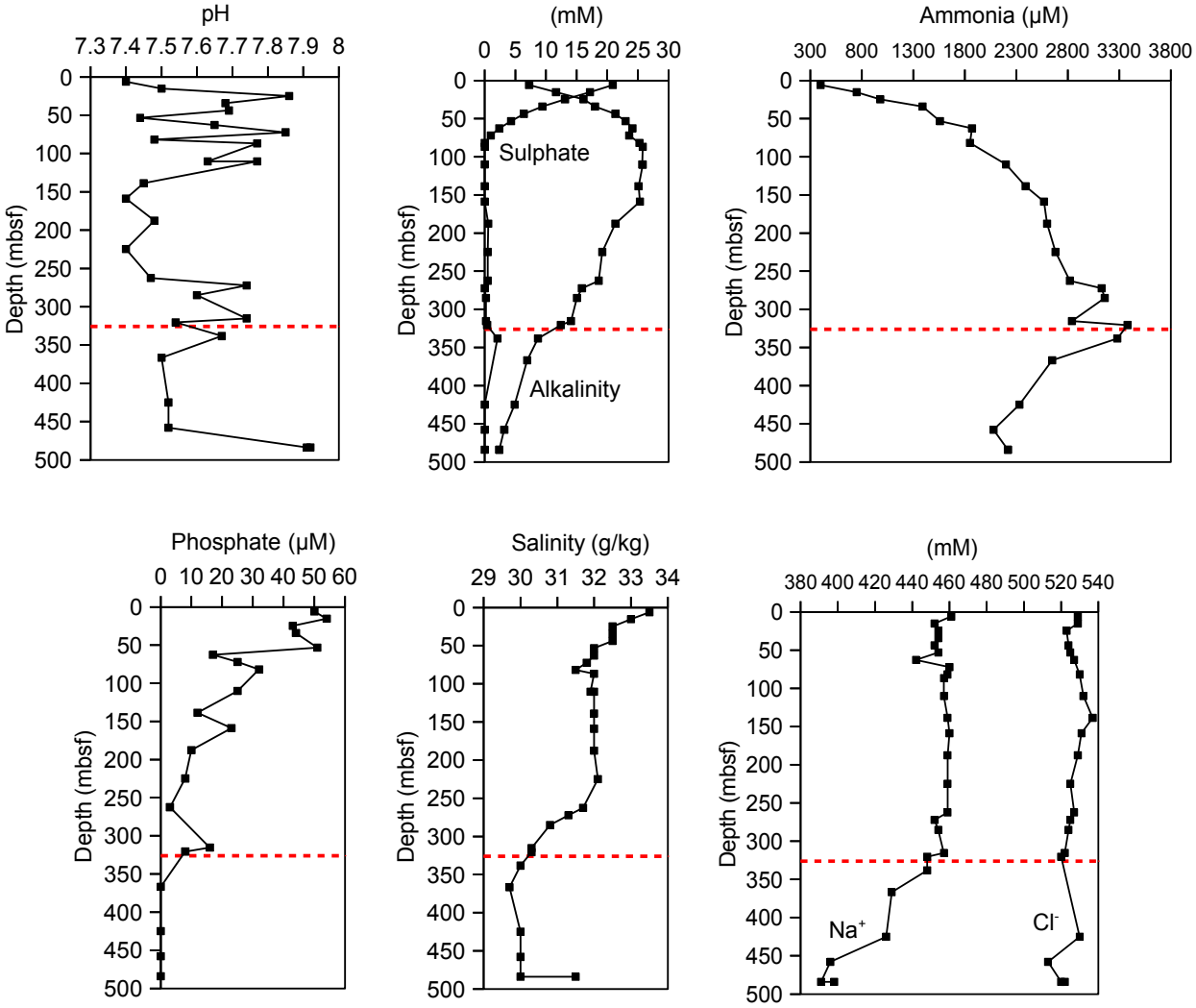


Figure 4.5. Continued.

I used the Reference Intensity Ratio (RIR) method, based upon scaling all diffraction data to the diffraction of standard reference material (often being corundum), to quantify crystalline components in the sediment samples containing multiple phases. The method assumes that the normalised weighted amounts of phases present in the sample add up to 100 wt% of the crystalline fraction. XRD cannot detect the

structure of the material during the early stage of diagenetic reactions as the starting material is non-crystalline silica, either volcanic ash or biosilica (Rice et al., 1995). Therefore, I utilised the results of smear-slides examination conducted by ODP to assess the relative abundance of opal-A present in the samples.

From the population of 67 core samples, I derived a subset of 10 representative samples (6 from Site 794 and 4 from Site 795) for scanning electron microscopy (SEM) examination. Carbon-coated, resin-impregnated polished blocks made from 1-cm-thick sub-sampled slabs were studied under the SEM which enabled the direct observation of breakage and progressive dissolution of diatom frustules constructed of opal-A and the formation of diagenetic silica. Details for the preparation of resin blocks from semi-lithified core samples are outlined in Chapter 3. An FEI Quanta 650 FEG scanning electron microscope, running in high vacuum mode and equipped with a secondary electron detector (ETD), was used to examine the samples.

4.5 Results

4.5.1 X-ray diffraction mineralogy

The primary silica phase in the Yamato and Japan Basins sediment is poorly-ordered amorphous opal-A, derived from the Pliocene clay-rich diatomaceous ooze. Particle composition of Site 794 sediments, as determined by smear-slide analyses, shows that biogenic silica is present in succession overlying the $TZ_{A/CT}$ in moderate to high proportions (50–55% of total volume in average; Shipboard Scientific Party, 1990a). Biosilica is present in the sediment pile above the $TZ_{A/CT}$ at Site 795 in moderate

quantities (~40%; Shipboard Scientific Party, 1990b). According to Singh and Gilkes (1993), the XRD band of opal-A is, however, overlapped by hk reflections of clays and volcanic ash in such sediment mixtures making opal undetectable by normal XRD procedures. X-ray diffraction patterns of volcanic ash in the sediments are grossly similar to those of opal-A and can only be distinguished if samples are devoid of detrital debris (Hein et al., 1978). Opal-CT has been analysed by the highest intensity peaks of d(101) cristobalite at 26.18–25.14° 2θ (3.95–4.11 Å) and d(110) tridymite lattice at 23.9° 2θ (4.32 Å) in the X-ray diffraction records of randomly-oriented bulk powder samples at Sites 794 and 795 (Fig. 4.6). The high intensity d(110) tridymite peak can only be seen on the lower angle shoulder of the d(100) quartz peak (24.27° 2θ at 4.255 Å). Representative diagnostic diffractions (mostly as low intensity peaks) are also present for other crystalline phases, such as albite, anorthite, chlorite, gypsum, halite, illite, phengite, and zeolite (Fig. 4.6; Appendix I). Recognition of both albite and anorthite in the same samples, as end-members of plagioclase series, implies a range of plagioclase minerals some of which giving relevant XRD patterns better refined to albite and some better refined to anorthite (Ward et al., 1999). Multi-phase features of the analysed sediments can cause the peaks of accessory minerals present in the diffraction records of some samples to overprint important low intensity opal-CT peaks. The d(101) cristobalite main peaks at 3.95–4.11 Å (mean = 4.03 Å) suffer from interference with a secondary albite peak (at ~25.51° 2θ). Measuring the most intense opal-CT peak, however, maximises the original signal to noise ratio, leading to a noticeable reduction in the common interference from accessory phases.

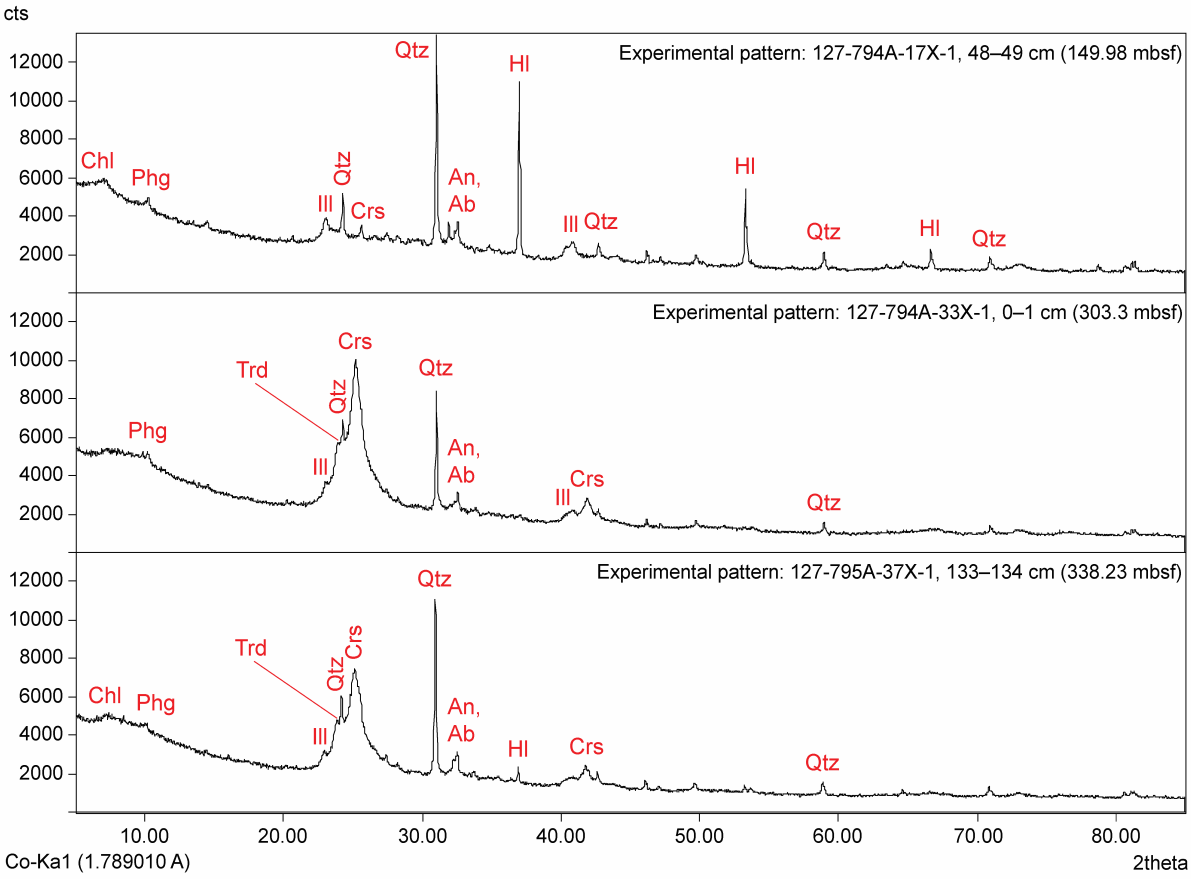


Figure 4.6. XRD integrated intensity versus 2θ for representative samples from opal-A zone (at Site 794) and opal-A to opal-CT transition zone (at Sites 794 and 795). The abbreviations represent: Ab = albite, An = anorthite, Chl = chlorite, Crs = cristobalite, Hl = halite, Ill = illite, Phg = phengite, Qtz = quartz, Trd = tridymite. The cristobalite peak at 25.58° (4.04 Å) recorded for sample 127-794A-17X-1, 48–49 cm suggests the presence of incipient opal-CT in opal-A-rich sediment unit. The opal-CT (tridymite and cristobalite) peaks rise sharply in samples 127-794A-33X-1, 0–1 cm and 127-795A-37X-1, 133–134 cm, respectively from Sites 794 and 795, across the opal-A to opal-CT transition.

The relative abundance of the most intense opal-CT peaks in the sediments from Sites 794 and 795, determined based on measuring absolute intensities, is shown in

Figure 4.7. The vertical intensity profiles for both tridymite and cristobalite indicate the incipient presence of diagenetic silica in both sites well above the abrupt transition in the physical state of the sediments (Fig. 4.7; the maximum values for cristobalite being 491.9 cts/s at 249.8 mbsf in Site 794 and 1717 cts/s at 321.6 mbsf in Site 795) in the set of low intensity peaks (for instance, the diffractogram of sample 127-794A-17X-1, 48–49 cm in Fig. 4.6). In Site 794, the absolute intensity across the $TZ_{A/CT}$ interval widely varies from 0 to 12307.3 cts/s for tridymite, and from 0 to 10257.5 cts/s for cristobalite. Except for three samples exhibiting remarkably-high intensity peaks (at ~303 mbsf), no significant increase is observed for opal-CT at other depths across the $TZ_{A/CT}$. Within the $TZ_{A/CT}$ at Site 795, the intensity values are ranged from 0 to 4132.5 cts/s for tridymite and from 0 to 3855.5 cts/s for cristobalite. In both sites, samples having little or no indication of diagenetic opal are present stratigraphically below samples that have clear signs of opal-CT presence. Such variations in the diffraction intensities of diagenetic silica suggest a non-uniform mineralogical transition from opal-A to opal-CT for Sites 794 and 795.

4.5.2 Quantitative XRD

Normalised percentages of five main mineral phases for Sites 794 and 795 samples are shown in Tables 4.2 and 4.3, separately. In Site 794, tridymite and cristobalite are identified in most of the samples, and in Site 795 in all of the samples. Tridymite is ranging in abundance from 3.5 to 32 wt% in Site 794, and from ~2 to about 27 wt% for cristobalite. In Site 795, tridymite varies between ~4 and ~29 wt% and a range of ~1 to ~30 wt% for cristobalite. Quartz and phengite are present in all samples from

these sites, in varying proportions. The percentages of quartz range between roughly 17 to about 46 wt% for Site 794 and from about 21 to 50 wt% for Site 795. Plagioclase (anorthite) content of the sediments is between ~20 and ~47 wt% for Site 794 and between 22 and ~39 wt% for Site 795. The abundance of phengite in the samples varies from 14 to ~36 wt% for Site 794 and from 11 to 25 wt% for Site 795.

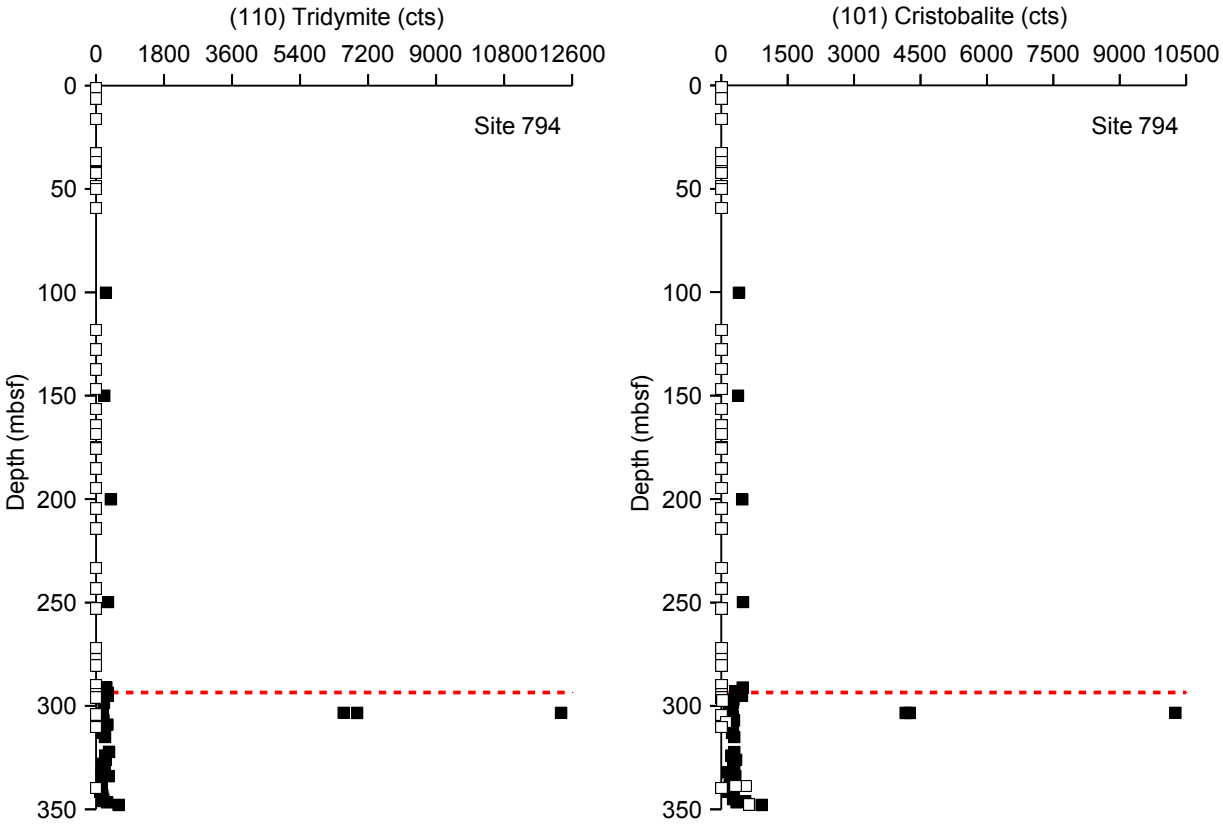


Figure 4.7. Relative abundance of tridymite and cristobalite in sediments at Sites 794 and 795 as determined by XRD analyses. Note that the XRD data from this study (solid squares) are co-plotted with the results of XRD analyses carried out by ODP (open squares; Shipboard Scientific Party, 1990a, b). Red dashed lines mark top of the petrophysical $TZ_{A/CT}$.

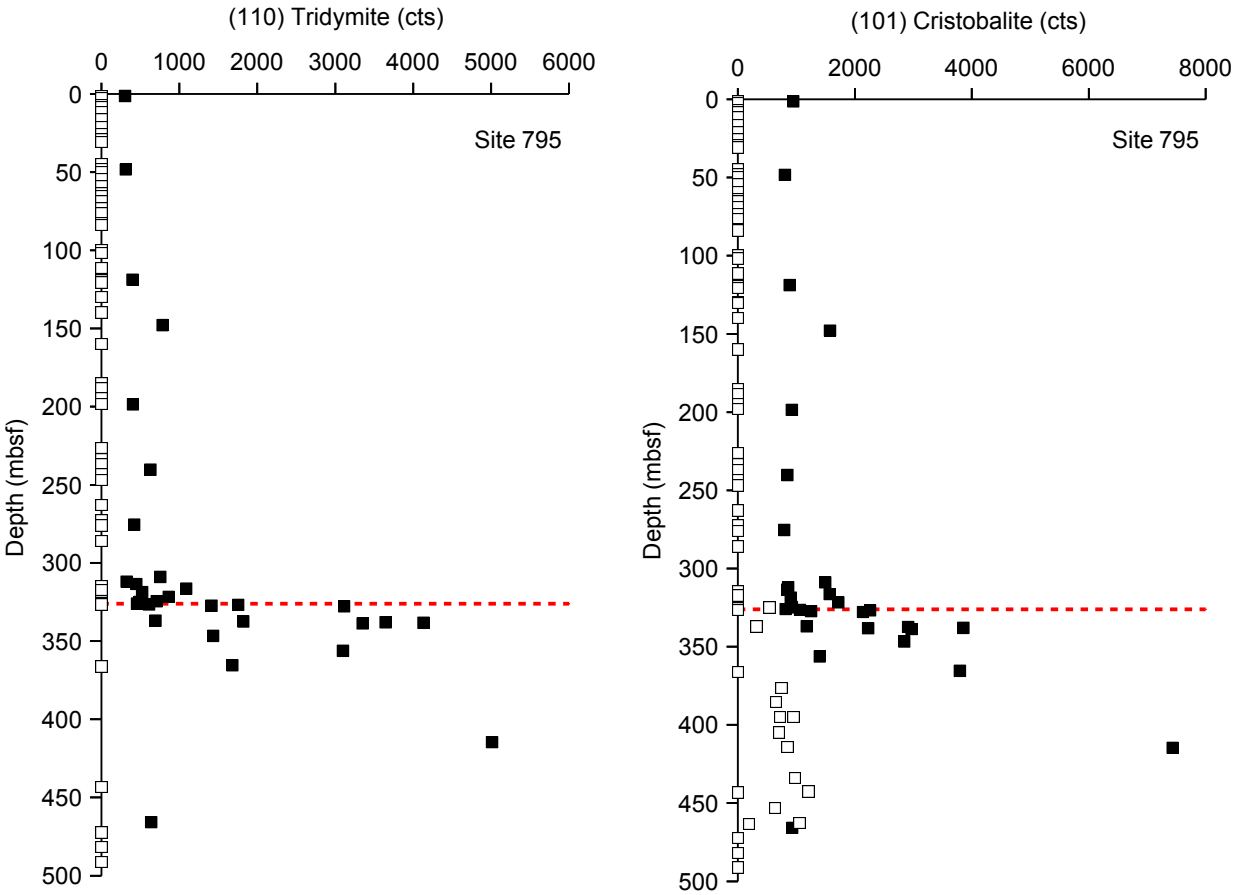


Figure 4.7. Continued.

Due to large sampling domains, the mean values of normalised relative mineral abundance in the depositional Unit II overlying the diagenetic transition at Site 794 provides only a rough estimate (Table 4.2): anorthite = 35 wt%, quartz = 34 wt%, phengite = 23 wt%, tridymite = 4.5 wt%, and cristobalite = 3.5 wt%. In Site 795, however, due to sufficient number of samples analysed (15 out of 30), the mean normalised abundance values for the interval sealing the transition zone (being Units I, II, and III) represent reliable estimates (Table 4.3): anorthite = 36 wt%, quartz = 36 wt%, phengite = 18 wt%, tridymite = 6 wt%, and cristobalite = 4 wt%. Quartz

Table 4.2. Normalised mineral content based on X-ray diffraction analysis of random bulk sediment samples, Site 794.

Lithologic unit	Core, section, interval, cm	Age	Depth, mbsf	Normalised mineral abundance, wt%				
				Anorthite	Cristobalite	Phengite	Quartz	Tridymite
IIA	127-794A-11H-6, 37–38	Late Pliocene	100.17	30.3	2.8	27.1	35.6	4.2
	127-794A-17X-1, 48–49	Early Pliocene	149.98	36	5.2	19.7	35.6	3.5
	127-794A-22X-2, 113–114	Late Miocene	200.13	35.3	1.9	23.9	33.6	5.3
IIB	127-794A-27X-3, 80–81	Late Miocene	249.8	38.2	3.5	25.3	28.8	4.2
	127-794A-31X-4, 100–101 *	Late Miocene	290.1	46.8	–	27.4	25.8	–
	127-794A-31X-5, 50–51	Late Miocene	291.1	36.9	3.1	22.5	33.5	4
	127-794A-31X-6, 90–91	Late Miocene	293	32.4	4.7	21	36.9	5
IIIA	127-794A-32X-1, 22–23	Late Miocene	293.72	27.9	4.4	25.5	28.2	14
	127-794A-32X-1, 100–101 *	Late Miocene	294.5	38.5	–	24.7	36.8	–
	127-794A-32X-2, 5–6	Late Miocene	295.05	33	4.7	22	32	8.3
	127-794A-32X-2, 100–101 *	Late Miocene	296	39.3	–	17.3	43.4	–
	127-794A-32X-3, 46–47	Late Miocene	296.96	32.5	6	21	32.5	8
	127-794A-32X-3, 100–101 *	Late Miocene	297.5	28.5	7	24.2	40.3	–
	127-794A-32X-CC, 34–35	Late Miocene	298.45	34.3	7.7	21	28	9
	127-794A-33X-1, 0–1	Late Miocene	303.3	–	22.9	16.5	28.6	32
	127-794A-33X-1, 5–6	Late Miocene	303.35	–	22.5	17.1	30.3	30.1
	127-794A-33X-1, 10–11	Late Miocene	303.4	–	19.1	20.3	30	30.6
	127-794A-33X-1, 35–36	Late Miocene	303.65	31.5	6	23	31	8.5
	127-794A-33X-1, 70–71	Late Miocene	304	30.5	5.4	21	30.5	12.6
	127-794A-33X-1, 100–101 *	Late Miocene	304.3	30	–	28.5	41.5	–
	127-794A-33X-1, 104–105	Late Miocene	304.34	26.3	5.9	32.5	26.3	9
	127-794A-33X-2, 9–10	Late Miocene	304.89	27.2	6.6	26.3	31.4	8.5
	127-794A-33X-3, 68–69	Late Miocene	306.98	32	6.6	20	33	8.4
	127-794A-33X-4, 12–13 *	Late Miocene	307.92	20.1	24.3	35.7	19.9	–
	127-794A-33X-4, 119–120	Late Miocene	308.99	29.9	7.5	25	29.8	7.8
	127-794A-33X-5, 100–101 *	Late Miocene	310.3	34.5	–	19.4	46.1	–
	127-794A-33X-6, 20–21	Late Miocene	311	28	6.4	26.1	31.1	8.4
	127-794A-34X-1, 40–41	Late Miocene	313	35	7.2	28.1	21.2	8.5
	127-794A-34X-2, 90–91	Late Miocene	315	30	6.5	24.9	31	7.6
	127-794A-35X-1, 5–6	Late Miocene	322.25	29.8	8	22	32	8.2
	127-794A-35X-2, 30–31	Late Miocene	324	30	7.6	22	32	8.4
	127-794A-35X-3, 80–81	Late Miocene	326	31.4	7.6	18.2	34.5	8.3

Table 4.2. Continued.

	127-794A-35X-4, 130–131	Late Miocene	328	30.5	6.1	22.8	33.9	6.7
	127-794A-35X-6, 38–39	Late Miocene	330.08	31.5	7.5	20	32.8	8.2
	127-794A-36X-1, 21–22	Late Miocene	332.11	30.8	8.2	22.2	27	11.8
	127-794A-36X-2, 55–56	Late Miocene	333.95	30.1	7.7	22.5	31	8.7
	127-794A-36X-3, 110–111	Late Miocene	336	32	7	22.7	30.5	7.8
	127-794A-36X-5, 54–55	Late Miocene	338.44	32.1	7.3	24.7	24.7	11.2
	127-794B-5R-1, 39–40 *	Late Miocene	338.69	24.6	24.6	15.8	35	–
IIIA	127-794B-5R-1, 49–50 *	Late Miocene	338.79	26	17.2	27.3	29.5	–
	127-794A-37X-1, 0–1	Late Miocene	341.6	38.4	6	24.6	24.9	6.1
	127-794A-37X-2, 19–20	Late Miocene	343.29	31.1	6.8	24.5	29.8	7.8
	127-794A-37X-3, 40–41	Late Miocene	345	26.6	7.9	32.6	17.4	15.5
	127-794A-37X-3, 140–141	Late Miocene	346	27.1	17.5	23.5	22.9	9
	127-794A-37X-CC, 30–31	Late Miocene	346.63	29.7	8.8	14	23	24.5
	127-794B-6R-CC, 5–6	Late Miocene	347.85	25.6	11.4	17.3	19.9	25.8
	127-794B-6R-CC, 7–8 *	Late Miocene	347.87	27.9	27.1	20.2	24.8	–

* Normalised abundance of minerals has been estimated from XRD analyses conducted by the ODP, available through the IODP core database.

content decreases slightly within the $TZ_{A/CT}$ at Site 794 (beneath 293.5 mbsf, in Subunit IIIA), the mean value being 30 wt%, whereas there is an abrupt increase in the average opal-CT content to twice that of opal-A sediment (the average amount of 9 and 7 wt% for tridymite and cristobalite, respectively). The percentage of anorthite gradually decreases across the $TZ_{A/CT}$ (the highest value being ~39 wt%), but the average phengite content of the $TZ_{A/CT}$ remains close to that of the opal-A section.

Likewise, at Site 795 the amount of quartz slightly decreases across the $TZ_{A/CT}$ while the average opal-CT content is significantly higher than that in the opal-A interval (the mean value of tridymite and cristobalite being 15 and 7 wt%, respectively).

Table 4.3. Mineral content based on X-ray diffraction analysis of bulk sediment samples, Site 795.

Lithologic unit	Core, section, interval, cm	Age	Depth, mbsf	Normalised mineral abundance, wt%				
				Anorthite	Cristobalite	Phengite	Quartz	Tridymite
IA	127-795A-1H-1, 124–125	Pleistocene	1.24	36.7	1.3	17	40.7	4.3
	127-795A-6H-1, 91–92	Pleistocene	48.21	31.1	3.9	21.5	39.1	4.4
IB	127-795A-13H-4, 43–44	Late Pliocene	118.73	37	3.2	20	34.1	5.7
II	127-795A-16H-4, 101–102	Late Pliocene	147.81	36.5	4.6	14.6	33.5	10.8
	127-795A-22X-5, 128–129	Early Pliocene	198.48	34.5	6	19.4	35	5.1
IIIA	127-795A-27X-1, 34–35	Early Pliocene	240.24	34	4.9	22.7	31.2	7.2
	127-795A-30X-5, 10–11	Early Pliocene	275.4	34	3.3	18.2	37.5	7
IIIB	127-795A-34X-1, 100–101	Early Pliocene	308.9	37	4.1	15.3	37.5	6.1
	127-795A-34X-3, 100–101	Early Pliocene	311.9	37.7	4.6	14.3	38.9	4.5
	127-795A-34X-4, 105–106	Early Pliocene	313.45	34.6	5	16.8	37.1	6.5
	127-795A-34X-6, 101–102	Early Pliocene	316.41	36.5	4	15.5	37.7	6.3
	127-795A-35X-1, 101–102	Early Pliocene	318.61	38	5	25	26.5	5.5
	127-795A-35X-3, 100–101	Early Pliocene	321.6	33.5	5	19.6	34.4	7.5
	127-795A-35X-5, 84–85	Early Pliocene	324.44	34.5	5.8	19	34.6	6.1
	127-795A-35X-5, 128–129	Early Pliocene	324.88	38	3.6	13.9	38	6.5
IVA	127-795A-35X-6, 84–85	Early Pliocene	325.94	38.5	4.5	16.9	32.9	7.2
	127-795A-35X-6, 136–137	Late Miocene	326.46	36.9	5	14	37.1	7
	127-795A-35X-CC, 14–15	Late Miocene	326.74	29	5.7	17.4	40	7.9
	127-795A-36X-1, 12–13	Late Miocene	327.32	25.9	7.3	14.9	26	25.9
	127-795A-36X-CC, 36–37	Late Miocene	327.78	25	12.1	13.5	25.4	24
	127-795A-37X-1, 0–1	Late Miocene	336.9	37.3	5.2	22	28.5	7
	127-795A-37X-1, 47–48	Late Miocene	337.37	33.9	7.3	15	36.8	7
	127-795A-37X-1, 101–102	Late Miocene	337.91	26	10.1	13.5	30.6	19.8
	127-795A-37X-1, 133–134	Late Miocene	338.23	24	9.3	20	21.3	25.4
	127-795A-37X-CC, 35–36	Late Miocene	338.68	27	8	17	38.5	9.5
	127-795A-38X-CC, 1–2	Late Miocene	346.61	29	6.5	14	35.5	15
	127-795A-39X-CC, 0–1	Late Miocene	356.2	35	8.3	12	29.1	15.6
	127-795B-1R-1, 18–19	Late Miocene	365.38	28.5	8	15	30.5	18
IVB	127-795B-6R-1, 80–81	Late Miocene	414.6	–	30.3	11	30.1	28.6
	127-795B-11R-3, 112–113	Late Miocene	465.82	22	5.9	17.5	50	4.6

Within the $TZ_{A/CT}$, the normalised abundance of anorthite (the average being 30 wt%) is well below the mean anorthite value of the overlying opal-A unit, the phengite content (16 wt%) but only slightly lower than that of the opal-A interval.

The cristobalite wt% to quartz wt% ratio slightly increases with depth within the Unit II in Site 794 (from 0.06 to 0.15), but decreases from very high values (maximum ratio = 1.22) to 0.15 in the first 55 m of Subunit IIIA, hosting the opal-A to opal-CT transition zone. In Site 795, the ratio slightly increases with depth within the opal-A zone (from 0.03 to 0.19) and then moderately increases within the $TZ_{A/CT}$ and the interval below (the peak ratio being 1.01). These values represent the likely-gradational opal-A to opal-CT mineralogical transformation for Sites 794 and 795.

4.6 Discussion

4.6.1 Source of dissolved silica

The release of dissolved silica in pore waters (H_4SiO_4) sampled at Sites 794 is regulated in essence by the presence of opaline silica. This is based on the most clearly-defined chemical signal of biogenic input through the diatomaceous sequence. Site 795 has the lowest signals of opal-A input among the drilled sites in Leg 127 (modified after Nobes et al., 1992) possibly because the deposits from this site have been more exposed to terrestrial than basinal sources.

The relatively-high abundance of diatoms in the interval above the transition zone at both Sites 794 and 795, interpreted from microscopic assessment of smear slides

(Shipboard Scientific Party, 1990a, b), suggests biogenic opal as the probable major source of dissolved silica in sediments. The large volume of Late Miocene to Late Pliocene diatomaceous sediment at Site 794 and comparable volumes of Pliocene diatom ooze at Site 795 display a strong stratigraphic correlation between their independently-determined distribution and the observed variations of dissolved silica concentrations. Thus, interstitial silica mirrors opal-A distribution (Figs. 4.8A, B), reflecting the release of silica during dissolution of siliceous frustules (and sporadic radiolaria). The implication is that under certain conditions, the volcaniclastic sediments (including volcanic glass, ash and tuff) mixed with the diatom-rich units may contribute silica to the pore waters at rates comparable to those of biogenic opal. However, the lack of correspondence between ash distribution and dissolved silica content in these two sites (especially at Site 794) denies this possibility (Figs. 4.8A, B).

Conversely, the progressive dissolution of diatoms with depth, from moderate-extensive corrosion to chemical deterioration of frustules (Figs. 4.9A–D, 4.9E–F), is very likely to release most of the dissolved silica to the sedimentary pore waters. Siliceous tests that are common in the porous Neogene sediments (Figs. 4.9G, H; Appendix II) are rarely found in the $TZ_{A/CT}$ and in the opal-CT interval below (Figs. 4.10A–B). This implies, in the context of silica diagenesis, a rather abrupt chemical transition from biogenic to diagenetic opal. The sudden chemical transition is followed by an abrupt transition in the physical state of sediment, particularly porosity, at Sites 794 and 795. The open cellular structure of diatoms contributes

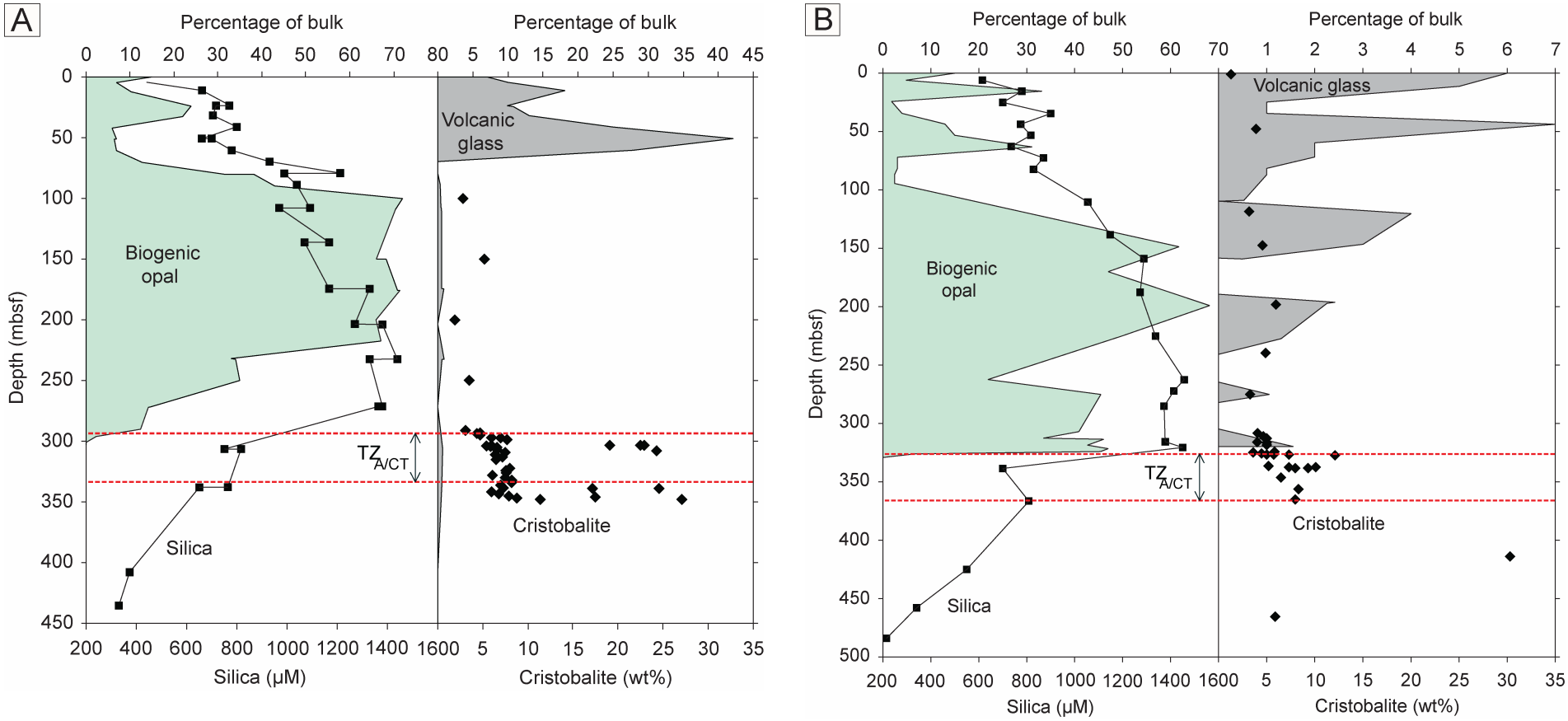


Figure 4.8. Depth profile for dissolved silica as well as the distribution of opal-A deposits (using smear-slides analyses; green shaded area) as estimated by Shipboard Scientific Party (1990a, b). Also shown are the distribution of volcanic glass (grey shaded area) (after Shipboard Scientific Party, 1990a, b) and normalised abundance of cristobalite (this study). A) Site 794. Red dashed lines mark top and base of the diagenetic transition zone as defined by petrophysical changes; B) Site 795. Red dashed lines denote top and base of the petrophysical $TZ_{A/CT}$.

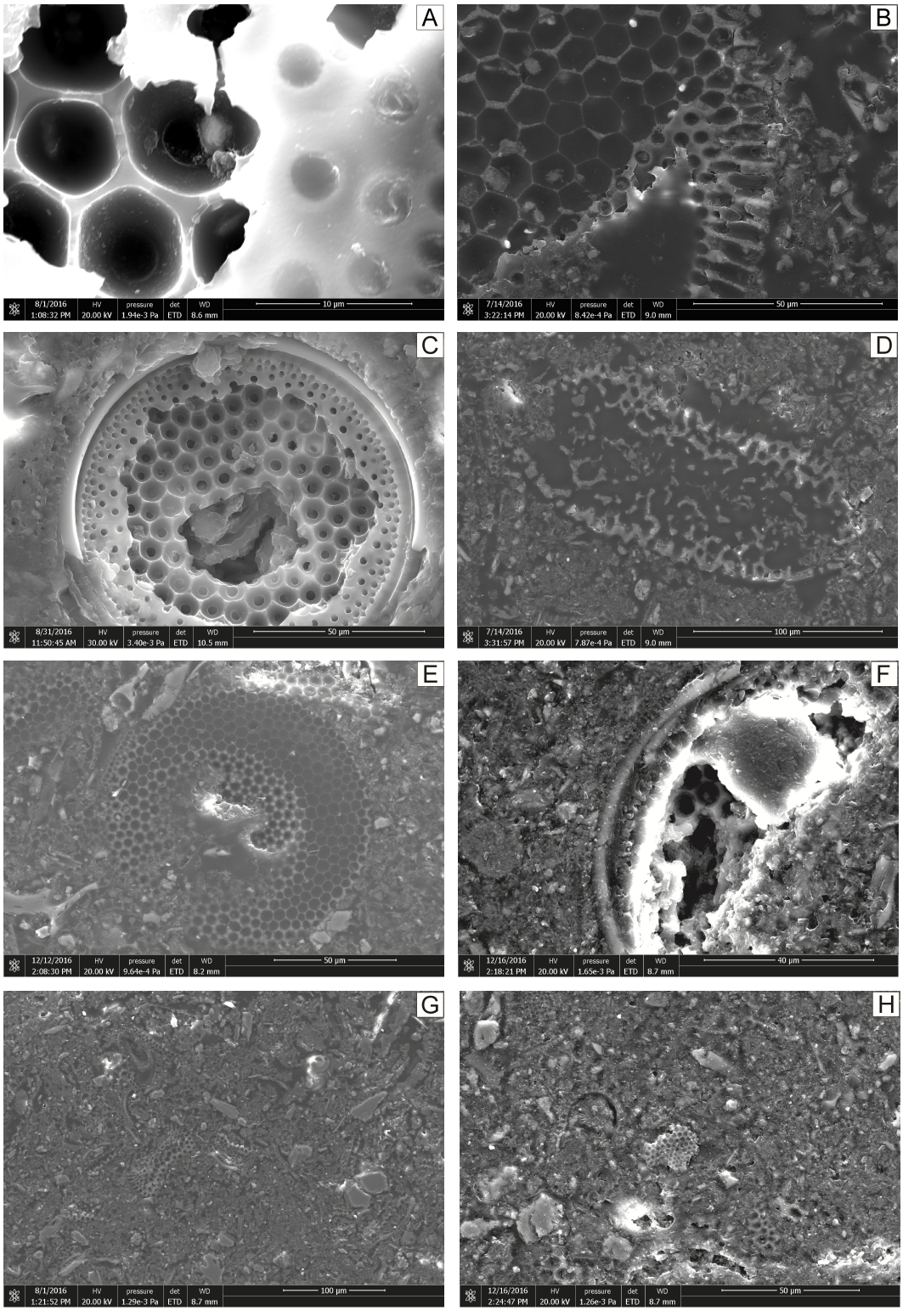


Figure 4.9. SEM photographs of diatom dissolution. A) Moderate dissolution of the outer portion of a diatom valve revealing the intact inner structure (Sample 127-

794A-11H-6, 37–38 cm, at 100.17 mbsf); B) Extensive dissolution of two outer layers of a diatom valve, and moderate dissolution of the inner structure starting from the edges (Sample 127-794A-17X-1, 48–49 cm, at 149.98 mbsf). Note that dissolution initially degrades the edges of diatom valves leading to progressive removal of outer layers and exposure of inner structure; C) Extensive dissolution of a diatom frustule. Note that even the innermost structure of the frustule is strongly affected by progressive dissolution (Sample 127-794A-22X-2, 113–114 cm, at 200.13 mbsf); D) Deterioration of a diatom valve due to dissolution (Sample 127-794A-27X-3, 80–81 cm, at 249.8 mbsf); E) An extensively-dissolved diatom (Sample 127-795A-16H-4, 101–102 cm, at 147.81 mbsf). Note that the outer layers are almost removed due to dissolution; F) A deteriorated diatom frustule under extensive dissolution (Sample 127-795A-22X-5, 128–129 cm, at 198.48 mbsf); G) Diatomaceous facies showing the dominance of fragmented and dissolved siliceous tests (Sample 127-794A-11H-6, 37–38 cm, at 100.17 mbsf); H) Diatomaceous facies displaying strongly dissolved and fragmented siliceous frustules (Sample 127-795A-22X-5, 128–129 cm, at 198.48 mbsf).

significantly to the high porosity of the diatom ooze (Figs. 4.9A–F), while their fragmentation with depth may help reduce the sediment porosity. There is a good correlation between the decrease in amount of biogenic silica and its degree of preservation (Shipboard Scientific Party, 1990b). A dramatic decrease of both the chemical and mechanical preservation of diatom frustules with depth corresponds to the lower diversity of their assemblages.

4.6.2 Silica concentration profile: diagenetic signals and implications

The variability of silica concentrations with burial depth is the key piece of evidence

showing the transition from metastable biosilica to an increasingly-ordered diagenetic silica. Dissolved silica concentrations exhibit a classic profile at Sites 794 and 795. Increasing silica concentrations within the uppermost few metres below the seafloor (from 440 μM at ~4 mbsf to 660 μM at ~10 mbsf for Site 794 and from 615 μM at ~6 mbsf to 780 μM at 15 mbsf for Site 795; Figs. 4.8A, B) may suggest that dissolved silica in the pore water has shifted nearly close to an equilibrium with opal-A. The chemical solution of diatoms is particularly strong at the sediment-water interface and in the upper few metres below seafloor, due to the effect of silica-undersaturated pore waters (Bohrmann, 1986). This may result in the increase of silica within the surficial sediment zone. Given the low sedimentation rate at Site 794 (~37 m/Ma; i.e., hemipelagic rates), most of diatoms in the upper sedimentary layers are likely consumed and the silica has been released into the pore waters. This is confirmed through the results of ODP-conducted smear-slides analysis showing the presence of low solid biosilica within the uppermost sediments (Shipboard Scientific Party, 1990a). At Site 795, smear-slides analyses also show that biogenic opal is at low content across the sediment-seawater interface and the few-metre-thick interval below (Fig. 4.8B). As the amount of dissolution is limited by the solubility of opal-A, which increases with depth and temperature (Tada et al., 2015), dissolved silica begins to steadily increase along the geothermal gradient from the near-surface silica maximum (being ~10 and 15 mbsf respectively at Sites 794 and 795) downwards to the depth of peak concentration in the profile (approximately 1400 μM at ~271 mbsf for Site 794 and 1450 μM at ~321 mbsf for Site 795). A consistent decrease in diatom preservation with depth (Figs. 4.9A–D, 4.9E–F) agrees with the

increased pore-water enrichment in silica across this interval. A strong case can be made that the dissolution of biogenic silica across the opal-A-rich sediment interval is an ongoing process; otherwise dissolved silica concentrations would have led to a definitive equilibrium in the pore water since the Late Miocene (and older) transformation of opal-A to opal-CT under sufficient rates of molecular diffusion or pore-water advection.

The abrupt decrease of dissolved silica starting from the depth of peak value (~23 m above the petrophysical $TZ_{A/CT}$ at Site 794) to a value of 750 μM (at 306 mbsf; Fig. 4.8A) indicates that silica is still being removed from the pore water. Similarly, the silica drop starting just from about 5 m above the transition zone to a value of 700 μM at roughly 338 mbsf (Fig. 4.8B) displays its current removal from the interstitial water in Site 795. The correspondence between the silica drop and distribution of opal-CT recorded at Sites 794 and 795 (Figs. 4.8A, B and 4.10A–E, 4.10F–G) implies that the present-day sink for the dissolved silica is due to the ongoing precipitation of diagenetic opal.

Under the conditions of slow to moderate sediment accumulation (ranging from 10 up to 100 m/Ma; Hesse, 1986), diffusion and pore-water advection are sufficiently rapid to smooth out records of non-steady-state interstitial silica sinks unless the reactions are still ongoing or occurred in the recent past (Lasaga and Holland, 1976; Lyons et al., 2000).

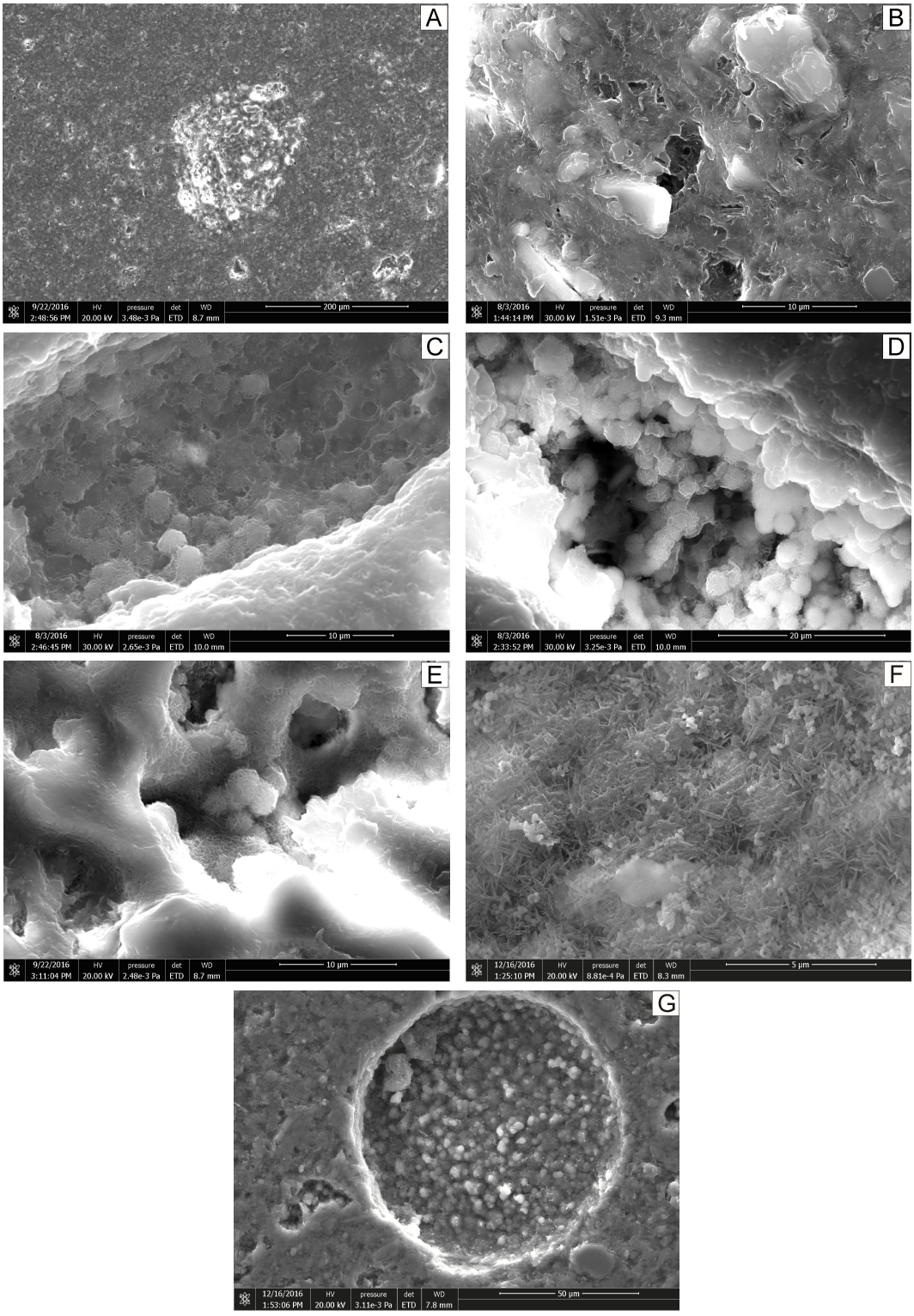


Figure 4.10. SEM photographs of opal-CT formation. A) Formation of opal-CT-cemented rock, following substantial removal of siliceous frustules due to dissolution

(Sample 127-794A-33X-1, 0–1 cm, at 303.3 mbsf); B) Opal-CT clay facies with minor remnants of a siliceous valve (Sample 127-794A-36X-3, 110–111 cm, at 336 mbsf); C) Opal-CT lepispheres partly filling a diatom void (Sample 127-794A-33X-1, 0–1 cm, at 303.3 mbsf); D) Growth of opal-CT lepispheres in a cavity (Sample 127-794A-33X-1, 0–1 cm, at 303.3 mbsf); E) Opal-CT lepispheres growing within a radiolarian skeleton (Sample 127-794A-33X-1, 0–1 cm, at 303.3 mbsf); F) Interlocking cristobalite blades (Sample 127-795A-36X-CC, 36–37 cm, at 327.78 mbsf); G) Opal-CT lepispheres filling a void developed following diatom dissolution (Sample 127-795A-37X-1, 133–134 cm, at 338.23 mbsf).

As such, I can conclude that the ongoing occurrence of opal-CT is related to the present-day burial depths as the sedimentary sections capturing the $TZ_{A/CT}$ at Sites 794 and 795 are presently at their maximum burial depth (due to lack of uplift and erosion). A stronger correlation between diagenetic silica-normalised abundance with present-day burial depth than with age supports this conclusion.

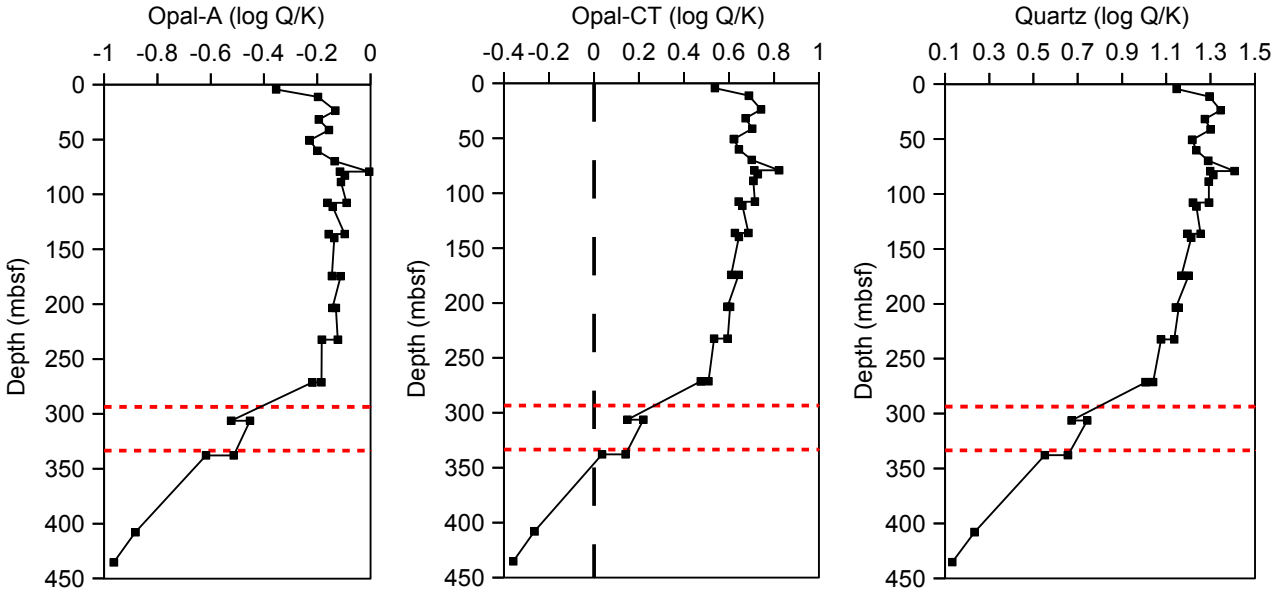
The exhibition of a steadily-decreasing silica content towards a minimum value, starting from the base of the silica sink downwards, suggests that H_4SiO_4 concentrations are close to or have reached an equilibrium with opal-CT. Negligible or no presence of siliceous frustules in the sediment corresponds to the silica minimum along this interval (for example, see Fig. 4.10B).

4.6.3 Pore-water saturation conditions

To determine whether the opal-A to opal-CT transformation thermodynamically occurs within the sediment accommodating the transition zone at the investigated

sites, the saturation index of SiO_2 polymorphs involved in silica diagenesis (opal-A, opal-CT, and quartz) was computed using the Geochemist's Workbench 11 (GWB 11). The software calculated the activity of SiO_2(aq) as well as the pore fluid saturation state with respect to silica polymorphs by using modern measured temperatures measured, pore-water contents of silica, major ions (being K^+, Ca^{2+}, Mg^{2+}) and primary indicators (being SO_4^{2-}, Na^+, Cl^-, pH), and background seawater matrix. The GWB 11 reads datasets of thermodynamic equilibrium constants (most commonly compiled from 0 to 300 °C along the steam saturation curve; after Bethke and Yeakel, 2016) with which it can translate the activity of silica into saturation states for the silica mineral phases. The present-day saturation index profiles (Fig. 4.11) indicate that opal-A should be dissolving thermodynamically in the pore waters above and across the transition zones at Sites 794 and 795. Pore waters above the transition at both sites are supersaturated with opal-CT and, in fact, are very close to the reference value (zero index) across the transition zone, which implies that solubility control might be reached in the pore waters with respect to opal-CT, and therefore opal-CT should still be precipitating within this zone. This is because the pore water is presently very close to the equilibrium with opal-CT at the depth of transition zones where it is most abundant. The solubility equilibration reached at the depth of transition is consistent with increased burial temperatures (pore-water saturation state calculations include temperature effects); as temperature increases, waters become closer to equilibrium with opal-CT. From this, a strong case can be made that the ongoing precipitation of opal-CT is dependent on the modern geothermal gradients at Sites 794 and 795. Excluding the last 20 m of quartz

Site 794



Site 795

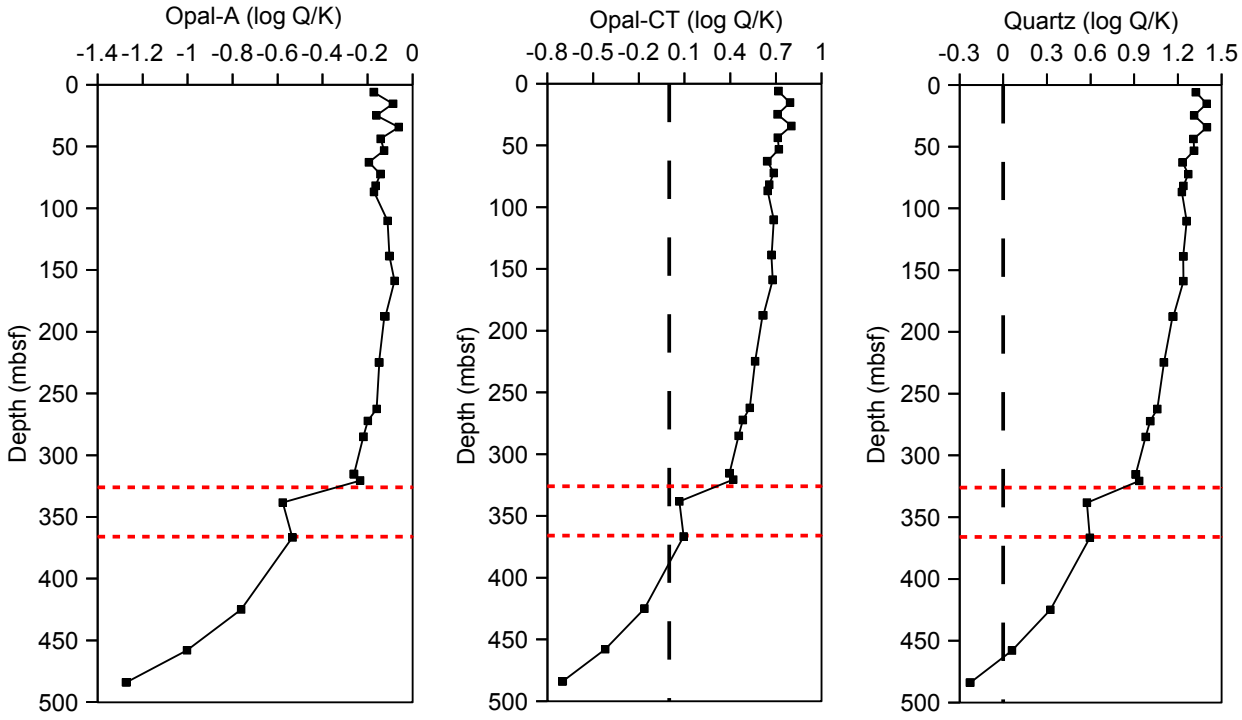


Figure 4.11. Pore-water saturation index versus burial depth for Sites 794 and 795. Black dashed lines represent solubility equilibrium (log Q/K = 0). Red dashed lines indicate top and base of the $TZ_{A/CT}$ as determined by abrupt petrophysical variations.

saturation index profile at Site 795 (from 464 to 484 mbsf; Fig. 4.11), the pore waters everywhere along the depth profiles of both sites are supersaturated with respect to quartz. Ideally, only the most stable polymorph can be present at one time, and quartz is the most stable phase. In reality, however, rates of transformation among silica polymorphs are quite slow under the diagenetic conditions such that the metastable polymorph (opal-CT) persists across the transition and is preferred over quartz due to its higher rates of nucleation and growth (after Williams et al., 1985). Below the $TZ_{A/CT}$, pore water is only supersaturated with respect to quartz, while undersaturated with both opal-A and opal-CT.

4.6.4 Role of authigenisation on silica concentration in sediment pore water

Formation of authigenic phases, namely the aluminosilicates, other than opal-CT, is an observed part of diagenesis in many biosiliceous oozes that are subjected to transformation from opal-A to opal-CT. These reactions which are referred to as 'reverse weathering processes' (e.g., Emerson and Hedges, 2008) often influence the pore-water solubility and chemical kinetics of dissolved silica. In accordance with previous studies on the role of fine detrital on silica solubility (e.g., Van Cappellen and Qiu, 1997a; Rickert, 2000), the SiO_2 pore-water values in the sediments from Sites 794 and 795 are dependent on the amount of clayey material present in the opal-rich zone (Fig. 4.12). Since it is well known that Al is a reactive element in marine sediments, this dependence implies that detrital aluminosilicates supply the aluminium necessary for the formation of authigenic aluminosilicates that occur soon after deposition. This relationship also strongly implies that sediments commonly

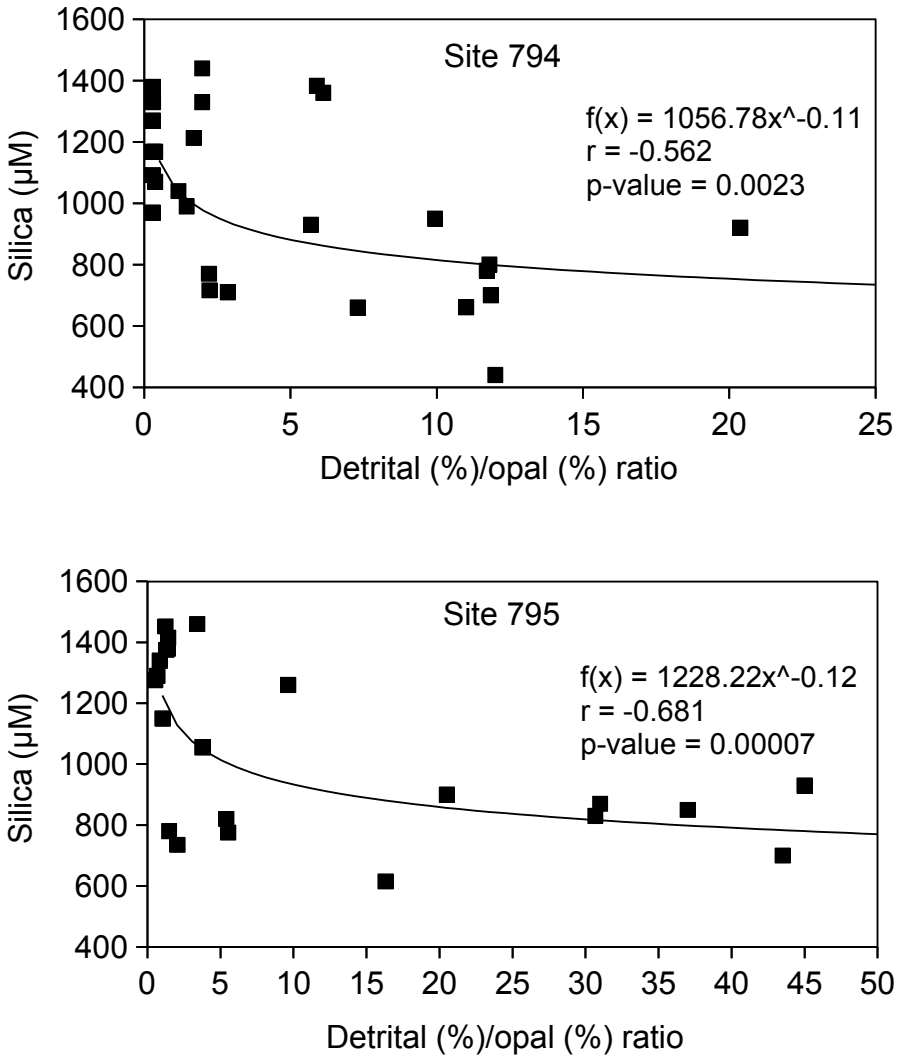


Figure 4.12. The relationship between the H_4SiO_4 concentration in pore waters of the sub-seabottom sediments is Sites 794 and 795 and the relative detrital content of the sediments. Sediments with more detrital (aluminosilicate) material support lower silica concentration values (the Pearson correlation coefficient (r) clearly indicates that the silica concentration and the relative detrital content for Sites 794 and 795 are inversely correlated; the p-value (< significance level 0.05) shows this relationship is statistically significant, according to Noymer, 2008). The detrital and opal content of the sediments were derived from the results of smear-slide analyses conducted by ODP (Shipboard Scientific Party, 1990a, b) to determine the sediment particle composition.

with the most detrital material (the highest detrital (%)/opal (%) ratios; Fig. 4.12) support the silica depression across the transition zone. During reverse weathering, some of the silica dissolved in the pore water is combined with Al, K, Mg, and other elements to precipitate less soluble early diagenetic clay minerals. Experimental works conducted by Dixit et al. (2001) on the opal-rich sediments from the Southern Ocean showed that the concentration of dissolved silica in these sediments is strongly influenced by the presence of the aluminosilicate phase. According to their study, pore-water silica concentration for a nearly-pure opal-A sediment was decreased up to 60% when the amount of authigenic aluminosilicate in the opal-A sediment was increased by 25% of the total volume.

Even though the indications of ongoing reverse weathering/diagenetic clay formation are observed, my temperature-dependent pore-water saturation state calculations clearly show that the depth of the transition zone is consistent and in both sites, corresponds to solubility equilibrium (i.e., log Q/K = 0) with respect to opal-CT. Thus, the silica drop within the transition zone represents a feature mainly controlled by an active precipitation of opal-CT mineral phase.

4.6.5 Interstitial-water signatures of other major ions

Due to significant petrophysical variations associated with the formation of opal-CT, the $TZ_{A/CT}$ at Sites 794 and 795 affects most of the interstitial-water chemical profiles. The similarity of Li and silica concentration profiles (Figs. 4.4 and 4.8A, B) demonstrates their close chemical relationship. Opal-A is the most probable carrier

phase for lithium at Sites 794 and 795 (Shipboard Scientific Party, 1990a, b). A relatively-large increase in Li^+ concentrations from the seafloor to the transition zone indicates a persistent release of lithium into the interstitial water during diatom dissolution. Though the change in relative concentrations of lithium and silica in Site 794 is positively correlated (r = 0.649; Fig. 4.13A), there are deviations from an ideal correlative pattern (r = 1) throughout the sediment column, especially within the upper part of the opal-A zone and across the $TZ_{A/CT}$. At Site 795, the concentrations of lithium and silica are poorly correlated (r = 0.145) such that their concentration ratio (Li:Si) strongly deviates from the correlative mixing line (the Li:Si ratio for mixing line is 1:6.7 (0.15); Fig. 4.13B). Such strong deviations from this ideal correlative behaviour represents a feature that is not altered by ion transport modes. For this to happen, it is required that the ongoing release of lithium and silica from the sediment occurs on timescales smaller than that at which diffusion or advection are effective. The current removal of dissolved lithium below the $TZ_{A/CT}$ is perhaps due to its incorporation into clay minerals (Steiness et al., 1972) or the cation-exchange processes in some newly-formed mineral phases. Gieskes (1983) and De Carlo (1992) suggested that the early diagenesis of biogenic opal-A has a major influence on dissolved Li^+ concentrations. I agree that the main cause of present lithium sink at Sites 794 and 795 is the reconstitution of the opal-A solid phase, as interstitial lithium mimics the opal-A distribution patterns (Figs. 4.4 and 4.8A, B). Further, the coincidence of non-correlative behaviour over the depth of transition zone for silica and lithium reflecting their distinct co-removal from the interstitial waters suggests the coherence of these peak deviations with ongoing silica

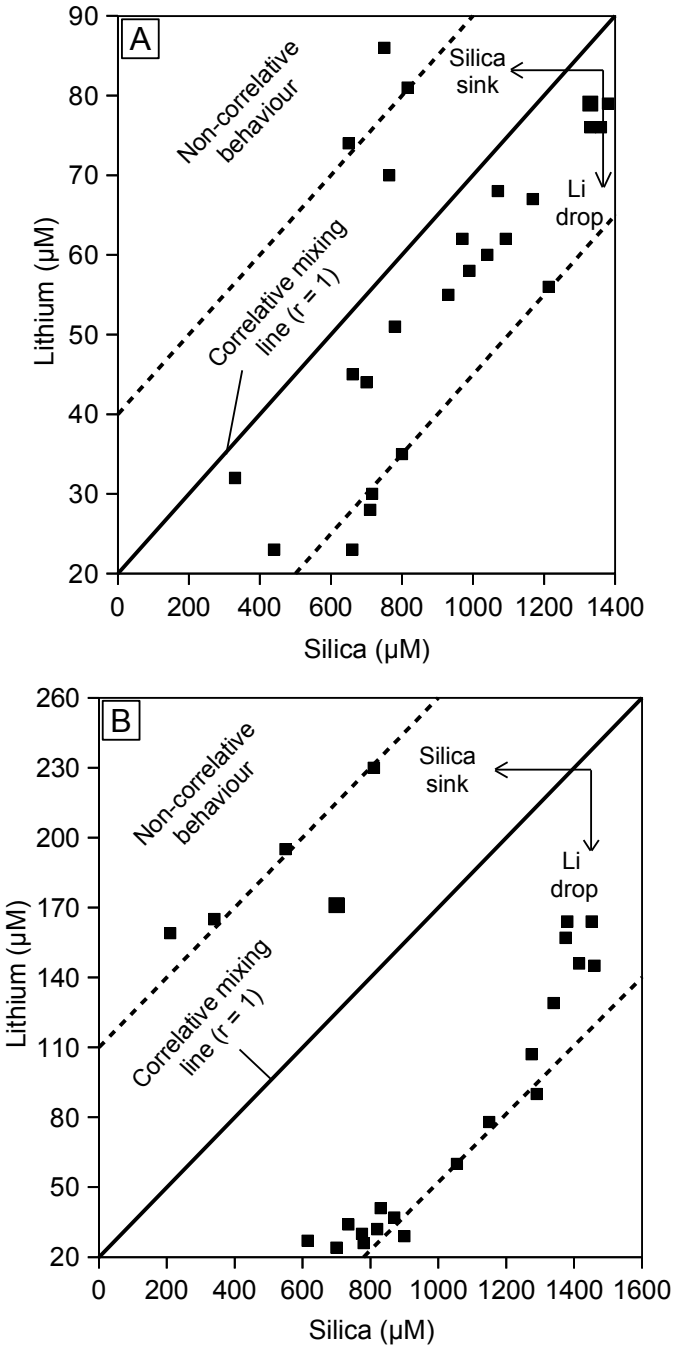


Figure 4.13. A) Lithium versus silica, Site 794. Sample points trend from shallow to deep sites in the sediment column from the lower left to the upper right in the figure. Black dashed lines denote the realm of deviation from the 1:20 (0.05) Li:Si ratio of ideal correlation; B) Lithium versus silica, Site 795. Note a weak correlation between the data points (r = 0.145) causing large deviations from the ideal mixing line. Dashed lines mark the domain of deviation from the 1:6.7 ratio of ideal correlation.

diagenesis (Figs. 4.13A, B).

The relatively-steep decrease in K concentrations (especially for Site 794) from the seafloor to the top of the $TZ_{A/CT}$ (Fig. 4.4) may result from alteration of the frequent volcanic ash layers present in the opal-A-rich sediment pile above the transition zone. The nearly-sharp decrease of K through the $TZ_{A/CT}$ likely indicates large-scale removal during interaction with phases undergoing ongoing silica diagenetic reactions. K concentrations are affected by ion transport modes that generally reduce the concentration gradients, unless a recent release of K to the pore water is predominant within the diagenetic system. Below the transition zone, a linear relationship occurs, a pattern typical for profiles influenced by basement alteration processes (McDuff and Gieskes, 1976).

Concentrations of Ca and Mg exhibit opposite trends (Figs. 4.4 and 4.14A, B) and suggest a chemical relationship. Relative concentrations of these two dissolved species are not entirely correlated along the conservative ratio ($r = -0.845$) exhibiting a slight deviation from the 1:1 (1) Ca:Mg ideal conservative line, particularly in the uppermost portion of the sediment column at Site 794. This would indicate some removal of both Ca and Mg from the interstitial waters. The change in relative Ca and Mg concentrations, however, shows marked deviations from the conservative pattern throughout the depth profile at Site 795 (the peak deviation being across the transition zone) ($r = -0.777$). To maintain deviations from conservative behaviour, the dissolved Ca and Mg profiles require a continuous input of these elements to the

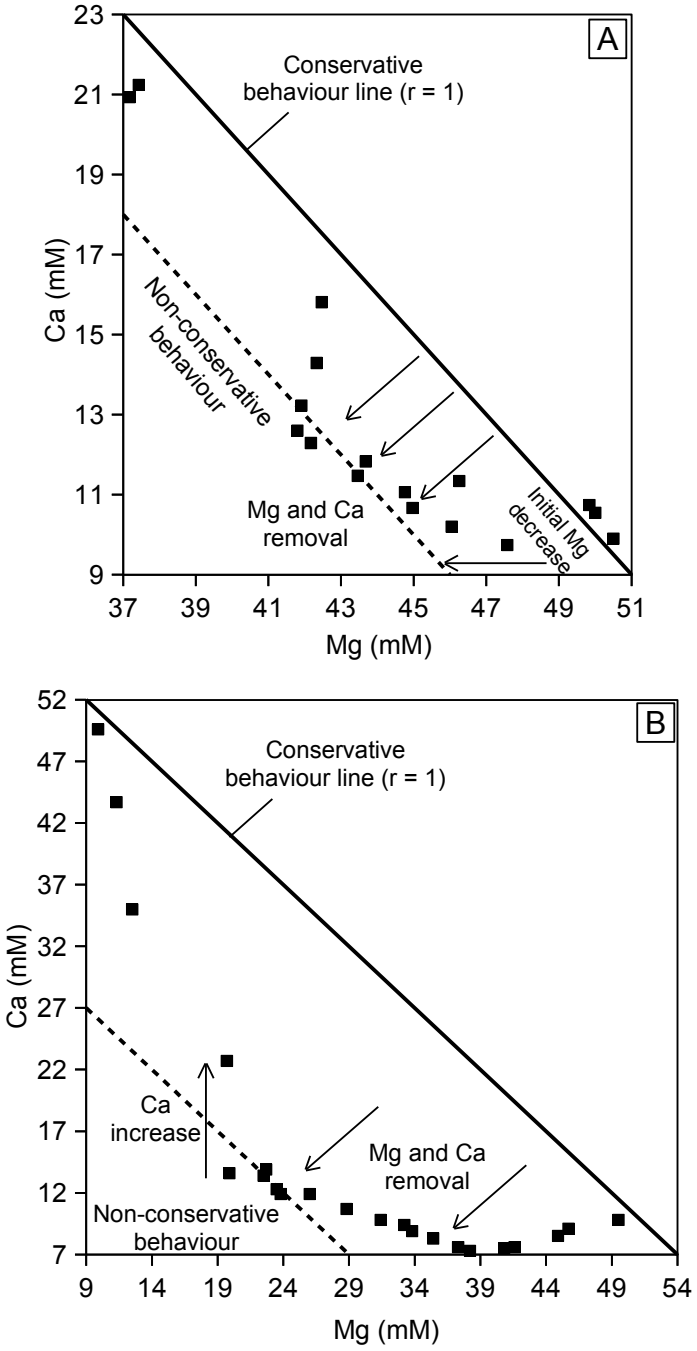


Figure 4.14. A) Calcium versus magnesium, Site 794. Sample points trend from shallow to deep in the sediment column from the lower right to the upper left in the figure. Black dashed line denotes the realm of deviation from the 1:1 Ca:Mg ratio of conservative line; B) Calcium versus magnesium, Site 795. Sample points trend from shallow to deep sites in the sediment column from the lower right to the upper left in the figure. Dashed line marks the limit of deviation from the 1:1 conservative line.

pore water. This may occur if Mg and Ca have been recently released to the interstitial waters and at rates faster than those for the pore-scale processes that smooth the concentration gradients.

The downhole gradients of pore-water Ca and Mg concentrations indicate that present-day composition of interstitial water is likely controlled by both mineralogical transformation of opal-A to opal-CT and formation of Mg clay minerals.

In both Sites 794 and 795, increased Ca concentrations with depth (Figs. 4.4 and 4.14A, B) suggest the dominance of silicate (plagioclase) alteration reactions, particularly the formation of clay minerals (Shipboard Scientific Party, 1990a), in the opal-A zone and in the $TZ_{A/CT}$. However, the continuity of decreasing Mg with depth across the $TZ_{A/CT}$ likely represents the precipitation of Mg-hydroxide lepispheres that serve as templates for opal-CT formation (Kastner et al., 1977).

It seems implausible that reactive formation of early diagenetic clay minerals is strongly retarding opal-CT precipitation as there is no additional pore-water sink for the dissolved Mg developed by silicate alteration reactions across the present silica sink. I assume that under highly-alkaline conditions, essentially achieved by the most intense sulphate reduction across the Neogene interval overlying the $TZ_{A/CT}$ (according to Shipboard Scientific Party, 1990a), seawater can provide a sufficient Mg source for the alteration reactions. Hence, the competition between clay minerals

and opal-CT for the available alkalinity from seawater decreases significantly.

Increased interstitial Sr with depth mimics the Ca trends and may reflect their mutual chemical association. Like Ca, the input of Sr is most likely from silicate alteration reactions (including the formation of clay minerals) as the overall carbonate extent of Sites 794 and 795 is low (Shipboard Scientific Party, 1990a, b). The similarity of Sr and Ca concentration patterns, especially below the opal-A to opal-CT diagenetic transition (Fig. 4.4), may suggest that the Sr profile is modified by the same set of diagenetic and transforming reactions as Ca.

4.6.6 Signals of ongoing reactions in pore-water primary indicators

Due to the highly-variable organic carbon content of the sediments from Sites 794 and 795, the changes in SO_4^{2-}, alkalinity, NH_4^+, and PO_4^{3-} profiles are a function of microbial-mediated organic matter degradation (in accordance with Shipboard Scientific Party, 2001a, b). As the dispersed organic matter embedded in the sediment provides an energy source for bacteria, bacterial decomposition of organic matter becomes the initial mechanism altering the chemical composition of pore water during early diagenesis (Hesse, 1986). Amongst primary indicators, dissolved sulphate exhibits a weak positive correlation with the organic matter content of sediment (Fig. 4.15). This may suggest that besides the availability of organic carbon, other factors, including sediment accumulation rates, can exert controls on the rate of sulphate reduction. However, the controls on pore-water organic matter are beyond the scope of this thesis.

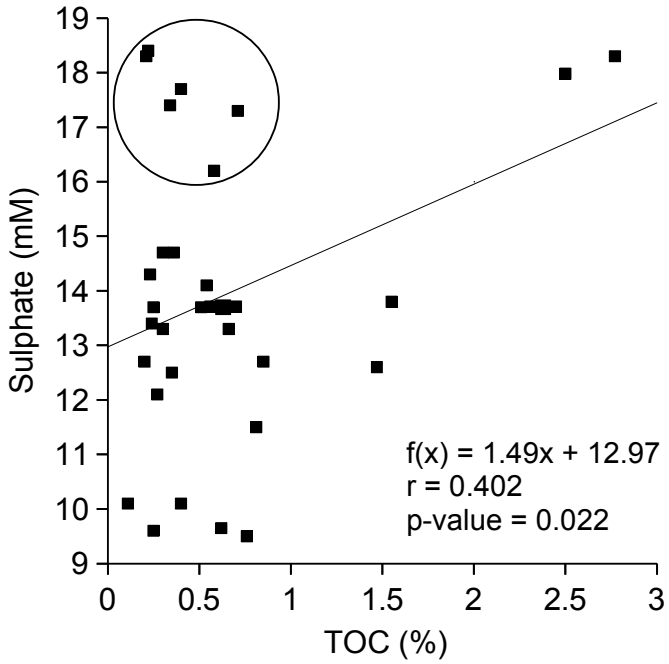


Figure 4.15. Sulphate reduction as a function of the organic carbon content of sediment samples, Site 794. Samples within this circle represent the shallowest sediment samples where the rate of sulphate reduction is greater. The data correlation is significant (p-value < significance cutoff 0.05, according to Noymer, 2008).

The patterns of concentration variability with depth also demonstrate essential controls from silica diagenetic reactions on primary chemical delegates (species). Sulphate reduction plays a major role during silicification through exerting a fundamental control on the alkalinity of interstitial waters. The higher the rate of sulphate removal, the higher the alkalinity of the pore water. Sulphate reduction is more effective in the opal-A-dominated sediment than in the opal-CT interval (Shipboard Scientific Party, 1990a), perhaps due to a porosity drop with silica diagenesis. The lower organic carbon content coupled with the low sedimentation rate, however, has limited the extent of pore-water sulphate depletion throughout Site

794. Conversely, high rate of sulphate removal from the sediment column at Site 795 has resulted in higher pore-water alkalinity values in this site.

The coincidence of the dissolved sulphate minimum with the present-day sink of silica (Figs. 4.5 and 4.8A, B) may emphasise the controls from sulphate reduction on ongoing silica diagenesis. For both Sites 794 and 795, the steadily-decreasing trend of alkalinity with depth across the transition zone occurs as silica diagenesis consumes the available pore-water alkalinity to precipitate opal-CT. It is generally accepted that the ammonia profile also corresponds to the ongoing silicification. The release of ammonia as a metabolic product of organic matter decay maintains relatively-constant alkaline pH values for interstitial waters (Fig. 4.5). The increased ammonia down to $TZ_{A/CT}$ raises the pH to levels sufficient for the solubility of amorphous silica to produce undissociated $Si(OH)_4$ (Williams et al., 1985; Taguchi et al., 1988). The steady decrease in ammonia below the $TZ_{A/CT}$, in coincidence with precipitation of diagenetic opal, is perhaps due to its incorporation into clay mineral interlayers (Wlotzka, 1972; Shipboard Scientific Party, 1990a).

At present, the lack of a response from the phosphate profile to silica diagenetic processes poses a challenge at Sites 794 and 795. Some researchers have shown that phosphorus is incorporated into biosiliceous diatom frustules as highly-phosphorylated proteins (silaffins, silacidins), which play a critical role in biosilica morphogenesis (Kröger et al., 2002; Sumper and Brunner, 2008; Wenzl et al., 2008; Richthammer et al., 2011; März et al., 2014). As such, phosphate may be propagated

into the pore water across the uppermost part of the sediment column (commonly up to the depth of ~10 mbsf) upon the dissolution of frustules. However, from this depth down to the depositional sections, the decreasing phosphate concentrations for both sites do not mirror the silica release trend. Rather, this trend indicates rather strong first-order removal, most likely into finely-disseminated sedimentary phosphatic phases (Shipboard Scientific Party, 1990a).

The decreasing salinity profile of interstitial waters from the surface towards the $TZ_{A/CT}$ and the continuity of this trend below the transition implies a contradictory trend of pore salinity under burial (Fig. 4.5). The moderate correlation of salinity index versus porosity under burial observed for Sites 794 and 795 (Fig. 4.16) displays a wide range of deviations from the ideal correlative pattern throughout the sediment column. Accumulation of minimum deviations from the ideal correlative pattern in Site 794 within the $TZ_{A/CT}$ while the occurrence of peak deviations at the $TZ_{A/CT}$ in Site 795 suggests that, in addition to porosity, other controls on salinity removal from the pore water may also be effective over the opal-A to opal-CT transition. It is well accepted that a considerable volume of interstitial solution has been expelled due to porosity decrease across the boundary between opal-A-rich and opal-CT-rich sediment units at Sites 794 and 795 (Tables 11 in Shipboard Scientific Party, 1990a, b). The small volumes of pore fluid left after porosity drop could be a very reasonable explanation for the salinity decrease with burial depth. This interpretation, however, can be challenged as the interstitial water pressed out under silica diagenesis leaves increased *in situ* salinity concentrations behind. Magara

(1974) explained that the salinity distribution in fine-grained sediments should be a reciprocal of the porosity, due to the ion infiltration effects of the clays. There is also the possibility that dominant clay mineral formation across the transition zone activates the salinity removal.

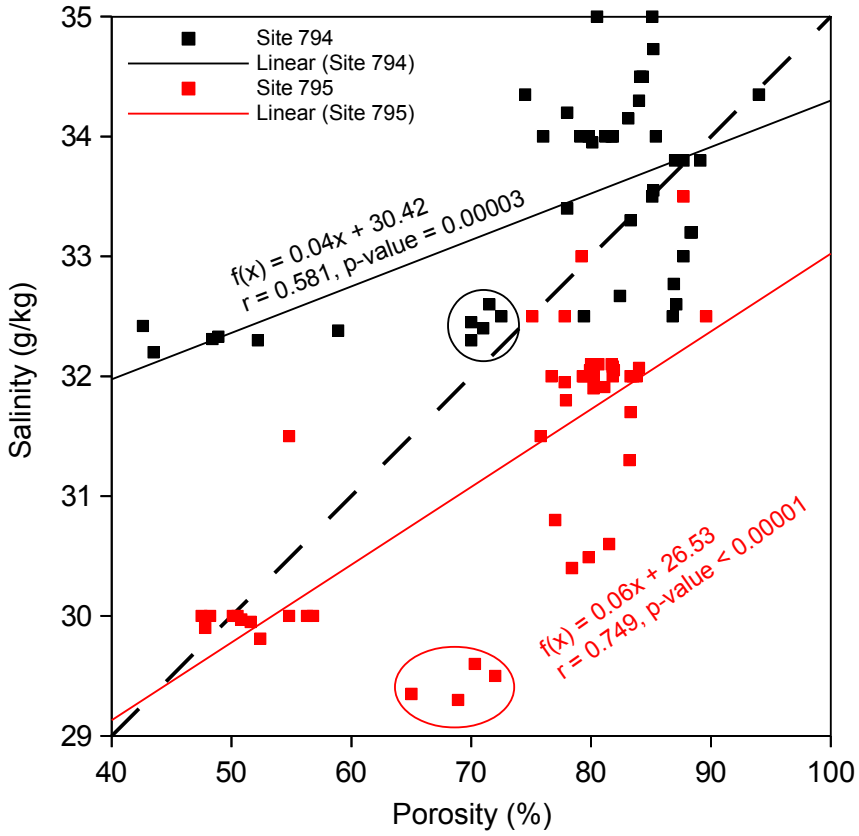


Figure 4.16. Pore-water salinity versus sediment porosity, Sites 794 and 795. Sample points trend from shallow to deep in the sediment column from the upper right to the lower left in the figure. Black dashed line marks the ideal correlative pattern (r = 1). Data points within the black circle and red oval represent the samples from the depth of transition zone at Sites 794 and 795, respectively. The p-values (< significance level 0.05) show the relationship between the data points is statistically significant (according to Noymer, 2008).

Rather conservative sodium and chlorine concentrations throughout the sediment column at Sites 794 and 795 reflect the nearly-constant high salt content of the pore water. The coincidence of pore-water salinity values remaining close to those of seawater and high amount of simple salts (Na^+ and Cl^- concentrations) with the silica sink (Figs. 4.5 and 4.8A, B) reflects the present-day precipitation of opal-CT. Alkaline pore waters having high salt concentrations are a key control on solubility of amorphous silica and the subsequent formation of silica gel (opal-CT precipitation) under burial (Williams and Crerar, 1985).

Following the same straightforward evidence presented for the profiles of the major ions, the interstitial-water profiles of primary indicators represent the ongoing release of these components into the pore water. The profiles that, until recently, have been neither affected by dissolution nor by precipitation (indicating fossilised diagenetic reactions) would have led to a thermochemical equilibrium of dissolved species concentrations in the pore waters, i.e., smoothed concentration gradients, under sufficient rate of molecular diffusion or pore-water advection.

4.6.7 Ongoing diagenesis signals from isotopic temperatures

A comparison of the isotopic temperatures of diagenetic silica formation and present-day *in situ* temperatures at comparable depths is the eminent set of evidence to evaluate whether silica diagenesis over the transition zone represents a currently-active process. The palaeo-temperatures of opal-CT formation can be deduced from $\delta^{18}O$ values using the expressions that relate temperature to oxygen isotope

fractionation for the silica-water system. The sudden change in oxygen isotopic composition of silica at the petrophysical $TZ_{A/CT}$ in Sites 794 and 795 (Figs. 4.17A, B) suggests that opal-CT acquires its $\delta^{18}O$ value through equilibration with the encompassing interstitial water at the transformation boundary, and maintains this isotopic signature with depth within the opal-CT-rich section, including the $TZ_{A/CT}$ and the interval below it (Murata et al., 1977; Pisciotto, 1981a; Pisciotto, 1981b; Pisciotto et al., 1992). Therefore, the mean $\delta^{18}O$ value across opal-CT-bearing zone approximates the temperatures of diagenetic silica formation.

Following the experimentally-determined fractionation expression of Kita et al. (1985), Pisciotto et al. (1992) computed the isotopic temperatures of opal-CT formation by pairing the pore-water $\delta^{18}O$ values at top of the opal-CT-bearing zone with each opal-CT $\delta^{18}O$ value within the zone. Due to their minute isotopic depletion gradients, the pore-waters samples from depths closest to each opal-CT sample would have made very little difference in the estimated temperatures of diagenetic silica formation (Pisciotto et al., 1992).

As a first estimation, the clustering of isotopically-determined temperatures close to the extrapolated present-day ambient temperatures in Site 794 (Fig. 4.17A) supports the hypothesis that the silica transition zone is roughly in equilibrium with the present-day geothermal gradient. At Site 795, isotopic temperatures are systematically lower than modern sediment temperatures at the depth of transition zone and the interval below, but the past temperature gradient (233 °C/km) is higher

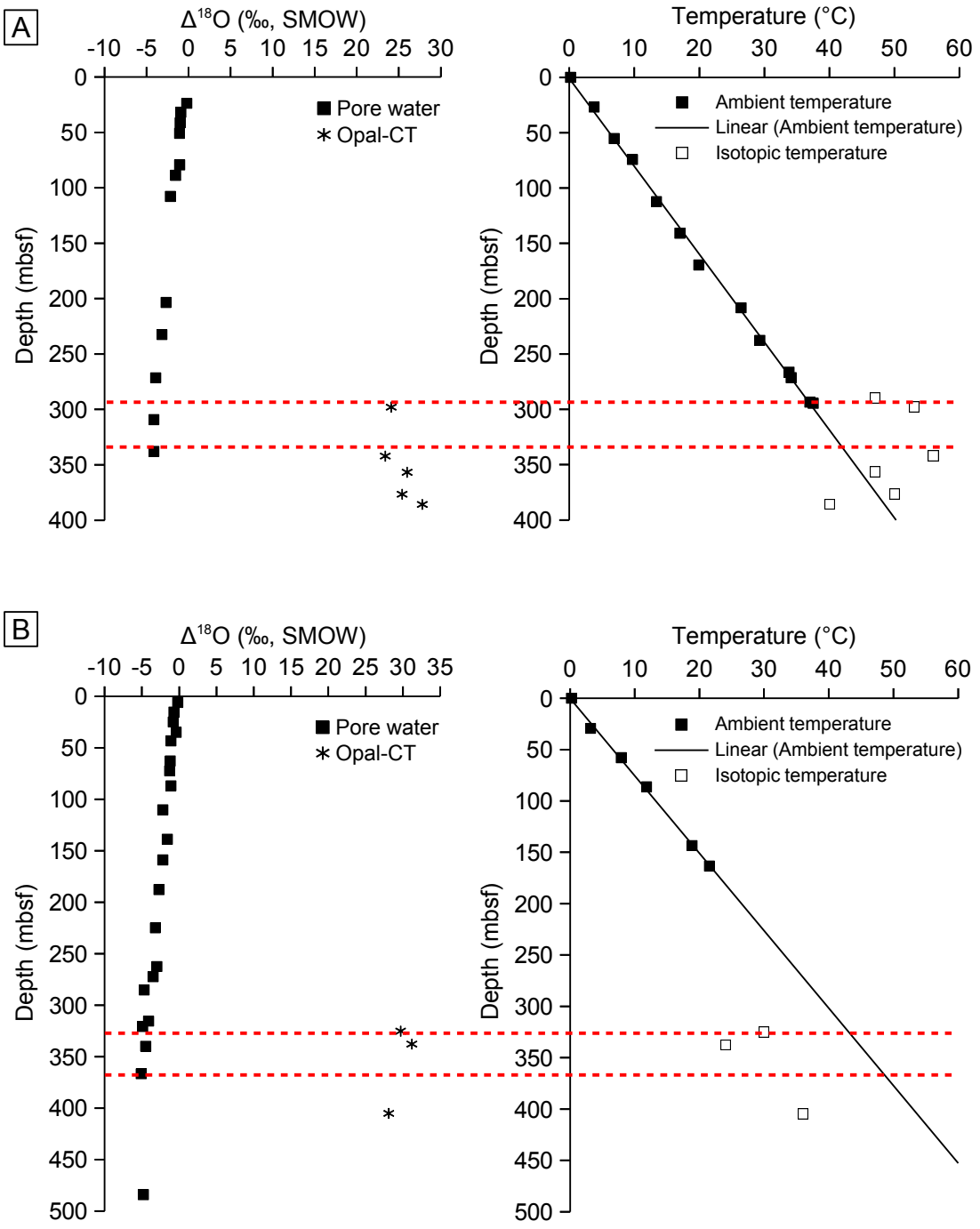


Figure 4.17. Oxygen isotope and temperature versus burial depth, Sites 794 (A) and 795 (B) (redrawn and modified from Pisciotto et al., 1992). The trend lines passing through ambient temperatures represent the modern thermal gradients which are 125 and 132 °C/km at Sites 794 and 795, respectively. Red lines mark top and base of the $TZ_{A/CT}$ as determined by abrupt petrophysical changes.

than the present-day gradient (132 °C/km). One possible explanation for this apparent inconsistency is that the silica transition formed during the early post-rift period in the Japan Basin has been rather rapidly buried, under an intermediate accumulation rate for the Neogene sediment sealing the transition (60 m/Ma), that it has yet to move towards equilibrium with the modern gradient (after Pisciotto et al., 1992). The temperature-dependent pattern of pore-water saturation with respect to opal-CT clearly supports this interpretation, showing that saturation index values are moving towards equilibrium near the depth of transition zone (Fig. 4.11).

In addition, the seismic geometrical attitude of the silica transition at these sites, which is a regional BSR, closely mimics the present-day isotherms, including those at the seafloor (Figs. 4.3A, B). The possible interpretation of these notions is that the opal-A to opal-CT depth interval at Sites 794 and 795 represents an approximate modern isotherms over which the silica phase change is an ongoing process, controlled by the present-day thermal regime. Since this currently-active $TZ_{A/CT}$ is not tectonically deformed, the isopleths─maturation lines of opal-CT (in particular cristobalite)─rationally take a concordant attitude in relation to the isothermal reflections (Mizutani, 1977). A transition zone that undergoes intense deformation prior to reaching a physicochemical equilibrium relative to the silica diagenetic reaction and having a much longer time period following deformation, will lead the isopleths to a discordant attitude relative to the modern isotherms, a situation that represents an arrested phase-change transition that is not in thermal equilibrium with the isothermal features.

4.6.8 Transport of dissolved species: advection versus diffusion

The presence of chemical signatures of opal-CT precipitation in the interstitial water heavily depends on the mechanisms that deal with the transport of solutes from the site of dissolution to the site of precipitation. The transition zone at Sites 794 (begins chemically at ~271 mbsf and petrophysically at ~293.5 mbsf) and 795 (begins chemically at ~321 mbsf and petrophysically at 326 mbsf) below which opal-CT is persistently precipitating, profoundly influences the composition of pore waters by regulating the concentration gradients of elements involved in the silica diagenesis process, as for instance silica, lithium, sulphate, and ammonia. Substantial silica and lithium additions to the pore water above and losses from the pore water below the $TZ_{A/CT}$ suggest that this boundary acts as an end point from which diffusional gradients can develop both upwards from the sediment into the water column and downwards below the transition (Figs. 4.4 and 4.8A, B). Due to variations in the sediment pore-water diffusion coefficients with burial depth (Table 4.4), the profiles connecting the concentration values above and below the $TZ_{A/CT}$ are essentially represented by curved lines. A depth dependency of the diffusion coefficient is expected from its relation to porosity (Hesse, 1986), implying remarkably-smaller coefficients for more compacted opal-CT sediments. As claimed by McManus et al. (1995), the interstitial chemical signals associated with silica diagenesis are diffusion dependent. According to Hesse (1986), under diagenetic conditions, diffusion is the main transport mechanism in pore water across the transition zone as the sediment column overlying the $TZ_{A/CT}$ becomes a seal for other modes of transport, including advection due to the significant decrease in porosity.

However, biogenic siliceous oozes are characterised by a very low permeability, and when we add the compaction effect, we can assume that diffusion rates will be even lower with depth (Williams et al., 1985; Hurd, 1973). In accordance with the observations of Hurd (1973), my estimated diffusion fluxes in the sediment pore water at Sites 794 and 795 are extremely low even at the sediment-water interface, and decrease rapidly down the stratigraphic column (Table 4.4). Given this data, and the low permeability features of biogenic opal, diffusion is considered a relatively-insignificant factor for bypassing opal-CT across the $TZ_{A/CT}$. The occurrence of an appreciable rate of water expulsion across the transition zone (Table 4.4), caused by an abrupt porosity contrast between the porous diatomaceous sediment and opal-CT units further supports the conclusion that the dissolved species has not been diffused in the sediment at rates comparable to those by other transport mechanisms, namely by pore-water advection. There is the possibility that pore water leaves the system both vertically and laterally. The low permeable nature of opal-A sediments may be an obstacle to the release of pore water during opal-A to opal-CT transformation. By contrast, Davies et al. (2008) indicated that the expulsion of water as opal-A converts to opal-CT is a function of overpressure. To generate overpressure, the rate of fluid production needs to exceed the rate of fluid seepage. In addition, the low permeability of fine-grained overburden permits the buildup and maintenance of elevated overpressure that drives the pore-water flow.

Most of the dissolved species with differing patterns of pore-water profiles are involved in ongoing reactions across the transition from opal-A to opal-CT in Sites

794 and 795, as evidenced by the concentration gradients with depth. Advective flow appears to have ceased recently or continues to operate at very low rates as it has failed to mask the effects of these reactions. As well, the reaction products (in particular dissolved silica) are consumed by the precipitation of progressively less soluble opal-CT over the $TZ_{A/CT}$ (see Fig. 4.10G, for instance). Even for the ion species whose profiles display slight gradients with depth, (e.g., calcium profile in Site 794), I assume that the existing gradients are been mostly initially dissipated by advection and then later by diffusion (Hesse, 1986). However, the failure of ion transport mechanisms to completely remove concentration gradients implies that the reactions are still ongoing. In essence, the retention of a silica gradient versus the gradient-erasing mechanisms along the sediment column is a major requirement for diagenesis to persist, as high advection (and or diffusion) rates prevent dissolved silica from concentrating *in situ*, and the critical concentrations needed for opal-CT precipitation cannot be achieved (Williams and Crerar, 1985).

4.6.9 Controls on sediment porosity

The pore-water silica profile specifies an abrupt chemical transition from opal-A and opal-CT, nearly coincident with a porosity decrease of as much as 14% (from 86 to 72%; these two values represent respectively the average porosities for the lithostratigraphic units just above and below the $TZ_{A/CT}$ (Table 4.4)) and 20% (from 80 to 60%; comparably, these values are averaged for the stratigraphic units just above and below the $TZ_{A/CT}$) respectively for Sites 794 and 795 that occurs within the transformation zone where opal-CT is the major silica polymorph. This significant

Table 4.4. Mean porosity, mean water content, and accumulation rate of the lithologic units, Sites 794 and 795 (Shipboard Scientific Party, 1990a, b). Also shown are the dependent parameters, including sediment diffusion coefficient and diffusion rate estimated for each unit.

Site	Depth, mbsf	Stratigraphic unit	Age *	Porosity, %	Water content, %	Sedimentation rate, m Ma^{-1}	Sediment diffusion ** coefficient, $cm^2 s^{-1}$	Diffusion flux, g $cm^{-2} yr^{-1}$
794	0	Seafloor	Quaternary (0 Ma)					
				79	55	31	3.43×10^{-6}	7×10^{-7}
	92.3	Base of alternating light bioturbated zones and dark laminated zones with common thin ash layers	Late Pliocene (2.99 Ma)					
				84	62	37	3.88×10^{-6}	1.9×10^{-7}
	216.9	Base of bioturbated ooze and clayey ooze with sparse ash layers	Late Miocene (6.4 Ma)					
				86	67	51	4.07×10^{-6}	-4×10^{-7}
	293.5	Base of diatomaceous clay	Late Miocene (7.9 Ma)					
				72	47	36	2.85×10^{-6}	-4×10^{-7}
	351.3	Base of bioturbated clay and siliceous claystone with minor ash, pyrite, and micritic carbonate	Late Miocene (9.65 Ma)					
				52	28	36	1.49×10^{-6}	-8.9×10^{-8}
	491.7	Base of bioturbated claystone with rare laminated intervals	Middle Miocene (14.3 Ma)					
795	0	Seafloor	Quaternary (0 Ma)					
				81	56	60	3.61×10^{-6}	5.4×10^{-7}
	123	Base of bioturbated silty clay and diatom clay	Late Pliocene (2.1 Ma)					
				82	58	65	3.7×10^{-6}	1.7×10^{-7}
	239	Base of bioturbated diatom ooze and silt-clay-diatom mixed sediment	Early Pliocene (3.95 Ma)					
				79	57	70	3.43×10^{-6}	0
	288.8	Base of bioturbated diatom claystone	Early Pliocene (4.7 Ma)					
				80	54	70	3.52×10^{-6}	-2.4×10^{-7}
	325	Base of diatom-silt-clay mixed sediment and diatom clayey siltstone	Early Pliocene (5.3 Ma)					
				60	29	47	1.98×10^{-6}	-2.8×10^{-7}

Table 4.4. Continued.

413	Base of siliceous silty claystone, porcellanite, and chert	Late Miocene (6.8 Ma)	45	25	36	1.11×10^{-6}	-4×10^{-8}
665	Base of bioturbated siliceous claystone, claystone, and subordinate silty siliceous claystone	Middle Miocene (12.8 Ma)					

* The numerical ages of stratigraphic units have been derived from the ODP initial reports for Sites 794 and 795 (see Shipboard Scientific Party, 1990a, b).
** The diffusion coefficient of sediment is calculated using the equation $D_s = \Phi^2 \times D$, where:
Φ, the sediment porosity (pore-water volume/total sediment volume) and D (= 5.5×10^{-6} cm^2/s; Wollast and Garrels, 1971; Rickert, 2000; Dixit and Van Cappellen, 2003) is the free solution diffusion coefficient of dissolved silica in the deep sea.

porosity reduction due to silica diagenesis is comparable to those estimated by previous studies; for example 15% in the sub-surface sections of Neogene marine non-calcareous siliceous rocks, northern Japan (Akita and Tenpoku oil fields; Tada and Iijima, 1983) and 20% in the Miocene siliceous shales, Temblor Range, California (Murata and Larson, 1975). The porosity drop observed in this study is consistent with the wet-bulk density and acoustic velocity increases associated with the transformation of amorphous silica to diagenetic opal, too. Since the amount of dissolved opal-A at a given burial depth(temperature) is limited by its solubility, the porosity reduction as a function of dissolved silica may also depend on the solubility (modified after Wrona et al., 2017). This dependence is acknowledged by the correspondence between the pore-water undersaturation state (a function of silica solubility) with respect to biogenic opal and porosity variations with depth (Fig. 4.18). The tendency for porosity preservation in the opal-A zone at both Sites 794

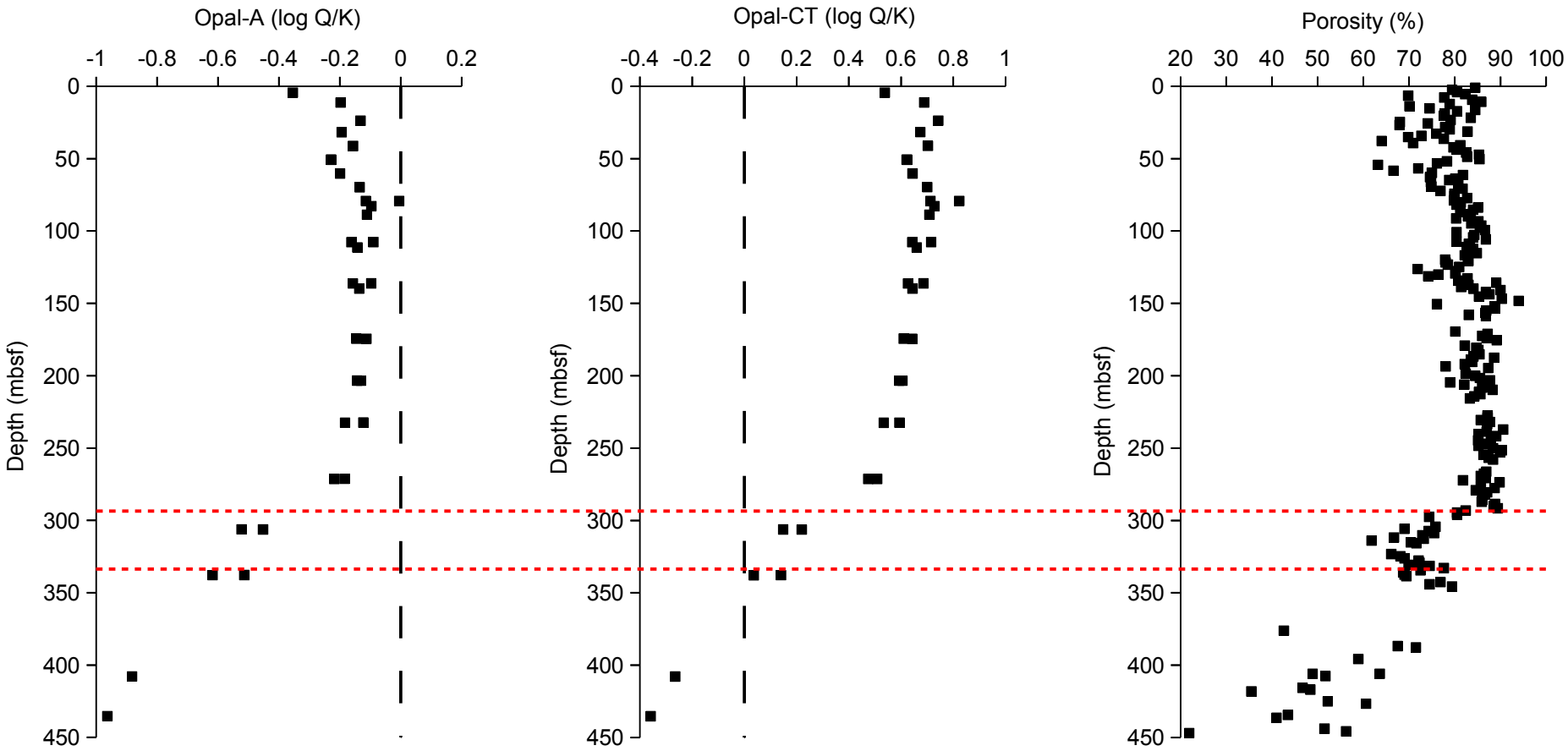


Figure 4.18. Correlation of pore-water saturation index with respect to silica polymorphs and the porosity values versus burial depth for Site 794. Black dashed lines represent solubility equilibrium (log Q/K = 0). Red dashed lines denote top and base of the $TZ_{A/CT}$ as determined by physical properties variations.

and 795 is attributed to the presence of highly-porous rigid siliceous tests (intragranular pores in the chambers) in the sediment (Figs. 4.19A, B). The diatom frustules within the opal-A interval continue to steadily dissolve in the interstitial water undersaturated with respect to biogenic opal. A sharp porosity change at the depth of transition zone is attributed to a sudden anomalous compactional event as amorphous silica dissolves and undergoes changes from opal-A to opal-CT. According to Isaacs (1981), such changes happen quickly, causing the sediment to lose its framework strength due to fragmentation and the extensive dissolution of siliceous frustules, and therefore allowing a compactional collapse of the clay matrix that supports the skeletal grains. The matrix collapse is essentially the main process that causes a sudden porosity drop. The subsequent precipitation of fine aggregates of opal-CT in the framework and skeletal components of host rock can further decrease the porosity (e.g., Fig. 4.10G). The occurrence of this compactional event is appreciated by the presence of an active silica sink close to the silica phase-change boundary (Figs. 4.8A, B); where the pore water is strongly undersaturated with respect to opal-A (which means the quick removal of diatom tests from the sediment), while reaching a solubility equilibrium with respect to opal-CT and thus the precipitation of this mineral phase (Figs. 4.11 and 4.18). The formation of opal-CT in the sediment interval overlying the transition zone (as evidenced by the XRD results) may disaccord with maintaining a high porosity condition. However, the increasing pattern of concentrations with depth in the opal-A zone indicates the initiation of the reaction but does not become expressed in terms of porosity and other physical changes until the reaction moves toward completion through extensive

in situ removal of siliceous tests and continuous re-precipitation of diagenetic opal.

It is also worth noting that due to the siliceous nature of the sub-seafloor sediments at Sites 794 and 795, the transformation of opal-A to opal-CT has occurred at relatively-shallow burial depths (according to Bohrmann et al., 1992). In such cases, silica diagenesis predates mechanical compaction of the host sediment (Wrona et al., 2017). Therefore, it might be possible that the mechanical compaction affects the petrophysical properties of the sediments after they have undergone chemically-induced anomalous compaction under silica diagenetic processes.

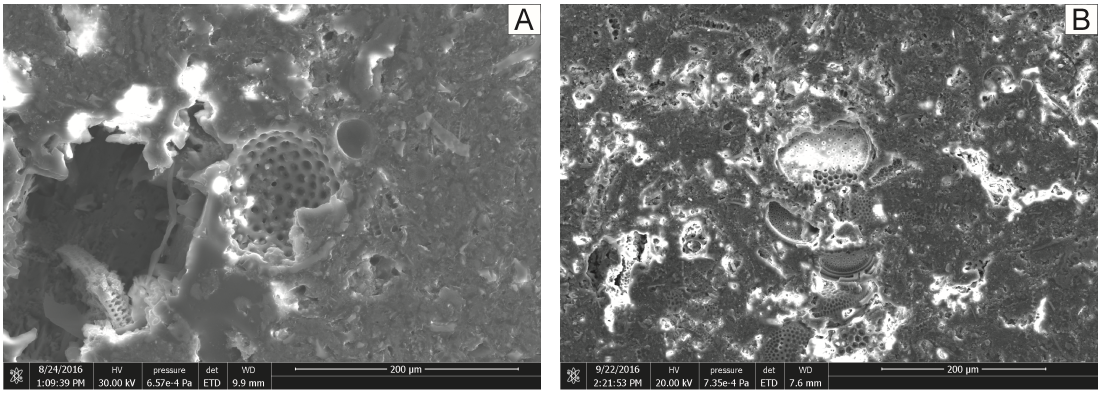


Figure 4.19. A) A porous opal-A facies from the biosiliceous ooze deposits in Site 794 (Sample 127-794A-11H-6, 37–38 cm, at 100.17 mbsf); B) Porous biosiliceous sediment from the opal-A zone in Site 795 (Sample 127-795A-16H-4, 101–102 cm, at 147.81 mbsf).

4.7 Conclusions

In this study, I used pore-water chemistry as a powerful diagnostic tool to

demonstrate ongoing silica diagenesis over the opal-A to opal-CT transition zone at Sites 794 and 795 in the Sea of Japan. Stratigraphic correlations between the distribution of Neogene diatomaceous ooze and the observed variations in dissolved silica concentration, authenticated with the SEM observations, reflect biogenic opal as the major source of silica released into the pore water. Integration of mineralogy, pore-water chemistry, and thermodynamic analyses indicates that solubility equilibrium has been reached with respect to opal-CT in the transition zone where it is most abundant; implying that the precipitation of opal-CT is an ongoing process. Although changes in silica concentration may occur with response to diagenetic formation of authigenic clay minerals, the pore-water saturation index corresponding to solubility equilibrium with respect to diagenetic opal strongly suggests that the silica sink across the transition zone is mainly controlled by an active silica diagenesis.

Due to an abrupt transition of the physical state of the sediments associated with opal-CT formation, ongoing silica diagenesis has profoundly affected most of the interstitial-water profiles, including those for major ions and primary indicators. Li exhibits a close connection to reconstitution of biosiliceous solid phases as it clearly mirrors opal-A and dissolved silica distribution patterns with depth. The opposite Ca and Mg concentration trends with depth indicate the present-day composition of interstitial water is controlled by both clay mineral formation and silica diagenesis. The steadily-decreasing trend of alkalinity synchronous with the zone of sulphate reduction across the depth of transition zone occurs as silica diagenesis consumes the

available pore-water alkalinity to precipitate diagenetic silica. The coincidence of pore-water salinity remaining similar to the overlying seawater and near constant amounts of salt with the silica sink at Sites 794 and 795 indicates a present-day precipitation of opal-CT.

Under low to intermediate accumulation rates of the sediments penetrated by the ODP 794 and 795, ion transport mechanisms can possibly smooth out the silica sink and the concentration gradients of major ions and primary indicators unless silica diagenesis still persists across the transition and the dissolved species are continuously released into the pore water at rates higher than those of interstitial transport mechanisms. Profiles affected neither by dissolution nor by precipitation over the recent past would have been smoothed out, i.e., fossil concentration gradients.

The clustering of isotopic temperatures of opal-CT formation at Site 794 close to ambient temperatures illustrates that the silica transition zone has equilibrated with the present-day geothermal gradient. At Site 795, isotopic temperatures are lower than sediment temperatures at the depth of $TZ_{A/CT}$ and the interval below it; suggesting that the transition formed during the early post-rift period has been nearly rapidly buried and has yet to equilibrate with the modern geothermal gradient. As the $TZ_{A/CT}$ at these sites is a regional BSR mirroring the present-day isotherms, it represents an approximate modern isotherm over which the silica phase change remains an ongoing process.

Given the extremely-low dissolved silica diffusion fluxes in the sediment pore water and the low permeability features of host lithology, diffusion is considered as a relatively-insignificant mechanism for precipitation of opal-CT at Sites 794 and 795. This conclusion is acknowledged by an appreciable pore-water expulsion across the transition zone, due to a sharp porosity reduction, suggesting that the dissolved species have not been diffused in the sediment at rates comparable to those by pore-water advection. The advective flow, however, appears to have ceased to operate recently or it is operating at very slow rates as it has failed to wipe out the signatures of active silica diagenetic reactions.

The sharply-reduced porosity of the Neogene biosiliceous sediments at the depth of $TZ_{A/CT}$ in Sites 794 and 795 is attributed to a sudden anomalous compaction event as amorphous silica dissolves and undergoes transformation from opal-A to opal-CT. Such a porosity drop occurs when the host sediment undergone extensive biosilica dissolution loses its framework strength, allowing a compactional collapse of the clay matrix. The porosity is further decreased through subsequent precipitation of pore-filling opal-CT lepispheres.

Chapter 5

Anomalous compaction due to silica diagenesis — Textural and mineralogical evidence from hemipelagic fine-grained deep-sea sediments

5.1 Abstract

Although anomalous compaction (sudden physical property variations) due to silica diagenesis is recognised from petrophysical profiles and cored/measured sections of biosiliceous deposits in sub-seafloor locations, controls on this event are not well understood. In order to investigate diagenetic controls on anomalous compaction, I analysed the microstructure and composition of hemipelagic sediments at the Ocean Drilling Program Sites 794 and 795 in the Sea of Japan. Textural and mineralogical examination of core samples obtained from these two sites indicate that opal-A and opal-CT are the two fundamental players in anomalous compaction and that other authigenic phases (i.e., clay minerals and pyrite) do not strongly impact petrophysical properties. Above the opal-A to opal-CT transition zone (anomalous compaction interval), opal-A-rich sediments import significant porosity to sediments. Because of high porosity and relative incompressibility of siliceous tests, burial mechanical compaction of biosiliceous clay-rich host sediment postdates silica diagenesis. Across the diagenetic transition, a sharp reduction in opal-A content due to progressive dissolution results in a significant reduction in the sediment

framework stability, allowing for its sudden collapse, abrupt porosity drop, and other associated physical property changes, including decreases in water content and density increases. Subsequent precipitation of opal-CT further affects sediment petrophysics. However, mineralogical analysis indicates that the formation of diagenetic silica has a little influence on the porosity of host sediment than opal-A dissolution, suggesting that anomalous compaction results principally from dissolution of biogenic silica. In the hemipelagic deposits analysed here, the high relative abundance of clay-sized material inhibits massive precipitation of opal-CT. Combined with the initially-porous nature of the clay-rich matrix, this accounts for the maintenance of high porosity within the diagenetic transition zone, despite a sharp porosity drop at the boundary. The decrease in d-spacing of opal-CT with depth in the $TZ_{A/CT}$ is because the external cations, which retard the transformation of disordered cristobalite to ordered phases, are possibly consumed by other authigenic reactions. Association of lower d-spacing values with denser rocks and higher values with higher porosities across the opal-CT zone suggests that burial temperature and time are also fundamental controls on structural ordering of diagenetic silica.

Keywords: Anomalous compaction, Silica diagenesis, Hemipelagic sediments, Ocean Drilling Program, Opal-A, Opal-CT

5.2 Introduction

Classical views of mechanical compaction and porosity loss in hemipelagic sediments generally treat the evolution of petrophysical properties, such as porosity,

density, permeability, and shear strength with increasing effective (burial) stress as a gradual process (e.g., after McSween et al., 2003; Fabricius, 2012; Wrona et al., 2017). Many basin-scale models are based on this fundamental notion of a gradual compaction of sediments with increasing depth (e.g., Velde, 1996; Revil et al., 2002). Continuously cored and measured sections of biosiliceous basinal deposits in many DSDP and ODP boreholes, however, indicate that anomalous compaction (i.e., abrupt and dramatic physical property variations) commonly occurs as a result of thermochemical diagenetic transformation of siliceous oozes (e.g., after Hein et al., 1978; Shipboard Scientific Party, 1990a, b; Littke et al., 1991; Nobes et al., 1992; Kim et al., 2007; Neagu, 2011). The anomalous compaction due to early silicification (the diagenetic transformation of opal-A to opal-CT) comprises a set of sudden petrophysical changes in the biosiliceous successions, including porosity and permeability reduction (e.g., Shipboard Scientific Party, 1990a), pore-water expulsion (Isaacs, 1981), density, velocity, and resistivity increase (e.g., Nobes et al., 1992), and mass transfer of silica (Tada, 1991; Davies, 2005).

Early silicification takes place under early burial in the upper few hundred metres of sediments that cover the ocean bottom (commonly < 1000 mbsf). The transformation occurs through a multi-step process that involves a series of dissolution-reprecipitation reactions (after Leeder, 1982; Williams et al., 1985). The extent and rate of silicification is thought to be predominantly controlled by increasing temperature and sedimentation rate (after Pisciotto, 1981a). Other factors, such as surface area of silica tests (e.g., Williams et al., 1985), host lithology, pore-fluid

chemistry (e.g., Kastner et al., 1977; Nobes et al., 1992), presence or absence of carbonate and clay (e.g., Kastner et al., 1977; Isaacs, 1982; Compton, 1991a), and organic matter (Bohrmann et al., 1994) may partially influence the reaction rate. In many sub-seabottom locations penetrated by the DSDP and ODP, exploration wells, and some on-land sections, silicification has led to the formation and advance of a $TZ_{A/CT}$, corresponding to rapid changes in the petrophysics of marine sediments. This anomalous compaction interval is a thin transitional boundary with a thickness commonly < 50 m across which opal-A and opal-CT co-exist, though highly composed of opal-CT.

It has been well documented that, in addition to changes in the sediment composition, the conversion of opal-A to opal-CT can result in enhanced rates of sediment compaction in depositional basins during early burial, relative to conventional predictions of porosity reduction and compaction with depth (e.g., after Compton, 1991b; Davies, 2005). It is also established that the anomalous compaction under silica diagenesis plays a functional role in the stratigraphic and structural evolution of basin fills (Davies, 2005). However, the precise controls under which the transformation of biogenic silica to cristobalite/tridymite leads to anomalous compaction are not well understood. Although several factors may influence this event, it is not clear which factors are most important. This is mainly due to a paucity of inclusive research on microscopic structure and composition of the principal sediment constructs involved in the silica diagenesis process. To date, only very few works have monitored the evolution in microstructure and composition as a means to

understand the petrophysical behaviour of the endpoints of early silicification (e.g., Wilkens et al., 1987; Nobes et al., 1992; Tribble et al., 1993).

Because biogenic silica is widely distributed in modern and ancient oceans (Chapter 4), investigating anomalous compaction in siliceous oozes is of great economic importance. In some situations, hydrocarbons have been largely produced from siliceous mudstones, porcellanites, and cherts where physical properties (in particular porosity and permeability) are heavily controlled by biosilica diagenetic reactions. For example, the Miocene Monterey Formation, the critical biosiliceous source rock in California (Chaika and Williams, 2001), is long known for capturing significant oil and gas reservoirs developed in the diagenetically-controlled chert and diatomite. From a basin analysis perspective, clarifying the physical and chemical controls on silica diagenesis and the effects on sediment petrophysics is key to understanding fluid flow, rock deformation, and thermal history in depositional basins (Wrona et al., 2017).

This chapter aims to elucidate the details of processes that are responsible for abrupt changes in physical properties through documenting these changes, and placing them in a diagenetic context. The geophysical well-logging programme carried out at Sites 794 and 795 of ODP Leg 127 in the Sea of Japan (Fig. 5.1) offers, in some sense, the best of both the laboratory and field experiment worlds. Marked changes in petrophysical and chemical properties, correlated with a distinct bottom-simulating reflector (BSR), have demonstrated the presence of a $TZ_{A/CT}$ at the sub-seabottom

position in each of these wells. Geochemical and thermodynamic analyses indicate that silica diagenesis is presently an ongoing process across the $TZ_{A/CT}$ at these sites (refer to Chapter 4). The focus here is to document and quantify petrophysical changes in the deep-sea sediments undergoing biogenic silica diagenesis from these two sites and to relate these changes to the evolution in microscopic fabric and sediment composition. This approach involves the study of microfabric and composition of the sediment, including the $TZ_{A/CT}$ and its overlying opal-A interval, as well as their variations with depth. Smear-slide analysis of the sediments is conducted to supplement the constraints from textural and mineralogical studies, and to facilitate links between sediment texture, composition, and petrophysics.

5.3 Tectono-stratigraphy and lithology of study sites

Site 794

Site 794 was drilled at 40° 11.41′N and 138° 13.86′E in the Japan Sea in the northeastern part of the Yamato Basin, south of Japan Basin, within or north of the abrupt transition between the continental crust of the Yamato Basin and oceanic crust of the Japan Basin (Fig. 5.1) and ~50 km west of the most active tectonic belt in the Sea of Japan (see Fig. 4.1B in Chapter 4). Based on single- and multi-channel seismic data, many of the faults within this tectonic zone are thrust or reverse faults with moderate to steep dips, and a number of them are coincident with seafloor escarpments and ridge flanks (Shipboard Scientific Party, 1990a). The central Japan Sea earthquake in 1983 occurred in association with an eastward-dipping thrust fault situated 50 km east of Site 794 (Tamaki and Honza, 1985). Occurrence of this

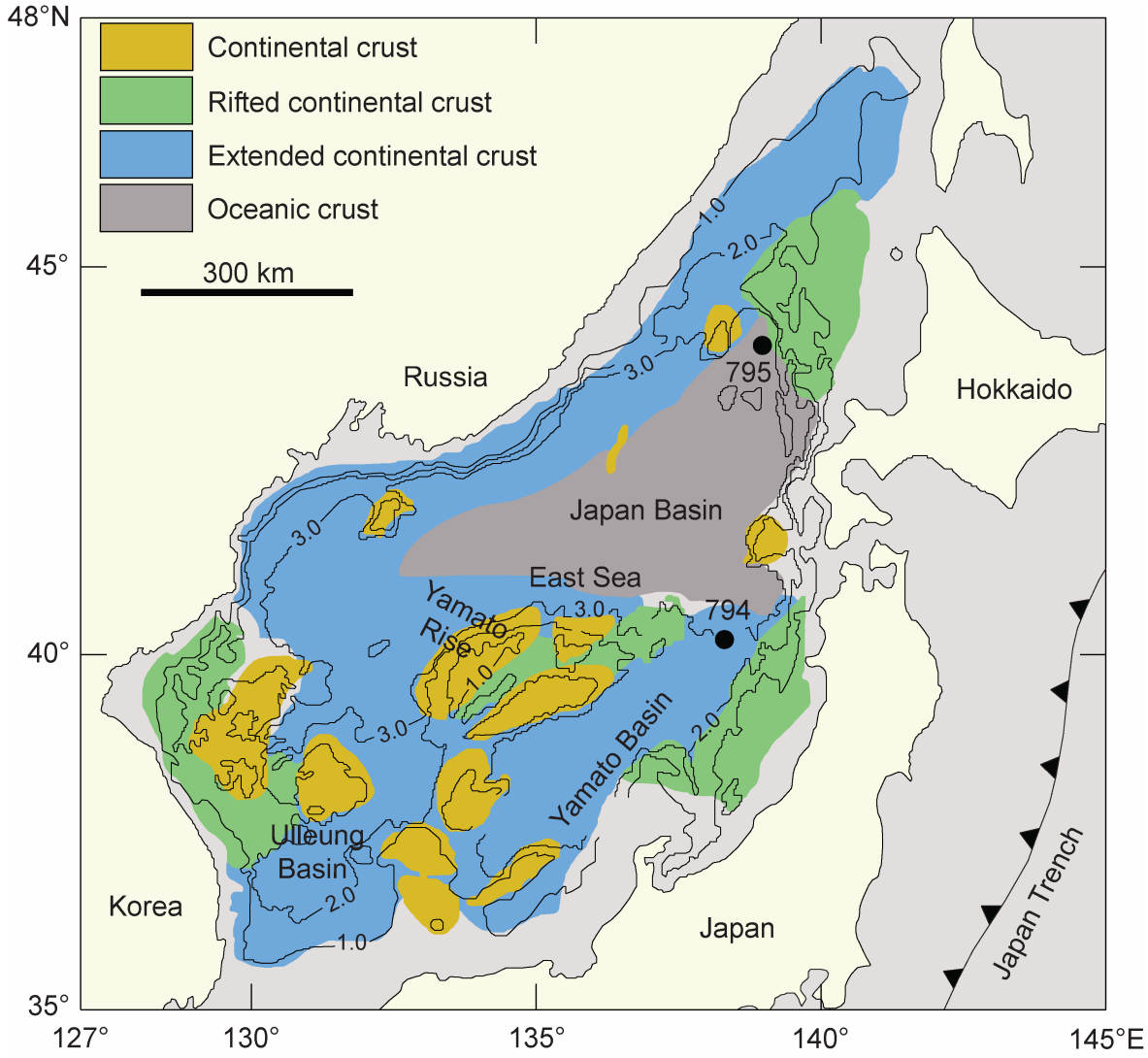


Figure 5.1. Location of ODP Sites 794 and 795 on crustal map of the Japan Sea (redrawn from Tamaki, 1988; Tamaki et al., 1992; Yoon et al., 2014). The discrimination of the crust type is based on seismic reflection/refraction data, bottom -sampling data, geomagnetic data, basement depth, and topography. Bathymetric contours are in kilometres.

earthquake indicates that the present-day compressional stress field trends east-west to northwest-southeast in this part of the Japan Sea. Associated with many of the faults in this tectonic zone are complex folds involving mostly pre-Quaternary units

(see Fig. 4.1B in Chapter 4). Faults are also present on the eastern Yamato Rise approximately 75 km west of Site 794. The faults in this area are mostly steep normal faults involving acoustic basement. In the immediate vicinity of the site, structural disruption of acoustic basement and the overlying sedimentary section is minimal. Except for minor irregularities in the basement surface, no significant faults or folds occur (Shipboard Scientific Party, 1990a).

The stratigraphic section encountered at Site 794 consists of 544 m of interbedded hemipelagic clay, silty clay, and diatomaceous clay and ooze, with lesser amounts of volcanic ash, tuff, and calcareous, siliceous, and glauconitic clay and claystone. The age of the sediment ranges from Quaternary to Middle Miocene, and basal sediments rest on plagioclase phyric dolerite. Mineralogy, grain size, microfossil abundance, and bedding characteristics are used to divide the stratigraphic section into five major lithologic units (in Fig. 5.2, the stratigraphic column shows only the three upper units in order to simplify the presentation). The last occurrence of diatoms (opal-A) in the fine-grained siliceous sediments from this site is coincident with the significant occurrence of opal-CT (Fig. 4.8A in Chapter 4). This important phase-change event occurs across a $TZ_{A/CT}$ that is located at 293.5 mbsf. The $TZ_{A/CT}$ coincides with the boundary between lithologic Subunits IIB (216.9–293.5 mbsf) and IIIA (293.5–351.3 mbsf), and across which a marked change in physical properties is observed (Fig. 5.2). These marked petrophysical variations correlate with significant changes in pore-fluid chemistry. Lithologically, the upper section of Unit III (Subunit IIIA), which captures the $TZ_{A/CT}$, is a ~58-m-thick interval composed of

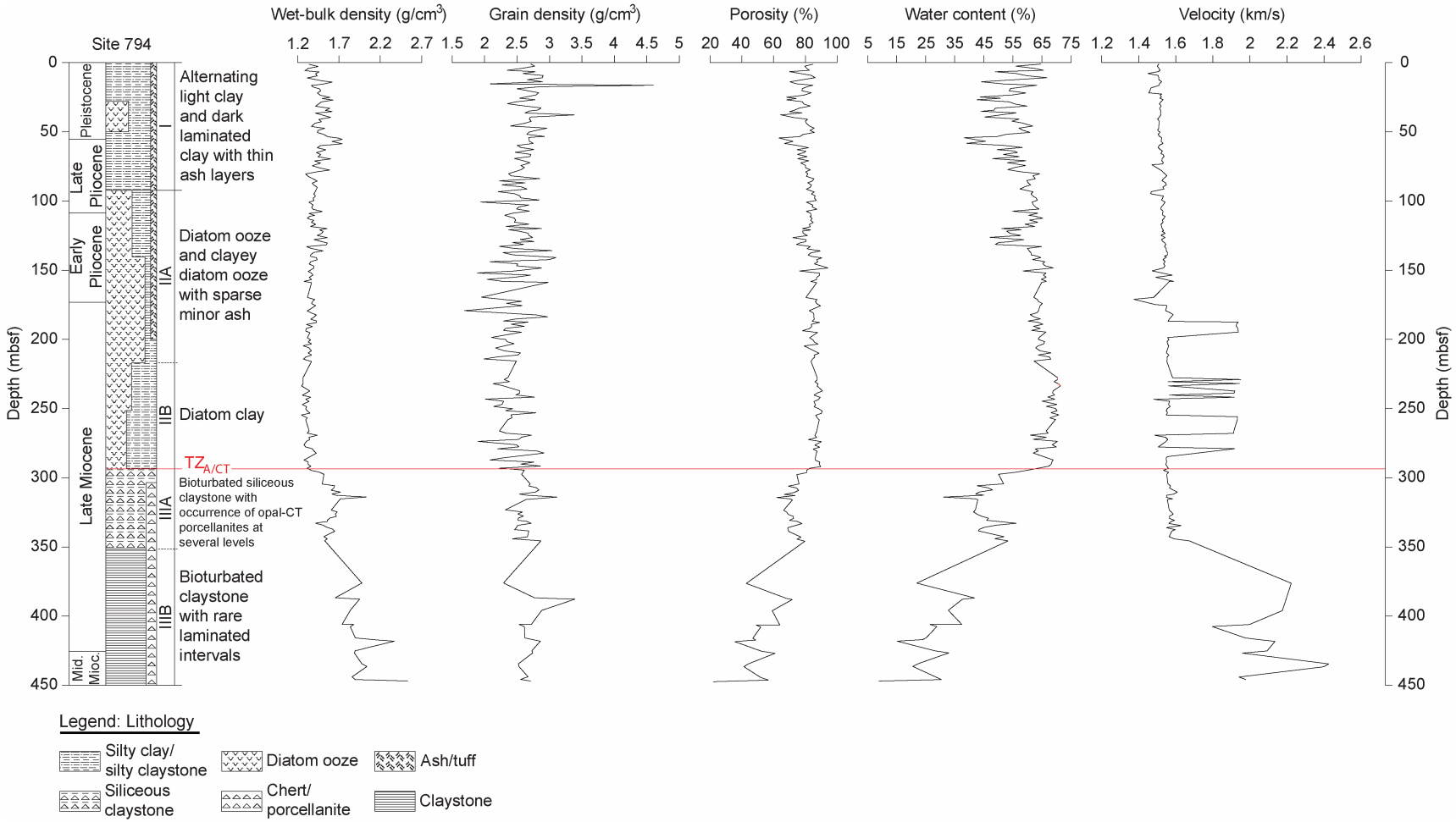


Figure 5.2. Correlation of petrophysical measurements with lithology in Sites 794 and 795 (redrawn and modified after Shipboard Scientific Party, 1990a, b). Except for a few measurements conducted using the Hamilton Frame apparatus (empty circles), no acoustic velocity measurements are available from ~230 to ~370 mbsf for Site 795. The sedimentary section in each of these sites is subdivided into five major lithologic units based on compositional and sedimentological criteria. To simplify the presentation, Units IV and V in Site 794 and Unit V in Site 795 are not shown in the stratigraphic columns. Units II and III in Site 794 and Units I, III, and IV in Site 795 are each divided into two subunits. Note the coincidence of $TZ_{A/CT}$ with sharp changes in physical properties of the sediments and the lithological boundary between Subunits IIB and IIIA at 293.5 mbsf in Site 794. The occurrence of $TZ_{A/CT}$ in Site 795 at ~326 mbsf is coincident with sudden changes in the physical state of the sediment.

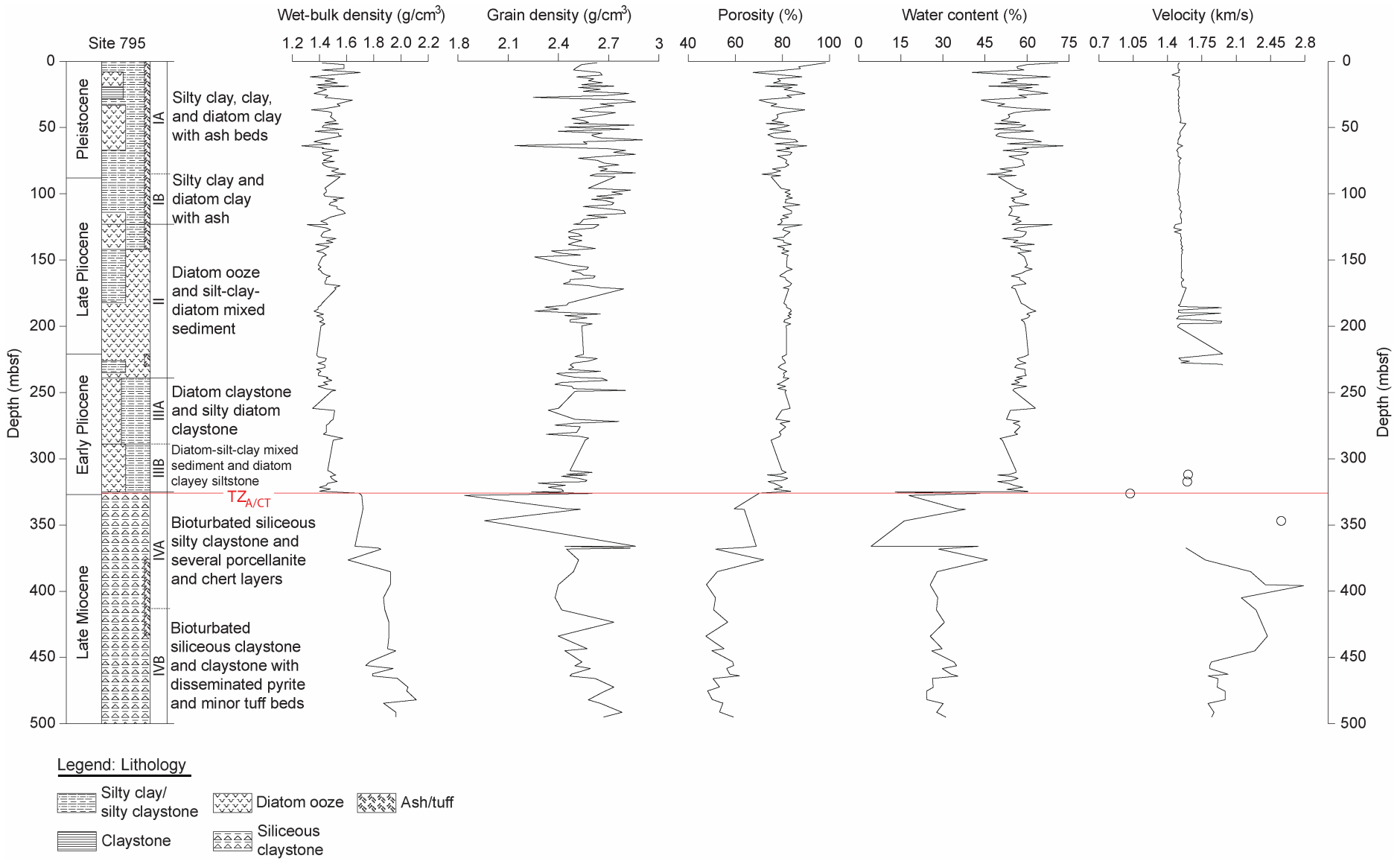


Figure 5.2. Continued.

olive grey to grey green clay and siliceous claystone (Fig. 5.3) with minor ash, pyrite, and micritic carbonate. Opal-CT porcellanites occur at several levels across this unit. The subunit can be distinguished from the overlying porous diatomaceous clay by its significantly-reduced biosilica content, its dominant diagenetic silica phase (opal-CT), its denser and more packed sediment matrix, and its lower porosity. In addition, the clay and claystone in Subunit IIIA are commonly bioturbated and mottled in layers from a few centimetres to a few metres thick.

Site 795

Site 795 is located at 43.99°N and 138.97°E in the bathymetric embayment in the northernmost Japan Basin (Fig. 5.1). The linear complex of north-trending ridges, basins, and escarpments lying east of the site are part of an active tectonic zone that extends over the western-northwestern part of Japan (Tamaki and Honza, 1985). Seismic data demonstrate that steep thrust or reverse faults coincide with many of the escarpments lying east and northeast of Site 795. The topographic and structural patterns near Site 795 indicate an area of active compression containing reverse faults (see Fig. 4.1C in Chapter 4), some of which cut the entire lithosphere. The large compressional earthquakes which have occurred recently in the tectonic zone east of Site 795 support the presence of such an active tectonism in the area. North, west, and south of Site 795, however, the structural style is less dramatic. The rise and the highs south of the site have steep flanks, appearing to be normal faults which formed during rifting of this part of the Japan Sea (modified from Shipboard Scientific Party, 1990b).

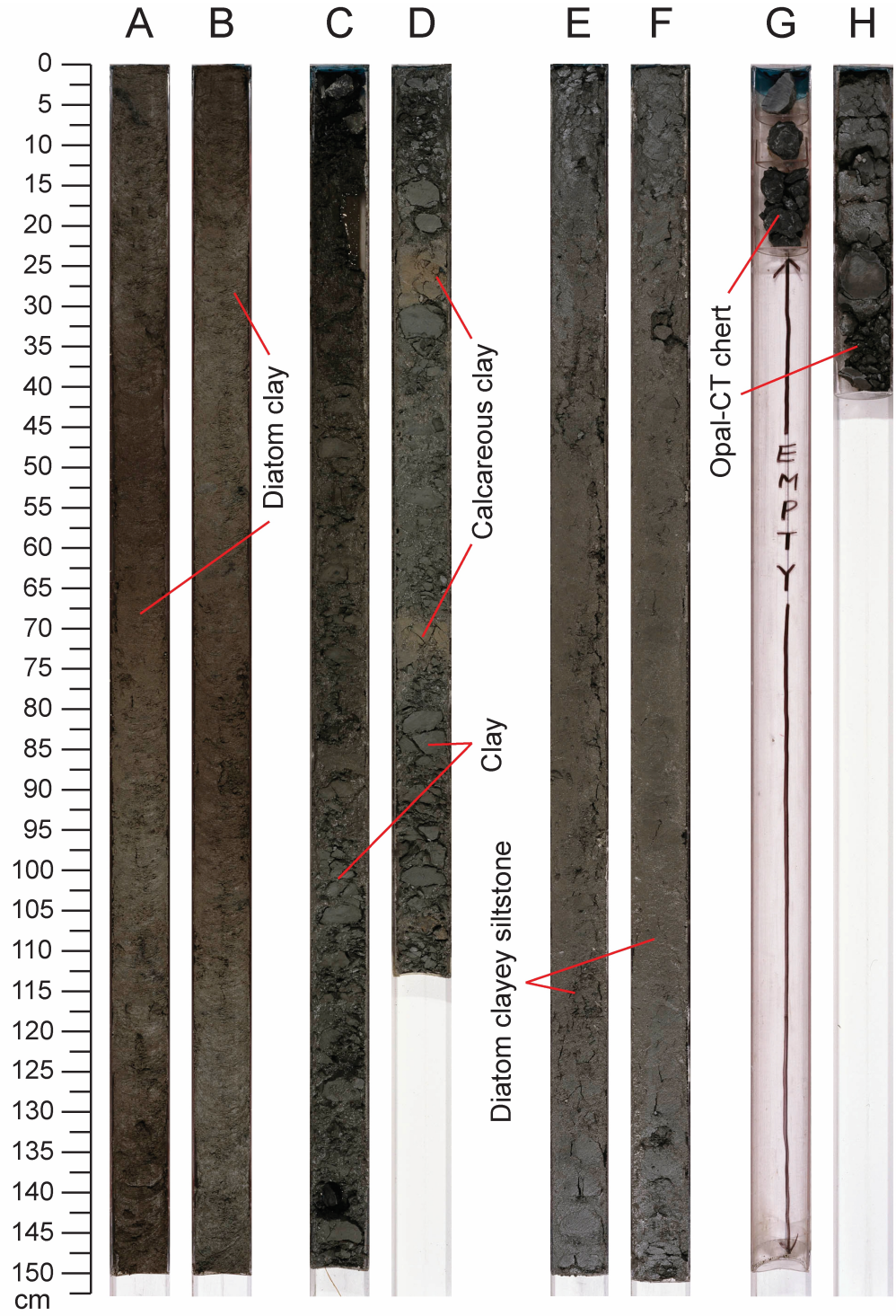


Figure 5.3. Core photo images from sediment intervals accommodating and overlying the $TZ_{A/CT}$ in Sites 794 and 795 (the images were taken by the ODP and are accessed from Core Photos (2014) at the IODP database). A) Brown to greyish brown locally semi-consolidated massive diatom clay (Core 127-794A-27X-3, at

249–250.5 mbsf); B) Brown to greyish brown diatom clay with fine disseminated pyrite at base (Core 127-794A-27X-4, at 250.5–252 mbsf); C) Grey to grey green clay and siliceous claystone (Core 127-794A-33X-1, at 303.3–304.8 mbsf). The first 15 cm is a very hard olive grey clay that is cut into small pieces during drilling. From 15 to 150 cm is a semi-lithified clay; D) Semi-lithified greyish green pyrite-bearing clay (Core 127-794A-33X-2, at 304.8–305.95 mbsf). The core is cut into pieces due to drilling. 2 beds (5–10 cm) of yellowish brown calcareous clay are also seen; E) Greyish olive green diatom clayey siltstone disturbed by drilling (Core 127-795A-34X-3, at 310.9–312.4 mbsf); F) Greyish olive green diatom clayey siltstone highly fragmented by drilling (Core 127-795A-34X-4, at 312.4–313.9 mbsf); G) Olive black bioturbated vitreous opal-CT chert (Core 127-795A-36X-1, at 327.2–327.42 mbsf); H) Greyish olive green to dark greenish grey opal-CT siliceous silty claystone and olive black opal-CT chert brecciated by drilling (Core 127-795A-36X-CC, at 327.42–327.82 mbsf)

Quaternary to Middle Miocene strata penetrated at Site 795 consist of 684 m of hemipelagic clay, silty clay, diatomaceous clay, and claystone with minor pyroclastic material. This succession is underlain by basalt breccia and basalt. The dramatic changes in physical state of the sediment at burial depth of 326 mbsf mark a $TZ_{A/CT}$ at this site. The coincidence of last occurrence of opal-A with a dramatic rise in opal-CT content of the sediment across the $TZ_{A/CT}$ is the most important mineralogical event for the site (Fig. 4.8B in Chapter 4). The $TZ_{A/CT}$ coincides with the lithologic boundary between the Subunits IIIB (288.8–325 mbsf) and IVA (325–413 mbsf) where, in addition to petrophysical changes (Fig. 5.2), variations in the lithification state and interstitial chemistry are significant. The Subunit IVA hosting the $TZ_{A/CT}$ is a 88-m-thick sedimentary succession consisting of siliceous silty claystone and

several chert layers that are highly disturbed by drilling (Fig. 5.3). This interval may contain abundant cherty layers that were not recovered during drilling by the ODP (based on observed drilling conditions and poor recovery; Shipboard Scientific Party, 1990b). The dominant silica phase in the unit is opal-CT. The subunit is bioturbated, with few faint laminae. It can be distinguished from the detrital/diatomaceous mixed sediment and diatom clayey siltstone interval overlying it based on its opal-CT enrichment, the paucity (or lack) of opal-A, its more compacted sediment matrix, and its bioturbation. The stratigraphic column at Site 795 is more or less similar to that at Site 794 in composition, however, the uppermost Pliocene through Quaternary succession in Site 795 is to some extent more coarser-grained than the comparable section in Site 794, suggesting a more proximal position to terrestrial sources and a more distal basinal setting for Site 795.

5.4 Data and methodology

An important source of the data for this study comes from the results of physical properties measurements for Sites 794 and 795 that are available through the ODP initial reports. A full programme of physical property measurements was conducted on Sites 794 and 795 cores, including magnetic susceptibility, GRAPE density, and compressional wave (P-wave) velocity on the multi-sensor track, index properties, thermal conductivity, P-wave velocity using the Hamilton Frame, and the formation factor. The ODP-conducted velocity measurements, index properties (including bulk density, grain density, porosity, water content, and void ratio), and GRAPE bulk density are used by this study to better understand the factors that control the

physical properties of marine sediments and rocks.

To allow cross-correlation of the results, index properties were obtained by the ODP once per section (each section being 1.5 m long) at a single location, on average, usually 100 cm from the top (Shipboard Scientific Party, 1990b). Typical sampling frequency for index properties measurements is two per section (Blum, 1997), however, with regard to the moderate to good recovery of Leg 127 and the staff assignments, one sample per section was considered sufficient. Two of the index property samples from each APC (advanced hydraulic piston corer) core and one for each XCB (Extended Core Barrel) and RCB (Rotary Core Barrel) core were analysed for grain size. The P-wave logger (PWL) measured P-wave velocity across the core sections using a sampling interval of 5 cm (4-s period), and the GRAPE bulk density was sampled every 5 cm (5-s period) (modified from Blum, 1997). These sampling spacings show their high resolution on acquisition of the sediment petrophysical properties from Sites 794 and 795.

Refer to the ODP technical note of Blum (1997) for an inclusive review of the details of methods used to collect, analyse, and compile all routine physical properties measurements on recovered materials.

Another important source of the data for this study comes from the results of textural and mineralogical analyses of the sub-seafloor core samples from these two sites that were reported in Chapter 4 of this thesis. The samples were acquired every ~40–50 m

within the opal-A interval at Site 794, but a wide range of sampling intervals (~1 to ~70 m) within the opal-A zone in Site 795. Within the opal-CT zone of the anomalous compaction interval ($TZ_{A/CT}$), samples were collected from small sampling intervals, being 0.05 to ~7 m in Site 794 and 0.28 to ~10 m in Site 795 (see Tables 4.2 and 4.3 in Chapter 4 for the position and identification of the samples). For a complete review of sampling and analytical methods performed on the core samples refer to Chapter 3 and the Data acquisition and methodology Section in Chapter 4. In addition to further interpretation and data acquisition from the results of XRD and SEM analyses presented in Chapter 4, this chapter focuses on textural and mineralogical analyses as described below:

SEM

A subset of 19 additional core samples (8 from Site 794 and 11 from Site 795) were selected for preparation of resin-impregnated polished blocks for SEM analysis. Resin blocks were made from a small piece of the sediment (1 cm thick) sub-sampled from each core. Details for the preparation of resin-impregnated polished blocks from these semi-lithified samples are described in Chapter 3. The polished blocks were carbon coated before the start of SEM examination. The various textural features of the sediment, particularly the presence and distribution of siliceous frustules constructed of biogenic silica in a fine detrital matrix, their dissolution and re-precipitation as diagenetic opal, and distribution of crystalline phases and pore spaces were studied under the SEM. The FEI Quanta 650 FEG scanning electron microscope, housed in the Department of Earth Sciences, University of Oxford, was

used to analyse the samples.

Smear slides

As a supplemental constraint, this study also describes major and minor compositions of the fine-grained sediments from these two sites and identifies their biogenic, mineral, and lithogenic components using smear slides. The abundance of these components is estimated by following the standard visual percentage estimation charts (Terry and Chilingarian, 1955). The relative abundance of biogenic silica in the sediment is given particular attention. The results of visual estimation based on smear slides prepared for all the 67 core samples obtained for this study are incorporated with the pre-existing results of ODP-conducted smear-slides examinations to more accurately quantify different components of the sediment hosting silica diagenetic reactions.

To prepare the smear slides, a 3 gram fraction of each core specimen was sub-sampled and submerged in a 15% solution of sodium hydrogen carbonate for disaggregation. The sample was left on a lab hotplate at the low temperature band for 72 hr. The suspension was then washed with deionised water a few times to make certain that no sodium hydrogen carbonate is left in the sediments. 2–3 drops of the slurry were deposited on a glass coverslip and left on the hotplate at the low temperature band for 5 minutes to dry. The coverslip was then affixed to a glass slide using an optical adhesive. Further details of the smear-slide preparation methods are given in Chapter 3. The suspension made for preparation of smear slides was also

used to determine the proportions of terrigenous grain-size groups in the sediment texture, including sand, silt, and clay. According to Marsaglia et al. (2013), sand- and silt-sized grains rapidly settle from the suspension, but clay remains suspended for a long period.

A polarizing Leica microscope, model DM750 P, was used for optical investigation of smear slides. Photomicrographs of the sediments acquired from Sites 794 and 795 were made using a high speed measurement colour HDMI camera, model TrueChrome Metrics, attached to a Leica DM750 P microscope.

5.5 Data presentation and results

5.5.1 Physical properties — General trends and features

At Site 794, the wet-bulk and grain densities both decrease from the seafloor down through the sedimentary section overlying the $TZ_{A/CT}$ (Fig. 5.2). The porosity and water content slightly increase, and the velocity moderately increases along this interval. However, from about 190 mbsf downward to the depths far below the transition zone, the variability in the velocity increases significantly. At the $TZ_{A/CT}$, at 293.5 mbsf, the trends in the index properties reverse, and wet-bulk and grain densities both increase, but porosity and water content rapidly decrease. Within the $TZ_{A/CT}$ interval where diatoms cease to be present in significant amounts, the velocity profile shows only a small increase.

At Site 795, the index property of wet-bulk density is nearly constant with depth in

the opal-A interval, but the grain density, porosity, and water content show a very slight decrease with depth within this section (Fig. 5.2). The P-wave logger on the multi-sensor track could only be used reliably at Site 795 to a depth of ~160 mbsf (Shipboard Scientific Party, 1990b). Deeper in the sediment section, the velocity was therefore measured using the Hamilton Frame apparatus. As a consequence, almost no velocity measurements were made between 230 and 370 mbsf. The velocity profile indicates a slight increase with depth within the first 230 m from the seafloor down through the depositional section. At the $TZ_{A/CT}$, at 326 mbsf, all of the measured index properties, with the exception of grain density, show an abrupt change. Bulk density increases sharply and there are significant complementary decreases in porosity and water content. The velocity measurements on discrete core samples are too sparse across the $TZ_{A/CT}$ to define the variation. The average of velocity values below the depth 370 mbsf down to the stratigraphic column in Site 795 is markedly higher than that of the first 230 m interval.

5.5.1.1 Correlation with stratigraphic units

The first-order statistical parameters, including mean, median, mode, standard deviation, variance, minimum, maximum, and range values for physical properties of the stratigraphic units overlying and capturing the $TZ_{A/CT}$ in Sites 794 and 795 were listed in Tables 5.1 and 5.2, respectively. The standard deviation, in particular, is representative of the degree of variability in the petrophysical properties of a given unit (Shipboard Scientific Party, 1990a).

Site 794

Unit I (0–92.3 mbsf, Pleistocene to Late Pliocene) is described by highly-variable index properties (see the standard deviation values in Table 5.1). The velocity increases moderately, on average, the porosity, water content, and void ratio increase very slightly, the wet-bulk density remains nearly constant, the dry-bulk and GRAPE density slightly decrease, but the grain density moderately decreases with depth. A number of ash layers occur and can be discerned as peaks in the index properties and P-wave velocity (Fig. 5.2). The porosity and water content indicate markedly-high variabilities, and the standard deviations are correspondingly the highest in this unit (Table 5.1). A general trend of increasing diatom content with depth begins from the middle part of this unit (Fig. 4.8A in Chapter 4), along with the associated changes in the physical properties. Unit II (92.3–293.5 mbsf, Late Pliocene to Late Miocene) is dominantly a diatomaceous ooze and clay. The velocity and void ratio generally increase, the porosity and water content increase very slightly, the wet-bulk, grain, and GRAPE densities decrease very slightly, and the dry-bulk density decreases moderately throughout this unit. Porosities and water contents are higher, but they show variabilities less than those within Unit I. The maximum average porosity, water content, and void ratio and the minimum average densities occur within this unit (Table 5.1). The grain density is highly variable (the standard deviation being 0.27), but the lowest grain densities, representative of almost pure diatomaceous ooze, occur in this unit. The base of Unit II is marked by the $TZ_{A/CT}$. Below the $TZ_{A/CT}$, in Subunit IIIA (293.5–351.3 mbsf, Late Miocene), the porosity, water content, and void ratio are lower than in the overlying units, and the densities are

Table 5.1. Statistics for physical properties of the lithologic units capturing silica diagenesis at Site 794.

Unit I								
Physical property	Average	Median	Mode	Standard deviation	Variance	Minimum	Maximum	Range
Wet-bulk density (g/cm^3)	1.47	1.45	1.44	0.1	0.01	1.29	1.74	0.45
Dry-bulk density (g/cm^3)	0.68	0.64	0.63	0.17	0.03	0.44	1.5	1.06
Grain density (g/cm^3)	2.68	2.66	2.62	0.32	0.1	2.09	4.6	2.51
GRAPE density (g/cm^3)	1.44	1.43	1.36	0.1	0.01	1.23	1.67	0.44
Porosity (%)	78.53	79.7	69.8	5.34	28.55	63.2	85.8	22.6
Water content (%)	55.02	56.1	56.1	6.43	41.38	38.3	66.6	28.3
Void ratio	3.84	3.92	2.31	1.08	1.17	1.72	6.05	4.33
Acoustic velocity (km/s)	1.52	1.52	1.51	0.02	0	1.45	1.55	0.1
Unit II								
Physical property	Average	Median	Mode	Standard deviation	Variance	Minimum	Maximum	Range
Wet-bulk density (g/cm^3)	1.37	1.36	1.37	0.07	0	1.25	1.56	0.31
Dry-bulk density (g/cm^3)	0.5	0.49	0.51	0.09	0.01	0.36	0.82	0.46
Grain density (g/cm^3)	2.45	2.46	2.48	0.27	0.07	1.69	3.1	1.41
GRAPE density (g/cm^3)	1.29	1.29	1.29	0.08	0.01	1.06	1.54	0.48
Porosity (%)	84.9	85.45	85.2	3.64	13.27	71.9	94	22.1
Water content (%)	63.9	64	63.4	4.68	21.94	47.2	71.4	24.4
Void ratio	6.01	5.86	3.55	1.75	3.07	2.56	15.6	13.04
Acoustic velocity (km/s)	1.59	1.55	1.55	0.14	0.02	1.37	1.95	0.58

Table 5.1. Continued.

Subunit IIIA								
Physical property	Average	Median	Mode	Standard deviation	Variance	Minimum	Maximum	Range
Wet-bulk density (g/cm^3)	1.61	1.61	1.56	0.12	0.01	1.37	2.03	0.66
Dry-bulk density (g/cm^3)	0.86	0.87	0.94	0.16	0.03	0.54	1.4	0.86
Grain density (g/cm^3)	2.64	2.63	2.51	0.16	0.03	2.32	3.11	0.79
GRAPE density (g/cm^3)	1.59	1.59	1.61	0.12	0.01	1.38	1.89	0.51
Porosity (%)	72.38	72.4	69	4.46	19.9	61.8	80.5	18.7
Water content (%)	46.59	45.5	43.4	5.79	33.55	31.2	60.2	29
Void ratio	2.72	2.63	2.23	0.63	0.4	1.62	4.12	2.5
Acoustic velocity (km/s)	1.58	1.57	1.57	0.03	0	1.53	1.67	0.14

higher. The acoustic velocity increases steadily through this unit. This trend continues into Unit IIIB (351.3–491.7 mbsf, Late to Middle Miocene).

Site 795

Unit I (0–123 mbsf) is constructed of an unconsolidated silty clay with zones of diatomaceous ooze and frequent occurrences of thin layers of tephra (Shipboard Scientific Party, 1990b). The index properties in this unit show a high variability (see the standard deviation values in Table 5.2), but the mean values show no significant trend with depth. Due to lack of measurements along the interval from 230 to 370 mbsf, the velocity profile is not a good indication for discussing the magnitude and variations within the lithostratigraphic units. Nevertheless, the first 180 m

Table 5.2. Statistics for petrophysical properties of the lithostratigraphic units overlying and capturing silica diagenetic transition zone at Site 795.

Unit I								
Physical property	Average	Median	Mode	Standard deviation	Variance	Minimum	Maximum	Range
Wet-bulk density (g/cm^3)	1.48	1.48	1.53	0.07	0.01	1.27	1.7	0.43
Dry-bulk density (g/cm^3)	0.65	0.64	0.58	0.11	0.01	0.35	1.01	0.66
Grain density (g/cm^3)	2.63	2.64	2.55	0.13	0.02	2.14	2.9	0.76
GRAPE density (g/cm^3)	1.4	1.41	1.37	0.1	0.01	1.1	1.57	0.47
Porosity (%)	80.75	80.9	79.4	5.15	26.53	67.5	98.4	30.9
Water content (%)	56.15	56.4	50.9	5.76	33.21	40.6	72.8	32.2
Void ratio	5.22	4.24	3.85	6.57	43.15	2.08	61.5	59.42
Acoustic velocity (km/s)	1.52	1.52	1.52	0.02	0	1.45	1.59	0.14
Unit II								
Physical property	Average	Median	Mode	Standard deviation	Variance	Minimum	Maximum	Range
Wet-bulk density (g/cm^3)	1.43	1.42	1.39	0.04	0	1.31	1.55	0.24
Dry-bulk density (g/cm^3)	0.59	0.59	0.57	0.05	0	0.41	0.74	0.33
Grain density (g/cm^3)	2.51	2.5	2.47	0.1	0.01	2.26	2.79	0.53
GRAPE density (g/cm^3)	1.32	1.33	1.28	0.09	0.01	0.98	1.48	0.5
Porosity (%)	81.5	81.2	81.8	2.12	4.5	76.1	88.4	12.3
Water content (%)	58.46	58.9	59.3	2.69	7.25	51.2	69	17.8
Void ratio	4.44	4.32	4.49	0.64	0.4	3.18	7.62	4.44
Acoustic velocity (km/s)	1.59	1.54	1.54	0.15	0.02	1.46	1.96	0.5

Table 5.2. Continued.

Unit III								
Physical property	Average	Median	Mode	Standard deviation	Variance	Minimum	Maximum	Range
Wet-bulk density (g/cm^3)	1.47	1.48	1.45	0.04	0	1.35	1.57	0.22
Dry-bulk density (g/cm^3)	0.66	0.66	0.66	0.06	0	0.5	0.78	0.28
Grain density (g/cm^3)	2.49	2.49	2.42	0.12	0.01	2.28	2.8	0.52
GRAPE density (g/cm^3)	1.32	1.33	1.31	0.09	0.01	1.07	1.45	0.38
Porosity (%)	79.26	79.6	79.8	2.68	7.17	73.6	83.5	9.9
Water content (%)	55.26	55.5	55.6	2.98	8.87	49.7	63.1	13.4
Void ratio	3.9	3.9	3.95	0.62	0.38	2.79	5.06	2.27
Acoustic velocity (km/s)	1.61	1.61	–	0.01	0	1.6	1.61	0.01
Subunit IVA								
Physical property	Average	Median	Mode	Standard deviation	Variance	Minimum	Maximum	Range
Wet-bulk density (g/cm^3)	1.77	1.72	1.72	0.11	0.01	1.61	1.92	0.31
Dry-bulk density (g/cm^3)	1.38	1.33	0.95	0.52	0.27	0.87	2.82	1.95
Grain density (g/cm^3)	2.43	2.45	2.45	0.28	0.08	1.84	2.86	1.02
GRAPE density (g/cm^3)	1.4	1.49	–	0.18	0.03	1.19	1.53	0.34
Porosity (%)	60.02	60.9	51.6	8.8	77.44	47.8	72	24.2
Water content (%)	28.72	28.4	–	12.33	151.97	4.4	45.8	41.4
Void ratio	1.27	1.09	1.07	0.77	0.6	0.15	2.57	2.42
Acoustic velocity (km/s)	2.07	2.2	–	0.58	0.33	1.02	2.79	1.77

of the velocity profile exhibits low scatter with values close to that of seawater (being ~1.52 km/s). Unit II (123–239 mbsf) is dominantly a diatom ooze. The index properties are remarkably uniform with depth in this unit and exhibit low variability, with the standard deviation changing within a narrow range from 0.04 to 2.69. The mean values of wet- and dry-bulk densities in the unit, 1.43 and 0.59 g/cm^3 respectively, are the lowest measured in the entire depositional section. Unit III (239–325 mbsf) sediments are a mixture of silt, silty clay, and diatomaceous ooze. The physical properties have nearly the same mean values as Unit II, but variability with depth is slightly greater. The boundary between Units III and IVA at ~326 mbsf is the transition from opal-A to opal-CT. Subunit IVA (325–413 mbsf) is composed of siliceous silty claystone and several porcellanite and chert layers that are disturbed by drilling. With the exception of void ratio, the variability of all physical properties in Subunit IVA is the greatest in the entire sedimentary column from seafloor to the base of this unit. Among the four lithologic units (I, II, III, and IVA), the minimum average porosity, water content, and void ratio are reached in the Subunit IVA from Site 795.

5.5.2 $TZ_{A/CT}$ thickness

The depths to the top and bottom of the $TZ_{A/CT}$ at Sites 794 and 795 were identified based on petrophysical profiles according to the methodology of Neagu (2011) (Fig. 5.4). The method defines the top of the $TZ_{A/CT}$ on porosity profiles, for instance, by a significant negative deflection, followed by a positive deflection at the base of the $TZ_{A/CT}$ (refer to Chapter 4). The $TZ_{A/CT}$ thickness can therefore be quantified on the

porosity profiles from the depth of most negative gradient between two adjacent values within a lithologic interval (representing onset of the $TZ_{A/CT}$) to the depth where the subsequent positive porosity gradient terminates (representing base of the $TZ_{A/CT}$) (Fig. 5.2). The agreement between qualitative estimation of the $TZ_{A/CT}$ based on physical changes and the peak quantitative gradient between two adjacent values within this depth interval suggests that the Neagu (2011) approach is a reliable means for the $TZ_{A/CT}$ thickness determination. Due to the high resolution of data, the different petrophysical parameters yielded nearly-similar values for the $TZ_{A/CT}$ thickness in each of these two sites (Fig. 5.4). The maximum thickness of the $TZ_{A/CT}$ (which is defined from minimum depth of the $TZ_{A/CT}$ top to maximum depth of the $TZ_{A/CT}$ base) ranges from 33.2 to 42.8 m at Site 794 and from 38 to 44.4 m at Site 795, according to the depth profiles of physical properties variations. An important observation is the remarkable difference between the variability of minimum $TZ_{A/CT}$ thickness (which can be defined from minimum depth of the $TZ_{A/CT}$ top to minimum depth of the $TZ_{A/CT}$ base) in Sites 794 and 795. At Site 794, the minimum thickness values range between 18.7 and 22.6 m, with the standard deviation of 1.21, while a wide range of the minimum thickness at Site 795 (12.2–25.2 m), with a standard deviation of 5.17. In accordance with Nobes et al. (1992) and Neagu (2011), this study considers the maximum thickness values as representative of the $TZ_{A/CT}$ thickness. The maximum thickness ensures that the diagenetic transition zone has been constrained well between the point where a clear-cut petrophysical change starts and the point where the changes are indistinguishable from the natural background variability. Given the direct dependence of porosity on water content

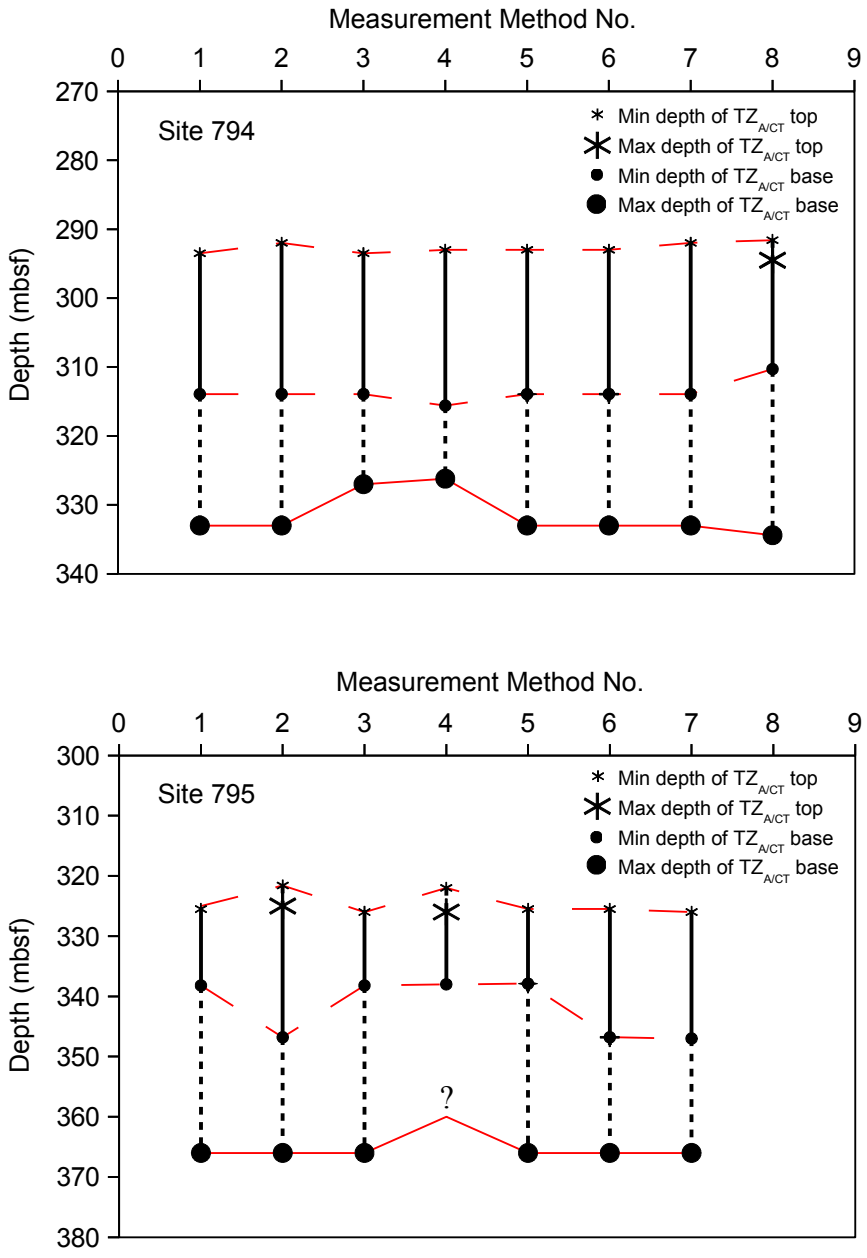


Figure 5.4. $TZ_{A/CT}$ thickness quantified using petrophysical properties of the sediments in Wells 794 and 795. Red dashed lines mark the minimum top and base of the $TZ_{A/CT}$. The continuous red lines mark the maximum base of the $TZ_{A/CT}$.

Numbers on the abscissa represent the physical property measurement methods (1 = wet-bulk density, 2 = dry-bulk density, 3 = grain density, 4 = GRAPE bulk density, 5 = porosity, 6 = water content, 7 = void ratio, 8 = acoustic velocity). The paucity of data does not allow for thickness determination using the velocity profile in Site 795.

reduction as well as its high variability and sensitivity under silica diagenesis, the thickness values estimated using porosity profiles closely represent the $TZ_{A/CT}$ thickness in Sites 794 and 795 (being ~40 m in each of these two sites).

5.5.3 Smear-slides observations

The biogenic and siliciclastic components of the sediment samples acquired from Wells 794 and 795 were identified using smear-slide analysis. Biogenic silica, in particular diatom tests, are a major biogenic component of the sediments from these two sites (Figs. 5.5A–F). With the exception of one sample from the depth of the $TZ_{A/CT}$ in Site 794 and a few samples from Site 795 containing low to minor fractions of organic debris, no other biogenic grains were found in the smear slides prepared for the samples acquired from these two sites. In both sites, clayey materials are the principal siliciclastic component observed in all analysed samples (Figs. 5.5 and 5.6A–D; Appendix III).

The relative abundances of siliciclastic and biogenic components of the sediment were estimated using a visual estimation approach that follows the standard visual comparison charts of Terry and Chilingarian (1955) (Appendix IV). The maximum amount of siliceous tests in the sediment pile overlying the $TZ_{A/CT}$ in Site 794 (72%) was observed at ~100 mbsf in a sample composed of diatom ooze (or clayey diatom ooze) (Fig. 5.5A). In Site 795, biogenic silica has reached peak values up to 68% at roughly 200 mbsf in a diatom ooze sample with subordinate clay; here, diatom frustules constitute more than 90% of the siliceous tests present in the sample (Fig.

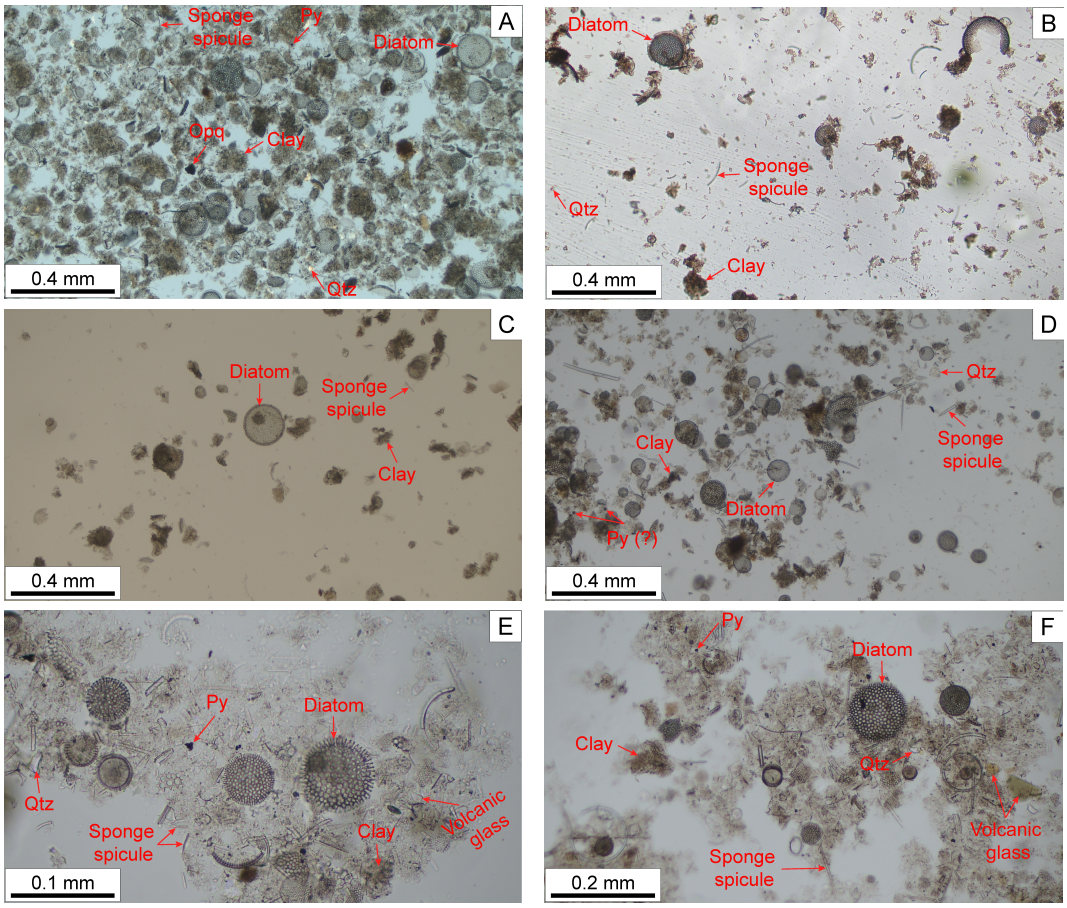


Figure 5.5. Photomicrographs of biosiliceous sediments. A) Siliceous ooze containing biosilica (especially diatoms, but also minor sponge spicules), clayey particles, and low fractions of detrital quartz and opaque minerals (Sample 127-794A-11H-6, 37–38 cm, at 100.17 mbsf); B) Diatom ooze (also containing a low content of sponge spicules) with clay-sized fractions and low quartz content (Sample 127-794A-17X-1, 48–49 cm, at 149.98 mbsf); C) Clayey diatom sediment containing diatoms as the dominant biosilica and low amounts of sponge spicules (Sample 127-794A-22X-2, 113–114 cm, at 200.13 mbsf); D) Diatom ooze (also having low amounts of sponge spicules) containing clayey material, low content of detrital quartz, and minor pyrite (?) (Sample 127-795A-16H-4, 101–102 cm, at 147.81 mbsf); E) Diatom-rich clayey ooze with low contents of sponge spicules, quartz, volcanic glass, and pyrite (Sample 127-795A-22X-5, 128–129 cm, at 198.48 mbsf); F) Diatom clay with clayey material and low amounts of sponge spicules, quartz, volcanic glass, and pyrite (Sample 127-795A-30X-5, 10–11 cm, at 275.4 mbsf).
The abbreviations represent: Opq = opaque, Py = pyrite, Qtz = quartz.

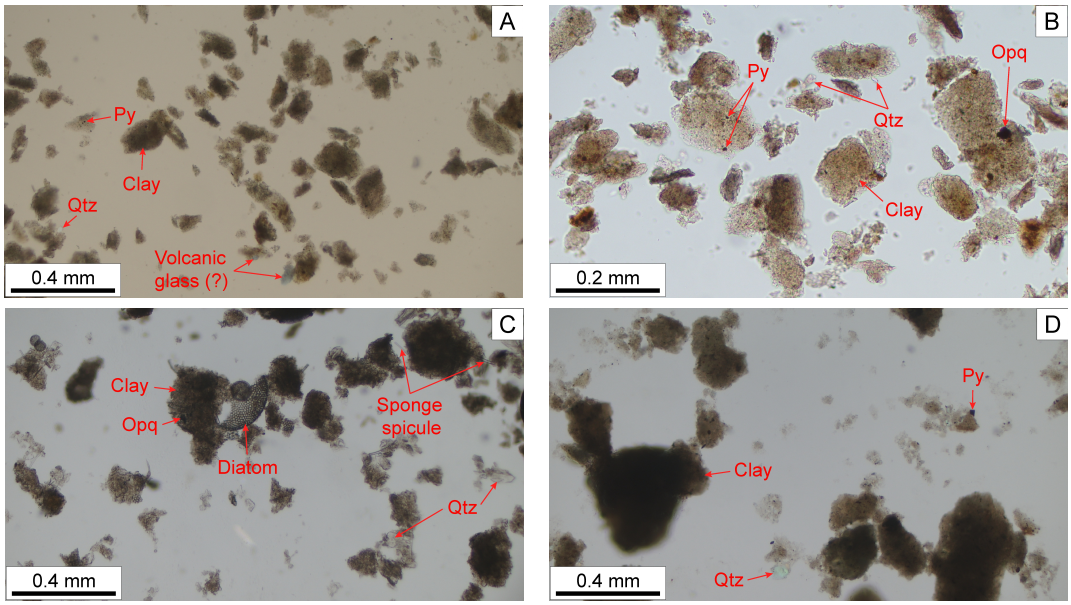


Figure 5.6. Photomicrographs of siliceous sediments. A) Siliceous clay dominated by clay-sized material and minor contents of quartz, volcanic glass (?), and pyrite (Sample 127-794A-33X-1, 70–71 cm, at 304 mbsf); B) Partly-calcareous (?) clay with high amounts of clay-sized material and low contents of quartz and minor fractions of pyrite and opaque minerals (Sample 127-794A-36X-2, 55–56 cm, at 333.95 mbsf); C) Siliceous clay with dominant fraction of clay-sized particles and containing detrital quartz, low content of biogenic silica, and minor opaque minerals (Sample 127-795A-35X-6, 84–85 cm, at 325.94 mbsf); D) Siliceous claystone with high contents of clay-sized material and low amounts of quartz and pyrite (127-795A-37X-CC, 35–36 cm, at 338.68 mbsf).
The abbreviations represent: Opq = opaque, Py = pyrite, Qtz = quartz.

5.5E). The biogenic silica content of the sediment drops to a low value of 7% just at the $TZ_{A/CT}$ in Well 795, but in Site 794 the onset of an abrupt opal-A decrease (from 35 to ~12%) occurs ~3.5 m above the $TZ_{A/CT}$ (Appendix IV). At Site 794, the clay-sized fraction has an average abundance of ~57.5% in the opal-A interval, but jumps to a high value of 93% within the $TZ_{A/CT}$ and the interval below it. At Site 795, there

is an abrupt increase in the clay fraction to more than twice that of the opal-A zone when shifting from the opal-A unit to the $TZ_{A/CT}$ and the opal-CT zone (from ~42 to ~86%). Among the rock-forming mineral fraction of the siliciclastic component, quartz was found in all analysed samples from each site. Compared to Site 795, quartz content of the analysed sediments from Site 794 is lower. The mean quartz abundance of the opal-A interval is 2.5% and increases to ~4% in the $TZ_{A/CT}$ and the interval below in Well 794, but decreases from ~14.5 to ~11.5% from opal-A to opal-CT unit in Site 795.

5.5.4 Sediment microfabric

Observations of sediment microfabric were made using SEM imaging with a secondary electron detector, which can distinguish between sources of X-ray amorphous phases (biogenic silica and volcanic ash) and their crystalline alteration products (in particular diagenetic silica). This also reveals changes in the nature and distribution of physical parameters (especially porosity) in response to silica diagenesis. This method thus permits assessment of diagenetic processes responsible for chemical and petrophysical changes to the sediment. These observations are discussed in order of appearance by increasing depth within the opal-A-rich interval and the opal-CT-rich sediment (including the $TZ_{A/CT}$ and the opal-CT unit). For reference, the location of each SEM image is indicated on the porosity profiles as the most conspicuous representative of petrophysical changes with depth in Sites 794 and 795 (Fig. 5.7A, B).

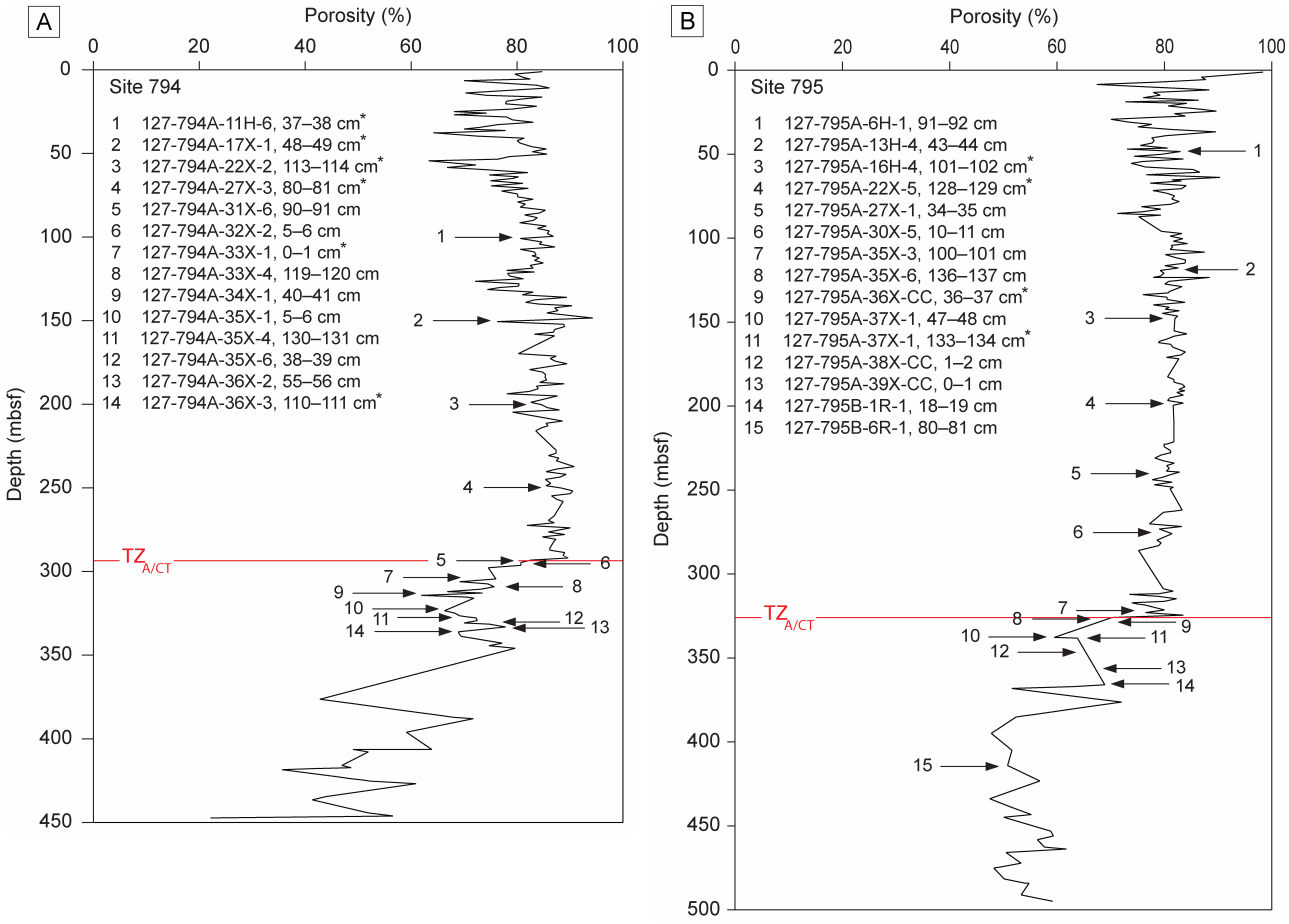


Figure 5.7. Variation of porosity versus sub-seafloor depth. A) Site 794; B) Site 795. Depth locations of samples analysed by SEM are indicated by arrows and the appropriate sample identifier.

* SEM analysis conducted on the sample is presented in Chapter 4.

Site 794

Due to lack of any material left from the main working-half sections, no core sample from the first 100 mbsf at Site 794 is available for analysis. The shallowest sample examined within the opal-A unit in Well 794 is therefore placed at 100.17 mbsf (Chapter 4) where the sediment porosity is ~85% (Fig. 5.7A). Other examined samples below this depth to the base of the opal-A zone (Samples 2 to 5 in Fig.

5.7A) have porosities more or less close to this value, ranging from 80 to 88%. In all these analysed samples, the sediment matrix is made up of fine-grained clayey material (Figs. 5.8A–E). These clayey particles are interspersed with pore spaces of different dimensions and must also have substantial amounts of intergranular porosity. Except for Sample 127-794A-31X-6, 90–91 cm taken just near the top of the $TZ_{A/CT}$, samples within the opal-A interval contain significant fractions of biosilica. The siliceous tests, however, are commonly fragmented and partly dissolved. Extensive dissolution of biosilica (especially diatom frustules) is evident from the burial depth of ~150 mbsf down to the base of the opal-A zone (Figs. 5.8B–E), and subsequent nearly-complete dissolution of the tests created large voids in deeper sections. Volcanic glass was not observed in the samples from the opal-A unit in Site 794 examined by SEM. Silt-sized quartz and siliceous sponge spicules are dispersed throughout the samples within the opal-A zone in minor to small amounts.

The nature of porosity and the matrix both change as the sediments undergo transformation from opal-A to opal-CT. Despite sudden decreases due to opal-A dissolution and opal-CT precipitation, the porosities of sediments across the $TZ_{A/CT}$ and the interval just below are still high (a mean value of ~72%; Fig. 5.7A), but pore spaces visible at SEM scale are generally smaller than in opal-A sediments (Figs. 5.9A–I). The clayey materials in the matrix have lost their network of clay domains (see for instance Figs. 5.8B–D) and instead form a densly-packed interlocking appearance (For example Figs. 5.9H–I) with a decreased matrix porosity. The microfabric of the samples from the depth of the transition zone and the interval

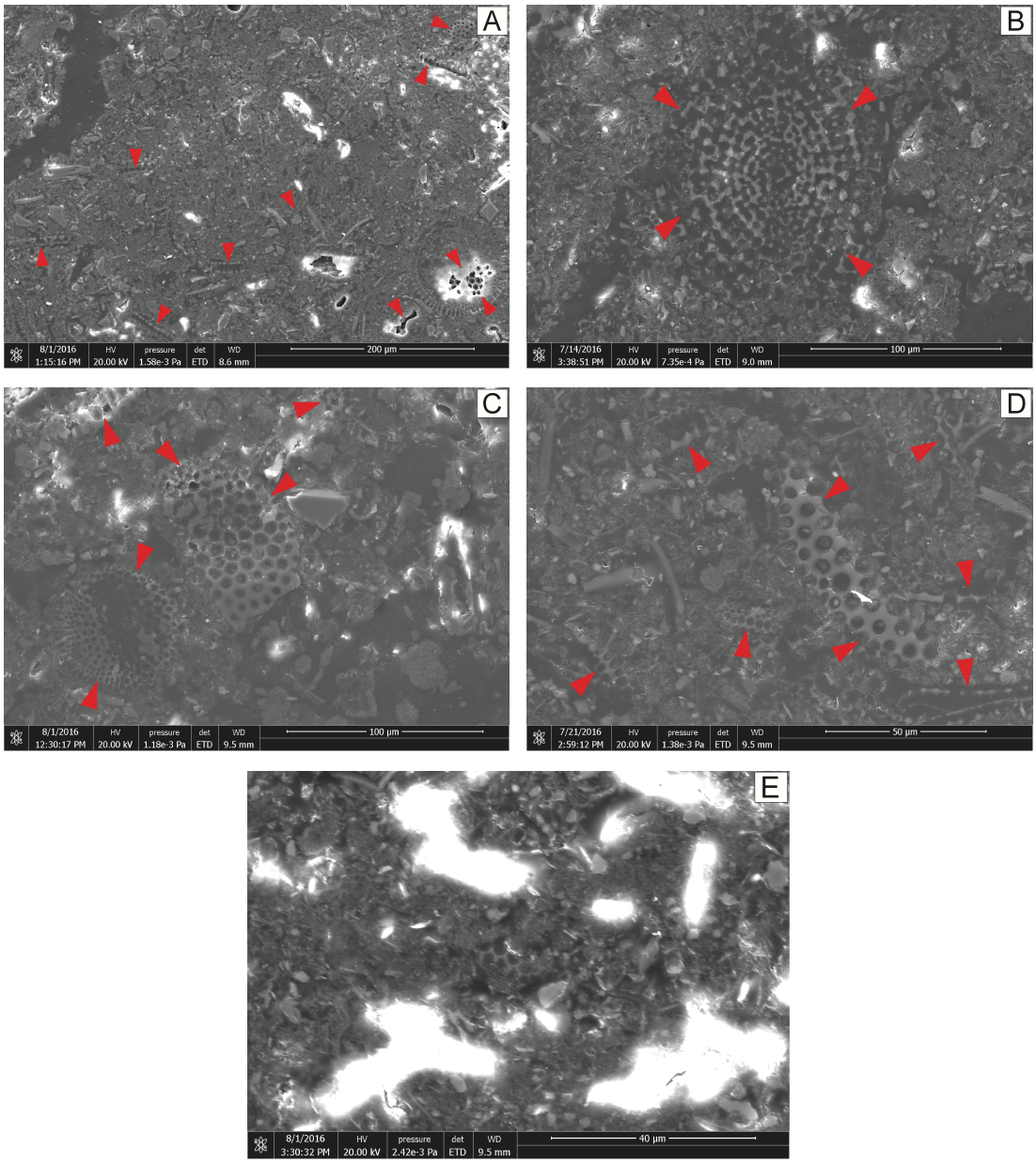
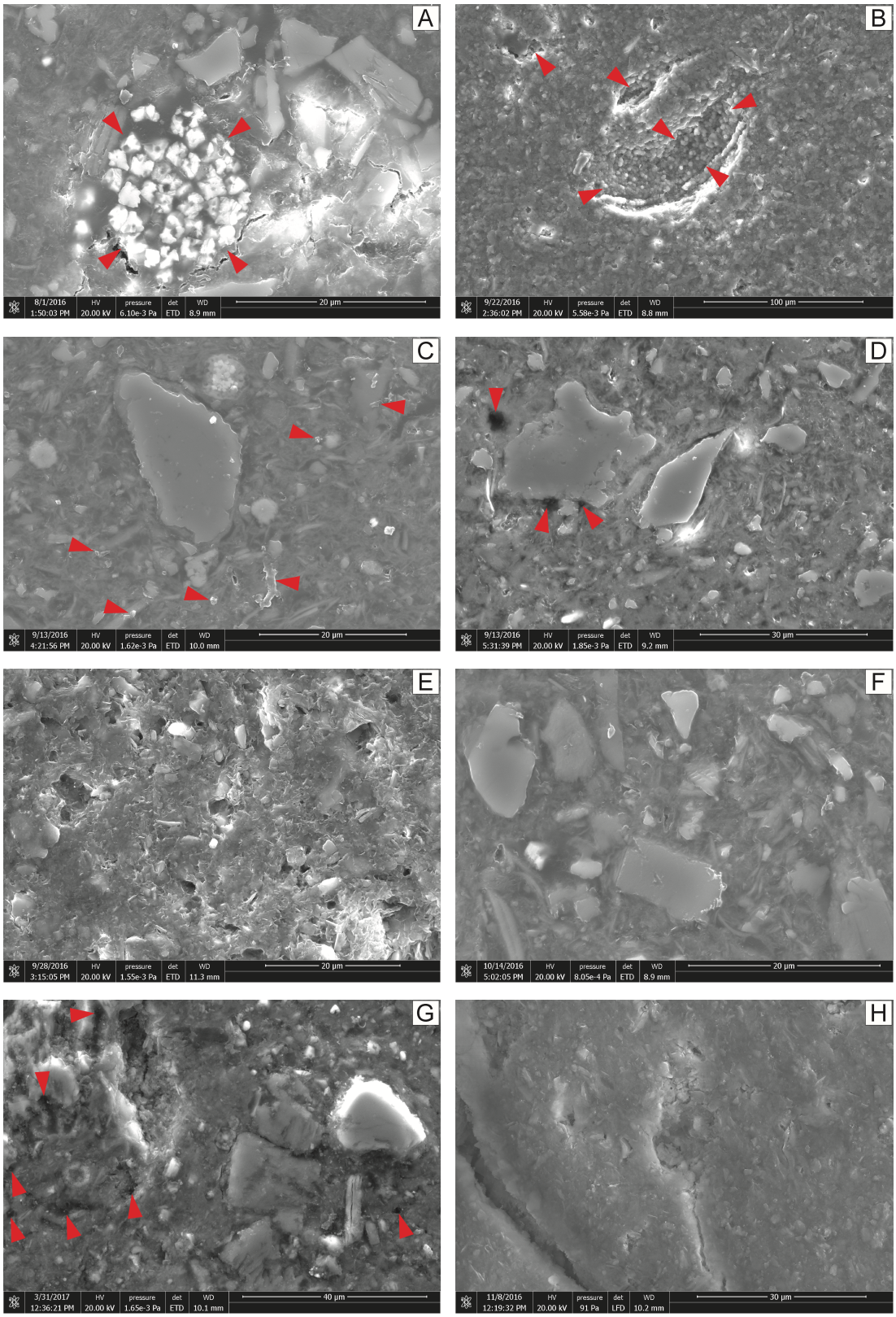


Figure 5.8. Porous biosiliceous sediments from the opal-A succession in Site 794. A) High porosity massive clayey diatom ooze (Sample 127-794A-11H-6, 37–38 cm, at 100.17 mbsf). The sediment matrix is made up of fine-grained clay minerals. Low amounts of sponge spicules and silt-sized quartz are also seen in the sediment. Note that fragmented and dissolved diatom frustules are dominant within the facies (some of them are shown with red arrows); B) High porosity (80%) diatom ooze with low amounts of detrital quartz. Note the extensive dissolution of siliceous tests in the sample (especially a deteriorated diatom valve in the centre of the photo (red

arrows)) (Sample 127-794A-17X-1, 48–49 cm, at 149.98 mbsf); C) Highly-porous (~85%) clayey diatom ooze with sedimentary matrix made up of clay-sized material (Sample 127-794A-22X-2, 113–114 cm, at 200.13 mbsf). Diatom frustules are extensively dissolved and in parts of the sediment texture are deteriorated (red arrows); D) Highly-porous (~88%) massive diatom clay (Sample 127-794A-27X-3, 80–81 cm, at 249.8 mbsf). Sponge spicules are also seen in the texture in small amounts. Note strong deterioration of diatom frustules under dissolution (red arrows); E) High porosity (~83%) clay just above the $TZ_{A/CT}$ top (Sample 127-794A-31X-6, 90–91 cm, at 293 mbsf). Note minor content of siliceous tests in the sediment (mostly dissolved and deteriorated due to progressive dissolution). Low amounts of detrital quartz occur in this sample.

below it is characterised by presence of opal-CT sediments (Appendix V) and a dense clayey matrix in which other particles, such as silt-sized quartz, pyrite, and volcanic glass were commonly observed in small amounts. Pyrite occurs in the samples as isolated framboids (up to 20 μm in diameter) (e.g., see Fig. 5.9A), dispersed submicron-sized crystals, aggregations of octahedral crystals filling the intergranular cavities in trace to small amounts, and cubic crystals filling porous biosiliceous skeletons (e.g., V.1E in Appendix V). Where voids are developed in the sediment fabric from the opal-CT-rich interval due to nearly-complete dissolution of siliceous tests (up to 120 μm in their longest dimension), their infilling by growth of cristobalite lepispheres were commonly observed (see Fig. 5.9B). These voids generally have sharp contacts with the matrix.


A
8/1/2016 1:50:03 PM HV 20.00 kV pressure 6.10e-3 Pa det ETD WD 8.9 mm 20 µm
B
9/22/2016 2:36:02 PM HV 20.00 kV pressure 5.58e-3 Pa det ETD WD 8.8 mm 100 µm
C
9/13/2016 4:21:56 PM HV 20.00 kV pressure 1.62e-3 Pa det ETD WD 10.0 mm 20 µm
D
9/13/2016 5:31:39 PM HV 20.00 kV pressure 1.85e-3 Pa det ETD WD 9.2 mm 30 µm
E
9/28/2016 3:15:05 PM HV 20.00 kV pressure 1.55e-3 Pa det ETD WD 11.3 mm 20 µm
F
10/14/2016 5:02:05 PM HV 20.00 kV pressure 8.05e-4 Pa det ETD WD 8.9 mm 20 µm
G
3/31/2017 12:36:21 PM HV 20.00 kV pressure 1.65e-3 Pa det ETD WD 10.1 mm 40 µm
H
11/8/2016 12:19:32 PM HV 20.00 kV pressure 91 Pa det LFD WD 10.2 mm 30 µm

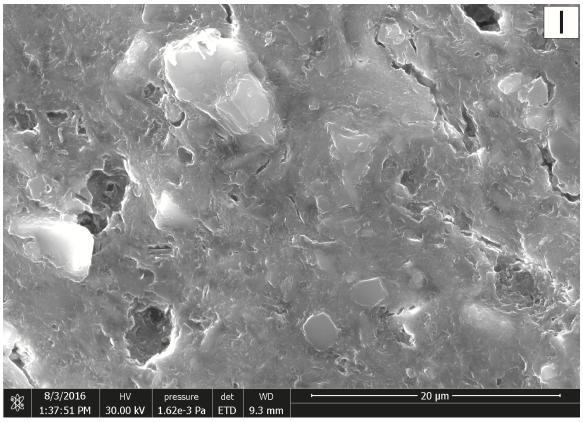


Figure 5.9. Siliceous sediments from the opal-CT-rich interval in Site 794. A) Clayey facies across the upper part of the $TZ_{A/CT}$ (Sample 127-794A-32X-2, 5–6 cm, at 295.05 mbsf). Note that the sample is devoid of siliceous tests. Fine-grained clayey material is the dominant groundmass. Low contents of silt-sized detrital quartz are also seen. The spherical aggregate composed of small bright crystals (red arrows) corresponds to framboidal pyrite; B) Opal-CT claystone (Sample 127-794A-33X-1, 0–1 cm, at 303.3 mbsf). Note the presence of cavities partly filled with opal-CT lepispheres, especially an oval-shaped void in the centre of the picture (red arrows). Clayey material is the dominant sediment component. Due to substantial removal by dissolution, the sample contains no remnants of siliceous tests; C) Opal-CT clay (Sample 127-794A-33X-4, 119–120 cm, at 308.99 mbsf). Note the presence of xenomorphic microcrystalline dolomite also its fine-grained aggregates (middle lower part of the photo) in the sediment texture (red arrows). Pyrite occurs both as framboids and discrete grains in the sediment. The sedimentary matrix is dominated by clayey material. Because of extensive dissolution and deterioration, no remnants of siliceous valves are observed in the sediment; D) Bioturbated siliceous clay (Sample 127-794A-34X-1, 40–41 cm, at 313 mbsf). Burrows can be seen on the left hand side of the photo (red arrows). Clayey matrix is dominant in the sediment. Silt-sized quartz grains and volcanic glass occur in low amounts; E) Clay (Sample 127-794A-35X-1, 5–6 cm, at 322.25 mbsf). Boring-like features are scattered in the sediment. The depositional matrix is composed of clayey material. Low amounts of detrital quartz grains and pyrite are observed in the texture; F) Sapropel-bearing clay

(Sample 127-794A-35X-4, 130–131 cm, at 328 mbsf). The sediment matrix is made up of clayey material. Note low abundance of quartz and pyrite; G) Bioturbated sapropelic clay (Sample 127-794A-35X-6, 38–39 cm, at 330.08 mbsf). Clayey matrix is dominant in the texture. Some burrows occur (red arrows). Quartz (also overgrowth), pyrite, and volcanic glass are present in minor amounts; H) Homogenous clay just below the base of the $TZ_{A/CT}$ (Sample 127-794A-36X-2, 55–56 cm, at 333.95 mbsf). Silt-sized quartz and pyrite can be seen in very small amounts; I) Opal-CT-cemented clay with minor remnants of a siliceous frustule (Sample 127-794A-36X-3, 110–111 cm, at 336 mbsf). Little detrital quartz occurs in the sediment.

Site 795

The shallowest sample analysed within the opal-A unit at Site 795 is located at 48.21 mbsf where the sediment porosity is ~82% (Fig. 5.7B). The examined samples below this depth to the base of the opal-A zone (Samples 2 to 7 in Fig. 5.7B) have porosities close to this value, ranging from 78 to 84%. Like that observed for Site 794, the sediment matrix is composed of clayey material in all examined samples (Figs. 5.10A–G). The clayey matrix is assumed to have substantial amounts of intergranular porosity. The biosilica content of the sediments analysed within the opal-A interval ranges in frequency from common to dominant, with the peak value being observed in Sample 127-795A-22X-5, 128–129 cm, at 198.48 mbsf. The siliceous tests in all the examined samples from the opal-A interval are mostly fragmented and dissolved. The evidence of extensive and progressive dissolution of siliceous frustules is observed from the burial depth of ~48 mbsf down-section to the base of the opal-A unit (Fig. 5.10). An important observation is that despite the development of large pores under dissolution deeper in the sediment at 118.73 mbsf

(see Fig. 5.10B), overall porosity is somewhat lower compared to the shallower samples (see Fig. 5.10A), presumably because of reduced matrix porosity. Volcanic glass was commonly observed in small fractions in the samples from the opal-A unit in Site 795 examined by SEM. Silt-sized quartz and pyrite are dispersed throughout the samples from the opal-A zone in small amounts.

The dramatic reduction in sediment porosity beginning across the $TZ_{A/CT}$ down-core to the opal-CT sediment (the mean value for the opal-CT-rich sediments examined being ~60%) (Fig. 5.7B) is due to diagenetic transformation of opal-A to opal-CT. The matrix appears dense in the sediments examined across the transition zone and the interval below (Fig. 5.11; see also V.2D in Appendix V), and the pore spaces developed under complete or nearly-complete dissolution of biosilica (up to 120 μm in their longest dimension) are partly filled with opal-CT lepispheres (Figs. 5.11B, D) and blades (Fig. 4.10F in Chapter 4). These pores commonly have sharp contacts with the matrix (Figs. 5.11B, D, H). In Sample 127-795B-6R-1, 80–81 cm, at 414.6 mbsf, the circular cavity (developed presumably due to complete dissolution of a diatom) is extensively filled with pyrite crystals. The microfabric of the sediments across the transition zone and the interval below is characterised by presence of opal-CT (see Appendix V) and a depositional matrix constructed of densly-packed clayey material in which other particles, including quartz (in small amounts, but sometimes as a common constituent) and pyrite (in small amounts) were commonly observed.

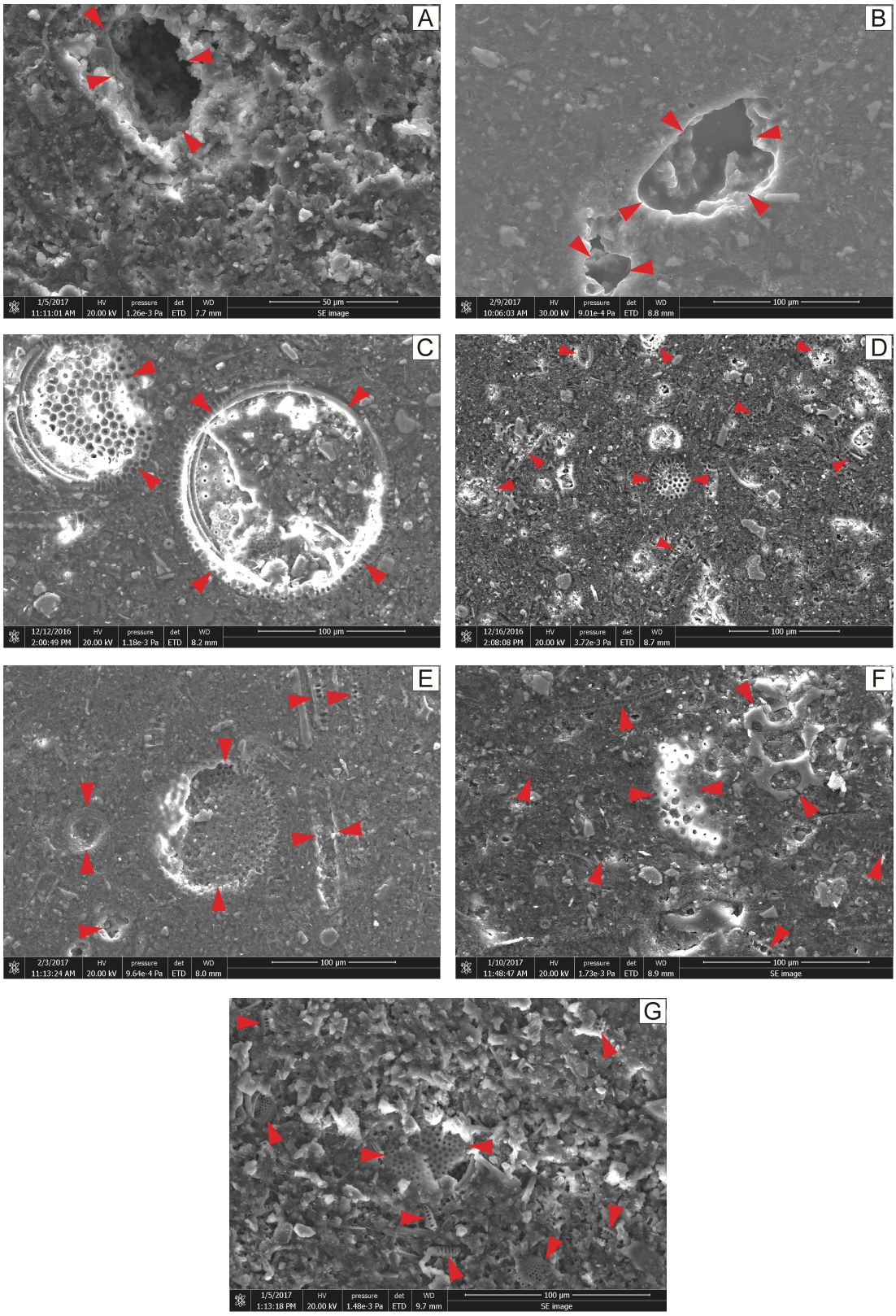

A
1/5/2017 11:11:01 AM | HV 20.00 kV | pressure 1.26e-3 Pa | det ETD | WD 7.7 mm | 50 µm | SE image
B
2/9/2017 10:06:03 AM | HV 30.00 kV | pressure 9.01e-4 Pa | det ETD | WD 8.8 mm | 100 µm
C
12/12/2016 2:00:49 PM | HV 20.00 kV | pressure 1.18e-3 Pa | det ETD | WD 8.2 mm | 100 µm
D
12/16/2016 2:08:08 PM | HV 20.00 kV | pressure 3.72e-3 Pa | det ETD | WD 8.7 mm | 100 µm
E
2/3/2017 11:13:24 AM | HV 20.00 kV | pressure 9.64e-4 Pa | det ETD | WD 8.0 mm | 100 µm
F
1/10/2017 11:48:47 AM | HV 20.00 kV | pressure 1.73e-3 Pa | det ETD | WD 8.9 mm | 100 µm | SE image
G
1/5/2017 1:13:18 PM | HV 20.00 kV | pressure 1.48e-3 Pa | det ETD | WD 9.7 mm | 100 µm | SE image

Figure 5.10. Biosiliceous sediments from the opal-A zone in Site 795. A) High porosity (~82%) silty clay (Sample 127-795A-6H-1, 91–92 cm, at 48.21 mbsf). The sediment matrix is composed of fine-grained clay particles. Note low amounts of diatom fragments, quartz, volcanic glass, and pyrite. The vertical hole in the sediment on the upper part of the picture (red arrows) can be a sign of burrow; B) High porosity (80%) silty clay (Sample 127-795A-13H-4, 43–44 cm, at 118.73 mbsf). Note two irregular cavity pores in the texture (red arrows) due to extensive dissolution of siliceous tests. Clayey material is abundant in the sediment groundmass. Quartz is present in the sample in small contents; C) High porosity (~82%) diatom ooze (Sample 127-795A-16H-4, 101–102 cm, at 147.81 mbsf). Sediment on the right side of the picture is mottled. Note extensive dissolution of siliceous frustules (especially two large circular diatoms (red arrows)). Clayey particles are common. Low amounts of sponge spicules, quartz, and volcanic glass are also present; D) High porosity (83%) diatom ooze (Sample 127-795A-22X-5, 128–129 cm, at 198.48 mbsf). Diatom frustules are mostly deteriorated and fragmented (some of them are shown with red arrows). Clayey material is common in the sediment. Sponge spicules, quartz, volcanic glass, and pyrite occur in low amounts; E) High porosity (~82%) diatom claystone (Sample 127-795A-27X-1, 34–35 cm, at 240.24 mbsf). Diatom tests are highly deteriorated under dissolution (red arrows). Groundmass is composed of clayey material. Small amounts of quartz and pyrite are seen in the sediment texture; F) High porosity (~81%) diatom clay (Sample 127-795A-30X-5, 10–11 cm, at 275.4 mbsf). Diatom valves are heavily fragmented and deteriorated (red arrows). The groundmass of sediment texture is clayey material. Sponge spicules, quartz, and pyrite are observed in low amounts; G) High porosity (~80%) diatom clayey silt mixed sediment (Sample 127-795A-35X-3, 100–101 cm, at 321.6 mbsf). Diatom fragments are dominant in the sediment and are extensively deteriorated by dissolution (red arrows). The sediment matrix is composed of clayey material. Sponge spicules and detrital quartz are common.

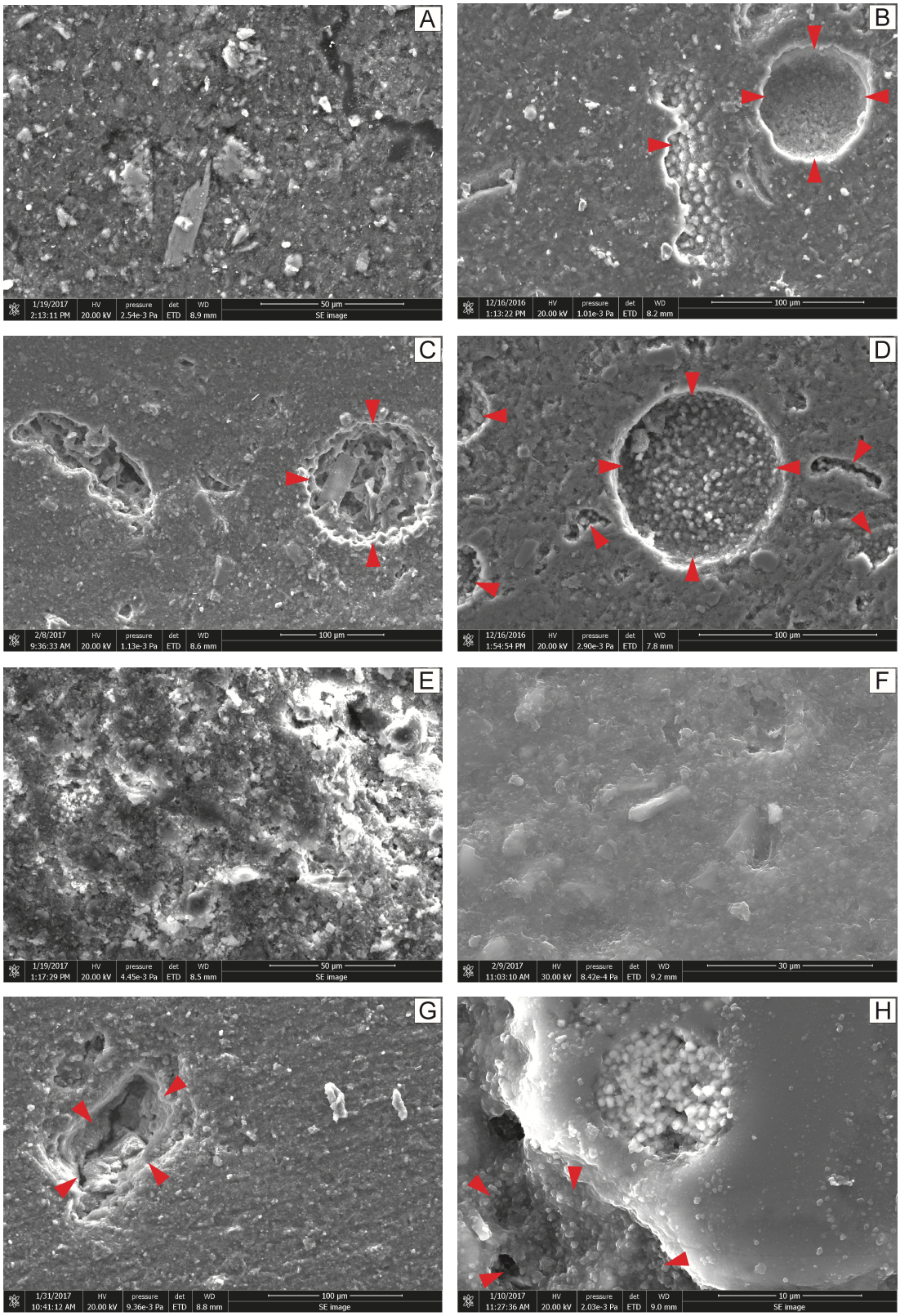

A
1/19/2017 2:13:11 PM HV 20.00 kV pressure 2.54e-3 Pa det ETD WD 8.9 mm 50 µm SE image
B
12/16/2016 1:13:22 PM HV 20.00 kV pressure 1.01e-3 Pa det ETD WD 8.2 mm 100 µm
C
2/8/2017 9:36:33 AM HV 20.00 kV pressure 1.13e-3 Pa det ETD WD 8.6 mm 100 µm
D
12/16/2016 1:54:54 PM HV 20.00 kV pressure 2.90e-3 Pa det ETD WD 7.8 mm 100 µm
E
1/19/2017 1:17:29 PM HV 20.00 kV pressure 4.45e-3 Pa det ETD WD 8.5 mm 50 µm SE image
F
2/9/2017 11:03:10 AM HV 30.00 kV pressure 8.42e-4 Pa det ETD WD 9.2 mm 30 µm
G
1/31/2017 10:41:12 AM HV 20.00 kV pressure 9.36e-3 Pa det ETD WD 8.8 mm 100 µm SE image
H
1/10/2017 11:27:36 AM HV 20.00 kV pressure 2.03e-3 Pa det ETD WD 9.0 mm 10 µm SE image

Figure 5.11. Siliceous sediments from the opal-CT-rich interval in Site 795. A) Siliceous silty claystone (Sample 127-795A-35X-6, 136–137 cm, at 326.46 mbsf) from the uppermost part of the $TZ_{A/CT}$. Quartz and low fractions of pyrite are observed. Note the burrow-like features in the sediment texture; B) Opal-CT chert (Sample 127-795A-36X-CC, 36–37 cm, at 327.78 mbsf). Note in particular the two large cavities partly filled with opal-CT lepispheres (red arrows). Quartz and little amounts of pyrite are also observed; C) Siliceous silty claystone with small remnants of strongly dissolved and deteriorated siliceous tests (Sample 127-795A-37X-1, 47–48 cm, at 337.37 mbsf). Note the remnants of a deteriorated radiolarian on the right hand side of the photo (red arrows). Clayey material forms the sediment matrix. Quartz and small amounts of pyrite are observed in the sediment; D) Opal-CT siliceous claystone (Sample 127-795A-37X-1, 133–134 cm, at 338.23 mbsf). Note the opal-CT lepispheres partly filling a large circular void and smaller voids around it (red arrows). Clayey material making up the sediment matrix are dominant in the sample. Low amounts of quartz are seen in the texture; E) Siliceous claystone (Sample 127-795A-38X-CC, 1–2 cm, at 346.61 mbsf) with the dominance of clayey groundmass material. Note the presence of boring-like structures in the sediment. Silt-sized quartz is seen in small amounts; F) Opal-CT siliceous claystone with minor remnants of siliceous frustules (Sample 127-795A-39X-CC, 0–1 cm, at 356.2 mbsf). Detrital quartz is present in small amounts. Clayey material form the sediment matrix; G) Silty siliceous claystone from the base of the $TZ_{A/CT}$ (Sample 127-795B-1R-1, 18–19 cm, at 365.38 mbsf). Note a deep cavity on the left side of the photo formed after dissolution of biogenic silica (red arrows). The sediment matrix is composed of clayey material. Quartz and pyrite are observed is low amounts; H) Siliceous claystone from the opal-CT interval below the base of the $TZ_{A/CT}$ (Sample 127-795B-6R-1, 80–81 cm, at 414.6 mbsf). Note an assemblage of pyrite crystals filling a circular cavity. The collapsed-like structure on the left hand side of the photo (red arrows) shows weathered part of the sediment, revealing fine rounded grains which can be a sign of leaching. Quartz and volcanic glass are present only in small contents.

5.6 Interpretation and discussion

5.6.1 Silica diagenetic controls on sediment petrophysics — Textural evidence

It is accepted that the formation of authigenic phases during silica diagenesis increases sediment strength (Spinelli et al., 2007). Among authigenic mineral phases identified in the SEM-examined samples from Sites 794 and 795 (including opal-A, opal-CT, and pyrite), the commonly-trace abundance and disseminated nature of the pyrite in both opal-A- and opal-CT-rich sediment units (e.g., Figs. 5.5E–F, 5.6D, 5.9G, 5.10E–F, and 5.11A–B) suggests that this authigenic phase is not a substantial factor in sediment strengthening. Dolomite in total was found only in four samples (2 samples from each of these sites) in minor to common amounts (Appendices III and IV), and its formation is considered to be only a subordinate control on sediment diagenesis. Other authigenic components are, however, critical in the process. Fragmentation of siliceous tests (opal-A) with burial (commonly less than 500 m sediment overburden) and mechanical compaction of clay should in theory reduce the sediment porosity across the opal-A zone in Sites 794 and 795 (according to Compton, 1991b; Chaika and Dvorkin, 2000). Bjørlykke et al. (2017) suggest mechanical compaction as the fundamental control on porosity at relatively-shallow depth. In highly-siliceous clay-dominated sediments from Sites 794 and 795, however, the highly-porous cellular structure of biosilica (Figs. 5.8A–D, 5.10B–G, and Figs. 4.9A–F in Chapter 4) and its relative incompressibility in comparison to the host detrital material mean that mechanical compaction of clayey sediments rich in biosilica progresses to completion only after they have been influenced by silica diagenetic reactions (see Chapter 4, also Wrona et al., 2017). This explains why high

porosity has been maintained across the opal-A zone. Supporting this claim, Compton (1991b) suggests a positive correlation between the porosity of clay-rich sediments and their content of biogenic silica. The relationship between porosity and biogenic silica content of the opal-A-rich and opal-CT-rich sediments from Sites 794 and 795 is also in agreement with this suggestion (Fig. 5.12). In contrast to its relative incompressibility, biogenic silica is susceptible to dissolution during shallow burial (Figs. 5.8A–D and 5.10B–G). Slight increases in porosity, water content, and void ratio, combined with slight sediment density decreases with depth in the diatomaceous unit from Sites 794 and 795 are consistent with the rate increase of opal-A dissolution within this interval.

Across the diagenetic $TZ_{A/CT}$ in Sites 794 and 795, the opal-A content of the sediment decreases due to dissolution; this causes failure of the depositional matrix in protecting the sediment framework under the overburden load. This leads to the collapse of porous sediment framework (Fig. 5.13), a process that reflects major changes in microstructure. The matrix collapse due to silica fragmentation and significant dissolution is the fundamental process resulting in anomalous compaction during which the porosity of sediment drops abruptly and dramatically. The porosity is further influenced through subsequent re-precipitation of dissolved silica as opal-CT. Due to the paucity of knowledge about the relative timing of biogenic silica dissolution and diagenetic silica precipitation, it is, however, difficult to separate the effects of framework collapse and formation of opaline lepispheres on anomalous compaction phenomenon in biosiliceous sediments.

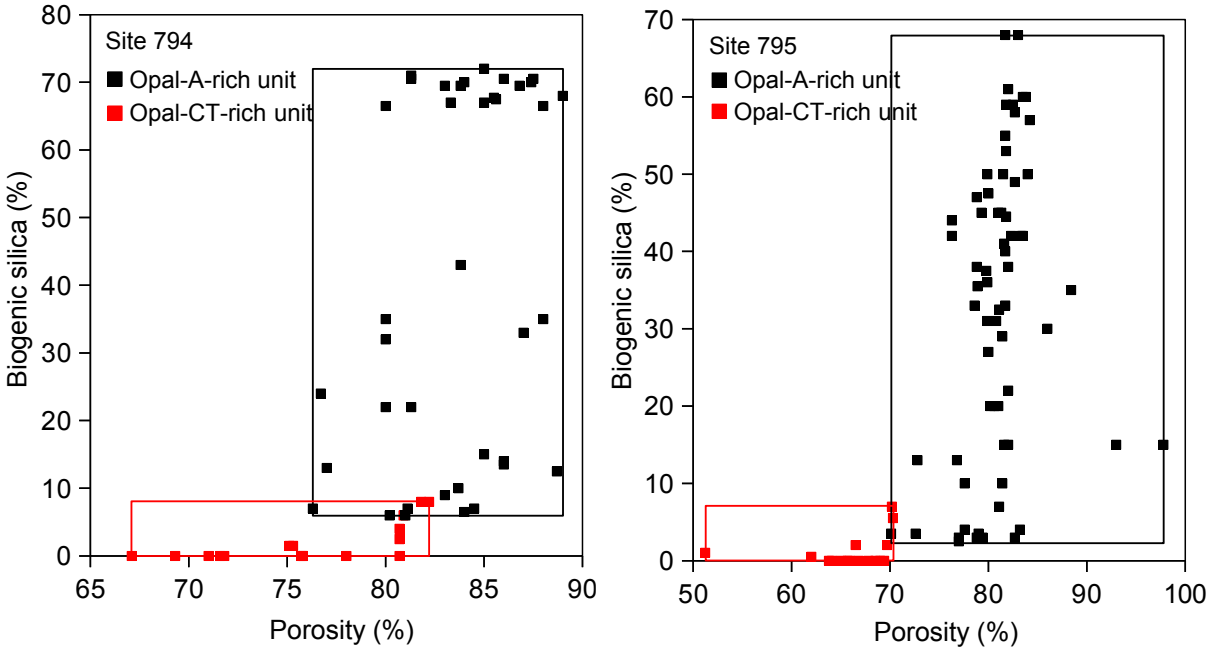


Figure 5.12. Relationships between porosity and biogenic silica content of the sediments from Sites 794 and 795. Black and red boxes outline ranges for the opal-A- and opal-CT-rich sediments, respectively. Note the mean porosity for the assemblage of red squares is markedly lower than that for the black squares (opal-A-rich unit), corresponding to a significant reduction in opal-A content within the opal-CT-rich sediment unit. The opal-A content values used on ordinates of the graphs are based on the results of smear-slides analysis assembled in Appendix IV.

As illustrated in Figure 5.12, the porosity drop during sediment framework collapse requires a substantial reduction in biogenic silica content of the sediment. This porosity reduction is therefore consistent with large decreases in biogenic silica content of the sediment relative to fine (clayey) matrix (Fig. 5.14). Since opal-A content of the sediment is very low across the $TZ_{A/CT}$ and is absent below this interval (Appendix IV; Figs. 5.6, 5.9, and 5.11; also see Fig. 4.10A–B in Chapter 4), the

relative abundance of fine-grained matrix greatly increases. As a consequence, the ratio of opal-A to clay matrix strongly drops, which results in a markedly-lower mean preserved porosity.

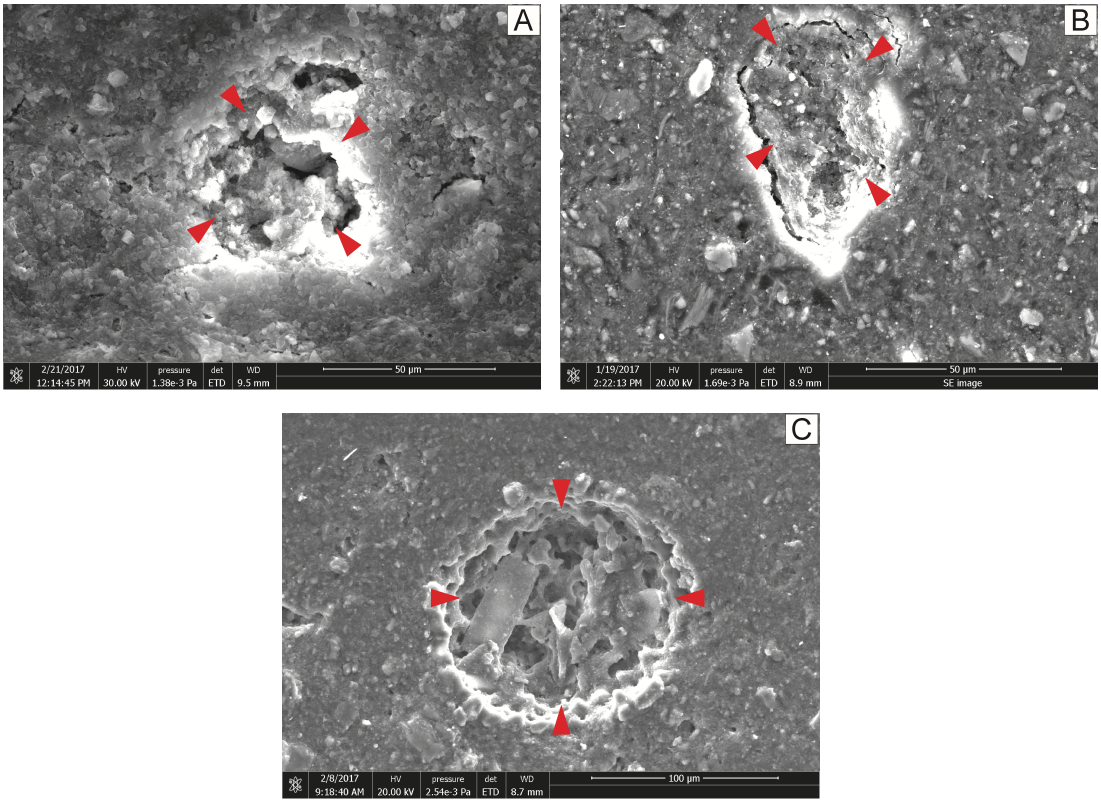


Figure 5.13. Sediment framework collapse due to silica diagenesis. A) Clayey facies from the $TZ_{A/CT}$ in Site 794 (Sample 127-794A-35X-1, 5–6 cm, at 322.25 mbsf). The depositional matrix is collapsing (red arrows) due to dissolution of opal; B) A siliceous silty claystone facies across top of the $TZ_{A/CT}$ in Site 795 illustrating evidence of matrix collapse (red arrows) following dissolution of biogenic silica (Sample 127-795A-35X-6, 136–137 cm, at 326.46 mbsf); C) A siliceous silty claystone within the $TZ_{A/CT}$ in Site 795 showing the collapse of framework in a circular pore space (red arrows) after extensive dissolution and destruction of a radiolarian (Sample 127-795A-37X-1, 47–48 cm, at 337.37 mbsf).

The reduced mean porosity across the anomalous compaction interval (represented by the red data points in Fig. 5.14) is lower than that of the opal-A-rich sediments (black data points in Fig. 5.14), corresponding to their extremely-low opal/clay ratios (< 0.11 in both Sites 794 and 795). The sediment continues to steadily increase in velocity within this interval, owing to subsequent cementation of collapsed framework by diagenetic opal, and an abrupt increase in bulk density, as a result of porosity reduction.

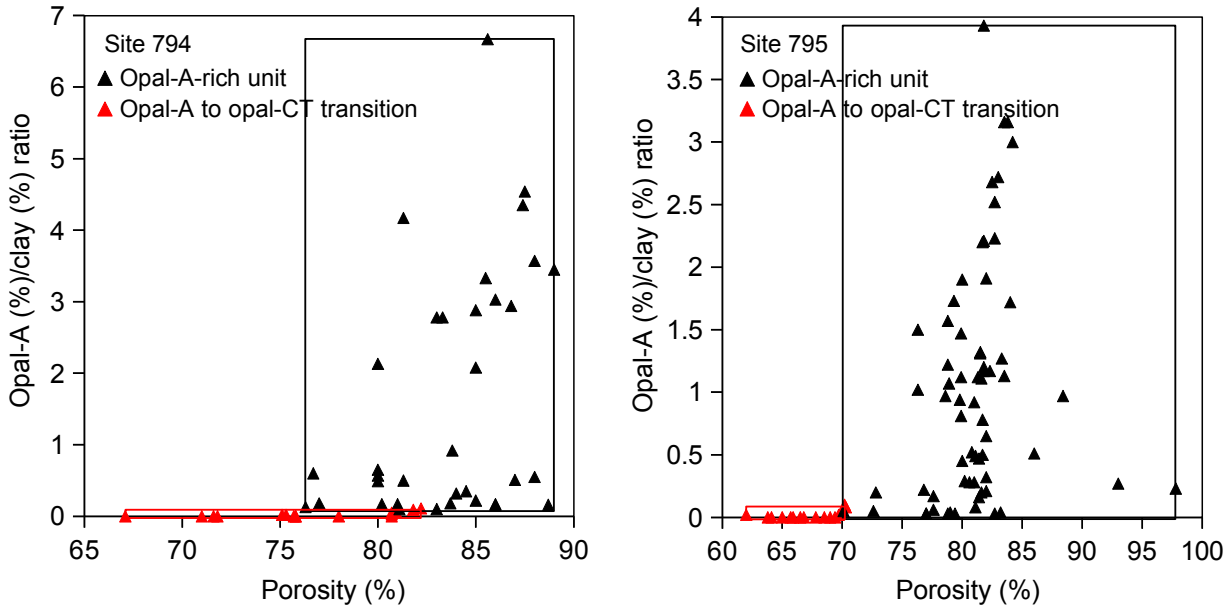


Figure 5.14. Porosity variations with opal/clay ratios of the sediments, Sites 794 and 795. Black and red boxes outline ranges for the opal-A and $TZ_{A/CT}$ sediments, respectively. The ratios used on ordinates of the diagrams were calculated using opal-A and clay percentages of the sediment estimated based on the results of smear-slides analysis assembled in Appendix IV and those reported by Shipboard Scientific Party (1990a, b).

Although the sediment matrix collapse and the preferential precipitation of opal-CT lepispheres have been translated into sharp petrophysical changes, in particular porosity and water content decreases, these physical parameters still represent relatively-high values within the $TZ_{A/CT}$ (Fig. 5.2). This can be partly because of the porous nature of the sediment matrix itself which is dominantly composed of fine-grained clayey materials that form an important component of the sediment in the diagenetic transformation zone and in the interval below it. Furthermore, the post-diagenetic nature of regular mechanical compaction of biosiliceous sediments can partially preserve porosity in the shallow burial anomalous compaction interval and the sediment unit below in Sites 794 and 795.

5.6.2 Sediment composition and physical properties

As discussed in the previous section (Silica diagenetic controls on sediment petrophysics — Textural evidence), the main difficulty in identifying drivers of matrix collapse and opal-CT precipitation on petrophysical variations relates to the relative timing of dissolution and precipitation of opaline phases during silica diagenesis. This issue is further complicated also by the relation between sediment composition and petrophysics (in particular porosity) for biosiliceous deposits from the investigated ODP sites. The extent of the porosity reduction during silica diagenesis only approximately corresponds to the XRD-determined diagenetic silica content of the examined sediments from Sites 794 and 795 (Fig. 5.15), though this relationship is more distinct at Site 795 possibly due to its lower content of clayey material. From this, a case can be made that the precipitation of opal-CT has a

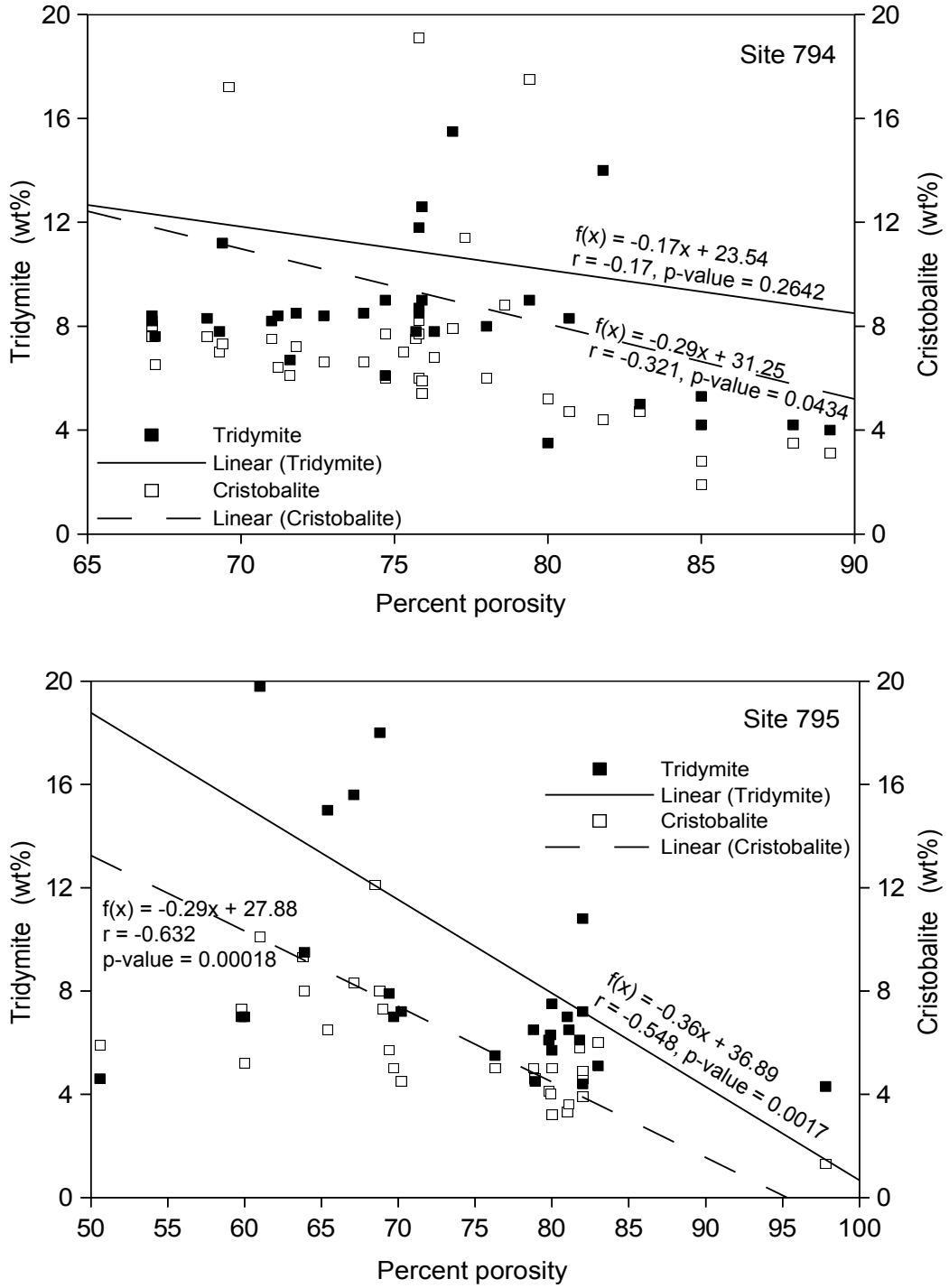


Figure 5.15. Diagenetic silica (tridymite and cristobalite from Tables 4.2 and 4.3 in Chapter 4) versus percent porosity for sediment samples from Sites 794 and 795. Except for the tridymite data points from Site 794, the inverse correlation between silica content and porosity for Sites 794 and 795 is significant at p-values < 0.05.

considerably-smaller influence on porosity reduction than opal-A dissolution during the anomalous compaction process. The relationship between porosity and tridymite/cristobalite abundance is slightly stronger for cristobalite than tridymite in Sites 794 and 795 possibly because of its ordering during the early stage of diagenesis through elimination of tridymite stacking in the cristobalite-like structure of opal-CT (Rice et al., 1995).

In general, the poor to moderate correlation observed between opal-CT content and porosity for Sites 794 and 795 appears to be linked to the grain size and composition of the non-silica fraction of the sediment. Due to the hemipelagic nature of the deep-sea sediments from Sites 794 and 795, mostly composed of diatomaceous siliceous oozes and fine-grained non-silica detrital material, the compaction is significant across the $TZ_{A/CT}$ in these sites. In the diatomaceous sediments, complete dissolution of the rigid and highly-porous siliceous frustules, matrix collapse, and precipitation of cryptocrystalline opal-CT have resulted in a reduction of ~15 and 20% porosity across the depth of the $TZ_{A/CT}$ in Sites 794 and 795, respectively. The extent of porosity decrease following the aforementioned processes, however, depends on the grain size and composition of the non-silica fraction of sediment and how susceptible it is to alteration during silica diagenesis (modified after Compton, 1991b). The fine-grained detrital fraction of the sediment in Sites 794 and 795 (originated from terrigenous sediments and altered oceanic basement) constitutes the dominant non-silica component that controls sediment porosity through interfering with compaction.

In addition to its natural porous structure, the proportion of clay- to silt-sized grains in the detrital fraction is a key variable that influences the compressibility of the sediment. It is accepted that high clay/silt ratios prohibit the extensive crystallisation of opal-CT in the biosiliceous sediments (e.g., Compton, 1991b). Isaacs (1981) observed that clay minerals in the sediment inhibit the massive crystallisation of opal-CT. The increasing abundance of clay-sized grains with depth relative to the silt-sized fraction observed for the investigated sites in this study (Fig. 5.16) is in agreement with these observations.

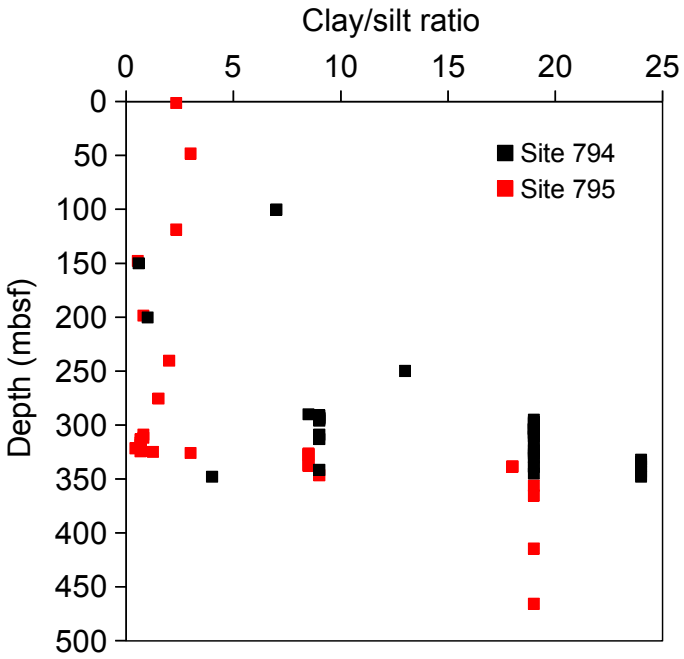


Figure 5.16. Variation in clay- to silt-sized grains ratios of sediment detrital fraction versus burial depth, Sites 794 and 795. The ratios were derived based on proportions of size fractions, forming terrigenous texture of the sediment, presented in Appendix IV. The terrigenous clay and silt fractions were quantified using suspension made for the preparation of smear slide, following the methodology of Marsaglia et al. (2013).

In addition, SEM examination of sediments from $TZ_{A/CT}$ and deeper indicates that the fine detrital component of the sediment provides grain support and inhibits massive cementation of the host sediment by opal-CT crystals (Figs. 5.9B, 5.11B, D, and 5.17A–B).

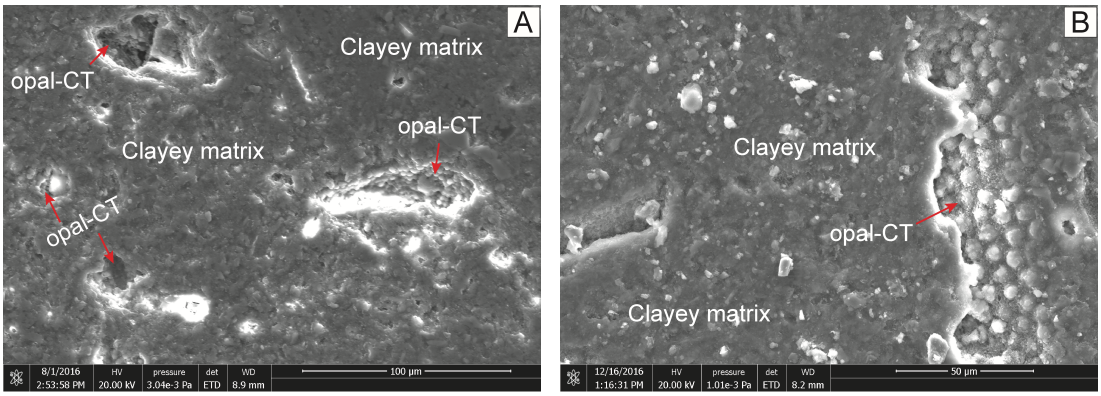


Figure 5.17. A) SEM photomicrograph of a claystone (Sample 127-794A-33X-1, 0–1 cm, at 303.3 mbsf), showing pore spaces (some of which only partly filled with opal-CT lepispheres). The pores are formed following complete dissolution of siliceous frustules. Clayey matrix is the dominant component of the sediment and clearly supports the grains; B) A chert (Sample 127-795A-36X-CC, 36–37 cm, at 327.78 mbsf), showing a cavity part of which filled with opal-CT lepispheres. The sediment groundmass is composed of fine-grained clayey material. Due to complete dissolution, no remnants of siliceous test are observed.

The opal-CT in clay-rich deep-sea sediment from Sites 794 and 795 occurs commonly as lepispheres grown in pore spaces formed following dissolution of diatom tests (and rarely radiolarians) that were supported by the fine-grained detrital component of the sediment. This contribution of diagenetic opal-CT to porosity

decreases leads to partial resistance to significant additional porosity reduction below the depth of anomalous compaction interval (the zone of porosity drop) until the clay-rich host sediment undergoes mechanical compaction by deeper burial (probably across the zone of opal-CT recrystallisation to quartz). The pattern of rough correspondence between porosity reduction and precipitated opal-CT content of the sediment (Fig. 5.15) supports this inference. This rough negative correlation is more or less similar to the negative correlation between porosity and diagenetic silica content observed by Isaacs (1980) for opal-CT rocks along the Santa Barbara coast and by Compton (1991b) for opal-CT sediments at Point Pedernales (Fig. 5.18). With the exception of the least siliceous samples from the Santa Barbara coastal area, the data points from Isaacs (1980) and Compton (1991b) fall nearly within the same porosity-composition field. The samples from the present study, however, are more porous than those examined by previous works, despite the similarity of their trend to lower porosity with increasing opal-CT content. This is related to the markedly-lower levels of diagenetic silica precipitated in the sediments from this study (the mean value of ~7.5 wt% within the $TZ_{A/CT}$), as compared to the opal-CT rocks of intermediate silica content (50–75 wt%) in the Santa Barbara coast and Point Pedernales. The siliceous sediments in this study which have undergone anomalous compaction still have a greater porosity than that of comparable studies mentioned above because the non-silica clay-rich material supports the sediment framework and less opal-CT is available to fill the porosity. In fact, the clay-rich matrix inhibits massive crystallisation of diagenetic silica as an intergranular cement, leading to higher porosity for the opal-CT sediments in Sites 794 and 795.

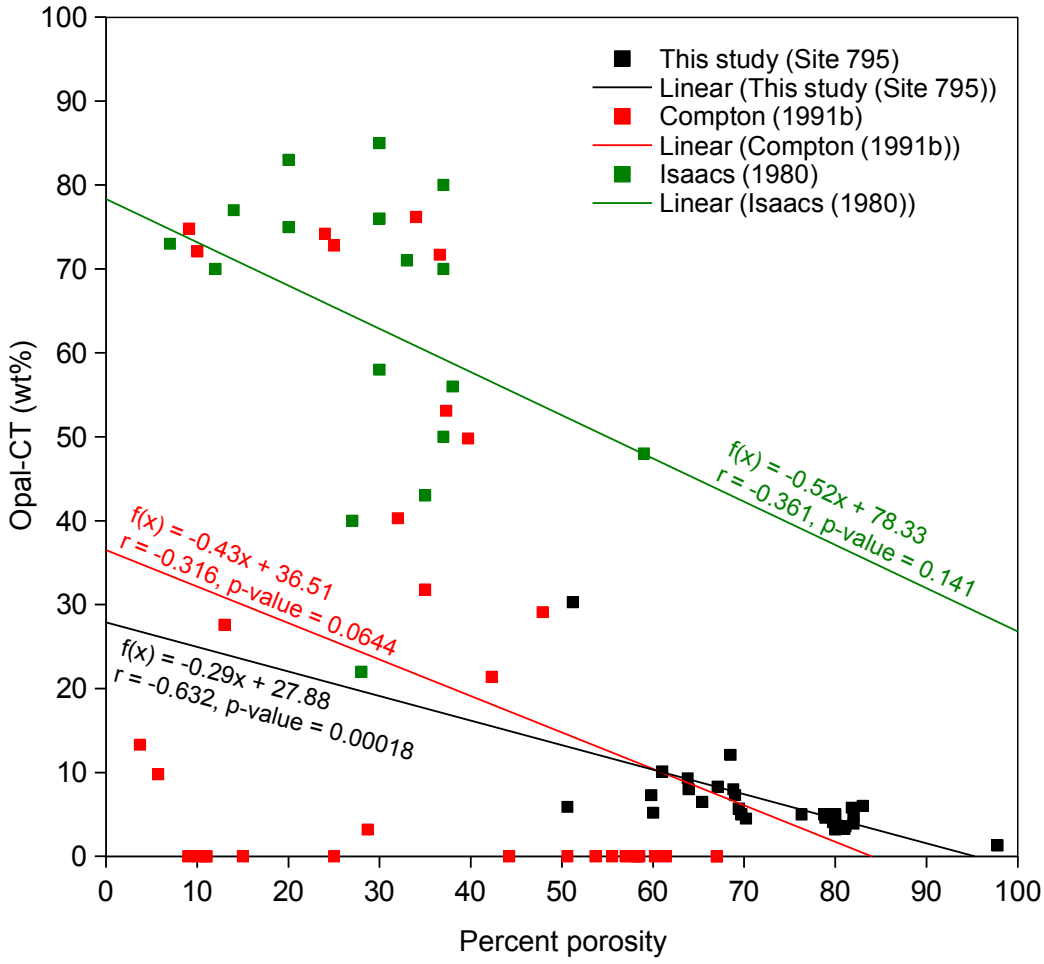


Figure 5.18. Opal-CT versus percent porosity for the sediments examined in this study. The values on the abscissa marking opal-CT wt% are the weight percents of cristobalite as the representative of opal-CT (cristobalite from Table 4.3 in Chapter 4). Opal-CT sediment data from the Santa Barbara coastal area (Isaacs, 1980) and the Point Pedernales (Compton, 1991b) are plotted for comparison.

5.6.2.1 Diagenetic silica d-spacing and implications for petrophysical changes

According to Kastner et al. (1977), the disorder of opal-CT at the time of formation in clay-rich deep-sea sediments results from the incorporation of abundant extraneous ions (especially metallic cations that are mainly the constituents of clayey material) to the crystal structure of silica. Once formed, the disordered silica

polymorph opal-CT undergoes an ordering process (i.e., the d-spacing decrease) that occurs under higher burial temperature and elapsing time where large amounts of impurity phases (commonly as exchangeable cations) are not present in the sediment (Rice et al., 1995).

The prominent (101) planar spacing (d) of α-cristobalite is widely accepted as the representative of opal-CT and used to track the diagenetic silica ordering in the sediment by XRD (e.g., after Rice et al., 1995; Damby et al., 2014). Supporting this, Flörke (1955) and Graetsch et al. (1987) suggested that opal-CT is a cristobalite-like structure incorporating randomly-intergrown tridymite. The d(101) cristobalite peaks of highest intensity are commonly observed at 4.02–4.11 Å in the X-ray diffraction records of bulk powder samples (e.g., Hein et al., 1978; Hesse and Schacht, 2011). The position of the (101) cristobalite peak is affected by the overlap of minor plagioclase peaks, however, measuring the most intense opal-CT peak maximises the original signal to noise ratio, leading to a significant reduction in the interference from accessory phases (after Damby et al., 2014; Chapter 4).

Although the (101) cristobalite in sediments from Sites 794 and 795 has a fluctuating d(101) spacing (3.95–4.11 Å and 3.98–4.05 Å in Sites 794 and 795, respectively) throughout the sub-seafloor section accommodating the opal-CT-rich zone (Fig. 5.19), it decreases with burial depth within the $TZ_{A/CT}$. The decrease in the d(101) spacing is impressive in light of the considerable fractions of fine-grained detrital that are typically present in the sediment from these sites (ranging from 25 to 97%

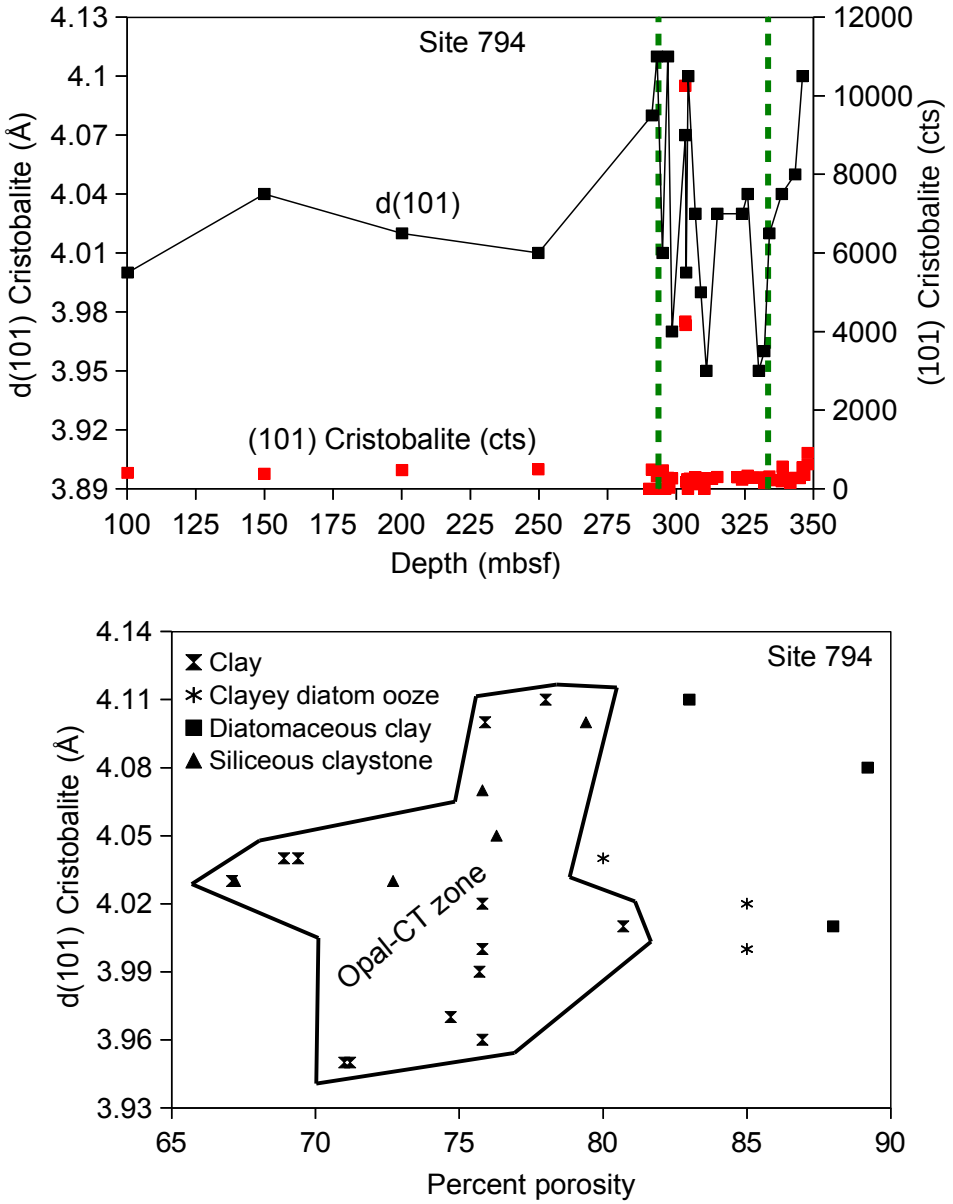


Figure 5.19. d(101) spacing and integrated intensity of opal-CT versus burial depth of siliceous sediments; d(101) spacing versus porosity, Sites 794 and 795. The integrated intensity values were derived from Figure 4.7 in Chapter 4. The analytical software Match! 3.4.2 Build 96 was used to derive the d(101) spacings from the XRD analysis conducted on the core samples (Chapter 4). The d(101) values were then corrected against the position of the quartz reflection at 3.34 Å using Bragg's law (Bragg and Bragg, 1913): $2d \times sin\theta = n \times \lambda$, where: d = the interplanar distance (Å), θ = the scattering angle (°), n = a positive integer (=1), and λ = the wavelength of the incident wave (Å). Green dotted lines in the opal-CT-depth diagrams mark top and base of the petrophysical $TZ_{A/CT}$.

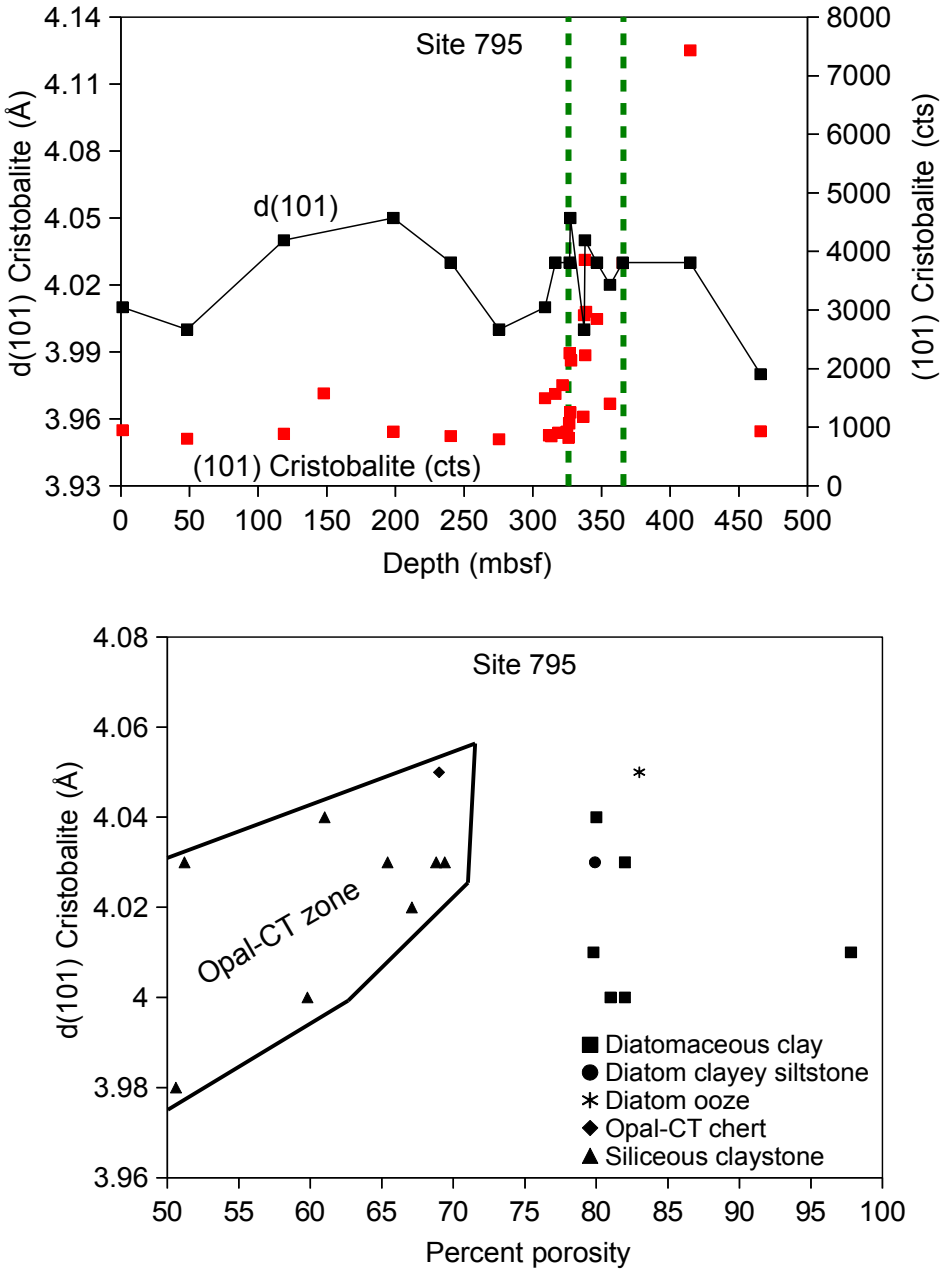


Figure 5.19. Continued.

in Site 794 and from 25 to 95% in Site 795; Appendix IV). Not only is massive opal-CT precipitation inhibited within the opal-CT-rich zone by detrital materials (except for a few samples with significant intensity peaks, no remarkable increase is

observed for opal-CT across the $TZ_{A/CT}$, especially in Site 794; Fig. 5.19; also see Fig. 4.7 in Chapter 4), but the smaller d(101) spacings are associated with increased detrital content of the sediment with depth (Appendix IV) within this interval. In accordance with Isaacs (1982), the decrease of opal-CT d-spacing in presence of large amounts of detrital material in these carbonate-free sediments is because the extraneous cations, which retard the transformation of disordered cristobalite to ordered polymorphs, are possibly consumed by other authigenic reactions, such as formation of clay minerals. According to Shipboard Scientific Party (1990a), smectite, chlorite, and mixed-layer clays are present in the sediments from Sites 794 in minor to small amounts, and are probably authigenic.

Although the d(101) spacing of cristobalite tends to generally increase with increasing porosity across the entire opal-CT-rich zone in Sites 794 and 795 (data points in the polygons on the d(101) spacing versus porosity diagram, Fig. 5.19), the relation between the d(101) spacings and porosity is more robust in denser rocks, such as siliceous claystones and cherts, than in clayey sediments from this interval. This is because the denser rocks have experienced a deeper burial, which is an essential component to both porosity decrease and the depth-dependent ordering of opal-CT. Compared to the high porosity diatom oozes and clays within the opal-A zone, the lower mean d(101) of cristobalite (more ordered) for lower porosity sediments from the opal-CT zone is, in addition to higher burial temperature and time, a possible result of the diminishing influence of non-crystalline phases (Rice et al., 1995).

Due to the paucity of knowledge about the crystalline structure of opal-CT and the mineralogical significance of its d-spacing, the relationships between cristobalite ordering and sediment petrophysics (in particular porosity) are only slightly understood. For example, the sharpening of the d(101) cristobalite XRD peak with increasing burial results from the gradual dissolution of smaller crystals and re-deposition of the dissolved silica on larger ones, and reflects a growing crystallite size of the opal-CT, which may entail changes in sediment petrophysics (Hesse and Schacht, 2011). However, according to Murata and Larson (1975), Murata et al. (1977), and Isaacs (1980, 1982), such variations are minor as ordering process is a structural solid-state adjustment within the opal-CT stage that does not basically involve changes in the amount of pore-filling silica per unit volume of sediment.

5.6.3 Authigenisation reactions associated with silica diagenesis

According to many researchers (e.g., Hurd, 1973; Papavasiliou, 1979; Iijima and Tada, 1981; Williams et al., 1985; Stamatakis et al., 1988; Compton, 1991a), the formation of authigenic minerals such as clays (and also zeolites) in most of the sub-seafloor biosiliceous deposits accompanies the transformation of opal-A to opal-CT. The precipitation of authigenic clay minerals in these deposits has been cited as an example of reverse weathering reactions under which amorphous aluminosilicates are precipitated and transformed into crystalline aluminosilicates (Mackenzie et al., 1981; DeMaster, 2003). In marine settings, neoformation of smectite is the prominent authigenic process that begins early in post-depositional diagenesis and is fuelled by the silica dissolved from siliceous tests (Krystinik, 1981; Williams et al.,

1985). In the context of Sites 794 and 795, the main source for production of smectite is alteration of volcanic glass that coincides with the transformation of biogenic opal-A (mostly diatoms) to opal-CT. The formation of smectite causes the uptake and release of cations and increases the pH which can then promote the precipitation of zeolites (Hay, 1963; Surdam and Hall, 1984). The markedly-lower abundance of smectite minerals compared to zeolite in the clay-rich ODP Sites 794 and 795 (Fig. 5.20) may indicate that the smectite is largely authigenic and that other reactions may not buffer the pH below values that enhance zeolite precipitation (Compton, 1991a).

In clay-rich sediments, clay minerals, in particular smectites, would initially compete for the available magnesium. As a result, the pore-water solution will be depleted in alkalinity which in the absence of $CaCO_3$ can be replenished only through bicarbonate diffusion (Kastner et al., 1977). Consequently, this effect leads to a great reduction in transformation rate of opal-A to opal-CT because the Mg-hydroxide nuclei aiding in the crystallisation of opal-CT are less likely to form where clay minerals take up much of the available alkalinity. In Sites 794 and 795, however, no additional pore-water Mg sink due to silicate alteration is developed across silica drop at the $TZ_{A/CT}$ (see Chapter 4). Therefore, the authigenisation of smectite and its associated zeolites formation is likely to be only a subordinate control on the rate of silica diagenesis. This assumption is supported by the low abundances of these mineral phases and their variations with depth for the investigated sites. Due to the low amounts of volcaniclastic materials (in particular volcanic glass and ash) mixed

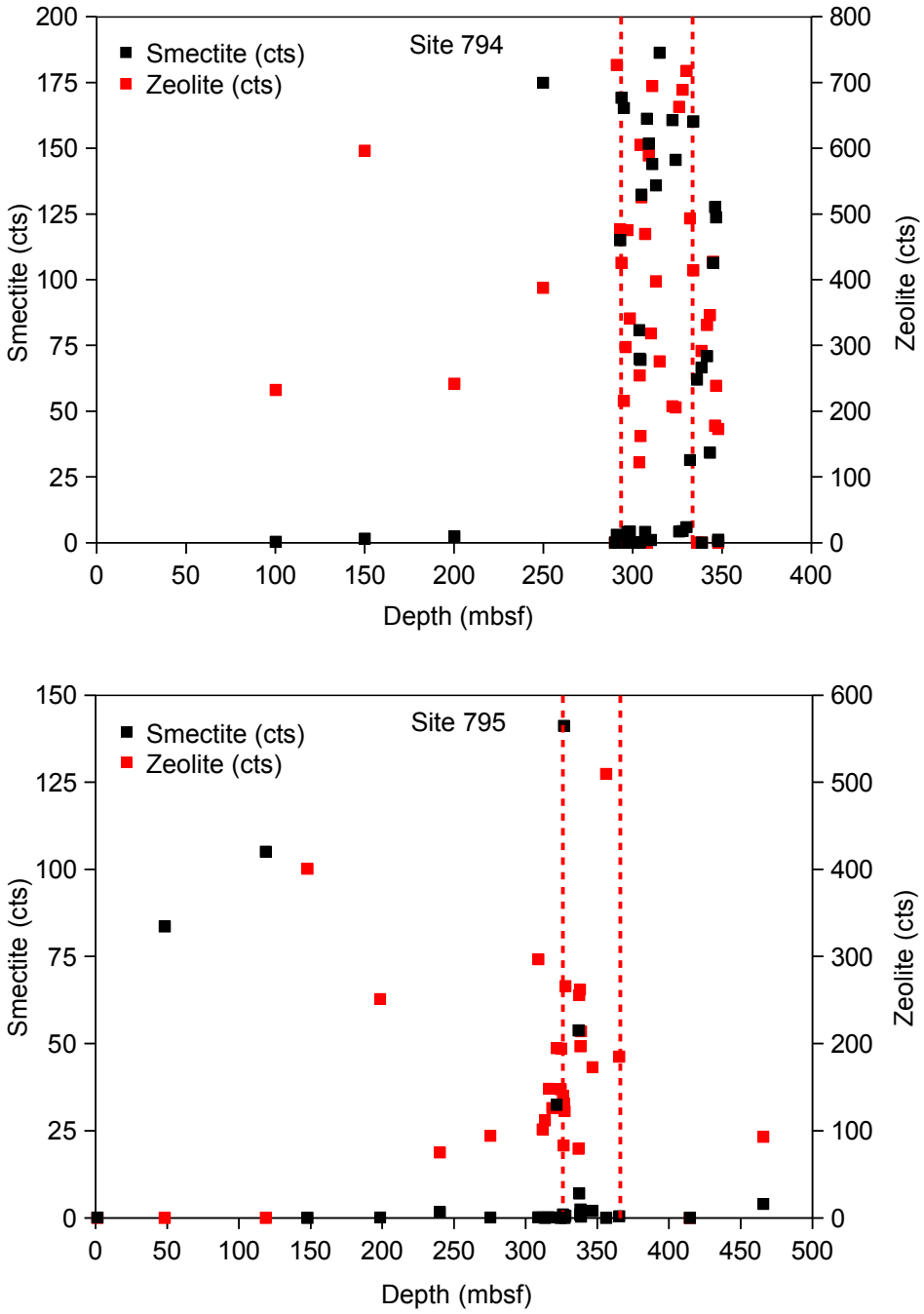


Figure 5.20. Integrated intensities of smectite and zeolite versus burial depth, Sites 794 and 795. The software Match! 3.4.2 Build 96 was used to derive the integrated intensity values from the XRD analysis conducted on the core samples (Chapter 4). The value for each data point on the primary ordinate is the sum of the integrated intensities of montmorillonite, nontronite, and hectorite which are the most important species of smectite group. The values on the secondary ordinate are the integrated

intensities of clinoptilolite-Na as the representative of zeolite in the deep-sea sediments. Red dotted lines represent top and base of the $TZ_{A/CT}$ as determined based on sharp changes in physical properties of the sediment. Note the intensity values decreasing with depth along the opal-CT-rich interval in Sites 794 and 795.

with the biosiliceous sediments in Sites 794 and 795, the contribution of dissolved silica to the interstitial water through this source is not comparable to the dissolution of biogenic silica (Chapter 4). Accordingly, the authigenic minerals produced from alteration of volcanic glass and ash constitute only minor fractions of the sediment in these sites. The low diffraction intensities of smectite and zeolite across the $TZ_{A/CT}$ and the interval below it in Site 794 decrease with burial depth (Fig. 5.20, Site 794). In Site 795, the rate of authigenisation within the zone of porosity drop is strongly reduced and the integrated intensities decrease within this interval (Fig. 5.20, Site 795).

The decreasing contents of these mineral phases with burial depth across the anomalous compaction interval in Sites 794 and 795 may also suggest that the pore filling by authigenic clay minerals has minor impacts on sediment petrophysics, and the sharp variation in physical state of the sediments (especially porosity drop) occur predominantly through extensive dissolution of biogenic opal, matrix collapse, and subsequent additions of diagenetic silica to the sediment.

5.7 Conclusions

Textural and mineralogical analysis of core samples from opal-A- and opal-CT-rich

sediment constructs in Sites 794 and 795 show that biogenic and diagenetic silica are the two critical components involved in the anomalous compaction phenomenon occurred across the $TZ_{A/CT}$. Other authigenic mineral contents have no measurable effect on abrupt variations in sediment petrophysics. In contrast to general trend of porosity dependence on burial mechanical compaction, the highly-porous structure of biogenic silica and its relative incompressibility compared to the clay-dominated host sediment lead to high porosity within the opal-A-rich interval. Significant reduction in biogenic silica content within the $TZ_{A/CT}$ results from opal-A dissolution and causes failure in the strength of porous sediment matrix, sudden framework collapse, and therefore abrupt porosity reduction. Other petrophysical changes, such as bulk density increase, void ratio decrease, and pore-water expulsion owe to porosity drop at the $TZ_{A/CT}$. Porosity of collapsed framework is further influenced through subsequent cementation of diagenetic silica, leading to velocity increase within the anomalous compaction interval.

Quantitative mineralogical analysis, however, shows that opal-CT content has a smaller influence on the sediment porosity decreases, suggesting that opal-A dissolution contributes most to the process of anomalous compaction. In addition to the porous nature of hemipelagic deposits combining biosiliceous material and fine-grained detrital, the increasing abundance of clay- versus silt-sized fraction in the detrital component with depth inhibits extensive crystallisation of opal-CT; thus less opal-CT is available to fill the pore spaces of sediments in Sites 794 and 795. This process results in resistance to additional porosity drop below the $TZ_{A/CT}$. As a

consequence, despite matrix collapse and re-precipitation of dissolved silica, porosity is still relatively high within the $TZ_{A/CT}$ at these sites.

The structural ordering of opal-CT with depth at the $TZ_{A/CT}$ in Sites 794 and 795 in presence of high fractions of fine detrital materials is because the extraneous ions (metallic cations that constitute clayey material), which retard the transformation of disordered cristobalite to ordered polymorphs, are removed from the structure of silica possibly by formation of authigenic minerals. Association of lower opal-CT d-spacings with denser sediments, such as siliceous claystones and cherts, across the anomalous compaction interval suggests that higher burial temperature and longer time are also essential controls on internal ordering of diagenetic opal.

Mineralogical analysis of clay-rich sediments from Sites 794 and 795 also suggests that the authigenisation of clay minerals, in particular smectite and formation of zeolites, accompanying the transformation of opal-A to opal-CT exerts only a subordinate control on silica diagenesis and its associated petrophysical variations.

Chapter 6

Bottom-water temperature controls on biogenic silica dissolution and recycling in surficial deep-sea sediments

6.1 Abstract

This study calculated the dissolution rates of biogenic silica deposited on the seafloor and the silicic acid benthic flux for 22 Ocean Drilling Program sites. Simple diagenetic models developed for two host sediment types—detrital and carbonate—were used to explain the variability of biogenic silica dissolution and recycling under present-day bottom-water temperatures. The kinetic constants describing silicic acid release and the silicic acid saturation concentration increased systematically with increasing bottom-water temperatures. When these temperature effects were incorporated into the diagenetic models, the prediction of dissolution rates and diffusive fluxes was more robust. This demonstrates that temperature acts as a primary control that decreases the relative degree of pore-water saturation with respect to biogenic silica while increasing the concentration of dissolved silica in pore water. The positive correlation between the dissolution rate and benthic flux with temperature was particularly pronounced at sites where biogenic opal is accommodated in surficial sediments mostly comprised of biogenic carbonates. The most likely explanation for this contrast is that in carbonate sediments, the dissolution of carbonates provides the alkalinity necessary for both silica dissolution

and clay formation; thus strongly reducing the retarding influence of clay minerals on opal dissolution as the competition between these reactions for the available alkalinity decreases. The model prediction of a first-order, early transformation reaction for silica in the sediment suggests that there may be controls from surface temperatures on unusual accumulation at low temperatures (0–4 °C) of opal-CT porcellanites over a short period of geological time (< 4 Ma) at a few sub-seabottom positions close to the seafloor in the Antarctic. The model attains close agreement between transformation ratios and temperatures with depth within the uppermost sediments at the Antarctic ODP Site 751. The role of temperature, however, may not be critical as the established inverse correlation between temperature and time, requiring opal-CT formation in young sediments at higher temperatures, denies the possibility of a major control from low bottom-water temperature on precipitation of opal-CT in the near-surface sediments. The relationship between solubility and surface area might better explain the formation of opal-CT in this situation, where time possibly plays a major role. Since the solubility and surface area of opal-A decrease with time in the sediment, it is possible that a < 4 Ma elapsed time has aged biogenic silica to the point that further changes in specific surface area have caused only minor effects on solubility, which may allow for earlier precipitation of opal-CT from the interstitial water at low temperature sub-seafloor locations near the seabed in the Antarctic.

Keywords: Bottom-water temperature, Biogenic silica, Dissolution rate, Benthic flux, Ocean Drilling Program

6.2 Introduction

Only a fraction of siliceous marine tests produced by planktonic organisms such as diatoms, radiolarians, and silicoflagellates in the surface ocean reach the seafloor after avoiding dissolution in the upper ocean and the lengthy passage through the water column. Even then, this small percentage of solution-resistant biogenic silica (opal-A) undergoes progressive dissolution across the water-sediment interface, especially within the top few centimetres of the sediment column, where 70–95% of the opal rain arriving at the seafloor dissolves prior to burial (modified after Ragueneau et al., 2000). The extensive dissolution of siliceous tests in surficial deep-sea sediments—including at the water-sediment interface and the first centimetres below it—constitutes part of the early diagenesis process of silica during which a considerable volume of the silicic acid produced by the dissolution of biogenic opal is released back to the overlying ocean water column through diffusion (after Dixit and Van Cappellen, 2003). This recycling (benthic flux) of dissolved silica (23×10^{12} moles of silicon per year) is estimated to be at least three times greater than the total amount of biogenic silica arriving and being preserved on the seafloor (Tréguer et al., 1995). Tréguer et al. (1995) estimate that globally, only 7.1×10^{12} moles of silicon per year or about 3% of the gross production of biogenic opal ends up buried in the sediment column (burial flux).

Interest in the dissolution of sedimentary biogenic silica within surficial deep-sea sediments arises mainly because of its importance as a mechanism by which the generated silicic acid contributes as a major component of the nutrient silicon cycle

in the world oceans.

The dissolution rate of biogenic silica depends on a variety of chemical and physical factors, including temperature, time, reactive surface area, pore-water chemistry, host lithology, and sediment permeability (e.g., Hurd, 1973; Lancelot, 1973; Kastner et al., 1977; Hein et al., 1978; Williams and Crerar, 1985; Nobes et al., 1992; Neagu, 2011). Among these, temperature is widely accepted as the dominant control (e.g., Kastner et al., 1977; Williams and Crerar, 1985; Neagu et al., 2010). The solubility of biogenic opal substantially increases with increasing temperature (Iler, 1979; Erez et al., 1982; Williams and Crerar, 1985; Atkins and de Paola, 2006; Park et al., 2006; Boggs, 2009). Laboratory-based experiments by Van Cappellen and Qiu (1997a), using a flow-through reactor, provided constraints for the development of mechanistic models of the early diagenesis of silica in deep-sea sediments. They suggest that silica solubility is dependent on bottom-water temperature for the modern highly-siliceous uppermost sediments (the top 10 cm) of the Southern Ocean. Comparable experiments performed by Rickert (2000), at an *in situ* temperature of 2 °C to simulate the bottom-water conditions, also demonstrated a significant temperature dependence on dissolution rate of sedimentary opal from the Arabian Sea.

To date, the basis for most models that account for the early diagenetic reactive transport of silica through the surficial sediments is derived from a first-order kinetic dissolution rate law (e.g., Schink et al., 1975; Berner, 1980; Rabouille et al., 1997;

Van Cappellen and Qiu, 1997a; Rickert, 2000; Dixit and Van Cappellen, 2003):

$$R_{diss} = k\left(1 - \frac{C}{C_{sat}}\right) \qquad (1.1)$$

where R_{diss} is the rate of biogenic opal dissolution in the sediment (in s^{-1}), k is the temperature-dependent first-order kinetic constant (in s^{-1}), C is the dissolved silica concentration (in μM), and C_{sat} is the asymptotic pore-water dissolved silica concentration (in μM).

The major assumption is that the dissolution of biogenic opal in the sediment produces dissolved silica. This kinetic expression of the reaction rate highlights the dependence of the dissolution rate on the relative departure from equilibrium with opal—given by the contrast between pore-water silicic acid concentrations and the saturation value (that equates to the asymptotic concentration of silicic acid)—and on the kinetic rate constant. The mathematical expansion of the standard kinetic rate law for opal dissolution also forms the basis of most models that deal with the benthic flux of silicic acid. Dixit and Van Cappellen (2003) have presented the most comprehensive expansion of the first-order congruent rate law for biogenic silica. Their expression for the benthic fluxes of dissolved silica combines the expanded dissolution rate equation (including the effects of biogenic silica content of the sediment and the petrophysical properties in the magnitude of the standard kinetic rate) with Fick's first law for diffusion through a porous medium.

Silica dissolution and its associated benthic flux in deep-sea sediments, as predicted by Dixit and Van Cappellen's (2003) model and the other aforementioned works, are often modified by sediment composition (namely, by relative detrital fraction of the sediment), implying an inverse correlation between dissolution rate and the mass ratio of lithogenic matter (detrital) to biogenic opal.

Though the presence of detrital material plays an undeniable rate-limiting role in the early diagenesis of silica within the uppermost deep-sea sediments as well as deeper in the sediment column, there are some indications that bottom-water temperatures may exert a stronger control on early diagenetic silica dissolution and recycling; this control under some circumstances may be stronger than the concentration of dissolved silica in pore water. Evidence for a strong temperature control includes:

(1) A shift in relative saturation observed within the surficial sediments from the ODP cores (at least for Sites 794 and 795; refer to Chapter 4) where detrital matter is the dominant component of the sediment. This implies a strong control by bottom-water temperature on the dissolution of biogenic opal, even in the presence of high detrital content;

(2) Seasonal variations of the silica dissolution rate and silicic acid effluxes at the water-sediment interface and within the uppermost sediment layers reported from some ocean regions (e.g., the southern North Sea) suggest a strong relationship between these processes and bottom-water temperatures. This relationship reflects low silicic acid fluxes in winter and markedly-high fluxes in summer (Oehler, 2014). The increased silicic acid fluxes during summer might be inconsistent with primary

production of diatoms as phytoplankton blooms during summer lead to the silicic acid depletion within the water column (Oehler, 2014). However, as described by Joint and Pomroy (1993), the concentration of silica can further be increased after phytoplankton blooms by the settling of diatoms at the seafloor and their dissolution at the sediment surface and within the sediment, which can explain temperature-related seasonal variations in silicic acid fluxes. There is also a clear decrease in the silica dissolution reaction rate with a seasonal bottom-temperature drop of 10 °C (Wollast, 1974; Gehlen et al., 1995);

(3) Finally, there is evidence that the accumulation of ancient early diagenetic opal—the formation of opal-CT due to transformation of opal-A—in marine settings over time has been strongly responsive to bottom-water temperature following a drastic shift in silica cycle to a diatom-dominated pattern in the Late Jurassic and Cretaceous (e.g., Hein and Parrish, 1987; Kidder and Erwin, 2001; Muttoni and Kent, 2007). Such a shift also argues that pre-Cretaceous oceans must have had higher levels of dissolved silica than younger oceans (after Siever, 1957, 1992), and therefore greater silica recycling. Effects of temperature, however, receive less focus because of limited variability in modern systems.

The major objective of this chapter is to investigate the role of bottom-water temperature in controlling the rates of silica dissolution and recycling across the uppermost few centimetres of the sediment record. Here, I interrogate accessible ODP sources to compile, analyse, and discuss data regarding the lithology, temperature, dissolved silica concentrations of pore water, and the petrophysical

properties of the surficial layer of biosiliceous deep-sea sediments cored by the ODP. Neagu et al. (2011) report that about 100 ODP wells around the globe have been drilled within sediment units containing a silica diagenesis transition zone, an interval where biogenic opal is transformed into diagenetic opal-CT (co-existence of opal-A and opal-CT within this boundary). Among these ODP stations, I chose 22 sites where the diagenetic transition zones are located in Neogene deposits for which there was existing ODP data regarding the uppermost sediment composition, bottom-water temperatures, silicic acid levels of pore water, sediment porosity, and density.

The dissolution rates of reactive silica across the benthic boundary layer were calculated for all 22 sites using the first-order kinetic rate law, the diffusive effluxes using the early diagenetic model expression of Dixit and Van Cappellen (2003), the burial fluxes of biogenic opal using the mass accumulation rate expression (e.g., Oehler, 2014), and the early diagenetic transformation using the linear expression of Arrhenius' Law (1889) for first-order reactions. Diagenetic models, specified for two different host lithologies (i.e., detrital and carbonate) and accounting for the temperature dependence of the kinetic dissolution rate coefficient (k), were formulated to predict the dissolution rate of sedimentary opal and the related benthic fluxes in relation to present-day bottom-water temperatures. These results were then used to predict the transformation of biogenic opal and explain unusual occurrences of low temperature (commonly from 0 to 4 °C) young (between 0.4 and < 4 Ma; e.g., Botz and Bohrmann, 1991) opal-CT porcellanite and chert precipitated at some sub-seabottom locations.

6.3 Environmental setting

The distribution of the 22 ODP sites studied here is indicated on Figure 6.1. Half of the investigated sites were drilled off the western continental margins of North and South America and within the northern Pacific, while almost 40% were drilled in the Sea of Japan and its surrounding basins. The remaining 10% were cored within the Southern Ocean and around the Antarctic peninsula. The geographic locations, ocean depth, and lithology of sediment cores recovered at the sites are provided in Table 6.1. The study sites represent exceptional depositional environments with highly-porous frequently-biosiliceous uppermost sediments that shift abruptly to less permeable lower porosity units deeper in the sediment following silica diagenetic reactions (e.g., Shipboard Scientific Party, 1990a).

A few of the study sites are located beneath the largest and most intense zone of equatorial upwelling on Earth (Sites 846, 847, 1225, and 1226). This matter is of special significance as the equatorial eastern rims of the North and South Pacific Ocean were some of the major depocentres of biogenic silica during the Middle Miocene to Early Pliocene (after Ingle, 1980, 1981; Behl, 1999). For 2/3 of the sites chosen for this study (15 sites), biogenic silica is deposited with fine-grained detrital material (siliceous oozes that are commonly accompanied by clay, silt, and sometimes volcanic ash). Though detrital-based, fractions of calcareous nannofossils (and sometimes foraminifers) are admixed with the diatomaceous sediments for Sites 798, 1016, 1022, 1165, 1175, and 1208.

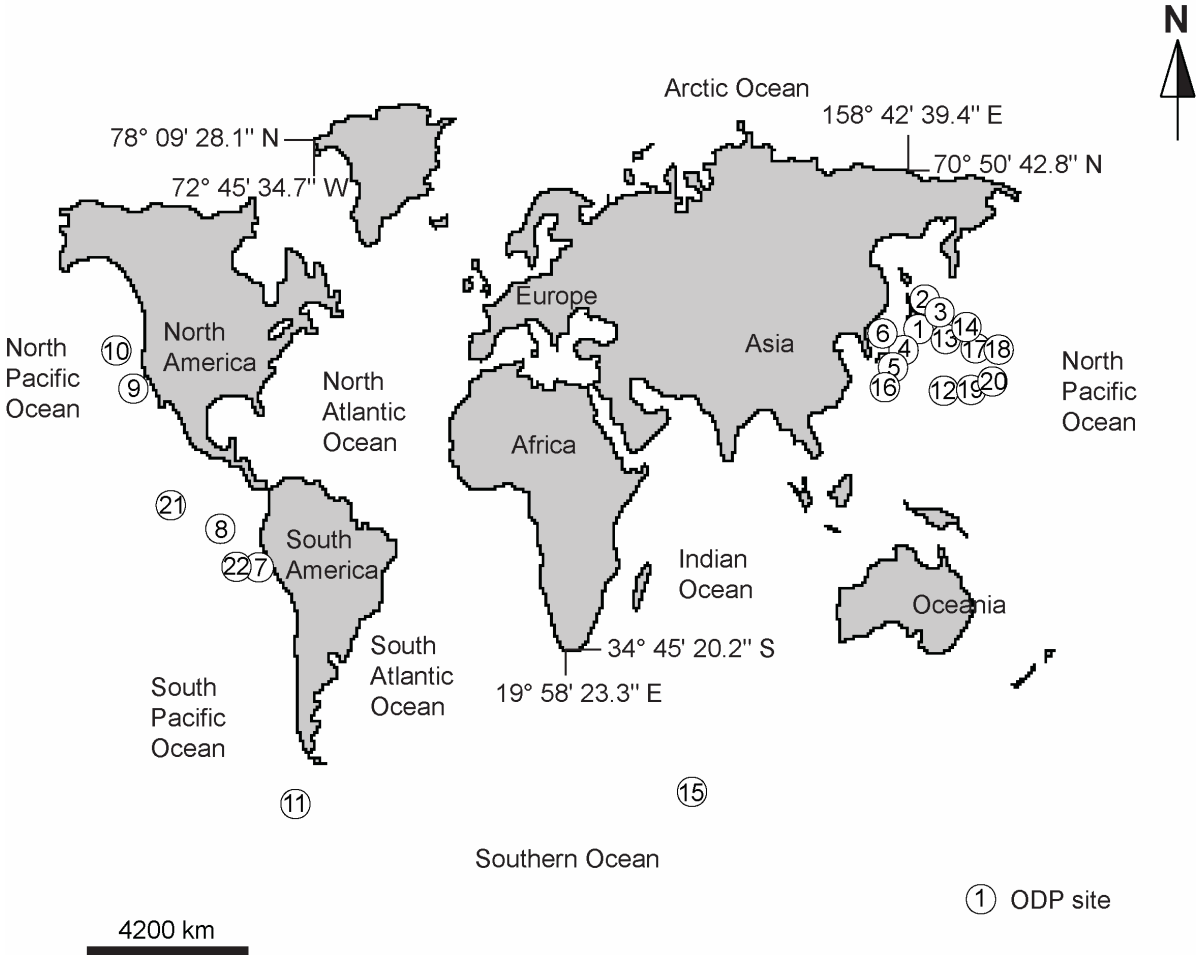


Figure 6.1. Location of the investigated ODP borehole sites.

ODP sites (circled numbers): 1) 794/Leg 127, 2) 795/Leg 127, 3) 796/Leg 127, 4) 797/Leg 127, 5) 798/Leg 128, 6) 799/Leg 128, 7) 846/Leg 138, 8) 847/Leg 138, 9) 1016/Leg 167, 10) 1022/Leg 167, 11) 1095/Leg 178, 12) 1149/Leg 185, 13) 1150/Leg 186, 14) 1151/Leg 186, 15) 1165/Leg 188, 16) 1175/Leg 190, 17) 1207/Leg 198, 18) 1208/Leg 198, 19) 1211/Leg 198, 20) 1212/Leg 198, 21) 1225/Leg 201, and 22) 1226/Leg 201.

Given that the sample sites reflect deep-sea zones (excluding Site 798 with a water depth of 911 m, the depths range between ~2200 and ~5800 m; Table 6.1), the surface sediments are not commonly reworked nor are disturbed by tidal currents and

Table 6.1. Description of ODP sites investigated in this study, including latitude and longitude, water depth, geographic location, and description of the first lithologic unit. No. = the identification number of the ODP sites as presented in Figure 6.1.

No.	Site/Leg	Latitude	Longitude	Water depth, m	Geographic location	Sediment type
1	794/127	40° 11.41´N	138° 13.86´E	2822	Yamato Basin, southeastern Japan Sea	Clay and silty clay with a significant admixture of vitric ash
2	795/127	43.99°N	138.97°E	3310	Japan Sea	Silty clay with subordinate diatom clay, ashy clay, and diatom ooze
3	796/127	42.89°N	139.41°E	2596	Japan Sea	Diatom-bearing clay and silty clay
4	797/127	38.62°N	134.54°E	2876	Yamato Basin, south-central Japan Sea	Clay and silty clay with a minor admixture of vitric ash and diatoms
5	798/128	37.04°N	134.8°E	911	Oki Ridge, southeastern Japan Sea	Clay, silty clay, and diatom clay with occurrence of calcareous nannofossils and foraminifers
6	799/128	39° 22.05´N	133° 86.69´E	2985	Yamato Rise, Japan Sea	Diatomaceous ooze and diatomaceous clay with carbonate and siliciclastic sands
7	846/138	3° 5.7´S	90° 49.08´W	3387	Galapagos Islands, equatorial Pacific	Nannofossil ooze, diatom nannofossil ooze, nannofossil diatom ooze, and clayey diatom ooze
8	847/138	0° 11.59´N	95° 19.23´W	3346	Galapagos Islands, equatorial Pacific	Diatom nannofossil ooze and nannofossil ooze with minor amounts of radiolarians and foraminifers
9	1016/167	34° 32.42´N	122° 16.59´W	4162	Point Conception, California	Diatom ooze with clay, diatom clay, and clayey diatom ooze, and diatom nannofossil ooze with clay
10	1022/167	40° 4.85´N	125° 20.56´W	2325	Cape Mendocino, California	Nannofossils and siliciclastic clay with diatoms

Table 6.1. Continued.

11	1095/178	66° 59.13´S	78° 29.27´W	3863	Antarctic Peninsula, Pacific margin	Diatom-bearing silty clay, silty clay, and clay with minor siliceous ooze
12	1149/185	31° 20.52´N	143° 21.08´E	5829	Nadezhda Basin, northwestern Pacific	Clay with varying amounts of siliceous microfossils and volcanic grains
13	1150/186	39° 10.91´N	143° 19.92´E	2692	Japan Trench, off northeast Japan	Diatom ooze and diatom clay with tephra
14	1151/186	38° 45´N	143° 20´E	2182	Japan Trench, off northeast Japan	Diatomaceous silty clay with occurrence of sand, silt, and pumice as minor lithologies
15	1165/188	64° 22.22´S	67° 13.14´E	3549	Prydz Bay, Antarctic Ocean	Transition from diatomaceous ooze to diatom clay
16	1175/190	32.6°N	134.64°E	3024	Nankai Trough, southwestern Japan	Nannofossil-rich hemipelagic mud
17	1207/198	37° 47.43´N	162° 45.05´E	3112	Shatsky Rise Northern High, northern Pacific	Nannofossil ooze and clayey nannofossil ooze
18	1208/198	36° 7.63´N	158° 12.1´E	3346	Shatsky Rise Central High, northern Pacific	Alternation of nannofossil clay and ooze with siliceous tests
19	1211/198	32° 0.13´N	157° 51´E	2907	Shatsky Rise Southern High, northern Pacific	Alternation of nannofossil clay and nannofossil ooze
20	1212/198	32° 26.90´N	157° 42.70´E	2681	Shatsky Rise Southern High, northern Pacific	Nannofossil ooze with clay
21	1225/201	2° 46.25´N	110° 34.29´W	3772	East Pacific Rise	Alternation of nannofossil ooze and diatom- and radiolarian-rich nannofossil ooze
22	1226/201	3° 5.67´S	90° 49.08´W	3297	East equatorial Pacific	Alternation of diatom-rich nannofossil ooze and nannofossil-rich diatom ooze

storms (Oehler, 2014). Therefore, the accumulated sediments, silica dissolution, and subsequent benthic nutrient fluxes from the sediment pore water reflect processes in the overlying water column (e.g., primary production or opal rain arriving at the seafloor). In addition, irrigation by macrofauna is thought to be only a minor effect on benthic solute-exchange fluxes at these sites (according to Dixit and Van Cappellen, 2003; Meile and Van Cappellen, 2003). Even in the case of uplifted sediments at Site 798, subjected to a sudden shallowing in water depth, possible low oxygen levels in the bottom water decrease the quality of the infaunal habitat (Shipboard Scientific Party, 1990d), and consequently exclude bioturbation and pore- water irrigation.

6.4 Data acquisition and methods

ODP resources (including initial reports and scientific results) and the IODP databank provided the mineralogical composition, temperature, pore-water silica concentration, and physical properties (in particular porosity and density) for the surface and uppermost sediments of the 22 selected borehole sites. Much of the baseline information acquired during the ODP cruises through downhole and onboard-ship measurements and measurements on water and core samples is available through open access (see International Ocean Discovery Program, 2018).

The various sediment and water measurements used in this study have been described in ODP technical notes (e.g., Rabinowitz and Garrison, 1985; Mazzullo and Graham, 1988; Gieskes et al., 1991; Fisher and Becker, 1993; Blum, 1997).

Below, a brief description is given for the ODP methodology concerning the sediment parameters reported in this study (Table 6.2).

In situ temperatures were measured using an APC (advanced hydraulic piston core) temperature tool designed to assess the bottom-sediment temperature during the process of cutting a hydraulic piston core. The temperature probe contained in one of the prongs at the base of the APC tool case was used to measure the sediment temperature during coring. The APC was held in place for at least 15 minutes to obtain enough data to extrapolate to the *in situ* sediment temperature (Fisher and Becker, 1993).

Once on deck, sediment cores were cut into 1.5-m-long sections and stored in racks for temperature equilibration. Whole-round 5- to 10-cm-long samples of core sections (usually taken from the bottom of a section) were removed for organic and interstitial-water analyses (Mazzullo and Graham, 1988). ODP shipboard inorganic geochemistry involves the extraction of interstitial-water samples from the whole-round core samples by ODP squeezers (after Rabinowitz and Garrison, 1985). Determination of silica concentrations was carried out on the pore-water samples by colorimetry using a wavelength range from 190 to 950 nm and analytical techniques described by following Gieskes et al. (1991). Silica concentrations were derived for the surficial sediments through the IODP databank.

Initial analyses conducted on the 1.5-m-long core sections usually include physical

properties measurements. Multi-sensor track logged physical properties, including gamma ray density, compressional wave velocity, magnetic susceptibility, and natural gamma radiation. The soft sediment cores were then split into two half-cores one half designated as 'archive', the other as 'working'. The final measured physical properties obtained from the working-half were moisture content and average mineral density (MAD). Parameters measured at the MAD station include the wet-bulk mass and dry mass of the specimen (for moisture content and density) and volume of dry (and optionally wet-bulk) sample (using gas pycnometry) (Blum, 1997). From these measurements, basic phase relationships, including porosity, bulk density, grain density, dry density, and void ratio were then calculated. These data are available through both ODP initial reports and IODP database.

Smear slides of unconsolidated sediments (usually taken from the archive-halves) were prepared aboard ship to document the lithology of recovered material and to aid in the description of cores. Beginning with Leg 119, the petrographic results were directly transferred into the shipboard computer system in a format like that reported on the ODP sediment smear-slide description forms for older Legs (Mazzullo and Graham, 1988). A visual estimation technique, based on using comparator charts (see Terry and Chilingarian, 1955), has been applied by the ODP to determine the relative percentages of minerals, skeletal grains, and other sediment components. The composition of the surficial sediments was derived from results of this approach.

Dissolution rates and benthic effluxes of dissolved silica and the burial fluxes of opal

were calculated and modelled based on the sediment parameter described above. In the following section, relevant equations required for these calculations are introduced.

6.4.1 Early diagenetic equations for silica

A first-order kinetic rate law (Equation 1.1) is the most widely-used rate expression for the dissolution of biogenic silica. This relates the dissolution rate to a linear function of the degree of pore-water undersaturation with respect to opal.

Whether stated explicitly or not, it is typically assumed that C in Equation 1.1 is equal to the bottom-water silicic acid concentration. The C_{sat} equates to the near constant concentration of dissolved silica at depths a few centimetres, usually < 10 cm below the sediment surface, and represents the equilibrium solubility of deposited biogenic silica (i.e., asymptotic silica concentration).

Temperature dependence on the kinetic rate constant is typically expressed using the Arrhenius' Law (1889):

$$k = Ae^{\frac{-Ea}{RT}} \qquad (1.2)$$

where A is the pre-exponential factor (in s^{-1}), E_a is the apparent activation energy of the dissolution reaction (in J mol^{-1}), R is the universal gas constant (8.314 J K^{-1} mol^{-1}), and T is absolute temperature (in K).

Temperature exerts a control on the kinetic rate constant through interaction with activation energy for the specific reaction of silica dissolution. This allows for basic predictions regarding variations in the dissolution rate coefficient with temperature. The exponent $-E_a/RT$ is simply the ratio of the activation energy to the average kinetic energy (RT) and as this ratio increases, the coefficient decreases. This implies that higher temperatures and lower activation energies favour larger rate constants; thus speeding up the reaction. As these terms occur in an exponent, their effects on the rate constant can be substantial. For example, assuming a decrease in activation energy for amorphous silica dissolution from 50 KJ mol^{-1} to a modest value of 40 KJ mol^{-1} at a slight seafloor temperature change from 0 to 0.1 °C, the rate coefficient increases by a factor of 10^2.

The mathematical expansion of Equation 1.1 combined with the Fick's first law of diffusion yields an expression for the benthic fluxes of silicic acid (Dixit and Van Cappellen, 2003):

$$J_0 = \left(kM_{opal} C_{sat} D_s \phi \left(1-\phi\right) \rho_b \right)^{0.5} \left(1 - \frac{C_{bw}}{C_{sat}} \right) \qquad (1.3)$$

where J_0 is the benthic flux of silicic acid (in mol m^{-2} yr^{-1}), k is the first-order rate coefficient (for Equation 1.3, the unit is converted from s^{-1} into yr^{-1}), M_{opal} is particulate biogenic silica concentration (in volume %), D_s is the sediment diffusion coefficient (in m^2 yr^{-1}), Φ is the sediment porosity (in %), ρ_b is the grain density of the sediment (in kg m^{-3}), C_{bw} is the bottom-water dissolved silica concentration (in

μM), and C_{sat} is the asymptotic silica concentration (saturation concentration) (in μM).

Although based on a simplified model of silica diagenesis, Equation 1.3 incorporates the main properties and variables of the early diagenetic system that affect the benthic fluxes of dissolved silica diffused from marine sediments back to the seawater.

The fraction of the opaline rain flux that reaches the water-sediment interface and that is neither dissolved nor diffused back to the water column is then buried within the sediment. This burial flux of biogenic silica is estimated using the mass accumulation equation (after Rabouille et al., 1997; Oehler, 2014):

$$BSi_{acc} = M_{opal}\omega\left(1-\phi\right)\rho_b \qquad (1.4)$$

where BSi_{acc} is the accumulation rate of biogenic silica within the sediment (in kg m^{-2} yr^{-1}), M_{opal} is the amount of biogenic silica (in volume %), ω is sedimentation rate (in m yr^{-1}), Φ is the sediment porosity (in %), and ρ_b is the sediment density (kg m^{-3}).

The rain rate of biogenic silica arriving at the seabed can then be calculated using the mass balance equation for silica (e.g., Rabouille et al., 1997; Ragueneau et al., 2009; Oehler, 2014):

$$BSi_{rain} = J_0 + BSi_{acc} \quad (1.5)$$

where BSi_{rain} is the rain rate of biogenic silica reaching the seafloor (in mol m^{-2} yr^{-1}), J_0 is the diffusive flux of silicic acid at water-sediment interface (in mol m^{-2} yr^{-1}), and BSi_{acc} is the accumulation rate of opal in the sediment (for Equation 1.5, the accumulated biogenic silica is converted from kg m^{-2} yr^{-1} into mol m^{-2} yr^{-1}).

6.5 Results

6.5.1 ODP-derived dataset

To calculate opal dissolution rates as well as benthic and burial fluxes, a dataset was assembled for the 22 study sites (Table 6.2). Sites were selected at which opal-A to opal-CT diagenesis takes place within the Neogene host sediments and for which sediment composition, bottom-water temperatures, pore-water silicic acid concentrations, and the results of sediment porosity and density measurements have been reported. The lithology of the sediment unit accommodating the biogenic silica within the uppermost benthic layers was categorised into two groups: detrital and carbonate. Almost 70% of the benthic sediment layers are hosted by detrital lithologies; the others hosted by biogenic carbonate.

Modifying the ODP approach for partitioning the sediment components (Mazzullo and Graham, 1988), sediment sample composition was divided into three fractions: biogenic opal (consisting of diatoms, radiolarians, silicoflagellates, and sponge spicules), detrital material (composed mainly of aluminosilicates (especially clays),

Table 6.2. Dataset assembled from the ODP data sources for the uppermost sediment of the 22 study sites. No. = the identification number of the ODP sites presented in Figure 6.1, M_{opal} = biogenic silica content of the uppermost sediment layer, T = present-day *in situ* bottom-water temperature, C_{bw} = bottom-water concentration of silicic acid, C_{sat} = asymptotic pore-water concentration of silicic acid, Φ = porosity of the uppermost sediment layer, ρ_b = grain density of the uppermost sediment layer, D_s = diffusion coefficient of sediment, and ω = sedimentation rate of the lithologic unit hosting the uppermost sediment layer. With the exception of C_{bw} values for Sites 794 through 799 that were extracted from Sarmiento et al. (2007), all other values in the table were obtained from the ODP.

No.	Site	Host [a] lithology	M_{opal}, %	Detrital, [b] %	Carbonate, [b] %	T, K	C_{bw}, µM	C_{sat}, µM	Φ, %	ρ_b, kg m^{-3}	$D_s \times 10^{-10}$, [c] m^2 s^{-1}	$\omega \times 10^{-5}$, m yr^{-1}
1	794	Detrital	15	84	0	273.36	70	440	85	2660	3.97	3.5
2	795	Detrital	15	83	0	273.35	70	615	93	2550	4.76	4.8
3	796	Detrital	7	91	0	273.15	70	740	77	2500	3.26	7.4
4	797	Detrital	10	89	0	273.35	70	540	81	2620	3.61	4.6
5	798	Detrital	17	75	7	274.55	60	620	77	2360	3.26	12.2
6	799	Detrital	29	65	3	273.29	70	537	88	2700	4.26	7.1
9	1016	Detrital	20	69	9	274.45	170	804	80	2770	3.52	5.3
10	1022	Detrital	5	83	10	275.05	160	702	65	2750	2.32	10.1
11	1095	Detrital	10	88	0	273.34	140	380	74	2730	3.01	2.2
12	1149	Detrital	21	76	2	274.21	190	559	81	2680	3.61	3.4
13	1150	Detrital	65	32	2	275.29	140	550	83	2420	3.79	20.5
14	1151	Detrital	33	63	3	275.26	140	500	77	2700	3.26	7.2
15	1165	Detrital	71	20	8	272.85	140	522	75	2700	3.09	1.5
16	1175	Detrital	15	74	10	274.77	140	556	67	2640	2.47	52
18	1208	Detrital	15	53	30	274.3	160	726	80	2670	3.52	4.2
7	846	Carbonate	39	5	55	274.96	160	892	84	2490	3.88	4
8	847	Carbonate	27	6	65	274.95	160	901	85	2700	3.97	3.2
17	1207	Carbonate	17	29	53	274.4	160	584	73	2690	2.93	1.4
19	1211	Carbonate	14	20	64	274.2	160	540	66	2690	2.4	0.9
20	1212	Carbonate	10	26	63	274.25	160	552	70	2710	2.7	1.4
21	1225	Carbonate	32	1	66	274.55	160	625	78	2700	3.35	8.9
22	1226	Carbonate	51	0	49	274.85	160	772	84	2580	3.88	4

[a] Lithological composition of the sediment hosting biogenic silica.

[b] Detrital (in percent of total volume) and biogenic carbonate (in percent of total volume) components of the uppermost sediment layer.

[c] Diffusion coefficient of sediment determined using equation $D_s = \Phi^2 \times D$, where Φ is the porosity value (derived from the ODP database), and D (5.5×10^{-10} m^2 s^{-1}; Wollast and Garrels, 1971; Rickert, 2000) is the free-solution molecular diffusion coefficient for silicic acid.

detrital quartz, oxides, volcanic ash, and volcanic glass), and biogenic carbonate (commonly calcareous nannofossils and foraminifers). When combined with accessory particles (organic debris, plant debris, and accessory minerals), the total is 100% for solid sediment volume. The sediments exhibit a wide compositional range. Biogenic silica content varies from 5 to 71%, detrital from 0 to 91%, and biogenic carbonate from 0 to 66%. The obtained values for accessory particles are not provided (Table 6.2). Given the research aims, the lithologic composition of the sites was divided into two categories; detrital and carbonate. On this basis, the detrital-dominated sites having a mean of 70% detrital matter contain on average 23% biogenic silica and only 5% carbonate. Conversely, the carbonate-dominant sites having a mean carbonate mineral content of 60% include an average of 12% detrital material and 27% opal. The highest contribution of biogenic opal to the sediment composition is reported from the detrital-based Site 1165 in the Southern Ocean. This site is situated at a sub-polar latitude beneath a major upwelling zone where there are high rates of opal rain. Relatively-lower rates of detrital particle rain account for high concentration of solid opaline silica in the surficial sediments (modified after Rashid, 1985; Libes, 1992). The highest detrital matter content is reported from Sites 796 and 797 in the Sea of Japan and Yamato Basin, respectively, where clay particles are the principal constituent of detrital sediment, formed through the chemical alteration of either windblown volcanic ash or volcanic glass on the seafloor, in addition to products of continental weathering from the source region. The highest biogenic carbonate content in the sediments is reported from Site 1225 in the Eastern Pacific Rise where nannofossil oozes alternate with layers rich in

diatoms and radiolarians.

The present-day temperature at the water-sediment interface for the investigated ODP sites varies from 272.85 to 275.29 K. The maximum temperature was recorded in the deep-sea terrace of the Japan Trench (Site 1150), where heat flow is anomalously high, averaging 60–70 mW/m^2, appreciably higher than typical heat flow values for seafloors aged 135 Ma. The probable cause of the higher bottom-water temperatures at this site is an efficient vertical heat transport by hydrothermal circulation within a permeable layer in the oceanic crust, gradually developed by fracturing due to plate bending (Yamano et al., 2014). The lowest temperature was recorded in diatom ooze to diatom clay sediments of Prydz Bay in the Antarctic.

The bottom-water silicic acid concentrations vary from 60 to 190 μM, with the maximum values observed in the uppermost sediments of the Nadezhda Basin in the northern Pacific Ocean. Minimum values are found in the Sea of Japan. The asymptotic silicic acid concentrations of sediments range from 380 to ca. 900 μM. The highest values are observed in diatomaceous nannofossil oozes of the Galapagos Islands in the equatorial Pacific Ocean, the lowest in the diatom-bearing fine-grained detrital sediments of the Antarctic Peninsula. However, even within the same oceanic region the asymptotic concentrations of silica can vary widely. For instance, in the Sea of Japan, concentrations differ by as much as 300 μM.

Porosity and sediment grain densities vary between 65 and 93% and 2360 to 2770 kg

m^{-3}, respectively. The highest benthic porosity is observed in the surficial silty clay sediments of the Japan Sea that contain subordinate diatom clay and diatom ooze. Grain density is highest in the diatomaceous ooze containing clay, diatom clay, diatom ooze, and diatom nannofossil ooze from the western Point Conception in California.

The sediment diffusion coefficient (Table 6.2), corrected for tortuosity using the ODP-reported porosity values, varies from 2.32×10^{-10} to 4.76×10^{-10} m^2 s^{-1}, with the peak value associated with the silty clay sediments of Site 795 in the Sea of Japan. The estimated sedimentation rates range between 0.9×10^{-5} and 20.5×10^{-5} m yr^{-1}, with the highest rates observed for the diatom ooze and clay deposits in Japan Trench. The lowest rates are found for the nannofossil clay and ooze from the Southern High of Shatsky Rise in northern Pacific (Sites 1211 and 1212).

6.6 Discussion

6.6.1 Model parameters: Calibration

One of the problems in the modelling of the early diagenesis of silica is the kinetic coefficient *k* of opal dissolution that is poorly constrained and commonly used as a fitting parameter in the diagenetic models (Dixit and Van Cappellen, 2003). The kinetic coefficients obtained through fitting of pore-water profiles vary greatly between different sediments (e.g., Schink et al., 1975). This is usually due to differences in temperature and the mineralogical nature of the sediments. To limit such a marked variability, the kinetic rate constant has been adjusted separately for

each studied ODP site using the site-specific bottom-water temperatures, a common activation energy of approximately 50 KJ mol^{-1} (50000 J mol^{-1}) for the dissolution of biogenic silica (following Dove and Rimstidt, 1994; Van Cappellen and Qiu, 1997b) and a first-order pre-exponential factor of ~30 s^{-1}. The linear variability of adjusted kinetic coefficient values due to differences in modern bottom-water temperatures (Fig. 6.2) deviates from the general trend of an exponential relationship with temperature for the solubility of silica. This is related to the narrow range of low seafloor temperatures (272.85–275.29 K), the presence of detrital matter in most sediments (this puts a constraint on the dissolution kinetics of opal, according to Dixit and Van Cappellen, 2003), and a common activation energy set for dissolution of opal within the benthic layer of investigated sites.

Observed variations in the asymptotic concentrations C_{sat} of silicic acid across the study sites poses another challenge for modelling the early diagenesis of silica. Despite temperature differences across the water-sediment interface and large variations in the asymptotic concentrations of dissolved silica, even where the lithologic composition of biosiliceous sediments is very similar, the relationship between C_{sat} and bottom-water temperature (T) remains robust across the range of deep-sea environments, especially across the carbonate-hosted settings included in this study (Fig. 6.3). This relationship was therefore used to calibrate the C_{sat} values against sediment temperature when calculating the dissolution rate and benthic fluxes of silica through Equations 1.1 and 1.3, respectively.

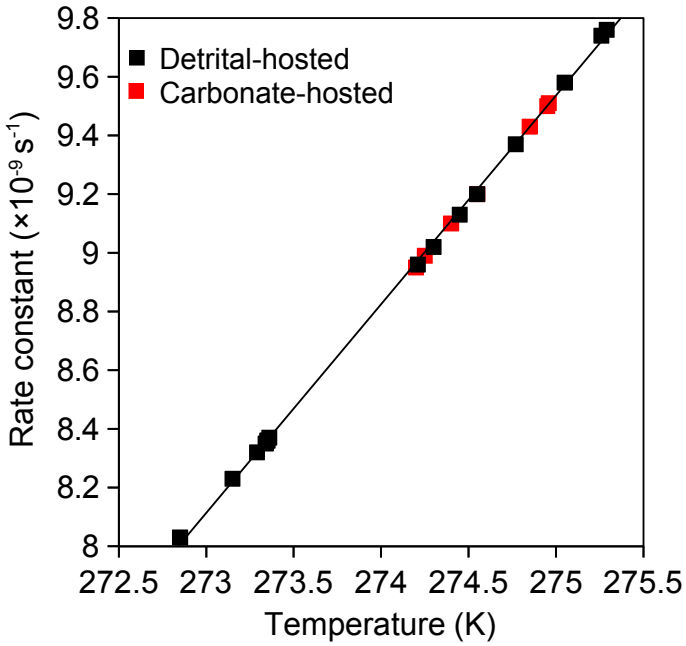


Figure 6.2. The first-order variability of dissolution rate coefficient with bottom-water temperature at the detrital- and carbonate-hosted 22 selected ODP sites. The rate constant values were calculated using the Arrhenius' (1889) equation.

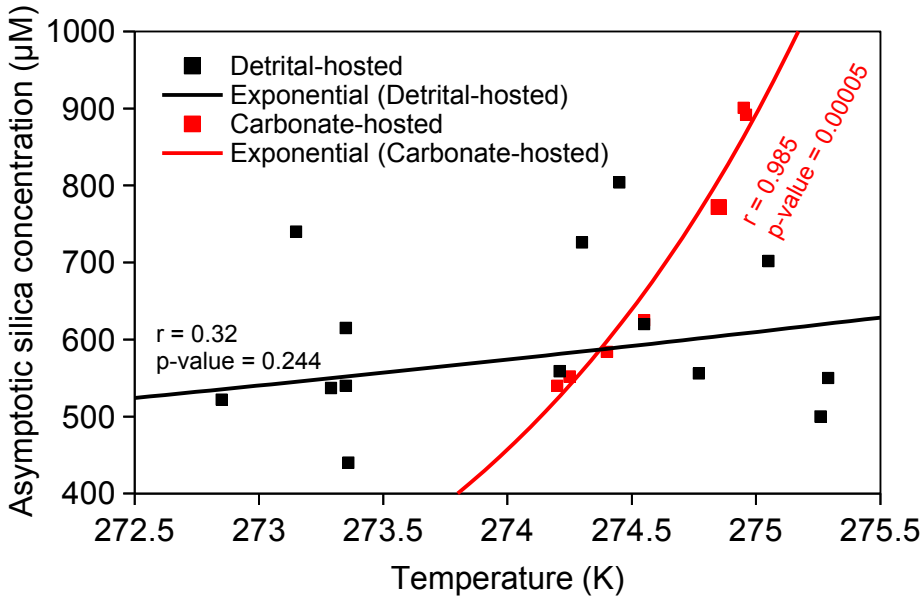


Figure 6.3. Asymptotic silicic acid concentration as a function of present-day temperature of the clay- and carbonate-based surface sediments. The p-value (< 0.05, according to Noymer, 2008) shows the relationship between the data points for carbonate sediments is more significant than that for detrital sediments.

Empirical equations relating C_{sat} to the T values in clay- and carbonate-hosted sites fit through the data points (representing the regression lines in Figure 6.3) are:

$C_{sat} = 3.607 \times 10^{-5} e^{0.0605T}$ $R^2 = 0.1$, for detrital-hosted sediments, and

$C_{sat} = 1.101 \times 10^{-77} e^{0.669T}$ $R^2 = 0.97$, for carbonate-hosted sediments

where C_{sat} is expressed in μM.

The exponential best fit overpredicted the ODP-reported asymptotic concentrations of silicic acid in the clayey sediments of Yamato Basin by as much as 9 μM. The best fit for carbonate-hosted sediments predicted very well (only 0.5 μM overprediction) the concentrations measured by the ODP for nannofossil oozes from the Northern High of Shatsky Rise in the northern Pacific Ocean.

6.6.2 Dissolution rate and benthic efflux: Empirical models

Dissolution rates for biogenic opal and the benthic fluxes of produced dissolved silica were predicted through the diagenetic equations 1.1 and 1.3, respectively. Values of solid opal content, porosity, density, and the diffusion coefficient of the uppermost sediment layer as well as the bottom-water and asymptotic concentrations for silicic acid were taken from Table 6.2. The asymptotic concentrations from Table 6.2 were calibrated based on empirical relationships defined in Figure 6.3, and the values of site-specific temperature-dependent kinetic rate constants were based on the Arrhenius Law.

Two different scenarios were used to calculate the dissolution rate and benthic efflux of biogenic silica. In the first scenario, the normalised asymptotic silicic acid concentration (C^*_{sat}) was kept constant and values were set as equal to the estimated peak amounts within the uppermost sediments of Sites 1150 and 846 for clay and carbonate host sediments, respectively. This scenario thus assumes that the thermodynamic properties of sedimentary biogenic silica are unaffected by the present-day temperature and composition of the sediment. As far as silica dissolution is concerned, bottom-water temperatures vary across the sites, and the sediments differ by their contents of detrital, carbonate, and biogenic opal (Table 6.2). In the second scenario, the asymptotic concentration depends on the temperature, implying that the increase in C^*_{sat} (and also k) with observed increases in bottom-water temperatures (Figs. 6.2 and 6.3) follows the common dependency observed through laboratory experiments for samples recovered from different basins (e.g., Rabouille et al., 1997; Van Cappellen and Qiu, 1997a). The second scenario best represents the effect of bottom-water temperature on the dissolution and efflux of silica during early diagenesis (Figs. 6.4 and 6.5). When thermodynamic and kinetic effects on the production of silicic acid are considered, a better association is observed between the predicted dissolution rate and diffusive flux and temperature. A slight increase in dissolution rates and benthic fluxes with temperature for detrital-based sediments—as compared with a significant increase in carbonate sites for both scenarios—strongly suggests the rate-limiting effects of the presence of detrital matter in the sediment. The incorporation of fine detritus into the surface lattice of biosiliceous tests significantly alters their solubility and reactivity. The transition from a linear to

an exponential increase of the dissolution rate and flux values in carbonate-based sediments when shifting from the first to the second scenario is because the variability in saturation levels of silica is involved in the early diagenetic reactions.

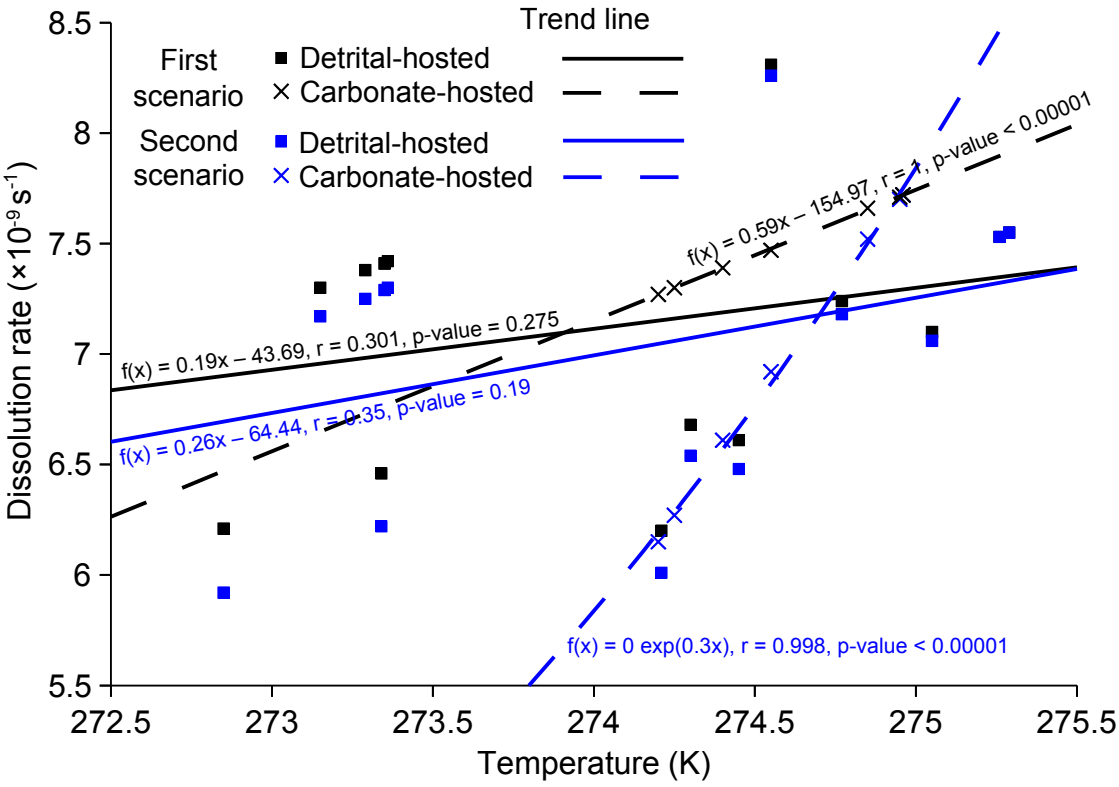


Figure 6.4. Calculated dissolution rate of sedimentary biogenic opal versus bottom-water temperature for the investigated sites. Note the difference between the rate variabilities with temperature, particularly for the carbonate-hosted sites, when shifting from the first (constant calibrated asymptotic concentration of silica) to the second scenario (asymptotic concentration varies with temperature). The p-values (< 0.05, Noymer, 2008) show the dissolution rate-temperature relation in carbonate-dominated sites for both scenarios is more significant than that for detrital-dominated sites. These values also indicate that the correlation between the data points is more significant in the second scenario than the first scenario.

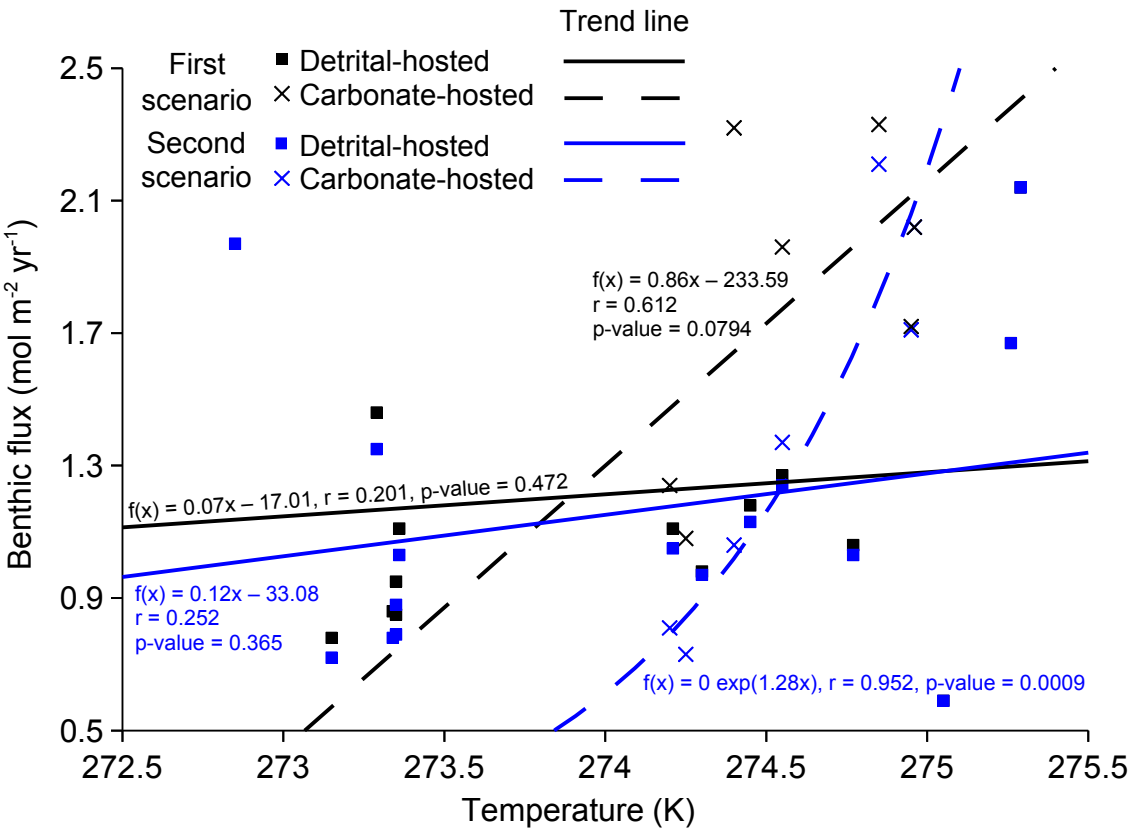


Figure 6.5. Calculated benthic flux of silicic acid versus bottom-water temperatures at the investigated ODP sites. Note the variability of flux, particularly for carbonate-hosted sites, when shifting from the first scenario (constant asymptotic concentration of silica) to the second scenario (site-specific asymptotic silica concentration). The p-values show the relationship between the data points for carbonate-dominated sites for both scenarios is statistically more significant than that for detrital sites. These values also show the correlation between the data points for the second scenario is more significant than that for the first scenario.

The dissolution rates and benthic fluxes predicted from the second scenario were recalculated separately for two host sediment types assuming average values for porosity, density, and bottom-water silica concentrations (average Φ, ρ_b, and C_{bw} in detrital-hosted sediments being 80%, 2600 kg m^{-3}, and 120 μM, respectively;

carbonate-hosted sediment had average values of 77%, 2650 kg m^{-3}, and 160 μM for Φ, ρ_b, and C_{bw}, respectively).

The dissolution rates calculated with the average parameter values in carbonate sites match perfectly those calculated with the site-specific values reported in Table 6.2 (Fig. 6.6). This occurs as bottom-water silicic acid concentrations remain constant among all the carbonate-based sites. However, for detrital-dominated sites, based on: 1) an observed shift from a weakly-positive correlation between dissolution rates and temperature to a strong linear correlation for the properties, and 2) recalculation of dissolution rates using average values produces rates that are generally higher than for site-specific values, a strong case can be made that variations in the pore-water concentrations of dissolved silica is an important source of variability for the dissolution rate of biogenic opal.

At detrital-hosted sites, the corresponding benthic fluxes predicted either using site-specific parameters or using average values exhibiting a slight increase with temperature (Fig. 6.7), highlight effects of detrital matter admixed with biogenic silica in confining the diffusive flux of silicic acid from the seafloor. The presence of sufficient fractions of detrital material (especially aluminosilicates) in the sediment causes a reduction in the rate of silicic acid production under the temperature-dependent dissolution kinetics of biogenic opal. This, in turn, affects the benthic flux. In such cases, variations in porosity, grain density, and bottom-water silicic acid concentration can only be a subordinate source of variability for benthic fluxes

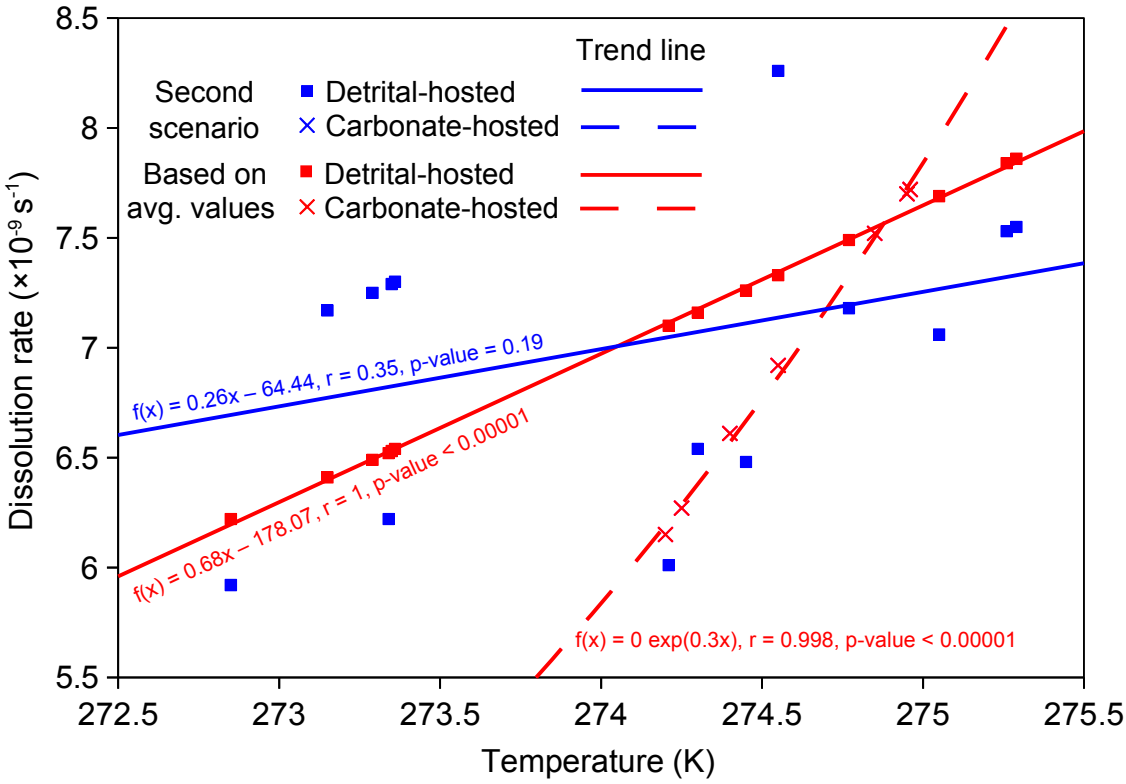


Figure 6.6. Dissolution rates of biogenic silica as a function of bottom-water temperature at the investigated sites. Note a transition from a weak positive correlation to a strong positive linear correlation at the clay-hosted sites when shifting from rate values calculated based on the second scenario (variable asymptotic concentration of silica with temperature) to those calculated using average parameter values (average bottom-water silica concentration). The dissolution rates at the carbonate-dominated sites do not change when shifting from a second scenario to those predicted based on average parameter values. The p-values (< 0.05, Noymer, 2008) show the relationship between the data points for carbonate-dominated sites is statistically more significant than that for detrital sites. These values also show the correlation between the data points determined based on average parameter values is more significant.

of silicic acid. Conversely, in carbonate sites, the close correspondence between the increasing effluxes of dissolved silica, predicted using either the average or site-

specific parameters, shows an exponential trend. This suggests a much more important role for bottom-water temperature in increasing silicic acid concentrations, thereby leading to the higher benthic fluxes. In addition, appearing directly from Equation 1.3, the amount of solid biogenic silica in the sediment also plays a key role in the evolution of silicic acid benthic flux as k and C_{sat} are dependent on the mineralogical composition of the sediment. An increase in the biogenic opal content of the sediment increases the access rate of pore water to the reactive surface areas of siliceous shells (even when the sediment contains detrital particles). This, in turn, helps these kinetic and thermodynamic parameters of biogenic opal to actively increase under the present-day bottom temperatures.

As inferred from Figures 6.6 and 6.7, the linear dependence on *in situ* temperatures of opal dissolution rate and associated diffusive fluxes in detrital-hosted benthic layers, while showing a substantial dependence on temperature in carbonate sites, are best represented by the values predicted using average parameter values. Unfortunately, no measured values of dissolution rates and benthic fluxes of silica are available for these study sites. Therefore, values obtained from other ocean regions were used for comparison. As seen in Figures 6.8 and 6.9, the measured parameters deviate markedly from the predicted values at the investigated ODP sites (except for a very few detrital-based sites clustered close to the modelled curves for benthic fluxes). This deviation is due to temperature differences and large discrepancies between the composition of the sediments sampled in this study and that of comparable works.

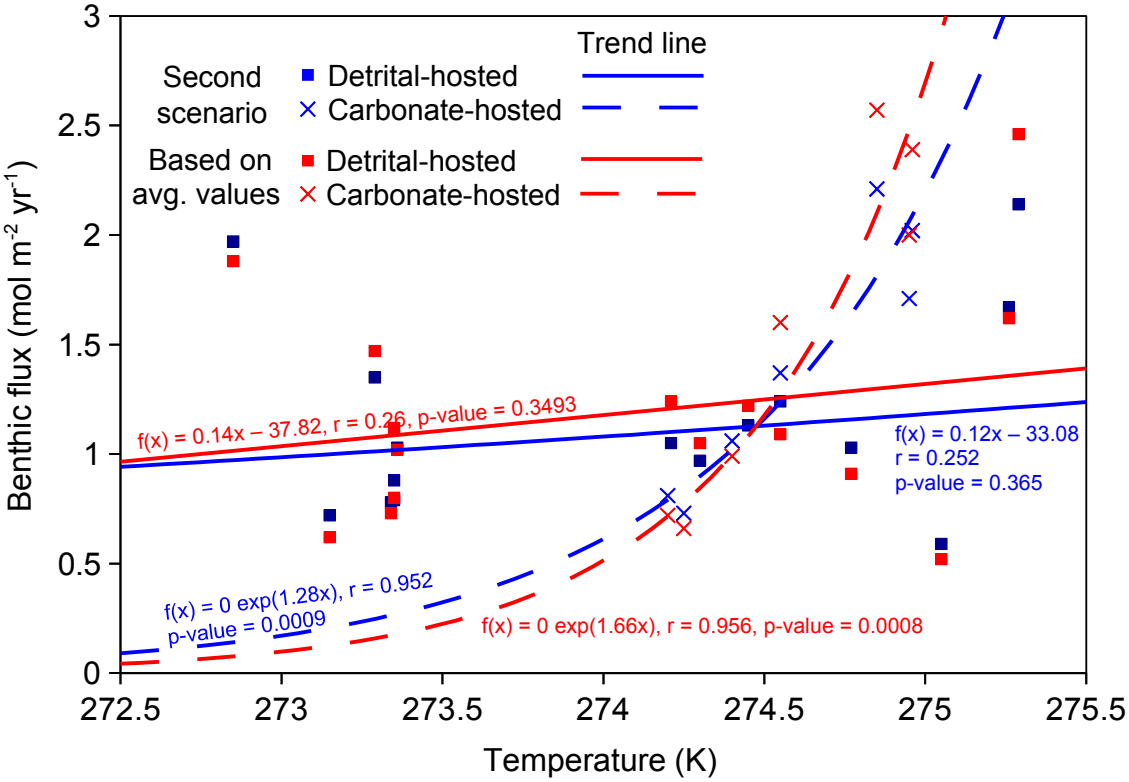


Figure 6.7. Benthic fluxes of dissolved silica as a function of bottom-water temperature at the studied sites. Note the closely-corresponding flux values for the detrital-hosted sites when shifting from the second scenario (site-specific parameter values) to values calculated based on average parameters (including average porosity, density, and bottom-water silica concentration). In carbonate-hosted sites, the flux values based on average parameters mimic those calculated using site-specific parameters. The p-values show the relationship between the data points for carbonate-dominated sites is more significant than that for detrital sites. The values also indicate that the correlation between the data points determined using average values is more significant than that between the data points from the second scenario.

6.6.3 Effects of pore-water undersaturation

The model-predicted increased dissolution rate of opal with bottom-water temperature in detrital-hosted sediments (Figs. 6.6 and 6.8) is consistent with the

variability of dissolution rate constant and fits well with the linear dissolution rate law. The pore-water undersaturation state with respect to the dissolving opal phase within the surface sediments could explain this linear pattern (Fig. 6.10). According to Van Cappellen and Qiu (1997b), only at very high levels of undersaturation (commonly > 0.85) do the dissolution kinetics of biogenic silica deviate from the linear rate law, which then increases in a non-linear manner with increasing undersaturation. In carbonate sites, conversely, very high degrees of pore-water undersaturation with biogenic silica account for the transition from a linear to non-linear exponential dissolution trend. Excluding the lithological composition of the host sediments, Williams and Crerar (1985) suggest temperature as a primary control mainly by influencing the biogenic opal saturation state in pore-water solution as well as increasing dissolved silica concentration at higher dissolution rates.

The slower increase in the opal dissolution rate with bottom-water temperature in detrital-hosted sediments relative to carbonate sediments can be attributed to the complementary active role of clays that slow the dissolution rate of biogenic opal, as they compete with silica dissolution for the available alkalinity from ocean water (Kastner et al., 1977). As a result, aluminosilicates present in the sediment (especially clay minerals) provide an additional sink for the alkalinity and the rate of opal dissolution is thereby reduced. They also react with dissolved silica to form coatings on diatom frustules (see Michalopoulos and Aller, 1995). The presence of an elevated detrital fraction in biosiliceous sediment can prevent pore waters from reaching equilibrium with biogenic silica under bottom-water temperatures because

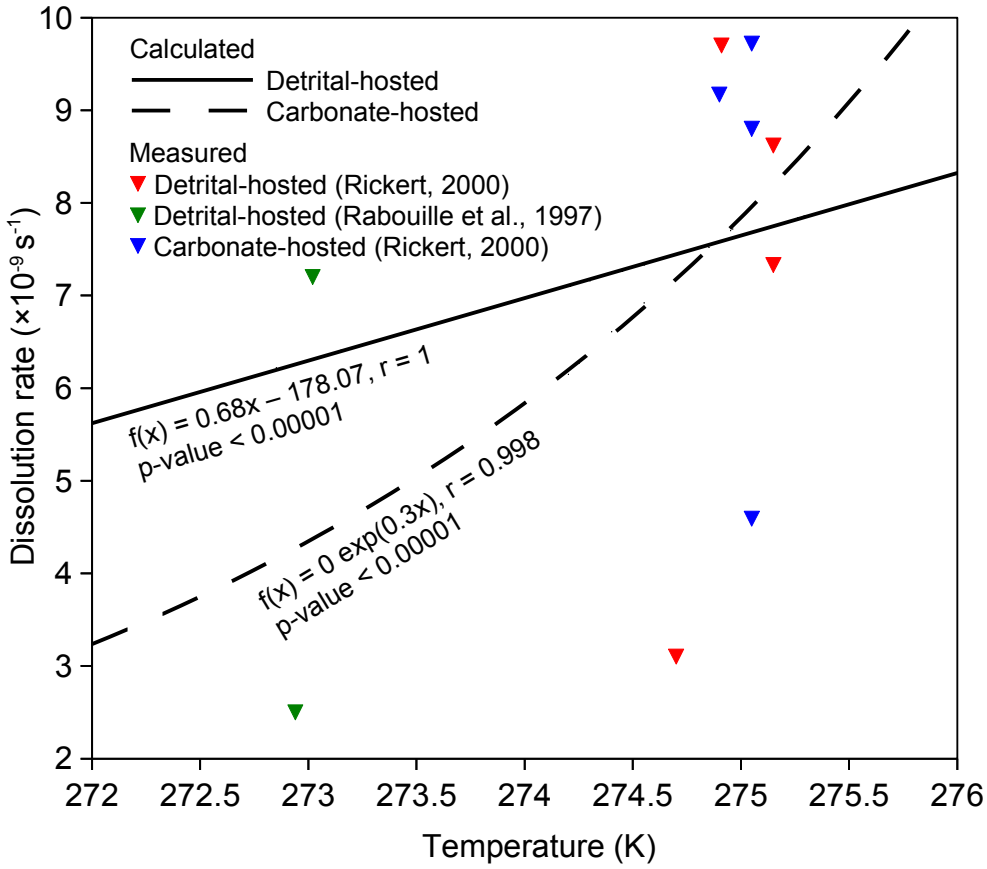


Figure 6.8. Dissolution rate of opal predicted using average parameter values versus bottom-water temperature at the studied ODP sites. The linear and exponential lines correspond to the model-predicted dissolution rates for detrital- and carbonate-dominated host lithologies, respectively. Also plotted are the dissolution rates determined for other ocean regions.

it confines the maximum levels of silicic acid (Dixit et al., 2001). Thus, pore waters remain undersaturated with respect to the *in situ* solubility of biogenic silica. However, in carbonate-hosted sediment, the dissolution of carbonate provides the required alkalinity for both silica dissolution and the formation of aluminosilicates. As such, the influence of clay minerals is strikingly reduced. This leads to the

rapidly-increasing saturation concentrations of silicic acid (although pore waters remain highly undersaturated with respect to opal) at lower seafloor temperatures in carbonate- versus detrital-based sediments (Fig. 6.3).

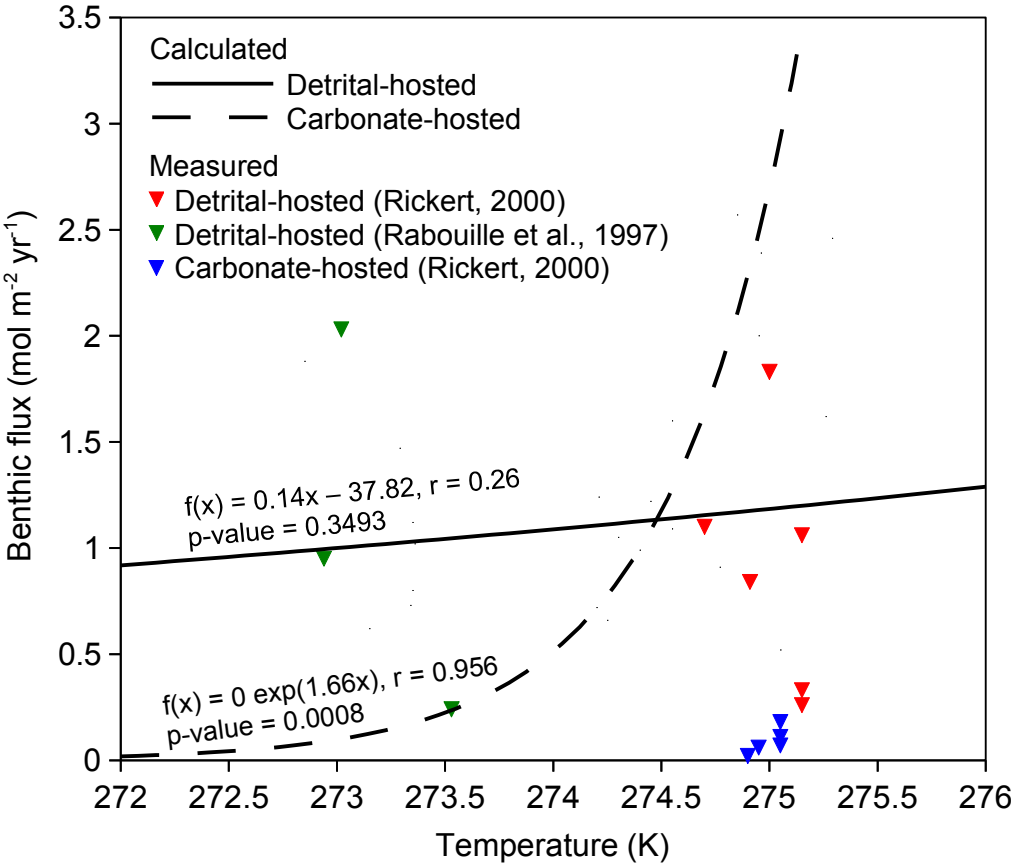


Figure 6.9. Benthic fluxes of silicic acid versus bottom-water temperature for the various studied ocean regions. The lines correspond to model-predicted fluxes, calculated using average porosity, density, and bottom-water silica concentrations, for clay- (solid line) and carbonate-hosted (dashed line) sites. Also shown are the benthic fluxes determined for other ocean basins.

Since both the dissolution rate and the benthic flux of silicic acid depend positively on the bottom-water temperatures (Figs. 6.4–6.9), a positive relationship is expected

between them. The model-predicted benthic fluxes confirm this expected relationship (Figs. 6.7 and 6.9). Compared to the slight increases in benthic fluxes with temperature at clay-dominated sites, the exponential trend of increased benthic fluxes with temperature for carbonate sites is related to the higher rates of silicic acid production in pore waters that are highly undersaturated with respect to biosilica.

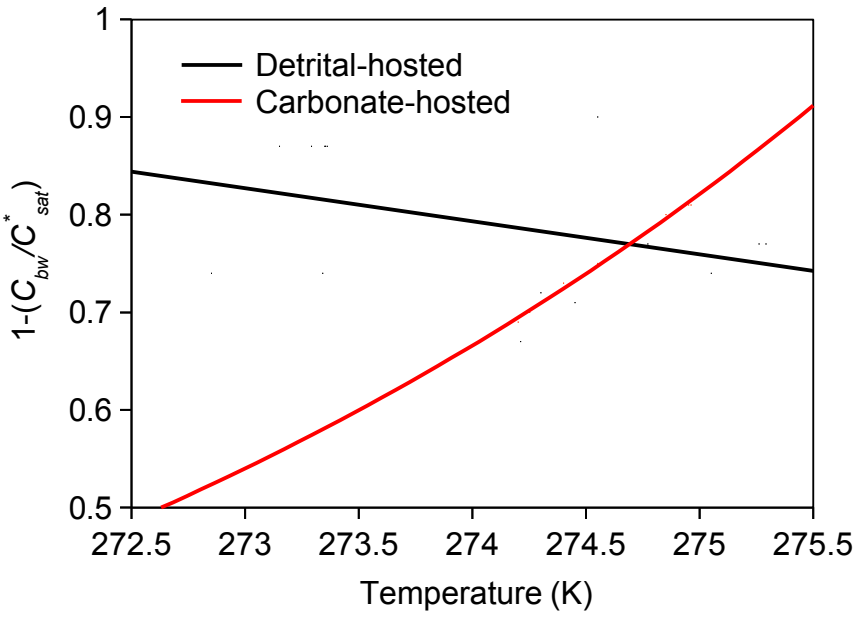


Figure 6.10. Degree of undersaturation with respect to opal versus bottom-water temperature at the studied ODP sites. Note the transition from a linear to non-linear trend at very high levels of undersaturation in carbonate sediments.

6.6.4 Biogenic silica burial efficiency

The fractions of biogenic silica recycled and buried in the sediment are clearly a function of the opal rain rate (Table 6.3 and Fig. 6.11), but this relationship is not straightforward. At low sedimentation rates, corresponding to lower biogenic silica rain rates in this study, a reduced fraction of the biogenic opal becomes buried due to

its prolonged exposure across the benthic layer. At sites having relatively-high sedimentation rates for opal, the burial of opal is maximised as the deposited opal particles remain at the water-sediment interface only for a short period of time. In addition, the detrital nature of the benthic layers that have the highest sedimentation rates among the studied ODP sites (Sites 1150 and 1175) significantly reduces the removal by dissolution of biosilica from sediment to the water column.

Table 6.3. Site-specific benthic flux, burial flux, and rain rate of biogenic opal calculated using the early diagenetic equations 1.3, 1.4, and 1.5, respectively. Also shown are the relative diffused and buried fluxes (in percentage) at each site. No. = the identification number of the ODP sites presented in Figure 6.1, J_0 = benthic flux of dissolved silica, BSi_{acc} = opal burial flux, and BSi_{rain} = opal rain rate.

No.	Host lithology	J_0, mol m^{-2} yr^{-1}	BSi_{acc}, kg m^{-2} yr^{-1}	BSi_{rain}, mol m^{-2} yr^{-1}	Recycled flux, %	Buried flux, %
1	Detrital	1.03	0.002	1.06	97.2	2.8
2	Detrital	0.79	0.001	0.81	97.5	2.5
3	Detrital	0.72	0.003	0.77	93.5	6.5
4	Detrital	0.88	0.002	0.91	96.7	3.3
5	Detrital	1.24	0.01	1.39	89.2	10.8
6	Detrital	1.35	0.007	1.46	92.5	7.5
9	Detrital	1.13	0.006	1.22	92.6	7.4
10	Detrital	0.59	0.005	0.67	88.1	11.9
11	Detrital	0.78	0.002	0.81	96.3	3.7
12	Detrital	1.05	0.004	1.11	94.6	5.4
13	Detrital	2.14	0.05	2.97	72	28
14	Detrital	1.67	0.01	1.82	91.8	8.2
15	Detrital	1.97	0.007	2.08	94.7	5.3
16	Detrital	1.03	0.07	2.19	47	53
18	Detrital	0.97	0.003	1.02	95.1	4.9
7	Carbonate	2.02	0.006	2.11	95.7	4.3
8	Carbonate	1.71	0.003	1.76	97.2	2.8
17	Carbonate	1.06	0.002	1.09	97.2	2.8
19	Carbonate	0.81	0.001	0.83	97.6	2.4
20	Carbonate	0.73	0.001	0.75	97.3	2.7
21	Carbonate	1.37	0.02	1.67	82	18
22	Carbonate	2.21	0.008	2.33	94.8	5.2

High sedimentation rates combined with the detrital-dominated composition of the host sediment thus causes biogenic silica to dissolve slowly near the water-sediment interface as it is removed from the dissolution zone due to comparatively-rapid burial (after Rabouille et al., 1997). This process increases the preservation rate of opal in the surface sediments and results in a rather elevated burial efficiency (the burial efficiency of opal in the sediments from this study reached elevated values up to 53%; Fig. 6.11).

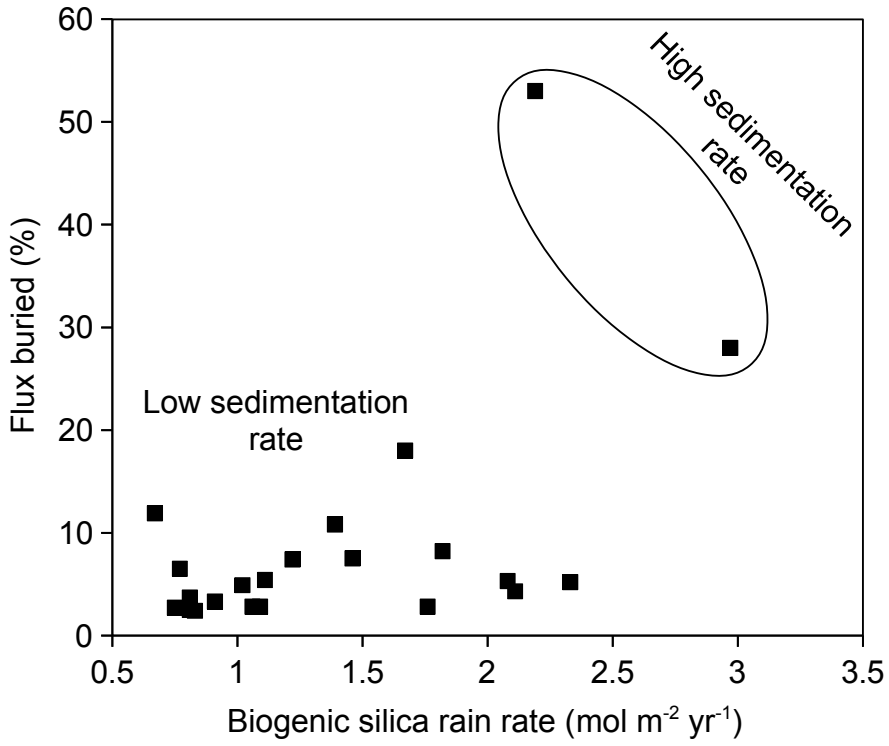


Figure 6.11. The fraction of solid silica buried as a function of the opal rain rate emphasising the role of sedimentation rate in the preservation of biogenic silica.

6.6.5 Controls on the precipitation of low temperature near-surface opal-CT

The transformation of biogenic to diagenetic opal (opal-CT) is the most significant process for biosiliceous particles preserved in the sediment. This transformation generally occurs during deeper burial when oversaturation is reached with respect to opal-CT within the pore space of the sediment. The transformation includes a series of thermochemical reactions, which are controlled by several drivers, though numerous studies have shown temperature and time to be the most efficient controls on the precipitation of opal-CT (e.g., Kastner et al., 1977; Kastner and Gieskes, 1983; Littke et al., 1991; Kuramoto et al., 1992; Nobes et al., 1992; Hesse and Schacht, 2011). According to many researchers (e.g., Kastner et al., 1977; Kastner and Gieskes, 1983; Williams et al., 1985; Hinman, 1998; Wrona et al., 2017), the dissolution rate of opal-A typically controls the overall rate of the transformation from opal-A to opal-CT under different chemical conditions. Kastner et al. (1977) and Kastner and Gieskes (1983) indicated that the dissolution rate of opal-A is the rate-controlling step that brings the dissolved silica in pore waters to values approaching the solubility value of disordered opal-CT. Hinman (1998) also certified the greater the silica concentration (under a higher opal-A dissolution rate) above saturation, the more rapidly the precipitation of opal-CT proceeds. Opal-A dissolution is the rate-determining step in silica diagenesis because the reactive surface area of opal-A obviously decreases under dissolution, and opal-CT enters the accumulation stage (Hinman, 1998).

Opal-CT precipitates following the dissolution of opal-A, when sediment

temperatures are generally between 35–50 °C (equal to burial depths of hundreds of metres) (e.g., Behl, 1999; DeMaster, 2003), although in some depositional settings this may be as low as 17–21 °C (e.g., Matheney and Knauth, 1993). Nevertheless, there are uncommon occurrences of early diagenetic young (0.4–4 Ma) opal-CT deposits (porcellanite and chert) at very low temperatures generally between 0 and 4 °C (Botz and Bohrmann, 1991) within near-surface sediments. The best known near-surface recordings of opal-CT chert growth have been reported from Antarctic marine sediments (Weaver and Wise, 1973, Bohrmann et al., 1990; Botz and Bohrmann, 1991).

Until now, there has only been speculation concerning the controls on precipitation of diagenetic opal-CT in these near-surface sediments. Model predictions of early diagenetic silica precipitation within the uppermost layers of ODP cores have attempted to clarify whether or not bottom-water and near-surface temperatures can account for the accumulation of opal-CT chert and porcellanite in the uppermost sediments. The transformation rate of opal-A to opal-CT has been best described using the Arrhenius' Law (Equation 1.2; e.g., Dralus et al., 2015; Wrona et al., 2017). As the Arrhenius plot of the early transformation rate of silica (represented by *ln k*) over a narrow range of temperature (0–3 °C) is based on 22 studied ODP surficial sediments (Fig. 6.12) having a global distribution, it should be applicable to other sites and ocean basin settings. Here, this linear model is used to predict the early diagenetic transformation of silica at the ODP Leg 120 Site 751 from the Kerguelen Plateau in the Antarctic region. Botz and Bohrmann (1991) report the

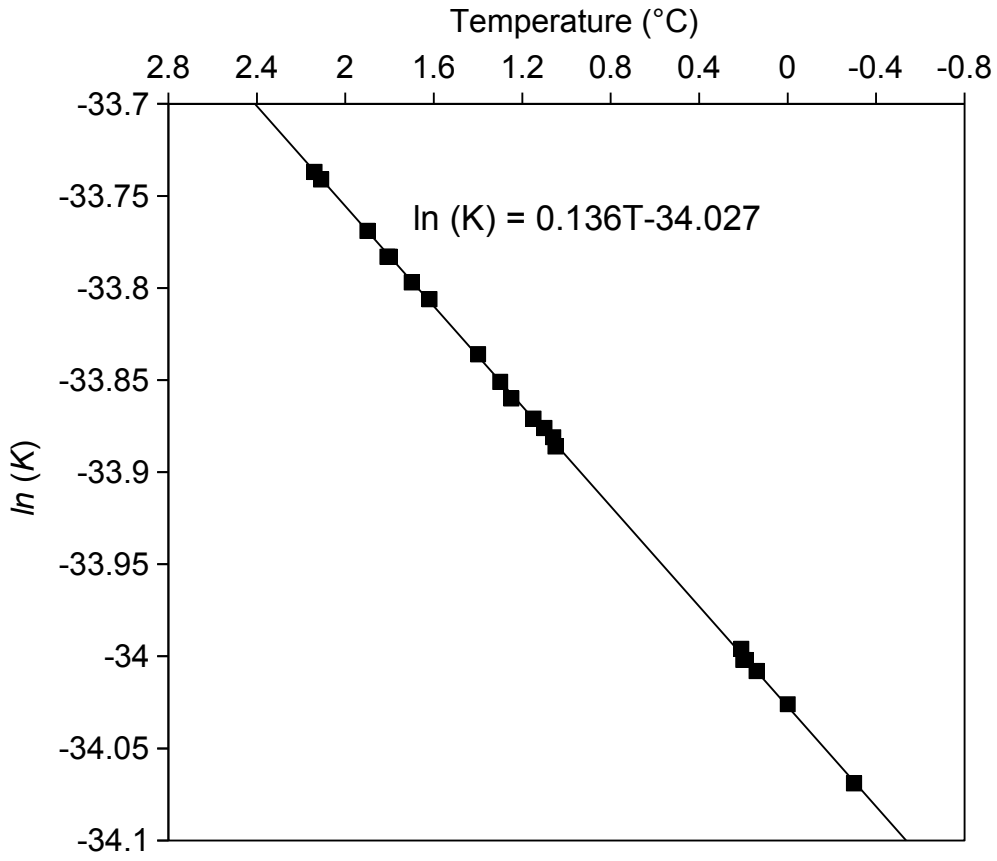


Figure 6.12. Linear transformation rate in the analysed surface sediments. The rate coefficient values were adjusted using an activation energy of 85000 J mol^{-1} (modified after Icenhower and Dove, 2000) to represent the early diagenetic re-precipitation process within the sediment.

occurrence of pure white porcellanite (almost completely composed of opal-CT) at the depth of ~14 mbsf for this site. This does not represent a transition zone from opal-A to opal-CT sediments as diatom ooze persists well below this horizon to a penetration depth of 166.2 mbsf. The linear regression for silica diagenesis, with the slope (activation energy) and intercept (pre-exponential factor) being 0.136 and ~-34.03, respectively, estimates a transformation rate constant of 1.7×10^{-15} s^{-1} for the

sediments at ~14 mbsf (equal to ~0.12 °C) for Site 751. Assuming an age of 3 Ma (Pliocene) for the porcellanites, the opal-A to opal-CT transformation at this site was predicted using the first-order translation of precipitation rate coefficient into a transformation ratio following:

$$1-e^{-kt}=1-e^{-(1.7\times10^{-15}\times3\times10^{6}\times365\times24\times3600)}=\sim0.15 \quad (1.6)$$

where k is the precipitation rate constant (in s^{-1}) and t is time (in s). The term e^{-kt} in Equation 1.6 is the relative amount of untransformed biogenic silica (according to the first-order rate law: $A/A_0 = e^{-kt}$, where A and A_0 are the remaining and initial amount of biogenic opal (in volume %), respectively).

The linear reaction rate law (Fig. 6.12 and Equation 1.6) slightly overpredicted the ODP-extracted transformation ratio of ~0.1 for Site 751 (Shipboard Scientific Party, 1989) by 0.05. The ODP-derived transformation ratio is set as equal to the opal-CT content of the sediment (in volume % or fraction) at a given depth over the total amount of opal-A and opal-CT at that depth (in volume % or fraction). At the water-sediment interface (a bottom-water temperature of -0.3 °C and Late Pleistocene in age), the linear regression model predicted quite well the transformation ratio equal to the measured value of 0, and at 3 mbsf (temperature = -0.21 °C) slightly overpredicted the measured opal-A to opal-CT transformation ratio of 0 by 0.03. The close correspondence between the predicted and measured values (r = 0.98; Fig. 6.13) validates this linear model for estimating the silica diagenesis transformation

rate and ratio in near-surface sediments for different ocean regions.

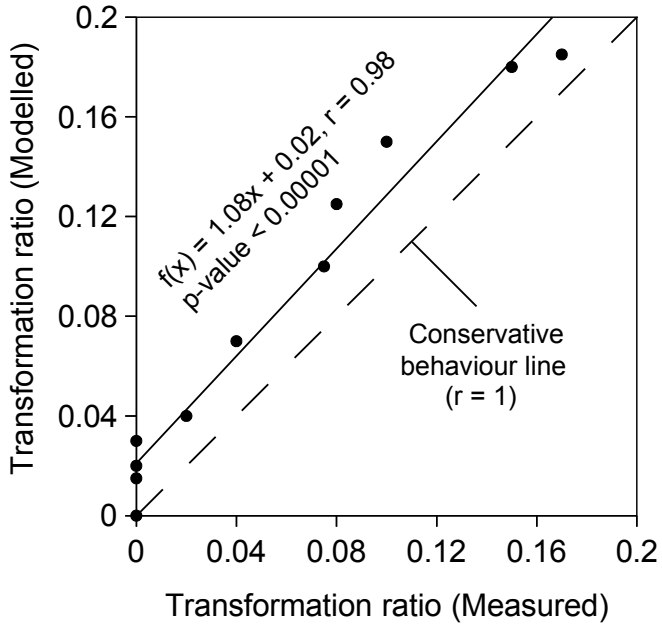


Figure 6.13. Comparison of model-predicted and measured transformation ratios of opal-A to opal-CT, ODP Site 751. The measured values were derived based on the data from Shipboard Scientific Party (1989).

The agreement between the depth variability of model-predicted transformation ratios observed at Site 751 and the temperature increase in the near-surface sediments initiated from the seafloor down-core along the site-specific geothermal gradient to the depth of opal-CT formation suggests that there may be controls from these low temperatures on accumulation of opal-CT porcellanite layers close to the seabed. In addition, the model-predicted temperature agrees well with both present-day temperatures measured at the depth of opal-CT porcellanite and the calculated

isotopic opal-CT formation temperature range of 0 to 1 °C based on $\delta^{18}O$ data (after Friedman and O'Neil, 1976), suggesting no deviation from the general trend of temperature change parallel to the geothermal gradient with the precipitation of opal-CT.

The accumulation of chert and porcellanite deposits containing diagenetic silica under such a low temperature condition is, however, in contrast with the established models of the later diagenetic precipitation of opal-CT within deep-sea sediments where the dominance of higher temperatures (generally between 18 and 56 °C, as determined by Pisciotto, 1981a) is a major requirement for the transformation. Furthermore, the widely-accepted inverse relationship between age and the formation temperature of opal-CT in deep-sea sediments, implying the occurrence of silica transformation at higher temperatures in young sediments and vice versa (e.g., Hein et al., 1978; Giles, 1997; Neagu, 2011), challenges the idea of low temperatures being a major control on the precipitation of young opal-CT sediments.

Botz and Bohrmann (1991) argue that temperatures, although important for the actual rate of opal-A to opal-CT transformation, are probably not the critical factor controlling the precipitation of opal-CT within the Antarctic deep-sea sediments. A likely explanation for such unusual formation of surficial opal-CT deposits in the Antarctic sediments may be drawn based on the relationship between solubility and surface area of biogenic silica. The tests of diatoms dominate in the sediments from Site 751 (the opal content of surficial layer being at least 80%; Shipboard Scientific

Party, 1989). Considering the surface area of biogenic silica is ranging between 19 and 350 m^2/g (Hurd, 1973), the steady-state solubility of skeletal silica in pore waters is likely to quickly approach the equilibrium solubility for this surface area (i.e., 120 ppm, according to Siever, 1957) . Dissolution is assumed to be rapid relative to nucleation and growth of other silica-containing phases (Williams et al., 1985). The likely role of low surface temperatures is to maintain the relative degree of undersaturation of pore water in respect to biogenic opal, while increasing silica solubility (modified after Ernst and Calvert, 1969; Stein and Kirkpatrick, 1976; Williams and Crerar, 1985). It is, however, assumed that time(age) plays a critical role, more important than temperature, in the context of near-surface opal-CT sediments in the Antarctic. Hurd (1983) showed that the solubility and specific area decrease with age in biogenic siliceous sediments. It is therefore possible that an elapsed time of near 4 Ma for the Antarctic sediments has aged opal-A to the point that further changes in particle size or specific surface area have produced minor effects on solubility (in accordance with Williams et al., 1985). This process could possibly speed up the rate of silica transformation, allowing opal-CT of a specific surface area within the range of the opal-A surface area to nucleate from the pore water supersaturated with respect to opal-CT earlier than it otherwise would.

It is also noteworthy to mention that despite the high rate of biogenic silica rain towards the seafloor (2.27 mol m^{-2} yr^{-1}), the burial efficiency of opal in Site 751 is low (~4.5%), comparable to values calculated for the ODP sites having low sedimentation rates included in this study (Fig. 6.11). This appears to be in contrast

with the considerable amounts of biogenic silica preserved in the sediments. A likely reason for this exceptional situation is the extremely-low rate of detrital material rain towards the seafloor (modified after Libes, 1992) and very low amounts of organic matter in the opaline sediments (Shipboard Scientific Party, 1989) that, in the presence of very high rain rates of opal, lead to a marked dilution of these components and great enrichment in biogenic silica even when the sedimentation rate is low.

6.7 Conclusions

Dissolution rates of deposited biogenic opal and the associated benthic flux of produced silicic acid in the deep sea are calculated for 22 ODP sites. Empirical diagenetic models specified for two sediment types that host biogenic silica—detrital and carbonate—are developed to predict variations in these parameters with present-day bottom-water temperatures. The most important variables in these models are the opal-A content of the benthic layer (especially for the benthic flux model), the temperature-dependent kinetic rate constant that describes the dissolution of biogenic silica, the asymptotic concentration of dissolved silica in pore water, and bottom-water temperature. Variability in the dissolution rate and the benthic flux in relation to present-day surface temperatures across the benthic layer is more pronounced when the functional association of temperature on asymptotic concentration and the dissolution kinetics is involved in the prediction of dissolution rate and benthic flux. A subtler increase in dissolution rates and benthic fluxes with increased temperature in detrital-hosted sediments (as opposed to the large increases in the dissolution rates

and benthic fluxes for carbonate-based sites) is due to the rate-limiting influence of detrital material as it is incorporated into the surface lattice of biosilica, markedly altering its solubility and reactivity. The mismatch between the model-predicted dissolution rates and benthic fluxes determined in this study and previous values obtained from other research is attributed to the temperature differences and large discrepancies in sediment composition between this study and the others. The transition from a linear to exponential increasing dissolution rate and benthic flux under low seafloor temperatures in carbonate- versus detrital-hosted sediments is related to the higher rates of silicic acid accumulation in the pore waters that are highly undersaturated in biogenic silica.

The linear expression of Arrhenius' Law for the potential early diagenetic transformation of biogenic to diagenetic silica suggests that there may be controls from bottom-water and near-surface temperatures on unusual accumulation of low temperature (0–4 °C) opal-CT porcellanite (and chert) in young sediments (< 4 Ma) near the seabed at some locations in the Antarctic. Variation in the model-calculated transformation ratios with depth in the surface deep-sea sediments from the Antarctic Site 751 agrees with the temperature increase from the seafloor down-core to the depth of opal-CT formation. However, the role of temperature in this situation is not as critical as previously thought as the established inverse temperature-time relationship in silica diagenesis, requiring the precipitation of opal-CT in young sediments at higher temperatures, denies a major control from temperature on precipitation of opal-CT in near-surface sediments. Here, the relationship between

solubility and surface area might be sufficient to explain the formation of opal-CT in the Antarctic Site 751, where time seems to play a critical role, more important than temperature. Since dissolution is assumed rapid relative to nucleation of other silica phases, the equilibrium solubility of biogenic silica in pore water is likely to be quickly approached. As the solubility and surface area both decrease with age in the sediments, it might be possible that a < 4 Ma time has been sufficient to reach opal-A the point that further decrease in surface area has produced negligible effects on solubility, which may allow for earlier precipitation of opal-CT from the pore water.

Chapter 7

Temperature-time relationships in biogenic silica diagenesis

7.1 Abstract

67 Ocean Drilling Program and Deep Sea Drilling Project sites were investigated to determine the relationship between temperature and time for silica diagenesis. The selected sites cover a variety of settings where the opal-A to opal-CT transition zone lies in Cenozoic sediments. This transition zone is a thin interval ranging in thickness from 10 to 40 m. The opal-A to opal-CT transition leads to an abrupt change in the sediment petrophysics. These changes are used to identify the diagenetic interval at the study sites. Controls on transition zone thickness are analysed and temperature was found to be the fundamental driver. This study also extends the reference time-temperature stability field for the onset of opal-CT precipitation more generally. Active silica diagenesis persists over a long period of time (> 35 Ma) at low temperatures (< 30 °C), within 3 Ma at moderate temperatures (35–55 °C), and much more rapidly at high temperatures (> 55 °C) regardless of burial depth. Geothermal gradients and sediment accumulation rates are the principal controls of the rate of silica diagenesis transformation. The reconstructed thermal evolution of sediments at the Sites 794 and 795 in the Japan Sea, which capture active transitions, demonstrates that the rapid increase in temperatures from the Late Miocene onwards occurred in response to high accumulation rates in the opal-A interval. The higher burial temperatures achieved for the opal-A sediment under higher sedimentation

rates and a steeper thermal gradient led to an earlier transition at Site 795 (~5 Ma) as compared to Site 794 (~8 Ma). Kinetic-based models are formulated to illustrate the time-temperature dependence of silica diagenesis. One of the main findings based on this model is that although opal-CT precipitation reaches its peak levels across the transition zone at 8 and 5 Ma after initial deposition of opal-A at Sites 794 and 795, respectively, the transformation is not completed until 14 Ma at Site 794 and ca. 9.5 Ma at Site 795 after initial sedimentation. Given the temperature and elapsed time, the model allows the transformation status of opal-containing sediments to be successfully predicted at any depth in these two sites.

Keywords: Biogenic silica diagenesis, Ocean Drilling Program, Deep Sea Drilling Project, Opal-A, Opal-CT

7.2 Introduction

Biogenic opal-A is diagenetically a metastable hydrous cryptocrystalline silica polymorph with sub-microscopic pores. It is usually produced by silica-secreting microorganisms, specifically diatoms, radiolaria, silicoflagellates, and siliceous sponges. With burial, opal-A dissolves and re-deposits as metastable opal-CT (cristobalite and tridymite) (e.g., Wise et al., 1972; Murata and Nakata, 1974; Kastner et al., 1977; Leeder, 1982; Williams and Crerar, 1985; Williams et al., 1985; Tada, 1991; Chaika and Williams, 2001; Weller and Behl, 2015). These diagenetic processes lead to the formation and development of an opal-A to opal-CT transition zone ($TZ_{A/CT}$) within the sediment record. This transition zone is often tens of metres

in thickness (see Chapters 4 and 5 of this thesis) across which opal-A and opal-CT co-exist, though mostly composed of opal-CT.

The sharp contrasts between the petrophysical properties of these two silica polymorphs (opal-A and opal-CT) strongly control the overall character of the sediment. For instance, sediments rich in opal-A are commonly identified by their high porosity. As such, the $TZ_{A/CT}$ is mostly characterised by a dramatic reduction in porosity (or increase in density) (e.g., after Nobes et al., 1992; Chaika, 1998; Chaika and Dvorkin, 2000; Davies and Cartwright, 2002; Davies et al., 2008; Meadows and Davies, 2010; Neagu, 2011; Weller and Behl, 2015). Silica-rich rocks abruptly lose porosity at these transitions due to sudden anomalous compaction under the *in situ* dissolution of opal-A, allowing for compactional collapse of the sediment matrix supporting the porous structure of siliceous frustules (after Isaacs, 1981; also see Chapters 4 and 5 of this thesis).

The dissolution-reprecipitation pathway involved in the diagenetic inversion from opal-A toward opal-CT (and eventually to quartz) is controlled by temperature, geological time (age), the surface area of biosilica, interstitial-water chemistry, and host lithology (e.g., Kastner et al., 1977; Hein et al., 1978; Williams and Crerar, 1985; Nobes et al., 1992). Increased temperature and geological time are thought to be the dominant drivers (e.g., Kuramoto et al., 1992; Nobes et al., 1992; Hesse and Schacht, 2011).

The interactions of temperature and time in silica diagenesis have been studied over the past five decades. The dependence of the silica diagenetic reactions on the thermal history of sediments (temperature vs time) was first stressed by Mizutani (1977). The current view is that the transformation of opal-A to opal-CT occurs at lower temperatures in older sediments, while higher temperatures are required in younger successions. Hein et al. (1978) estimated the time and temperature of this transformation reaction for moderately- to highly-biosiliceous Cenozoic deposits. They defined a reference temperature-time stability field for the formation of diagenetic silica.

Although the inverse relationship between temperature and time in ocean sediment settings is intuitive, we lack sufficient quantitative data to permit the prediction of silica diagenesis in response to both time and temperature. For example, Hein et al.'s (1978) stability field for the opal-A to opal-CT transformation was based only on six data points. Furthermore, noted mismatches between their reference diagram and data derived from comparable studies at ODP sites (e.g., Neagu, 2011) suggest a need to update this relationship and provide a more comprehensive model.

Predicting temperature-time relationships for silica diagenesis has implications for the reconstruction of the geothermal evolution of depositional basins accommodating the opal-A to opal-CT transformation. This also affects the determination of the likely diagenetic status of a $TZ_{A/CT}$, i.e., active versus fossilised transition zones. Silica diagenetic reactions occur over thermodynamically-active transitions, in

motion recently relative to the host lithology, at a recognisable rate (after Neagu et al., 2010). Conversely, the opal-A to opal-CT conversion has been stopped along the fossilised fronts; this is known from the stratigraphic relationships between the transition zone and host lithology (Davies and Cartwright, 2002).

High resolution experimental data demonstrate that the rate of silica phase change is controlled by the kinetic dissolution of biogenic silica in the sediment (Hinman, 1998), which is dependent primarily on temperature and time (e.g., after Kastner et al., 1977; Kastner and Gieskes, 1983; Williams et al., 1985; Dove and Rimstidt, 1994). It is also accepted that several driving factors of silica solubility control the overall rate of opal-A to opal-CT transformation. It is therefore possible, as a first-order estimation, to model the transformation of biosilica as a time-temperature function. This modelling approach is important for tracking the evolution of silica phase-change reactions and temperature over time in sediment record and to further constrain the thermal history of host basins.

The underlying aim of this study is to investigate the influence of thermal variations over time on buried sediment during silica diagenesis. The main goals of this study are threefold: (1) to modify the time-temperature domain of opal-CT formation, (2) to approximate the thermal history of silica diagenesis, and (3) to model the early burial transformation of amorphous silica to opal-CT.

To achieve these goals, my work mines the ODP and DSDP databases. The $TZ_{A/CT}$

has been drilled through by more than 100 ODP and DSDP boreholes, distributed worldwide. From these locations, I have selected 67 sites where the Cenozoic deposits accommodate the $TZ_{A/CT}$. For most of these sites, multiple parameters (e.g., petrophysical and thermal parameters of the sediment hosting the $TZ_{A/CT}$ as well as the $TZ_{A/CT}$ characteristics) are available to act as indicators of silica diagenesis. I use these datasets to identify the $TZ_{A/CT}$ within the sediment records and to derive the required information. Due to limited availability and quality of the reflection seismic profiles acquired by the ODP and DSDP legs, seismic recognition of the $TZ_{A/CT}$ is not considered by this study. As the temperature domain of silica diagenesis can be deduced based on the thickness and depth of the $TZ_{A/CT}$ (Neagu, 2011), this chapter reports and discusses, in a preliminary way, variations observed in terms of the thickness of the transition zone and its controlling factors.

7.3 Data and methods

Sixty-seven ODP and DSDP borehole sites, where the $TZ_{A/CT}$ was recovered in Pliocene to Palaeocene deep-sea core deposits, were selected for study (Fig. 7.1). Almost 3/4 of the sites were drilled along the continental margins of North and South America, western-northwestern Africa, and east-southeast Asia. The remaining sites are located mostly within Oceania and the Southern Ocean. Initial reports and related sources for the ODP and DSDP legs contain data regarding lithology, age, petrophysical properties, thickness, and thermal information for the intervals of interest ($TZ_{A/CT}$ and its under- and overlying sections). This information is compiled in Table 7.1. Methods used to assess those parameters assembled in Table 7.1 are

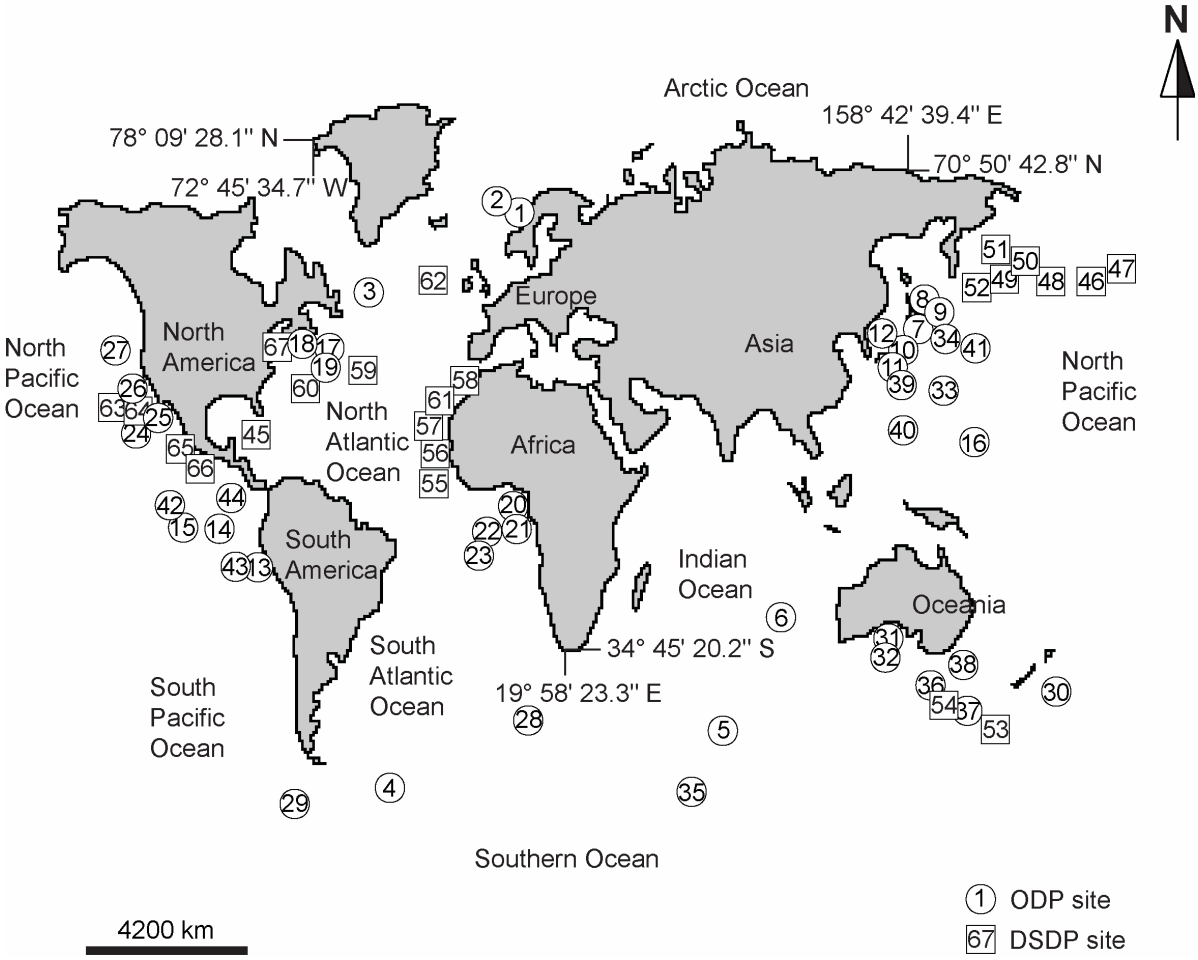


Figure 7.1. Location of the investigated borehole sites.

ODP sites (circled numbers): 1) 642/Leg 104, 2) 643/Leg 104, 3) 647/Leg 105, 4) 696/Leg 113, 5) 748/Leg 120, 6) 752/Leg 121, 7) 794/Leg 127, 8) 795/Leg 127, 9) 796/Leg 127, 10) 797/Leg 127, 11) 798/Leg 128, 12) 799/Leg 128, 13) 846/Leg 138, 14) 847/Leg 138, 15) 850/Leg 138, 16) 869/Leg 143, 17) 902/Leg 150, 18) 903/Leg 150, 19) 904/Leg 150, 20) 959/Leg 159, 21) 960/Leg 159, 22) 961/Leg 159, 23) 962/Leg 159, 24) 1010/Leg 167, 25) 1011/Leg 167, 26) 1016/Leg 167, 27) 1022/Leg 167, 28) 1090/Leg 177, 29) 1095/Leg 178, 30) 1122/Leg 181, 31) 1132/Leg 182, 32) 1133/Leg 182, 33) 1149/Leg 185, 34) 1150/Leg 186, 35) 1165/Leg 188, 36) 1170/Leg 189, 37) 1171/Leg 189, 38) 1172/Leg 189, 39) 1173/Leg 190, 40) 1201/Leg 195, 41) 1207/Leg 198, 42) 1225/Leg 201, 43) 1226/Leg 201, 44) 1256/Leg 206;
DSDP sites (numbers inside squares): 45) 98/Leg 11, 46) 184/Leg 19, 47) 185/Leg 19, 48) 188/Leg 19, 49) 189/Leg 19, 50) 190/Leg 19, 51) 191/Leg 19, 52) 192/Leg 19, 53) 277/Leg 29, 54) 280/Leg 29, 55) 366/Leg 41, 56) 367/Leg 41, 57) 368/Leg 41, 58) 370/Leg 41, 59) 385/Leg 43, 60) 387/Leg 43, 61) 397/Leg 47, 62) 405/Leg 48, 63) 467/Leg 63, 64) 469/Leg 63, 65) 471/Leg 63, 66) 473/Leg 63, 67) 603/Leg 93

described in the ODP technical notes (e.g., Mazzullo and Graham, 1988; Fisher and Becker, 1993; Blum, 1997).

Due to its association with abrupt petrophysical variations, determining the top and bottom of the $TZ_{A/CT}$ at each site was based on the approach of Neagu (2011). For example, according to Neagu (2011), the top of the $TZ_{A/CT}$ occurs where there is a great positive deflection of the bulk sediment density. This is followed by a negative deflection near the base of the $TZ_{A/CT}$ as observed on the sediment density curve (see the physical property profiles in Fig. 1.9 in Chapter 1, Fig. 4.2 in Chapter 4, and Fig. 5.2 in Chapter 5). The thickness of the $TZ_{A/CT}$ can thus be estimated via the density profile from the depth of the marked positive gradient between two adjacent values within a specific lithologic interval to the point where the subsequent negative density deflection ends.

Below, with reference to the principal function of age and *in situ* temperature of drilled sediments for the framework of present study, the methodology of ODP for measuring these parameters is briefly described.

7.3.1 Temperature estimates

The procedure to estimate downhole temperatures of ODP- and DSDP-drilled sediments follows Fisher and Becker (1993). Two types of ODP tools are available for measuring the downhole temperatures: (1) the APC (advanced piston corer) and (2) the WSTP (water-sampling temperature probe). Generally, the tools are used

Table 7.1. Parameters of the ODP and DSDP sites comprising the opal-A to opal-CT transition zone. The values were mostly extracted or derived from ODP and DSDP datasets. Values for some of the ODP sites were derived or modified from Neagu (2011). No. = the identification number of the sites presented in Figure 7.1, M_{opal} = mean biogenic silica in the total volume of the sediment column hosting the silica transition, Φ_A = mean porosity of the sediments rich in opal-A, Φ_{CT} = mean porosity of the sediments rich in opal-CT, $\Delta\Phi$ = difference between the mean porosity of opal-CT- and opal-A-rich sediments, ρ_A = mean bulk density of the sediments rich in opal-A, ρ_{CT} = mean bulk density of sediments rich in opal-CT, $\Delta\rho$ = difference between the mean bulk density of opal-CT- and opal-A-rich sediments, V_A = mean velocity in the sediments rich in opal-A, V_{CT} = mean velocity in the sediments rich in opal-CT, ΔV = difference between the mean velocity in opal-CT- and opal-A-rich sediments, R_A = mean resistivity of sediments rich in opal-A, R_{CT} = mean resistivity of sediments rich in opal-CT, ΔR = difference between the mean resistivity of opal-CT- and opal-A-rich sediments, G = present-day geothermal gradient of the sediment column hosting the silica diagenetic transition, Q = present-day heat flow of the sediment column hosting the silica transition zone, ω = mean sedimentation rate for the period immediately following the deposition of biogenic opal

No.	Leg	Site	Water depth, m	Dominant lithology	$TZ_{A/CT}$ depth, mbsf	$TZ_{A/CT}$ age, Ma	M_{opal}, %	Φ_A, %	Φ_{CT}, %	$\Delta\Phi$, %	ρ_A, g cm^{-3}	ρ_{CT}, g cm^{-3}	$\Delta\rho$, g cm^{-3}	V_A, km s^{-1}	V_{CT}, km s^{-1}	ΔV, km s^{-1}	R_A, Ω.m	R_{CT}, Ω.m	ΔR, Ω.m	$TZ_{A/CT}$ temperature, °C	$TZ_{A/CT}$* thickness, m	G, °C km^{-1}	Q, mW m^{-2}	ω, m Ma^{-1}
1	ODP 104	642	1292	Clay	275	23	35	78	62	16	1.45	1.8	0.35	1.7	1.85	0.15	–	–	–	11	15	40	90.4	18
2	ODP 104	643	2768	Clay	270	19.5	55	70	45	25	1.4	1.65	0.25	1.5	2	0.5	–	–	–	11	12	40	90.4	30
3	ODP 105	647	3869	Clay	240	28.5	45	70	55	15	1.45	1.8	0.35	1.6	1.65	0.05	–	–	–	8	20	35	–	20
4	ODP 113	696	661	Clay	525	11	60	70	45	25	1.45	2	0.55	1.65	1.85	0.2	–	–	–	27.6	25	52	63	38
5	ODP 120	748	1301	Carbonate	190	42.9	20	70	40	30	1.6	2.2	0.6	1.55	1.9	0.35	–	–	–	13.5	10	71.2	90	5.5
6	ODP 121	752	1086	Carbonate	290	60.4	20	50	30	20	1.85	2.1	0.25	2	2.45	0.45	–	–	–	14.5	15	33.9	46.1	12.5
7	ODP 127	794	2822	Clay	293.5	7.9	55	86	72	14	1.27	1.7	0.43	1.58	1.85	0.27	0.4	0.6	0.2	37.5	40	125	103	36
8	ODP 127	795	3310	Clay	326	5.3	40	80	60	20	1.75	1.85	0.1	1.55	1.85	0.3	–	–	–	43.2	40	132	113	61
9	ODP 127	796	2596	Clay	212.5	5.5	35	70	55	15	1.55	1.9	0.35	1.7	1.9	0.2	0.6	0.8	0.2	38	25	178	156	62
10	ODP 127	797	2876	Clay	303	8	45	85	65	20	1.4	1.8	0.4	1.8	2	0.2	0.4	0.6	0.2	36.9	30	121	101	49.5
11	ODP 128	798	911	Clay	451	3.4	35	65	55	10	1.7	1.85	0.15	2	2.3	0.3	0.17	0.17	0	38.8	30	83	98	121
12	ODP 128	799	2985	Clay	450	6.2	60	77	57	20	1.5	1.8	0.3	1.71	1.83	0.12	–	–	–	44.2	40	98	96	70
13	ODP 138	846	3387	Carbonate	370	12	40	70	60	10	1.55	1.7	0.15	1.75	1.85	0.1	0.55	0.8	0.25	16.2	20	39	37.8	15
14	ODP 138	847	3346	Carbonate	233	6.6	30	70	–	–	1.45	–	–	1.52	–	–	0.42	–	–	19.2	–	76	74.5	42
15	ODP 138	850	3798	Carbonate	215	8.5	45	75	65	10	1.45	1.55	0.1	1.55	1.65	0.1	0.6	0.65	0.05	3.2	15	7.8	8.4	64.5
16	ODP 143	869	4838	Carbonate	140	37.5	–	60	40	20	1.3	1.5	0.2	1.55	1.55	0	–	–	–	–	10	173	166.8	6.5
17	ODP 150	902	808	Clay	680	28.5	30	60	45	15	1.85	2.05	0.2	1.85	2	0.15	0.9	1	0.1	27	25	40	48	13
18	ODP 150	903	703	Clay	1050	25.5	25	65	45	20	1.7	1.9	0.2	1.8	1.9	0.1	–	–	–	42.2	40	40	–	12.5
19	ODP 150	904	577	Clay	525	31.5	20	60	50	10	1.7	1.95	0.25	1.85	2.2	0.35	1	1.5	0.5	21.2	15	40	52	12.5
20	ODP 159	959	2102	Carbonate	430	31.5	20	60	30	30	1.5	1.9	0.4	1.5	1.75	0.25	0.8	0.9	0.1	22	25	48	56.2	–
21	ODP 159	960	2060	Carbonate	140	38	10	65	40	25	1.7	1.9	0.2	1.5	1.75	0.25	0.8	0.9	0.1	8.1	30	48	52.8	–
22	ODP 159	961	3612	Carbonate	150	19.5	5	65	35	30	1.6	2.05	0.45	1.6	2.2	0.6	–	–	–	–	30	–	–	–
23	ODP 159	962	4649	Clay	55	19.5	15	70	40	30	1.4	1.8	0.4	1.55	–	–	0.2	0.25	0.05	5.8	25	15	18	10
24	ODP 167	1010	3690	Clay	180	13.1	60	73	67	6	1.5	1.7	0.2	–	–	–	–	–	–	23.4	15	122	118	15
25	ODP 167	1011	2021	Clay	205	7.5	30	65	62	3	1.62	1.64	0.02	–	–	–	0.75	–	–	24.8	15	108	111	22.5
26	ODP 167	1016	4162	Clay	282	7.2	50	75	65	10	1.4	1.65	0.25	–	–	–	0.5	0.6	0.1	30.9	–	105	88	30
27	ODP 167	1022	2325	Clay	360	8	10	65	58	7	1.55	1.75	0.2	–	–	–	0.55	0.8	0.25	33.6	–	88	84	–

Table 7.1. Continued.

28	ODP 177	1090	3710	Carbonate	290	35	40	83	77	6	1.6	–	–	–	–	–	–	–	2	15	8	7	30
29	ODP 178	1095	3863	Clay	490	6.5	20	57	45	12	1.75	1.9	0.15	1.7	1.9	0.2	0.65	0.7	0.05	16.4	20	33	–	110
30	ODP 181	1122	4432	Clay	585	15	40	52	–	–	1.85	2.05	0.2	2.3	2.5	0.2	–	–	–	–	20	–	–	20
31	ODP 182	1132	230	Carbonate	255	13.8	–	44	26	18	1.55	1.65	0.1	1.9	2.3	0.4	0.49	0.98	0.49	23.2	15	41.6	43.3	–
32	ODP 182	1133	1049	Carbonate	40	13.8	–	55	–	–	1.86	1.9	0.04	1.59	–	–	–	–	–	13.2	–	41.6	–	–
33	ODP 185	1149	5829	Clay	180	14	35	70	30	40	1.5	2	0.5	–	–	–	0.9	1.8	0.9	6.5	18	33	28.1	10
34	ODP 186	1150	2692	Clay	1050	8.3	35	65	55	10	1.55	1.7	0.15	1.8	2	0.2	1	1.4	0.4	32.3	25	28.9	20.1	70
35	ODP 188	1165	3549	Clay	600	19.5	20	60	42	18	1.75	2	0.25	1.7	1.85	0.15	0.7	0.9	0.2	19.2	15	32	51.4	13.5
36	ODP 189	1170	2716	Carbonate	475	37.5	20	60	50	10	1.65	1.8	0.15	1.7	1.9	0.2	–	–	–	27	40	52	56	10
37	ODP 189	1171	2159	Carbonate	375	42.9	30	65	45	20	1.4	1.7	0.3	1.6	1.9	0.3	0.6	2	1.4	26.3	35	62	68	8
38	ODP 189	1172	2633	Carbonate	500	44	30	60	48	12	1.55	1.75	0.2	1.85	1.9	0.05	1	1.15	0.15	25.7	30	46.6	55	18
39	ODP 190	1173	4802	Clay	344	3.5	40	65	51	14	1.6	1.8	0.2	1.7	1.8	0.1	0.3	0.55	0.25	60	35	170	180	52
40	ODP 195	1201	5721	Clay	25	4.5	–	85	55	30	1.25	1.7	0.45	1.62	2.2	0.58	–	–	–	4.8	15	125	98	3
41	ODP 198	1207	3112	Carbonate	150	16.5	25	60	55	5	1.9	2.18	0.28	1.5	1.7	0.2	0.45	0.5	0.05	–	20	–	–	5
42	ODP 201	1225	3772	Carbonate	275	13	50	80	70	10	1.45	1.55	0.1	1.52	1.55	0.03	0.55	0.65	0.1	6.3	15	17.4	15.5	43
43	ODP 201	1226	3297	Carbonate	370	13	45	78	61	17	1.55	1.7	0.15	1.75	1.8	0.05	0.55	0.75	0.2	22.9	20	57.2	48.7	16
44	ODP 206	1256	3645	Carbonate	175	12.5	35	81	68	13	1.3	1.45	0.15	1.55	1.62	0.07	0.35	0.38	0.03	27	10	146	113	27
45	DSDP 11	98	2769	Carbonate	165	51.9	25	65	60	5	1.55	1.8	0.25	1.92	1.92	0	–	–	–	–	–	–	–	6
46	DSDP 19	184	1910	Clay	600	5.3	80	65	–	–	1.5	2	0.5	1.8	2.2	0.4	–	–	–	51.2	–	82	74	–
47	DSDP 19	185	2110	Clay	640	5.3	65	60	–	–	1.6	1.75	0.15	1.63	2.02	0.39	–	–	–	35	–	50.4	42.7	–
48	DSDP 19	188	2649	Clay	550	4.5	75	70	–	–	1.35	1.8	0.45	1.6	2	0.4	–	–	–	–	–	–	–	–
49	DSDP 19	189	3437	Clay	540	4.5	20	55	–	–	1.64	2.05	0.41	1.63	2.2	0.57	–	–	–	53.7	–	95.8	–	–
50	DSDP 19	190	3875	Clay	610	5.3	40	60	–	–	1.5	–	–	1.6	–	–	–	–	–	–	–	–	–	–
51	DSDP 19	191	3854	Clay	520	3.1	25	55	–	–	1.75	2	0.25	1.75	2.05	0.3	–	–	–	–	–	–	–	–
52	DSDP 19	192	3014	Clay	600	8.5	60	60	–	–	1.55	1.9	0.35	1.5	1.7	0.2	–	–	–	–	–	–	–	–
53	DSDP 29	277	1214	Carbonate	246	38	10	85	78	7	1.28	1.52	0.24	–	–	–	–	–	–	–	–	–	–	13.5
54	DSDP 29	280	4176	Carbonate	160	33.9	45	85	–	–	1.05	–	–	–	–	–	–	–	–	–	–	–	–	39
55	DSDP 41	366	2853	Carbonate	520	42.9	35	54	34	20	–	–	–	1.9	2.3	0.4	–	–	–	–	35	–	–	19
56	DSDP 41	367	4758	Carbonate	330	42.9	20	57	42	15	–	–	–	1.6	1.71	0.11	–	–	–	–	30	–	–	6.5
57	DSDP 41	368	3366	Carbonate	355	42.9	15	64	52	12	1.65	1.8	0.15	1.7	2	0.3	–	–	–	–	35	–	–	–
58	DSDP 41	370	4214	Carbonate	425	36	10	49	33	16	–	–	–	1.84	2.14	0.3	–	–	–	–	35	–	–	8
59	DSDP 43	385	4936	Clay	165	51.9	30	82	60	22	1.42	1.65	0.23	1.54	1.74	0.2	–	–	–	–	15	–	–	27.5
60	DSDP 43	387	5117	Clay	225	42.9	20	68	41	27	1.6	1.85	0.25	1.66	1.9	0.24	–	–	–	–	20	–	–	26
61	DSDP 47	397	2900	Carbonate	700	13.8	20	57	40	17	1.7	2	0.3	1.55	1.8	0.25	–	–	–	–	15	–	–	50
62	DSDP 48	405	2958	Carbonate	265	51.9	10	65	50	15	1.45	1.65	0.2	–	1.8	–	0.8	1.1	0.3	–	15	–	–	74
63	DSDP 63	467	2128	Clay	550	8.5	50	65	35	30	1.6	1.95	0.35	1.65	2.2	0.55	–	–	–	39.2	20	63	–	87.5
64	DSDP 63	469	3790	Clay	225	13.8	50	–	42	–	1.6	1.89	0.29	1.5	2.2	0.7	–	–	–	–	–	–	–	20
65	DSDP 63	471	3101	Clay	155	11.6	55	–	30	–	1.5	1.82	0.32	1.64	1.99	0.35	–	0.3	–	22.5	–	132	119.1	20
66	DSDP 63	473	3249	Clay	181	8.5	15	63	40	23	1.51	1.73	0.22	1.56	1.98	0.42	–	–	–	13	10	64	56.2	30
67	DSDP 93	603	4633	Clay	950	36	20	54	34	20	1.85	2.1	0.25	1.7	2.1	0.4	–	–	–	41.7	10	41.8	–	35

* The thickness of the silica transition zone as estimated from the porosity depth profiles.

separately to measure sediment temperature at different depths during a coring sequence.

The *in situ* temperatures at the ODP sites were measured using the APC tool (Fig. 7.2A) designed to assess the sediment temperature as a piston core is taken. The two steel prongs at the base of the APC tool case fit into the borehole at the bottom of the annular cell in the cutting shoe of the piston corer. The instrument is fixed in the annular cell with the help of the prongs. The resistance temperature apparatus contained in one of the prongs is used to measure the sediment temperature. The wall thickness of the cutting shoe outside the annular cavity is about 1.5 cm, giving it a few minutes of time constant in the sediment. The APC was thus held in place for 15–20 minutes to obtain enough data for extrapolating the sediment *in situ* temperature.

The temperature of the sediment of the analysed DSDP boreholes was measured using the WSTP tool (sometimes referred to as the Barnes/Uyeda probe) (Fig. 7.2B). The WSTP, connected to the end of a core barrel, was lowered down the drill column and run on the coring line; thus requiring a break in coring (commonly 2 hours) to collect a fluid sample. The probe landed in the bottom-hole assembly, extending about 1 m into the sediment in front of the drill bit. As the fluid sample is driven into a sample cell by the difference between hydrostatic and atmospheric pressures, only one sampling effort was possible during each extension (deployment). The fluid was pulled into the WSTP through a series of filters and mounted near the tip of the

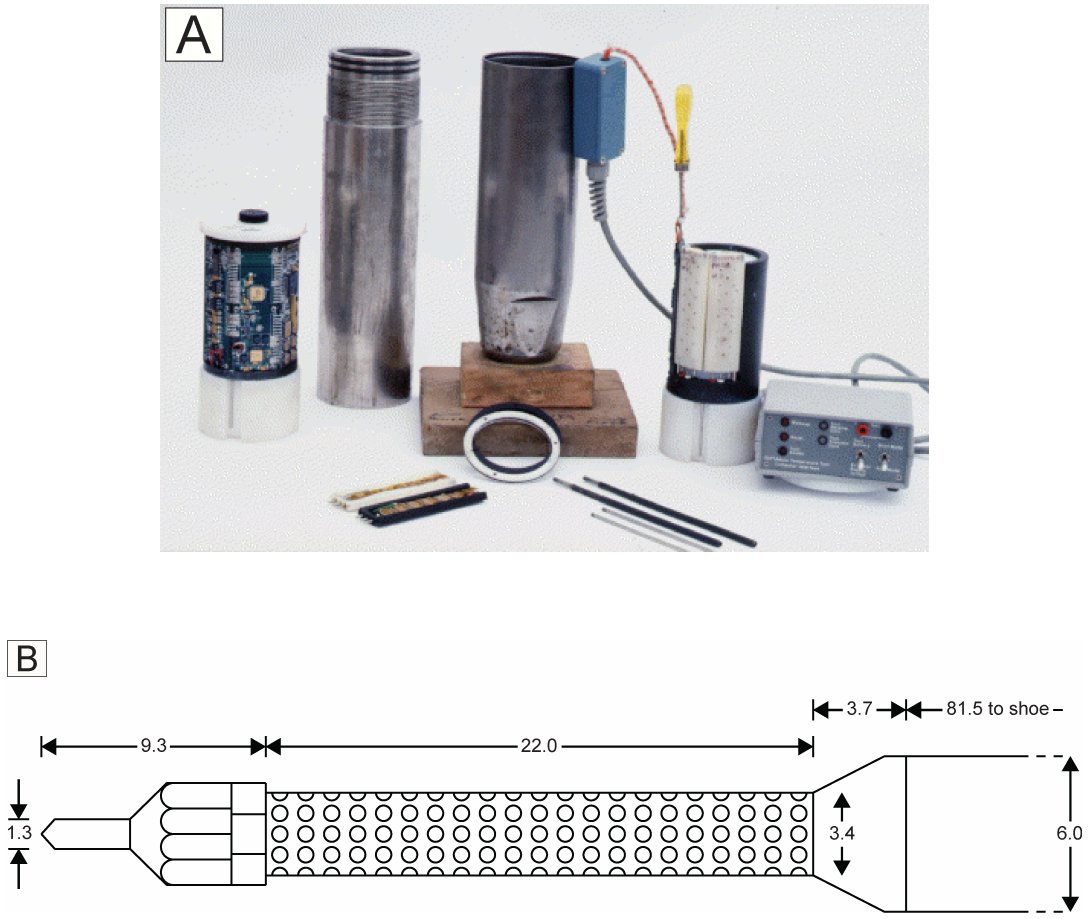


Figure 7.2. A) APC tool components (left to right background): APC tool on cylindrical holder, APC landing sub, APC coring shoe (with internal annular cavity), interface cable attached to another APC tool (turned to show battery packs), and interface box. (left to right in the foreground): battery packs, tool retaining rings, and extraction tools (photograph from Fisher and Becker, 1993); B) WSTP probe assembly for temperature measurement and fluid sampling. All dimensions in centimetres (redrawn and slightly modified from Fisher and Becker, 1993).

probe through the end of a sampling tube. The WSTP data logger continually sampled the resistance of the thermistors placed in the probe. The probe was then held in place for 15 minutes to gain enough data allowing for reliable extrapolation

to the sediment temperature.

7.3.2 Age determination

Sediments hosting the $TZ_{A/CT}$ were dated using biostratigraphic evidence from diatoms, radiolarians, calcareous nannofossils, and planktonic foraminifera. Combining the biostratigraphic patterns of these different microfossils provides a well constrained chronology for nearly all of the studied borehole sites. Based on the zonation scheme of Okada and Bukry (1980), calcareous nannofossils were often used to develop the biostratigraphic framework of sequences. Due to notable contrasts in abundance above and below the $TZ_{A/CT}$, diatom assemblages were specifically used at sites where sufficient biosilica was contained in the sediment. Sediment ages determined by these methods are available through open access to the DSDP and ODP databanks. The present study has relied on the numerical ages provided by these sources, and the numerical stratigraphic ages of the deep-sea sediments for each ODP and/or DSDP site involved in this project have been derived directly from its respective ODP and/or DSDP initial report. In this case, each initial report has used a different version of the geological timescale.

7.4 Results

7.4.1 Overview of the silica diagenesis transition zone

For the studied cores, the sub-seafloor depth of the $TZ_{A/CT}$ was identified based on the contrasting physical properties of the opal-A and opal-CT sediment units (Table 7.1). The depth of the $TZ_{A/CT}$ was generally 25 to 1050 mbsf, with the deepest transition

zones (1050 mbsf) hosted by clay-dominated sediments at the ODP Site 903 on the New Jersey continental slope (North America) and ODP Site 1150 from a deep-sea terrace of the Japan Trench. In detrital-rich basins, $TZ_{A/CT}$ depth varied mainly from 200 to 600 mbsf. In carbonate-dominated settings, the transition zone depth ranged chiefly from 150 to 500 mbsf (Fig. 7.3). Due to the small measurement intervals (e.g., 0.7–1.5 m for density stations and ~30 cm for the downhole logging tools, according to Blum, 1997; Neagu, 2011; Chapter 5), the thickness of the $TZ_{A/CT}$ was primarily determined using the profiles of the down-core physical properties (see Chapters 4 and 5). The various physical parameters mirror values of $TZ_{A/CT}$ thickness (Fig. 7.4). The present study assumes the porosity profile to be representative of the physical properties for determining the $TZ_{A/CT}$ thickness (Chapter 5). For all the studied ODP and DSDP sites $TZ_{A/CT}$ thickness was consistent across sites, ranging between 10 and 40 m (Table 7.1) with a mean value of ~23 m, despite having different dominant lithologies (Refer to Appendix VI for statistics related to $TZ_{A/CT}$ thickness for clay- and carbonate-dominated cases as well as statistics for all ODP and DSDP sites used in this study, regardless of the host sediment type). Almost 80% of the clay-hosted transition zones and 60% of those hosted by carbonate-dominated lithologies were relatively-narrow intervals having a thickness varying from 5 < to 25 m (Fig. 7.5). Almost 30% of transition zones were more than 25 m thick, regardless of the host lithology. Remarkably, it was found that for both dominant host sediment types, i.e., clay versus carbonate, the modal value of $TZ_{A/CT}$ thickness fell within the 10–15 m range (Fig. 7.5). The studied opal-A to opal-CT diagenetic transitions ranged in age from the Middle Palaeocene (Selandian) to the

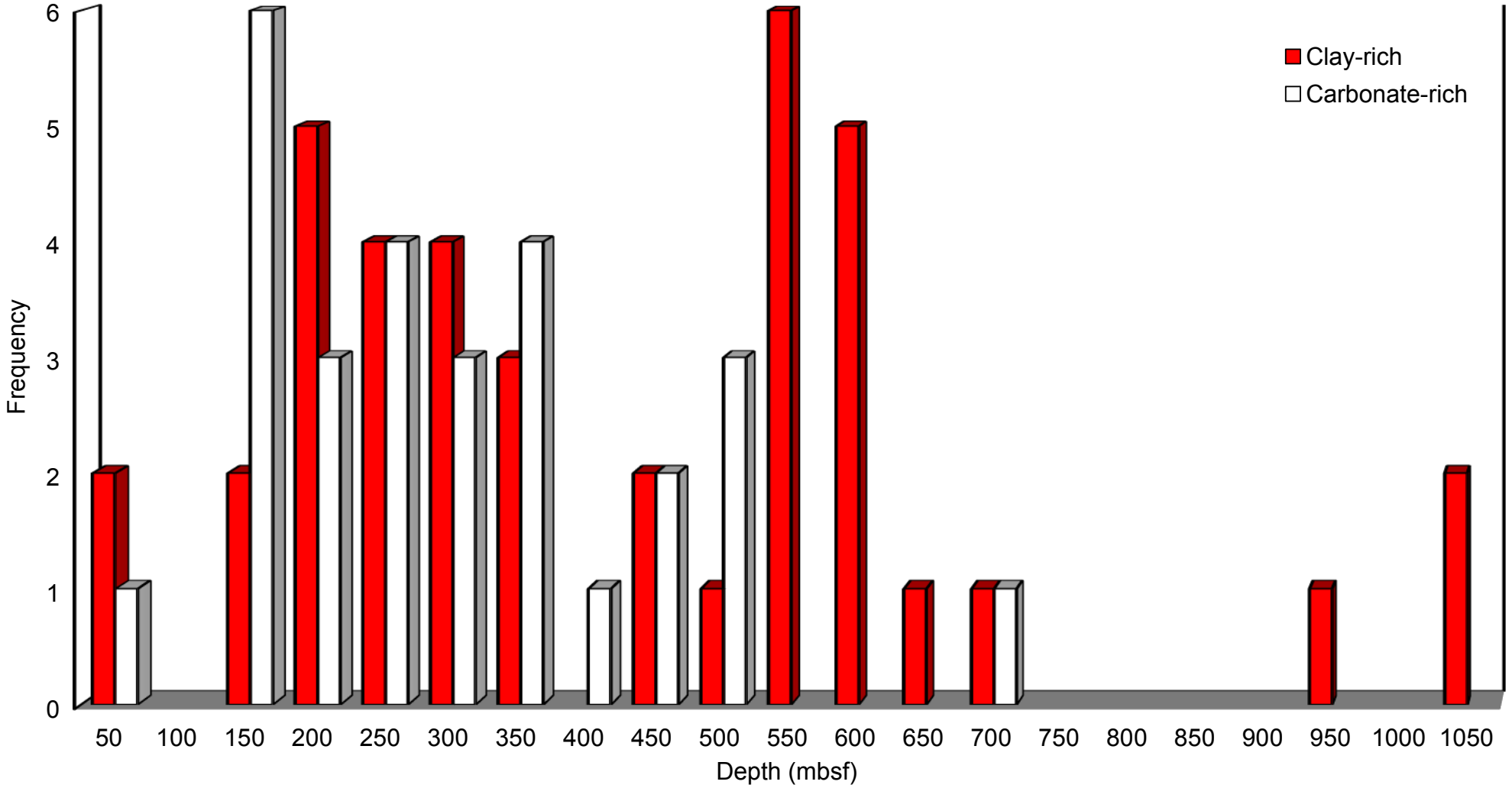


Figure 7.3. Depth distribution of the opal-A to opal-CT transition zones in clay- and carbonate-rich sediments drilled at the studied borehole sites.

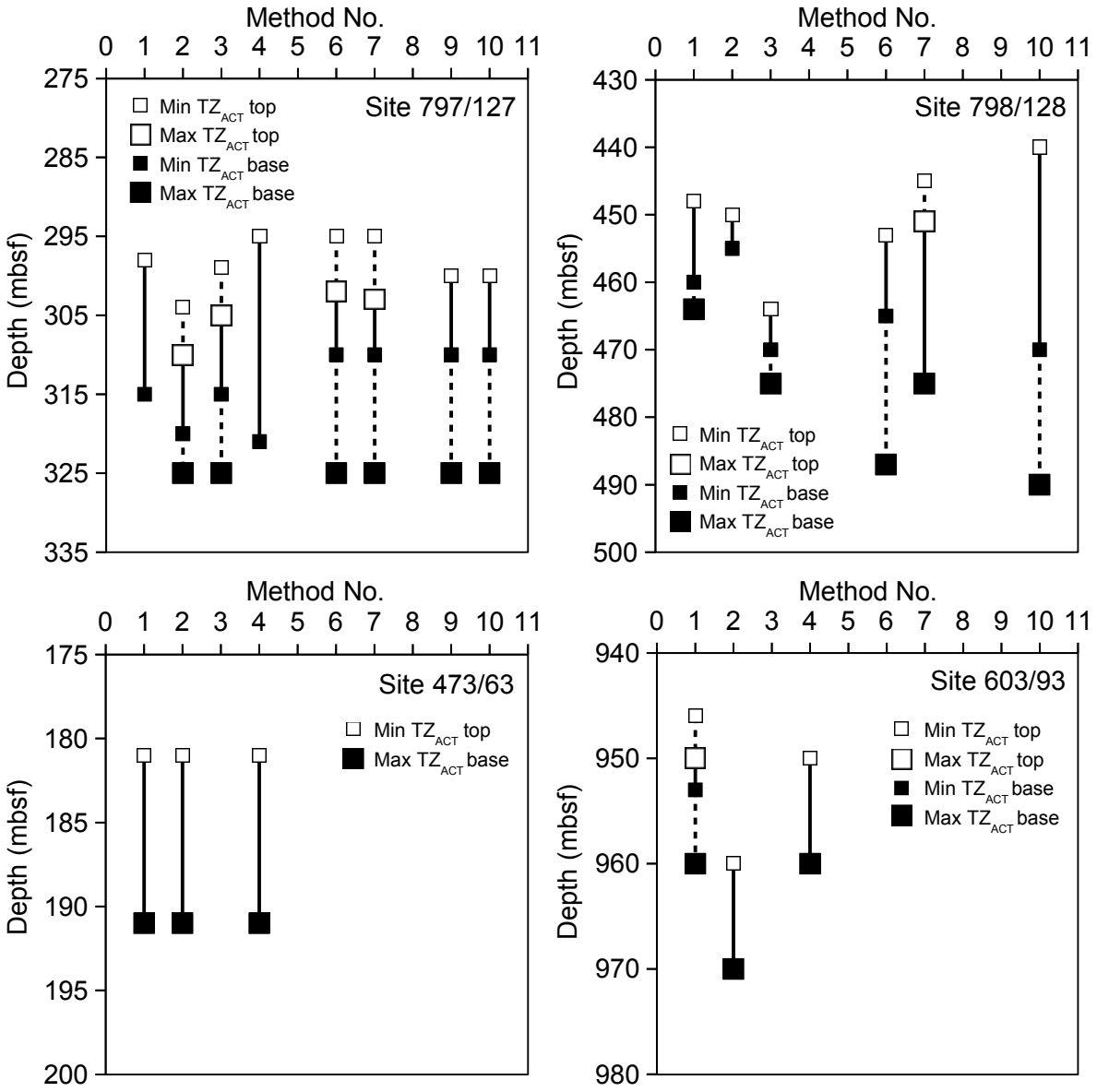


Figure 7.4. $TZ_{A/CT}$ thickness as estimated by changes in the physical properties of the sediments for four representative borehole sites. Given the poor recovery of the core samples, measurements of physical properties for the DSDP sites are often absent. Numbers on the abscissa represent the downhole measurement methods (1 = bulk density, 2 = P-wave velocity, 3 = gamma ray, 4 = porosity, 5: resistivity) and measurements directly on core samples (6 = wet-bulk density, 7 = porosity, 8 = P-wave velocity, 9 = gamma ray, 10 = thermal conductivity) used for determining the thickness of the $TZ_{A/CT}$.

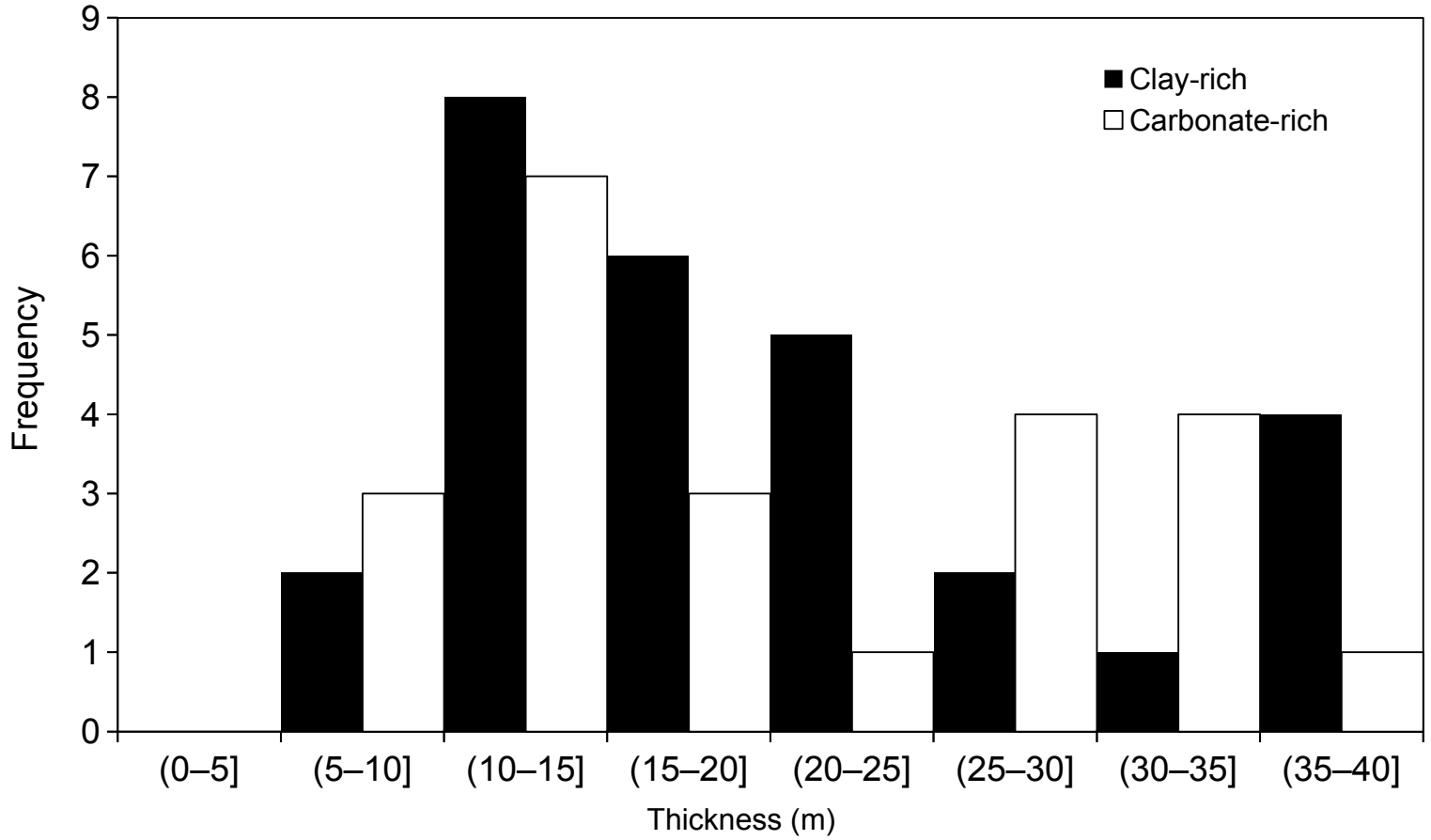


Figure 7.5. Histogram showing the distribution of $TZ_{A/CT}$ thickness categories in clay-hosted (black bars) and carbonate-hosted (white bars) lithologies. Each half-open thickness interval on the abscissa also includes its upper (right hand side) end point.

Late Pliocene (Piacenzian) (Fig. 7.6). The silica transitions found within mainly-carbonate sediments had wider age ranges than transitions embedded in clay-rich sediments. The oldest (Middle Palaeocene) and the youngest (Late Pliocene) transitions appeared in carbonate-rich and clay-rich host lithologies, respectively. The most frequent transitions in clay-dominated and carbonate-rich sediment types were found to occur during the Late Miocene and Middle Miocene, respectively.

For all study sites, the age of the sediments in which the diagenetic transition was embedded was neither correlated with the thickness of the $TZ_{A/CT}$ nor with the opal-A content of the sediment (correlation coefficients being -0.02 and -0.499; Figs. 7.7A, B, respectively). However, when the sediment age was compared to thickness for carbonate-dominated sites, a weak correlation was observed (r = 0.327; Fig. 7.7A).

The present-day *in situ* temperature of the studied transition zones varies between 2 and 60 °C (Table 7.1), with an average of ~25 °C (Refer to Appendix VI for the statistics related to the $TZ_{A/CT}$ temperature values presented in Table 7.1). The maximum temperature, 60 °C, was recorded at the clay-hosted Site 1173 in the Nankai Trough, northwestern Pacific Ocean where the actual geothermal gradient is very high (170 °C/km; Table 7.1). However, according to Neagu (2011), the 60 °C recorded at this site is not very reliable as it is estimated based on shallower temperature measurements that were then extrapolated to the $TZ_{A/CT}$ depth. The lowest temperature (2 °C) was recorded at the carbonate-dominated Site 1090 near the Agulhas Ridge in the Southern Ocean where the geothermal gradient is

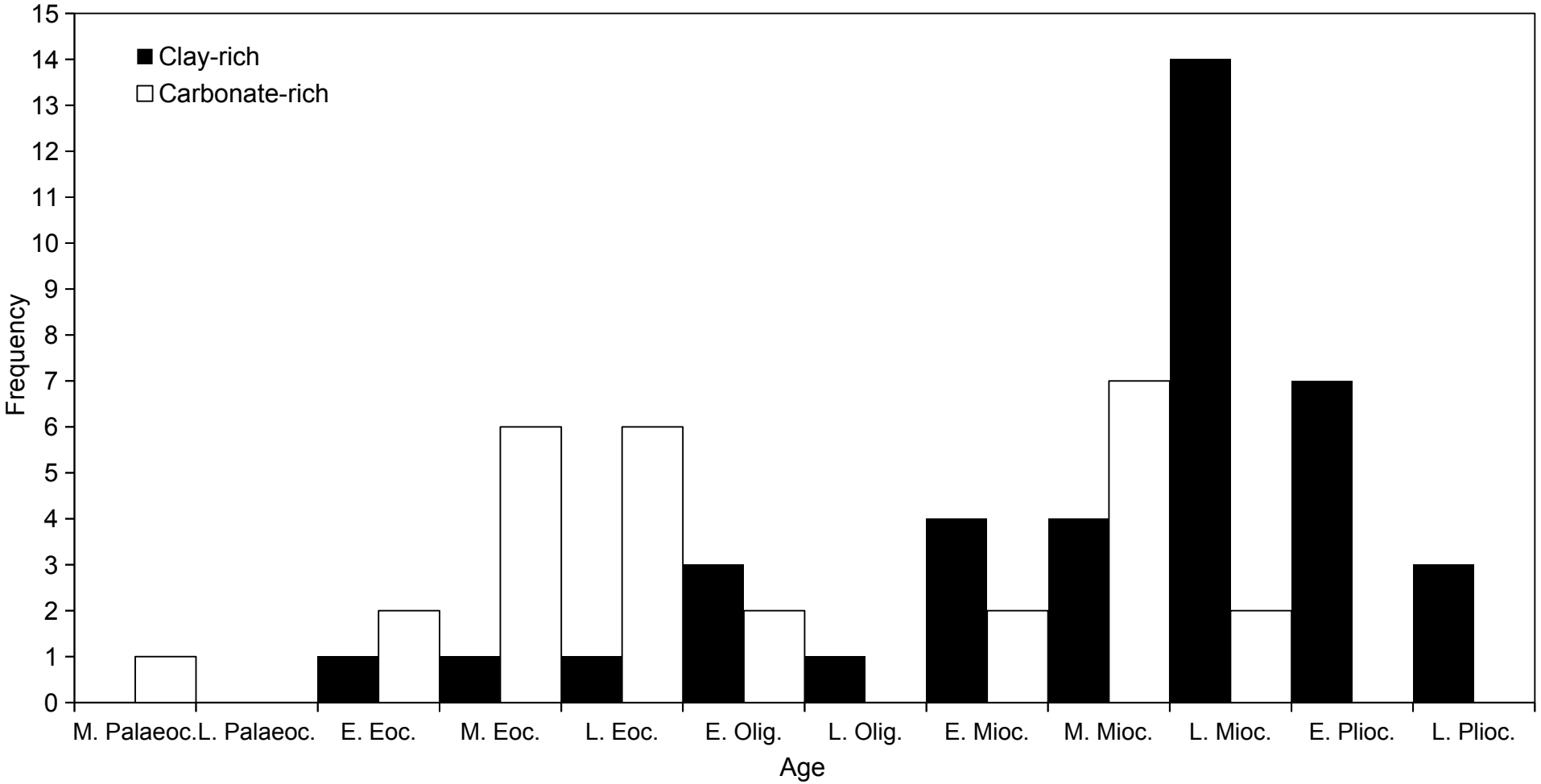


Figure 7.6. Age distribution of silica diagenetic transition zones within the studied ODP and DSDP boreholes. The abbreviations represent: M. Palaeoc. = Middle Palaeocene, L. Palaeoc. = Late Palaeocene, E. Eoc. = Early Eocene, M. Eoc. = Middle Eocene, L. Eoc. = Late Eocene, E. Olig. = Early Oligocene, L. Oligocene = Late Oligocene, E. Mioc. = Early Miocene, M. Mioc. = Middle Miocene, L. Mioc. = Late Miocene, E. Plioc. = Early Pliocene, L. Plioc. = Late Pliocene

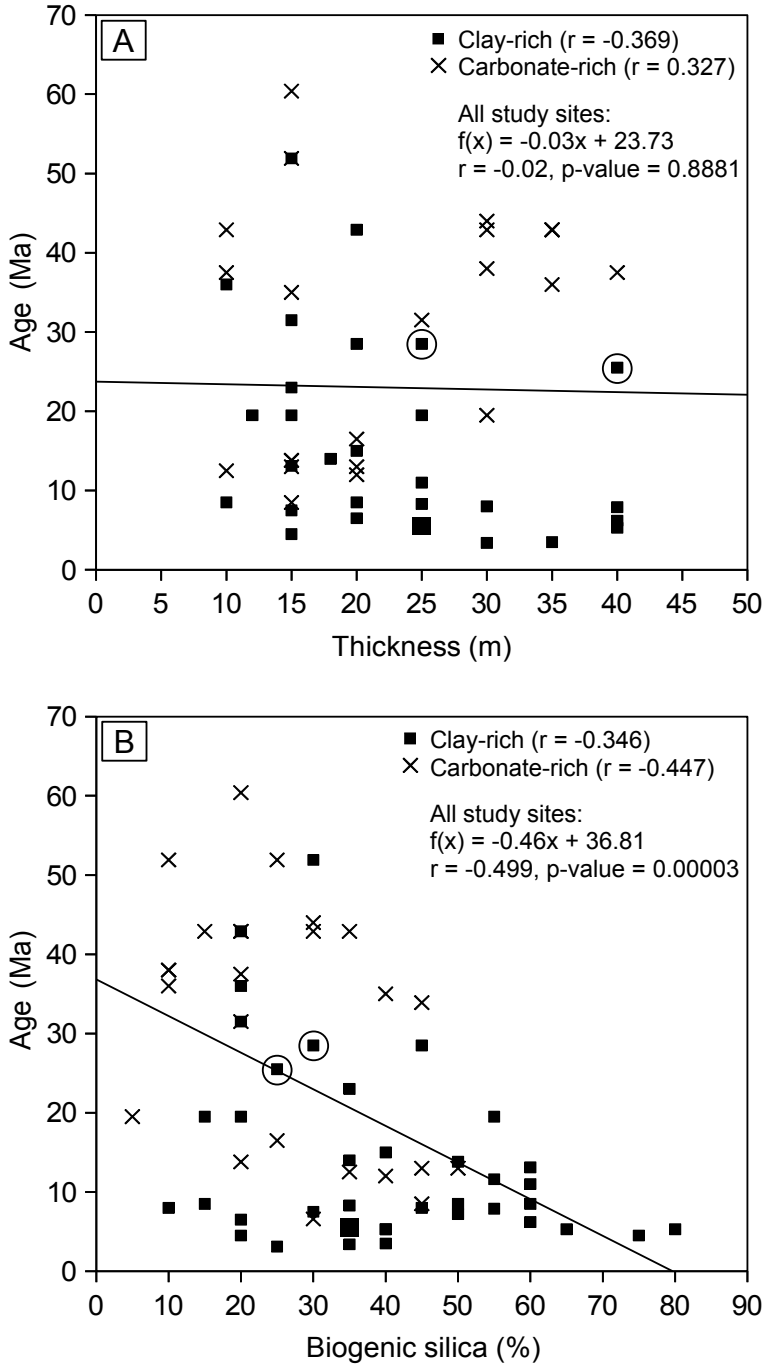


Figure 7.7. A) Cross-plot illustrating the relationship between the $TZ_{A/CT}$ age and thickness in clay-dominated (solid squares) and carbonate-dominated (× marks) sediments. Circled data points represent Sites 902/150 and 903/150 where the position of the $TZ_{A/CT}$ was uncertain; B) Age of the $TZ_{A/CT}$ relative to the opal content of the sediment hosting the $TZ_{A/CT}$. Circled squares denote Sites 902/150 and 903/150 where $TZ_{A/CT}$ depth was uncertain.

anomalously low (8 °C/km; Table 7.1). The temperatures at the depth of the transitions found in clay-rich sediments ranged widely (~5–60 °C; Appendix VI and Fig. 7.8), far more than for transitions hosted by carbonate lithologies. A modal value of 35–4 0 °C was observed for the study sites having the clay-dominated transitions (Fig. 7.8). The frequency of carbonate-hosted transition zones increased with higher temperatures, while there was no apparent relationship between frequency and temperature for clay-dominated sites.

Regardless of the dominant lithology, the present-day $TZ_{A/CT}$ temperature was moderately correlated with $TZ_{A/CT}$ thickness (r = 0.588) (Fig. 7.9). Clay-hosted $TZ_{A/CT}$ showed a much stronger relationship between $TZ_{A/CT}$ temperature and thickness (r = 0.659) than did carbonate-embedded transition zones (r = 0.424).

7.4.2 Temperature-age relationship

The relationship between *in situ* temperatures at the $TZ_{A/CT}$ and the age of the sediment hosting this diagenetic boundary followed the general trend previously shown by Hein et al. (1978) exhibiting an inverse correlation between these two variables (i.e., the older the diagenetic transition zone, the lower its measured temperature). Figure 7.10A follows the general trend of the reference temperature-age relationship presented by Hein et al. (1978), and exhibits an overall inverse correlation between these two variables; i.e., the older the diagenetic transition zone, the lower its current temperature. However, a series of silica transitions younger than the Middle Miocene were almost evenly distributed across the 3–40 °C temperature

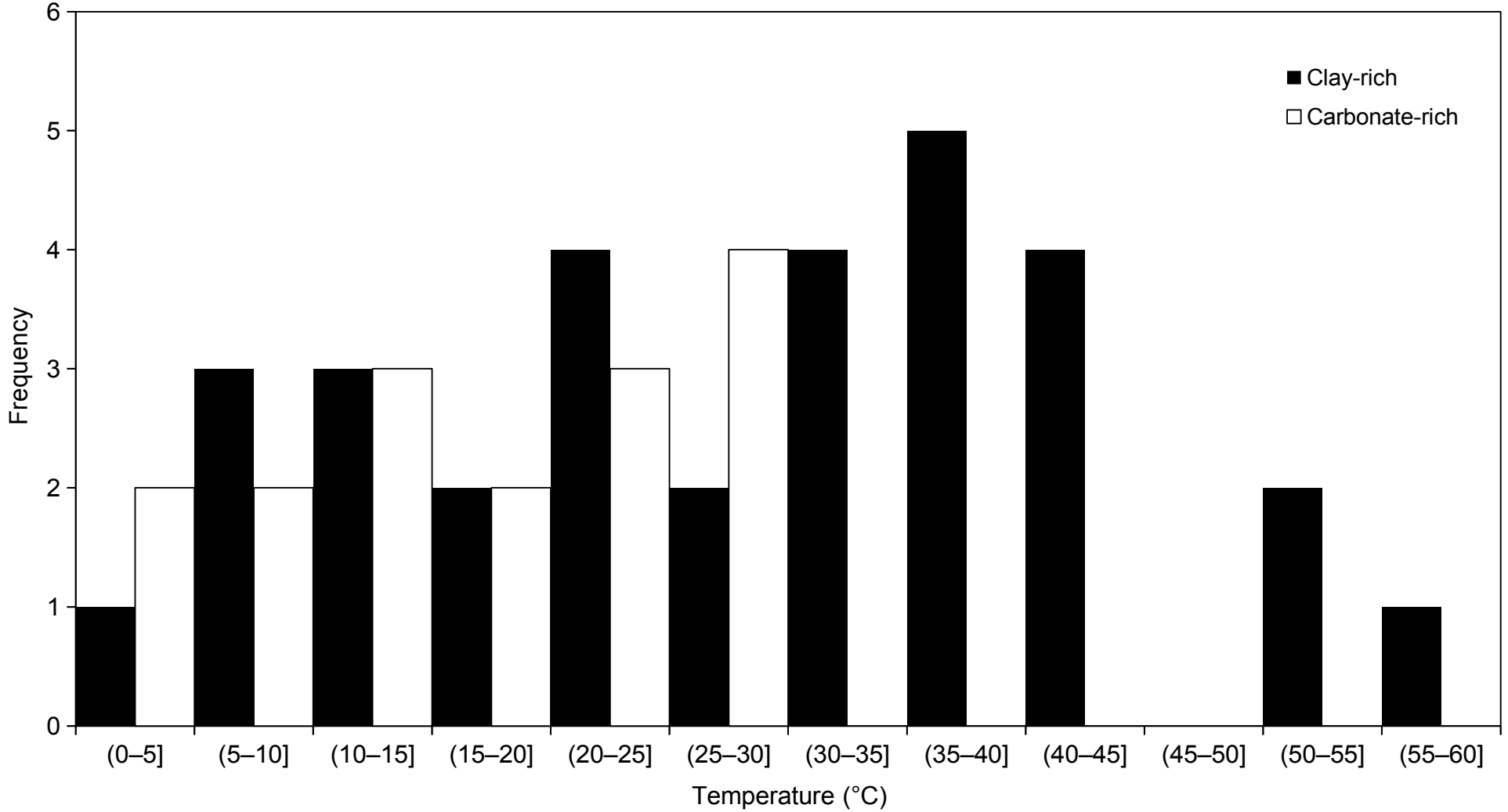


Figure 7.8. Bar graph showing the distribution of temperature at $TZ_{A/CT}$ depth for clay-hosted (black bars) and carbonate-hosted (white bars) sites. Each half-open temperature interval on the abscissa also includes its upper end point.

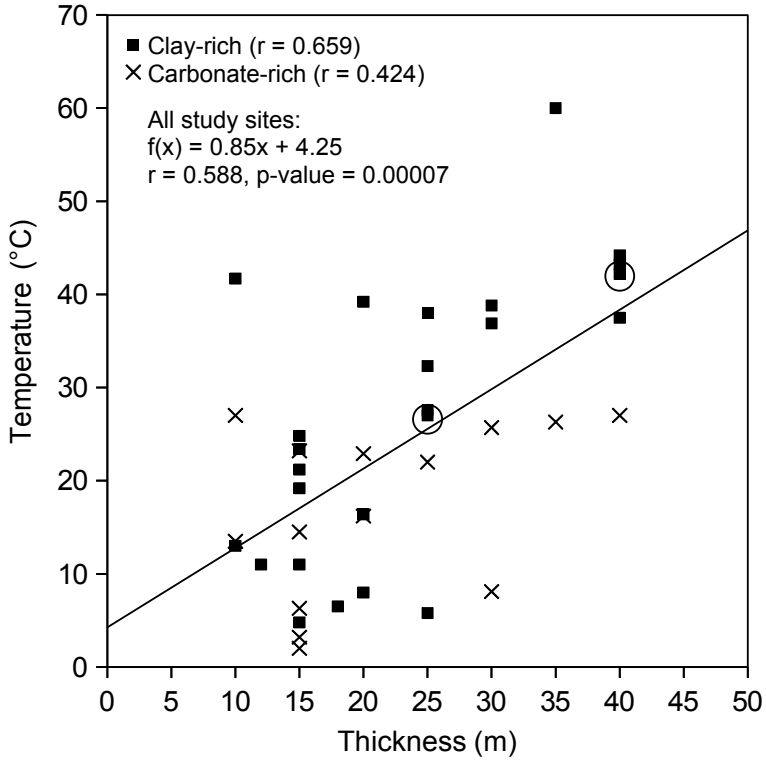


Figure 7.9. Scatterplot showing the $TZ_{A/CT}$ temperature-zone thickness relationship in clay- and carbonate-dominated ODP and DSDP study sites. The explanations for the circled data points are given in Figure 7.7.

range. Though the data points in Figure 7.10A generally have error bars representing the possible age range of the sediment, this inverse relationship remains statistically valid. When clay- and carbonate-dominated sites were assessed separately, no correlation between temperature and age was found (Fig. 7.10B; correlation coefficient values being -0.35 and 0.08 for clay- and carbonate-dominated sites, respectively).

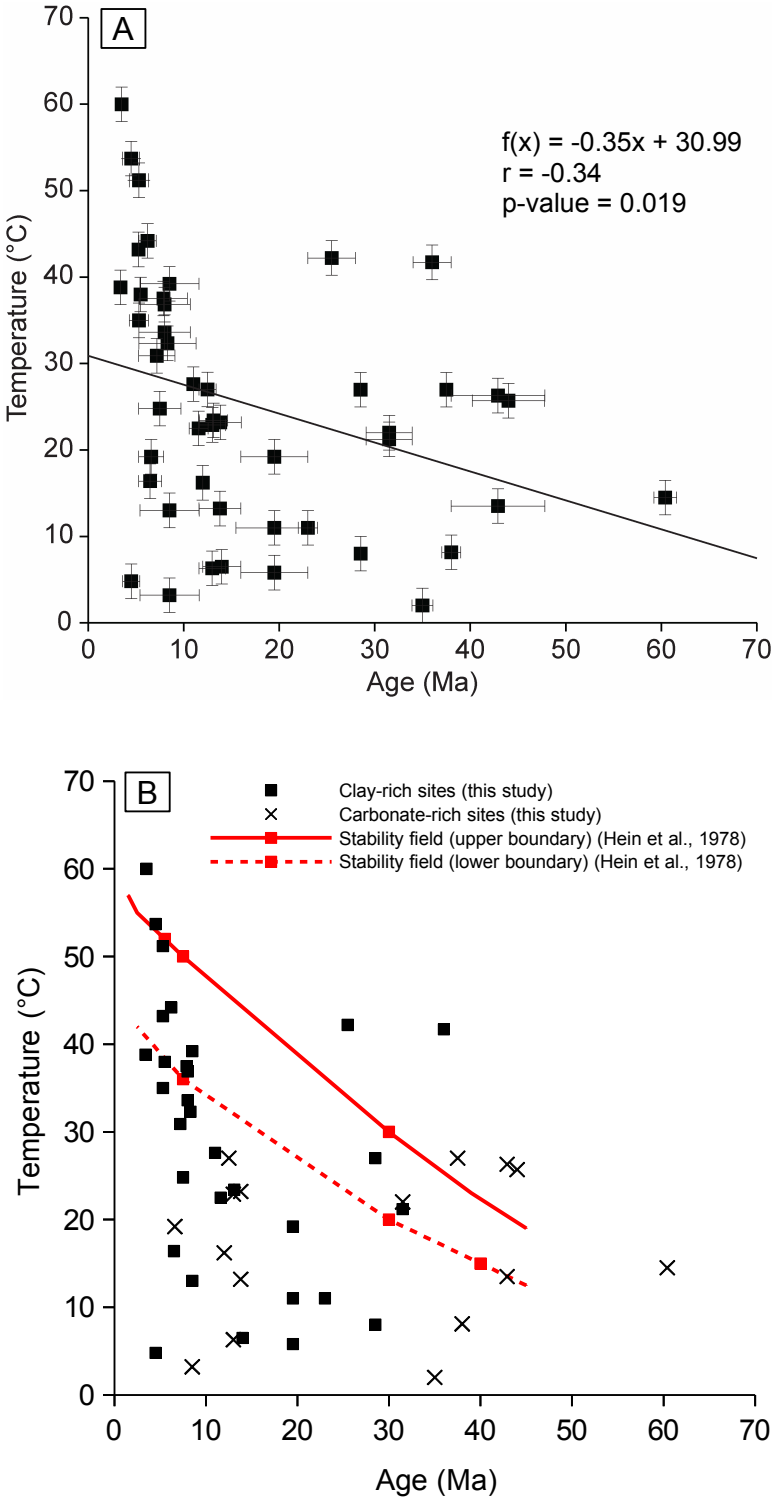


Figure 7.10. A) Inverse relationship between age and *in situ* temperature across the $TZ_{A/CT}$ at the studied ODP and DSDP sites. The p-value (< significance level 0.05) shows this relationship is statistically significant (according to Noymer, 2008). The

X- and Y-error bars represent the possible age ranges of the sediment and the standard errors, respectively; B) The age-temperature data points of Figure 7.10A as classified by their dominant host sediment types. There was no correlation between these variables for both clay- and carbonate-rich sediments. The reference data of Hein et al. (1978) are also plotted for comparison. The continuous and dashed red lines represent the upper and lower limits of opal-CT formation as determined by the reference data.

7.5 Discussion and implications

7.5.1 Controls on $TZ_{A/CT}$ thickness

As the rate of opal-A to opal-CT transformation reactions is predominantly temperature dependent (e.g., Kastner and Gieskes, 1983), it can be inferred that temperature exerts a major control on the thickness of the $TZ_{A/CT}$ as well. This inference is supported by the studied transition zones being relatively-narrow intervals (maximum thickness = 40 m; Table 7.1), regardless of the dominant host sediment type, age, and/or biogenic silica content. According to Littke et al. (1991), temperature is a first-order control on thickness where the $TZ_{A/CT}$ is relatively narrow. The correlation observed between the $TZ_{A/CT}$ temperature and thickness values (Fig. 7.9) further supports temperature being a primary control. A wide range of differences in temperature between the top and bottom of the $TZ_{A/CT}$ (0.12–5.9 °C; Table 7.1) suggests that other diagenetic drivers, such as time, surface area, pore chemistry, and host lithology may partially affect $TZ_{A/CT}$ thickness.

One of the most significant observations is that the temperature contrast between the

top and bottom of the $TZ_{A/CT}$ is correlated to the $TZ_{A/CT}$ thickness (Fig. 7.11). Temperature variability within the $TZ_{A/CT}$ may reflect variations in the thermal regime of the host sediment (after Neagu, 2011), i.e., the higher the temperature contrast over the $TZ_{A/CT}$, the higher the heat flow within the sediment (and vice versa). As seen in Figure 7.11, the $TZ_{A/CT}$ intervals are distributed in both low and high heat flow regimes.

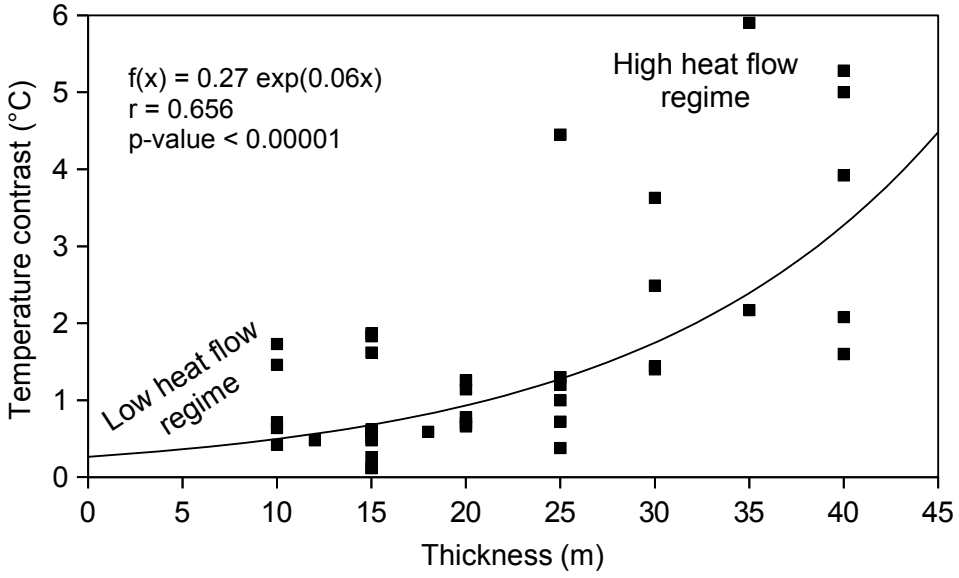


Figure 7.11. Temperature contrast through the $TZ_{A/CT}$ versus zone thickness for the studied ODP and DSDP sites. The temperature contrast between top and bottom of the $TZ_{A/CT}$ was calculated using the equation: $\Delta T = G\delta$, where ΔT is the temperature difference (°C) between the top and bottom of the zone, G is the geothermal gradient of the sediment column hosting the $TZ_{A/CT}$ (in °C m^{-1}), and δ is the $TZ_{A/CT}$ thickness (in m). Note that the low and high values of temperature difference between the top and bottom of the $TZ_{A/CT}$ correspond to low and high heat flow conditions in the host sediment, respectively.

The association of $TZ_{A/CT}$ thicknesses with high temperature contrasts agrees with the observations of Littke et al. (1991) linking narrow intervals to areas marked by high geothermal gradients. However, a group of the analysed narrow transition zones are clustered around values having a minimal temperature difference (< 1 °C temperature contrast; Fig. 7.11). Littke et al. (1991) suggest that silica diagenesis across some of these transition zones occurred when the geothermal gradient was significantly higher than at present. Therefore, the temperature contrast through the $TZ_{A/CT}$ would not be representative of the actual diagenetic temperature of opal-A to opal-CT transformation. This type of transition zone is discussed in the next section.

7.5.2 Revisiting the silica diagenesis stability field

The temperature-time relationship during diagenetic silica formation has been studied extensively (e.g., Mizutani, 1970; Hein et al., 1978; Mizutani, 1977; Pisciotto, 1981a). Hein et al. (1978) were the first to propose a diagenetic stability field necessary for initiation of opal-A to opal-CT transformation. They estimated the age and present-day temperatures at opal-CT formation depth for siliceous marine deposits from the southern Bering Sea, the Monterey Formation, and some North Pacific chert and porcellanite sediments. Their stability field was based on the strong negative correlation of time and temperature during the ongoing precipitation of opal-CT (i.e., active diagenetic processes) and included the upper and lower boundaries of diagenetic silica formation (see Fig. 7.10B). According to Hein et al. (1978), early silicification (formation of opal-CT) takes place at relatively-deep burial depths (> 500 mbsf) and moderate temperatures (35–55 °C) within 10 Ma,

while more than 30 Ma is required for opal-A to opal-CT transformation at shallow burial depths (< 300 mbsf) and low temperatures (< 30 °C) (Fig. 7.10B).

My negatively-correlated age and temperature data points fit poorly within the Hein et al. (1978) time-temperature field (Fig. 7.10B). My data match the lower boundary of the stability domain slightly better than the upper boundary. The low temperature (< 30 °C) data points, however, are located mostly outside the original lower boundary. I postulate that this non-conformity is because the Hein et al. (1978) time-temperature relationship field was based on limited data. As the initial reference diagram was based on only six data points, it needs to be modified for use in constraining the stability realm of diagenetic silica.

The approach taken here is to expand the reference diagram by including the age and temperatures of a set of $TZ_{A/CT}$ intervals that I believe are diagenetically the most plausible active candidates (those zones across which silica diagenesis is still occurring). Due to lack of uplift and erosion, the sedimentary columns hosting the active transitions are presently at their maximum burial depth, and the onset of silica diagenesis at these sites is not concurrent with unconformities. As such, the ongoing precipitation of opal-CT is thus related to the present-day burial depth. Therefore, the age and present-day temperature at the depth of an active $TZ_{A/CT}$ can roughly represent the time and temperature when formation of opal-CT across the $TZ_{A/CT}$ was first initiated. This assumption is possible as the active transitions represent modern isothermal features that are in near equilibrium with the present-day geothermal

gradients (after Pisciotto et al., 1992; also see Chapter 4 of this thesis).

The likely-active $TZ_{A/CT}$ intervals and the criteria used to select these intervals are presented in Table 7.2. Seismic identification criteria were not used as, due to their low quality, the $TZ_{A/CT}$ is often difficult to identify from DSDP and ODP seismic profiles (except for Sites 794 and 795 where the $TZ_{A/CT}$ is clear on seismic profiles; see Chapter 4). Only a limited number of the investigated transition zones (21 sites) were considered to be presently active (Table 7.2). These likely-active boundaries were found in continuous stratigraphic sections where there are no major breaks or unconformities in sedimentation. These transitions are found in young sediments (Middle Miocene and younger) marked by high geothermal gradients and generally containing sufficient amounts of biogenic silica. Moreover, the concentration of silicic acid sharply decreases across the active transitions (this issue is discussed in Chapter 4 of this thesis).

The proposed stability field is defined mainly on the time-temperature data from likely-active transitions and represents an expanded version of the Hein et al. (1978) diagram (Fig. 7.12). Among the active sites used for modifying the reference diagram, the clay-dominated Site 1173 has the highest $TZ_{A/CT}$ temperature (60 °C). However, according to Neagu (2011), the temperature recorded for the transition zone at this site cannot be fully trusted as it has been estimated based on shallower temperature measurements that were extrapolated to the $TZ_{A/CT}$ depth using a linear geothermal gradient of 170 °C/km estimated for the upper 300 m.

Table 7.2. Likely-active opal-A to opal-CT transition zones involved in this study and their characteristics. The data were extracted from the ODP and DSDP database. No. = the identification number of the sites presented in Figure 7.1. The symbols represent: ✓ = yes, – = no data, ? = uncertain

No.	Site	Stratigraphic continuity	Sediment age, Ma	Biosilica, %	Geothermal gradient, °C km^{-1}	*In situ* temperature, °C	Silica concentration drop at the $TZ_{A/CT}$
7	794	✓	7.9	55	125	37.5	✓
8	795	✓	5.3	40	132	43.2	✓
9	796	✓	5.5	35	178	38	✓
10	797	✓	8	45	121	36.9	✓
11	798	✓	3.4	35	83	38.8	✓
12	799	✓	6.2	60	98	44.2	✓
24	1010	✓	13.1	60	122	23.4	?
26	1016	✓	7.2	50	105	30.9	✓
27	1022	✓	8	10	88	33.6	?
39	1173	✓	3.5	40	170	60	✓
43	1226	✓	13	45	57.2	22.9	✓
44	1256	✓	12.5	35	146	27	✓
46	184*	✓	5.3	80	82	51.2	–
47	185*	✓	5.3	65	50.4	35	–
48	188*	✓	4.5	75	–	–	–
49	189*	✓	4.5	20	95.8	53.7	–
50	190*	✓	5.3	40	–	–	–
51	191*	✓	3.1	25	–	–	–
52	192*	✓	8.5	60	–	–	–
63	467	✓	8.5	50	63	39.2	–
65	471	✓	11.6	55	132	22.5	–

* The temperature and age data from Sites 184–192 (DSDP Leg 19) are a major component of the Hein et al. (1978) reference stability field. The values estimated by Hein et al. (1978) for these sites were slightly modified in this study, using them to define the new stability field for the initiation of opal-CT precipitation.

It is acknowledged that deeper than 300 mbsf at Site 1173 thermal conductivities have increased by 30–50% (Shipboard Scientific Party, 2001c), so the thermal

gradient should decrease proportionally, and the $TZ_{A/CT}$ temperature should be somewhat lower than that reported by the ODP. In addition, magnetostratigraphy shows that the age of the sediment hosting the $TZ_{A/CT}$ has been slightly overestimated using biostratigraphic data. Therefore, the temperature and age of the $TZ_{A/CT}$ at Site 1173 were slightly modified to fit the upper boundary of the stability field.

Insufficient time to reach an equilibrium temperature while drilling as well as the temperature estimation based on shallower temperatures extrapolated to the $TZ_{A/CT}$ depth (Shipboard Scientific Party, 1981) are the two major sources that have affected the DSDP-reported $TZ_{A/CT}$ temperature value for Site 471. Also, some uncertainties in constraining the $TZ_{A/CT}$ depth have led to slightly-underestimated and -overestimated $TZ_{A/CT}$ temperatures at Sites 184 and 1172, respectively (Hein et al., 1978; Shipboard Scientific Party, 2001b). The $TZ_{A/CT}$ temperatures for Sites 184 and 471 were thus slightly modified, and placed very close to the upper and lower boundaries of the modified opal-CT stability field, respectively. The $TZ_{A/CT}$ temperature at Site 1172 was also slightly modified to fit the upper boundary of the revised stability field.

This modified diagram follows the general trend of a progressive and ongoing transformation from opal-A to opal-CT, implying the negative correlation between temperature and time, valid for all diagenetic processes (after Giles, 1997). Since the data points from active transitions cover only the younger age zone of the modified stability field (< 13 Ma; Middle Miocene onwards), the boundaries of this diagram were extrapolated to older ages (from the Middle Miocene to Middle Eocene) using

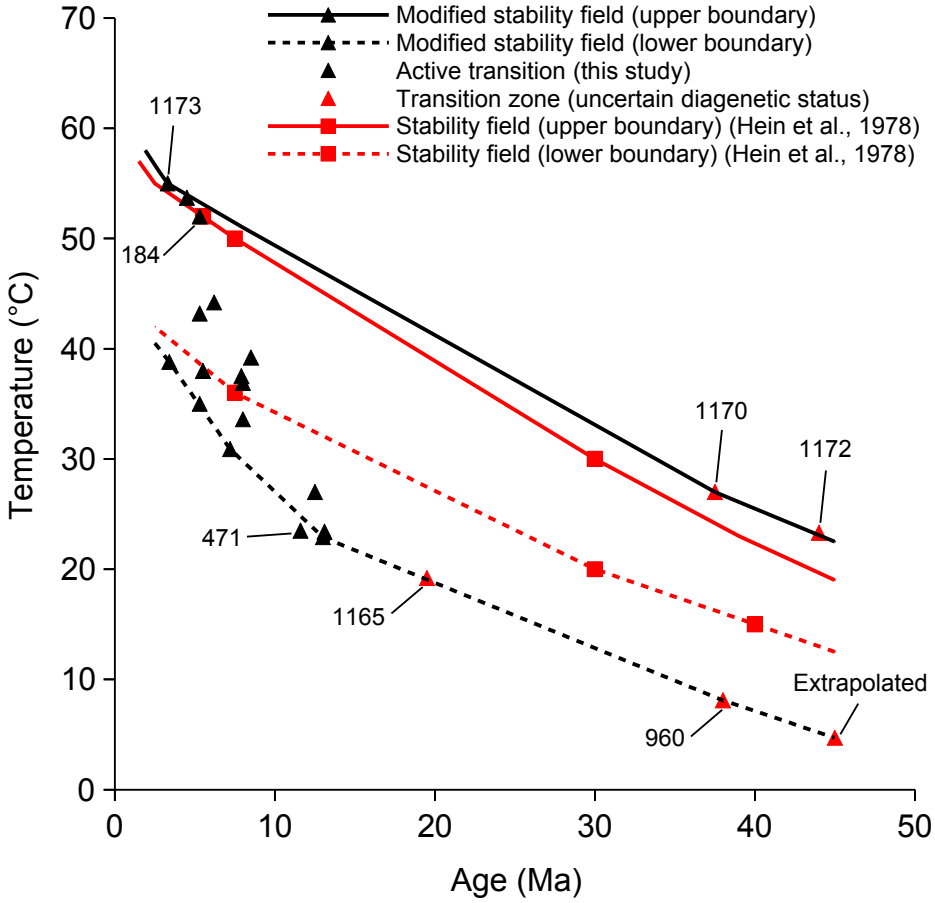


Figure 7.12. Stability field of diagenetic silica (opal-CT) formation based on age and temperature values at the $TZ_{A/CT}$ depths analysed in this study. The continuous and dashed black lines represent the upper and lower boundaries of this stability field, respectively. The age and temperature of the $TZ_{A/CT}$ at Site 1173 as well as the $TZ_{A/CT}$ temperature at Sites 184, 471, and 1172 were slightly modified (these sites are labelled on the diagram). The reference data of Hein et al. (1978) are shown for comparison. The continuous and dashed red lines represent the original upper and lower limits of the reference opal-CT stability field.

the age-temperature data from some of diagenetic transformation boundaries that do not meet the applicable recognition criteria for active transition zones (see Table 7.2 and Chapter 4), but fit well the inverse correlation pattern of temperature and age

established for ongoing silica diagenetic reactions (transition zones with uncertain diagenetic status, shown by labelled red triangles in Fig. 7.12). Here, I give explanations why these data points (red triangles in Fig. 7.12) were chosen for the extrapolation of the stability field to > 13 Ma rather than any of the others shown in Figure 7.13:

1) these data points persist following the trend of temperature-time relationship observed for the younger part of the stability field better than others.
2) low temperature nature of these old transitions (Early Miocene and older) shows it is very unlikely that these boundaries to be presently fossilised (according to Neagu, 2011 and literature there in).
3) trend of temperature evolution in time among these data points shows a nearly-consistent variability pattern, with the least deviation from parallelism to the reference stability field.

The upper boundary of the extended stability field was defined by connecting data points of the higher-temperature zone that best express the inverse trend of temperature and age relationship. Similarly, data points from the lower- temperature part best describing the inverse correlation of temperature and time were connected with lines to define the lower boundary of the stability field. Due to the limited number of data points, I was conservative with regard to determining the upper boundary of the modified opal-CT zone, and I shifted the upper boundary somewhat closer to that of the reference stability field (Fig. 7.12).

Given its narrower temperature range, the reference stability field is captured within my opal-A to opal-CT age-temperature stability field. Comparable to transition zones studied by Hein et al. (1978), the transitions from this study are mostly ranged in age from the Middle Eocene to Late Pliocene; the time range for the extended stability field was therefore defined the same as that of Hein et al. (1978) diagram. According to the extended stability field, ongoing opal-A to opal-CT transformation under shallow burial conditions at low temperatures (< 30 °C) requires more than 35 Ma. (Fig. 7.12). This is in broad agreement with Hein et al. (1978). They claim that the silicification reaction, under the constraints of a shallow burial depth and low temperatures, depends mainly on time. However, an increase in the rate of silica diagenesis relative to the sedimentation rate would still be needed to sustain the active transformation of opal-A to opal-CT following the initial opal-CT precipitation. Thus, time cannot be the first-order control for increasing the reaction rate. Therefore, even at low temperature conditions, the opal-A to opal-CT reaction has been primarily caused by temperature, of course it is also partly influenced by other agents such as sediment age, geochemical, and lithological factors. Based on the revised stability field, the active precipitation of opal-CT at moderate temperatures (ranging from 35 to 55 °C) under shallow burial settings takes place within a 3 Ma period, a much shorter period than the transformation time estimated by the reference diagram for moderate temperature conditions. The modified diagram shows that at high temperatures (> 55 °C), the transformation will likely occur rapidly (< 1–2 Ma) regardless of burial depth. Thus, an earlier transformation occurs at higher temperatures.

To confirm that the negative temperature-age relationship illustrated by the extended opal-CT stability diagram adequately describes the study data, time and temperature values for the $TZ_{A/CT}$ depths of the study sites were re-plotted on the modified diagram (Fig. 7.13). Although showing a better fit to the lower boundary of the modified stability field than to the upper boundary, these data points (red triangles in Fig. 7.13) do not fit the stability field. In general, these data do not follow the trend of decreasing temperature with age (and vice versa) under ongoing silica diagenesis. Due to the limited availability of thermal and geochemical data, the current diagenetic status of the $TZ_{A/CT}$ at these sites is not known. It should be noted that a significant fraction of these data points (red triangles) fall outside the stability zone of active opal-CT precipitation, more explicitly below the lower boundary of the temperature-time field. The temperature and age of some of these sites are certainly not representative of an active opal-A to opal-CT diagenetic process (after Neagu, 2011). The $TZ_{A/CT}$ at these boreholes is characterised by low temperatures (< 20 °C) and is found in young sediments (Middle Miocene and younger; circled data points in Fig. 7.13). According to Neagu (2011), such opal-A to opal-CT transition zones having present-day low temperatures and younger ages are likely to represent fossilised features. Although there are no published supporting data, it seems that the fossilisation of the $TZ_{A/CT}$ at these sites occurred due to a remarkable drop in the palaeo-geothermal regimes that are possibly associated with past events of increased heat flow (after Neagu et al., 2010). This inference assumes that the thermal gradient has significantly decreased since the time of fossilisation (Davies and Cartwright, 2002) and that the magnitude of palaeo-geothermal gradients was markedly higher

than the present at the burial depth of these fossilised transition zones.

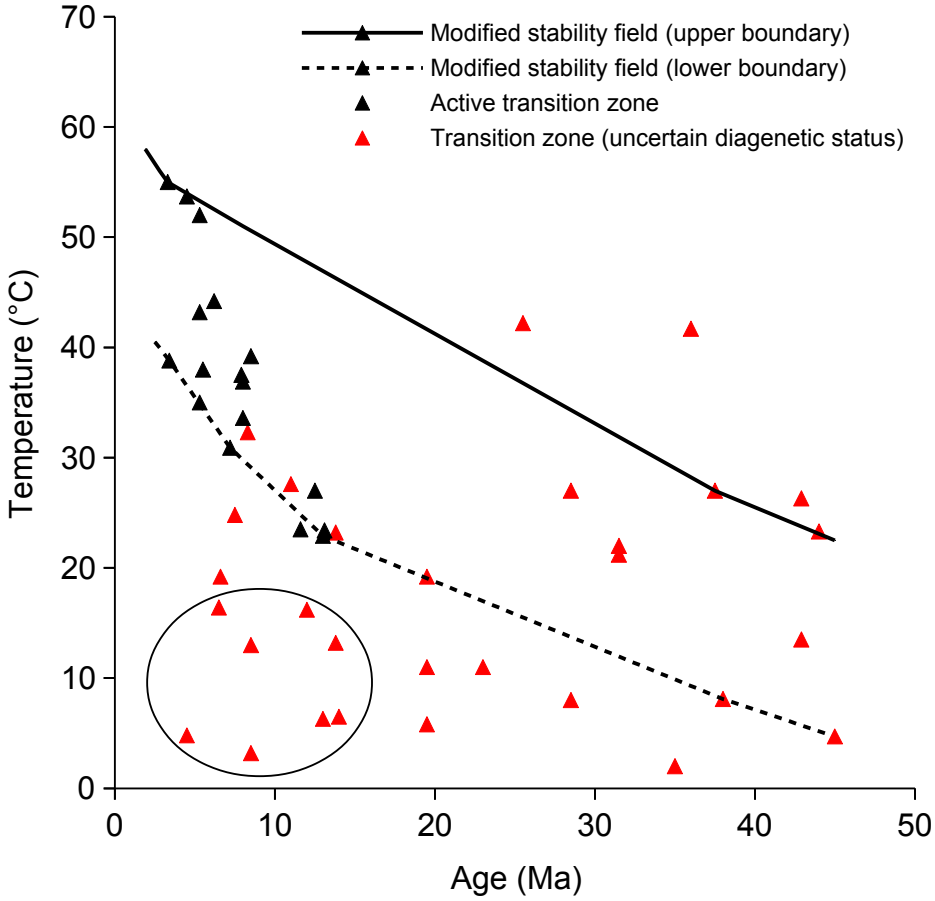


Figure 7.13. Distribution of the $TZ_{A/CT}$ temperature and time data from the studied ODP and DSDP sites within and around the modified stability field of opal-CT formation. The continuous and dashed black lines represent the upper and lower boundaries of the stability field, respectively. These boundaries are based on the data points from active transitions, and extrapolated using the data points representing transitions with uncertain diagenetic status, but fitting the inverse temperature-age correlation for ongoing silica diagenesis (red triangles connected with continuous and dashed black lines). The circled data points represent likely-fossilised transitions (Sites 473, 846, 850, 1095, 1133, 1149, 1201, 1225; Table 7.1).

Davies and Cartwright (2002) explain how significant decreases in palaeo-geothermal gradients and a cooling to modern values have possibly led to fossil silica diagenesis by presenting arguments for an arrested transition zone from the Faeroe-Shetland Channel, northeast Atlantic margin. Based on constraints of overburden thickness accumulated during the Late Miocene and Early Pliocene, seabed temperature, and present-day geothermal gradient (38 °C/km), Davies and Cartwright (2002) calculate that a minimum thermal gradient of 60 °C/km would have been required to initiate active diagenetic transitions during the Middle and Late Miocene. Given the present-day temperature of this boundary (24 °C), a minimum 60 °C/km palaeo-thermal gradient would have been necessary to raise the palaeo-temperature of the transition above 24 °C. This argument also incorporates a palaeo-seafloor temperature of 5 °C during the initiation of active silica diagenesis; a postulation that leads to an elevated palaeo-temperature for the transition (29 °C at 400 mbsf), higher than that of its present-day depth (24 °C at 700 mbsf), when the boundary was closer to the seafloor. From this, Davies and Cartwright (2002) conclude that the opal-A to opal-CT transition might have been warmer early in deposition, and then much colder later in its history when fossilisation occurred, possibly due to sudden decreases in the extreme palaeo-geothermal gradient. However, up to the present no supportive thermochronological evidence is available to support this.

The idea of an elevated palaeo-geothermal when the transformation from opal-A to opal-CT initiated can also explain why particular fossilised sites exhibit young

transition zones. The long established view of the development of an active silica diagenetic transition (prior to fossilisation) originates from the theoretically-based reasoning that temperature was the principal rate-controlling factor for growth and up-section migration of the transition zone through biosiliceous sediments (e.g., Kastner et al., 1977; Meadows and Davies, 2007; Neagu et al., 2010). This reasoning clearly supports the assumption that the rate of transformation from biogenic to diagenetic silica prior to fossilisation has been fundamentally controlled by the palaeo-geothermal gradients and thereby the palaeo-temperatures. From this, we can conclude that the exceptionally-elevated palaeo-geothermal gradients have favoured rapid (high rate) transformation of opal-A to opal-CT, and therefore earlier formation of silica diagenetic boundaries (young transition zones).

It is also noteworthy to mention that the opal-A to opal-CT transition zones are developed in many continental margin depositional basins worldwide and according to many studies in the past three decades (e.g., Roaldset and He, 1995; Brekke, 2000; Davies and Cartwright, 2002; Berndt et al., 2004; Neagu et al., 2010), the $TZ_{A/CT}$ is not presently related to an active diagenetic reaction but is in fact fossilised in its current position. However, most of the transition zones from different geographic regions are apparently bottom-simulating reflectors; in such situations the $TZ_{A/CT}$ is commonly concordant with the host strata and it is extremely difficult to make a case that the $TZ_{A/CT}$ is fossilised at all (as evident from Neagu et al., 2010). Nevertheless, where the $TZ_{A/CT}$ cross-cuts stratigraphy or it is deformed contemporaneous with its fossilisation (in highly-structured tectonic settings where local variations in heat flow

and thermal conductivity result in a complex shallow thermal structure, according to Meadows and Davies, 2007, 2010; Neagu et al., 2010), the nature of fossil diagenesis can be determined.

7.5.3 Geothermal history of silica diagenesis

Mizutani (1970, 1971) proposed that the silica mineral phases of siliceous deposits are controlled by the thermal history experienced by the deposits during silica diagenesis. Accordingly, the location and temperature of the $TZ_{A/CT}$ primarily depends on the integrated geothermal history of the layer in which the transition zone is presently found (Tada, 1991; Langseth and Tamaki, 1992).

Amorphous silica has been transformed to opal-CT at all the studied ODP and DSDP sites. However, the $TZ_{A/CT}$ occurred at different depths in host sediments that ranged in age and depth (temperature) (e.g., Figs. 7.6 and 7.8). To further examine temperature variations in these sediments over time, the thermal history was estimated by multiplying the geothermal gradient and sedimentation rate ($G \times \omega$; as suggested by Mizutani, 1970) at the $TZ_{A/CT}$ depth and the results were plotted versus the age of the transition zone (Fig. 7.14). The accuracy of the temperature history values for those DSDP and ODP sites plotted in Figure 7.14 depends strongly on to what degree the variables (G and ω) can be estimated. I have used the gradients measured by the DSDP and ODP and the sedimentary histories were estimated based on the magnetostratigraphic and biostratigraphic datum levels recognised at each site (available through the DSDP and ODP initial reports) that have been modelled

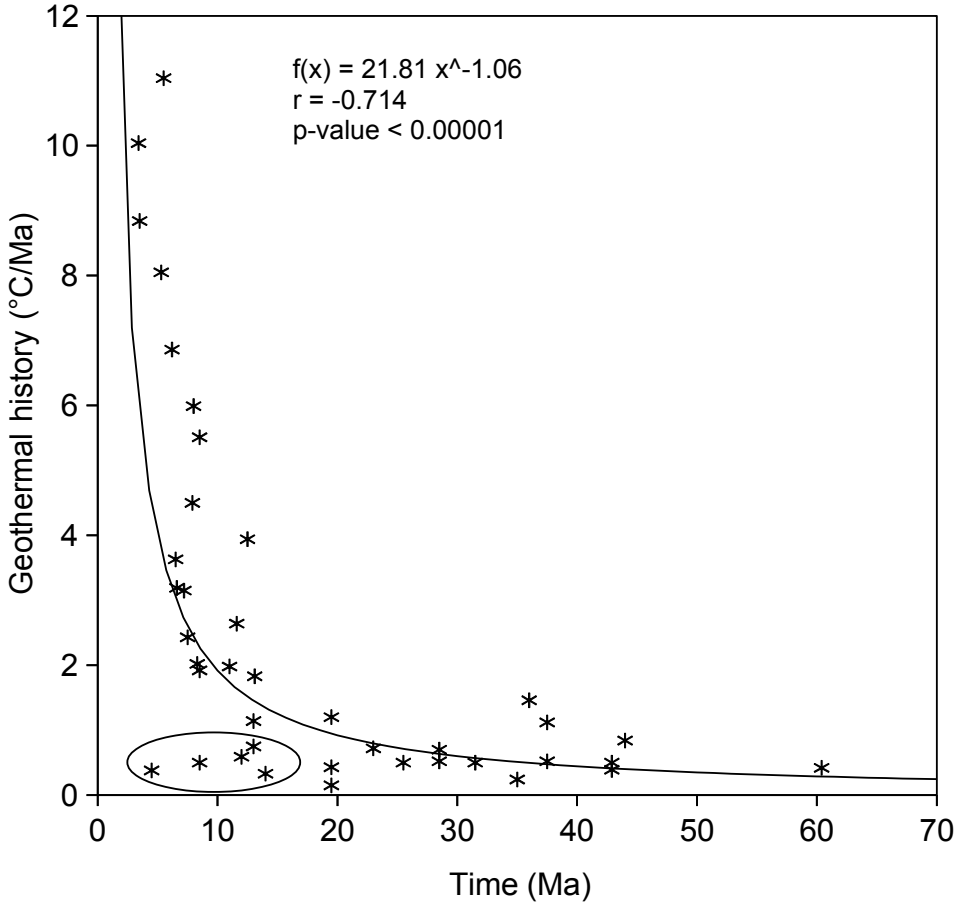


Figure 7.14. Geothermal evolution versus age at the $TZ_{A/CT}$ for the study sites. The temperature history values on the Y-axis are the product of geothermal gradient (in °C/m) and sedimentation rate (in m/Ma) at each site. Note the negative correlation between the two variables. The correlation is significant at p-value < significance level 0.05. The circled data points represent likely-fossilised transitions.

versus subsea-bottom depth (e.g., Figure 30 in Shipboard Scientific Party, 1990a). The inverse relationship between the age and temperature history is represented by the power function (Fig. 7.14; correlation coefficient squared (R^2) ≈ 0.51). This pattern agrees with the age and temperature history relationships observed for the siliceous sediments by Pisciotto (1981b) who suggested that higher geothermal

gradients in sediments with higher burial rates can account for the increased rates of opal-A to opal-CT transformation. Thus, high rates of silica diagenetic transformation correspond to high geothermal gradients and high sedimentation rates.

This study proposes a pattern of opal-A to opal-CT transformation that has active silica diagenesis at higher temperature gradients and higher sedimentation rates in younger sediments (Middle Miocene and younger), while silica transformation in sediments having low thermal gradients and low burial rates, corresponding to lower temperature history values, requires a much longer period of time (starting in sediments of Early Miocene age or older). The pattern is best illustrated by the power function showing a near steady upward trend when the $TZ_{A/CT}$ is found in younger sediments (a temperature history > 4 °C/Ma; Fig. 7.14), and a nearly-constant trend in older sediments (a temperature history < 1 °C/Ma). Some of the transition zones characterised by a low temperature evolution and a young age (younger than 14 Ma) that do not fit this opposing pattern of temperature and time can be characterised as likely-fossil candidates (circled data points in Fig. 7.14; also see Fig. 7.13). Although the present-day temperatures of the young fossilised $TZ_{A/CT}$ are low (Fig. 7.13), it is supposed that the palaeo-geothermal gradients of the sediment in which these transitions are contained were significantly higher than the present-day gradients (e.g., Davies and Cartwright, 2002). This supports the view that the rate of silica diagenesis prior to fossilisation was basically controlled by the palaeo-temperatures, and that these palaeo-geothermal gradients caused a rapid transformation from opal-A

to opal-CT (notice that the transformation occurred within young sediments at that time).

7.5.3.1 Thermal history: Case study

Given that silica diagenesis continues, over time, to advance upward above the active $TZ_{A/CT}$ and that increasing burial depth leads to higher temperatures (Langseth and Tamaki, 1992), a main control of this diagenetic process must be related to the host sediment temperature history. Reconstructing the thermal history of host sediments, on a case by case basis, can provide further evidence to support this idea.

This section focuses particularly on the geothermal history of the sediments in the Sea of Japan, recovered by ODP 794 and 795, where the depositional sections display a full spectrum of siliceous lithologies and silica minerals (e.g., Shipboard Scientific Party, 1990a, b) and where the geochemical and thermodynamic records suggest a currently-active $TZ_{A/CT}$ within these biosiliceous sediments (refer to Chapter 4). These two boreholes represent a relatively-uncomplicated natural laboratory to investigate the relation between temperature and time during silica diagenesis. It requires that the accumulation of biosiliceous sediments be nearly continuous with little or no removal of sediment overburden (see Chapter 4); the $TZ_{A/CT}$ (and hosting sediments) is thus currently at its maximum burial depth. As such, the present-day thermal gradient and the sediment accumulation rates under which the opal-A to opal-CT transformation occurs can be used to accurately reconstruct the thermal history. This reconstruction relied on the approach of

Mizutani (1970) (see Section 7.5.3).

The most striking aspect of this reconstruction is the rapid acceleration of the thermal history during Late Miocene in response to the peak rates of sedimentation in the biosiliceous interval just above the active $TZ_{A/CT}$ at Site 794 (Fig. 7.15).

In comparison, at Site 795 the temperature history values for the opal-A sediment unit above and across the $TZ_{A/CT}$ are higher than for Site 794, but are still in agreement with the high accumulation rates. The consistently-higher rates of sedimentation at Site 795 from the Late Miocene to Recent coupled with a higher geothermal gradient—relative to the sedimentation rates and geothermal gradient at Site 794—resulted in a greater burial temperature for sediment overlying the $TZ_{A/CT}$. Thus, at Site 795 maximum diagenetic silica concentrations occurred ca. 5 Ma after deposition, whereas at Site 794, opal-CT reached a peak concentration only after ca. 8 Ma post-deposition. Although it is noted that minor amounts of opal-CT were precipitated in the opal-A interval well above the $TZ_{A/CT}$, peak concentrations occurred only within the $TZ_{A/CT}$ (refer to Chapter 4 for a comprehensive review). The higher thermal gradient at Site 795 caused the $TZ_{A/CT}$ to reach its present-day depth faster than at Site 794.

7.5.4 Modelling of silica diagenesis

According to earlier works (e.g., Kastner et al., 1977), the transformation of opal-A to opal-CT requires the dissolution of siliceous tests into pore waters and

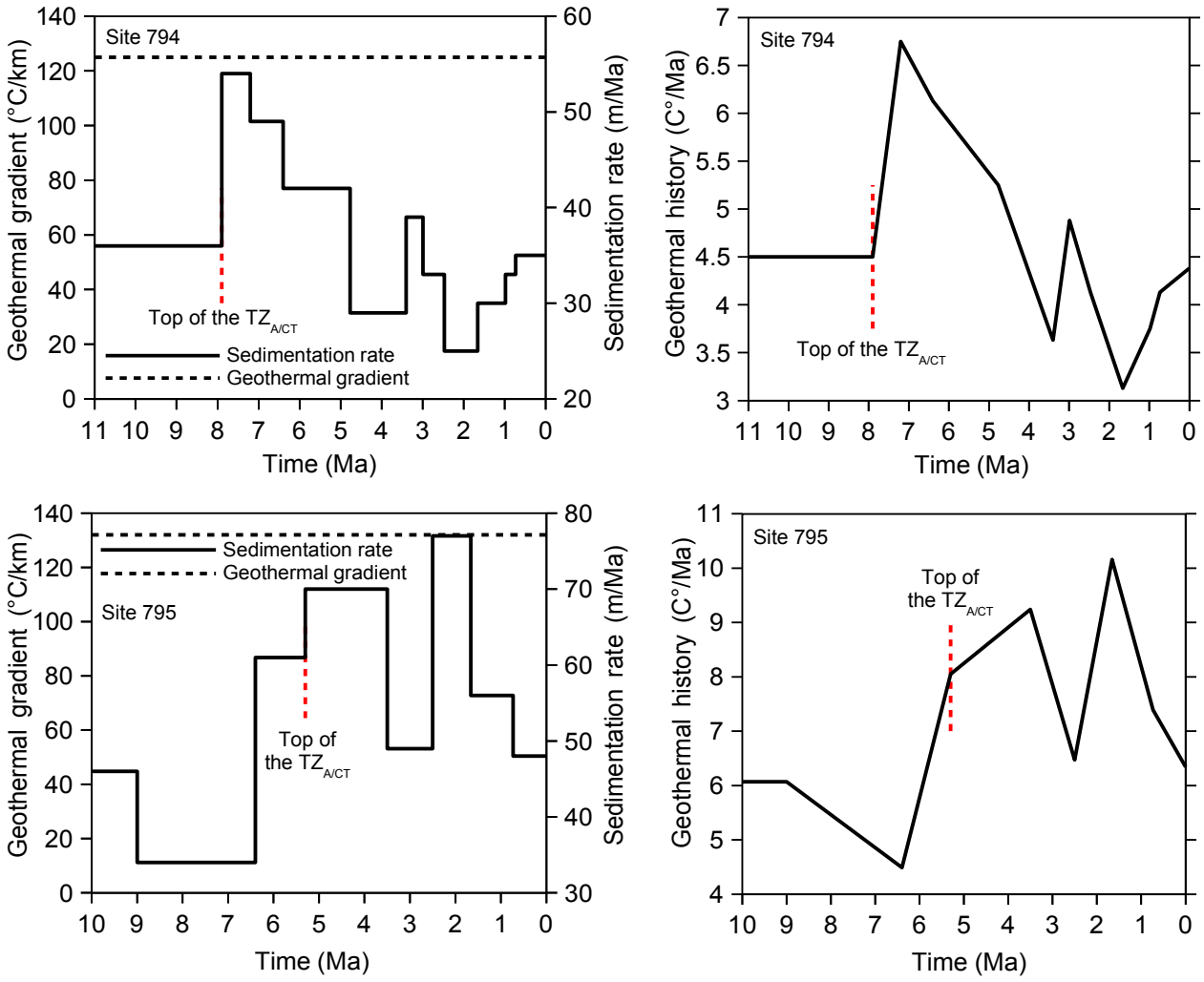


Figure 7.15. Reconstructed burial and thermal histories for the sediments hosting the $TZ_{A/CT}$ at Sites 794 and 795. The dotted red line marks the top of the $TZ_{A/CT}$. The numerical age of the sediments was derived from the depth profiles of diatom zones and magnetostratigraphic datum levels provided in the ODP 794 and 795 initial reports (see Shipboard Scientific Party, 1990a, b).

reprecipitation of the dissolved silica, as dispersed crystalline cristobalite, within the sediment matrix (Langseth and Tamaki, 1992). The precipitation of opal-CT is the target transformation process in silica diagenesis, and is substantially influenced by

the dissolution rate of biogenic silica that controls silicic acid concentrations being released into the pore water. The rate of diagenetic silica precipitation from aqueous solutions is a clear function of temperature and time (e.g., Littke et al., 1991; Kuramoto et al., 1992). The temperature-time dependence of this reaction can be described by the Arrhenius equation:

$$k = Ae^{\frac{-Ea}{RT}} \qquad (1.1)$$

where k is the first-order kinetic coefficient (in Ma^{-1}), A is the pre-exponential factor (7.18×10^{13} Ma^{-1} for dissolution of biogenic silica in the marine sediments, according to Icenhower and Dove, 2000), Ea is the activation energy (92000 J mol^{-1} for opal-A dissolution during later diagenesis, according to Wrona et al., 2017), R is the gas constant (8.314 J K^{-1} mol^{-1}), and T is the temperature (in K).

There are two key parameters in this equation: a) the pre-exponential factor that represents the frequency of collisions between reactant molecules (Chang, 2005), this being a function of temperature, and b) the apparent activation energy, which is the minimum amount of energy required to start the chemical reaction.

The kinetic coefficient, k, in the equation represents the transformation rate, and it describes how fast (time function) opal-A can be transformed into opal-CT at a given temperature. The first step toward the modelling of time-temperature dependent silica diagenesis is the evaluation of the silica transformation rate, which can be best

estimated by k values. The second step is to estimate the transformation ratio that represents the relative amount of opal-A transformed to opal-CT at a certain point. This reacted opal-A content can be extracted based on the first-order rate law:

$$A = A_0 e^{-kt} \qquad (1.2)$$

where A is the amount of biogenic silica at time $t \neq 0$ (in volume %), A_0 is the initial amount of biogenic silica (in volume %), k is the rate coefficient (in Ma^{-1}), and t is the elapsed time (in Ma).

The key parameters in the rate law equation are time and the transformation rate (k), clearly illustrating the relevance of time and temperature during silica diagenetic transformation.

The transformation ratio can then be simply calculated using equation $k' = 1 - (A/A_0)$, where k' is the transformation ratio and A/A_0 is the relative amount of unreacted opal-A.

The Arrhenius equation and the first-order reaction rate law were used to predict the transformation from opal-A to opal-CT in the sediments at ODP Sites 794 and 795. The values chosen for the key parameters in the Arrhenius equation seem reasonable as increased transformation rates are associated with higher temperatures (Fig. 7.16), a pattern that has been previously documented (e.g., Pisciotto, 1981a, b; Dralus et al., 2015). The model predictions of the type of variability of transformation ratios with

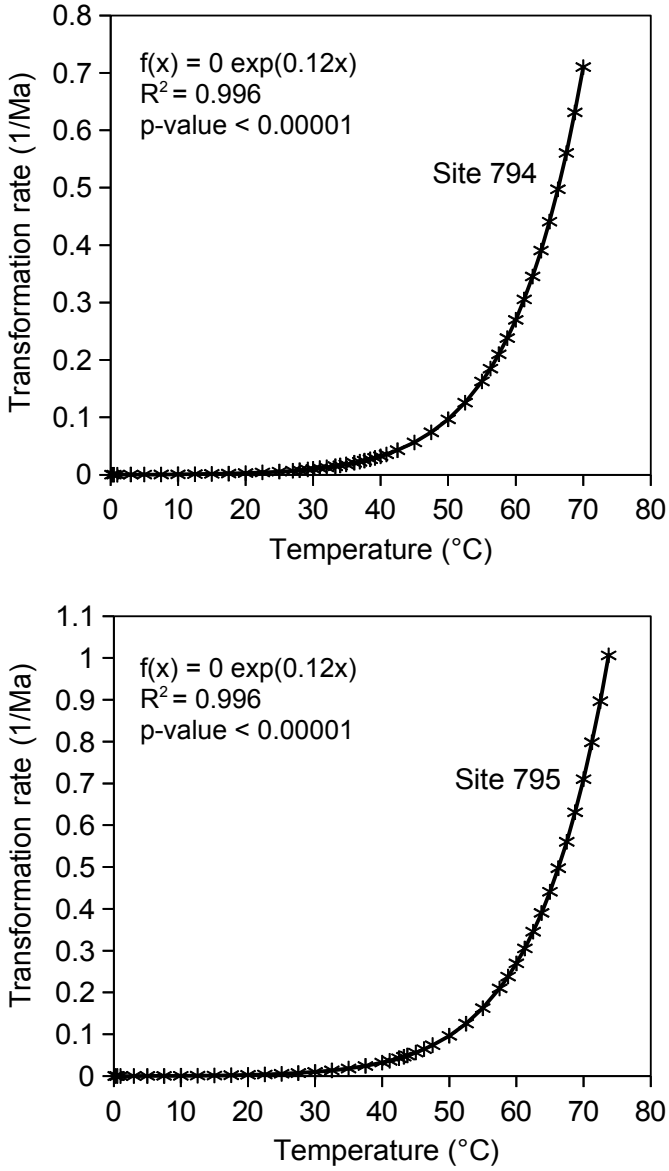


Figure 7.16. Calculated opal-A to opal-CT transformation rates versus *in situ* temperature measurements at ODP Sites 794 and 795.

temperature (Fig. 7.17A) closely mimics the previously-documented variabilities versus temperature (e.g., Dralus et al., 2015; Wrona et al., 2017). The temperatures of opal-A to opal-CT transformations also vary in the range of those established by reference silica diagenesis phase diagrams (Fig. 7.17B). This approach is further

validated by the match between the modelled and observed opal-A to opal-CT transformation ratios in the ODP Sites 794 and 795 (Figs. 7.17C, D).

An important result is the precision of the suggested transformation ratio model for predicting the temperature at the present-day depth of the $TZ_{A/CT}$. The model only slightly underpredicted the *in situ* $TZ_{A/CT}$ temperature at Site 794, being ~37 °C at 293.5 mbsf (the ODP-measured value at the comparable depth is 37.5 °C; Table 7.1), while precisely predicting the temperature for Site 795 (ODP estimate of 43.2 °C at 326 mbsf; Table 7.1). At Site 794, the model predicts opal-CT began precipitating in the biosiliceous facies above the $TZ_{A/CT}$ with almost 16% (which corresponds to the transformation ratio of 0.16, Fig. 7.17A) of opal-A converted into opal-CT prior to reaching the $TZ_{A/CT}$. At Site 795, this value was somewhat higher (22%). The low transformation ratios within the opal-A zone for both sites are due to low transformation rates of biogenic silica in this zone, where the burial heating is lower than that within the opal-CT zone (the $TZ_{A/CT}$ and the interval below up to the depth of the opal-CT to quartz transition). The slight difference in the transformation rates between these sites can be attributed to the warmer thermal history of Site 795. Though both values are low, the transformation rate above the $TZ_{A/CT}$ at Site 795 (being ~ 0.05 Ma^{-1}), is more than double that of the $TZ_{A/CT}$ at Site 794. At a greater depth, a significant increase in the reaction rate (Fig. 7.16) within the opal-CT zone —under increased burial heating—caused ~75% progress in the transformation at Site 795 (Fig. 7.17A), while the rate increase in the comparable interval from Site 794 promoted the opal-A to opal-CT ratio to about 0.63 (~45% progress). The

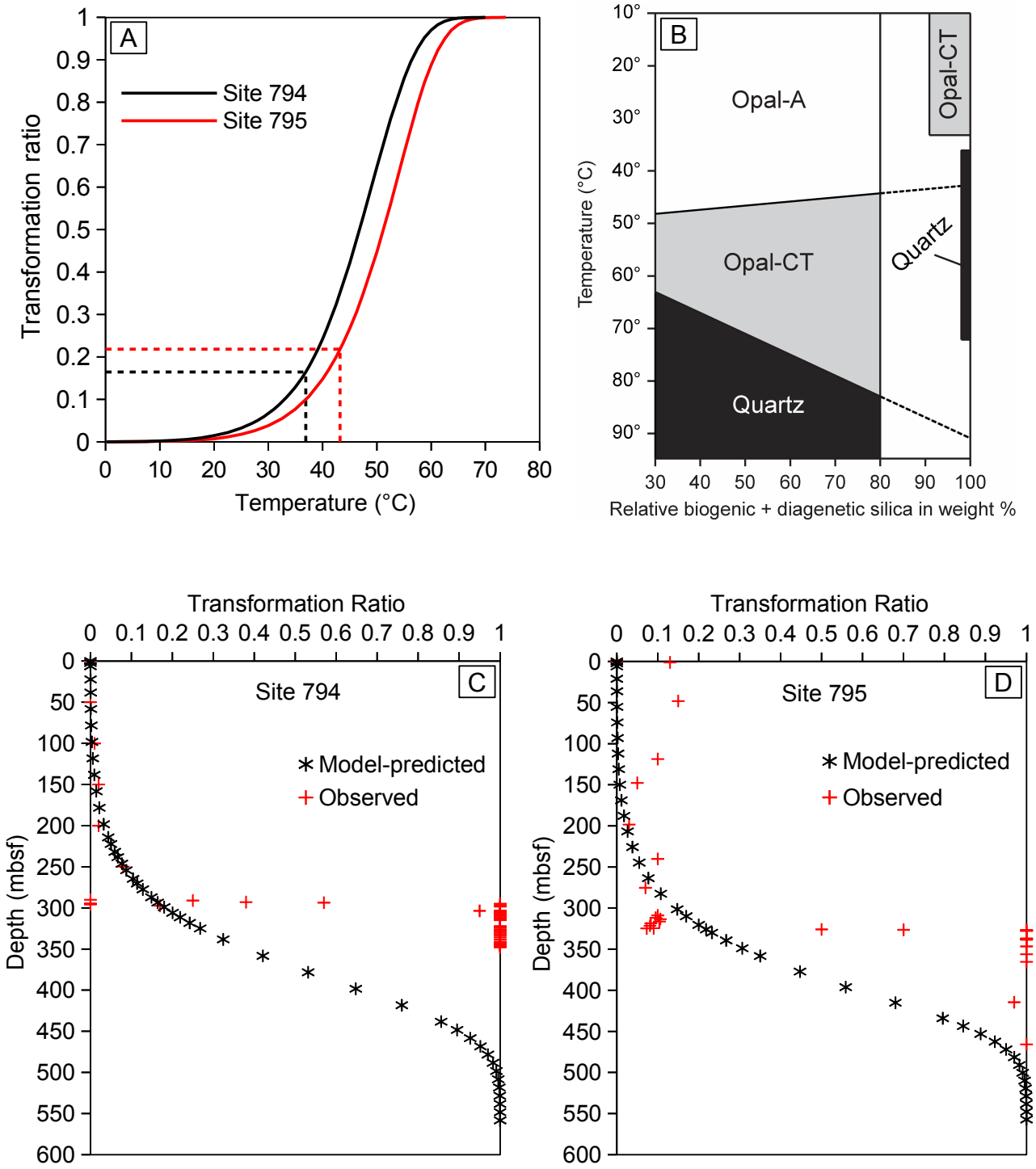


Figure 7.17. A) Modelled opal-A to opal-CT transformation at ODP Sites 794 and 795. Black and red dotted lines mark the coordinates of the $TZ_{A/CT}$ at Sites 794 and 795, respectively; B) Reference phase diagram for silica diagenesis (redrawn from Behl, 1999); C) Comparison between modelled and observed transformation ratios in

Site 794; D) Comparison of modelled and observed transformation ratios at Site 795. The observed transformation ratios plotted in Figures. 7.17C, D have been approximated by combining the results of smear-slide analyses (Chapter 5 and Appendix IV) and the results of the quantitative X-ray diffraction of the sediments from these two sites (Chapter 4) to determine the amount of biogenic and diagenetic silica within the sediment.

remarkably-warmer geothermal history of opal-CT zone in Site 795 as compared to that of Site 794 can account for a significant contrast between the amounts of reacted opal-A within this zone at these two sites. Following the deposition of biosiliceous sediments, transformation was completed within 9.5 Ma for Site 795, while ca. 14 Ma was required for the full opal-A to opal-CT conversion at Site 794 (Fig. 7.18). Although the peak concentrations of opal-CT occurred at the $TZ_{A/CT}$ 8 and 5.3 Ma following the sediment deposition at Sites 794 and 795, respectively (see Chapter 4), the transformation of opal-A to opal-CT was not fully complete until 14 Ma for Site 794 and 9.5 Ma for Site 795 after initial deposition.

Relating to the cooperative function of time and temperature in the silica diagenesis process, the strong correlation for opal-CT formation between temperature (present burial depth) and age (Fig. 7.18) suggests that thermal burial (present-day temperature) and sediment accumulation rates are the principal controls of the transformation ratio of opal-A to opal-CT.

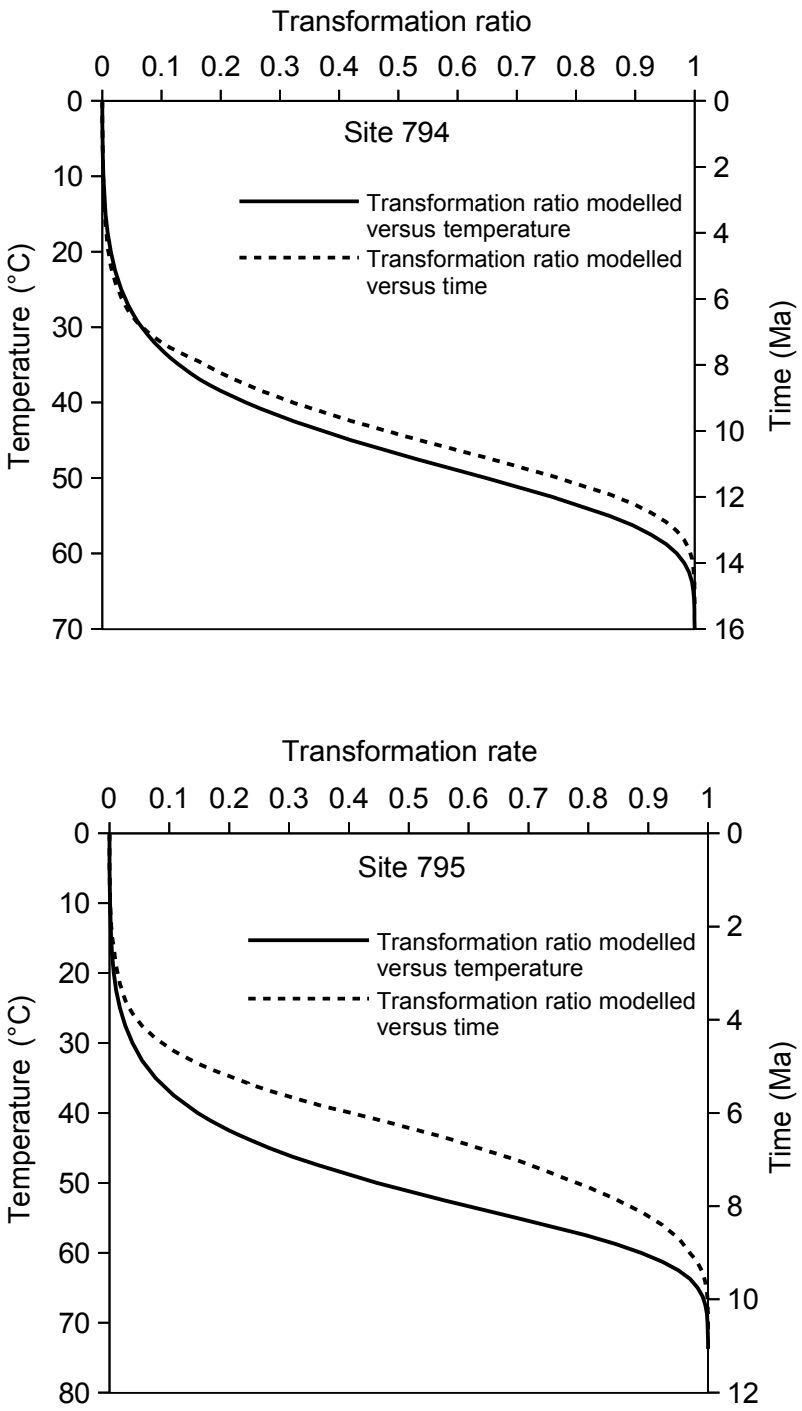


Figure 7.18. Modelled transformation of opal-A to opal-CT as a function of temperature and time. Sediment numerical ages were derived from the ODP 794 and 795 initial reports (see Shipboard Scientific Party, 1990a, b).

7.6 Conclusions

Based on an exploration of the ODP and DSDP database, 67 globally-distributed sites having an opal-A to opal-CT transition zone within Palaeocene- to Pliocene-aged sediments, were selected and examined for temperature-time relationships during silica diagenesis. The transition zone at these sites represents a narrow depth interval (up to 40 m in thickness) across which opal-A is transformed into opal-CT. This zone was recognised in down-core profiles by its association with dramatic petrophysical variations in the host sediment. Regardless of the dominant lithology in which the transition zone was found (e.g., clay- or carbonate-rich sediments), the observation that all transition zones were relatively narrow and that their thickness was correlated to present-day temperatures suggest that temperature is the leading control on the thickness of these diagenetic boundaries.

Through this work, I used data mined from the ODP and DSDP programmes to modify the reference temperature-time stability field of Hein et al. (1978) used for the initiation of opal-CT formation. This new diagenetic opal stability field is an extension of the original reference diagram, modified by adding the age and temperature data of the active transition zones and transitions with uncertain diagenetic status fitting the inverse temperature-age correlation determined in this study. The new stability field follows the widely-accepted pattern of temperature variability over time for biogenic silica progressive diagenesis, implying an inverse relationship between temperature and time, valid for all diagenetic processes. According to the extended stability field, ongoing silica diagenesis under shallow

burial occurs over 35 Ma at low temperatures (< 30 °C), within 3 Ma at moderate temperatures (35–55 °C), and rapidly, regardless of the burial depth, at higher temperatures (> 55 °C). However, most data points from this study do not fit the modified stability field. The transition zones at some of these borehole sites, characterised by very low temperatures and captured in young sediments (Middle Miocene or younger), are likely to represent currently-fossilised features.

The thermal history is a principal control on the rates at which the silica diagenetic transformations occur. The geothermal history is primarily a function of sediment accumulation and thermal gradient. The analysis of thermal history for the studied borehole sites suggests silica diagenesis occurs at high temperature gradients and high sedimentation rates in younger sediments (Middle Miocene and younger), while occurring over a longer time (Early Miocene and older) in sediments having low thermal gradients and lower rates of burial. Reconstruction of the temperature history of two representative wells having active transitions, ODP Sites 794 and 795, indicated that an accelerated thermal history during the Late Miocene and later occurred in response to the peak sedimentation rates in the opal-A interval overlying the transition zone. Compared to Site 794, ODP Site 795 had higher accumulation rates from the Late Miocene to Recent and a higher thermal gradient that resulted in a greater burial temperature for the opal-A sediment unit, leading to an earlier onset of the diagenetic transition zone.

The time and temperature dependent transformation of opal-A to opal-CT was

modelled for Sites 794 and 795 using fundamental kinetic principles. According to this model, the ratio of opal-A that is converted to opal-CT increased significantly within the opal-CT sediment interval below the transition zone, in comparison with the low precipitation of this mineral phase in the opal-A sediments above the transition zone. This was due to the higher burial temperature, and therefore higher transformation rates, in the opal-CT zone. One of the main findings based on this kinetic model is that although the peak levels of opal-CT were achieved across the transition zones at 8 and 5 Ma after initial biogenic silica deposition at Sites 794 and 795, respectively, the transformation of opal-A to opal-CT was not complete until 14 Ma (Site 794) and 9.5 Ma (Site 795) after initial sedimentation.

Chapter 8

Conclusions and future research

The present work addresses several challenging aspects of biogenic silica diagenetic studies. Above all, this study represents the first novel work on the applicability of inorganic pore-water chemistry as a potential tool to assess whether the diagenetic transformation of biogenic silica to opal-CT at the sub-seafloor locations is presently an ongoing reaction or it is arrested. Secondly, this research introduces textural and mineralogical evidence, derived from microscopic and XRD analyses on core samples obtained from the ODP Sites 794 and 795 in the Sea of Japan. These data unravel the poorly understood and controversial issue of linking the silica diagenetic processes to anomalous compaction (sudden petrophysical variations), especially porosity reductions, across the opal-A to opal-CT transition zone ($TZ_{A/CT}$). Thirdly, the empirical diagenetic models formulated in this work, based on the data from ODP sources, demonstrate the role of present-day bottom-water temperatures in early diagenetic reactions of opal-A for two dominant sediment types (i.e., detrital and carbonate). Finally, based on a compilation of wellbore data from the ODP and DSDP sites penetrating the $TZ_{A/CT}$ across which silica diagenesis is currently ongoing, the temperature-time relationships for biogenic silica diagenesis have been further constrained. This relationship was used to evaluate the thermal history and model the transformation of opal-A to opal-CT in the sediments penetrated by these scientific drilling projects. In summary, the integration of ODP- and DSDP-derived

data and new data generated in this study to investigate the associated chemical signatures of silica diagenesis in the interstitial water (Chapter 4), controls on the anomalous compaction (Chapter 5), temperature controls (Chapter 6), and temperature-time relations on transformation of biogenic to diagenetic silica (Chapter 7) represents a valuable approach to diagenetic studies. Figure 8.1 illustrates the connections between the headlines of research presented in this thesis (Chapters 4–7) and the pathway that links this research to basinal and environmental studies. The conclusions of this thesis are presented in the next section, followed by limitations of the data and methods employed by the present work, and a suggestion for future research.

8.1 Thesis conclusions

8.1.1 Conclusions of Chapter 4

- Interstitial-water inorganic chemistry was used as a powerful proxy to demonstrate that silica diagenesis over the $TZ_{A/CT}$ at the ODP Sites 794 and 795 in the Sea of Japan is still ongoing (i.e., active $TZ_{A/CT}$).

- The distribution of Neogene diatom ooze and the variations in pore-water dissolved silica concentration are stratigraphically correlated; implying that biogenic opal is the major source of silica released into the pore water.

- Mineralogy, pore-water chemistry, and thermodynamic analyses show that solubility equilibrium has been reached with respect to diagenetic opal in the $TZ_{A/CT}$; implying that opal-CT is currently precipitating.

- Although dissolved silica concentration may change due to the neoformation of

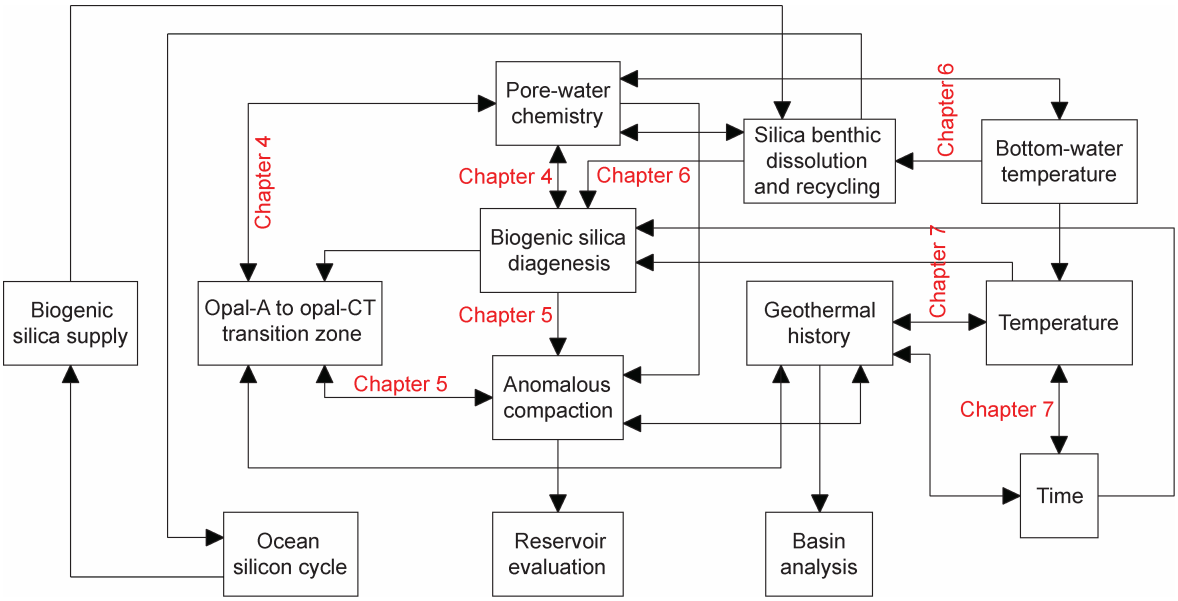


Figure 8.1. Connections between the research topics presented in this work, also their links to basinal and environmental research.

clay minerals, the pore-water saturation index corresponding to solubility equilibrium with respect to opal-CT suggests that the silica sink (drop) across the $TZ_{A/CT}$ is essentially controlled by an active biogenic silica diagenesis.

- The association of a sudden transition in the sediment petrophysics with opal-CT precipitation has caused ongoing silica diagenesis to significantly affect most of the pore-water chemistry profiles, including those for major ions and primary chemical indicators.

- The clustering of isotopic temperatures of opal-CT formation at Site 794 close to present-day sediment temperatures demonstrates that the $TZ_{A/CT}$ has equilibrated with the modern thermal gradient. At Site 795, isotopic temperatures are lower than temperatures at the depth of the $TZ_{A/CT}$ and the opal-CT-rich interval below it,

suggesting that the $TZ_{A/CT}$ has been rather rapidly buried and has yet to move towards equilibrium with the present-day thermal gradient.

- The significantly-low silica diffusion fluxes in the pore water and the low permeable nature of host sediment suggest that diffusion is a relatively-insignificant mechanism for precipitation of opal-CT in Sites 794 and 795. In turn, a considerable expulsion of pore water across the $TZ_{A/CT}$ suggests that the dissolved species have not been diffused in the sediment at rates comparable to those by pore-water advection. The advection, however, seems to have ceased to operate recently or it is functioning very slowly as it has clearly failed to eliminate the signatures of ongoing silica diagenesis.

- The abruptly-reduced porosity of biosiliceous sediments at the depth of the $TZ_{A/CT}$ in Sites 794 and 795 is related to a sudden anomalous compaction phenomenon as biogenic silica dissolves and undergoes transformation to opal-CT. This porosity drop occurs when the host sediment has undergone remarkable dissolution of biogenic opal losing its framework strength, allowing for the collapse of fine-grained sediment matrix. The porosity is further decreased through subsequent precipitation of opal-CT.

- Due to their significance for constraining the diagenetic drivers that cause anomalous compaction and for reconstructing the thermal history of depositional basins hosting silica diagenesis, the recognition and study of active $TZ_{A/CT}$ are considered an essential element of basin analysis.

8.1.2 Conclusions of Chapter 5

- Textural and mineralogical examination of opal-A and opal-CT sediments in Sites 794 and 795 indicates that biogenic and diagenetic silica are the two substantial components involved in the occurrence of anomalous compaction across the $TZ_{A/CT}$.

- Highly-porous structure of biogenic opal and its relative incompressibility as compared to the clay-dominated host sediment in Sites 794 and 795 result in a high porosity condition within the opal-A sediment unit.

- An abrupt decrease in opal-A content of the sediment within the $TZ_{A/CT}$ results from biosilica dissolution which causes failure in the strength of sediment matrix, sudden framework collapse, and therefore sharp porosity reduction.

- Owing to porosity drop, other physical properties, including bulk density, void ratio, and water content change at the $TZ_{A/CT}$ also a velocity increase following cementation of opal-CT across the $TZ_{A/CT}$.

- Quantitative mineralogical analysis of sediments in Sites 794 and 795 indicates that opal-CT content has a small influence on the host sediment porosity decrease, suggesting that opal-A dissolution contributes most to the initiation of anomalous compaction.

- Mineralogical analysis of the sediments from Sites 794 and 795 also suggests that the authigenisation of clay minerals and formation of zeolites are only a subsidiary control on silica diagenesis and its related porosity decrease.

- Due to hydrocarbon production from some opal-CT porcellanite and chert deposits associated with marked petrophysical changes, potential for silica diagenesis to generate anomalous compaction and its controlling factors are regarded key elements

in reservoir evaluation. The controls on anomalous compaction should be considered essential to understanding the implications on fluid flow, rock deformation, and thermal history, too.

8.1.3 Conclusions of Chapter 6

- The rates of silica early diagenetic processes, including dissolution rates of deposited opal-A and the benthic flux of produced silicic acid in the deep-sea position, were calculated for 22 ODP sites.
- Empirical models specified for two host sediment types—detrital and carbonate—were developed to predict variations in the dissolution rate and benthic flux of silica versus modern bottom-water temperatures. The most important variables in the models are the biogenic silica content of the benthic layer (for the benthic flux model), the kinetic coefficient, the asymptotic concentration of silicic acid in pore water, and bottom-water temperature.
- Variability in the dissolution rate and the benthic flux in relation to temperatures across the benthic layer is more distinct when the association of asymptotic concentration and kinetic coefficient with temperature is involved in the prediction of these parameters.
- A subtler increase in dissolution rates and benthic fluxes with temperature in detrital-dominated sediments as opposed to the large increases in these parameters for carbonate-hosted sites is due to the rate-limiting influence of detrital material because it significantly alters the solubility and reactivity of biogenic silica.
- The mismatch between the modelled dissolution rates and benthic fluxes in this

study and previous values obtained from other studies is due to the temperature differences and large discrepancies in sediment composition between this study and comparable works.

- Using the model expression for early diagenetic transformation of opal-A to opal-CT, the present study showed that there may be a relationship between the uncommon precipitation of opal-CT porcellanite and chert in near-surface sediments and bottom-water temperatures at some locations in the Antarctic deep-sea deposits. However, disagreement between the established models of inverse temperature-time relationship in silica diagenesis and precipitation of opal-CT at low temperatures (0–4 °C) over a geological time less than 4 Ma noticed for the Antarctic sediments suggests that temperature cannot be a major control. It seems that age plays a critical role in this situation via influencing the solubility and surface area of opal. Since the solubility and surface area both decrease with age, a < 4 Ma elapsed time has been sufficient for opal-A to age to the point of its minimum solubility, which possibly allows for opal-CT earlier precipitation near the seabed.

- Due to its importance for silica phase change reactions that occur deeper in the sediment and its major contribution to the nutrient silicon cycle in the world ocean, dissolution and recycling of dissolved silica in the benthic zone is regarded a critical component of biogenic silica diagenesis and silicon biogeochemical cycles.

8.1.4 Conclusions of Chapter 7

- 67 representative ODP and DSDP wells from various geographic locations where the $TZ_{A/CT}$ is hosted by Palaeocene to Pliocene deep-sea sediments allowed the

examination of temperature-time relationships during silica diagenesis.

- The $TZ_{A/CT}$ in these sites represents a narrow interval (≤ 40m) across which biogenic silica is transformed into opal-CT and was recognised in the sub-seafloor locations by its association with sudden changes in the physical state of host sediment.

- The thickness of the diagenetic transition zones involved in this study and its correlation with the present-day temperatures support temperature as the main control on the $TZ_{A/CT}$ thickness.

- The present study developed a new temperature-time stability field for the initiation of opal-CT formation mainly using the age and temperature data from the diagenetic transition zones believed to be presently the most likely active candidates. The new stability field follows the widely-accepted pattern of inverse correlation between temperature and time that is valid for all diagenetic processes.

- Based on the extended stability field, during shallow burial silica diagenesis takes place at low temperatures (< 30 °C) over 35 Ma, at moderate temperatures (35–55 °C) within 3 Ma, and at high temperatures (> 55 °C) occurs rapidly regardless of the depth of burial. Most of the temperature-time data points in this study do not fit the modified stability field, and at some of these sites the transition zones with very low temperature and young age (Middle Miocene and younger) are likely to be currently fossilised.

- This study demonstrated that the thermal history is the leading control on rate of silica diagenetic transformation. The analysis of thermal history for the borehole sites from this study suggested the occurrence of silica diagenesis at high thermal gradients and high sedimentation rates in younger sediments (Middle Miocene and

younger), while over a longer time (Early Miocene and older) in sediments with low thermal gradients and low burial rates.

- Temperature-time dependent transformation of opal-A to opal-CT was modelled for Sites 794 and 795 using kinetic principles. Compared to the opal-A unit, the ratio of opal-A converted to opal-CT highly increased in the opal-CT interval due to a higher burial heating and therefore a higher transformation rate reached in this zone. Though the peak amounts of opal-CT were reached across the $TZ_{A/CT}$ 8 and 5 Ma following the deposition at Sites 794 and 795, respectively, the transformation of opal-A to opal-CT did not go completion until 14 and 9.5 Ma had elapsed from the initiation of opal-A deposition.

- The review of temperature and time relationships in silica diagenesis should be considered as an essential component for the analysis of the geothermal evolution of depositional basins hosting biosiliceous sediments.

8.2 Research limitations

Integration of the information derived from open accessed ODP and DSDP databank mining and the results of textural and mineralogical analyses conducted on discrete core samples obtained from Sites 794 and 795 allowed for researching some significant aspects of silica diagenesis under remit of this D.Phil. work. Nevertheless, there have been specific limitations for the results Chapters 4, 5, and 6 of this thesis that are discussed below.

While XRD determined well the presence and abundance of diagenetic silica in the

core samples obtained from Sites 794 and 795, it could not detect the presence of non-crystalline material, including opal-A and volcanic ash in the sediment. Amongst these, opal-A is a key component of silica diagenetic reactions, and therefore Chapters 4 and 5 had to rely on the results of smear-slides analysis to determine the amount of biogenic silica in the samples. Another impediment to Chapters 4 and 5 was the lack of core samples from the first 100 mbsf at Site 794 as the main working-half section had no longer any material. To compensate this drawback, required data related to this depth interval were derived from the ODP sources. Also, an incomplete velocity profile in Site 795 did not allow for its accurate correlation with stratigraphic units and the determination of $TZ_{A/CT}$ thickness using velocity in Chapter 5.

Chapter 6 is based on the study of only a limited number of ODP wells drilling the Neogene sediments that host diagenetic silica of 22 sites total. This is because the relevant data needed for evaluation of bottom-water temperature controls on silica diagenetic reactions and for modelling approach were only available for a restricted number of the boreholes penetrating Neogene silica diagenesis. In addition, the data required for the purpose of this chapter (especially bottom-water chemical data) were mostly absent for the DSDP wells. However, based on lithology, petrophysical properties, and seismic data, it was considered that these selected 22 ODP sites are broadly representative of the $TZ_{A/CT}$ in the Neogene sub-seafloor deposits.

8.3 Future outlook

The aim of conducting the present project was to develop the knowledge around some poorly understood, and at the same time, challenging aspects of biogenic silica diagenesis, such as pore-water chemical signatures of active silica diagenesis, controls on anomalous compaction, bottom-water temperature controls on silica early diagenesis reactions, and temperature-time relationships for silica later diagenesis. The outcome of this work is considered a complement to former research focused on biogenic silica diagenesis using core samples analysis, experimental, and outcrop studies. The results of this thesis provide the basis for future studies on the complicated process of silica diagenesis in the deep-sea settings. The paragraph below makes a suggestion for future research.

Textural and geochemical characterisation of the opal-CT to microcrystalline quartz transition ($TZ_{CT/Q}$) that develops below the $TZ_{A/CT}$ deeper in the sediment column is suggested as an interesting topic for future work as, to the author's knowledge, so far very little work has been conducted on the $TZ_{CT/Q}$ (e.g., Dralus et al., 2011), and independent research particularly concentrated on internal structure, mineralogy, and or geochemistry of this depth interval are absent in the literature. The paucity of research on the $TZ_{CT/Q}$ simply arises from the difficulty of recognising this diagenetic boundary in the subsurface positions. Due to its very limited thickness (commonly less than 3 m thick, modified after Nobes et al., 1992) as compared to the much higher thickness of the $TZ_{A/CT}$ (tens of m thick) and the fact that this boundary is not commonly represented by an identifiable reflection on seismic profiles, the $TZ_{CT/Q}$

cannot be easily recognised. However, petrophysical variations associated with the $TZ_{CT/Q}$, though less significant than those noticed across the $TZ_{A/CT}$, allow for the recognition of this boundary on the physical properties profiles. In addition, this interval has been penetrated and sampled by some ODP wells worldwide (e.g., ODP Legs 127 and 128), and its location in these scientific boreholes has been determined. Therefore, the boundary can be investigated for its textural and geochemical features. Researching the characteristics of this diagenetic transition zone is of great significance for petroleum exploration and basin modelling. The permeability increases during the transformation of opal-CT to microcrystalline quartz (Reid and McIntyre, 2001) may result in diagenetic seals and stratigraphic traps for petroleum where no structural traps exist (Grau et al., 2003; Kidney et al. 2003; Peters et al., 2011). The locations of these diagenetic traps can be predicted using a basin modelling approach. The kinetics of opal-CT to quartz phase transformation reaction is a key component in basin modelling for identifying and predicting the type of diagenetic trapping (Dralus et al., 2011).

References

Abe, K., and Kanamori, H. 1970. Mantle structure beneath the Japan Sea as revealed by surface wave, *Tokyo Daigaku Jishin Kenkyusho Iho*, v. 48, p. 1011–1021.

Arrhenius, S. 1889. Über die Reaktionsgeschwindigkeit bei der Inversion von Rohrzucker durch Säuren, *Zeitschrift für Physikalische Chemie*, v. 4, p. 226–248.

Atkins, P., and de Paola, J. 2006. Physical Chemistry (8th Edition), Oxford University Press, Oxford, 1149 p.

Behl, R. J. 1992. Chertification in the Monterey Formation of California and Deep-Sea Sediments of the West Pacific, PhD thesis, University of California, Santa Cruz, 287 p.

Behl, R. J. 1999. Since Bramlette (1946): The Miocene Monterey Formation of California revisited. *In* Moores, E. M., Sloan, D., and Stout, D. L. (Eds.), Classic Cordilleran Concepts: A View from California, Geological Society of America Special Papers, v. 338, p. 301–313.

Behl, R. J., and Garrison, R. E. 1994. The origin of chert in the Monterey Formation of California (USA). *In* Iijima, A., Abed, A., and Garrison, R. (Eds.), Siliceous, phosphatic and glauconitic sediments of the Tertiary and Mesozoic, Proceedings of the 29th International Geological Congress, Part C, Utrecht, The Netherlands, p. 101–

132.

Berndt, C., Bunz, S., Clayton, T., Mienert, J., and Saunders, M. 2004. Seismic character of bottom simulating reflectors: examples from the mid-Norwegian margin, *Marine and Petroleum Geology*, v. 21, p. 723–733.

Berner, R. A. 1980. Early Diagenesis: A Theoretical Approach, Princeton University Press, Princeton, 241 p.

Bethke, C. M., and Yeakel, S. 2016. The Geochemist's Workbench®, Release 11: GWB Essentials Guide, Aqueous Solutions LLC, Champaign, Illinois, 188 p.

Bidle, K. D., and Azam, F. 1999. Accelerated dissolution of diatom silica by marine bacterial assemblages, *Nature*, v. 397, p. 508–512.

Bjørlykke, K., Jahren, J., Mondol, N., Hellevang, H., and Aagaard, P. 2017. Mechanical Compaction of Sand and Clay: Constraints From Experimental Compaction, Chemical Reactions and Fluid Flow During Burial – An Overview, Search and Discovery Article #90291, American Association of Petroleum Geologists Annual Convention and Exhibition, Houston, Texas.

Blum, P. 1997. Physical properties handbook: A guide to the shipboard measurement of physical properties of deep-sea cores, Ocean Drilling Program, Texas A&M University, Technical Note 26, 117 p.

Boggs, S. 2009. Petrology of Sedimentary rocks (2nd Edition), Cambridge University

Press, Cambridge, 600 p.

Bohrmann, G. 1986. Accumulation of biogenic silica and opal dissolution in upper Quaternary Skagerrak sediments, *Geo-Marine Letters*, v. 6, p. 165–172.

Bohrmann, G., Abelmann, A., Gersonde, R., Hubberten, H., and Kuhn, G. 1994. Pure siliceous ooze, a diagenetic environment for early chert formation, *Geology*, v. 22, p. 207–210.

Bohrmann, G., Kuhn, G., Abelmann, A., Gersonde, R., and Fütterer, D. 1990. A Young Porcellanite Occurrence from the Southwest Indian Ridge, *Marine Geology*, v. 92, p. 155–163.

Bohrmann, G., Spiess, V. , Hinze, H., and Kuhn, G. 1992. Reflector Pc a prominent feature in the Maud Rise sediment sequence (eastern Weddell Sea) Occurrence, regional distribution and implications to silica diagenesis, *Marine Geology*, v. 106 , p. 69–87.

Botz, R., and Bohrmann, G. 1991. Low-temperature opal-CT precipitation in Antarctic deep-sea sediments: evidence from oxygen isotopes, *Earth and Planetary Science Letters*, v. 107, p. 612–617.

Bragg, W. H., and Bragg, W. L. 1913. The Reflexion of X-rays by Crystals, *Proceedings of the Royal Society of London Series A*, v. 88, p. 428–438.

Brekke, H. 2000. The Tectonic Evolution of the Norwegian Sea Continental Margin

with Emphasis on the Vøring and Møre Basins, *Geological Society Special Publications*, v. 167, p. 327–378.

Celaya, M., and McCabe, R. 1987. Kinematic model for the opening of the Sea of Japan and the bending of the Japanese Islands, *Geology*, v. 15, p. 53–57.

Chaika, C. 1998. Physical Properties and Silica Diagenesis, PhD thesis, Stanford University, 130 p.

Chaika, C., and Dvorkin, J. 1997. Ultrasonic velocities of opaline rocks undergoing silica diagenesis, *Geophysical Research Letters*, v. 24, p. 2039–2042.

Chaika, C., and Dvorkin, J. 2000. Porosity reduction during diagenesis of diatomaceous rocks, *American Association of Petroleum Geologists Bulletin*, v. 84, p. 1173–1184.

Chaika, C., and Williams, L. A. 2001. Density and mineralogy variations as a function of porosity in Miocene Monterey Formation oil and gas reservoirs in California, *American Association of Petroleum Geologists Bulletin*, v. 85, p. 149–167.

Chang, R. 2005. Physical Chemistry for the Biosciences, University Science Books, Sausalito, California, 772 p.

Chinzei, K. 1986. Opening of the Japan Sea and marine biogeography during the Miocene, *Journal of geomagnetism and geoelectricity*, v. 38, p. 487–494.

Chough, S. K., Lee, H. J., and Hoon, S. H. 2000. Marine Geology of Korean Seas (2nd Edition), Elsevier, Amsterdam, 313 p.

Chung, F. H., and Smith, D. K. 2000. The Practice of Diffraction Analysis. *In* Chung, F. H., and Smith, D. K. (Eds.), Industrial Applications of X-Ray Diffraction, Marcel Dekker, New York, p. 13–35.

Chung, S. l., Lee, T. Y., Lo, C. H., Wang, P. L., Chen, C. Y., Yem, N. T., Hoa, T. T., and Wu, G. Y. 1997. Intraplate extension prior to continental extrusion along the Alao Shan-Red River shear zone, *Geology*, v. 25, p. 311–314.

Compton, J. S. 1991a. Origin and Diagenesis of Clay Minerals in the Monterey Formation, Santa Maria Basin Area, California, *Clay and Clay Minerals*, v. 39, p. 449–466.

Compton, J. S. 1991b. Porosity reduction and burial history of siliceous rocks from the Monterey and Sisquoc Formation, Point Pedernales area, California, *Geological Society of America Bulletin*, v. 103, p. 625–636.

Core Photos. 2014. *In* International Ocean Discovery Program, Accessed 20 January 2015, http://web.iodp.tamu.edu/janusweb/imaging/photo.shtml

Damby, D. E., Llewellin, E. W., Horwell, C. J., Williamson, B. J., Najorka, J., Cressey, G., and Carpenter, M. A. 2014. The α–β phase transition in volcanic cristobalite, *Journal of Applied Crystallography*, v. 47, p. 1205–1215.

Davies, R. J. 2005. Differential compaction and subsidence in sedimentary basins due to silica diagenesis: A case study, *Geological Society of America Bulletin*, v. 117, p. 1146–1155.

Davies, R. J., and Cartwright, J. 2002. A fossilized Opal A to Opal C/T transformation on the northeast Atlantic margin: Support for a significantly elevated palaeogeothermal gradient during the Neogene?, *Basin Research*, v. 14, p. 467–486.

Davies, R. J., Goulty, N. R., and Meadows, D. 2008. Fluid flow due to the advance of basin-scale silica reaction zones, *Geological Society of America Bulletin*, v. 120, p. 195–206.

De Carlo, E. H. 1992. Geochemistry of pore water and sediments recovered from the Exmouth Plateau. *In* von Rad, U., Haq, B. U., et al. (Eds.), Proceedings of the Ocean Drilling Program, Scientific Results, College Station, Texas, v. 122, p. 295–308.

DeMaster, D. J. 2001. Marine silica cycle. *In* Steele, J. H., Thorpe, S. A., and Turekian, K. K. (Eds.), Encyclopedia of Ocean Sciences, Academic Press, San Diego, p. 1659–1667.

DeMaster, D. J. 2003. The Diagenesis of Biogenic Silica: Chemical Transformations Occurring in the Water Column, Seabed, and Crust. *In* Holland, H. D., and Turekian, K. K. (Eds.), Treatise on Geochemistry, v. 7, p. 87–98.

de Wolff, P. M., and Visser, J. W. 1964. Absolute Intensities—Outline of a Recommended Practice, Report 641.109, Technisch Physische Dienst, Delft,

Holland.

Deyhle, A., Kopf, A., Frape, S., and Hesse, R. 2004. Evidence for fluid flow in the Japan Trench forearc using isotope geochemistry (Cl, Sr, B): results from ODP Site 1150, *The Island Arc,* v. 13, p. 258–270.

Dillon, W. P., Lee, M. W., Fehlhaber, K. and Coleman, D. F. 1993. Gas hydrates on the Atlantic margin of the United States - controls on concentration. *In* Howell, D. G. (Ed.), The Future of Energy Gases, U.S. Geological Survey Professional Paper 1570, p. 313–330.

Dixit, S., and Van Cappellen, P. 2003. Predicting benthic fluxes of silicic acid from deep-sea sediments, *Journal of Geophysical Research: Oceans*, v. 108, No. C10, 3334, doi: 10.1029/2002JC001309.

Dixit, S., Van Cappellen, P., and van Bennekom, A. J. 2001. Processes controlling solubility of biogenic silica and pore water build-up of silicic acid in marine sediments, *Marine Chemistry*, v. 73, p. 333–352.

Dove, P. M. 1999. The dissolution kinetics of quartz in aqueous mixed cation solutions, *Geochimica et Cosmochimica Acta*, v. 63, p. 3715–3727.

Dove, P. M., and Crerar, D. A. 1990. Kinetics of quartz dissolution in electrolyte solutions using a hydrothermal mixed flow reactor, *Geochimica et Cosmochimica Acta*, v. 54, p. 955–969.

Dove, P. M., and Elston, S. F. 1992. Dissolution kinetics of quartz in sodium-chloride solutions – analysis of existing data and a rate model for 25-Degrees-C, *Geochimica et Cosmochimica Acta*, v. 56, p. 4147–4156.

Dove, P. M., and Nix, C. J. 1997. The influence of the alkaline earth cations, magnesium, calcium, and barium on the dissolution kinetics of quartz, *Geochimica et Cosmochimica Acta*, v. 61, p. 3329–3340.

Dove P. M., and Rimstidt. J. D. 1994. Silica-water interactions. *In* Heaney, P. J., Prewitt, C. T., and Gibbs, G. V. (Eds.), Silica: Physical behavior, geochemistry, and materials applications, Reviews in Mineralogy, Mineralogical Society of America, Washington, v. 29, p. 259–308.

Dralus, D., Lewan, M. D., and Peters, K. 2015. Kinetics of the Opal-A to Opal-CT Phase Transition in Low- and High-TOC Siliceous Shale Source Rocks, American Association of Petroleum Geologists Annual Convention & Exhibition, Denver, Colorado.

Dralus, D., Peters, K. E., Lewan, M. D., Schenk, O., Herron, M., and Tsuchida, K. 2011. Kinetics of the Opal-CT to Quartz Phase Transition Control Diagenetic Traps in Siliceous Shale Source Rock from the San Joaquin Basin and Hokkaido, American Association of Petroleum Geologists Search and Discovery Article #40771.

Dugdale, R. C., and Wilkerson, F. P. 1998. Silicate regulation of new production in the equatorial Pacific upwelling, *Nature*, v. 391, p. 270–273.

Edmond, J. M., Jacobs, S. S., Gordon, A. L., Mantyla, A. W., and Weiss, R. F. 1979. Water column anomalies in dissolved silica over opaline pelagic sediments and the origin of the deep silica maximum, *Journal of Geophysical Research: Oceans*, v. 84, p. 7809–7826.

Emeis, K.-C., Morse, J. W., and Mays, L. L. 1991. Organic carbon, reduced sulfur, and iron in Miocene to Holocene upwelling sediments from the Oman and Benguela upwelling systems. *In* Prell, W. L., Niitsuma, N., et al. (Eds.), Proceedings of the Ocean Drilling Program, Scientific Results, College Station, Texas, v. 117, p. 517–527.

Emerson, S. R., and Hedges, J. I. 2008. Chemical Oceanography and the Marine Carbon Cycle, Cambridge University Press, Cambridge, 453 p.

Erez, J., Takahashi, K., and Honjo, S. 1982. In-situ dissolution experiment of radiolaria in the central North Pacific ocean, *Earth and Planetary Science Letters*, v. 59, p. 245–254.

Ernst, W. G., and Calvert, S. E. 1969. An experimental study of the recrystallization of porcelanite and its bearing on the origin of some bedded cherts, *American Journal of Science*, v. 267A, p. 114–133.

Fabricius, I. L. 2012. Pore Size and Permeability of Experimentally Compacted Smectire and Kaolinite Clay. Permeability and Elastic Moduli. Proceedings of Third EAGE Shale Workshop Shale Physics and Shale Chemistry.

Fisher, A. T., and Becker, K. 1993. A guide to ODP tools for downhole measurements, Ocean Drilling Program, Texas A&M University, Technical Note 10 (Revised), 131 p.

Flörke, O. W. 1955. Zur Frage des "Hoch"-Cristobalit in Opalen, Bentoniten und Gläsern. *Nenes Jahrbuch for Mineralogie, Monatshefte*, Heft 10, p. 217–223.

Flörke, O. W., Hollmann, R., von Rad, U., and Rösch, H. 1976. Intergrowth and twinning in opal-CT lepispheres, *Contributions to Mineralogy and Petrology*, v. 58, p. 235–242.

Flower, M., Tamaki, K., and Hoang, N. 1998. Mantle extrusion: a model for dispersed volcanism and DUPAL-like asthenosphere in east Asia and the western Pacific. *In* Flower, M. F. J., Chung, S. L., Ho, C. H., and Lee, T. Y. (Eds.), Mantle Dynamics and Plate Interactions in East Asia, American Geophysical Union, p. 67–86.

Fournier, R. O., and Rowe, J. J. 1962. The solubility of cristobalite along the three-phase curve, gas plus liquid plus cristobalite, *American Mineralogist*, v. 47, p. 897–902.

Friedman, I., and O'Neil, J. R. 1976. Compilation of stable isotope fractionation factors of geochemical interest. *In* Fleischer, M. (Ed.), Data of Geochemistry (6th Edition), United States Geological Survey, Professional Paper 440–KK.

Fütterer, D. K. 2006. The solid phase of marine sediments. *In* Schulz, H. D., and

Zabel, M. (Eds.), Marine Geochemistry, Springer Verlag, Berlin-Heidelberg, p. 1–25.

Fukao, Y., and Furamoto, M. 1975. Mechanism of large earthquakes along the eastern margin of the Japan Sea, *Tectonophysics*, v. 25, p. 247–266.

Gallinari, M., Ragueneau, O., Corrin, L., DeMaster, D. J., and Tréguer, P. 2002. The importance of water column processes on the dissolution properties of biogenic silica in deep-sea sediments I. Solubility, *Geochimica et Cosmochimica Acta*, v. 66, p. 2701–2717.

Gehlen, M., Malschaert, H., and Van Raaphorst, W. R. 1995. Spatial and temporal variability of benthic silica fluxes in the southeastern North Sea, *Continental Shelf Research*, v. 15, p. 1675–1696.

Gieskes, J. M. 1983. The chemistry of interstitial waters of deep-sea sediments: interpretation of deep-sea drilling data. *In* Riley, J. P., and Chester, R. (Eds.), Chemical Oceanography, v. 8, Academic Press, London, p. 221–269.

Gieskes, J. M., Gamo, T., and Brumsack, H. 1991. Chemical Methods for Interstitial Water Analysis aboard JOIDES Resolution, Ocean Drilling Program, Texas A&M University, Technical Note 15, 60 p.

Giles, M. R. 1997. Diagenesis: A Quantitative Perspective, Kluwer Academic Publishers, Dordrecht, The Netherlands, 526 p.

Gnibidenko, H. 1979. The tectonics of the Japan Sea, *Marine Geology*, v. 32, p. 71–87.

Google Earth Pro 7.3. 2017. Sea of Japan, 38° 52' 54.17"N and 135° 00' 43.46"E. Available from google.co.uk/intl/en_uk/earth

Graetsch, H . , Flörke, O. W., and Miehe, G. 1987. Structural defects in microcrystalline silica, *Physics and Chemistry of Minerals*, v. 14, p. 249–257.

Grau, A. R., Sterling, R., and Kidney, R. 2003. Success! Using seismic attributes and horizontal drilling to delineate and exploit a diagenetic trap, Monterey Shale, San Joaquin Valley, California, American Association of Petroleum Geologists Search and Discovery Article #20011.

Guerin, G., and Goldberg, D. 1996. Acoustic and elastic properties of calcareous sediments across a siliceous diagenetic front on the eastern U.S. continental slope, *Geophysical Research Letters*, v. 23, p. 2697–2700.

Hamilton, E. L. 1976. Shear-wave velocity versus depth in marine sediments; a review, *Geophysics*, v. 41, p. 985–996.

Hawkings, J. R., Wadham, J. L., Benning, L. G., Hendry, K. R., Tranter, M., Tedstone, A., Nienow, P., and Raiswell, R. 2017. Ice sheets as a missing source of silica to the polar oceans, *Nature Communications*, v. 8, doi:10.1038/ncomms14198.

Hay, R. L. 1963. Stratigraphy and zeolitic diagenesis of the John Day Formation of

Oregon, *University of California Publications in Geological Sciences*. v. 42, p. 199–262.

Hayakawa, H., and Takemura, A. 1987. The Neogene system in the Yatsuo area Toyama Prefecture, central Japan, *The Journal of the Geological Society of Japan*, v. 93, p. 717–732.

Hayashida, A., and Ito, Y. 1984. Paleoposition of Southwest Japan at 16Ma: Implication from paleomagnetism on the Miocene Ichishi Group, *Earth and Planetary Science Letters*, v. 68, p. 335–342.

Hedges, J. I., and Keil, R. G. 1995. Sedimentary organic matter preservation: An assessment and speculative synthesis, *Marine Chemistry*, v. 49, p. 81–115.

Hein, J. R., and Parrish, J. T. 1987. Distribution of siliceous deposits in space and time. *In* Hein, J. R. (Ed.), Siliceous Sedimentary Rock-Hosted Ores and Petroleum, Van Nostrand Reinhold, New York, p. 10–57.

Hein, J. R., Scholl, D. W., Barron, J. A., Jones, M. G., and Miller, J. 1978. Diagenesis of late Cenozoic diatomaceous deposits and formation of the bottom simulating reflector in the southern Bering Sea, *Sedimentology*, v. 25, p. 155–181.

Hendry, K. R., and Andersen, M. B. 2013. The zinc isotopic composition of siliceous marine sponges: Investigating nature's sediment traps, *Chemical Geology*, v. 354, p. 33–41.

Hesse, R. 1986. Hydrochemistry, origin and evolution of sedimentary subsurface fluids: I. Early diagenetic pore-water evolution in low-sedimentation rate offshore basins, *Chinese Journal of Geochemistry*, v. 5, p. 297–319.

Hesse, R. 1988. Origin of chert. I: Diagenesis of biogenic siliceous sediments, *Geosciences Canada*, v. 15, p. 171–192.

Hesse, R., and Schacht, U. 2011. Early diagenesis of deep-sea sediments. *In* Hüneke, H., Mudler, T., et al. (Eds.), Deep-sea sediments, Developments in Sedimentology, v. 63, Elsevier, Amsterdam, p. 557–713.

Hilde, T. W. C., and Wageman, J. M. 1975. Structure and origin of the Japan Sea. *In* Coleman, P. J. (Ed.), The Western Pacific, Island Arcs, Marginal Seas, Geochemistry, University of Western Australia Press, p. 415–434.

Hinman, N. W. 1987. Organic and inorganic chemical controls on the rates of silica diagenesis: a comparison of a natural system with experimental results, PhD thesis, University of California, San Diego, 381p.

Hinman, N. W. 1998. Sequences of silica phase transitions: effects of Na, Mg, K, Al, and Fe ions, *Marine Geology*, v. 147, p. 13–24.

Hirata, N., Karp, B. Y., Yamaguchi, T, Kanazawa, T, Suyehiro, K., Kasahara, J., Shiobara, H., Shinohara, M., Koresawa, S., and Kinoshita, H. 1991. Seismic structure of the Japan basin in the Japan Sea by the 1990 Japan–USSR expedition, Abstract, IUGG 20th Symposium, Ull.

Hirata, N., Tokuyama, H., and Chung, T. W. 1989. An anomalously thick layering of the crust of the Yamato Basin, southeastern Japan Sea: the final stage of back-arc spreading, *Tectonophysics*, v. 165, p. 303–314.

Hüneke, H., and Henrich, R. 2011. Pelagic Sedimentation in Modern and Ancient Oceans. *In* Hüneke, H., and Mudler, T. (Eds.), Deep-Sea Sediments, Developments in Sedimentology, v. 63, Elsevier, Amsterdam, p. 215–351.

Hurd, D. C. 1973. Interactions of biogenic opal, sediment and seawater in the Central Equatorial Pacific, *Geochimica et Cosmochimica Acta*, v. 37, p. 2257–2282.

Hurd, D. C. 1983. Physical and chemical properties of siliceous skeletons. *In* Aston, S. R. (Ed.), Silicon Geochemistry and Biogeochemistry, Academic Press, London, p. 187–244.

Hurd, D. C., and Theyer, F. 1977. Changes in the physical and chemical properties of biogenic silica from the central equatorial Pacific: Part II. Refractive index, density, and water content of acid-cleaned samples, *American Journal of Science*, v. 277, p. 1168–1202.

Icenhower, J. P., and, Dove, P. M. 2000. The dissolution kinetics of amorphous silica into sodium chloride solutions: effects of temperature and ionic strength, *Geochimica et Cosmochimica Acta*, v. 64, p. 4193–4203.

Ichikawa, M. 1971. Reanalysis of mechanism of earthquakes which occurred in and near Japan, and statistical studies on the nodal plane solutions obtained, 1929-1968,

Geophysical Magazine, v. 35, p. 207–273.

Iijima, A., and Tada, R. 1981. Silica diagenesis of Neogene diatomaceous and volcaniclastic sediments in northern Japan, *Sedimentology*, v. 28, p. 185–200.

Iler, R. K. 1979. The Chemistry of Silica, John Wiley and Sons, New York, 667 p.

Ingle, J. C., Jr. 1980. Cenozoic paleobathymetry and depositional history of selected sequences within the southern California continental borderland, *Cushman Foundation for foraminiferal Research Special Publication*, no. 19, p. 163–195.

Ingle, J. C., Jr. 1981. Origin of Neogene diatomites around the north Pacific rim. *In* Garrison, R. E., and Douglas, R. G. (Eds.), The Monterey Formation and related siliceous rocks of California, Society of Economic Paleontologists and Mineralogists Publication, Pacific Section, v. 15, p. 159–180.

International Ocean Discovery Program. 2018. http://iodp.tamu.edu/database/

Interstitial Water. 2014. *In* International Ocean Discovery Program, Accessed 10 November 2014, http://web.iodp.tamu.edu/janusweb/chemistry/chemiw.shtml

Ireland, M. T., Goulty, N. R., and Davies, R. J. 2010. Influence of pore water chemistry on silica diagenesis: evidence from the interaction of diagenetic reaction zones with polygonal fault systems, *Journal of the Geological Society*, v. 167, p. 273–279.

Isaacs, C. M. 1980. Diagenesis in the Monterey Formation examined laterally along

the coast near Santa Barbara, California, PhD dissertation, Stanford University, Stanford, California, 329 p.

Isaacs, C. M. 1981. Porosity reduction during diagenesis of the Monterey Formation, Santa Barbara coastal area, California. *In* Garrison, R. E., Douglas, R. G., Pisciotto, K. E., Isaacs, C. M., and Ingle, J. C., Jr. (Eds.), The Monterey Formation and Related Siliceous Rocks of California, SEPM Research Symposium, San Francisco, California, v. 15, p. 257–272.

Isaacs, C. M. 1982, Influence of rock composition on kinetics of silica phase changes in the Monterey Formation, Santa Barbara area, California, *Geology*, v. 10, p. 304–308.

Isaacs, C. M., Pisciotto, K. A., and Garrison, R. E. 1983. Facies and diagenesis of the Monterey Formation, California: a summary. *In* Iijima, A., Hein, J. R., and Siever, R. (Eds.), Siliceous Deposits in the Pacific Region, Elsevier, Amsterdam, p. 247–282.

Ishikawa, Y., Takeo, M., Hamada, N., Katsumata, M., Satake, K., Abe, K., Kikuchi, M., Sudo, K., Takahashi, M., Kashiwabara, S., and Mikami, N. 1984. Mechanism of the central Japan Sea earthquake, 1983, *Chikyu (The Earth Monthly)*, v. 6. p. 11–17 (in Japanese).

James, R. 2005. Marine Biogeochemical Cycles (2nd Edition), Elsevier, 130 p.

Jantschke, A., Fischer, C., Hensel, R., Braun, H.-G., and Brunner, E. 2014. Directed assembly of nanoparticles to isolated diatom valves using the non-wetting

characteristics after pyrolysis, *Nanoscale*, v. 6, p. 11637–11645.

Joint, I., and A. Pomroy. 1993. Phytoplankton biomass and production in the southern North Sea, *Marine Ecology Progress Series*, v. 99, p. 169–182.

Jones, J. B., and Segnit, E. R. 1971. The nature of opal I. Nomenclature and constituent phases, *Journal of the Geological Society of Australia*, v. 18, p. 57–68.

Kamiya, H., and Shimokata, K. 1976. The role of salts in the dissolution of powdered quartz. *In* J, C. and T, P. (Eds.), International symposium on Water-Rock Interactions, Czechoslovakian Geological Survey, Prague, Czechoslovakia.

Kankeu, B., Bassahak, J., Hell, J. V., and Runge, J. 2012. Geological and tectonic history of Western Central Africa since the Palaeozoic. *In* Runge, J. (Ed.), Landscape Evolution, Neotectonics and Quaternary Environmental Change in Southern Cameroon, Palaeoecology of Africa, v. 31, p. 7–30.

Kastner, M, and Gieskes, J. M. 1983. Opal-A to opal-CT transformation: A kinetic study. *In* Iijima, A., Hein, J. R., and Siever, R. (Eds.), Siliceous Deposits in the Pacific Region, Amsterdam, Elsevier Science Publishing Company, p. 211–227.

Kastner, M., Keene, J. B., and Gieskes, J. M. 1977. Diagenesis of siliceous oozes – I. Chemical controls on the rate of opal-A to opal-CT transformation – an experimental study, *Geochimica et Cosmochimica Acta*, v. 41, p. 1041–1059.

Keene, J. B. 1976. Distribution, mineralogy, and petrography of biogenic and

authigenic silica in the Pacific Basin, PhD thesis, University of California, San Diego, 264 p.

Keller, M. A., and Isaacs, C. M. 1985. An evaluation of temperature scales for silica diagenesis in diatomaceous sequences including a new approach based on the Miocene Monterey Formation, California, *Geo-Marine Letters*, v. 5, p. 31–35.

Kemp, A. E. S., Dean, J. M., Pearce, R. B., and Pike, J. 2001. Recognition and analysis of bedding and sediment fabric features. *In* Last, W. M., and Smol, J. P. (Eds.), Tracking Environmental Change Using Lake Sediments, v. 2, Physical and Geochemical Methods, Kluwer Academic Publishers, Dordrecht, p. 7–22.

Kershaw, S., and Cundy, A. 2000. Oceanography: an Earth Science perspective, Stanley Thornes, Cheltenham, 276 p.

Kidder, D. L., and Erwin, D. H. 2001. Secular distribution of biogenic silica through the Phanerozoic: comparison of silica-replaced fossils and bedded cherts at the series level, *The Journal of Geology*, v. 109, p. 509–522.

Kidney, R. J., Arestad, J., Grau, A., and Sterling, R. 2003. Delineation of a diagenetic trap using P-wave and converted-wave seismic data in the Miocene McLure Shale, San Joaquin Basin, California, American Association of Petroleum Geologists Search and Discovery Article #20012.

Kim, G. Y., Yoo, D. G., Lee, H. Y., Lee, Y. J., and Kim, D. C. 2007. The relationship between silica diagenesis and physical properties in the East/Japan Sea:

ODP Legs 127/128, *Journal of Asian Earth Sciences*, v. 30, p. 448–456.

Kimura, M., Matsuda, T., Sato, H., Kaneoka, I., Tokuyama, H., Kuramoto, S., Oshida, A., Shimamura, K., Tamaki, K., Kinoshita, H., and Uyeda, S. 1987. Report on DELP 1985 cruises in the Japan Sea Part VII: Topography and geology of the Yamato Basin and its vicinity, *Bulletin of the Earthquake Research Institute*, University of Tokyo, v. 62, p. 447–483.

Kita, I., Taguchi, S., and Matsubaya, O. 1985. Oxygen isotope fractionation between amorphous silica and water at 34°-93°C, *Nature*, v. 314, p. 83–84.

Kobayashi, K. 1983. Spreading of the Sea of Japan and drift of the Japanese islands: a synthesis and speculation, *Mining Geology Special Issue*, v. 11, p. 23–36 (in Japanese with English abstract).

Kobayashi, K., and Isezaki, N. 1976. Magnetic anomalies in the Sea of Japan and the Shikoku Basin: possible tectonic implications. *In* Sutton, G. H., Manghnani, M. H., Moberly, R., and Mcafee, E. U. (Eds.), The Geophysics of the Pacific Ocean and Its Margins, American Geophysical Union, Washington, v. 19, p. 235–251.

Kong, L. S. L., Kasahara,J., and Katao, H. 1991. Crustal Structure of the Yamato Basin, Japan Sea, from P-Wave Travel Time Tomography, *Journal of Physics of the Earth*, v. 39, p. 515–536.

Kröger, N., Lorenz, S., Brunner, E., and Sumper, M. 2002. Self-assembly of highly phosphorylated silaffins and their function in biosilica morphogenesis, *Science*, v.

298, p. 584–586.

Krystinik, L. F. 1981. Pore-filling cements in turbidites of southern California: products of early diagenesis and dewatering of shale, PhD thesis, Princeton University, 153 p.

Kuramoto, S., Tamaki, K., Langseth, M. G., Nobes, D. C., Toluyama, H., Pisciotto, K. A., and Taira, A. 1992. Can opal-A/opal-CT BSR be an indicator of the thermal structure of the Yamato Basin, Japan Sea?. *In* Tamaki, K., Suyehiro, K., Allan, J., McWilliams, M., et al. (Eds.), Proceedings of the Ocean Drilling Program, Scientific Results, College Station, Texas , v. 127/128, p. 1145–1156.

Kvenvolden, K. A., Golan-Bac, M., McDonald, T. J., Pflaum, R. C., and Brooks, J. M. 1989. Hydrocarbon Gases in Sediment of the Vøring Plateau, Norwegian Sea. *In* Eldholm, O., Thiede, J., Taylor, E., et al. (Eds.), Proceedings of the Ocean Drilling Program, Scientific Results, College Station, Texas, v. 104, p. 319–326.

Lallemand, S., and Jolivet, L. 1986. Japan Sea: A pull-apart basin?, *Earth and Planetary Science Letters*, v. 76, p. 375–389.

Lancelot, Y. 1973. Chert and silica diagenesis in sediments from the central Pacific. *In* Winterer P. L., Ewing, J. I., et al. (Eds.), Initial Reports of the Deep Sea Drilling Project, U.S. Government Printing Office, Washington, v. 17, p. 377–405.

Langseth, M. G., and Tamaki, K. 1992. Geothermal measurements: thermal evolution of the Japan Sea basins and sediments. *In* Tamaki, K., Suyehiro, K., Allan,

J., McWilliams, M., et al. (Eds.), Proceedings of the Ocean Drilling Program, Scientific Results, College Station, Texas, v. 127/128 (Pt. 2), p. 1297–1309.

Lasaga, A. C., and Holland, H. D. 1976. Mathematical aspects of non-steady state diagenesis. *Geochimica et Cosmochimica Acta*, v. 40, p. 257–266.

Leeder, M. R. 1982. Sedimentology: Process and Product, Allen and Unwin, London, 344 p.

Leinen, M., Cwienk, D., Heath, G. R., Biscaye, P. E., Kolla, V., Thiede, J., and Dauphin, J. P., 1986. Distribution of biogenic silica and quartz in recent deep-sea sediments, *Geology*, v. 14, p. 199–203.

Lewin, J. C. 1962. Silicification. *In* Lewin, R. E. (Ed.), Physiology and Biochemistry of Algae, Academic Press, New York, p. 445–455.

Lewin, J. C., and Chen C.-H. 1968. Silicon metabolism in diatoms. VI. Silicic acid uptake by a colorless marine diatom, *Nitzschia alba* Lewin & Lewin, *Journal of Phycology*, v. 4, p. 161–166.

Libes, S. M. 1992. An Introduction to Marine Biogeochemistry, John Wiley and Sons, New York, 734 p.

Littke, R., Fourtanier, E., Thurow, J., and Taylor, E. 1991. Silica diagenesis and its effects on lithification of Broken Ridge deposits, Central Indian Ocean. *In* Peirce, J., Weissel, J., et al. (Eds.), Proceedings of the Ocean Drilling Program, Scientific

Results, College Station, Texas, v. 121, p. 261–272.

Longhurst, A. R., and W. G. Harrison, 1989. The biological pump: Profiles of plankton production and consumption in the upper ocean, *Progress in Oceanography*, v. 22, p. 47–123.

Loucaides, S. 2009. Dissolution of biogenic silica: Roles of pH, salinity, pressure, electrical charging and reverse weathering, PhD thesis, Utrecht University, 137 p.

Ludwig, W. J., Murauchi, S., and Houtz, R. E. 1975. Sediments and structure of the Japan Sea, *Geological Society of America Bulletin*, v. 86, p. 651–664.

Lyons, T. W., Murray, R. W., and Pearson, D. G. 2000. A comparative study of diagenetic pathways in sediments of the Caribbean Sea: highlights from pore-water results. *In* Leckie, R. M., Sigurdsson, H., Acton, G. D., and Draper, G. (Eds.), Proceedings of the Ocean Drilling Program, Scientific Results, College Station, Texas, v. 165, p. 287–298.

Mackenzie, F. T., Ristvet, B. L., Thorstenson, D. C., Lerman, A., and Leeper, R. H. 1981. Reverse weathering and chemical mass balance in a coastal environment. *In* Marten, J. M., Burton, J. D., and Eisma. D. (Eds.), River Inputs to Ocean Systems, UNEP and UNESCO, Switzerland, p. 152–187.

März, C., Poulton, S. W., Wagner, T., Schnetger, B., and Brumsack, H-J. 2014. Phosphorus burial and diagenesis in the central Bering Sea (Bowers Ridge, IODP Site U1341): Perspectives on the marine P cycle, *Chemical Geology*, v. 363, p. 270–

282.

Magara, K. 1974. Compaction, ion filtration, and osmosis in shale and their significance in primary migration, *American Association of Petroleum Geologists Bulletin*, v. 58, p. 283–290.

Manheim, F. T., and Sayles, F. L. 1974. Composition and origin of interstitial waters of marine sediments based on deep sea drill cores. *In* Goldberg, E. D. (Ed.), The Sea (Vol. 5), Wiley, New York, p. 527–568.

Marsaglia, K., Milliken, K., and Doran, L. 2013. Smear slides of marine mud for IODP core description, Volume I. Part 1: Methodology and atlas of siliciclastic and volcanogenic components. Integrated Ocean Drilling Program, Technical Note 1, 236 p.

Matheney, R. K., and Knauth, L. P. 1993. New isotopic temperature estimates for early silica diagenesis in bedded cherts, *Geology*, v. 21, p. 519–522.

Maynard, J. B. 1975. Kinetics of silica sorption by kaolinite with application to seawater chemistry, *American Journal of Science*, v. 275, p. 1028–1048.

Mazzullo, J. M., and Graham, A. G. 1988. Handbook for shipboard sedimentologists, Ocean Drilling Program, Texas A&M University, Technical Note 8, 70 p.

McDuff, R. E., and Gieskes, J. M. 1976. Calcium and magnesium profiles in DSDP interstitial waters: diffusion or reaction?, *Earth and Planetary Science Letters*, v. 33,

p. 1–10.

McManus, J., Berelson, W. M., Hammond, D. E., Kilgore, T. E., Ragueneau, O. G., DeMaster, D. J., and Collier, R. W. 1995. Early diagenesis of biogenic opal: Dissolution rates, kinetics, and paleoceanographic implications, *Deep Sea Research Part II: Topical Studies in Oceanography*, v. 42, p. 871–903.

McSween, H. Y. Jr., Richardson, S. M., and Uhle, M. E. 2003. Geochemistry: Pathways and Processes (2nd Edition), Columbia University Press, New York, 432 p.

Meadows, D., and Davies, R. J. 2007, Morphological development of basin-scale silica diagenetic fronts revealed with 2D seismic reflection data: offshore Sakhalin, Russian Far East, *Journal of the Geological Society*, v. 164, p. 1193–1206.

Meadows, D., and Davies, R. J. 2010. The limited suitability of silica diagenetic boundaries as isothermal markers: Insights from seismic reflection imaging, Offshore Sakhalin, Russian Far East, *Marine and Petroleum Geology*, v. 27, p. 1028–1039.

Meile, C., and Van Cappellen, P. 2003. Global estimates of enhanced solute transport in marine sediments, *Limnology and Oceanography*, v. 48, p. 777–786.

Michalopoulos, P., and Aller, R. C. 1995. Rapid Clay Mineral Formation in Amazon Delta Sediments, *Science*, v. 270, p. 614–617.

Mizutani, S. 1970. Silica minerals in the early stage of diagenesis, *Sedimentology*, v.

15, p. 419–436.

Mizutani, S. 1971. Silica minerals in diagenesis, Memoir 6, The Geological Society of Japan, p. 151–163 (in Japanese).

Mizutani, S. 1977. Progressive ordering of cristobalitic silica in the early stage of diagenesis, *Contributions to Mineralogy and Petrology*, v. 61, p. 129–140.

Molnar, P., Burchfiel, B. C., Ziyun, Z., K'uangyi, L., Shuji, W., and Minmin, H. 1987. The geologic evolution of northern Tibet: Results from an expedition to Ulugh Muztagh, *Science*, v. 235, p. 299–304.

Morey, G. W., Fournier, R. O., and Rowe, J. J. 1962. The solubility of quartz in water in the temperature interval from 25° to 300° C, *Geochimica et Cosmochimica Acta*, v. 26, p. 1029–1043.

Mortlock, R. A., and Froelich, P. N. 1989. A simple method for the rapid determination of biogenic opal in pelagic marine sediments, *Deep-Sea Research Part I: Oceanographic Research Papers*, v. 36, p. 1415–1426.

Murata, K. J., and Larson, R. R. 1975. Diagenesis of Miocene siliceous shales Temblor Range, California, *Journal of Research of the U.S. Geological Survey*, v. 3, p. 553–566.

Murata, K. J., and Nakata, J. K. 1974. Cristobalitic stage in the diagenesis of diatomaceous shale, *Science*, v. 184, p. 567–568.

Murata, K. J., Friedman, I., and Gleason, J. D. 1977. Oxygen isotope relations between diagenetic silica minerals in Monterey Shale, Temblor Range, California, *American Journal of Science*, v. 277, p. 259–272.

Murauchi, S. 1972. Seismic crustal structure of the Japan Sea by controlled source experiment, *Kagaku*, v. 42, p. 367–375 (in Japanese).

Muttoni, G., and Kent, D. V. 2007. Widespread formation of cherts during the early Eocene climate optimum, *Palaeogeography, Palaeoclimatology, Palaeoecology*, v. 253, p. 348–362.

Neagu, R. C. 2011. The relationship between biogenic silica diagenesis and the physical properties of sediments studied using seismic and well data, PhD thesis, Cardiff University, 275 p.

Neagu, R. C., Cartwright, J., Davies, R. J., and Jensen, L. 2010. Fossilisation of a silica diagenesis reaction front on the mid-Norwegian margin, *Marine and Petroleum Geology*, v. 27, p. 2141–2155.

Nelson, J. 2004. The Geology of Western North America (Abridged Version). *In* Simandl, G. J., McMillan, W. J., and Robinson, N. D. (Eds.), 37th Annual Forum on Industrial Minerals Proceedings, Industrial Minerals with emphasis on Western North America, British Columbia Ministry of Energy and Mines, Geological Survey Branch, Paper 2004-2, p. 1–2.

Nelson, J., and Colpron, M. 2007. Tectonics and metallogeny of the British

Columbia, Yukon and Alaskan Cordillera, 1.8 Ga to the present. *In* Goodfellow, W. D. (Ed.), Mineral Deposits of Canada: A Synthesis of Major Deposit-Types, District Metallogeny, the Evolution of Geological Provinces, and Exploration Methods, Geological Association of Canada, Mineral Deposits Division, Special Publication No. 5, p. 755–791.

Nobes, D. C., Murray, R. W., Kuramoto, S., Pisciotto, K. A., and Holler, P. 1992. Impact of silica diagenesis on physical property variations. *In* Pisciotto, K. A., Ingle, J. C., Jr., von Breymann, M. T., Barron, J., et al. (Eds.), Proceedings of the Ocean Drilling Program, Scientific Results, College Station, Texas, v. 127/128 (Pt. 1), p. 3–31.

Noymer, A. 2008. Alpha, Significance Level of Test. *In* P. J., Lavrakas (Ed.), Encyclopedia of Survey Research Methods, Sage Publications, Thousand Oaks, California.

O'Brien, D. K., Manghnani, M. H., and Schoonmaker–Tribble, J. 1989. Irregular trends of physical properties in homogeneous clay – rich sediments of DSDP Leg 87 Hole 584, midslope terrace in the Japan Trench, *Marine Geology*, v. 87, p. 183–194.

Ocean Drilling Program Site Maps. 2009. [Drawing]. *In* Ocean Drilling Program, Accessed 5 October 2017, http://www-odp.tamu.edu/sitemap/sitemap.html

Oehler, T. 2014. Seasonal variations of benthic carbon and nutrient fluxes in the southern North Sea, PhD thesis, University of Bremen, 116 p.

Okada, H., and Bukry, D. 1980. Supplementary modification and introduction of code numbers to the low-latitude coccolith biostratigraphic zonation, *Marine Micropaleontology*, v. 5, p. 321–325.

Olivarez Lyle, A., and Lyle, M. W. 2002. Determination of biogenic opal in pelagic marine sediments: A simple method revisited. *In* Lyle, M., Wilson, P. A., Janecek, T. R., et al. (Eds.), Proceedings of the Ocean Drilling Program, Initial Reports, College Station, Texas, v. 199, p. 1–21.

Otofuji, Y., and Matsuda, T. 1983. Paleomagnetic evidence for the clockwise rotation of Southwest Japan, *Earth and Planetary Science Letters*, v. 62, p. 349–359.

Otofuji, Y., and Matsuda, T. 1984. Timing and rotational motion of Southwest Japan inferred from paleomagnetism, *Earth and Planetary Science Letters*, v. 70, p. 373–382.

Otofuji, Y., Matsuda, T., and Nohda, S. 1985. Opening mode of the Japan Sea inferred from the paleomagnetism of the Japan Arc, *Nature*, v. 317, p. 603–604.

Papavasiliou, C. 1979. The Geochemistry and mineralogy of some NW Indian Ocean DSDP cores (Sites 222 and 223, Leg 23 DSDP), PhD thesis, University of Southampton, 520 p.

Park, C. H., Kim, H. J., Yang, C. S., Suk, B. C., and Isezaki, N. 1996. Crustal structure of the Ulleung Basin, the East Sea (Japan Sea), from gravity and ocean bottom seismometer data, *Journal of the Geological Society of Korea*, v. 32, p. 276–

290.

Park, J., Norman, D., McLin, K., and Moore, J. 2006. Modelling amorphous silica precipitation: a strategy to reduce silica precipitation near Coso injection wells, Proceedings, Thirty-First Workshop on Geothermal Reservoir Engineering, Stanford University, California, January 30-February 1, p. 267–274.

Peters, K. E., Dralus, D., Lewan, M. D., Magoon, L. B., and Schenk, O. 2011. The Opal-CT to Quartz Phase Transition and Unconventional Oil in Siliceous Shale Source Rock, San Joaquin Basin, California, American Association of Petroleum Geologists Search and Discovery Article #90122.

Pisciotto, K. A. 1981a. Diagenetic trends in the siliceous facies of the Monterey Shale in the Santa Maria region, California, *Sedimentology*, v. 28, p. 547–571.

Pisciotto, K. A. 1981b. Distribution, thermal histories, isotopic compositions and reflection characteristics of siliceous rocks recovered by the Deep Sea Drilling Project. *In* Warme, J. E., Douglas, R. G., and Winterer, E. L. (Eds.), The Deep Sea Drilling Project: A Decade of Progress, Society of Economic Paleontologists and Mineralogists Special Publications No. 32, p. 129–147.

Pisciotto, K. A., Murray, R. W., and Brumsack, H. J. 1992. Thermal history of Japan Sea sediments from isotopic studies of diagenetic silica and associated pore waters. *In* Pisciotto, K. A., Ingle, J. C., Jr., von Breymann, M. T., Barron, J., et al. (Eds.), Proceedings of the Ocean Drilling Program, Scientific Results, College Station,

Texas, v. 127/128 (Pt. 1), p. 49–56.

Pletsch, T., Erbacher, J., Holbourn, A. E. J., Kuhnt, W., Moullade, M., Oboh-Ikuenobe, F. E., Söding, E., and Wagner, T. 2001. Cretaceous separation of Africa and South America: the view from the West African margin (ODP Leg 159), *Journal of South American Earth Sciences*, v. 14, p. 147–174.

Rabinowitz, P. D., and Garrison, L. E. 1985. Operational and Laboratory Capabilities of "JOIDES Resolution", Ocean Drilling Program, Texas A&M University, Technical Note 2, 34 p.

Rabinowitz, P. D., Garrison, L. E., and Meyer, A. W. 1990. Shipboard Scienticts' Handbook, Ocean Drilling Program, Texas A&M University, Technical Note 3 (Revised), 170 p.

Rabouille, C., Gaillard, J.-F., Tréguer, P., and Vincendeau, M.-A. 1997. Biogenic silica cycling in surfacial sediments across the Polar Front of the Southern Ocean (Indian Sector), *Deep Sea Research Part II: Topical Studies in Oceanography*, v. 44, p. 1151–1176.

Ragueneau, O., Dittert, N., Pondaven, P., Tréguer, P., and Corrin, L. 2002. Si:C decoupling in the world ocean: Is the Southern Ocean different?, *Deep Sea Research Part II: Topical Studies in Oceanography*, v. 49, p. 3127–3154.

Ragueneau, O., Regaudie-de-Gioux, A., Moriceau, B., Gallinari, M., Vangriesheim, A., Baurand, F., and Khripounoff. A. 2009. A benthic Si mass balance on the Congo

margin: Origin of the 4000m Dsi anomaly and implications for the transfer of Si from land to ocean, *Deep Sea Research Part II: Topical Studies in Oceanography*, v 56, p. 2197–2207.

Ragueneau, O., Tréguer, P., Leynaert, A., Anderson, R. F., Brzezinski, M. A., DeMaster, D. J., Dugdale, R. C., Dymond, J., Fischer, G., François, R., Heinze, C., Maier-Reimer, E., Martin-Jézéquel, V., Nelson, D. M., and Quéquiner, B. 2000. A review of the Si cycle in the modern ocean: recent progress and missing gaps in the application of biogenic opal as a paleoproductivity proxy, *Global and Planetary Change*, v. 26, p. 317–365.

Railkin, A. I. 2003. Marine Biofouling: Colonization Processes and Defenses, CRC Press, Boca Raton, 320 p.

Rashid, M. A. 1985. Geochemistry of Marine Humic Compounds, Springer-Verlag, New York, 300 p.

Reid, S., and McIntyre, J. 2001. Monterey Formation porcelanite reservoirs of the Elk Hills field, Kern County, California, *American Association of Petroleum Geologists Bulletin*, v. 85, p. 169–189.

Revil, A., Grauls, D., and Brévart, O. 2002. Mechanical compaction of sand/clay mixtures, *Journal of Geophysical Research: Solid Earth*, v. 107, 2293, p. ECV 11-1–ECV 11-15.

Rice, S. B., Freund, H., Huang, W. L., Clouse, J. A., and Isaacs, C. M. 1995.

Application of Fourier Transform Infrared Spectroscopy to silica diagenesis: The opal-A to opal-CT transformation, *Journal of Sedimentary Research*, v. A65, p. 639–647.

Richthammer, P., Börmel, M., Brunner, E., and Van Pee, K.-H. 2011. Biomineralisation in diatoms: the role of silacidins, *ChemBioChem*, v. 12, p. 1362–1366.

Rickert, D. 2000. Dissolution kinetics of biogenic silica in marine environments (Reports on Polar Research 351), PhD thesis, Alfred Wegener Institute for Polar and Marine Research, 211 p.

Roaldset, E., and He, W. 1995. Silica-phase Transformation of Opal-A to Opal-CT to Quartz− An Experimental Approach, Report, Department of Geology and Mineral Resources Engineering, Norwegian Institute of Technology, Trondheim.

Robert, C. M. 2009. Global Sedimentology of the Ocean: An Interplay between Geodynamics and Paleoenvironment, Developments in Marine Geology, v. 4, Elsevier, 487 p.

Sarmiento, J. L., and Gruber, N. 2006. Ocean Biogeochemical Dynamics, Princeton University Press, Princeton, New Jersey, 528 p.

Sarmiento, J. L., Simeon, J., Gnanadesikan, A., Gruber, N., Key, R. M., and Schlitzer, R. 2007. Deep ocean biogeochemistry of silicic acid and nitrate, *Global Biogeochemical Cycles*, v. 21, GB1S90, doi:10.1029/2006GB002720.

Sato, T., No, T., Kodaira, S., Takahashi, N., and Kaneda, Y. 2014. Seismic constraints of the formation process on the back-arc basin in the southeastern Japan Sea, *Journal of Geophysical Research: Solid Earth*, v. 119, p. 1563–1579.

Schink, D. R., Guinasso, N. L., Jr., and Fanning, K. A. 1975. Processes affecting the concentration of silica at the sediment-water interface of the Atlantic Ocean, *Journal of Geophysical Research*, v. 80, p. 3013–3031.

Schlee, J. S. 1980. A Comparison of Two Atlantic-type Continental Margins, United States Geological Survey, Professional Paper 1167, U.S. Government Printing Office, 21 p.

Seno, T., and Eguchi, T. 1983. Seismotectonics of the western Pacific region. *In* Hilde, T. W. C., and Uyeda, S. (Eds.), Geodynamics of the western Pacific, American Geophysical Union-Geological Society of America Geodynamics Series, v. 11, p. 5–40.

Shinohara, M., Hirata, N., Nambu, H., Suyehiro, K., Kanazawa, T., and Kinoshita, H. 1992. Detailed crustal structure of northern Yamato Basin. *In* Tamaki, K., Suyehiro, K., Allan, J., McWilliams, M., et al. (Eds.), Proceedings of the Ocean Drilling Program, Scientific Results, College Station, Texas, v. 127/127 (pt. 2), p. 1075–1106.

Shipboard Scientific Party. 1981. Site 471: Offshore Magdalena Bay. *In* Yeats, R. S., Haq, B. U., et al. (Eds.), Initial Reports of the Deep Sea Drilling Project, U.S.

Government Printing Office, Washington, v. 63, p. 269–349.

Shipboard Scientific Party. 1987. Site 642: Norwegian Sea. *In* Eldholm, O., Thiede, J., Taylor, E., et al. (Eds.), Proceedings of the Ocean Drilling Program, Initial Reports, College Station, Texas, v. 104, p. 53–453.

Shipboard Scientific Party. 1989. Site 751. *In* Schlich, R., Wise, S. W., Jr., et al. (Eds.), Proceedings of the Ocean Drilling Program, Initial Reports, College Station, Texas, v. 120, p. 339–373.

Shipboard Scientific Party. 1990a. Site 794. *In* Tamaki, K., Pisciotto, K., Allan, J., et al. (Eds.), Proceedings of the Ocean Drilling Program, Initial Reports, College Station, Texas, v. 127, p. 71–167.

Shipboard Scientific Party. 1990b. Site 795. *In* Tamaki, K., Pisciotto, K., Allan, J., et al. (Eds.), Proceedings of the Ocean Drilling Program, Initial Reports, College Station, Texas, v. 127, p. 169–245.

Shipboard Scientific Party. 1990c. Site 797. *In* Tamaki, K., Pisciotto, K., Allan, J., et al. (Eds.), Proceedings of the Ocean Drilling Program, Initial Reports, College Station, Texas, v. 127, p. 323–421.

Shipboard Scientific Party. 1990d. Site 798. *In* Ingle, J. C., Jr., Suyehiro, K., von Breymann, M. T., et al. (Eds.), Proceedings of the Ocean Drilling Program, Initial Reports, College Station, Texas, v. 128, p. 121–236.

Shipboard Scientific Party. 1990e. Site 799. *In* Ingle, J. C., Jr., Suyehiro, K., von Breymann, M. T., et al. (Eds.), Proceedings of the Ocean Drilling Program, Initial Reports, College Station, Texas, v. 128, p. 237–402.

Shipboard Scientific Party. 2001a. Site 1170. *In* Exon, N. F., Kennett, J. P., Malone, M. J., et al. (Eds.), Proceedings of the Ocean Drilling Program, Initial Reports, College Station, Texas, v. 189, p. 1–167.

Shipboard Scientific Party. 2001b. Site 1172. *In* Exon, N. F., Kennett, J. P., Malone, M. J., et al. (Eds.), Proceedings of the Ocean Drilling Program, Initial Reports, College Station, Texas, v. 189, p. 1–149.

Shipboard Scientific Party. 2001c. Site 1173. *In* Moore, G. F., Taira, A., Klaus, A., et al. (Eds.), Proceedings of the Ocean Drilling Program, Initial Reports, College Station, Texas, v. 190, p. 1–147.

Shipboard Scientific Party. 2003. Site 1225. *In* D'Hondt, S. L., Jørgensen, B. B., Miller, D. J., et al. (Eds.), Proceedings of the Ocean Drilling Program, Initial Reports, College Station, Texas, v. 201, p. 1–86.

Siever, R. 1957. The silica budget in the sedimentary cycle, *American Mineralogist*, v. 42, p. 821–841.

Siever, R. 1992. The silica cycle in the Precambrian, *Geochimica et Cosmochimica Acta*, v. 56, p. 3265–3272.

Siever, R., and Woodford, N. 1973. Sorption of silica by clay minerals, *Geochimica et Cosmochimica Acta*, v. 37, p. 1851–1880.

Singh, B., and R. J. Gilkes. 1993. The recognition of amorphous silica in indurated soil profiles, *Clay Minerals*, v. 28, p. 461–474.

Son, M., Song, C. W., Kim, M.-C., Cheon, Y., Cho, H., and Sohn, Y. K. 2015. Miocene tectonic evolution of the basins and fault systems, SE Korea: dextral, simple shear during the East Sea (Sea of Japan) opening, *Journal of the Geological Society*, v. 172, p. 664–680.

Spinelli, G. A., Mozley, P. S, Tobin, H. J., Underwood, M. B., Hoffman, N. W., and Bellew, G. M. 2007. Diagenesis, sediment strength, and pore collapse in sediment approaching the Nankai Trough subduction zone, *Geological Society of America Bulletin*, v. 119, p. 377–390.

Stamatakis, M. G., Dermitzakis, M., Economou-Amilli, A., and Magganas, A. 1988. Petrology and diagenetic changes in Miocene marine diatomaceous deposits from Zakynthos Island, Greece. *In* Hein, J. R., and Obradovic, J. A. (Eds.), Siliceous deposits of Tethys and Pacific regions, Springer-Verlag, New York, p. 130–139.

Stein, C. L., and Kirkpatrick, R. J. 1976. Experimental porcelanite recrystallization kinetics: a nucleation and growth model, *Journal of Sedimentary Petrology*, v. 46, p. 430–435.

Steiness, E., Heier, K. S., and Billings, G. K. 1972. Lithium. *In* Wedepohl, K. H.

(Ed.), Handbook of Geochemistry (Vol. 2), Springer-Verlag, Berlin, looseleaf.

Sumper, M., and Brunner, E. 2008. Silica biomineralisation in diatoms: the model organism *Thalassiosira pseudonana*, *ChemBioChem*, v. 9, p. 1187–1194.

Sumper, M., and Kröger, N. 2004. Silica formation in diatoms: the function of long-chain polyamines and silaffins, *Journal of Materials Chemistry*, v. 14, p. 2059–2065.

Surdam, R. C., and Hall, C. A., Jr. 1984. Diagenesis of the Miocene Obispo Formation, Coast Range, California. *In* Surdam, R. C. (Ed.), A Guidebook to the Stratigraphic, Tectonic, Thermal, and Diagenetic Histories of the Monterey Formation, Pismo and Hausna Basin, California, SEPM Guidebook No. 2, p. 8–20.

Swann, G. E. A., Pike, J., Leng, M. J., Sloane, H. J., and Snelling, A. M. 2017. Temporal controls on silicic acid utilisation along the West Antarctic Peninsula. *Nature Communications*, v. 8, p. 1–8.

Tada, R. 1991. Compaction and cementation in siliceous rocks and their possible effect on bedding enhancement. *In* Einsele, G., Ricken, W., and Seilacher, A. (Eds.), Cycles and Events in Stratigraphy, Springer-Verlag, Berlin, Heidelberg, p. 480–491.

Tada, R., and Iijima, A. 1983. Petrology and diagenetic changes of Neogene siliceous rocks in northern Japan, *Journal of Sedimentary Petrology*, v. 53, p. 911–930.

Tada, R., Murray, R. W., Alvarez Zarikian, C. A., Anderson, W. T., Jr., Bassetti, M.-

A., Brace, B. J., Clemens, S. C., da Costa Gurgel, M. H., Dickens, G. R., Dunlea, A. G., Gallagher, S. J., Giosan, L., Henderson, A. C. G., Holbourn, A. E., Ikehara, K., Irino, T., Itaki, T., Karasuda, A., Kinsley, C. W., Kubota, Y., Lee, G. S., Lee, K. E., Lofi, J., Lopes, C. I. C. D., Peterson, L. C., Saavedra-Pellitero, M., Sagawa, T., Singh, R. K., Sugisaki, S., Toucanne, S., Wan, S., Xuan, C., Zheng, H., and Ziegler, M. 2015. Site U1425. *In* Tada, R., Murray, R. W., Alvarez Zarikian, C. A., and the Expedition 346 Scientists (Eds.), Proceedings of the Integrated Ocean Drilling Program, College Station, Texas, v. 346, p. 1–137.

Taguchi, K., Hasegawa, K., and Suzuki, T. 1988. The relationship between silica minerals and organic matter diagenesis: its implications for the origin of oil, *Organic Geochemistry*, v. 13, p. 97–107.

Taira, A., Ohara, Y., Wallis, S. R., Ishiwatari, A., and Iryu, Y. 2016. Geological evolution of Japan: an Overvierw. *In* Moreno, T., Wallis, S. R., Kojima, T., and Gibbons, W. (Eds.), The Geology of Japan, Geological Society of London, p. 1–24.

Tamaki, K. 1988. Geological structure of the Japan Sea and its implications, *Bulletin of the Geological Survey of Japan*, v. 39, p. 269–365.

Tamaki, K., and Honza, E. 1985. Incipient subduction and obduction along the eastern margin of the Japan Sea, *Tectonophysics*, v. 119, p. 381–406.

Tamaki, K., Suyehiro, K., Allan, J., Ingle, J.C., Jr., and Pisciotto, K. A. 1992. Tectonic synthesis and implications of Japan Sea ODP drilling. *In* Tamaki, K.,

Suyehiro, K., Allan, J., McWilliams, M., et al. (Eds.), Proceedings of the Ocean Drilling Program, Scientific Results, College Station, Texas, v. 127/128 (Pt. 2), p. 1333–1348.

Tanaka, C., and Ogawa, Y. 2006. Data report: Silica mineral crystallization with textural change of Cretaceous siliceous/calcareous pelagic sedimentary rocks recovered from the northwest Pacific, ODP Leg 185. *In* Ludden, J. N., Plank, T., and Escutia, C. (Eds.), Proceedings of the Ocean Drilling Program, Scientific Results, College Station, Texas, v. 185, p. 1–11.

Tapponnier, P., Peltzer, G., Le Dain, A.Y., Armijo, R., and Cobbold, P. 1982. Propagating extrusion tectonics in Asia: new insights from simple experiments with plasticine, *Geology*, v. 10, p. 611–616.

Terry, R. D., and Chilingarian, G. V. 1955. Summary of "Concerning some additional aids in studying sedimentary formations" by M. S. Shvetsov, *Journal of Sedimentary Petrology*, v. 25, p. 229–234.

Thein, J., and von Rad, U. 1987. Silica Diagenesis in Continental Slope and Rise Sediments off Eastern North America (Sites 603 and 605, Leg 93; Sites 612 and 613, Leg 95). *In* Poag, C. W., Watts, A. B., et al. (Eds.), Initial Reports of the Deep Sea Drilling Project, U.S. Government Printing Office, Washington, v. 95, p. 501–525.

Tréguer, P. J., and De La Rocha, C. L. 2013. The world ocean silica cycle, *Annual Review of Marine Science*, v. 5, p. 477–501.

Tréguer, P., Nelson, D. M., van Bennekom, A. J., DeMaster, D. J., Leynaert, A., and Quéguiner, B. 1995. The silica balance in the world ocean: A reestimate, *Science*, v. 268, p. 375–379.

Tribble, J. S., Wilkens, R., Arvidson, R. S., and Busing, C. J. 1993. Sediments of the Hawaiian arch: X-ray mineralogy and microfabric. *In* Wilkens, R. H., Firth, J., Bender, J., et al. (Eds.), Proceedings of the Ocean Drilling Program, Scientific Results, College Station, Texas, v. 136, p. 65–76.

TrueChrome Metrics. 2015. *In* Tucsen, Accessed 5 October 2017, http://www.tucsen .com/products/TrueChromeMetrics%20.html

Van Cappellen, P. 1996. Reactive surface area control of the dissolution kinetics of biogenic silica in deep-sea sediments, *Chemical Geology*, v. 132, p. 125–130.

Van Cappellen, P., and Qiu, L. 1997a. Biogenic silica dissolution in sediments of the Southern Ocean: I. Solubility, *Deep Sea Research Part II: Topical Studies in Oceanography*, v. 44, p. 1109–1128.

Van Cappellen, P., and Qiu, L. 1997b. Biogenic silica dissolution in sediments of the Southern Ocean: II. Kinetics, *Deep Sea Research Part II: Topical Studies in Oceanography*, v. 44, p. 1129–1149.

Van Lier, J. A., De Bruyn, P. L., and Overbeek, J. TH. G. 1960. The solubility of quartz, *Journal of Physical Chemistry*, v. 64, p. 1675–1682.

Velde, B. 1996. Compaction trends of clay-rich deep sea sediments, *Marine Geology*, v. 133, p. 193–201.

von Rad, U., Riech, V., and Rösch, H. 1978. Silica diagenesis in continental margin sediments off Northwest Africa, Initial Reports of the Deep Sea Drilling Project, U.S. Government Printing Office, Washington, v. 41, p. 879–905.

Ward, C. R., Taylor, J. C., and Cohen, D. R. 1999. Quantitative mineralogy of sandstones by X-ray diffractometry and normative analysis, *Journal of Sedimentary Research*, v. 69, p. 1050–1062.

Weaver, F. M., and Wise, S. W., Jr. 1973. Early diagenesis of deep sea bedded chert, *Antarctic Journal of the United States*, v. 8, p. 298–300.

Weishampel, D. B, and Jianu, C-M. 2011. Transylvanian Dinosaurs, Johns Hopkins University Press, Baltimore, 328 p.

Weller, R., and Behl, R. J. 2015. Physical and Mechanical Characteristics of the Opal-A to Opal-CT Transition Zone: Enhanced Diatomite Permeability from Heterogeneous Diagenetic Embrittlement, Pacific Section AAPG, SEG and SEPM Joint Technical Conference, Oxnard, California.

Wenzl, S., Hett, R., Richthammer, P., and Sumper, M. 2008. Silacidins: highly acidic phosphopeptides from diatom shells assist in silica precipitation in vitro, *Angewandte Chemie International Edition*, v. 47, p. 1729–1732.

Wilkens, R. H., Schreiber, B. C., Caruso, L., and Simmons, G. 1987. The effects of diagenesis on the microstructure of Eocene sediments border- ing the Baltimore Canyon Trough. *In* Poag, C. W., Watts, A. B., et al. (Eds.), Initial Reports of the Deep Sea Drilling Project, U.S. Government Printing Office, Washington, v. 95, p. 527–547.

Williams, L. A., and Crerar, D. A. 1985. Silica diagenesis, II. General mechanisms, *Journal of Sedimentary Petrology*, v. 55, p. 312–321.

Williams, L. A., Parks, G. A., and Crerar, D. A. 1985. Silica diagenesis, I. Solubility controls, *Journal of Sedimentary Petrology*, v. 55, p. 301–311.

Wilson, M. J. 2014. The structure of opal-CT revisited, *Journal of Non-Crystalline Solids*, v. 405, p. 68–75.

Wise, S. W., and Kelts, K. R. 1971. Submarine lithification of middle Tertiary chalks in the South Atlantic Ocean basin, VIII International Sedimentological Congress, Heidelberg, p. 110.

Wise, S. W., and Weaver, F. M. 1974. Chertification of oceanic sediments, *International Association of Sedimentologists Special Publication*, v. 1, p. 301–326.

Wise, S. W., Buie, B. F., and Weaver, F. M. 1972. Chemically precipitated sedimentary cristobalite and the origin of chert, *Eclogae Geologicae Helvetiae*, v. 65 , p. 157–163.

Wlotzka, F. 1972. Nitrogen. *In* Wedepohl, K. H. (Ed.), Handbook of Geochemistry (Vol. 2), Springer-Verlag, Berlin, looseleaf.

Wollast, R. 1974. The Silica Problem. *In* Goldberg, E. D. (Ed.), The sea, Ideas and observations on progress in the study of the seas, Wiley-Interscience, New York, v. 5, p. 359–392.

Wollast, R., and Garrels, R.M. 1971. Diffusion coefficient of silica in sea water, *Nature Physical Science*, v. 229, p. 94–94.

Wrona, T., Jackson, C. A.-L., Huuse, M., and Taylor, K. G. 2017. Silica diagenesis in Cenozoic mudstones of the North Viking Graben: physical properties and basin modelling, *Basin Research*, v. 29, p. 556–575.

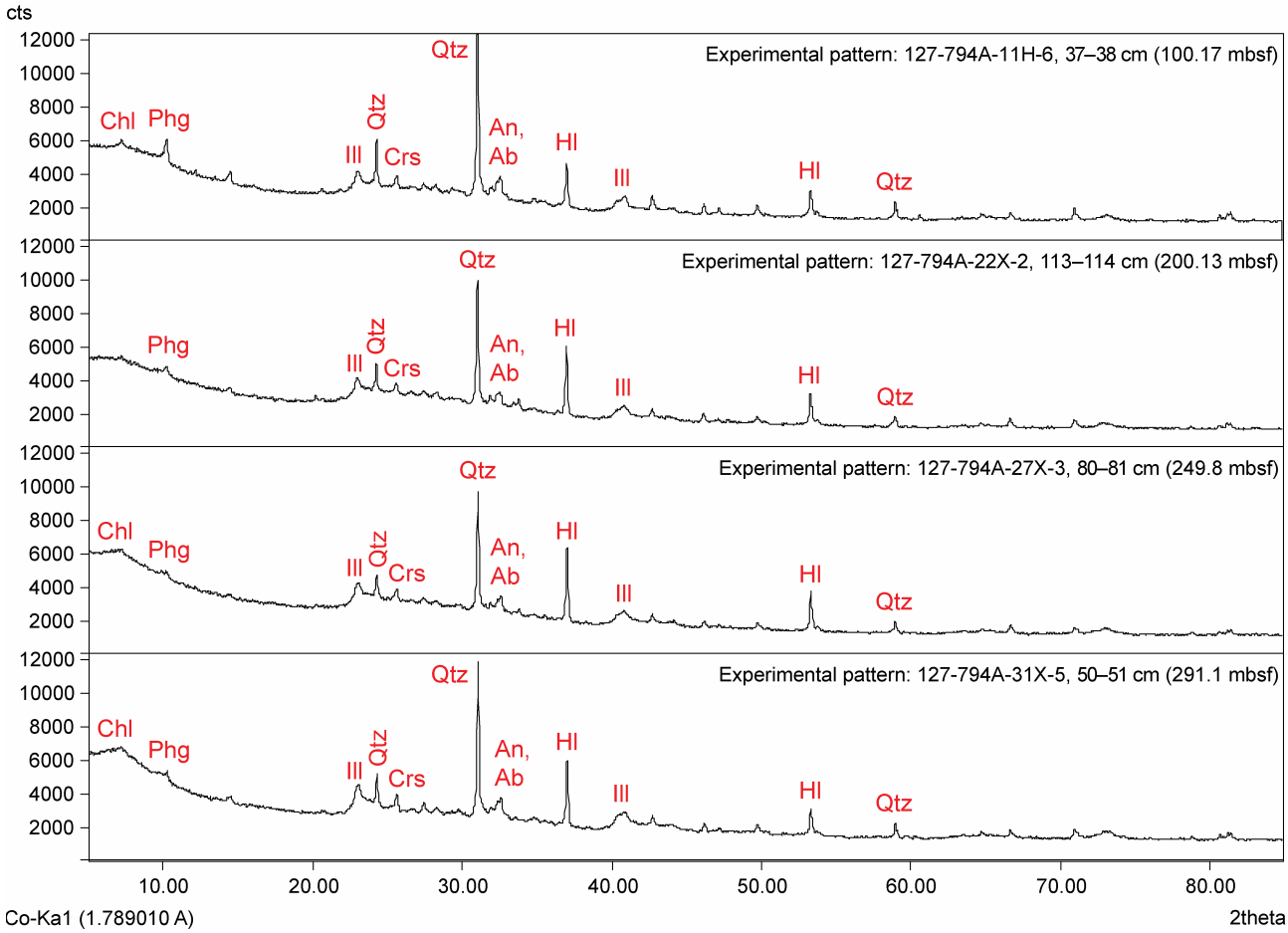
Yamano, M., Hamamoto, H., Kawada, Y., and Goto, S. 2014. Heat flow anomaly on the seaward side of the Japan Trench associated with deformation of the incoming Pacific plate, *Earth and Planetary Science Letters*, v. 407, p. 196–204.

Yin, A. 2010. Cenozoic tectonic evolution of Asia: A preliminary synthesis, *Tectonophysics*, v. 488, p. 293–325.

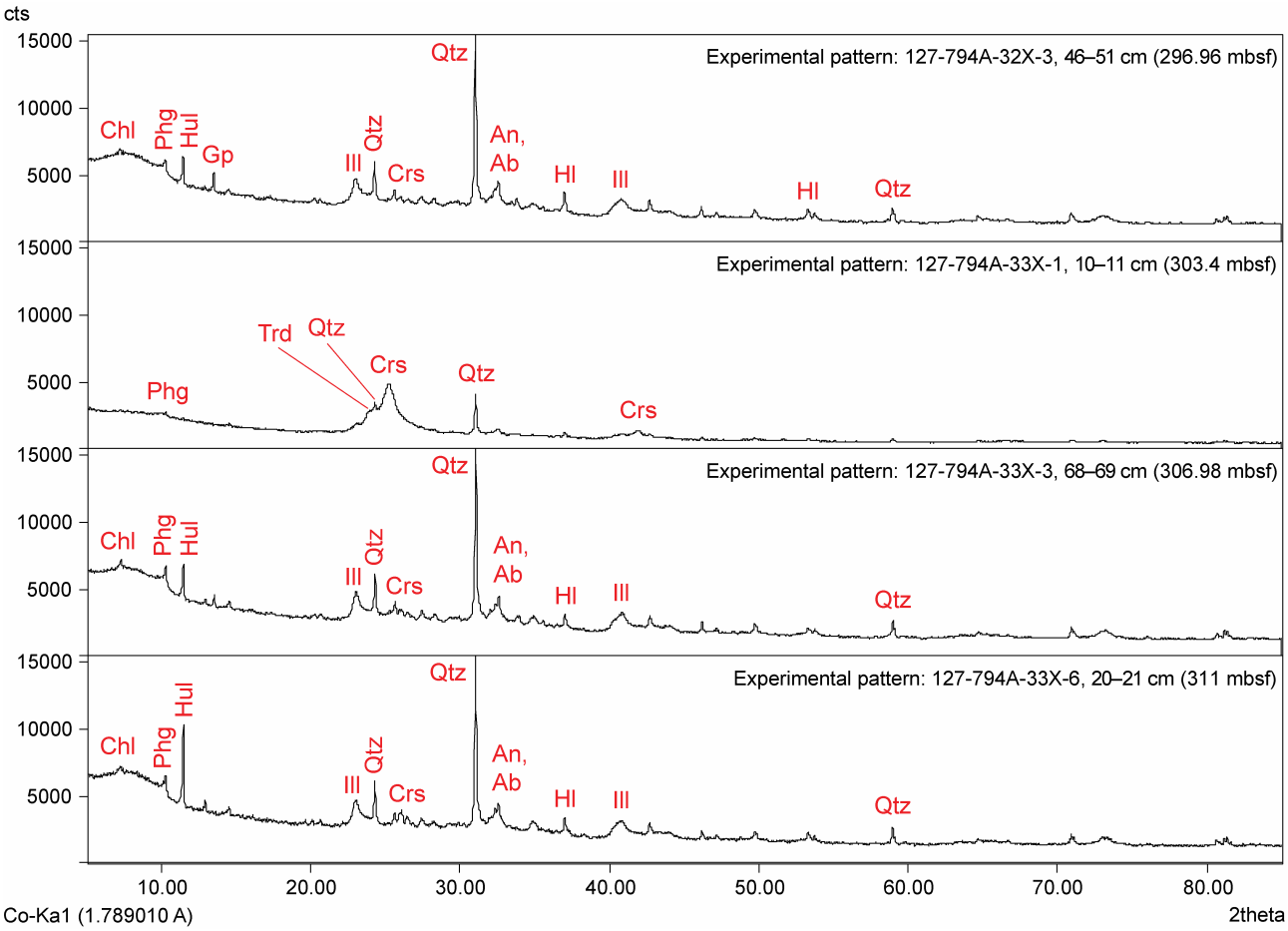
Yoon, S. H., Sohn, Y. K., and Choughc, S. K. 2014. Tectonic, sedimentary, and volcanic evolution of a back-arc basin in the East Sea (Sea of Japan), *Marine Geology*, v. 352, p. 70–88.

Appendices

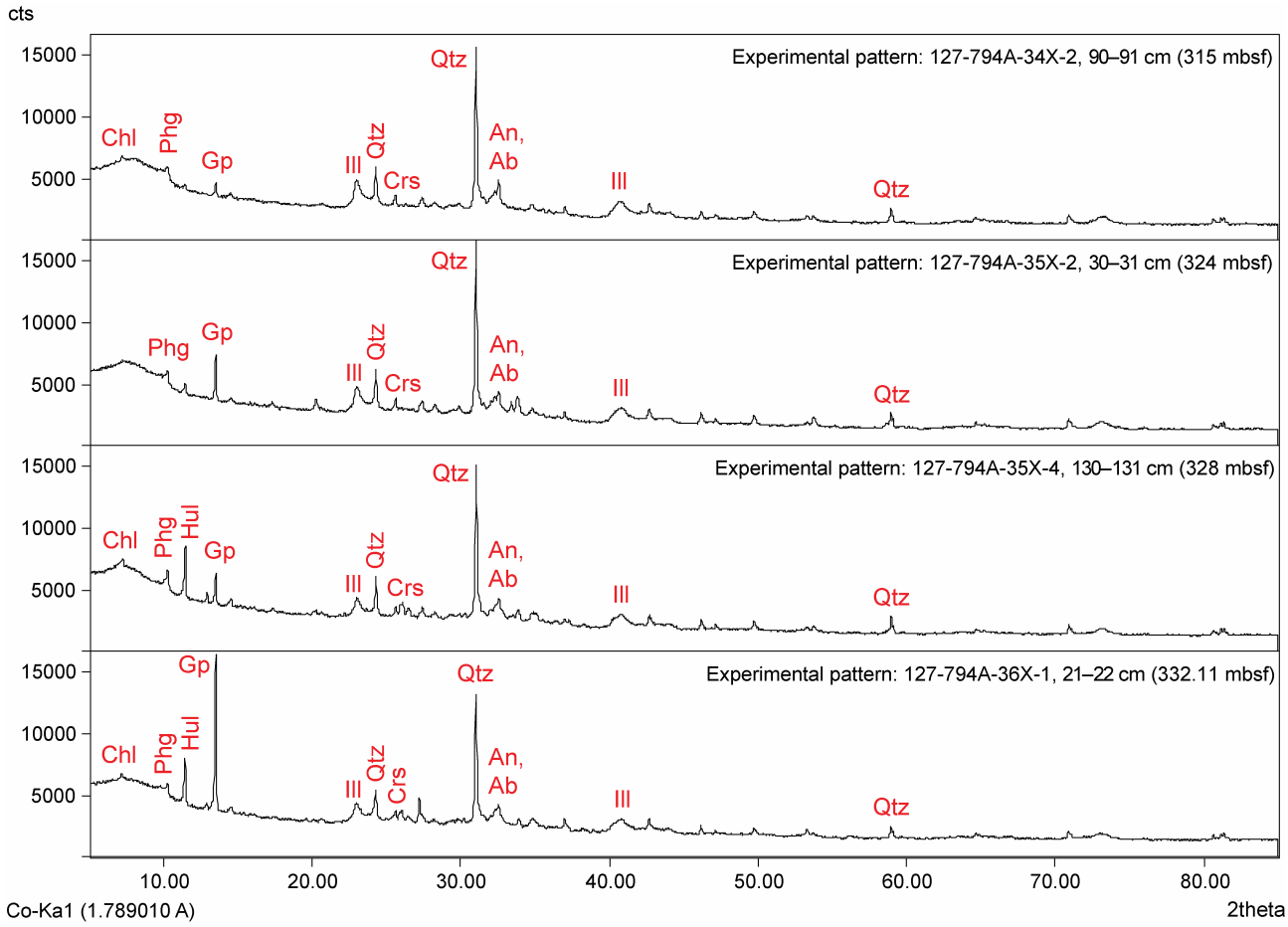
Appendix I (Chapter 4)



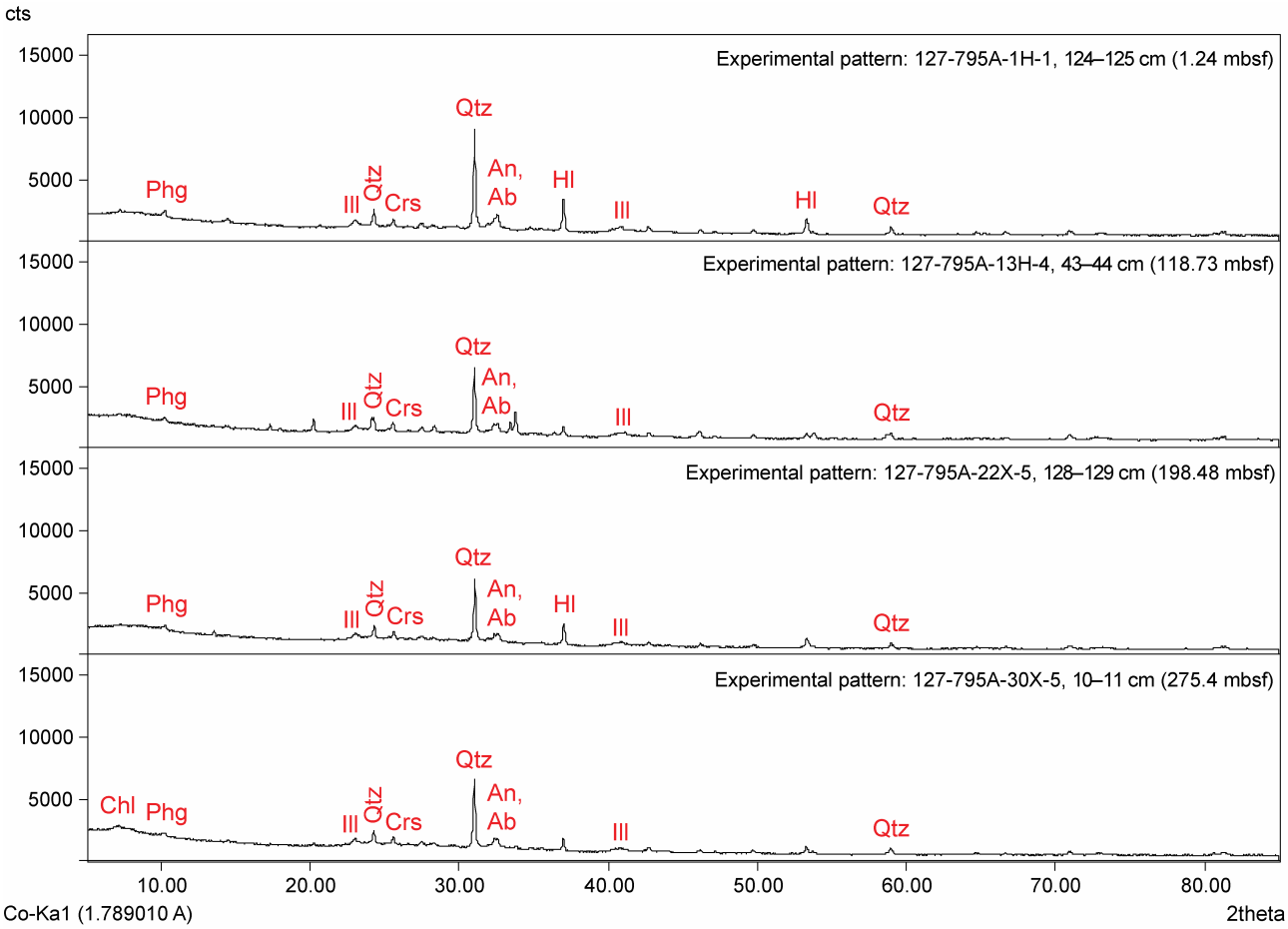
I.1. XRD integrated intensity versus 2θ for sediment core samples from opal-A-rich interval at Site 794. The XRD graphs were plotted using the software Match! 3.2.1 Build 70. The abbreviations represent: Ab = albite, An = anorthite, Chl = chlorite, Crs = cristobalite, Hl = halite, Ill = illite, Phg = phengite, Qtz = quartz.



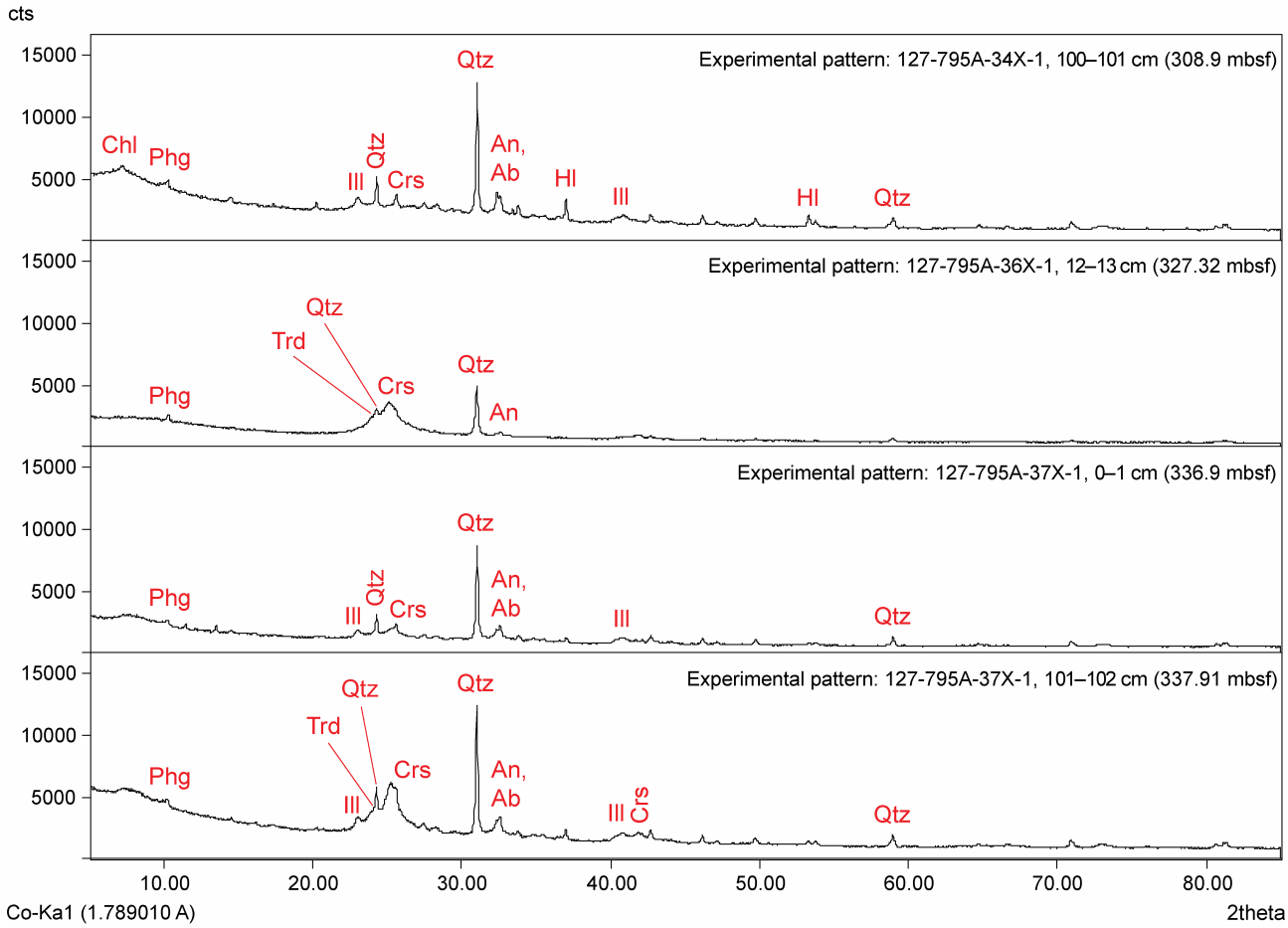
I.2. XRD integrated intensity versus 2θ for sediment core samples from the upper part of the $TZ_{A/CT}$ at Site 794. The XRD graphs were drawn using the Match! 3.4.2 Build 96. The abbreviations represent: Ab = albite, An = anorthite, Chl = chlorite, Crs = cristobalite, Gp = gypsum, Hl = halite, Hul = heulandite, Ill = illite, Phg = phengite, Qtz = quartz, Trd = tridymite.



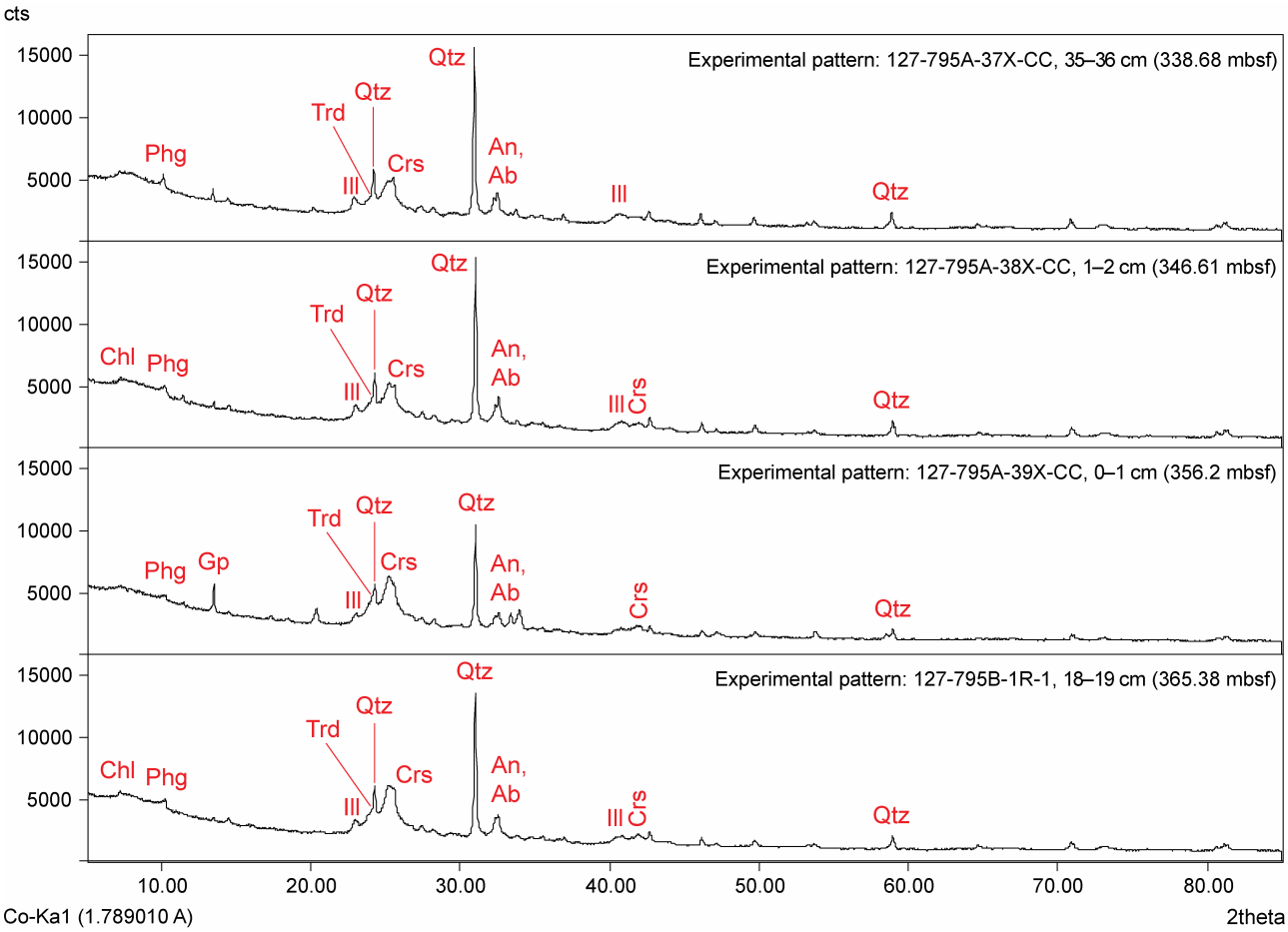
I.3. XRD integrated intensity versus 2θ for sediment core samples from the lower part of the $TZ_{A/CT}$ at Site 794. The XRD graphs were drawn using the Match! 3.4.2 Build 96. The abbreviations represent: Ab = albite, An = anorthite, Chl = chlorite, Crs = cristobalite, Gp = gypsum, Hul = heulandite, Ill = illite, Phg = phengite, Qtz = quartz.



I.4. XRD integrated intensity versus 2θ for sediment core samples from opal-A-rich interval at Site 795. The XRD graphs were plotted using the software Match! 3.4.2 Build 96. The abbreviations represent: Ab = albite, An = anorthite, Chl = chlorite, Crs = cristobalite, Hl = halite, Ill = illite, Phg = phengite, Qtz = quartz.

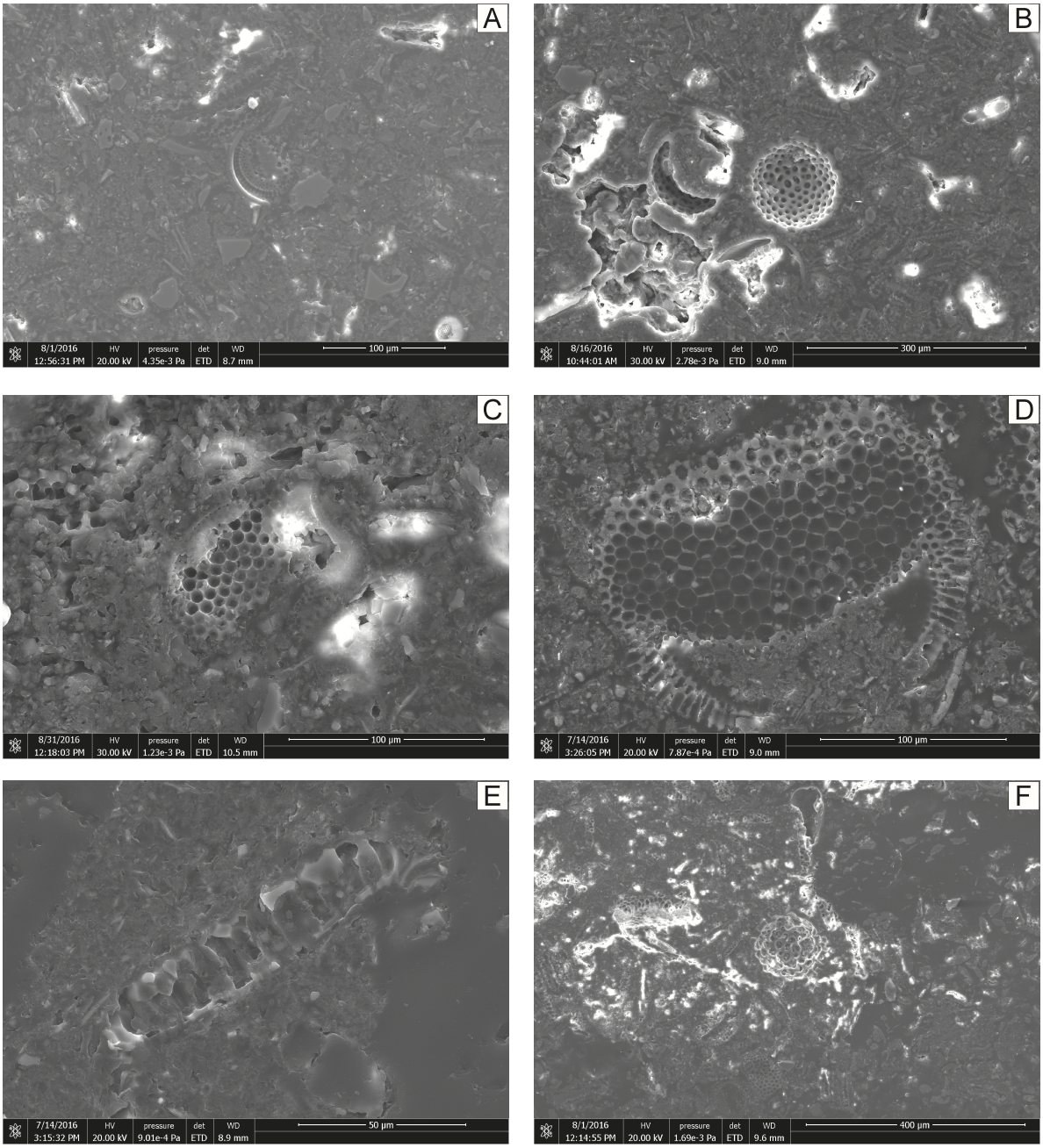


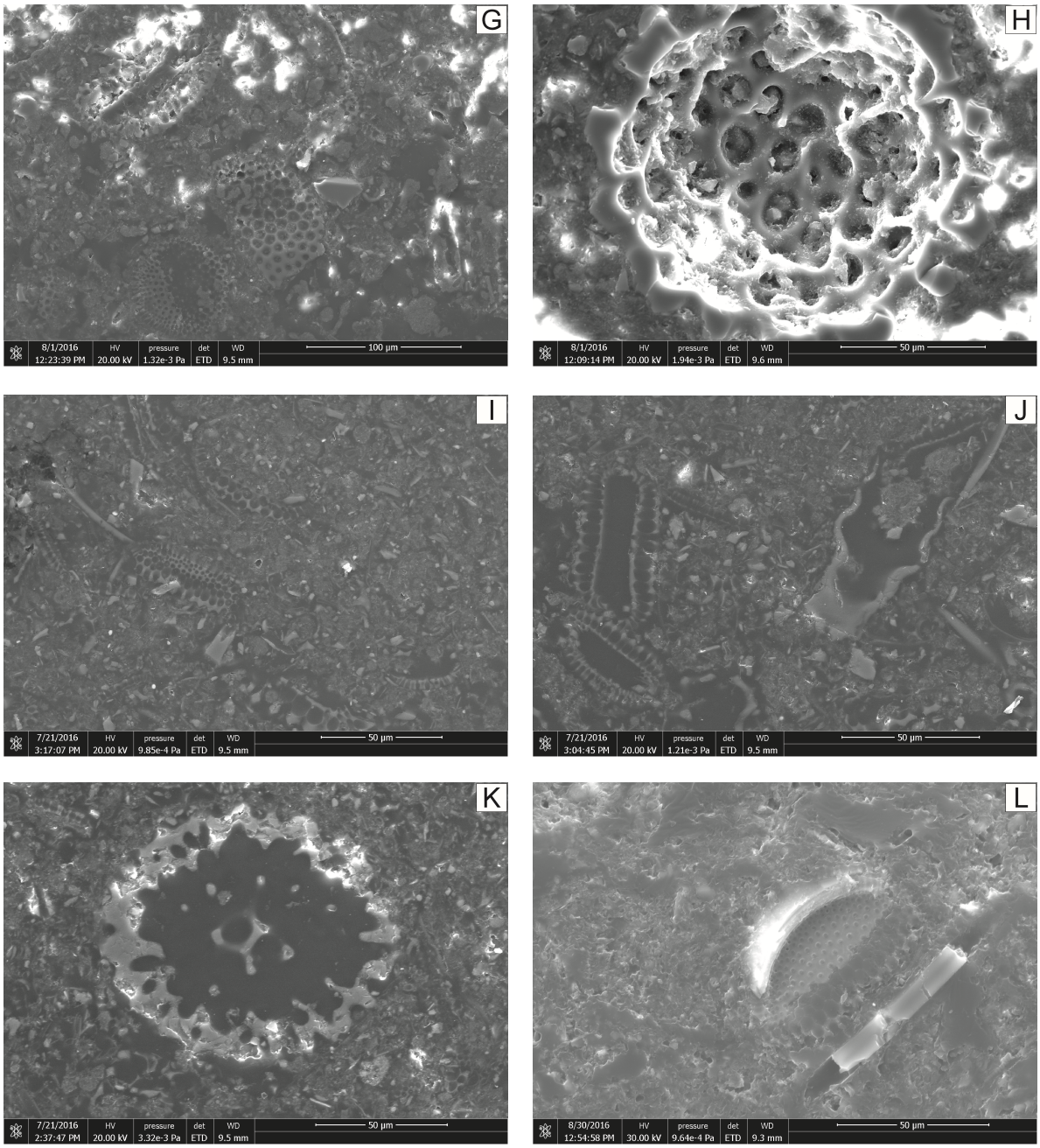
I.5. XRD integrated intensity versus 2θ for sediment core samples from the lower part of opal-A zone (the uppermost (first) XRD graph in the photo) and the upper part of the $TZ_{A/CT}$ at Site 795. The XRD graphs were plotted using the Match! 3.4.2 Build 96. The abbreviations represent: Ab = albite, An = anorthite, Chl = chlorite, Crs = cristobalite, Hl = halite, Ill = illite, Phg = phengite, Qtz = quartz, Trd = tridymite.



I.6. XRD integrated intensity versus 2θ for sediment core samples from the $TZ_{A/CT}$ (upper and lower parts) at Site 795. The XRD graphs were plotted using the software Match! 3.4.2 Build 96. The abbreviations represent: Ab = albite, An = anorthite, Chl = chlorite, Crs = cristobalite, Gp = gypsum, Ill = illite, Phg = phengite, Qtz = quartz, Trd = tridymite.

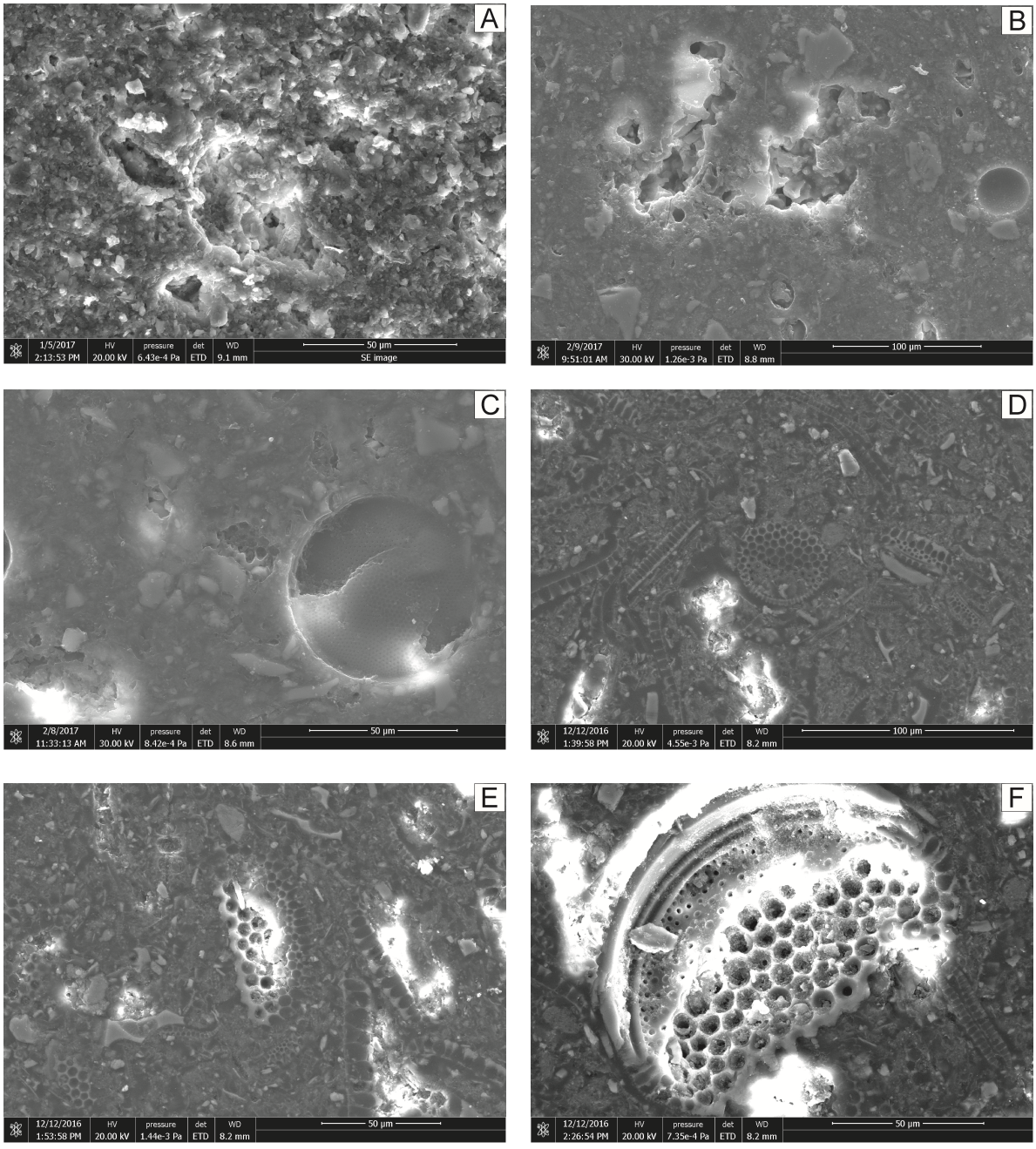
Appendix II (Chapter 4)

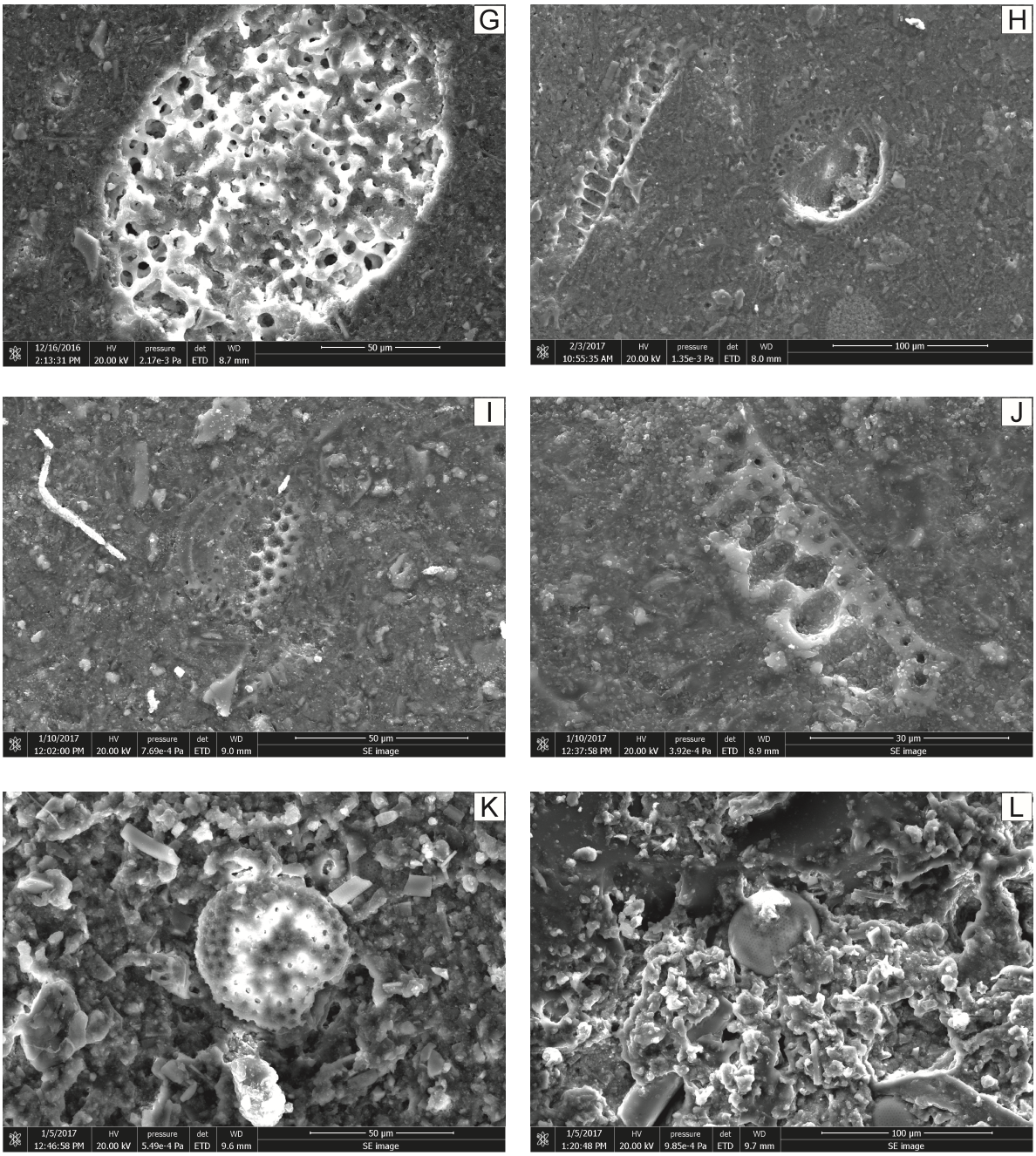




II.1. Additional SEM photomicrographs of biosiliceous sediments (opal-A interval) from Site 794. A) Clayey diatom ooze with fragmented and dissolved siliceous tests (Sample 127-794A-11H-6, 37–38 cm, at 100.17 mbsf); B) Development of large cavities due to dissolution of diatoms and radiolarians in the porous diatom ooze (Sample 127-794A-11H-6, 37–38 cm, at 100.17 mbsf); C) Deterioration of a diatom frustule under extensive dissolution (Sample 127-794A-11H-6, 37–38 cm, at 100.17

mbsf); D) Extensive dissolution of a diatom valve (Sample 127-794A-17X-1, 48–49 cm, at 149.98 mbsf); E) Deterioration of a diatom valve due to extensive dissolution (Sample 127-794A-17X-1, 48–49 cm, at 149.98 mbsf); F) High porosity clayey diatom ooze with extensively-dissolved (and in some places deteriorated) siliceous tests (Sample 127-794A-22X-2, 113–114 cm, at 200.13 mbsf) ; G) Highly-porous clayey diatom ooze containing extensively dissolved and deteriorated siliceous frustules (Sample 127-794A-22X-2, 113–114 cm, at 200.13 mbsf); H) Extensive dissolution of a radiolarian (Sample 127-794A-22X-2, 113–114 cm, at 200.13 mbsf); I) High porosity diatom clay with dominance of fragmented and strongly-dissolved (mostly deteriorated) siliceous tests (Sample 127-794A-27X-3, 80–81 cm, at 249.8 mbsf); J) Diatom clay containing deteriorated diatoms (Sample Sample 127-794A-27X-3, 80–81 cm, at 249.8 mbsf); K) Deterioration of a diatom valve due to extensive dissolution (Sample 127-794A-27X-3, 80–81 cm, at 249.8 mbsf); L) Fragmentation and deterioration of diatom tests under dissolution (Sample 127-794A-27X-3, 80–81 cm, at 249.8 mbsf).

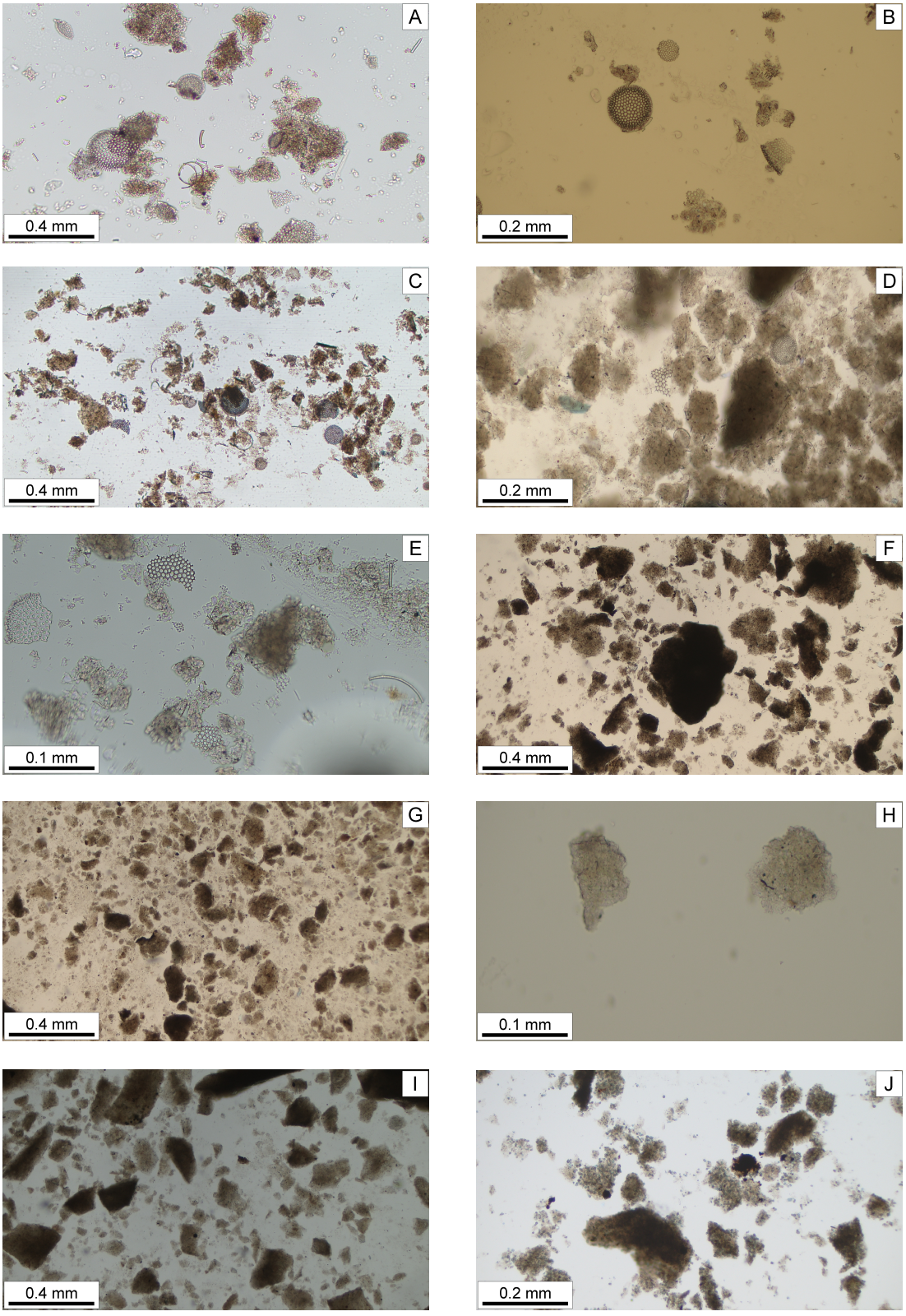

A
1/5/2017 2:13:53 PM | HV 20.00 kV | pressure 6.43e-4 Pa | det ETD | WD 9.1 mm | 50 µm | SE image
B
2/9/2017 9:51:01 AM | HV 30.00 kV | pressure 1.26e-3 Pa | det ETD | WD 8.8 mm | 100 µm
C
2/8/2017 11:33:13 AM | HV 30.00 kV | pressure 8.42e-4 Pa | det ETD | WD 8.6 mm | 50 µm
D
12/12/2016 1:39:58 PM | HV 20.00 kV | pressure 4.55e-3 Pa | det ETD | WD 8.2 mm | 100 µm
E
12/12/2016 1:53:58 PM | HV 20.00 kV | pressure 1.44e-3 Pa | det ETD | WD 8.2 mm | 50 µm
F
12/12/2016 2:26:54 PM | HV 20.00 kV | pressure 7.35e-4 Pa | det ETD | WD 8.2 mm | 50 µm

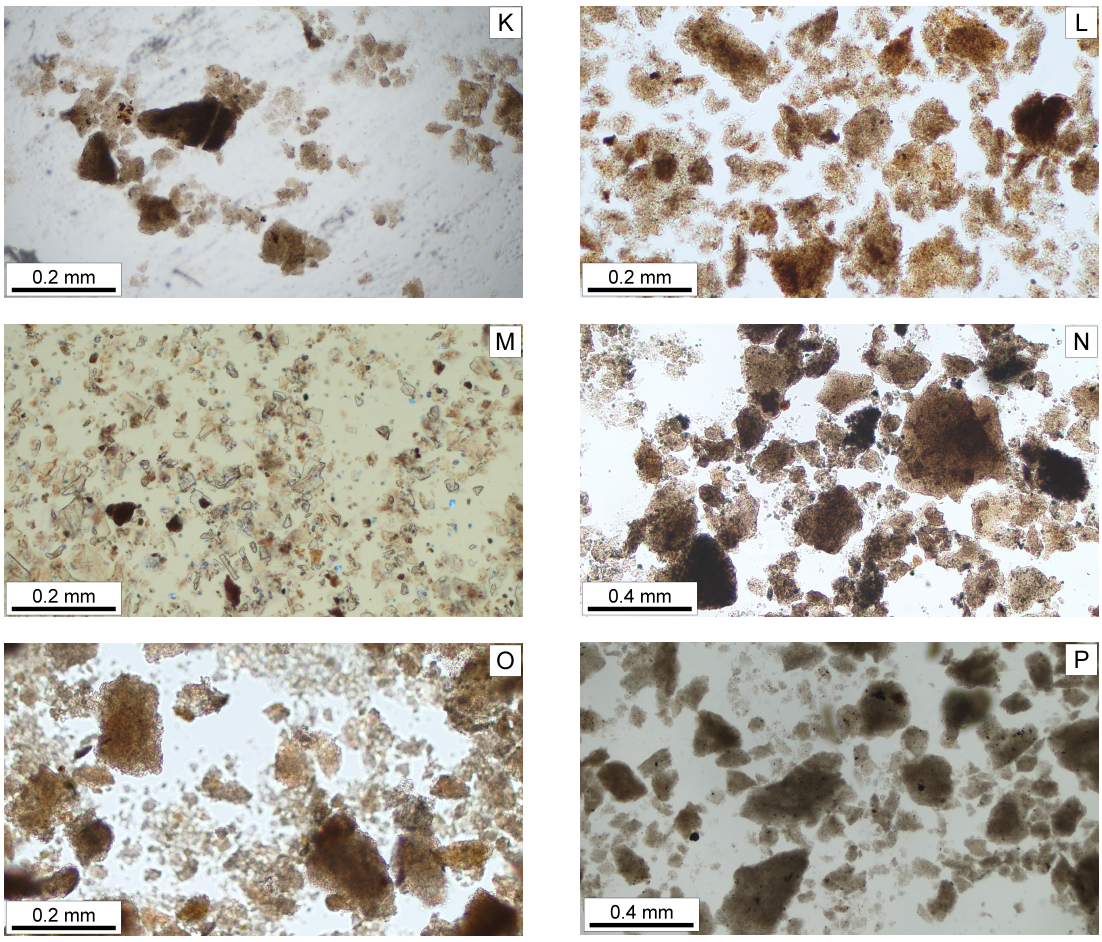


II.2. Additional SEM photomicrographs of biosiliceous sediments (opal-A interval) from Site 795. A) Highly-porous silty clay containing low content of diatom fragments (Sample 127-795A-6H-1, 91–92 cm, at 48.21 mbsf); B) Highly-porous biosiliceous silty clay with irregular cavities developed due to dissolution of siliceous tests (Sample 127-795A-13H-4, 43–44 cm, at 118.73 mbsf); C) Silty clay containing strongly dissolved and deteriorated diatoms (Sample 127-795A-13H-4,

43–44 cm at 118.73 mbsf); D) Highly-porous diatom ooze with fragmentation, extensive dissolution, and deterioration of siliceous tests (Sample 127-795A-16H-4, 101–102 cm, at 147.81 mbsf); E) Diatom ooze with fragmented and dissolved (deteriorated) tests (Sample 127-795A-16H-4, 101–102 cm, at 147.81 mbsf); F) Deterioration of a diatom valve under extensive dissolution (Sample 127-795A-16H-4, 101–102 cm, at 147.81 mbsf); G) Deterioration of a radiolarian due to extensive dissolution (Sample 127-795A-22X-5, 128–129 cm, at 198.48 mbsf); H) Porous diatom clay with diatom tests deteriorated under dissolution (Sample 127-795A-27X-1, 34–35 cm, at 240.24 mbsf); I) Highly-porous diatom clay with heavily-deteriorated diatoms (Sample 127-795A-30X-5, 10–11 cm, at 275.4 mbsf); J) A deteriorated diatom valve due to extensive dissolution (Sample 127-795A-30X-5, 10–11 cm, at 275.4 mbsf); K) Highly-porous diatom clayey silt mixed sediment with siliceous tests (commonly diatoms) fragmented and extensively deteriorated (Sample 127-795A-35X-3, 100–101, at 321.6 mbsf); L) High porosity diatom clayey silt mixed sediment with diatoms as the dominant siliceous test mostly fragmented and dissolved (Sample 127-795A-35X-3, 100–101, at 321.6 mbsf).

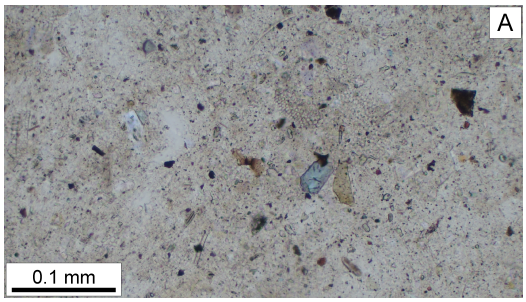
Appendix III (Chapter 5)

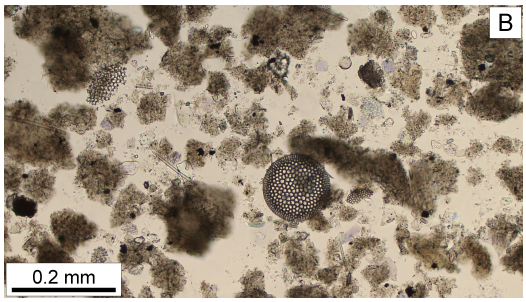


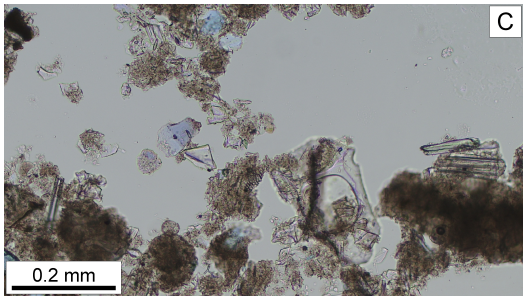


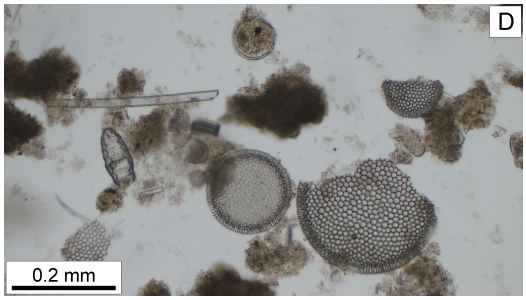
III.1. Additional photomicrographs of smear slides from Site 794. A) Diatom ooze (having also low amounts of sponge spicules) with low content of quartz and minor opaque minerals (Sample 127-794A-11H-6, 37–38 cm, at 100.17 mbsf); B) Siliceous tests (especially diatoms) and clayey particles in a diatom ooze (Sample 127-794A-17X-1, 48–49 cm, at 149.98 mbsf); C) Diatom clay with little amounts of sponge spicules and micro-quartz (Sample 127-794A-27X-3, 80–81 cm, at 249.8 mbsf); D) Clay with low amounts of diatoms, sponge spicules, pyrite, and quartz (Sample 127-794A-31X-6, 90–91 cm, at 293 mbsf); E) Diatom fragments, little amounts of sponge spicules, quartz, and minor pyrite and volcanic glass in a clayey facies (Sample 127-794A-32X-1, 22–23 cm, at 293.72 mbsf); F) Clay with little content of quartz and minor volcanic glass (?) (Sample 127-794A-32X-3, 46–47 cm, at 296.96 mbsf); G) Clay with low amounts of pyrite and quartz (Sample 127-794A-32X-CC, 34–35 cm, at 298.45 mbsf); H) Fragments of clayey material (Sample 127-794A-

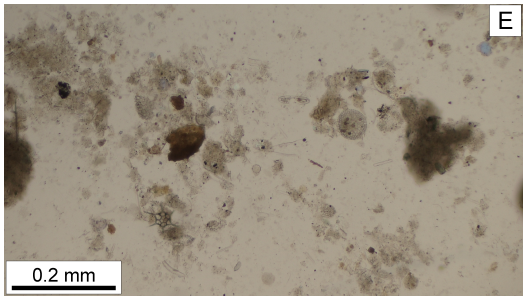
33X-1, 0–1 cm, at 303.3 mbsf); I) Claystone with low contents of pyrite and quartz (Sample 127-794A-33X-1, 10–11 cm, at 303.4 mbsf); J) Dolomite-bearing clay with low amounts of pyrite and opaque minerals (Sample 127-794A-33X-4, 119–120 cm, at 308.99 mbsf); K) Clay with low contents of pyrite, opaque minerals, and micro-quartz (?) (Sample 127-794A-34X-2, 90–91 cm, at 315 mbsf); L) Clay with low amounts of opaque minerals, pyrite, and quartz (Sample 127-794A-35X-2, 30–31 cm, at 324 mbsf); M) Ashy claystone with low contents of quartz, feldspar, volcanic glass, mica, pyrite, and opaque minerals (Sample 127-794A-37X-1, 0–1 cm, at 341.6 mbsf); N) Clay with low amounts of dolomite, pyrite, opaque minerals, and micro-quartz (?) (Sample 127-794A-37X-3, 40–41 cm, at 345 mbsf); O) Calcareous (?) clay (Sample 127-794A-37X-CC, 30–31 cm, at 346.63 mbsf); P) Siliceous clay with low amounts of pyrite and minor micro-quartz (Sample 127-794B-6R-CC, 5–6 cm, at 347.85 mbsf).


A
0.1 mm

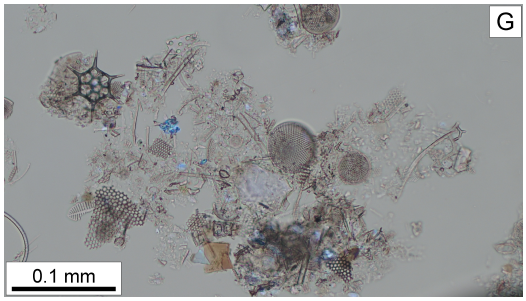

B
0.2 mm

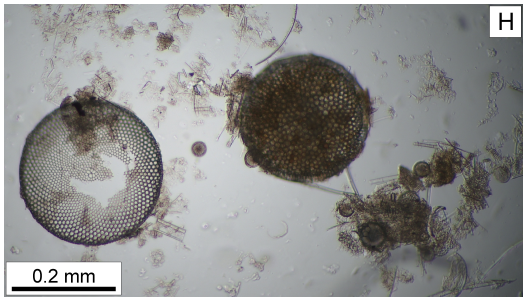

C
0.2 mm

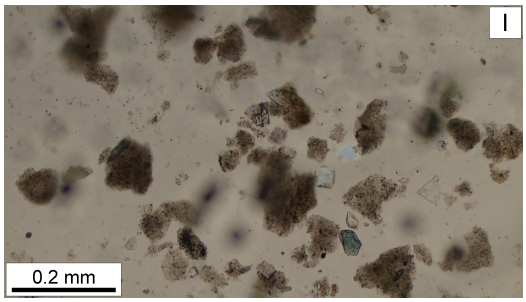

D
0.2 mm

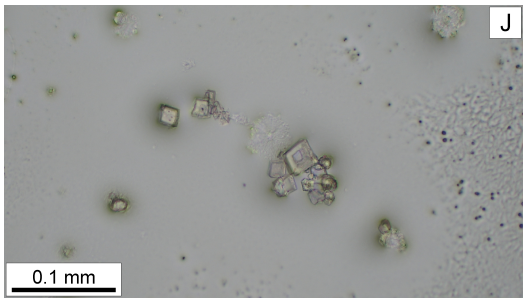

E
0.2 mm

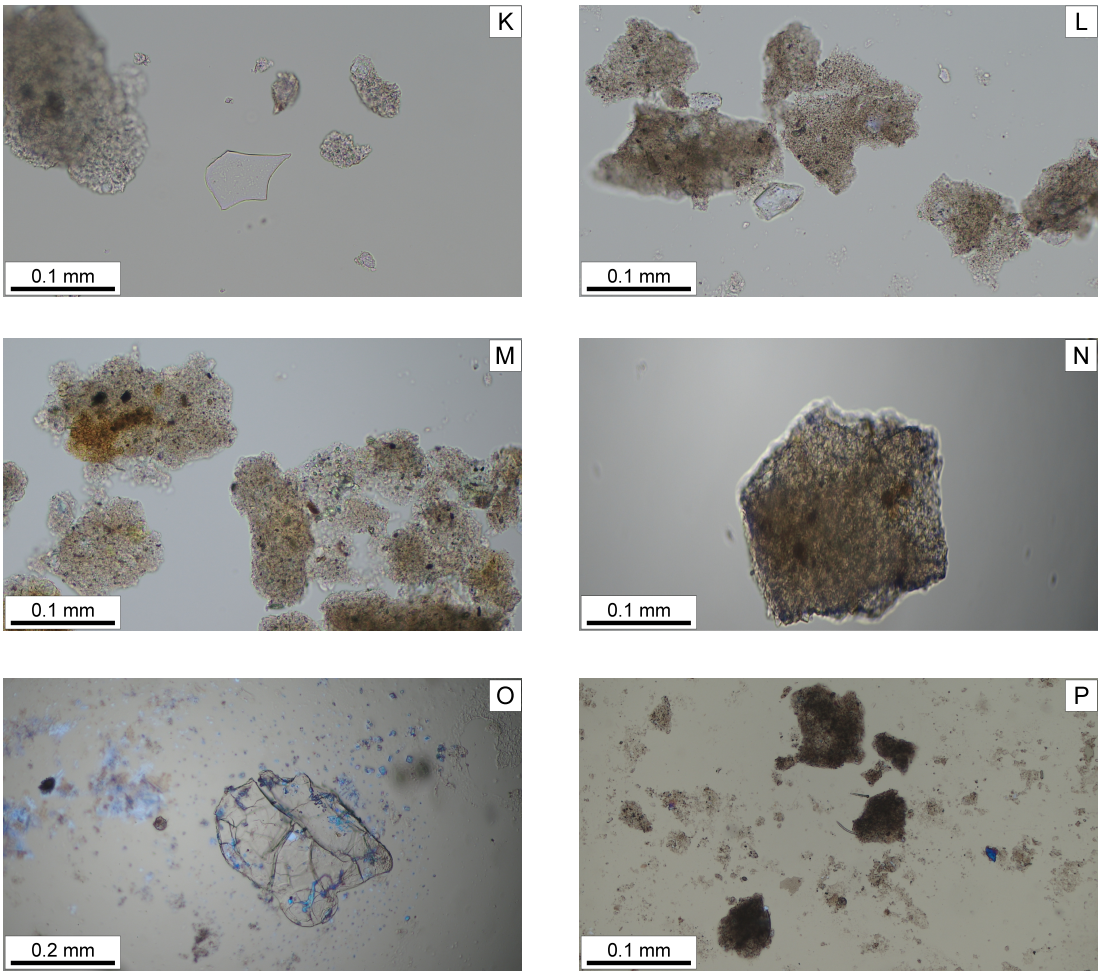

F
0.1 mm


G
0.1 mm


H
0.2 mm


I
0.2 mm


J
0.1 mm



III.2. Additional photomicrographs of smear slides from Site 795. A) Ashy diatom silty clay with low content of volcanic glass, quartz, mica, feldspar, pyrite, opaque minerals, and sponge spicules (Sample 127-795A-1H-1, 124–125 cm, at 1.24 mbsf); B) Diatom-bearing silty clay with low amount of volcanic glass, quartz, feldspar, pyrite, opaque minerals, and sponge spicules (Sample 127-795A-6H-1, 91–92 cm, at 48.21 mbsf); C) Volcanic glass, feldspar, quartz, and minor pyrite in a biosiliceous silty clay (Sample 127-795A-13H-4, 43–44 cm, at 118.73 mbsf); D) Diatoms, sponge spicules, and minor content of pyrite in a diatom clay facies (Sample 127-795A-27X-1, 34–35 cm, at 240.24 mbsf); E) Diatom clayey siltstone with micro-quartz, volcanic glass (?), mica, pyrite, opaque minerals, sponge spicules, and silicoflagellates (Sample 127-795A-34X-3, 100–101 cm, at 311.9 mbsf); F) Diatoms, sponge spicules, quartz, volcanic glass, micas (commonly chlorite (or possibly

chloritoid)), and minor amount of pyrite in a diatom clayey silt facies (Sample 127-795A-34X-4, 105–106 cm, at 313.45 mbsf); G) Diatom clayey siltstone with quartz, volcanic glass, mica, sponge spicules, and silicoflagellates (Sample 127-795A-35X-1, 101–102 cm, at 318.61 mbsf); H) Diatoms, sponge spicules, quartz, and minor pyrite in a diatom clayey siltstone (Sample 127-795A-35X-5, 128–129 cm, at 324.88 mbsf); I) Siliceous silty claystone with low amounts of quartz, volcanic glass, mica (chloritoid or maybe chlorite), and pyrite (Sample 127-795A-35X-CC, 14–15 cm, at 326.74 mbsf); J) Idiomorphic (rhombohedral) and xenomorphic dolomite (Sample 127-795A-36X-1, 12–13 cm, at 327.32 mbsf); K) Vitric and fragments of fine (clay/silt) material (Sample 127-795A-36X-CC, 36–37 cm, at 327.78 mbsf); L) Quartz and fragments of silty claystone (Sample 127-795A-37X-1, 0–1 cm, at 336.9 mbsf); M) Siliceous silty clay with inclusions of micro-quartz, pyrite, mica, and minor dolomite (Sample 127-795A-37X-1, 133–134 cm, at 338.23 mbsf); N) Fragment of a siliceous claystone (Sample 127-795A-38X-CC, 1–2 cm, at 346.61 mbsf); O) Quartz (sand-sized) grain (in the centre of photo) and dolomite (right side of the photo) (Sample 127-795A-39X-CC, 0–1 cm, at 356.2 mbsf); P) Siliceous claystone with low amounts of micro-quartz, volcanic glass, minor feldspar, pyrite, and siliceous tests (diatoms and sponge spicules) (Sample 127-795B-6R-1, 80–81, at 414.6 mbsf).

Appendix IV (Chapter 5)

IV.1. The abundance of various components of sediments from Site 794 estimated based on the study of smear slides. The percentages were estimated by following the standard visual estimation charts of Terry and Chilingarian (1955). The format of this table follows the smear-slide description sheet of Marsaglia et al. (2013). The percentages of quartz and volcanic glass for most of the samples listed in this table were derived and slightly modified from Shipboard Scientific Party (1990a).

Sample ID	Dept, mbsf	Terrigenous texture, %			Component, %																						
					Siliciclastic grains/minerals													Biogenic grains										
					Framework grains/minerals						Accessory and authigenic grains/minerals							Siliceous				Calcareous			Others		
		Sand	Silt	Clay	Quartz	Feldspar (undifferentiated)	Volcanic glass	Source lithic fragment	Micas (undifferentiated)	Pyroxene	Clay-size fraction	Opaque minerals	Zeolite	Pyrite	Inorganic calcite	Dolomite	Gypsum	Diatoms	Radiolarians	Silicoflagellates	Sponge spicules	Foraminifera	Nannofossils	Bioclast (undifferentiated)	Organic debris	Plant debris	Fish debris
127-794A-11H-6, 37–38	100.17	60	5	35	2	–	–	–	–	–	25	1	–	–	–	–	–	70	–	–	2	–	–	–	–	–	–
127-794A-17X-1, 48–49	149.98	5	60	35	2.5	–	–	–	–	–	31	–	–	–	–	–	–	64	0.5	–	2	–	–	–	–	–	–
127-794A-22X-2, 113–114	200.13	0	50	50	1	–	–	–	–	–	32	–	–	–	–	–	–	66	–	–	1	–	–	–	–	–	–
127-794A-27X-3, 80–81	249.8	30	5	65	1	–	–	–	–	–	64	–	–	–	–	–	–	33	–	–	2	–	–	–	–	–	–
127-794A-31X-4, 100–101 *	290.1	5	10	85	3.5	1	–	–	2	1	79	–	1	–	–	–	–	11	0.5	–	1	–	–	–	–	–	–
127-794A-31X-5, 50–51	291.1	0	10	90	3.5	–	–	–	–	–	85	–	–	–	–	–	–	10	0.5	–	1	–	–	–	–	–	–
127-794A-31X-6, 90–91	293	0	10	90	4	–	–	–	–	–	86	–	–	1	–	–	–	7	–	–	2	–	–	–	–	–	–
127-794A-32X-1, 22–23	293.72	0	10	90	4	–	–	–	–	–	88	–	–	–	–	–	–	7	–	–	1	–	–	–	–	–	–
127-794A-32X-1, 100–101 *	294.5	0	10	90	4	0.5	0.5	–	0.5	–	88	–	–	0.5	–	–	–	5.5	–	–	0.5	–	–	–	–	–	–
127-794A-32X-2, 5–6	295.05	0	5	95	6.5	–	0.5	–	–	–	92	–	–	1	–	–	–	–	–	–	–	–	–	–	–	–	–
127-794A-32X-2, 100–101 *	296	0	10	90	4.5	–	0.5	–	–	–	91	–	–	1.5	–	–	–	2	–	–	0.5	–	–	–	–	–	–
127-794A-32X-3, 46–47	296.96	0	5	95	4.5	–	0.5	–	–	–	94	–	–	–	1	–	–	–	–	–	–	–	–	–	–	–	–
127-794A-32X-3, 100–101 *	297.5	0	5	95	5	–	0.5	–	–	–	93	–	–	–	–	–	–	1	–	–	0.5	–	–	–	–	–	–
127-794A-32X-CC, 34–35	298.45	0	5	95	5	–	0.5	–	–	–	93	–	–	1.5	–	–	–	–	–	–	–	–	–	–	–	–	–
127-794A-33X-1, 0–1	303.3	0	5	95	5	–	0.5	–	–	–	93	–	–	1.5	–	–	–	–	–	–	–	–	–	–	–	–	–
127-794A-33X-1, 5–6	303.35	0	5	95	5	–	0.5	–	–	–	94	–	–	0.5	–	–	–	–	–	–	–	–	–	–	–	–	–
127-794A-33X-1, 10–11	303.4	0	5	95	5	–	0.5	–	–	–	94	–	–	0.5	–	–	–	–	–	–	–	–	–	–	–	–	–
127-794A-33X-1, 35–36	303.65	0	5	95	5	–	0.5	–	0.5	–	93	–	–	0.5	–	–	–	–	0.5	–	–	–	–	–	–	–	–
127-794A-33X-1, 70–71	304	0	5	95	5	–	0.5	–	–	–	94	–	–	0.5	–	–	–	–	–	–	–	–	–	–	–	–	–
127-794A-33X-1, 100–101 *	304.3	0	5	95	5	–	0.5	–	0.5	–	93	–	–	1	–	–	–	–	–	–	–	–	–	–	–	–	–
127-794A-33X-1, 104–105	304.34	0	5	95	5	–	0.5	–	0.5	–	93	–	–	1	–	–	–	–	–	–	–	–	–	–	–	–	–
127-794A-33X-2, 9–10	304.89	0	5	95	5	–	0.5	–	–	–	93	–	–	1.5	–	–	–	–	–	–	–	–	–	–	–	–	–
127-794A-33X-3, 68–69	306.98	0	5	95	5	–	0.5	–	1	–	93	–	–	0.5	–	–	–	–	–	–	–	–	–	–	–	–	–
127-794A-33X-4, 12–13 *	307.92	0	5	95	5	–	1	–	1	–	92	–	–	1	–	–	–	–	–	–	–	–	–	–	–	–	–
127-794A-33X-4, 119–120	308.99	0	10	90	5	–	0.5	–	–	–	76	2.5	–	3	–	13	–	–	–	–	–	–	–	–	–	–	–
127-794A-33X-5, 100–101 *	310.3	0	5	95	5	–	1	–	–	–	92	–	1	1	–	–	–	–	–	–	–	–	–	–	–	–	–
127-794A-33X-6, 20–21	311	0	5	95	5	–	0.5	–	–	–	94	–	–	0.5	–	–	–	–	–	–	–	–	–	–	–	–	–
127-794A-34X-1, 40–41	313	0	10	90	4	–	–	–	–	–	95	–	–	1	–	–	–	–	–	–	–	–	–	–	–	–	–
127-794A-34X-2, 90–91	315	0	5	95	4	–	0.5	–	–	–	93	–	–	2.5	–	–	–	–	–	–	–	–	–	–	–	–	–
127-794A-35X-1, 5–6	322.25	0	5	95	2.5	–	0.5	–	–	–	93	1	–	2	–	–	–	–	–	–	–	–	–	–	1	–	–
127-794A-35X-2, 30–31	324	0	5	95	5	–	0.5	–	–	–	93	1	–	0.5	–	–	–	–	–	–	–	–	–	–	–	–	–
127-794A-35X-3, 80–81	326	0	5	95	5	–	0.5	–	–	–	93	1.5	–	–	–	–	–	–	–	–	–	–	–	–	–	–	–
127-794A-35X-4, 130–131	328	0	5	95	4	–	0.5	–	–	–	92	2.5	–	1	–	–	–	–	–	–	–	–	–	–	–	–	–
127-794A-35X-6, 38–39	330.08	0	5	95	4	–	0.5	–	–	–	95	–	–	0.5	–	–	–	–	–	–	–	–	–	–	–	–	–
127-794A-36X-1, 21–22	332.11	0	4	96	3.5	–	0.5	–	–	–	96	–	–	–	–	–	–	–	–	–	–	–	–	–	–	–	–
127-794A-36X-2, 55–56	333.95	0	4	96	3	–	0.5	–	–	–	96	0.5	–	–	–	–	–	–	–	–	–	–	–	–	–	–	–

IV.1. Continued.

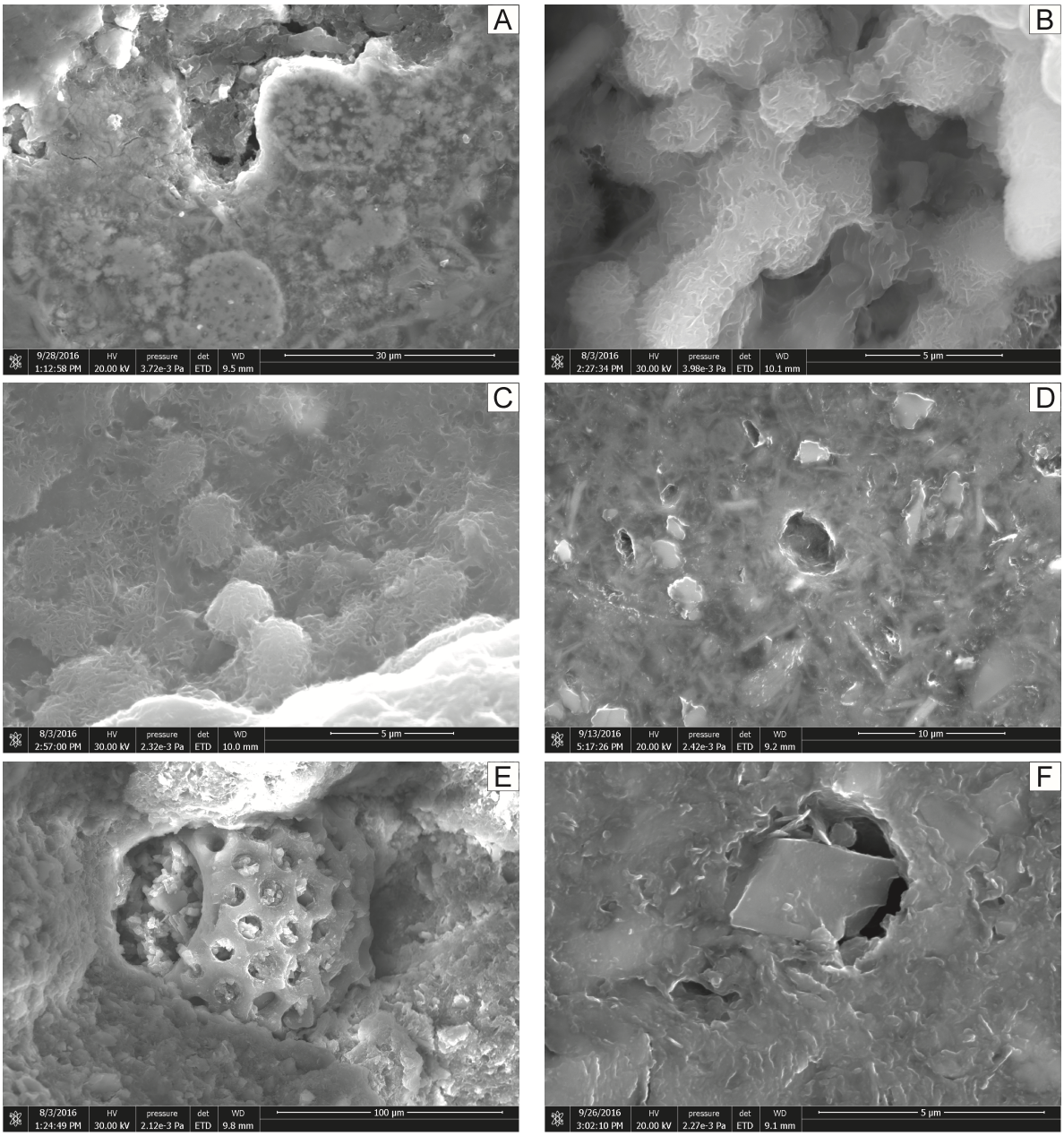
127-794A-36X-3, 110–111	336	0	4	96	3	–	0.5	–	–	–	96	–	–	0.5	–	–	–	–	–	–	–	–	–	–	–	–
127-794A-36X-5, 54–55	338.44	0	4	96	3	–	0.5	–	–	–	96	–	–	0.5	–	–	–	–	–	–	–	–	–	–	–	–
127-794B-5R-1, 39–40 *	338.69	0	5	95	3	–	1	–	1	–	94	–	–	1	–	–	–	–	–	–	–	–	–	–	–	–
127-794B-5R-1, 49–50 *	338.79	0	5	95	3	–	1	–	1.5	–	94	–	–	0.5	–	–	–	–	–	–	–	–	–	–	–	–
127-794A-37X-1, 0–1	341.6	0	10	90	7	5	2	–	1.5	–	81	1.5	–	2	–	–	–	–	–	–	–	–	–	–	–	–
127-794A-37X-2, 19–20	343.29	0	4	96	2.5	–	0.5	–	–	–	96	0.5	–	0.5	–	–	–	–	–	–	–	–	–	–	–	–
127-794A-37X-3, 40–41	345	0	5	95	2	–	0.5	–	–	–	91	1.5	–	1	–	4	–	–	–	–	–	–	–	–	–	–
127-794A-37X-3, 140–141	346	0	4	96	2.5	–	0.5	–	–	–	96	1	–	–	–	–	–	–	–	–	–	–	–	–	–	–
127-794A-37X-CC, 30–31	346.63	0	3	97	2.5	–	0.5	–	–	–	97	–	–	–	–	–	–	–	–	–	–	–	–	–	–	–
127-794B-6R-CC, 5–6	347.85	0	20	80	1.5	–	0.5	–	–	–	94	–	–	4	–	–	–	–	–	–	–	–	–	–	–	–
127-794B-6R-CC, 7–8 *	347.87	0	4	96	2.5	–	0.5	–	–	1	96	–	–	–	–	–	–	–	–	–	–	–	–	–	–	–

* Abundance of sediment components has been estimated from smear-slides analyses conducted by the ODP, available through the IODP core database.

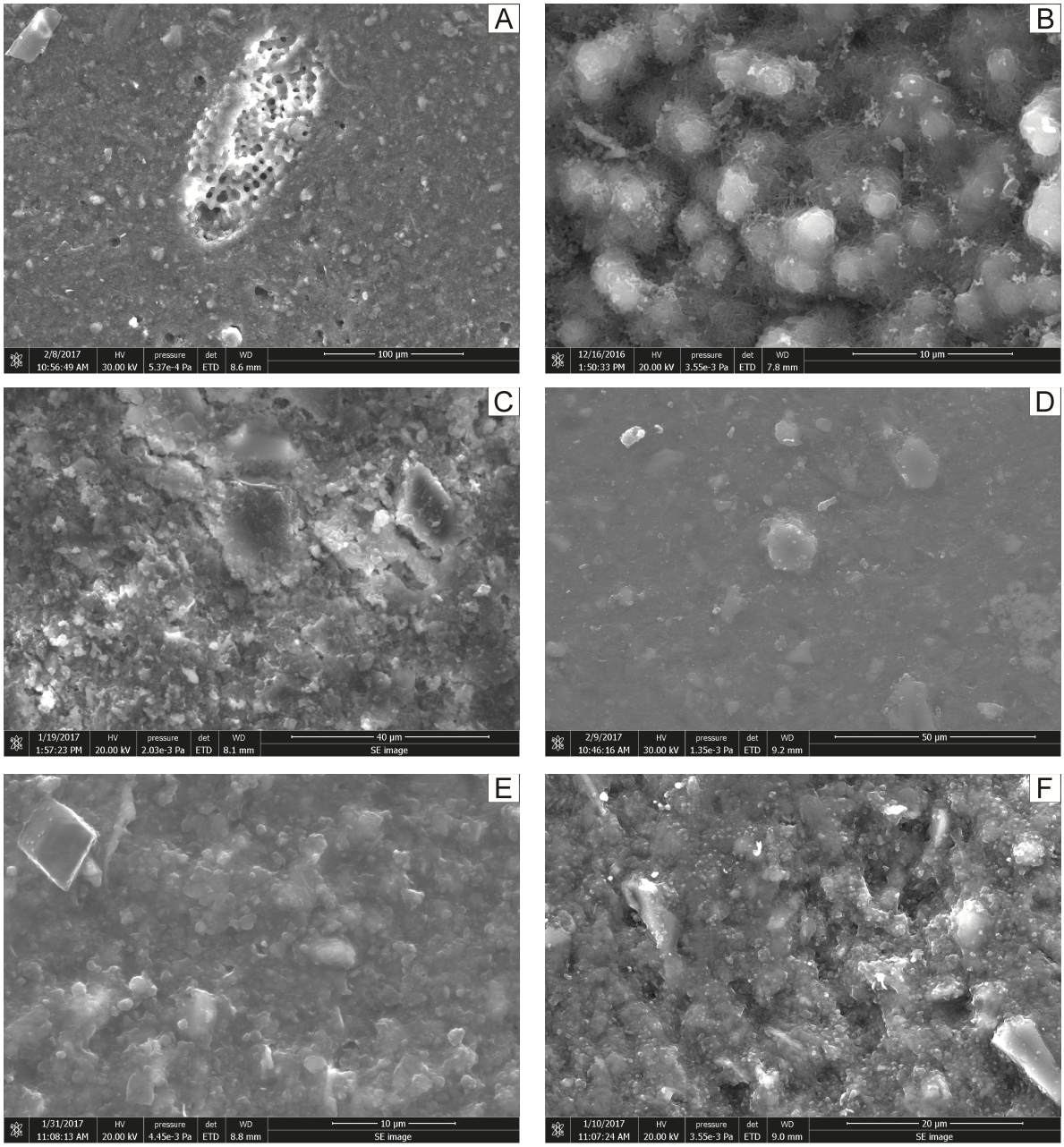
IV.2. The abundance of various components of sediments from Site 795 estimated based on the study of smear slides. The percentages were estimated by following the standard visual estimation charts of Terry and Chilingarian (1955). The format of this table follows the smear-slide description sheet of Marsaglia et al. (2013). The percentages of quartz and volcanic glass for most of the samples listed in this table were derived and slightly modified from Shipboard Scientific Party (1990b).

Sample ID	Dept, mbsf	Terrigenous texture, %			Component, %																							
					Siliciclastic grains/minerals													Biogenic grains											
					Framework grains/minerals						Accessory and authigenic grains/minerals							Siliceous				Calcareous			Others			
		Sand	Silt	Clay	Quartz	Feldspar (undifferentiated)	Volcanic glass	Source lithic fragment	Micas (undifferentiated)	Pyroxene	Clay-size fraction	Opaque minerals	Zeolite	Pyrite	Inorganic calcite	Dolomite	Gypsum	Diatoms	Radiolarians	Silicoflagellates	Sponge spicules	Foraminifera	Nannofossils	Bioclast (undifferentiated)	Organic debris	Plant debris	Fish debris
127-795A-1H-1, 124–125	1.24	0	30	70	5	0.5	6	–	1.5	–	66	2	–	3	–	–	–	14	–	–	1	–	–	–	1	–	–
127-795A-6H-1, 91–92	48.21	0	25	75	4	0.5	6	–	–	–	72	0.5	–	2	–	–	–	14	–	–	1	–	–	–	–	–	–
127-795A-13H-4, 43–44	118.73	0	30	70	5	3.5	4	–	–	–	60	–	–	0.5	–	–	–	26	–	–	1	–	–	–	–	–	–
127-795A-16H-4, 101–102	147.81	0	65	35	4	–	2.5	–	–	–	32	–	–	0.5	–	–	–	58	–	–	3	–	–	–	–	–	–
127-795A-22X-5, 128–129	198.48	10	50	40	3	–	2.5	–	0.5	–	25	–	–	1	–	–	–	63	1	–	4	–	–	–	–	–	–
127-795A-27X-1, 34–35	240.24	10	30	60	3	–	–	–	–	–	58	–	–	1	–	–	–	36	–	–	2	–	–	–	–	–	–
127-795A-30X-5, 10–11	275.4	0	40	60	3	–	2	–	–	–	49	–	–	1	–	–	–	42	–	–	3	–	–	–	–	–	–
127-795A-34X-1, 100–101	308.9	10	50	40	22	–	–	–	–	–	40	–	–	0.5	–	–	–	34	–	0.5	3	–	–	–	–	–	–
127-795A-34X-3, 100–101	311.9	10	50	40	28	–	0.5	–	1	–	33	1	–	1	–	–	–	32	–	0.5	3	–	–	–	–	–	–
127-795A-34X-4, 105–106	313.45	0	60	40	27	–	1	–	2.5	–	31	–	–	0.5	–	–	–	31	–	–	7	–	–	–	–	–	–
127-795A-34X-6, 101–102	316.41	0	60	40	26	2	1	–	2	–	32	–	–	1	–	–	–	34	–	–	2	–	–	–	–	–	–
127-795A-35X-1, 101–102	318.61	0	60	40	27	–	1.5	–	0.5	–	28	–	–	0.5	–	–	–	34	0.5	1.5	6	–	–	–	0.5	–	–
127-795A-35X-3, 100–101	321.6	0	70	30	27	–	–	–	0.5	–	25	–	–	–	–	–	–	40	–	0.5	7	–	–	–	–	–	–
127-795A-35X-5, 84–85	324.44	0	60	40	16	0.5	–	–	–	–	37	–	–	1	–	–	–	34	0.5	2	8	–	–	–	1	–	–
127-795A-35X-5, 128–129	324.88	10	40	50	16	0.5	–	–	–	–	37	–	–	0.5	–	–	–	35	–	2	8	–	–	–	1	–	–
127-795A-35X-6, 84–85	325.94	0	25	75	24	–	–	–	–	–	69	–	–	–	–	–	–	5	–	–	2	–	–	–	–	–	–
127-795A-35X-6, 136–137	326.46	5	10	85	15	–	–	–	–	–	82	–	–	1	–	–	–	1	–	–	1	–	–	–	–	–	–
127-795A-35X-CC, 14–15	326.74	5	10	85	15	0.5	1	–	3	–	79	–	–	1.5	–	–	–	–	–	–	–	–	–	–	–	–	–
127-795A-36X-1, 12–13	327.32	5	10	85	6	–	–	–	–	–	82	–	–	2	–	10	–	–	–	–	–	–	–	–	–	–	–
127-795A-36X-CC, 36–37	327.78	5	10	85	17	–	–	–	–	–	83	–	–	–	–	–	–	–	–	–	–	–	–	–	–	–	–
127-795A-37X-1, 0–1	336.9	5	10	85	13	1	–	–	–	–	85	–	–	1	–	–	–	–	–	–	–	–	–	–	–	–	–
127-795A-37X-1, 47–48	337.37	5	10	85	13	1	–	–	–	–	85	–	–	1	–	–	–	–	–	–	–	–	–	–	–	–	–
127-795A-37X-1, 101–102	337.91	5	10	85	13	1	–	–	–	–	85	–	–	1	–	–	–	–	–	–	–	–	–	–	–	–	–
127-795A-37X-1, 133–134	338.23	5	5	90	13	–	–	–	0.5	–	86	–	–	0.5	–	–	–	–	–	–	–	–	–	–	–	–	–
127-795A-37X-CC, 35–36	338.68	5	5	90	12	–	–	–	–	–	86	–	–	2	–	–	–	–	–	–	–	–	–	–	–	–	–
127-795A-38X-CC, 1–2	346.61	0	10	90	9	–	–	–	–	–	90	–	–	1	–	–	–	–	–	–	–	–	–	–	–	–	–
127-795A-39X-CC, 0–1	356.2	0	5	95	5	–	–	–	–	–	92	–	–	–	–	3	–	–	–	–	–	–	–	–	–	–	–
127-795B-1R-1, 18–19	365.38	0	5	95	4	–	–	–	–	–	95	–	–	0.5	–	–	–	–	–	–	–	–	–	–	0.5	–	–
127-795B-6R-1, 80–81	414.6	0	5	95	7	0.5	0.5	–	–	–	90	–	0.5	0.5	–	–	–	0.5	–	–	0.5	–	–	–	–	–	–
127-795B-11R-3, 112–113	465.82	0	5	95	3	–	–	–	1	–	95	–	–	1	–	–	–	–	–	–	–	–	–	–	–	–	–

Appendix V (Chapter 5)



V.1. Additional SEM photomicrographs of sediments from the opal-CT interval in Site 794. A) Opal-CT-cemented clayey facies with framboid distribution of pyrite (Sample 127-794A-32X-2, 5–6 cm, at 295.05 mbsf); B) Aggregates of opal-CT lepispheres (Sample 127-794A-33X-1, 0–1 cm, at 303.3 mbsf); C) Void-filling opal-CT (Sample 127-794A-33X-1, 0–1 cm, at 303.3 mbsf); D) Dense siliceous clay (Sample 127-794A-34X-1, 40–41 cm, at 313 mbsf); E) A radiolarian skeleton filled with pyrite crystals in a clayey sediment (Sample 127-794A-35X-4, 130–131 cm, at 328 mbsf); F) Opal-CT claystone (Sample 127-794A-36X-2, 55–56 cm, at 333.95 mbsf).



V.2. Additional SEM photomicrographs of sediments from the opal-CT interval in Site 795. A) Siliceous silty claystone with remnants of a deteriorated diatom (upper centre) (Sample 127-795A-37X-1, 47–48 cm, at 337.37 mbsf); B) Opal-CT lepispheres (Sample 127-795A-37X-1, 133–134 cm, at 338.23 mbsf); C) Opal-CT siliceous claystone (Sample 127-795A-38X-CC, 1–2 cm, at 346.61 mbsf); D) Dense claystone (Sample 127-795A-39X-CC, 0–1 cm, at 356.2 mbsf); E) Opal-CT silty siliceous claystone with minor dolomite revealing signs of leaching (fine rounded grains) (Sample 127-795B-1R-1, 18–19 cm, at 365.38 mbsf); F) Siliceous claystone with signs of leaching (Sample 127-795B-6R-1, 80–81, at 414.6 mbsf).

Appendix VI (Chapter 7)

VI.1. Statistics related to the $TZ_{A/CT}$ thickness values presented in Table 7.1 in Chapter 7.

Statistical parameters	Clay-dominated sites	Carbonate-dominated sites	All sites
Count	28	23	51
Sum	635	520	1155
Minimum	10	10	10
Maximum	40	40	40
Range	30	30	30
Average	22.68	22.61	22.65
Averagea	22.68	22.61	22.65
Average deviation	7.7	8.6	8.11
Median	20	20	20
Mode	15	15	15
Standard deviation	9.41	9.64	9.42
Population standard deviation	9.24	9.42	9.32
Variance	88.6	92.88	88.71
Population variance	85.43	88.85	86.97
Kurtosis	-0.54	-1.4	-0.96
Skewness	0.71	0.3	0.5

VI.2. Statistics related to the $TZ_{A/CT}$ temperature values presented in Table 7.1 in Chapter 7.

Statistical parameters	Clay-dominated sites	Carbonate-dominated sites	All sites
Count	31	16	47
Sum	900.6	270.3	1170.9
Minimum	4.8	2	2
Maximum	60	27	60
Range	55.2	25	58
Average	29.05	16.89	24.91
Averagea	29.05	16.89	24.91
Average deviation	12.49	7.27	11.53
Median	30.9	17.7	23.4
Mode	11	27	27
Standard deviation	14.95	8.59	14.28
Population standard deviation	14.71	8.32	14.12
Variance	223.58	73.85	203.81
Population variance	216.37	69.24	199.47
Kurtosis	-0.78	-1.12	-0.45
Skewness	0.03	-0.44	0.39